

~~X71-73654~~
~~71-73654~~
~~X71-73654~~
N72-14670

R-678

GUIDANCE AND NAVIGATION REQUIREMENTS
FOR UNMANNED FLYBY AND SWINGBY
MISSIONS TO THE OUTER PLANETS

VOLUME II Impulsive High Thrust Missions

MAY 1969

CABLE FILE
COPY

CHARLES STARK DRAPER
LABORATORY

MASSACHUSETTS INSTITUTE OF TECHNOLOGY

CAMBRIDGE, MASSACHUSETTS, 02139

GUIDANCE AND NAVIGATION REQUIREMENTS

FOR UNMANNED FLYBY AND SWINGBY

MISSIONS TO THE OUTER PLANETS

(Final Technical Report on Phase A of Contract NAS-2-5043)

VOLUME II IMPULSIVE HIGH THRUST MISSIONS

MAY 1969

CHARLES STARK DRAPER LABORATORY
MASSACHUSETTS INSTITUTE OF TECHNOLOGY
CAMBRIDGE, MASSACHUSETTS

Approved: Donald C Fraser Date: 19 October 1970

Dr. Donald C. Fraser, Program Manager

Approved: David G Hoag Date: 26 Oct 70

David G. Hoag, Associate Director
Charles Stark Draper Laboratory

Approved: Ralph R Ragan Date: 26 Oct 70

Ralph R. Ragan, Deputy Director
Charles Stark Draper Laboratory

ACKNOWLEDGEMENT

This report was prepared under DSR Project 55-32700, sponsored by the Ames Research Center, National Aeronautics and Space Administration through Contract NAS 2-5043.

The following are the contributors to this Phase B technical report:

James H. Flanders
Donald C. Fraser
Harvey L. Malchow
Glen Ogletree
Patricia C. Pollock
Mark A. Smith
Richard Tomplins
Michael Venturino
M. Edward Womble

The publication of this report does not constitute approval by the National Aeronautics and Space Administration of the findings or the conclusions contained therein. It is published only for the exchange and stimulation of ideas.

ABSTRACT

This is the impulsive, high thrust missions portion of a study on guidance and navigation requirements for unmanned flyby and swingby missions to the outer planets. The objective of this study is to define the proper balance between groundbased navigational capability, using the deep space network (DSN) alone, and an onboard navigational capability with and without supplemental use of DSN tracking, for unmanned missions to the outer planets of the solar system.

A general guidance and navigation requirements program is used to survey parametrically the characteristics associated with three types of navigation systems.

1. Totally onboard.
2. Totally Earth-based.
3. A combination of these two.

This is done by using estimated ephemeris and navigation error data and applying it to three outer planet missions which use impulsive, midcourse velocity corrections:

1. A 1973 low energy Jupiter flyby
2. A 1977 Saturn flyby using a Jupiter swingby.
3. A 1977 Grand Tour.

Selected concepts for onboard navigation capability are used to generate relationships between desired mission performance and onboard navigation subsystem power, weight, and volume requirements. In addition, requirements are defined for the attitude maneuvers, attitude hold, and navigation requirements.

The study results, presented both graphically and in tabular form, indicate predicted DSN performance for the 1970's to be of such quality that onboard navigational capability does not make important reductions in state vector uncertainty for interplanetary mission phases. These are defined to be those phases of the mission where the spacecraft is outside of one Laplacian sphere of influence of any planet. Furthermore, using an onboard navigation system together with Earth based tracking does not give significant reduction of errors inside the planetary spheres of influence until Saturn is reached on an outer planet mission. From this point and beyond, however, substantial reduction of navigational errors and midcourse fuel requirements are obtainable inside the planetary spheres of influence with the addition of a sufficiently accurate onboard navigation function.

TABLE OF CONTENTS

CHAPTER	PAGE
I. STATEMENT OF THE PROBLEM	1
A General	1
B Missions	2
C Guidance Sensitivities	8
D Navigation	15
E Guidance	15
F Subsystem Weight, Volume and Power	16
II. MODEL FOR THE MISSIONS, NAVIGATION TARGETS AND SYSTEMS	19
A Recursive Filtering with Unestimated Biases	19
B Guidance Uncertainty Error Model	21
C Navigation Target Uncertainties	23
1. Planetary Ephemeris Uncertainties	23
2. Planetary Radius Uncertainty	24
3. Planet Mass Uncertainty	27
4. Planetary Horizon Uncertainties	27
5. Satellite Ephemeris and Orbital Radius Uncertainties	30
6. Satellite Radii	34
D Combined Navigation Sighting Error Models	34
E Organization of the Trade-off Computation Procedure	37
F Measurement Schedule Optimization	46
III. ONBOARD NAVIGATION SYSTEM CONCEPTS	49
A Introduction	49
B A Matrix of Possibilities	50
C Sensor Design	56

CHAPTER	PAGE
III. D Matrix of Attitude Control Requirements	57
1. General	57
2. Body-Fixed Sensor	62
3. Single Degree of Freedom Sequential Sensor	62
4. Three Degree of Freedom Sequential Type Instrument	65
5. Single Degree of Freedom Sextant Sensor	67
6. Four Degree of Freedom Sextant Type of Instrument	69
7. Review	69
IV. SYSTEM REQUIREMENTS FOR THE 1973 JUPITER FLYBY	73
V. SYSTEM REQUIREMENTS FOR THE 1977 JUPITER SWINGBY TO SATURN	199
VI. SYSTEM REQUIREMENTS FOR THE 1977 GRAND TOUR	115
A Key Simulation Results	115
B Onboard System Requirements	149
VII. CONCLUSIONS AND RECOMMENDATIONS	165
A Conclusions	165
1. 1973 Jupiter Flyby	165
2. 1977 Jupiter Swingby to Saturn	165
3. 1977 Grand Tour	166
B Recommendations	167
1. Navigation	167
2. Guidance	168
3. Systems	169
A INTERPLANETARY TRAJECTORY GEOMETRIES	171
B PLANETARY PASSAGE TRAJECTORY GEOMETRIES	215

C	GUIDANCE ERROR SENSITIVITIES	307
D	ASPECT PROGRAM PLOTS	333
E	DERIVATION OF THE FILTER ALGORITHMS	345
	A Recursive Filtering with Unestimated Biases	345
	B Coordinate Definitions	361
	C The Measurement Partial and Data Compression	366
F	A COMPARISON OF FILTERING TECHNIQUES	379
G	SENSOR DESIGN CHARACTERISTICS	385
	G1 Navigation Sensor Physical Characteristics	385
	1. Weight	385
	2. Volume	387
	3. Power	387
	G2 Telescope Design	388
	1. Mechanical Features	388
	2. Aperture Area	388
	3. Planet Limb Sensor Slit Size and Shape	391
	4. Detector Selection	396
	G3 Navigation Sensor Accuracy	397
	1. Introduction	398
	2. Visible Horizon Locator Selection	398
	3. Visible Planet Limb Accuracy	404
	4. Visible Scan Rates	408
	5. Infrared Assumptions	408
	6. I. R. Horizon Locator Selection	406
	7. Infrared Accuracy	413
	8. Infrared Scan Rates	418
	9. Further Investigations - I. R. and Visible Accuracy	418
	10. Star Sensing Accuracy	423
	11. Angle Resolver Accuracy	423
H	OPTIMIZATION OF THE ONBOARD MEASUREMENT SCHEDULE	427
	REFERENCES	433

Page intentionally left blank

INTRODUCTION

There now exists, within both the National Aeronautics and Space Administration and the international scientific community in general, an increasing interest in the outer planets of the solar system. These constitute such a different class of bodies and physical phenomena that they create scientific questions of a general nature in addition to those questions specifically oriented towards the nature and origin of the solar system. Consideration of outer solar system planet missions is also timely because during the 1976 - 1979 period the relative positions of the outer planets will permit a low-energy flyby of Jupiter, Saturn, Uranus, and Neptune in one, long mission, the so-called Grand Tour.

The study reported on in this Volume represents part of a task funded by the NASA under contract NAS-2-5043 and directed by the Mission Analysis Division of the Office of Advanced Research and Technology. The study was divided into two phases. Phase A, reported on in this volume, studies the requirements placed on guidance and navigation by missions in which the post-transplanetary injection trajectory corrections are exclusively by means of short-duration, impulsive ΔV 's. Phase B, reported on in Volume III, studies the same requirements problem for planetary flyby missions in which the spacecraft uses continuous, low-thrust propulsion for the interplanetary mission phases.

With regard to the Phase A work on impulsive, high-thrust missions, the following objectives were set forth by the NASA's OART Mission Analysis Division:

1. Determine the characteristics associated with (a) totally onboard, (b) totally Earth-based, and (c) a combination of Earth-based and onboard navigation concepts.
2. Determine the associated navigation and guidance subsystems weight, volume, and power estimates for representative navigation and guidance subsystem concepts applied to mission objectives.

3. Determine the accuracy requirements placed upon the midcourse propulsion and attitude control subsystems by each of the combinations above.
4. Perform tradeoff analyses which compare on a total guidance and navigation subsystem basis, the three navigation concepts for each nominal mission, considering both the heliocentric and near-planet portions of the missions.

Volume II begins with a statement of the problem in Chapter I. There follows in Chapter II an extensive description of the way the various elements of the mission, navigation targets and systems were modeled. This includes descriptions of the overall analytical program, and how it was used, the error models associated with DSN, solar system body ephemerides, phenomena for navigation, and infrared and visible frequency range navigation data. Chapter III describes the navigation system concepts which were used in this study as a conceptual means for bridging the gap between onboard navigation requirements and the resulting penalties in weight, power, and volume. Chapters IV, V, and VI set forth, for each of three outer planet missions, the analytical program results and the resulting system requirements and tradeoff results. In Chapter VII are to be found the conclusions and recommendations for this study. Appendices A and B present details of the trajectories used, Appendix C gives the guidance error sensitivities for the three missions studied, and Appendix D illustrates typical navigation sighting geometry. In Appendix E, the filter equations are derived. Appendix F presents a comparison of filtering techniques. The design characteristics of the several onboard navigation sensors are discussed in Appendix G. Finally, the method used for optimization of the overall onboard measurement schedule is detailed in Appendix H.

CHAPTER I

STATEMENT OF THE PROBLEM

A. General

The assessment of guidance and navigation requirements for unmanned missions to the outer planets has been undertaken in this study to provide general guidelines for mission planners.

The unique features of the guidance and navigation problem for these missions arise out of general characteristics which are listed below:

- a) Given the restraints of reasonable times of flight, desired scientific objectives and payloads, and present booster limitations, it is of interest to consider swingby mission designs where the kinetic energy gained in one planetary passage is used to achieve a transition trajectory to the next planet.
- b) Precision is needed in the swingby mission trajectories to avoid excessive post-encounter corrections in the trajectory to the next planet.
- c) The long durations of interplanetary trajectories give small injection velocity errors opportunity to propagate into large terminal position errors.
- d) The missions are characterized by long flight times, which create unparalleled challenges in reliability and survivability.
- e) Communication to and from the spacecraft involve communication distances and round trip signal transmission times which are beyond present operational experience.

- f) Lack of knowledge of the position of the outer planets in a helio-centric coordinate system, i. e., ephemeris uncertainty, is great enough to limit the ability of the Deep Space Network (DSN) to determine, unaided by navigational sighting data from onboard sensors, the location of the spacecraft with respect to target planets.
- g) Concurrently, lack of knowledge about the target planets themselves with respect to radius, shape, physical composition, mass, atmospheric limb definition, etc. raise fundamental questions about suitable instruments for onboard navigation.

B. Missions

The study of impulsive-correction type mission requirements was based upon three nominal missions, the trajectory data for which was supplied by the NASA OART/MAD. The first mission is a 1973 Jupiter flyby. Basic mission trajectory characteristics are described in Table I-1, and in Figure I.1. The planetary passage itself occurs at a distance of two (2) Jovian radii and is described in Table I-2. The mission objectives here are to achieve an encounter passage along a major diameter or great circle as seen from earth in order to perform an occultation experiment.

The second mission examined in this study is a 1977 Jupiter swingby to Saturn. Basic characteristics of this mission are listed in Table I-3, and depicted in Figure I. 2. Mission performance requirements involve minimizing trajectory errors at the Jovian swingby in order to reduce the post-Jovian-encounter corrections necessary to achieve the desired passage of Saturn. The Saturn passage itself is targeted for three (3) radii. Details of this passage are shown in Table I-4. Again, the parameters of interest at this encounter are the deviation of the occultation track from a major diametral line and the uncertainty in the periapsis radius which is achieved.

The final mission chosen for this study is a 1977 Grand Tour involving successive swingbys of Jupiter, Saturn, and Uranus, with Neptune being the final target. Table I-5 describes general trajectory characteristics,

TABLE I-1

Basic Trajectory Data for the
1973 Low Energy Jupiter Flyby

Launch Date	27 April 1973
Arrival Date	6 July 1975
Flight Time (days)	800
Hyperbolic Excess Velocity at Earth (km/sec)	9.85
Eccentricity	0.673

TABLE I-2

Basic Trajectory Data for Jupiter Passage
on 1973 Low Energy Jupiter Flyby

Time Spent within Sphere of Influence (days)	148.2
Periplanet Radius (planet radii)	2.0
v_{∞} (km/sec)	6.31
Turn Angle	146.3°
Time Probe not Visible from Earth (hours)	1.39

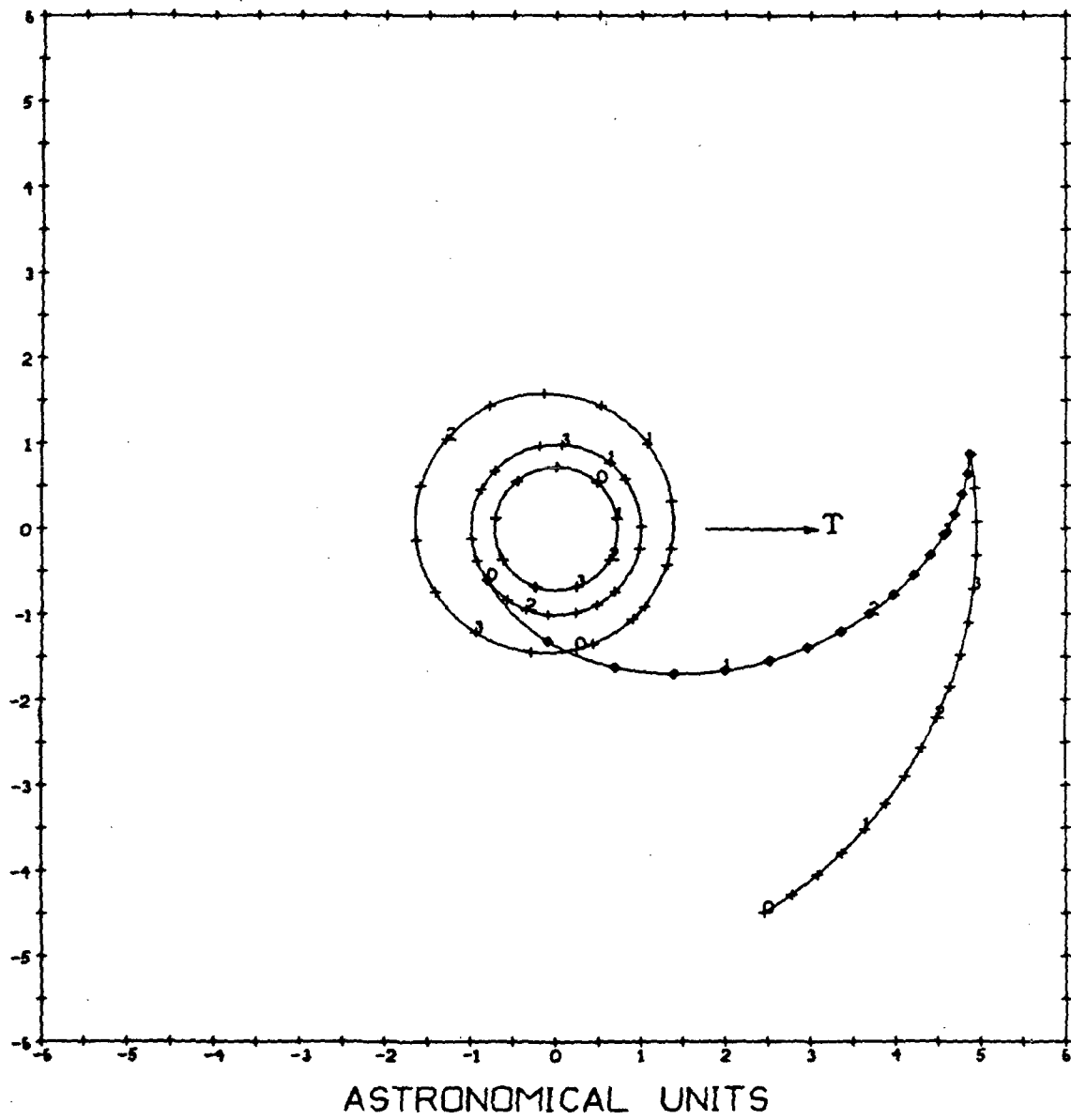


Fig. I.1 Trajectory Diagram for Low Energy Jupiter Flyby

TABLE I-3

Basic Trajectory Data for the 1977 Jupiter
Flyby to Saturn

Earth-Jupiter Leg

Launch Date	3 September 1977
Arrival Date	24 April 1979
Flight Time (days)	567
Hyperbolic Excess Velocity at Earth (km/sec)	10.1
Eccentricity	0.786

Jupiter Passage

Periplanet Radius (planet radii)	5.05
Time within sphere of influence (days)	99.5
Time probe not visible from Earth (hrs)	1.76

Jupiter-Saturn Leg

Departure Date	24 April 1979
Arrival Date	29 December 1980
Flight Time (days)	645.6
Eccentricity	2.10

TABLE I-4

Basic Trajectory Data for Saturn Flyby on the
Jupiter Swingby to Saturn

Time Spent within Sphere of Influence (days)	85.6
Periplanet Radius (planet radii)	3.0
v_{∞} (km/sec)	14.5
Turn Angle	59.718
Time Probe not Visible from Earth (hours)	1.8

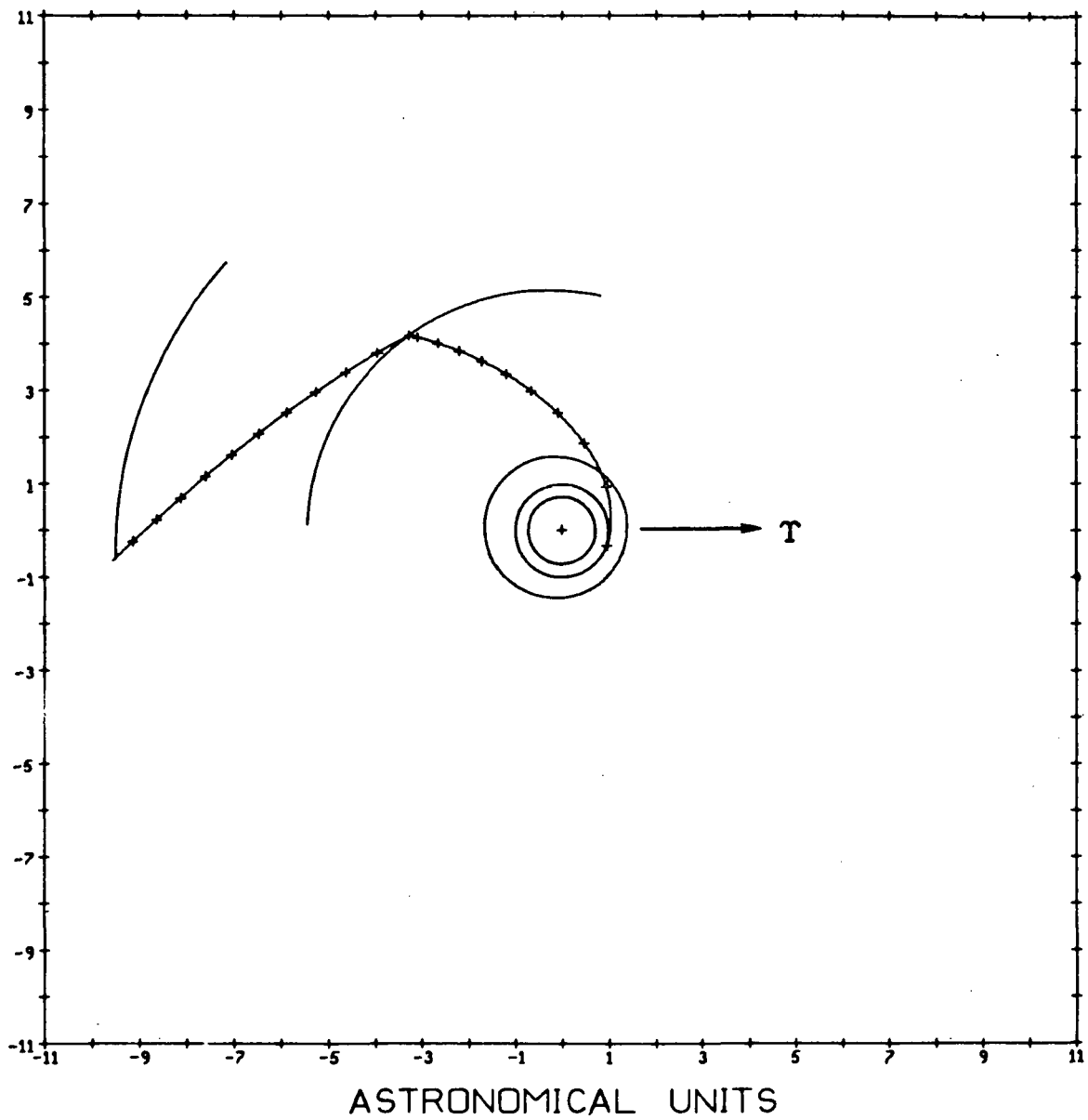


Fig. I.2 Trajectory Diagram for Jupiter Flyby to Saturn

TABLE I-5

Basic Trajectory Data for the 1977 Grand Tour

Earth-Jupiter Leg

Launch Date	5 September 1977
Arrival Date	23 January 1979
Flight Time (days)	504.6
Hyperbolic Excess Velocity at Earth (km/sec)	10.8
Eccentricity	0.844

Jupiter Passage

Periplanet Radius (planet radii)	3.5
Time within Sphere of Influence (days)	84.8
Time Probe Not Visible from Earth (hrs)	1.68

Jupiter-Saturn Leg

Flight Time (days)	580.4
Saturn Arrival Date	25 August 1980
Eccentricity	2.72

Saturn Passage

Periplanet Radius (planet radii)	1.06
Time within Sphere of Influence (days)	73.4
Time Probe not Visible from Earth (hrs)	1.02

Saturn-Uranus Leg

Flight Time (days)	1218.4
Uranus Arrival Date	26 December 1983
Eccentricity	6.52

while Figure I. 3 depicts the overall mission geometry. The mission specifications on each swingby of the Grand Tour are again the minimization of the position and velocity vector uncertainties so as to achieve the best fit to the reference trajectory to the next planet. Encounter at Neptune involves a planned passage at 2 radii (See Table I-6) and again the diametral passage and periapsis altitude are the relevant mission success parameters.

Additional information about the geometrical properties of all three missions is given in Appendices A and B. The characteristics summarized in these appendices are of prime importance to the scheduling of onboard navigation measurements.

C. Guidance Sensitivities

Mention has been made in the above paragraphs of the sensitivity of arrival state vector uncertainties to those uncertainties prevailing at the previous planetary departure. A tabular presentation of these uncertainties can be helpful in gaining a quantitative understanding of the trajectory sensitivities involved in these three missions. Such data has been assembled and is presented in Tables I-7, I-8, and I-9. In addition, more detailed sensitivity data is assembled in Appendix C.

Tables I-7, I-8, and I-9 give the magnitude of the position and velocity errors which would ensue at the arrival planet as a result of unit position and velocity errors in each coordinate direction at the previous planet. All interplanetary mission legs are described. The X coordinate direction in these tables is along the heliocentric departure velocity vector at the previous planet; the z component is in the direction of the orbital angular momentum of the interplanetary leg; and the y component is chosen to complete a right handed orthogonal coordinate system.

As an example of interpreting this data, Table I-7 shows that a one kilometer position error in the direction of the heliocentric velocity vector at departure from Earth results in an 11.21 km position error and a 17.67 m/sec velocity error upon arrival at Jupiter. Similarly,

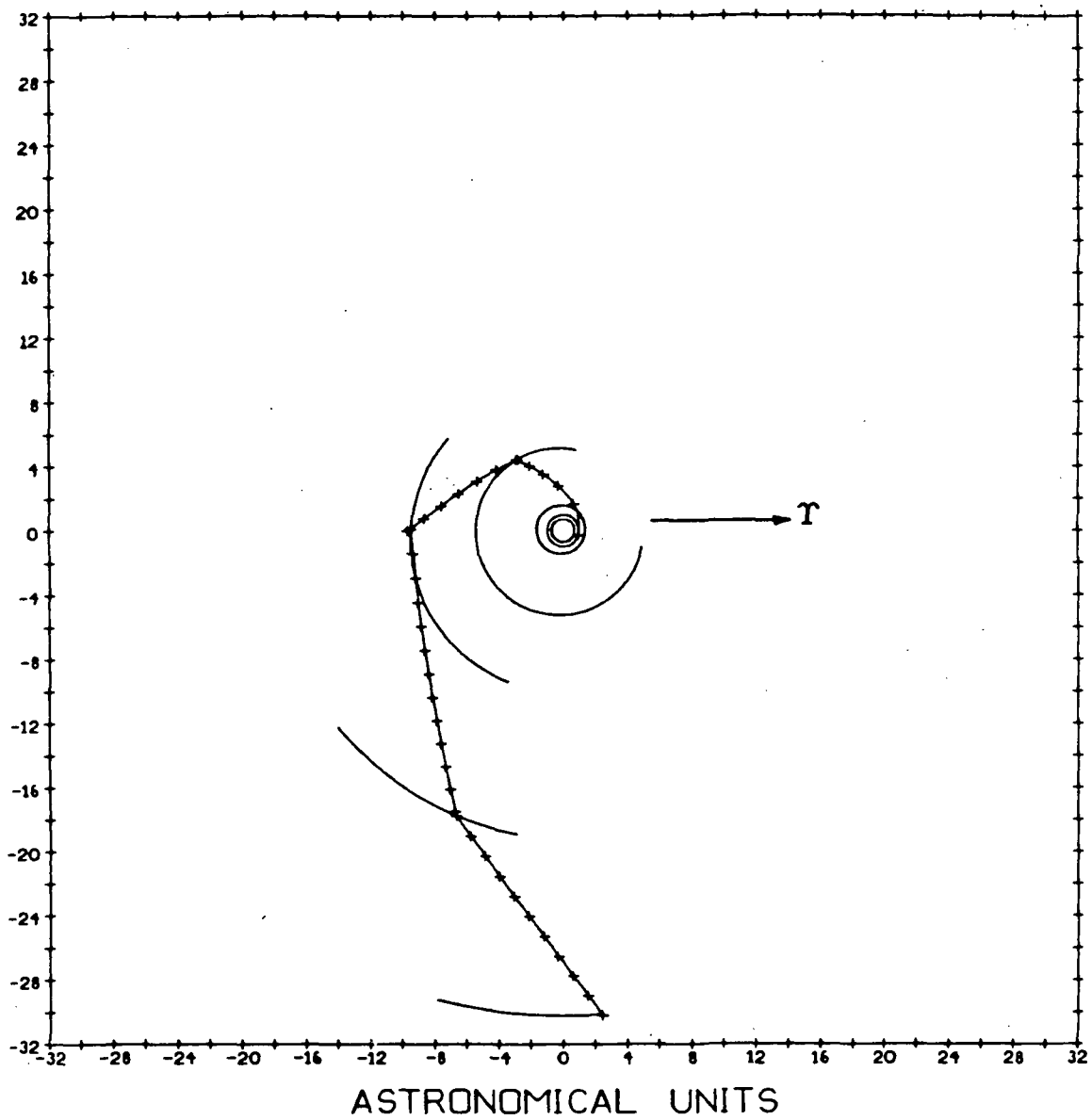


Fig. I.3 Trajectory Diagram for 1977 Grand Tour

TABLE I-6

Basic Trajectory Data for the Neptune Flyby on
the 1977 Grand Tour

Time Spent within Sphere of Influence (days)	83.4
Periplanet Radius (planet radii)	2.0
\underline{v}_{∞} (km/sec)	24.1
Turn Angle	24.35°
Time Probe not Visible from Earth (hrs)	0.68

TABLE I-7

Interplanetary Guidance Error Sensitivity

Ratios for the 1973 Jupiter Flyby

<u>INITIAL</u> <u>UNIT</u> <u>PERTURBATIONS</u>	<u>FINAL</u> <u>RSS POSITION</u> <u>DEVIATION (km)</u>	<u>FINAL</u> <u>RSS VELOCITY</u> <u>DEVIATION (m/sec)</u>
Δr_x (km)	11.21	17.67
Δr_y (km)	36.99	9.750
Δr_z (km)	4.700	1.142
ΔV_x (m/sec)	7248	6.426
ΔV_y (m/sec)	13,180	0.4632
ΔV_z (m/sec)	454.1	0.1590

TABLE I-8

Interplanetary Guidance Error Sensitivity Ratios for the

1977 Jupiter Swingby to Saturn

<u>UNIT</u> <u>PERTURBATIONS</u>	<u>EARTH-JUPITER</u>		<u>JUPITER-SATURN</u>	
	RSS Position Deviation (km)	RSS Velocity Deviation (m/sec)	RSS Position Deviation (km)	RSS Velocity Deviation (m/sec)
Δr_x (km)	6.242	3.899	1.003	0.1324
Δr_y (km)	21.02	1.353	1.382	0.2544
Δr_z (km)	4.418	2.523	0.7423	0.2205
ΔV_x (m/sec)	3,637	4.040	46.214	1.117
ΔV_y (m/sec)	10,480	0.6667	24,120	1.035
ΔV_z (m/sec)	72.72	0.0318	2,081	0.8567

TABLE I-9A

Interplanetary Guidance Error Sensitivity Ratios for the
First Two Legs of the 1977 Grand Tour

<u>UNIT</u> <u>PERTURBATIONS</u>	<u>EARTH-JUPITER</u>		<u>JUPITER-SATURN</u>	
	RSS Position Deviation (km)	RSS Velocity Deviation (m/sec)	RSS Position Deviation (km)	RSS Velocity Deviation (m/sec)
Δr_x (km)	5.785	2.846	0.9747	0.1179
Δr_y (km)	17.31	0.8763	1.326	0.2542
Δr_z (km)	4.034	2.932	0.7835	0.2071
ΔV_x (m/sec)	3686	3.579	42,970	1.084
ΔV_y (m/sec)	11,973	0.7425	19,957	1.073
ΔV_z (m/sec)	52.53	0.03836	1892	0.8795

TABLE I-9B

Interplanetary Guidance Error Sensitivity Ratios for the

Second Two Legs of the 1977 Grand Tour

UNIT PERTURBATIONS	<u>SATURN-URANUS</u>		<u>URANUS-NEPTUNE</u>	
	RSS Position Deviation (km)	RSS Velocity Deviation (m/sec)	RSS Position Deviation (km)	RSS Velocity Deviation (m/sec)
Δr_x (Km)	0.9267	0.0807	1.005	0.0133
Δr_y (km)	1.283	0.006043	1.009	0.0095
Δr_z (Km)	0.8241	0.07782	0.9860	0.0083
ΔV_x (m/sec)	6,313	1.041	49,560	1.007
ΔV_y (m/sec)	100,497	1.066	69,540	1.002
ΔV_z (m/sec)	3,988	0.9121	4,712	0.9912

a one meter per second velocity error in the plane of motion perpendicular to the reference departure velocity results in a 13,180 km position error and a .46 m/sec velocity error upon arrival at Jupiter.

The primary purpose of using these three tables here as a synopsis of the data given in Appendix C is to emphasize the enormous sensitivity of position errors at arrival to velocity errors upon departure. These are largest for the in plane components of departure velocity error and range from a minimum of 3637 km/m/sec for the along velocity component on the Earth-Jupiter leg of the 1977 Jupiter swingby to 100,497 km/m/sec for the cross velocity component on the Saturn Uranus leg of the 1977 Grand Tour. These guidance sensitivities, which are directly attributable to the long mission leg time, place primary importance on the ability to detect and precisely correct any trajectory errors which occur.

D. Navigation

Within this background of characteristics, the present study was structured to compare the navigation characteristics of three specific missions using impulsive, midcourse ΔV 's, and a space-stabilized spacecraft for 1) DSN-only navigation, 2) onboard-only navigation, and 3) a combination of the two. In the navigation area, the developers of outer planet mission plans need to be given quantitative data about the relative efficiency of these three approaches in terms of measuring the residual trajectory errors following transplanetary injection from earth, the build-up of deviations from the nominal or reference trajectory, the effect of midcourse propulsion burns, etc.

E. Guidance

The navigation problem involves the ability to determine the spacecraft state vector first with respect to a heliocentric coordinate system and then with respect to the swingby or target planet. The guidance problem involves system ability to eliminate a portion of the state vector error buildup as determined by the navigation process, whether DSN, onboard, or a combination of the two. In general terms, there must be balance

between navigation performance and guidance performance. It is not worthwhile to install a guidance system capable of precise ΔV adjustments, if the basic navigation capability is highly imprecise. Conversely, an accurate design for spacecraft navigation should be accompanied by a guidance scheme capable of reducing substantially and accurately the estimated state vector error. The guidance problem needs further definition in terms of actual requirements. The present study seeks to give parametric answers to this question, by varying the parameters of a strapdown guidance system as it executes velocity corrections in selected mission situations.

F. Subsystem Weight, Volume, and Power

Of further interest to mission planners, is the penalty that might have to be paid for onboard navigation capability or for enhancement of guidance capability. The outer planet missions are in a formative stage and there is a very real need for some means by which the mission benefits of onboard capability can be traded off against penalties to be incurred by the spacecraft and its other subsystems in weight, volume, and power.

For the present study, it was decided to assemble and describe candidate navigation instrument subsystems. It is important to realize that these candidates are concepts and not designs, the latter being outside the scope of the present contract. However, the candidate concepts have been used to establish estimates of power, weight, and volume in addition to basic figures of accuracy, utility, and flexibility which accompany these concepts. By this technique, it is thought that useful relationships have been created between desired onboard capability, and the accompanying penalties. These candidate concepts are discussed in Chapter III. Their application to the study missions is described in Chapters IV, V and VI.

It is significant to note here that no assessment has been specifically promised in the areas of reliability and survivability. Yet this is an area where all concerned with outer planet missions have identified a major challenge due to the requirement for deepspace operation over a period of years. Reliability and survivability considerations will have to be the central core of the next state of the onboard instrument evaluation. The

present contract was not directed toward this problem, and it is only noted in passing. Beyond the problem of achieving reliability and survivability lies the challenge of proving these qualities have been achieved in a test time span that is shorter than the nominal missions.

The outer planet mission guidance and navigation requirements problem has been described in terms of navigation, guidance, and subsystem parameter evaluation. In the next Chapter there follows a description of the analytical model around which the present study was built.

Page intentionally left blank

CHAPTER II

MODEL FOR THE MISSION, NAVIGATION TARGETS AND SYSTEMS

A detailed statistical error analysis of the outer planet missions under study was performed in order to determine the tradeoff between navigation via the use of the ground tracking system and a supplemental onboard navigation system. The purpose of this chapter is to define the various error models used to describe the physical phenomena which are important to this tradeoff study. In addition, a filter theory is summarized which makes it possible to treat the entire navigation process recursively. This filter theory is developed in detail in Appendix E. Together with actual mission parameters such as trajectory data and sighting and tracking schedules, these form the main ingredients for the mission guidance-navigation requirements simulation.

The entire requirements study is performed statistically by considering only the statistics of first order deviations from a reference trajectory; thus all the convenient and powerful techniques of modern linear filter theory can be employed in the analysis. By making the approximation that all random processes are Gauss-Markov processes, only second order statistics are necessary and it is possible to obtain recursion formulas for the filter which are extremely convenient for use on a digital computer. The reference trajectory used throughout is the nominal mission trajectory; measurements are linearized about nominal values which can be computed using the mission reference trajectory.

A. Recursive Filtering with Unestimated Biases

There are several ways in which a bias is important to the tradeoff study under discussion here. First, the fact that the masses of the outer planets are imperfectly known leads to a situation where the gravitational parameter of the attracting body may be in error by a constant amount. This bias affects the trajectory dynamics.

Second, a key parameter in the error model of the deep space network is knowledge of the locations of the tracking stations. In reality these stations may be offset from the locations used in the model by a constant amount. Thus two additional biases are introduced into the problem - the unknown offset of the station from the Earth's spin axis and the unknown offset in its longitude.

The usual artifice to avoid biases in a linear filtering problem is to adjoin the biases to the state and estimate them. In this way all the assumptions made in deriving the filter equations can be met - in particular the assumption that the noises have white distributions in time. This was not done in this instance primarily because if no method is included to put a lower bound on the estimation errors (e. g. driving these state variables with process noise) the estimation error continuously decreases. The point is soon reached where in a practical sense these biases are perfectly known and they should be dropped from the problem. In reality this would not occur - there are other physical phenomena such as pole wander of the Earth's spin axis and higher order terms in the expansion of the planetary potential functions which prevent this. These limiting phenomena are currently not well modeled. Therefore, to introduce them into the problem might give less realistic results than "considering"* but not estimating the biases. A filter theory for considering these biases in an optimal manner is derived in detail in Appendix E.

The biases mentioned above are, by definition, correlated in time. This causes all quantities which are driven by the biases (the estimation error, for example) to be correlated in time in a more complex way than is the result for the situation in which all the noises have white time distributions. The development of the filter equations in Appendix E consists of identifying all the cross correlation terms which must be included and evaluating recursion formulas which can be used to adjust them for each of the four prime steps of the simulation:

1. Extrapolation of statistics from one time to another.
2. Adjustment of statistics to account for a midcourse velocity correction.

* This term is borrowed from Reference 1. It is used here in the same sense but different technical detail than in the reference. An explanation is provided in Appendix F.

3. Adjustment of statistics to account for incorporation of an onboard measurement.
4. Adjustment of statistics to account for incorporation of a DSN measurement.

The recursion formulas for each of these cases are derived by using the relationships by which three basic quantities propagate through each of the four steps above:

1. The actual deviation of the spacecraft from the reference trajectory, ($\delta \underline{x}$).
2. The estimate of the deviation of the spacecraft from the reference trajectory, ($\delta \hat{\underline{x}}$).
3. The error in the estimate of the deviation of the spacecraft from the reference trajectory, (\underline{e}).

These difference equations are used to form the necessary correlations and by using the known statistics of the white noises and biases the desired recursion formulas are obtained.

The development of these recursive filter equations is followed in Appendix E by definitions of the state and coordinate systems employed in each mission phase. These coordinates are then used in a derivation of the equations which are necessary to process an Earth based doppler radar measurement according to a simple model of the information content of a DSN measurement which is due to Hamilton and Melbourne². The required measurement partial derivatives are derived directly from these equations and then an approximate method of compressing each pass of data is developed by assuming constant measurement geometry over the pass. The complete set of equations which result from this analysis is given in Appendix E.

B. Guidance Uncertainty Error Model

For the purposes of this study it is assumed that over an ensemble of missions, individual midcourse velocity corrections have equal probability of being in any direction. By making the additional assumption that the

noise involved in implementing an individual velocity correction is spherically distributed one has the result that the noise associated with a midcourse correction has a uniform distribution over the velocity space. Consequently, the guidance error sources which are of first order importance to the statistical analysis of those phases of the mission where the assumption of impulsive velocity corrections is reasonable, are those which affect the length of the velocity vector to first order. Accordingly, reference frame alignment and gyro drift factors were not included in the modelling of the velocity correction implementation. These were eliminated on the assumption that the initial alignment would be accurate enough and time since alignment small enough that the following sources would be the primary contributors to the error in making a midcourse velocity correction.

1. Accelerometer Bias
2. Accelerometer Scale Factor Error
3. Engine Cutoff Uncertainty

Current state of the art in alignment and construction of inertial navigation equipment for space applications supports this simple choice. One should not conclude from this, however, that there is not a need for precise means of reference frame alignment and for low gyro drift. These error sources are important in attitude control requirements and are discussed in Chapter III.

In terms of these parameters the implementation error in making a velocity correction has the following variance.

$$\sigma_{\text{imp}}^2 = \overline{\Delta SF^2} \overline{\Delta V^2} + \overline{a_b^2} \Delta t^2 + \overline{v_{co}^2}$$

where:

$$\sigma_{\text{imp}}^2 = \text{variance of velocity correction implementation errors.}$$

$$\overline{\Delta SF^2} = \text{variance of accelerometer scale factor errors.}$$

$\overline{\Delta V^2}$ = mean squared value of the velocity correction.

a_b^2 = variance of accelerometer bias errors.

Δt = duration of the velocity correction impulse.

$\overline{v_{co}^2}$ = mean squared value of the error attributable to thrust tailoff uncertainties.

Note that although the thrust tailoff uncertainty causes a guidance error it is observable with the accelerometers; hence it need not be added to the covariance matrix of state estimation errors when a velocity correction is made.

The term $\overline{v_{co}^2}$ is approximated by assuming the full thrust of the engine is on for T_{co} seconds longer (or less) than called for. A nominal value for T_{co} of .05 seconds is used.

C: Navigation Target Uncertainties

1. Planetary Ephemeris Uncertainties

During early and midcourse flight, the outer planet ephemeris uncertainties contribute the major portion of the phenomena errors. These errors result from the limiting accuracy to which planetary positions can be measured optically from earth.

Errors in optical measurements depend on a number of factors such as diffraction, atmospheric eddies, temperature discontinuities, wind turbulence, warm air leaving a telescope dome, and convection within the telescope tube. According to Ref. 3, limiting resolution, after taking into account all the error sources, seems to be around 0.1". This value is supported by other sources. For example the U. S. Naval Observatory (Ref. 4) has measured the positions of 64 reference stars with an uncertainty of 0.29", and the position of the asteroid Ceres with

a standard deviation of $\pm 0.17''$ in right ascension, and $\pm 0.11''$ in declination. Ref. 5 lists measurements to within $0.1''$ as a "good estimate" of the limiting stellar position uncertainty for a single measurement. The consensus of these sources is that $0.1''$ is approximately the minimum angular uncertainty occurring in astronomical position measurements. Applying this value (as was recommended in Ref. 7) to the outer planet orbital radii (Ref. 8), one obtains the ephemeris uncertainty values listed in Table II-1 and in Ref. 9.

When the planetary probe moves close enough to a planet to make accurate sightings on the planet limb, the ephemeris errors with respect to the earth will be diminished. This is due to the accurate position determination of the probe with respect to the planet using onboard navigation measurements, which are telemetered back to earth, and the accurate position determination of the probe with respect to earth via the DSN system.

2. Planetary Radius Uncertainty

The outer planet physical properties (especially mean density) lead to models of these planets that are characterized by deep, dense atmospheres which merge gradually into the liquid and solid gaseous phases with increasing depth (Ref. 10). There is no radius in the solid-gas interface sense. Radius values given in the literature represent the altitude of satellite or star occultations, or the apparent visible horizon altitude. But the radii derived by observing different phenomena show systematic differences (Ref. 11), therefore radius values can only be defined in terms of a specific phenomenon and a sensor of specific band-width. The idea of a "cloud top" radius has been expressed in various references, and alluded to in Ref. 12, however cloud height variability (Ref. 13), and possible absence (Ref. 14) make the cloud tops an unstable reference.

For Jupiter, the radius value provided by NASA (Ref. 12) is 71,370 km. This agrees closely with the value of 71,403 km obtained from Rabe's average (Ref. 11), however, the standard deviation of the 19 measurements

TABLE II-1 Planetary Ephemeris Errors

	3 σ values		
	tangent (km)	normal (km)	radial (km)
Jupiter	± 1150	± 1150	± 300
Saturn	± 2400	± 2400	± 600
Uranus	± 4200	± 4200	± 1200
Neptune	± 6600	± 6600	± 1800

made by various researchers (ignoring the "wild" Rabe's value) is 336 km. Even among researchers using the same technique (for example, the Filar micrometer in Ref. 11) the predicted radius values are spread over a range of 0.45" or about 1500 km. These data would seem to indicate that the 3σ uncertainty of 50 km assumed for Jupiter in Reference 12 could be considered optimistic.

Using the conventional diameter measuring techniques, namely, the heliometer, the double-image micrometer, the filar micrometer, and satellite eclipses, it would be expected that the diameter errors would be proportional to the earth-planet range. However, photoelectrically monitored star occultations have recently been used, and this technique promises to reduce radius uncertainties and make the errors range independent. Such a measurement was made on Neptune on 7 April 1968 (Ref. 15). Resultant diameters are given in terms of the fraction of starlight unextinguished. At $1/2$ light the diameter is listed as 50,100 \pm 200 km. In their error analysis it appears that the authors have neglected to include the normal component of the ephemeris error for Neptune. This is equivalent to assuming exact knowledge of the latitude of the point of star penetration into Neptune's atmosphere, and may be the reason that their diameter is 4600 km larger than the older values. This technique is also sensitive to the assumed atmosphere model. For example, the authors state that refraction by Neptune's atmosphere of 0.01" will change the answer by 400 km. Also, the diameter resulting from an occultation will depend on the magnitude and spectral class of the star, and the spectral bandpass of the detector. This implies that the ideal diameter measurement for outer planet probe purposes would be made with a star of the same magnitude and spectral class, and the same detector as one would be expected to use on the actual flight for a star occultation navigation measurement.

An often used onboard navigation measurement is the angle between the planet limb and a star. This measurement is combined with assumed radius values to yield range to planet information. Hence, if there is a radius error it acts as a bias in the range calculation. It is anticipated that this bias can be reduced in the filtering process, but the magnitude and direction of the bias prior to first onboard measurement remains

unknown. Table II-2 lists the estimated planetary radius uncertainties supplied by NASA along with their assumed nominal values.

3. Planet Mass Uncertainty

Estimated values of outer planet masses may differ from the real mass and as a result contribute a bias error to the positional error ellipsoid. The inverse masses and their estimated uncertainties used in the navigation simulation are displayed in Table II-3. These uncertainties lead to position uncertainties at planet passage of about 7 km (at Jupiter) to 130 km (at Neptune). Errors of this size are negligible with respect to the ephemeris errors, and have been consequently ignored in the simulation. An increase in inverse mass error by an order of magnitude would be required to make these errors significant. However, in Ref. 9 one can see that the range of mean values of inverse mass obtained by different measurement techniques is an order of magnitude larger than the estimated uncertainties of Table II-3.

4. Planetary Horizon Uncertainties.

There have been a large number of measurements of Jupiter radiation covering the whole spectrum, and including many absorption line profiles. For Saturn, the numbers of experiments have been considerably less, and for Uranus and Neptune, atmospheric characteristics are poorly known.

Navigation with respect to the outer planets will require sightings on the planet horizon. The uncertainty in the information about the altitude from which a given radiative intensity is emitted will derive from two sources. One is the uncertainty in the atmospheric models as derived from earth-based measurements, the other is the statistical fluctuation in the atmospheric meteorology which occurs even if the nominal atmosphere is well determined.

The altitude of the infrared profile's half-maximum intensity is uncertain because of uncertainty in the percentages of the absorbers methane and ammonia, and uncertainty in the total atmospheric pressure. If there were no atmosphere or absorbers above the cloud tops, the clouds would form a black body infrared surface.

TABLE II-2 Planetary Radius and Radius Uncertainty

	Radius (km)	3 σ Radius Uncert. (km)
Jupiter	71,370	± 50
Saturn	60,500	± 50
Uranus	24,850	± 50
Neptune	22,700	± 250

Table II-3 Planetary Mass Uncertainties

	Mass ⁻¹	3 σ Mass Uncert.
Jupiter	1047.39	± 0.03
Saturn	3497.6	± 0.3
Uranus	22,934	± 6
Neptune	18,889	± 62

On Jupiter, the methane and ammonia absorber percentages are estimated to be 3% and 1% respectively (Ref. 16). The mixing ratios on Jupiter and Saturn are estimated to be constant for H_2/CH_4 (Ref. 17). However, Saturn has a higher percentage of CH_4 . Uranus and Neptune appear to have deep methane atmospheres (Ibid., p. 374), and it has been postulated that H_2/CH_4 is 45 and H_2/H_e is 0.3 for these planets (p. 384). Aerosols in these atmospheres would be at some temperature near the black body equilibrium temperature, and would tend to make the radiant emission from the horizon less spectral. Ref. 17, P. 384, states that at 5900 \AA , aerosols account for one half of the scattering on Uranus and Neptune.

There is not enough radiation emitted in the infrared by the outer planets to allow one to use a small bandwidth detector (for example on the $10\mu - 11\mu$ NH_3 band on Jupiter). Thus the horizon altitude problem is complicated by the requirement to sense radiation which comes from different depths at different wavelengths. Vertical optical depth of the Jupiter atmosphere has been estimated to be 0.66 in the "far infrared" (Ref. 18). A further uncertainty is in the effective radiation temperature of the various parts of the atmospheres. In Ref. 19, an atmospheric temperature of $108^\circ K$ was found for Jupiter, with a cloud top temperature range of $140^\circ - 160^\circ K$. Ref. 20 gives an effective radiating temperature of $145^\circ K$ for Jupiter. Ref. 17, p. 379, lists the cloud top temperature of Jupiter at $165^\circ K$ or $168^\circ K$.

To select maximum and minimum values covering the range of expected infrared altitude uncertainty, the following argument was used. If the optical depths attributed to the absorbers are large enough so that there is essentially complete absorption over the 1μ to 30μ wavelength region, then the atmospheres are opaque, and the uncertainty in the altitude of a particular radiative intensity will depend on the uncertainty in the scale height. Bourne and Code (Ref. 21) observed a star occultation on Jupiter, and found a possible scale height range of 7 km based on an assumed temperature of $86^\circ K$. However, a temperature of $112^\circ K$ has been proposed in Ref. 22, and since scale height is directly proportional to temperature, this could increase the range of scale heights found in Ref. 21 to about 10 km.

Thus a 10 km 1σ uncertainty is representative. If the Jupiter atmosphere is not essentially opaque over the 1μ - 30μ range, then most of the infrared radiation will come from the cloud tops whose altitude has been estimated to vary over a 30 km (3σ) range (Ref. 13). For want of better data, the minimum uncertainty in the Saturn horizon altitude was taken equal to that of Jupiter, namely 10 km, 1σ . For Uranus and Neptune a scale height of 16.3 km has been found (Ref. 4, p. 384), and allowing for roughly a $\pm 50\%$ variation in this value, a rounded-off 20 km, 3σ , value was assumed giving a 1σ value of 6.66 km. To cover the range of uncertainty values, the maximum 1σ 's were chosen to be ten times the minimum values. Both IR and visible horizon altitude uncertainties are listed in Table II-4.

The visible horizon altitude uncertainties depend on uncertainties in cloud albedo and altitude, aerosol characteristics, and the density of Rayleigh scatterers. Geometrical albedos of Jupiter and Saturn are around 0.4 for Jupiter and Saturn in the visible light spectral region. If the clouds are earth-like in their scattering, they have albedos near 0.7. Both planets have been demonstrated to have aerosols (Ref. 4) but the quantity and physical characteristics such as size distribution and index of refraction are essentially unknown. Pressure at the cloud-top level on Jupiter has been determined with a wide range of results. Ref. 18 lists a cloud top value of 2 atmospheres based on CH_4 lines. Ref. 14 gives a value of 8.3 atm. In Ref. 22 the value is 2.3 atm. Ref. 23 gives 11 atmospheres. For the range of scale heights given in Ref. 21, this cloud-top pressure range essentially shifts the half-maximum intensity altitude up and down from 10 km to 20 km. We take the minimal visible horizon altitude to have an uncertainty of 10 km, 1σ accordingly. This value was extended to all the outer planets. The maximum uncertainty for the outer planets was taken to be 10 times minimum, or 100 km 1σ .

5. Satellite Ephemeris and Orbital Radius Uncertainties

The planetary satellites can be used in a number of ways as navigational objects. They can be used together with stars for "near body" type measurements, and they can be used together with the parent planet for range computations.

TABLE II-4 Planetary Horizon Altitude Uncertainty

	$\pm 3\sigma$ Visible (km)	$\pm \sigma$ I. R. (km)
Jupiter	30	30
Saturn	30	30
Uranus	20	20
Neptune	20	20

For "near body" measurements at long ranges the ephemeris errors are the most important phenomenon error source. According to Ref. 6 and 24 the 0.1" optical resolution capability is the limiting factor in position determination for the planetary satellites, therefore, the ephemeris errors are about the same as those listed for the corresponding planets in Table II-1.

For range type measurements the satellite orbital radius is assumed to be known, and the uncertainty in this value contributes to the range uncertainty. The orbital radius uncertainty is obtained from Kepler's law. If one takes:

$$T = 2\pi \frac{a^3}{\mu}$$

where $\mu = GM$, with M the mass of the planet, then

$$\frac{1}{\mu} = \frac{1}{GM} \cdot \frac{M_{\odot}}{M_{\odot}} = \frac{\rho}{GM_{\odot}} = \frac{\rho}{\mu_{\odot}}$$

If units of years and astronomical units are chosen for the calculation then $\mu_{\odot} = (2\pi)^2$. Consequently, for the planetary satellite,

$$T = a^{3/2} \rho^{1/2}.$$

Applying a linear error analysis gives the orbital radius error

$$\delta a = \frac{2}{3} \left[\sqrt{\frac{1}{\rho a}} \delta T - \frac{1}{2} \frac{a}{\rho} \delta \rho \right].$$

The worst value obtains when $\text{sign}(\delta T) = -\text{sgn}(\delta \rho)$. Substituting the values of ρ , a , δT , and $\delta \rho$ supplied by NASA for Triton of Neptune gives $\delta a = 388$ km.

For the navigation analysis, the values derived by this method were used, but to be conservative, they were rounded off to slightly larger values. Orbital radius uncertainties used are shown in Table II-5.

TABLE II-5. Satellite Orbital Radius Uncertainties

Planet	Satellite	1 σ Orb. Rad. Uncert.
Jupiter	Io	150 km
	Europa	
	Ganymede	
	Callisto	
Saturn	Titan	300 km
Uranus	Ariel	250 km
	Umbriel	300 km
	Titania	400 km
	Oberon	500 km
Neptune	Triton	500 km

The uncertainty in the outer radius of Saturn's rings, using the 0.1'' criterion, has been set at 600 km, 1σ .

6. Satellite Radii

Navigation sightings on the planetary satellites will be made on the satellite limb with the same instruments used for planet limb sensing. Since the satellites have non-negligible radii, the radius uncertainties need to be estimated. Statements about the diameters of the satellite are found in various places in the literature. Ref. 25 states that the diameters of the satellites of Saturn cannot be determined to better than the nearest 100 miles (p. 436), and gives micrometer measured results obtained in 1920 to within 0.16'' to 0.2'' (p. 367). In Ref. 26 it is stated that the diameters of Oberon and Triton have been determined only by assuming that their visual albedos are 0.3 and relating the measured brightness to radius.

Some of the satellites have, or may have atmospheres. According to Ref. 4, p. 309, the inner satellites of Jupiter may or may not have atmospheres. The question is still open at this time. They appear to have definite markings, but this does not rule out thin atmospheres. Titan of Saturn definitely has an atmosphere. The four moons of Uranus probably do not have atmospheres because of their small escape velocities. Neptune's Triton has a large escape velocity, and if its temperature has been properly estimated, it probably has an atmosphere.

It has been assumed for this effort that the satellite horizon fluctuations are negligible, and that the radius uncertainties are proportional to satellite size and the 100-mile value of Ref. 26. The assumptions lead to uncertainties in satellite radii as shown in Table II-6.

D. Combined Navigation Sighting Error Models.

The error associated with making each type of measurement is modeled on an appropriate combination of 1) the basic instrument error; including angle measurement deficiencies and out of measurement plane

TABLE II-6. Satellite Radius Uncertainties

Planet	Satellite	Radius Uncert.
Jupiter	Io	80 km
	Europa	75 km
	Ganymede	125 km
	Callisto	118 km
Saturn	Titan	122 km
Uranus	Ariel	60 km
	Umbriel	40 km
	Titania	100 km
	Oberon	80 km
Neptune	Triton	700 km

effects, and 2) the uncertainty involved in defining a planet limb. In this study, the basic instrument error is used parametrically to determine the sensitivity of the mission output quantities to instrument error. On the interplanetary legs (see Table IV-1, for example) a nominal instrument error of 10 seconds of arc in the visible light range is used. Values of 3 seconds and 1 second of arc are used in addition to establish sensitivity relationships. The onboard only and DSN plus onboard cases are then compared to the DSN only values as a basic requirement for this study.

On near planet legs (see Table IV-2 for example) onboard only (10 second accuracy with 60 second infrared) and DSN only cases are compared with a broader range of instrument error combinations. Visible light instrument errors of 10, 3 and 1 seconds of arc are evaluated without an infrared capability. The intent here is to map this type of instrument in comparison to two others:

- a) 10 second accuracy - visible light
60 second accuracy - infrared
and
- b) 60 second accuracy - visible and infrared.

Instrument (a) evaluates the benefit of adding an infrared capability and instrument (b) can be considered to be an all infrared candidate.

Thus, instrument and phenomena errors are in general different for the light and dark sides of a planet. If we let $(\sigma_A)^2$ be the variance associated with the combined instrument and phenomena error on one target planet limb and similarly let $(\sigma_B)^2$ be the variance for the other side, then the basic measurement variances are as follows:

Planet Diameter	$\sigma^2 = (\sigma_A)^2 + (\sigma_B)^2$
Planet - Star	$\sigma^2 = (\sigma_A)^2 (\sigma_B)^2 / [(\sigma_A)^2 + (\sigma_B)^2]$
Star occultation	$\sigma^2 = \text{dark side phenomena uncertainty variance}$
Star Elevation	$\sigma^2 = \sigma_A^2$

(It should be re-emphasized that the basic instrument error cited above includes the combined effects of instrument transducer error, spacecraft motion, cut of plane geometry, and detector uncertainty.)

The first of the combined errors is obtained by assuming the independence of the phenomena from the two sides of the planet. The second follows from minimizing the expectation of a weighted average. Instrument and phenomenon errors are assumed independent, and are combined simply as:

$$(\sigma_A, \text{ OR } \sigma_B)^2 = \sigma (\text{inst})^2 + \sigma(\text{phen})^2.$$

where the phenomena uncertainty used is different depending upon whether or not the target limb is sunlit.

E. Organization of the Trade-off Computation Procedure

The previous sections of this chapter have discussed error models for the various physical phenomena, instrument and system characteristics which are germane to this study. The purpose of this section is to describe the computation procedure in which all these ingredients are combined to perform the tradeoff studies.

Figure II. 1 gives a flow chart of the major elements of the computer program which performs the error analysis. This procedure begins with initial values for all the correlation matrices defined in the first section of this chapter. These could be the end result of a transplanetary injection or the terminal conditions from a previous leg of the same mission. The usual operating mode is to begin with the transplanetary injection errors and proceed through the mission, running successively each interplanetary and near planet leg. Each new leg is started from the terminal conditions of the previous leg.

As can be seen from Fig. II. 1 there is a main computation loop in the program. There are as many cycles through this main computation loop as there are predetermined "decision points" in the leg of the mission

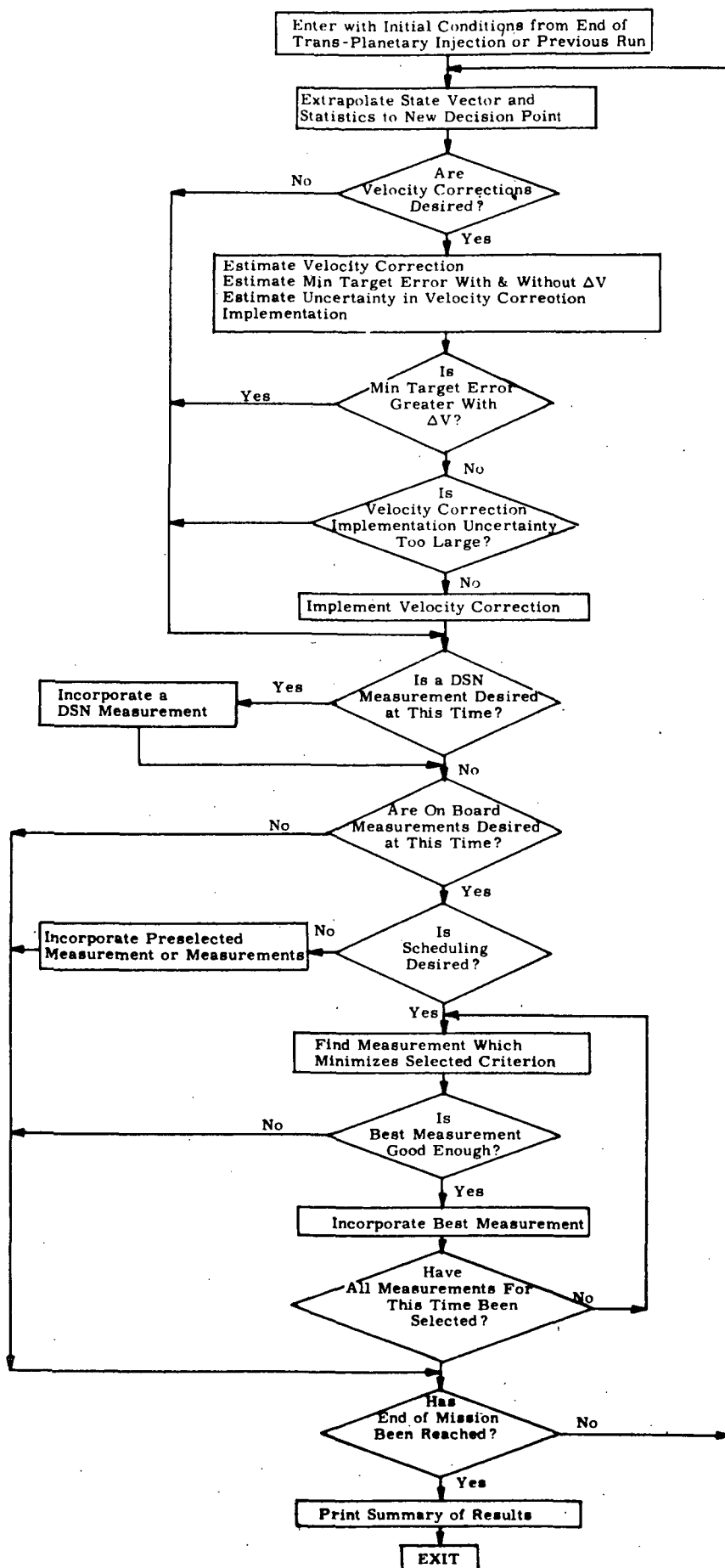


Figure II-1 Simulation Logic Diagram

under study. Central to the understanding of the error analysis computation procedure is the fact that the mission under consideration is divided into a number of such decision points. The frequency, spacing, and total number of these points is completely flexible but must be specified prior to run time. At each point a decision is made as to whether or not to make a velocity correction, whether or not to process a DSN measurement and what onboard measurement or measurements to take, if any. If it is decided to implement a measurement or a velocity correction at any point, this is done. Examples of how mission geometry influences the arrangement of these decision points is given in Appendices A and B.

The first step within the main computation loop is to extrapolate these initial conditions to the time of the first decision point under a two-body approximation to the free-fall situation. The reference state is extrapolated by solving Kepler's problem along the reference trajectory between the initial time and the time of first decision point. Simultaneously, a set of partial derivatives is computed which can be used to generate the state transition matrix associated with the solution to the linear perturbation equations between these two times. All this is done using a solution to Kepler's problem developed by Battin²⁷. A similar procedure has been published by Goodyear²⁸. The result of this computation are terms $\Phi_{n+1, n}$, $\underline{m}_{n+1, n}$ required to extrapolate the statistics in the above filter scheme. Using these formulas the statistics are all extrapolated to the next decision point.

Once the state and statistics have been extrapolated to the decision point, the mean squared value of the velocity correction which would be required at this time to cause the spacecraft to intersect the reference trajectory at a preassigned destination point is computed²⁹.

This mean squared velocity correction is then used to compute the expected mean squared error in implementing the velocity correction. Four additional quantities are then computed.

- 1) $\sigma_{\text{imp}}^2 / \overline{\Delta v^2}$ ($\sigma_{\text{imp}}^2 = \Delta v$ implementation variance)
- 2) Minimum obtainable terminal error without a velocity correction.
- 3) Minimum obtainable terminal error with a velocity correction of mean squared value $\overline{\Delta v^2}$
- 4) (Mean squared uncertainty in evaluating $\overline{\Delta v^2}$)

The computation procedure for the first quantity is evident from its definition. The second is obtained by projecting the X matrix ahead to the terminal time. The third is calculated by adding the expected implementation error to the E matrix and projecting this sum to the terminal time. The procedure for determining the mean squared uncertainty in the computation of the ΔV is given in reference 29. This is then used to form the ratio indicated in the fourth quantity above.

A velocity correction is then made only if the minimum obtainable error is smaller by making a correction (it could be more if the implementation errors are large), if the ratio $\sigma_{\text{imp}}^2 / \overline{\Delta v^2}$ is less than a pre-specified amount and if the ratio of the uncertainty in estimating the velocity correction to the velocity correction itself is smaller than a pre-specified amount. The purpose of the latter two tests is to inhibit corrections of marginal utility. At any desired time this entire procedure can be overridden and a velocity correction made without making any of these tests.

If a velocity correction is made it is "implemented" by processing the statistical formulas given in Appendix E for mid-course corrections. In these formulas:

$$Q_n = \begin{bmatrix} 0 & 0 & 0 \\ 0 & I & 0 \\ 0 & 0 & 0 \end{bmatrix} \sigma_g^2$$

$$Q_n^{\#} = \begin{bmatrix} 0 & 0 & 0 \\ 0 & I & 0 \\ 0 & 0 & 0 \end{bmatrix} \sigma_{\text{imp}}^2$$

where the matrices have been divided into their three by three partitions and:

$$\sigma_g^2 = \frac{1}{3} (\overline{\Delta SF^2} \overline{\Delta v^2} + \overline{a_b^2} \Delta t_v^2)$$

where

$$\overline{\Delta SF^2} = \text{accelerometer scale factor error variance}$$

$$\overline{a_b^2} = \text{accelerometer bias error variance}$$

$$\Delta t_v = \text{time required for velocity correction}$$

Note that the ability to measure the tailoff uncertainty causes less error to be introduced into the estimation of the deviation from the reference than into the actual deviation. The spherical distribution of the velocity error permits the use of the convenient diagonal form in the additive terms.

Once the velocity correction decision has been made the program continues to the question of whether or not to process a DSN measurement at this time. If it is determined that this is one of the predetermined times that such a ground tracking measurement is to be incorporated this is done by using the method outlined in the first three sections of this chapter.

After the DSN measurement choice has been made the program continues to the questions of whether to make a measurement at this time and what measurement to take. One of three options may be exercised at this point. The first is not to make a measurement at all. In this case the state and statistics are extrapolated to the next decision point and the entire process repeated. The second option is to incorporate a predetermined

measurement or sequence of measurements. Once this is completed the state and statistics are extrapolated along the reference trajectory to the time of the next decision point. The third option is to enter the measurement selection process. This will now be described.

Of prime importance in the selection of the individual measurements is the criterion function used to select them. Three criteria were implemented in this program; they are all to be minimized:

Method 1. the trace of the covariance matrix of estimation errors.

Method 2. the mean squared position estimation error at a preselected target point (Usually the destination point).

Method 3. the mean squared velocity estimation error at a preselected target point.

Only one may be used during any given run.

Method 1, as its description implies, is to incorporate trial measurements and choose the one which would result in the smallest value of $\text{tr}(E_n)$ after the measurement. This method is infrequently used because it doesn't relate directly to mission objectives and it is not physically appealing to directly add quantities which have different dimensions. It was implemented to determine whether approximately the same results as for method 2 could be obtained with fewer computations. Fewer computations are involved because it is not necessary to extrapolate the covariance matrix forward for each trial measurement as is described below. Unfortunately this approximation proved to be of insufficient accuracy for the cases studied.

For method 2, the procedure used to compute the mean squared position error at a preselected target point is to extrapolate the covariance matrix, which results after incorporating a trial measurement, forward to the time at which the vehicle will arrive at this target point on the reference trajectory. The best measurement is that which minimizes the trace of the upper left 3x3 matrix of the resulting extrapolated covariance matrix. The procedure for obtaining this 3x3 matrix without computing the full 6x6 state transition matrix is outlined in detail in reference 29. If the leg under study is an interplanetary leg then the lower right 3x3 of the E matrix is added to the upper left before the trace operation is performed. This is to permit the potential reduction of the ephemeris error to play a part in the selection of the measurement.

The computation procedure for the mean squared velocity error at a pre-selected target point is completely analagous to the projected position error just described except, of course, no ephemeris error is added in.

One of the above criteria is selected in any given computer run to select measurements. The measurements are chosen from one of the following types:

1. Planet/Moon diameter
2. Planet/Moon-star (planet/moon center to star).
3. Star occultation
4. Star-elevation (planet/moon limb to star).
5. Sun-star.

The possibility of using sun-planet measurements was eliminated because of the large uncertainty involved in defining the limb of both the sun and the planets. The first eight planets of the solar system and the 37 Apollo navigational stars can be used for planets and stars. Planet position and velocity information is generated using a Fourier-Bessel series expansion of the planetary orbits ⁽²⁹⁾. A list of the Apollo navigational stars is given in Table II-7. Star locations were obtained from Reference 30. Table II-8 lists the available planetary satellites. Their orbital elements were obtained from references 29, 30, 31, and 32. The planetary orbital elements were also obtained from reference 31.

A number of constraints are used to eliminate measurements which should be rejected for physical reasons. These include:

1. Two lines of sight farther apart than the optical instrument can permit.
2. Line of sight to a star too close to the line of sight to the sun.
3. Star behind the planet/moon.
4. Line of sight to a star too close to the line of sight to the planet/moon limb.
5. Line of sight to a planet/moon edge too close to the line of sight to the sun. (Not made if the spacecraft is in the planet/moon shadow).
6. Planet/moon or star behind the sun.
7. Lines of sight to dark edges of planets/moon are rejected in those cases where infrared equipment is not assumed.

TABLE II-7.
List of Navigational Stars

<u>Catalogue No.</u>	<u>Star Name</u>	<u>Vis. Mag.</u>
1	Andromedae	2.1
2	Ceti	2.2
3	Cassiopeiae	2.2
4	Eridani (chernar)	0.6
5	Vrsae Minoris (Polaris)	2.1
6	Eridani	3.4
7	Ceti	2.8
8	Persei	1.9
9	Tauri (Aldebaran)	1.1
10	Orionis (Rigel)	0.3
11	Aurigae (Capella)	0.2
12	Carinae (Canopus)	-0.9
13	Canis Majoris (Sirius)	-1.6
14	Canis Minoris (Procyon)	0.5
15	Velorum	1.9
16	Ursae Majoris	3.1
17	Hydrae	2.2
18	Leonis	1.3
19	Leonis	2.2
20	Corvi	2.8
21	Crucis	1.6
22	Virginis (Spica)	1.2
23	Ursae Majoris	1.9
24	Centauri	2.3
25	Bootis (Arcturus)	0.2
26	Coronae Borealis	2.3
27	Scorpii (Antares)	1.2
28	Trainguli Austr.	1.9
29	Ophiuchi	2.1
30	Lyrae (Vega)	0.1
31	Sagittarii	2.1
32	Aquilae (Altair)	0.9
33	Capricorni	3.2
34	Pavonis	2.1
35	Cygni (Deneb)	1.3
36	Pegasi	2.5
37	Piscis Austr. (Fomalhaut)	1.3

TABLE II-8. List of Available Planetary Satellites

<u>Planet</u>	<u>Satellite</u>
Earth	Moon
Mars	None
Jupiter	Io Europa Ganymede Callisto
Saturn	Titan Rings
Uranus	Ariel Umbriel Titania Oberon
Neptune	Triton

8. Star occultation occurs too close to the sun terminator on a body with an atmosphere.
9. Star occultation occurs too close to the edge of the planet disc as it enters the star field.

The error associated with making each type of measurement is modeled as an appropriate combination of the basic instrument pointing error and the uncertainty involved in defining a planet limb as discussed above. Different numerical values are used for each planet and for the dark and light edge sightings.

Once the best measurement is found, it is incorporated if it gives a sufficient reduction in the selection criterion. Once the required number of measurements for this decision point have been selected and incorporated, the state and statistics are extrapolated to the time of the next decision point and the entire process is repeated until all decision points have been processed.

F. Measurement Schedule Optimization

In the navigational measurement technique thus far described in this chapter (and in greater detail in Appendix E), measurements were taken at specified intervals throughout the period in which the spacecraft was in a planet's sphere of influence. At any specified point, a large number of measurements would be possible, and from these possibilities was chosen the one measurement that would result in the smallest rms terminal position estimation error. By definition, this was the "optimal measurement" at the specified point. Measurements took into account the optimal measurements at all previous points, but not, of course, those measurements yet to be made. Thus, this method built up a set of optimal individual measurements.

For two of the missions, an added step was undertaken to reduce even further the terminal position error when onboard navigation alone was used. This step, described in greater detail in Appendix H, used the set of optimal measurements resulting from the previous method, as a

starting point, to specify how those measurements might be changed to result in the smallest possible rms terminal position estimation error. The basic difference between the two methods is that the first results in a set of measurements which are individually optimal; the second gives the optimal overall measurement schedule. By building upon the foundation laid by the first method, the second method reduced the final estimation error to its smallest possible value.

Page intentionally left blank

CHAPTER III

ONBOARD NAVIGATION SYSTEM CONCEPTS

A. Introduction

The basic function of the navigation system is to measure angles between astronomical bodies. This function can be performed in at least two basic ways; namely by either viewing the two astronomical objects simultaneously with separate sensors having a measurable angular separation, or by viewing them in sequence, and noting either the change in angle with respect to an inertial reference or, knowing the scan rate, noting the time between appropriate signals. The process of choosing between these two basic types of navigation systems involves consideration of the total system design loop, and the aims and scope of the outer planet missions. Navigation system design is affected by the design and accuracy of the coarse attitude control system, by the requirements for pointing the communications antenna and the scientific packages, and by the gross thrust capability of the velocity correcting rockets. The question of required navigation accuracy is answered in part by the computer simulations, partly by the limits imposed by uncertainties in the planetary limbs, but also partly by the yet undefined requirements of the scientific packages. Fundamental to the navigation system design is the angular stabilization and control of the spacecraft, which is a major factor in determining the need for sensor dynamic isolation and target tracking capability.

It is the aim of this section to identify those navigation system elements that are common to most of the navigation concepts, and to define some plausible candidate systems. Probable candidate systems are the subject of the first part of the section, and are discussed within the framework of a trade of sensor degrees of freedom versus degrees of freedom of the entire spacecraft. Detector choice is discussed next, followed by a presentation of accuracy, physical characteristics, and telescope design for specific systems.

B. A Matrix of Possibilities

The combined effects of the limited scope of this study and the undefined nature of the missions and vehicles make it difficult to select the optimal navigation system here, but by examining navigation sensors in terms of their allotted controllable rotational degrees of freedom one can propose some systems that seem plausible, and extract and analyze the elements that are common to these systems. The device chosen for this exercise is called the possibilities matrix. The making of a navigation measurement involves lining up the optical axis of a radiation sensor with a desired astronomical object, and this alignment can be accomplished in a number of ways through various combinations of rotations of the spacecraft and sensor. Construction of the matrix of possibilities, therefore, represents an attempt to systematically display and consider the various possible combinations of rotational degrees of freedom assigned to the navigation sensor and the spacecraft. The rows and columns of the possibilities matrix represent the number of rotational degrees of freedom assigned to the spacecraft and navigation sensors respectively. Thus, a spacecraft having three rotational degrees of freedom can, upon command, orient itself in any given attitude in the same sense that a rigid body can be arbitrarily oriented by three Euler rotations about principal orthogonal axes. Similarly, a spacecraft having two degrees of rotational freedom can point one axis at a time in any selected direction. One degree of freedom allows the spacecraft only to roll about one axis, while a zero degree of freedom spacecraft has no capability to actively change its orientation. Figure III. 1 displays the matrix. It is assumed that no more than three D. O. F. are assigned to either spacecraft or sensor, i. e., that complete orientation is sufficient.

The lower portion of the matrix enclosed by the dark border, and representing spacecraft designs with two or three degrees of freedom is of major interest because the communications antenna is by far the largest dimensioned part of the craft and will contribute a significant portion of the moments of inertia; therefore, it makes sense to rigidly connect the antenna to other parts of the craft, and rotate the entire assembly for

		SENSOR R. D. O. F.			
		0	1	2	3
SPACECRAFT R. D. O. F.	0	0	1	2	3
	1	1	2	3	4
	2	2	3 Simple Scan System	4 Tracker & Scanner	5 Complete Dynamic Isolation
	3	3 Strapped Down System	4	5	6

Fig. III. 1 The Possibilities Matrix

communications antenna attitude control. Complete spacecraft orientation capability also allows thrusting for course corrections to be accomplished by one engine thrusting through the center of gyration. The Mariner spacecraft falls into this category, having two rotational degrees of freedom (pitch and roll control) which it uses to point the thruster for mid-course corrections. However, the Mariner has no operationally used on-board navigation sensor and therefore is not represented by an element of this matrix. In the two and three spacecraft D. O. F. region of the possibilities matrix there are essentially four different sensor system possibilities. Column one (zero sensor D. O. F.) represents the strapped down systems. In this configuration the attitude control system would have a reaction wheel with axis normal to the sensor scan plane to provide preselected scan rates about that axis which would typically be a spacecraft principal axis of greatest moment of inertia. Rotation rates must be accurately measured, possibly by a preliminary scan, to determine accurately the sequentially sampled navigation angle.

There would be a communications break while the on-board navigation measurements are being made, and following each navigation measurement the coarse attitude control objects (e. g. , Sun and Canopus) would have to be re-acquired. This system has the advantages associated with a minimum of degrees of freedom, such as increased mechanical reliability and simplicity. However, if there are problems with producing a smooth, accurately known spacecraft rotation, it may be necessary to move into the second column of the possibilities matrix and consider a sensor with one degree of freedom.

This device would have a rotational degree of freedom about an axis perpendicular to the scan plane containing the two navigational objects. The spacecraft, with its two degrees of freedom would align the sensor rotation axis with sufficient tolerance. The sensor would be swept about its scan axis through the proper angle, and the angle between objects would then be read out from a precision angle encoder. Star and planet limb signals can be sensed by separate detectors located at different places in the focal plane. A sensor of this type is shown in Figure III. 2. Design details for the sensor will be given below after the possibilities matrix

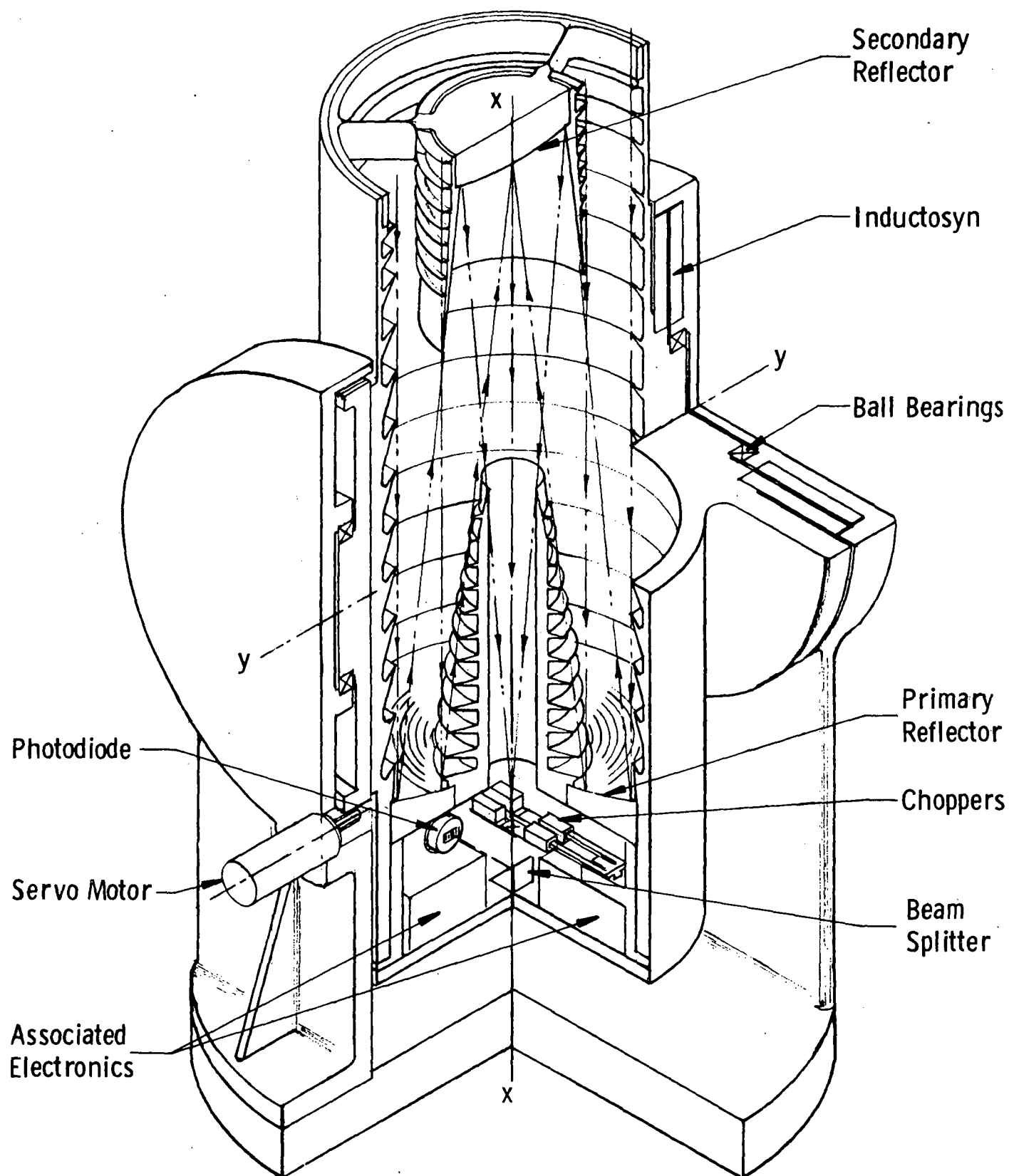


Fig. III.2 Single Degree of Freedom Sensor

discussion is completed. There are some other possibilities for a single degree of freedom sensor, for example, a combination one degree of freedom star tracker with a strapped down planet scanner. This system would however essentially double the weight, power, and volume, and would not increase the accuracy. If the accuracy can be shown to be sufficient for the single barrel system, it makes little sense to add a second telescope. With moderately accurate scan plane placement (within several minutes of arc), and a quiescent spacecraft, the single telescope, single degree of freedom sensor system is capable of "few arc second" accuracy (see system accuracy section below).

Adding a second degree of freedom to the sensor as in the third column of the possibilities matrix allows a star tracker to reduce the error in scan plane alignment. However, since this alignment need not be extremely accurate, the extra degree of freedom buys little total accuracy, but adds considerable complexity. In this system the sensor would acquire the subject star in the tracker mode, then orient the scan plane by rotating the spacecraft until the polar angle becomes zero. After this alignment the sensor would switch to a planet limb scan mode and complete the measurement. This system could be constructed in a sextant configuration, but given that most of the error in a star planet angle measurement resides in the planet limb signal, it makes little sense to attempt an extreme refinement of the star position. Also the second telescope adds a penalty in weight, power, and volume.

The last possibilities matrix column represents the full three degrees of freedom sensor. This device could be implemented in several different configurations depending on the characteristics of other parts of the spacecraft system. For example, if the spacecraft is quiescent with negligibly small amplitude vibrations, or large vibrations of extremely low angular velocity (much lower than the scan rate of the navigation sensor) then the three degrees of freedom might be used to provide a large sensor scan field without the necessity of rotating the spacecraft. Under these conditions the sensor becomes a copy of the single degree of freedom device shown in Figure III. 2 with two added gimbals. A sensor of this type is illustrated in Figure III. 3. The electronics ends of both sensors are the same.

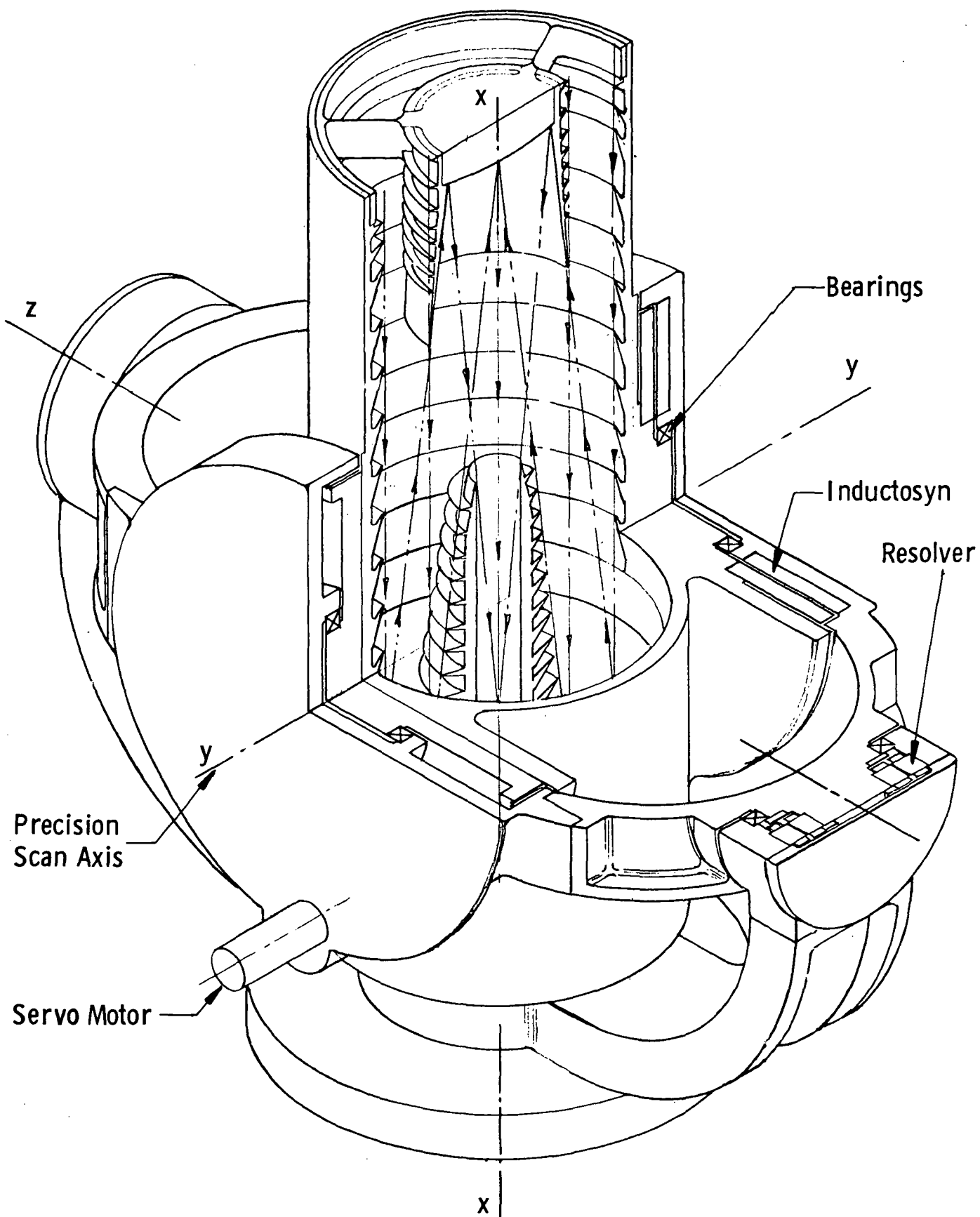


Fig. III.3 Three Gimbal Sensor

If the vibrational noise of the spacecraft is moderate, i. e. , of arc minute amplitude, and of an angular velocity of the order of the scan rate of the navigation sensor, then it will be possible to provide dynamic isolation of the sensor scan by servoing the three gimbal sensor package with respect to a set of inertial gyros.

Spacecraft vibrations of excessive amplitude at angular velocities of the order of sensor scan rates or higher would have to be dealt with by using a full scale isolation system. Such a system (Ref. 33) completely isolates the scan plane from the spacecraft by using a servo system in combination with a star tracker-planet scanner sextant. Hopefully, the spacecraft will be quiescent enough to avoid the need for such instrument complexity.

In Summary, it appears that the spacecraft will have at least two degrees of rotational freedom for thrust vector orientation, for communications antenna pointing, and possibly for navigation sensor and experimental package orientation. Control of the spacecraft attitude will be accomplished by a coarse, wide field, Sun-Canopus sensor system and momentum exchange flywheels. Because of wide field of view requirements in system wake up following dormancy this coarse system will be separate from the fine navigation system. If the coarse system is accurate enough, i. e. , capable of setting up a scan plane with a few minutes accuracy, it will be possible to navigate with a single degree of freedom sensor using a simple scan about an axis, with precision angle encoding. This is provided, of course, that the spacecraft is sufficiently quiescent during the scan. Either a requirement for simultaneous communications and navigation measurements, or a noisy attitude environment will require additional degrees of freedom on the navigation sensor.

C. Sensor Design

Detailed discussions of sensor design are given in Appendix G. Section G1 contains estimates of weight, power and volume requirements for sensors with 0, 1, and 3 rotational degrees of freedom. Section G2

discussed telescope design factors such as materials, aperture area requirements, field of view choices, and detector selection. Section G3 presents the results of some accuracy calculations.

D. Matrix of Attitude Control Requirements

1. General

It is now necessary to consider the relationship between navigation system concepts and attitude control requirements. At this point, system level questions arise to which answers are not available in a study of this kind. For example, if an onboard digital computer is proposed as a part of the navigation measurement and attitude control subsystem, the penalty of such a unit may be prohibitive if no other need for an onboard digital computer exists. However, the characteristics of outer planet missions suggest that a measure of onboard autonomy, through the provision of a digital computer, may be necessary for many mission phases, and for many functions, which could then properly include navigation and attitude control.

Spacecraft design concepts for outer planet missions usually include large parabolic antennas and planetary science packages. The rotational motion of either or both of these could be separated from the spacecraft by gimbals. Some planetary passage trajectories have geometry conflicts between requirements for maintaining radio lock on earth and surveillance of the planet both before and after passage. The constraints on the command attitude of the spacecraft are an unknown part of the situation in the discussion of attitude control requirements as given below.

Figure III. 4 is a follow-on matrix to the Possibilities Matrix set forth in Figure III.1. As before, the column index represents the number of rotational degrees of freedom assigned to the navigation sensor, while the row index represents the number of different orthogonal axes about which the spacecraft can change its attitude.

Sensor Degrees of Freedom

	0	1	2	3	4
0				Secondary Accuracy Except in Measurement Plane	Secondary Accuracy
1			Secondary Accuracy Except in Measurement Plane	Surplus Degrees of Freedom	Primary Accuracy - Attitude Error Appears 1:1 in Navigation Measurement Error.
2	Primary Accuracy	Secondary Accuracy Except in Measurement Plane	Surplus Degrees of Freedom	Surplus Degrees of Freedom	Secondary Accuracy - Attitude Error Only Causes Measurement in a Skewed Plane. Effect is $1 - \cos \theta$, Versine, for example.
3	Primary Accuracy	Secondary Accuracy Except in Measurement Plane	Surplus Degrees of Freedom	Surplus Degrees of Freedom	

Navigation Attitude Maneuver Degrees of Freedom.

Fig. III. 4 Spacecraft/Navigation-Sensor Combinations in Terms of Navigation Operational Maneuvers and Spacecraft Attitude Control Accuracy.

Within the matrix blocks the terms "primary accuracy" and "secondary accuracy" appear. These refer to the role that the spacecraft attitude control system plays in error buildup in the measurement. An attitude error in the measurement plane caused by the attitude system is primary, i. e., is producing a 1:1 effect inless that axis of the navigation instrument is gyro controlled. An attitude error which causes the measurement to be taken in a plane skewed from the desired measurement plane is secondary and is related to $(1 \cos \theta, \text{ the versine})$ in radians where θ is the skew angle.

It is anticipated that spacecraft attitude control requirements, particularly the requirement for thrust vector orientation, will necessitate the assigning of two or more rotational degrees of freedom to the spacecraft. With this type of spacecraft it is possible to make navigation measurements with sensors having zero to four degrees of freedom. Therefore, in absense of a specified spacecraft, and of specified scientific payload constraints, all that can be done with regard to navigation sensor specification is to present a shopping list of possible candidate systems and equipment, and trade off the features of the various configurations in a preliminary manner.

The discussion will now take up a series of candidate navigation systems having from zero (strapped down) to four (sextant) degrees of freedom and discuss their effects of the attitude control system. The basic sybssystem building blocks are set forth in Tables III-1, 2, 3.

Table III-1 shows the estimated weight, power and volume required for single line of sight sensors having 0, 1, and e degrees of freedom. Navigation angle measurements made by these sensors are carried out sequentially by pointing the optical axis first at one object then at the other by means of rotations of either the spacecraft or the sensor or a combination of both.

Table III-2 lists the same characteristics for sextant type sensors having two lines of sight and two sets of optics. Navigation angle measurements made with these devices are derived directly from the angle between the two lines of sight.

TABLE III-1

Single Telescope, Sequential-Type Onboard
Navigation System Candidates

	MASS (kg)	SIZE (cm ³)	POWER (Watts)
I. BODY FIXED TELESCOPE	5.4	6,556.0	1-2
II. SINGLE - D.O.F. TELESCOPE (Fig. III-2)	11.3	11,473.0	9
III. THREE - D.O.F. TELESCOPE (Fig. III-3)	18.1	21,307.0	22

TABLE III-2

Dual Telescope or Sextant Onboard Navigation
System Candidates

	WT. (kg)	SIZE (cm ³)	POWER (Watts)
I. SINGLE - D.O.F. SEXTANT	22.7	24,585.0	17
II. FOUR - D.O.F. SEXTANT (Figs. III-6 and III-7)	36.3	N/A	90

TABLE III-3

Onboard Guidance and Control Sybsytem Candidates

	MASS (kg)	SIZE (cm ³)	POWER (Watts)
Attitude Reference Units (ARU) Only			
Gimbaled	5.4	6,556.0	30
Floated	3.6	1,639.0	50
Structure-Mounted (1 axis at a time - 3 gyros)	N/A	N/A	N/A
Specific Force Units Only (Per Unit with Support Electronics)			
	1.1	1,195.0	7.5
Inertial Measurement Units (Attitude and Specific Force)			
Gimbaled	6.8	8,195.0	90
Floated	4.5	3,278.0	80
Structure Mounted (Including algorithm computer)	11.3	11,473.0	135
Computer Subsystem Multi-Processor Architecture			
Gnd-Based GNC Calcs.	4.1	4,097.5	30
Onboard GNC Calcs.	8.2	8,195.0	30

Table III-3 lists candidate onboard guidance and control units the use of which would be coincident with the various navigation sensors and concepts.

2. Body-Fixed Sensor

Referring now to Column 0 of Figure III. 4, one can visualize the telescope of Figure III. 2 removed from its mount and fastened rigidly to the spacecraft structure. Navigation angle measurements would then be possible if the spacecraft attitude could be controlled about two or three of its axes. Instrument weight would be minimum.

Measurements would be accomplished by spacecraft body rotation from one line-of-sight to the other. This implies a departure from cruise attitude and a loss of radio lock for each measurement. It also demands that body rotations not only be measured but also controlled in the measurement plane to primary accuracy. Onboard consummables might be depleted by such attitude maneuvers.

This configuration is identified by a minimum navigation sensor and a maximum attitude control requirement. The requirement is to establish orientation and precess the spacecraft to a measurement plane skewed less than 20 minutes of arc from the ideal plane, (see Figure III. 5) and to measure rotation in the measurement plane to primary accuracy. In actual practice, it may prove difficult to accomplish spacecraft precession in the measurement plane because of motion about non-principal axes. Motion skewed by 1 degree would add 30 arc seconds of angle measurement error. Weight, power, and volume estimates for the body fixed system and its associated attitude control system are given Table III-4.

3. Single Degree of Freedom Sequential Sensor

Referring now to Column 1 of Figure III. 4 and to the telescope as mounted in Figure III. 2, consideration can be given to the single degree of freedom navigation sensor. As in the body fixed sensor, the spacecraft is called upon to rotate for the navigation measurement to

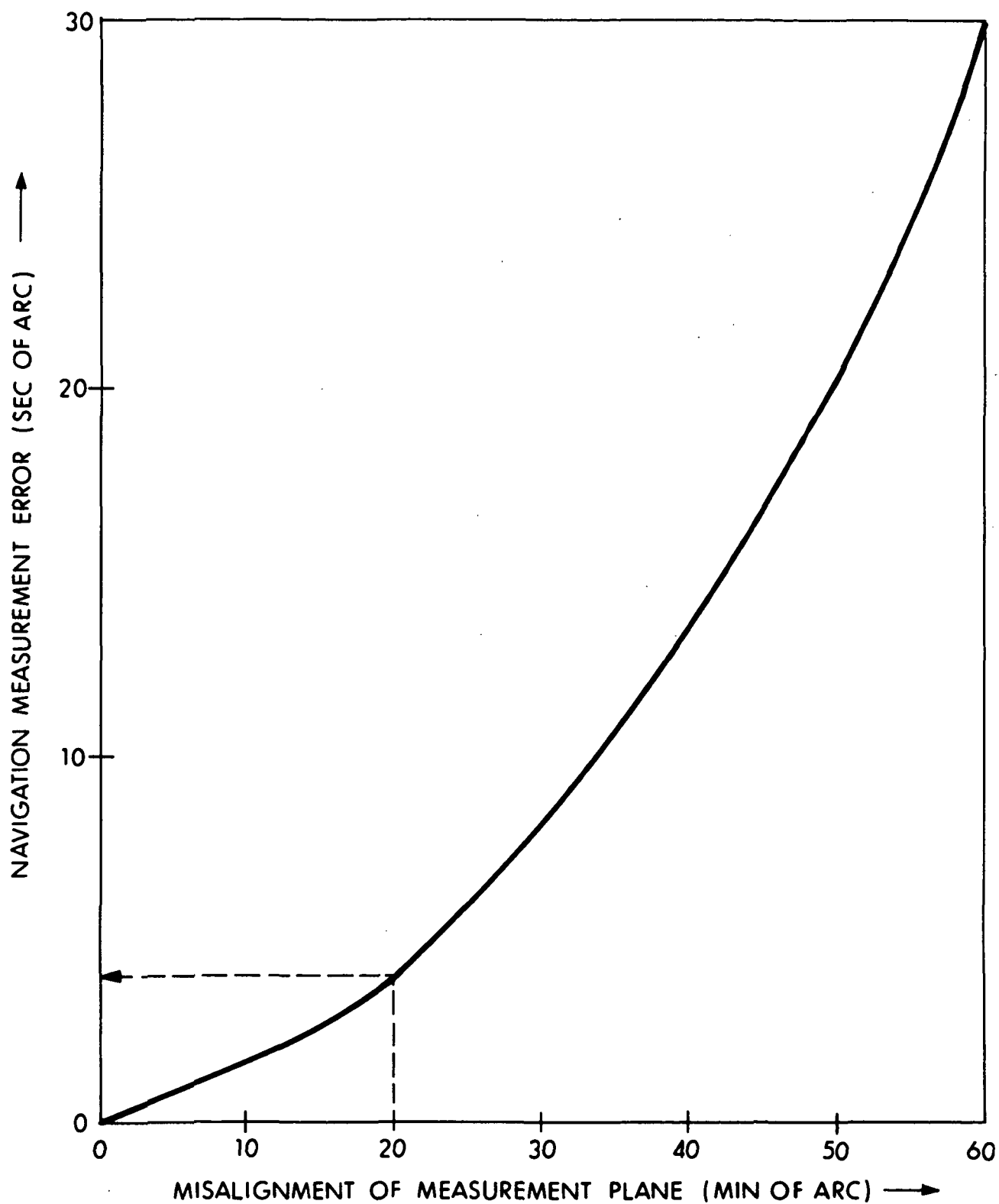


Fig. III. 5 Effect of Misalignment of Measurement Axis with Respect to Proper Plane (Versine Effect)

TABLE III-4

Subsystem Values for Body-Fixed Navigation Sensor
and Associated Attitude Control

	MASS (kg)	SIZE (cm ³)	POWER (Watts)
Nav. Sensor (Body Fixed)	5.4	6,554.8	2
Gimbaled	5.4	6,554.8	30
ARU			
Floated	3.6	1,638.7	50
Computer Subsystem	8.2	8,193.5	30
<hr/>			
(Gimbaled ARU)	19.1	21,303.1	62
Totals:			
(Floated ARU)	17.2	16,387.0	82

align the navigation sensor scan axis perpendicular to the plane containing the astronomical objects. The sensor then scans the objects, and the angle between them is determined by one of several techniques, each involving slightly different instrumentation. We consider three possibilities here.

In the first of these, the spacecraft has an attitude reference unit (ARU) by which it locates the proper scan axis direction. Less demands are placed on the attitude control system for this sensor than in the strapped down case, because the system is required only to maintain a chosen attitude accurately and is not required to produce an accurate roll rate about the scan axis. The requirement is for stability during sighting rather than precise rotation. Again a 20 minutes of arc measurement plane alignment reduces the versine error to less than 4 seconds of arc.

A second possibility is to equip the measurement axis with a pulse-torquing gyro loop. Thus navigation angles could be measured directly in inertial space by pulse-torquing the instrument and adding the pulsed angular increments. This requires a structure mounted ARU, and the accuracy is limited by the pulse size which it is felt can be made as small as 10 arc seconds.

Finally, it may be possible to operate the telescope in a star-tracking mode after the spacecraft has been placed in the measurement plane with some degree of quiescence. The residual drift rate could then be measured prior to and after swinging the line of sight down to the planet to measure the navigation angle. Theoretically, this type of navigation sensor configuration is capable of high accuracy, but additional control logic is required, hence a larger computer.

The characteristic weight, power, and volume of these variants of the single degree of freedom system are displayed in Table III-5.

4. Three Degree of Freedom Sequential Type Instrument

Reference is now made again to the Matrix of Attitude Control Requirements. The right hand column with its three degrees of freedom

TABLE III-5

Subsystem Values for Single-Degree of Freedom Sequential
Navigation Sensors and Attitude Control

	MASS (kg)	SIZE (cm ³)	POWER (Watts)
<u>A. Simple ARU System</u>			
SDOF Nav. Sensor	11.3	11,473.0	9
Gimbaled	5.4	6,556.0	30
ARU Floated	3.6	1,639.0	50
Computer Subsystem	<u>4.1</u>	<u>4,097.5</u>	<u>30</u>
Gimbaled	20.8	22,126.5	69
totals:			
Floated	19.0	17,209.5	89
<u>B. Pulse-Torque Gyro System</u>			
SDOF Nav. Sensor	11.8	11,473.0	10
ARU - Structure Mtd.	4.1	4,097.5	40
Computer Subsystem	<u>4.1</u>	<u>4,097.5</u>	<u>30</u>
totals:	20.0	19,668.0	80
<u>C. Star Tracking System</u>			
SDOF Nav. Sensor	11.3	11,473.0	9
ARU Structure Mtd.	4.1	4,097.5	40
Computer Subsystem	<u>8.2</u>	<u>8,195.0</u>	<u>30</u>
totals:	23.6	23,765.5	79

will be discussed. These three degrees of freedom give theoretical measurement capability for the Row 0 case where the spacecraft is not permitted to change attitude for the navigation measurement. In fact this is the most desirable operational situation. If the instrument (see Fig. III. 3) is equipped with a single precision measurement axis, and two more degrees of freedom with respect to the spacecraft, it becomes possible to make navigation measurements without having to disturb the spacecraft's cruising attitude. Thus the problems of depleted consumables and loss of radio lock mentioned above are avoided. As a practical matter, it might be necessary for some mission situations to rotate the spacecraft about the sun line (or the earth line) because a desired star or planetary direction was not attainable by the instrument for geometrical reasons.

Considering now the instrument system under discussion, the spacecraft will have to maintain its cruise attitude to primary accuracy values if the sensor gimbals are limited to a precision position servo loop. If the sensors measurement degree of freedom is equipped with either the gyro stabilization or the star tracking capability, then the spacecraft attitude stability can be set at the secondary level. Since these specifications are on the equilibrium cruise attitude, they are easier to attain than if they applied to re-orientation maneuvers. Subsystem specifications for the three-degree of freedom sequential instrument are set forth in Table III-6.

5. Single Degree of Freedom Sextant Sensor

Another alternative instrument is the use of two telescopes, a body-fixed precision star tracker and a single degree of freedom planetary limb scanner. Motion about the star line of sight into the desired measurement plane would initiate the measurement sequence. Then the planetary limb scanner would determine the angle to the limb by a precision transducer angle measurement between the two telescopes.

Attitude control requirements would require primary accuracy control to the star line of sight, unless off-axis draft during limit cycles could be digitally encoded as a star sensor output. Requirements about

TABLE III-6

Subsystem Values for Three Degree of Freedom Sequential
Navigation Sensor and Attitude Control

Note: ARU's are not listed below as a navigation measurement requirement, although necessary for velocity corrections. Cruise sun seekers and star trackers are not charged to navigation attitude control.

	MASS (kg)	SIZE (cm ³)	POWER (Watts)
<u>A. Primary ARU System</u>			
3 DOF Nav. Sensor	18.1	21,303.1	22
Computer Subsystem	<u>8.2</u>	<u>8,193.5</u>	<u>30</u>
totals:	26.3	29,496.6	52
<u>B. Gyro System</u>			
3 DOF Nav. Sensor	18.6	21,303.1	23
Computer Subsystem	<u>8.2</u>	<u>8,193.5</u>	<u>30</u>
totals:	26.8	29,496.6	53
<u>C. Star Tracking System</u>			
3 DOF Nav. Sensor	18.1	21,303.1	22
Computer Subsystem	<u>8.2</u>	<u>8,193.5</u>	<u>30</u>
totals:	26.3	29,496.6	52

the star line of sight would be for secondary attitude control. Table III-7 summarizes possible subsystem parameters associated with this configuration.

6. Four Degree of Freedom Sextant Type of Instrument

For the sake of completeness, Figure III. 6 and Fig. III. 7 show a four degree of freedom sextant instrument which contains gimbaling necessary to establish two telescopes in the measurement plane and an additional precision degree of freedom to measure the angle between them. This instrument also contains an array of inertial sensing instruments to make a compact guidance and navigation sensor assembly³⁴. The subsystem parameters for this instrument and its associated computer and attitude control equipment are listed in Table III-8.

7. Review

Five different candidate Navigation System Concepts have been outlined in the preceding paragraphs. It should be emphasized again that no real design work was a proper part of this effort. Consequently all values of power, weight, and volume are estimates. These estimates do have, however, the benefit of experience and consideration.

TABLE III-7

Subsystem Values for Single-Degree of Freedom Sextant
Navigation Sensor and Attitude Control

	MASS (kg)	SIZE (cm ³)	POWER (Watts)
SDOF Sextant	22.7	24,585.0	17
ARU Structure Mtd.	3.2	2,294.6	35
Computer Subsystem	<u>4.1</u>	<u>4,097.5</u>	<u>30</u>
totals:	30.0	30,977.1	82

TABLE III-8

Subsystem Values for Four Degree of Freedom Sextant
Navigation Sensor and Attitude Control

	MASS (kg)	SIZE (cm ³)	POWER (Watts)
4 DOF Sextant with Inertial Sensors	36.3	16,387.0	90
Computer Subsystem	<u>8.2</u>	<u>4,096.8</u>	<u>30</u>
totals:	44.5	20,483.8	120

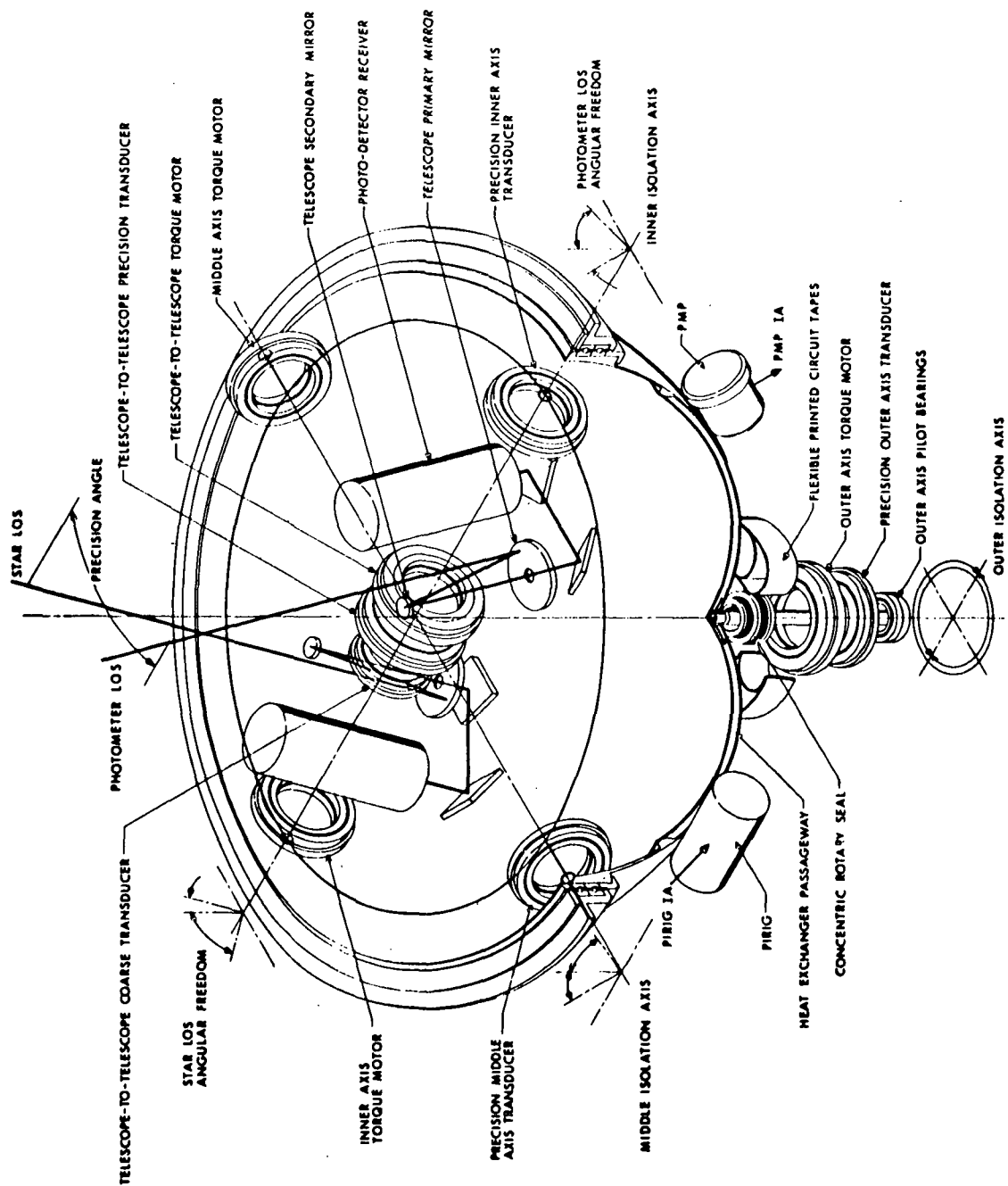


Fig. III-6 Schematic, design model RSS.

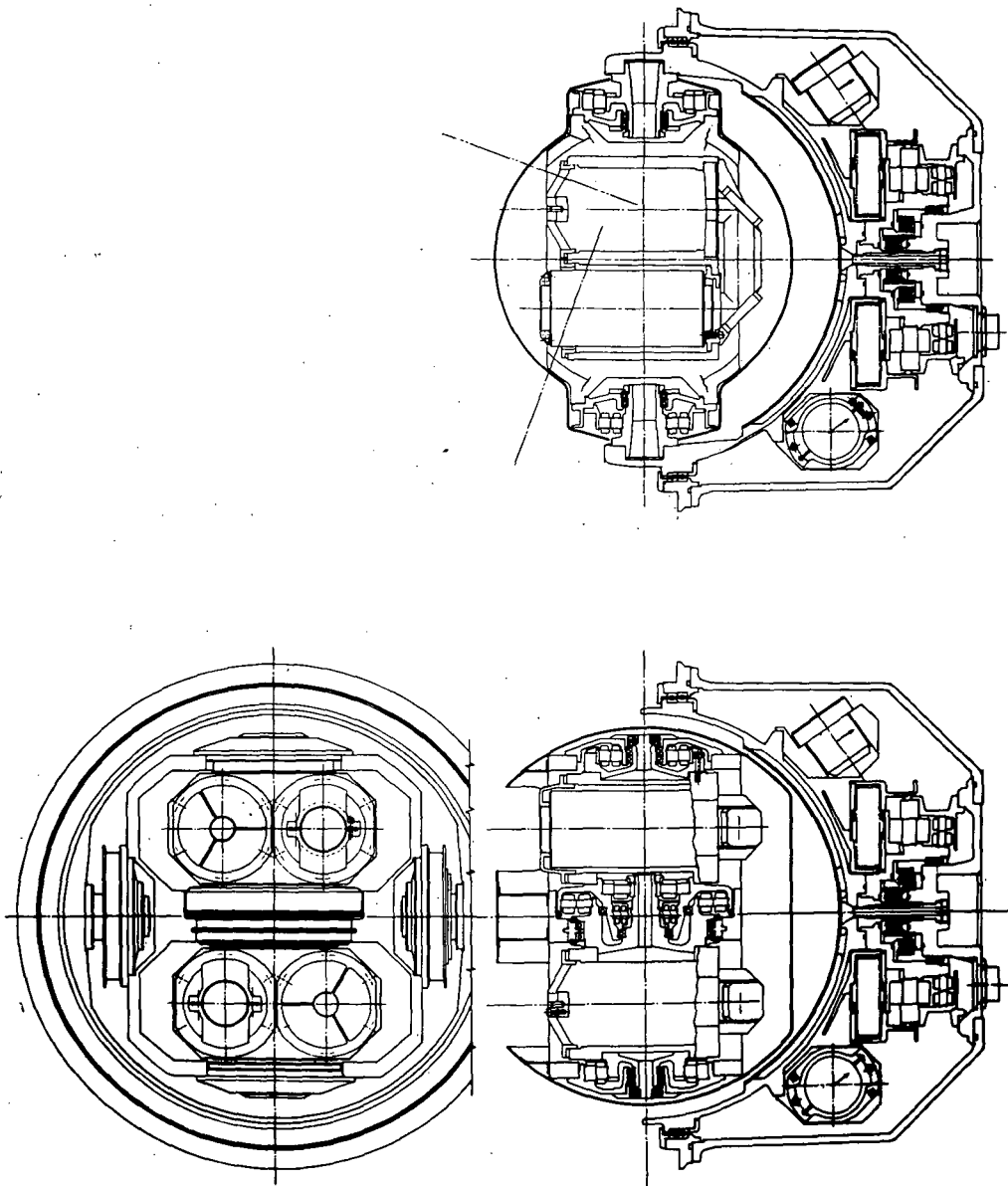


Fig. III. 7 Design layout of design model RSS.

CHAPTER IV

SYSTEM REQUIREMENTS FOR THE 1973 JUPITER FLYBY

This chapter presents the simulation results of the 1973 low-energy Jupiter flyby mission and discusses their implication on systems and mission requirements. Because many of the results presented here and in the next two chapters are in tabular form, the terms used in the tables will be defined at this point. Tables IV-1 and IV-2 serve as examples of the described tabular presentation. All entries in these tables are one-sigma values. The same is true for all statistical quantities used in this report.

Both "RMS Pos EST" and "Position Estimate" refer to the rms position-estimation error at the time indicated. These terms derive from the E matrix and reflect how well position is known. The column entitled "RMS Vel EST" gives the same information for the velocity. The two times involved are periplanet passage and the terminal time. By definition, terminal time is the time of arrival at the planetary sphere of influence, for interplanetary legs. For near-planet passages, terminal time is the arrival time at the outbound sphere of influence for all except the last passage of a mission, when it is the point at which the probe reappears from behind the planet.

The column entitled "FTA" denotes rms position error at the end of a specific leg resulting from fixed-time-of-arrival guidance for the number of midcourse corrections entered in the column headed "No.". These corrections require an amount of fuel entered under "Total FPS". The last correction was made at the time entered under "Days Last ΔV " or "Time of Last ΔV Days". The specific time is important because it effects both the FTA error and terminal-estimation errors. If the

TABLE IV-1

Earth Jupiter Leg of the 1973 Jupiter Flyby Mission *

Configuration	Terminal Errors					ΔV History			
	RMS Pos. EST (km)	RMS Vel EST (mps)	FTA (km)	RMS EPH. EST (km)	Total No.	Initial ΔV mps	Total ΔV mps	Time of Last ΔV (Days)	
OB Only	9433.64	0.2101	10082.5	551.8	6	59.16 **	115.68	700	
DSN Only	556.13	0.00085	559.7	555.1	8	52.29 ***	55.40	695	
DSN & OB 10" - 60"	535.57	0.00082	930.7	534.5	5	52.29 ***	55.07	534	
DSN & OB 3" - 60"	442.48	0.00082	928.4	441.1	5	52.29 ***	55.07	534	
DSN & OB 1" - 60"	270.43	0.00085	471.5	268.1	6	52.29 ***	55.20	640	

*Time to Sphere of Influence - 710 Days.

**at 50 days

***at 2 days

TABLE IV-2

Near Planet Results for Jupiter Passage of 1973 Jupiter Flyby Mission*

Configuration	Periapsis Error Values (km)			Terminal Error				ΔV History		
	Position Estimate	Out of Path	Out of Path Corrected	RMS Pos. EST (km)	RMS Vel. EST (mps)	FTA (km)	Ephemeris RMS EST (km)	No.	Total ΔV mps	Time of Last ΔV (Days)
OB only	16.28	788.74	8.11	16.29	6.5051	8753	551.5	2	105.4	71.35
DSN Only	2.75	42.31		2.75	2.6789	723.2	83.8	2	2.31	70
DSN & OB 10" - No IR	0.82	65.47	0.69	0.82	.7059	762.5	78.1	2	1.90	69
DSN & OB 3" - No IR	0.50	66.02	0.31	0.51	.3088	767.0	77.6	2	1.65	68
DSN & OB 1" - No IR	0.45	30.61	0.21	0.45	.2094	369.0	77.6	3	2.24	71.52
DSN & OB 10" - 60"	0.80	64.39	0.68	0.80	.6844	749.5	76.4	2	1.89	69
DSN & OB 60" - 60"	1.34	61.22	1.24	1.34	1.2578	723.1	79.0	2	2.31	70

*Terminal Time = 74.10 Days. Pericenter Time = 74.10 Days

last correction were made near the terminal time, the estimation error would be larger than expected and the FTA error smaller. The reverse would occur if the last correction were made far in advance of the terminal time.

The ephemeris error remaining at the terminal time is given under "RMS EPH EST" or Ephemeris RMS EST.

Entries in the column, "Out of Path", denote the deviation from the reference trajectory perpendicular to the path of the vehicle as viewed from Earth. If a suitable velocity correction had been made before periplanet, this deviation could have been reduced approximately to the value listed under "Out of Path Corrected". "Approximately" is used because only in theory can the actual deviations be reduced to precisely the estimation error.

Certain combinations of navigation capabilities were explored for all three outer-planet missions considered in this study, as discussed in Chapter II. The onboard-only case referred to in these tables assumes the availability of an instrument working in the visible spectrum with a pointing error of 10 seconds of arc and an infrared sensor with a 1-arc-minute pointing error. The notation, "DSN & OB", followed by two quantities separated by a dash, refers to cases where onboard navigation is performed in conjunction with ground-based radar tracking. The first of the two quantities is the pointing error of the optical device and the second is that of the infrared sensor, both given in seconds of arc. On interplanetary legs, the onboard system is activated at a range of 1 a.u. from the destination planet if ground tracking is also available. For the onboard-only case, the onboard system is always operating.

Table IV-1 contains the results of applying the simulation program described in Chapter II to the interplanetary leg of the 1973 Jupiter flyby mission. The rms position estimate at the sphere-of-influence arrival is given in the first column of the table. It can be seen that, with the nominal 10-arc-second visible light and 60-arc-second infrared light uncertainties chosen for the onboard instrument, the DSN navigation facility is vastly

superior to onboard navigation. The combination of DSN and onboard capabilities results in a modest enhancement of the overall position uncertainty.

Reference to the second column of Table IV-1 indicates the superiority of DSN over the onboard system in measuring velocity. Onboard-only velocity errors are two-hundred times as great as those on a DSN-only system. A combination of onboard with DSN does not enhance the velocity knowledge over that for DSN only. In regard to the rms ephemeris estimate, it is evident that on this interplanetary leg the onboard system is competitive in accuracy with DSN tracking and that the combination of DSN with onboard is more effective than either system alone.

Figure IV.1 displays a time history of the projected rms position error at the arrival at the Jovian sphere of influence for the onboard-only case and the DSN-only case. This projected error for any given time is the value which would result if, after that period of time, no further midcourse corrections were made and no navigation of any type was performed. This plot also shows that on this mission leg, ground-tracking-only is far superior to onboard-only navigation. It is also clear that the DSN very quickly reduces the projected error to the rms ephemeris error for Jupiter. This is the limiting value because until the probe is influenced by the gravity field of Jupiter, the ephemeris error is not observable through Earth-based tracking. This error value is reached so quickly because the position-fixing capability of the DSN is inversely proportional to the range to the probe, as is evident from inspection of the partial derivatives given in Appendix E. At the beginning of the Earth-Jupiter leg, the spacecraft is extremely close to Earth; hence the rapid error reduction.

Figure IV.2 provides a comparison of the projected rms terminal position error obtainable with various combinations of onboard and ground-tracking capabilities. The onboard system is active only from the point at which the range to Jupiter is less than 1 a.u. It is clear that the ability of an onboard system to reduce ephemeris error improves

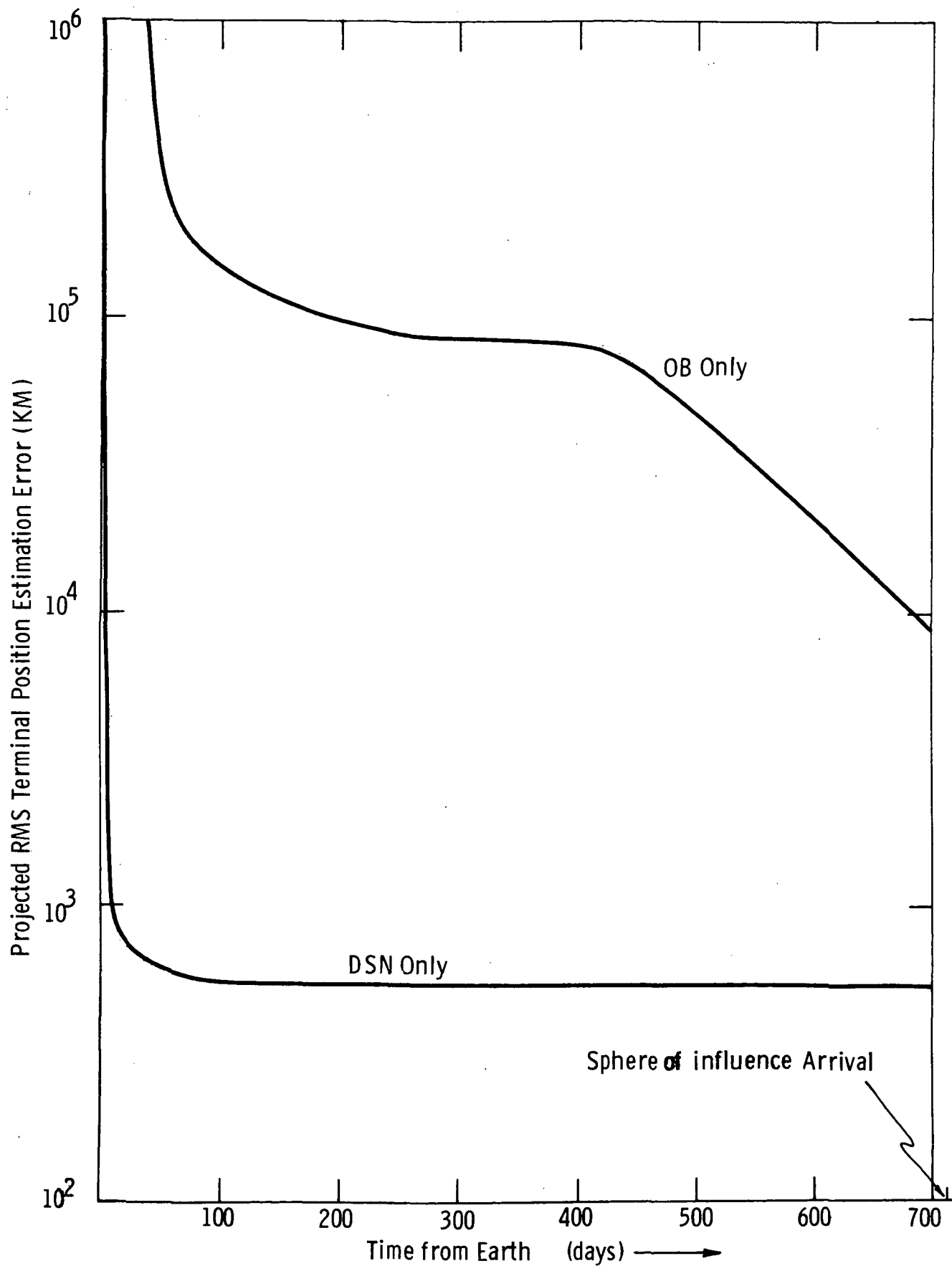


Fig. IV.1 Projected RMS Terminal Position Estimation Error Earth-Jupiter Leg

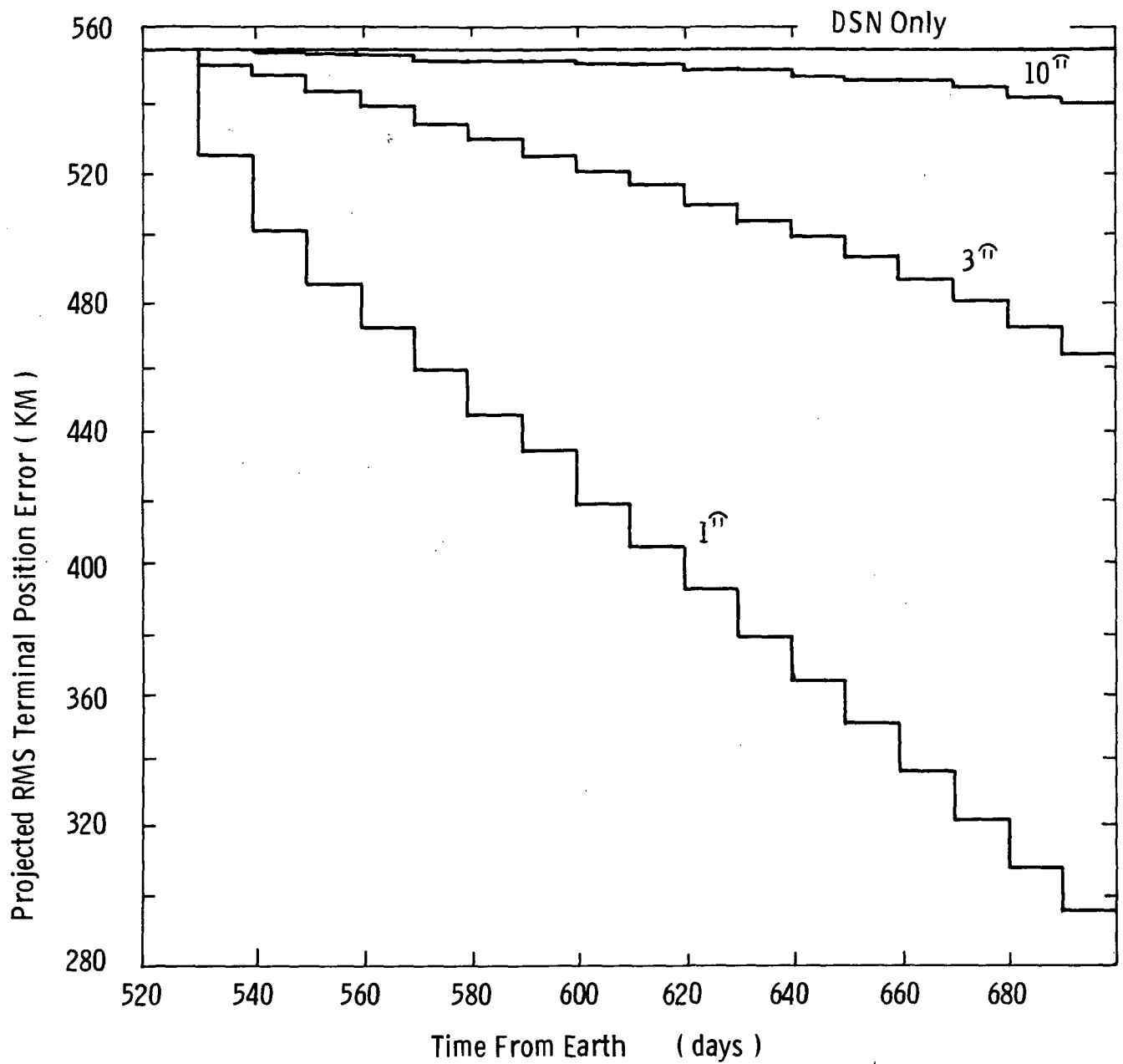


Fig. IV.2 Comparison of Error Reduction on Earth-Jupiter Leg of 1973 Jupiter Flyby

with better instrument quality and that a reduction of errors over the DSN-alone capability is thus possible. By waiting until the probe is under the gravitational influence of Jupiter, however, we can reduce the ephemeris error even more through the use of ground tracking. This is evident from inspection of the ephemeris-error column of Table IV-2. Thus, unless reduction of ephemeris error is important very early in the encounter, which seems unlikely, there appears to be no need for an onboard navigation system during any part of the interplanetary phase.

The column of Table IV-1 covering FTA guidance error refers to the actual position error of the spacecraft upon arrival at the Jovian sphere influence. These FTA values should be studied in connection with the ΔV history columns which give the number, fuel-consumption (initial and total), and timing data relative to enroute velocity corrections. The first velocity correction upon leaving Earth on each of these missions removes transplanetary injection errors. The size of this initial correction is, in all cases, trajectory-dependent and directly proportional to the injection error, assuming, of course, that sufficient time is provided before the correction for the navigation system to determine the errors. It is quite conclusive that total reliance on an onboard system results in a large terminal error and also in a substantial fuel penalty. The combination of onboard and DSN navigation produces an FTA error lower than that of DSN-only, provided that a second velocity correction is made after the onboard navigation system has reduced the ephemeris error.

It should be emphasized in this first reference to fuel requirements that the investigators are not recommending that the mission actually be flown with the number of midcourse corrections indicated in Tables IV-1 and IV-2. (The same comment applies to similar entries in the next two chapters.) The automatic midcourse-correction scheduling algorithm described in Chapter II is designed only to evaluate approximate total-fuel requirements and to assure, in the presence

of navigational uncertainties, a reasonable tradeoff between the total fuel required and the terminal-miss distance. This algorithm frequently gives more corrections than would actually be used; the one-sigma value of fuel consumed, however, is approximately the same as would be used in executing an actual correction schedule. A typical correction schedule, in this case for a DSN-onboard system, is given in Table IV-3. The 52.29 meters per second initial velocity correction at 2 days, is a consequence of the "worst case" transplanetary injection errors used to generate this particular set of data.

On an interplanetary leg, the ephemeris error is included in the targeting calculations for a potential midcourse correction only if onboard navigation is available. This algorithm performs least effectively in determining the location of the final velocity correction because timing at this point is very critical due to the rapid increase of ΔV required to correct a given miss as time to go becomes very small. For example, the FTA error for the DSN-only case is smaller than that for DSN with an onboard system of either a 3 or 10 arc-second visible-spectrum instrument capability. Table IV-4 compares the errors which result if, instead, the final midcourse velocity correction is made at the 700-day point used by the onboard-only navigation system. Note that, with no significant cost in fuel, the actual miss can be reduced to below the initial ephemeris error if both onboard navigation and ground tracking are used.

Despite the ability of the onboard system to reduce ephemeris errors, it appears that for the interplanetary leg of the 1973 Jupiter flyby, onboard navigation cannot make a significant contribution even when combined with DSN. It is felt that an FTA error of 291 Km upon arrival at the Jovian sphere of influence, compared with 558 Km, is not a justification for any of the candidate navigation systems discussed in Chapter III.

Guidance requirements for the interplanetary leg were evaluated in a series of special runs described in Table IV-5. In these runs the velocity correction was rather arbitrarily chosen at 112 days (corresponding to a fixed fuel consumption of 86.17 mps.) This was possible because

TABLE IV-3

1973 Jupiter Flyby

Correction Schedule for the Case
of DSN and Onboard 10" - 60"

Day	ΔV (mps)
2	52.29
3	2.44
146	.11
432	.11
534	.11

TABLE IV-4

Minimum Obtainable Miss for Final ΔV at 700 Days

Configuration	Minimum Obtainable FTA Error (km)	Total ΔV for Earth-Jupiter Leg (mps)
OB Only	10,082.5	115.68
DSN Only	558.1	55.46
DSN & OB 10" - 60"	540.6	55.86
DSN & OB 3" - 60"	457.2	55.91
DSN & OB 1" - 60"	290.8	55.60

TABLE IV-5

Guidance Error Survey for Earth-Jupiter Leg*

Guidance Error Value Used	FTA Error (km)
Nominal Values	6480.8
Engine Cutoff Uncertainty X10	31931.0
Engine Cutoff Uncertainty X100	314291.0
Accelerometer Bias X10	56407.6
Accelerometer Bias X100	563178.0
Accelerometer Scale Factor X10	7037.6
Accelerometer Scale Factor X100	28340.6

*DSN-only navigation with a single midcourse correction at 112 days.

the navigation uncertainties were identical to this point.

Nominal values for the guidance implementation were as follows:

Accelerometer Bias:	0.1 cm/sec ² or approximately 100 micro - g's
Accelerometer Scale Factor:	50 ppm
Engine Cutoff Implementation	
Uncertainty:	50 milliseconds of thrust time at full thrust

As explained in Chapter II, guidance errors for midcourse corrections are dominated by contributions affecting the length rather than the orientation of the ΔV vector. Accordingly, reference-frame alignment and gyro-drift factors were not included in the guidance error modelling. Accelerometer bias, accelerometer scale factor, and cutoff-uncertainty error contributions were evaluated parametrically and the results plotted in Fig. IV.3. The horizontal log scale is the ratio of guidance parameter error values to the nominal values listed above. Ten times and one hundred times nominal errors served as a useful range of examination.

From Fig. IV.3, it is apparent that the FTA error is insensitive to accelerometer scale-factor error until values in excess of 500 ppm are reached. The similarity shown by the accelerometer bias and cutoff-time curves is reasonable because the ΔV magnitude is the product of acceleration times burn-duration time. FTA error is thus directly affected by accelerometer bias and cutoff uncertainty.

Regarding the terminal phase or sphere-of-influence leg of the 1973 Jupiter flyby, the basic results for a nominal onboard system, DSN only, and a combination of both are given in Table IV-2. For this mission, the periapsis and terminal positions are the same point, since periplanet is encountered after the spacecraft reappears from behind the planet as viewed from Earth. Thus, the values of position uncertainty in the first and fourth columns are identical. Onboard-

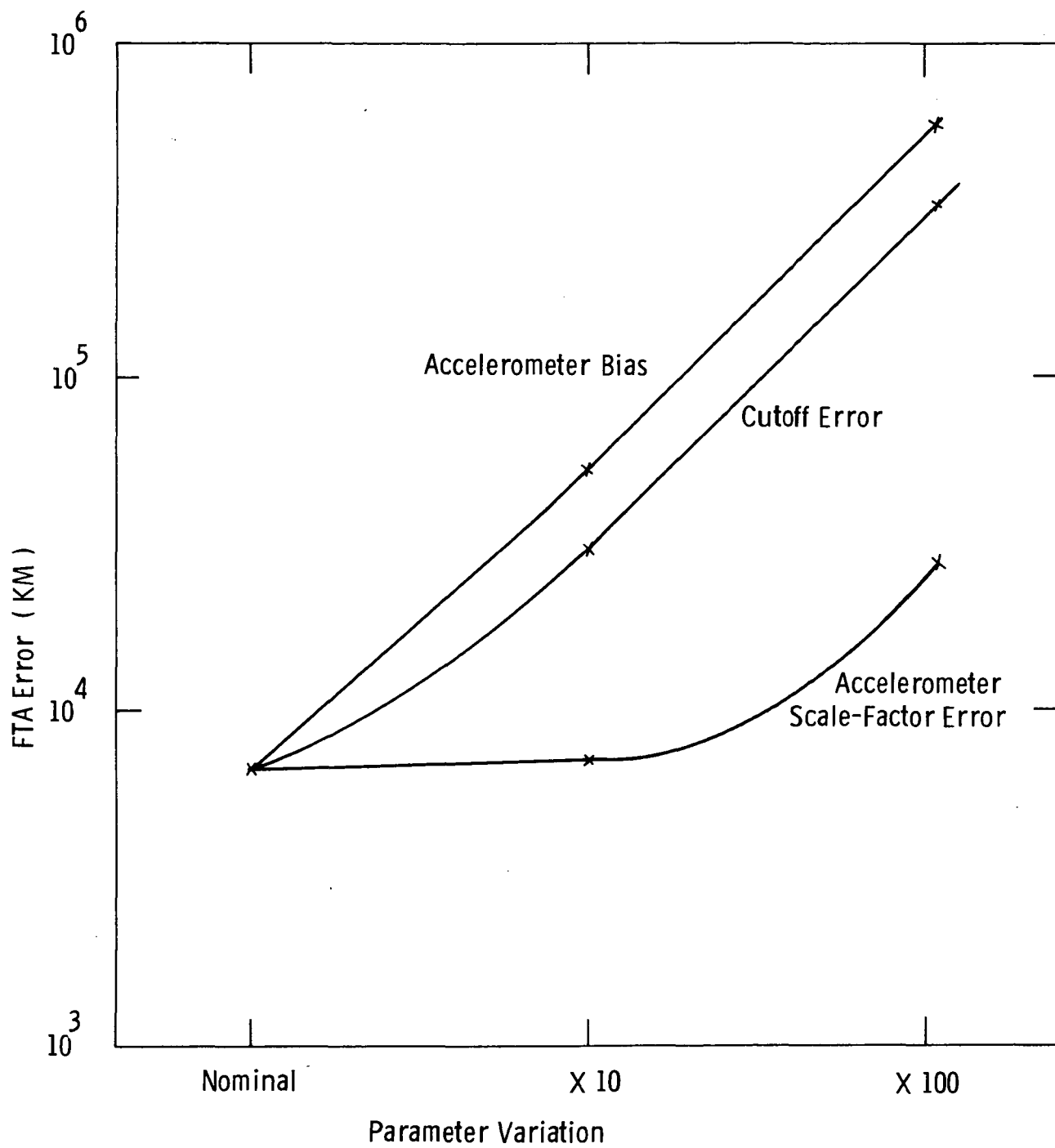


Fig. IV. 3 Sensitivity of FTA Error to Guidance Parameters on Earth-Jupiter Leg

only navigation yields position uncertainties greater by a factor of ten than the DSN-only case. The combined use of DSN and onboard produces the smallest errors. In this instance, the deletion of infrared sensing does not cause larger errors. Inspection of the passage geometry presented in Appendix B reveals that this lack of sensitivity to the availability of an IR sensor probably results from the fact that even though the approach is made to the dark side, a sunlit limb is at almost all times available.

The onboard system alone produces the largest velocity-estimate errors and the largest ephemeris errors. The velocity errors are larger simply because all the onboard-measurement strategies considered here observe directly some component of position; none directly gives any component of velocity. Ground tracking, on the other hand, provides an excellent observation of the component of velocity along the Earth-spacecraft line. The ephemeris error is so large in the onboard-only case because, once the spacecraft is totally affected by the gravity field of Jupiter, there is no reference to any body but Jupiter. Thus, there is no object with which to compare the location of Jupiter. Ground tracking, of course, always has Earth as a reference; once the probe is observed to be under the influence of Jupiter's gravity field, information on the location of Jupiter with respect to Earth can be gathered.

Comparison of the two capabilities shows that in all respects ground-tracking alone is superior to onboard-navigation only. One data point is missing -- the amount to which the out-of-path deviation from the reference trajectory as viewed from Earth is correctable in the DSN-only case. By definition of the variables, this value must be smaller than the position-estimation error of 2.75 km.

Table IV-2 indicates a fairly large discrepancy between the FTA error and the final rms position-estimation error. This difference can be substantially reduced if the final velocity correction is made approximately one-half day before the probe disappears behind Jupiter as viewed from Earth. Table IV-6 summarizes the FTA errors and fuel

TABLE IV-6

FTA Error Obtainable with Final ΔV One-Half

Day Before Spacecraft Passes Behind

Jupiter

Configuration	Minimum Obtainable FTA Error (km)	Total ΔV for Jupiter Passage (mps)
OB Only	445.1	152.4
DSN Only	31.1	6.07
DSN & OB 10'' - no I R	20.0	6.35
DSN & OB 3'' - no I R	18.7	6.11
DSN & OB 1'' - no I R	15.3	4.39
DSN & OB 10'' - 60''	20.0	6.27
DSN & OB 60'' - 60''	20.2	6.54

required for such a strategy. The out-of-path deviation, which is very significant from the standpoint of the occultation experiments, would also be reduced accordingly. Precise figures are not available for this parameter, but a reduction similar to that for the FTA error could be expected.

In general, with respect to navigation on the 1973 Jupiter mission, onboard instruments and the DSN both tend to gain information only in the last ten days, and then very rapidly. As seen in Fig. IV.4, during the last ten days the onboard instrument tends to drop the uncertainties faster, but not by much. The slightly smaller errors obtainable hardly justify the addition of an onboard capability to the Earth-based system.

In addition to the navigation technique involving individual optimal measurements, an additional method was employed for this mission, when onboard-only navigation was employed. As described in section F of Chapter II and in Appendix H, this optimization method uses the original set of measurements, as a starting point, to specify how these measurements might be changed to result in the smallest possible rms terminal position estimation error. Figure IV.5 illustrates the ratio of the rms terminal position estimation errors derivable from each of these methods.* As seen in this figure, the optimization method reduces rms terminal position estimation error by about 20 percent over the first method, by the time the spacecraft reappears from behind Jupiter. Note that the optimization technique is less effective at earlier portions of the mission than at later times, since the method purposefully trades off larger errors at earlier times to yield smaller errors at the terminal time. Also, the large transient near the end results from the fact that most information content occurs at periplanet passage and-- for this mission-- terminal time is at periplanet passage.

Table IV-7 presents the guidance errors associated with a study of the 74-day flyby. The effects of different guidance-parameter values were studied in connection with a single velocity correction made three

*ratio of ($\frac{\text{optimization cost}}{\text{individual measurement cost}}$), with cost being the rms terminal position estimation error.

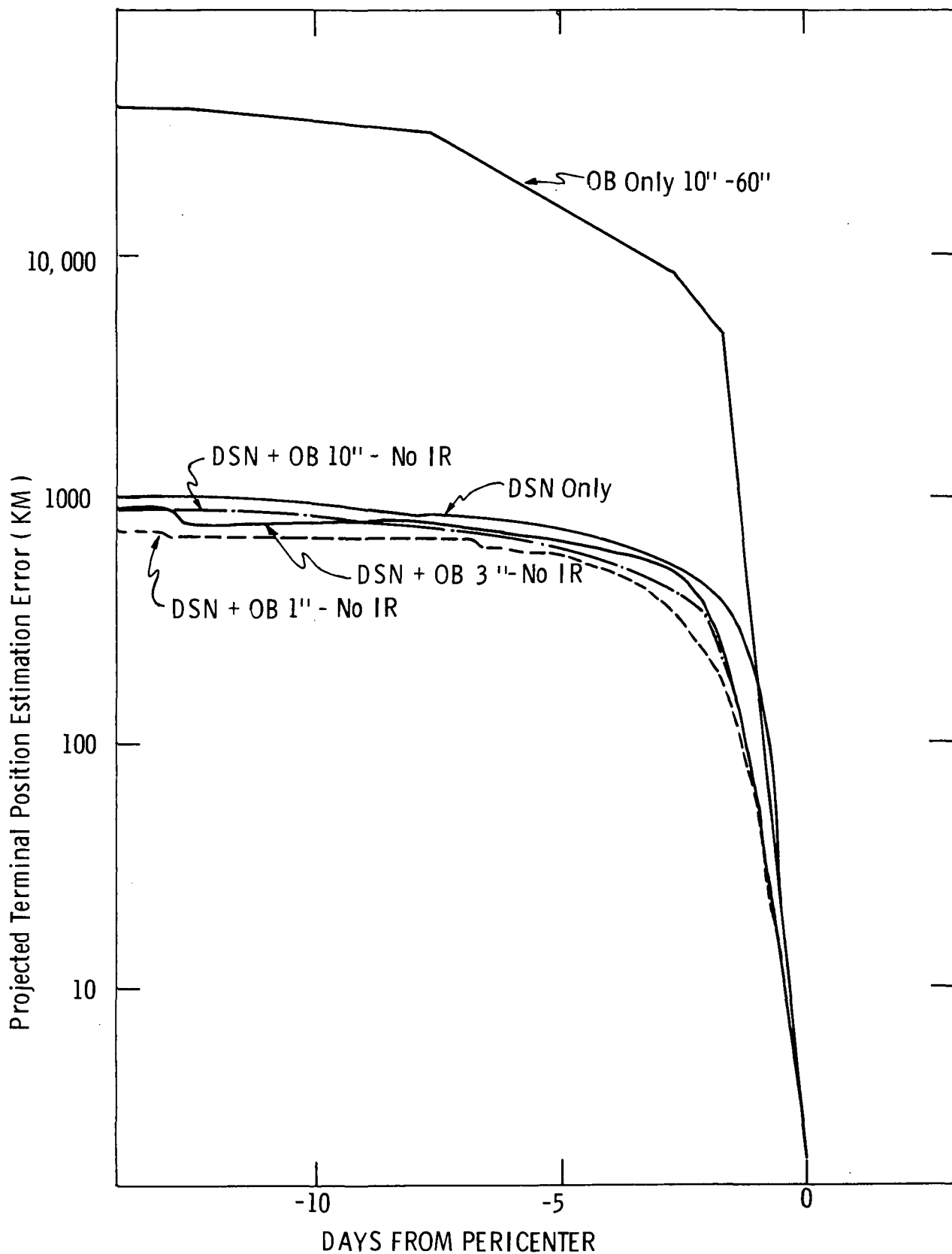


Fig. IV.4 Comparison of Terminal Error Reduction During Jovian Passage

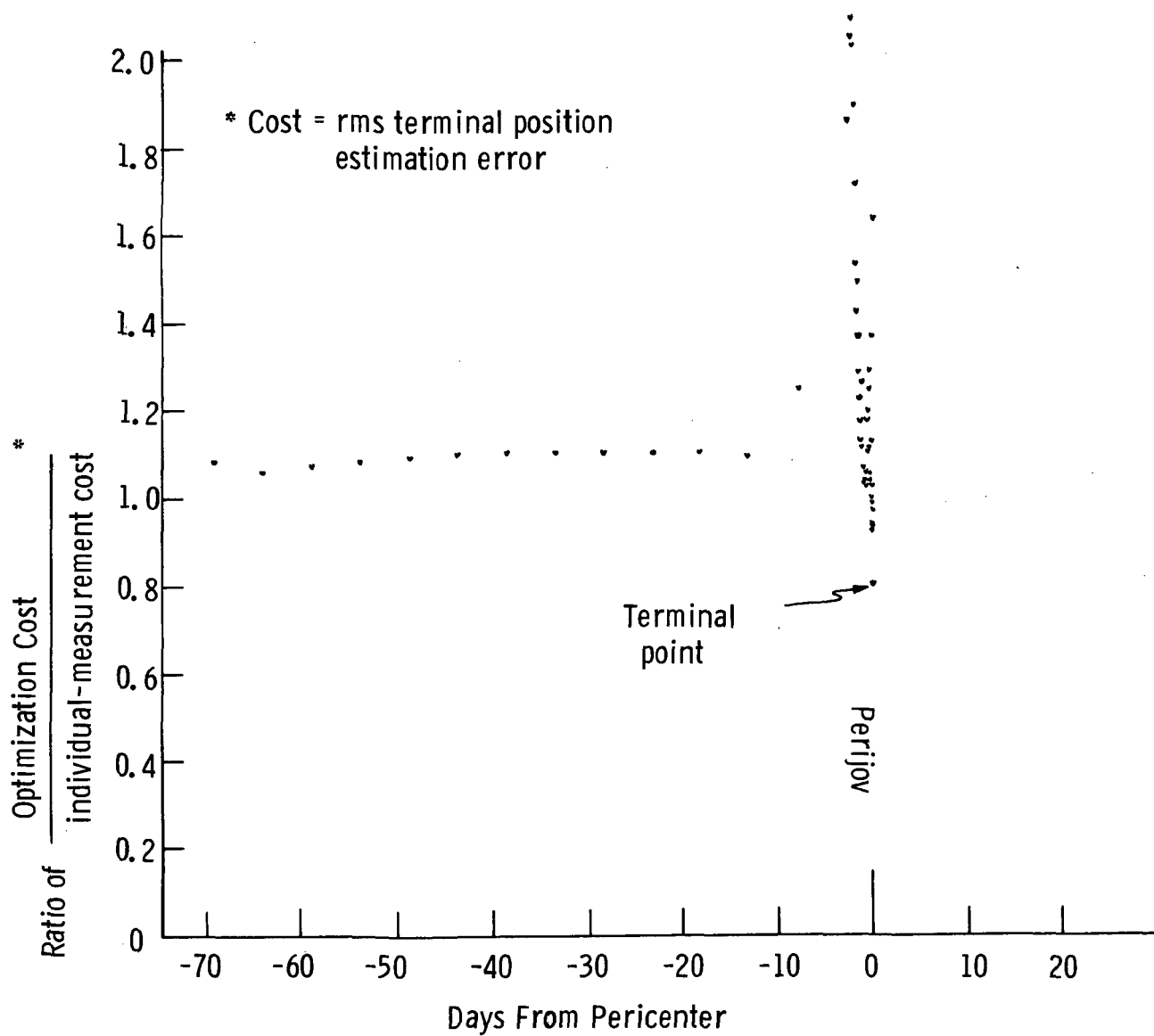


Fig. IV. 5 Comparison of rms Terminal Position Estimation Errors
Derivable through Two Navigation Methods -- Jupiter Flyby

TABLE IV-7

Guidance Error Survey for Jupiter Passage

Configuration	Error Values 40 Minutes Before Pericenter (km)			Terminal Error				ΔV History
	Position Estimate	Out of Path	Out of Path Corrected	RMS Pos. EST (km)	RMS Vel. EST (mps)	FTA (km)	Ephemeris RMS EST (km)	
Nominal	14.29	71.97	14.27	4.57	4.3923	1,577.8	135.3	49.42
Engine Cutoff Uncertainty x 10	14.56	357.42	14.53	4.67	4.4759	10,049.2	136.0	51.41
Engine Cutoff Uncertainty x 100	27.10	3,519.2	27.09	8.85	8.3269	99,754.9	163.2	150.41
Accelerometer Bias x 10	42.92	182.69	42.92	14.15	13.1055	3,837.3	186.5	55.54
Accelerometer Bias x 100	45.09	580.38	45.06	14.90	13.7597	163,995.0	189.3	259.35
Accelerometer Scale Factor x 10	15.05	72.39	15.02	4.83	4.6288	1,585.2	137.1	49.44
Accelerometer Scale Factor x 100	35.29	107.04	35.26	11.59	10.8015	2,233.8	176.5	50.97

days after entering Jupiter's sphere of influence. All these runs used the DSN-only navigation information and were started from the terminal conditions of the Earth-Jupiter leg which had the same guidance errors. In Fig. IV. 6, the out-of-path errors due to guidance effects at +3 days respond strongly to changes in accelerometer bias or cutoff uncertainty. Once again the scale factor has to increase beyond 500 ppm for a significant degradation to occur. Figure IV. 7 shows in the out-of-path corrected plots that the cut-off uncertainty effect can be minimized at ten times the nominal. The ten-times-nominal value for accelerometer bias seems to be out of place. One might ask why the engine cutoff uncertainty doesn't cause a similar increase in error at the ten-times-nominal value as it does for the uncorrected out-of-path error. The answer lies in the fact that the corrected out-of-path error is a function of the state estimation error (the E matrix), whereas the out-of-path miss is a function of the deviations from the reference trajectory (the X matrix). Thrust-tailoff uncertainties contribute to first order to the miss; since they are observable with the accelerometers, however, these uncertainties do not contribute to first order to the estimation error.

Figure IV. 8 depicts FTA guidance errors at mission termination near periapsis. Insensitivity to scale factor is again the dominant result.

Table IV. 8 displays the results of a parametric survey of key DSN parameters for the ground-tracking-only situation. The nominal case, which also appears in Table IV-2, has station-location errors of 1 meter off the spin axis and 2 meters in effective longitude. Continuous tracking with three stations is assumed. The results given in Table IV-8 show that the resulting errors are insensitive to increasing the station-location-errors even up to a factor of 50. However, if the tracking schedule is decreased, the velocity estimation error, ephemeris estimation error and minimum obtainable out-of-path miss distance increase noticeably. The two additional tracking-frequency values listed in Table IV-8 are continuous tracking with one station and one tracking-pass every three days.

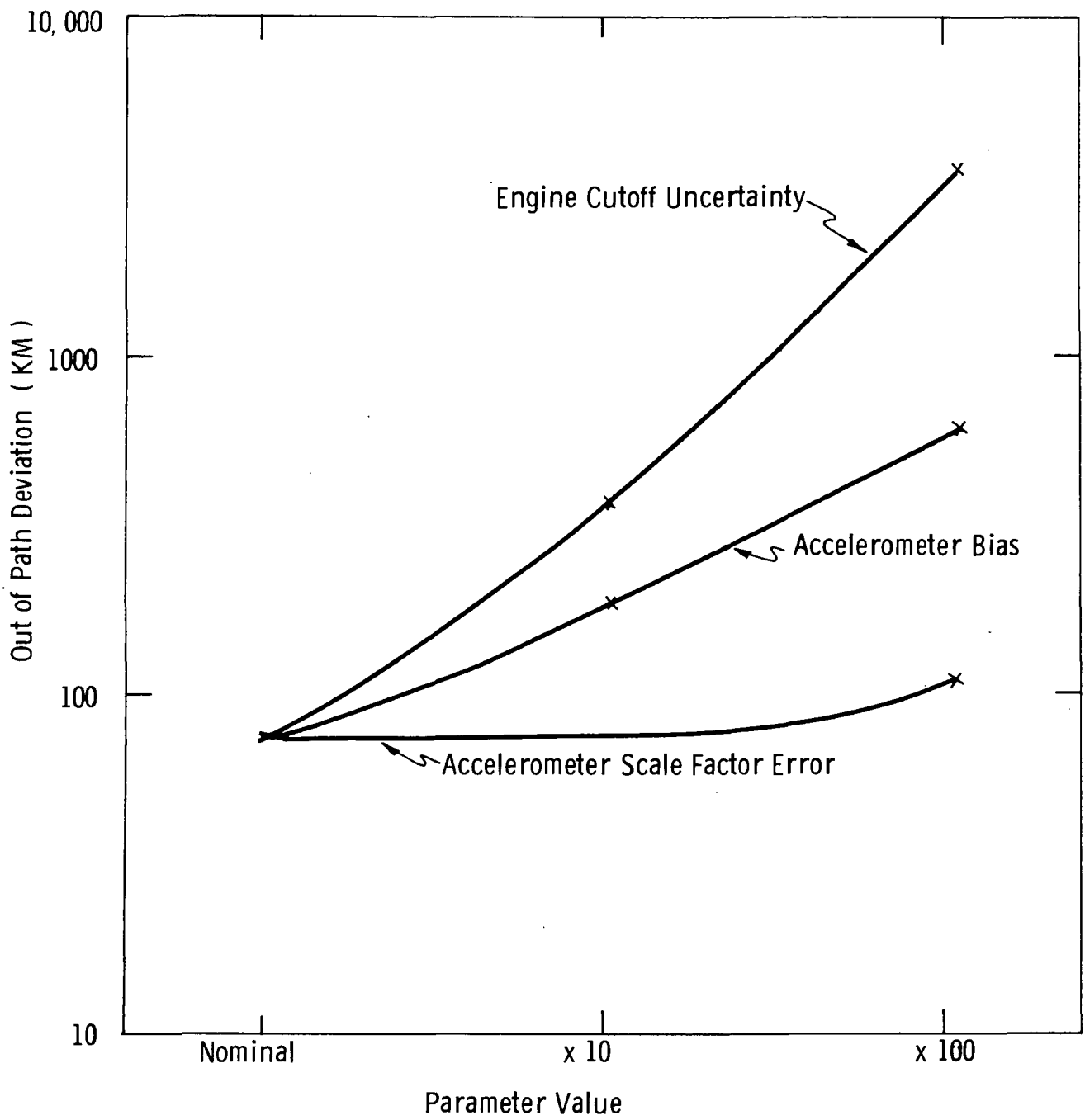


Fig. IV. 6 Sensitivity of out of Path Periapsis Errors to Guidance Parameters

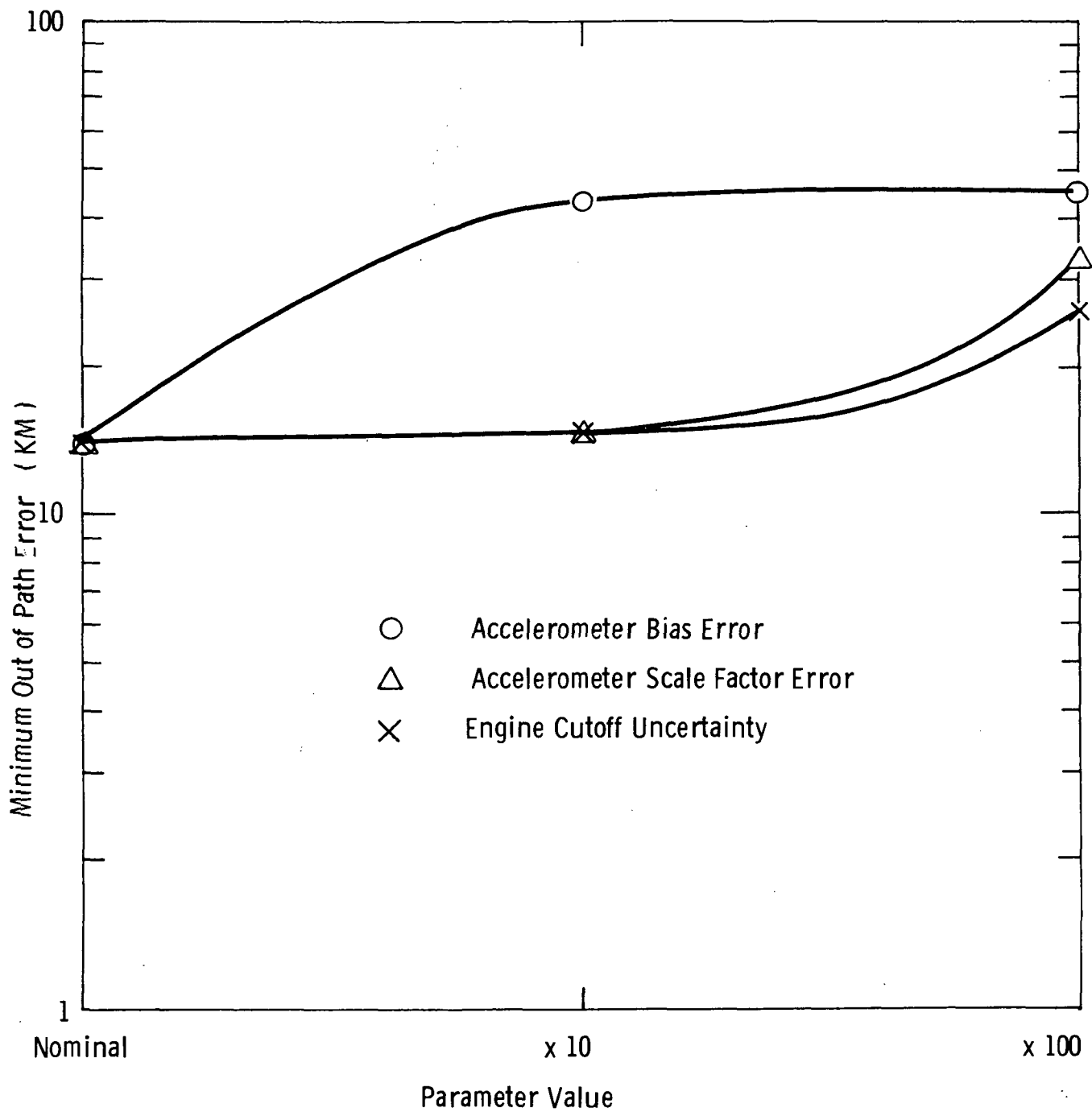


Fig. IV. 7 Sensitivity of Minimum Periapsis out of Path Errors to Guidance Parameters

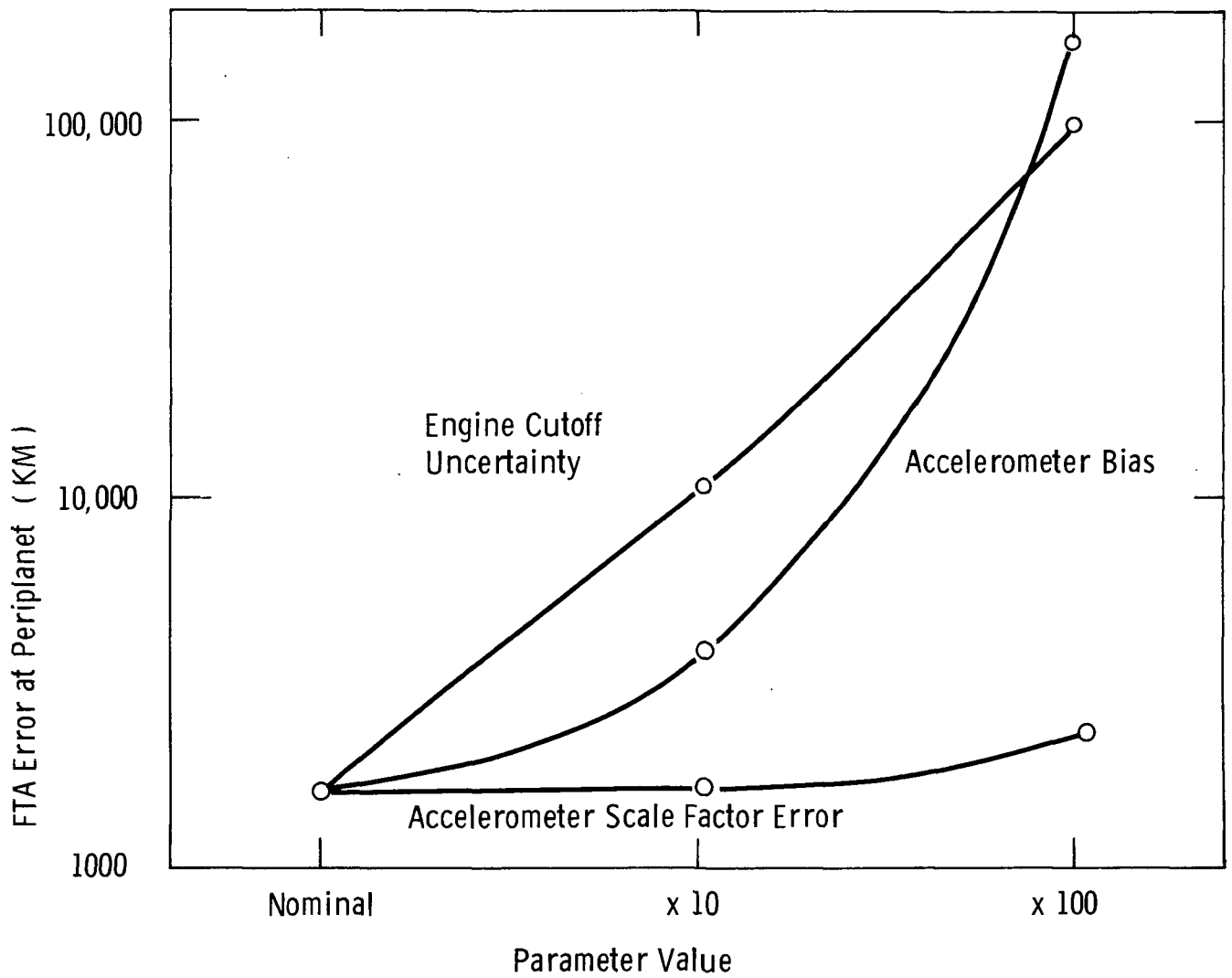


Figure IV.8 Sensitivity of Periapsis FTA Error to Guidance Parameters

TABLE IV-8

DSN Parameter Variation for DSN Only Case

Configuration	Error Values 40 Minutes Before Pericenter (km)			Terminal Error				ΔV History		
	Position Estimate	Out of Path	Out of Path Corrected	RMS Pos. EST (km)	RMS Vel. EST (mps)	FTA (km)	Ephemeris RMS EST (km)	No.	Total ΔV (mps)	Time of Last ΔV (Days)
Nominal	2.85	42.31	8.72	2.75	2.70	723.2	83.8	2	2.31	70
Station Location Errors x 10	9.29	43.58	9.25	2.96	2.85	739.2	90.3	2	2.31	70
Station Location Errors x 50	9.32	43.66	9.29	2.99	2.88	740.5	91.2	2	2.31	70
One Pass Per Day	13.15	42.63	13.13	4.12	4.03	722.6	112.8	2	3.02	70
One Pass Per Three Days	18.89	41.68	18.88	5.99	5.87	690.4	145.2	2	3.22	71.184

To summarize requirements for the 1973 Jupiter flyby, attention needs to be focussed on the passage of the planet itself. DSN-only navigation as described in Table IV-2 yields uncertainties in position, velocity, and ephemeris which are not excessive. The onboard-only case has large uncertainties and is unacceptable because of its poor performance on the interplanetary leg. The combination of onboard and DSN should be considered only if it is necessary to reduce the ephemeris error early in the encounter, as seems unlikely. The sensitivity of instrument design to early reduction of ephemeris error seems low and the 60" - 60" instrument is adequate to reduce the errors to the same order of magnitude as the 10" - 60" instrument.

The major issue in the guidance area is the use of an accelerometer to control engine shutdown as opposed to open-loop timing of propulsion on-time with no accelerometers. The guidance study assumed an accelerometer along the thrust direction with bias and scale-factor errors, and, in addition, an uncertainty in implementing cutoff via accelerometer command based on uncertainty in the actual cutoff pattern.

The results show that guidance errors are extremely responsive to bias and cutoff-time uncertainties, but not to changes in scale factor. An accelerometer is required, although 50 ppm scale factor is not needed. However, such a scale factor would be the concomitant result of requiring the bias to be at a nominal level of 100 micro-g's or better. Such an instrument is within the state of the art and could have a high probability of surviving the 800 - odd days of the 1973 mission. Table IV-9 contains the nominal parameters for such an accelerometer. Though maintenance of low uncertainties in engine cutoff implementation is a problem beyond the scope of this study, this error source may be of equal importance to accelerometer-bias effects.

TABLE IV-9

Nominal Accelerometer Parameters

Wt.	1.1 Kg
Size	1196.47 cm ³
Power	6.5 watts + 1 watt for Thermal Control

Page intentionally left blank

CHAPTER V

SYSTEM REQUIREMENTS FOR THE 1973 JUPITER SWINGBY TO SATURN

This chapter presents the simulation results of the 1977 Jupiter swingby to Saturn and discusses their implication on systems and mission requirements. Tables V-1 through V-4, containing the simulation results, use the same format as Tables IV-1 and IV-2.

Inspection of Tables V-1 and V-3 immediately reveals that navigating on either interplanetary leg with only an onboard navigation system yields far poorer results than using Earth-based tracking alone. This conclusion is true both in terms of navigational errors and fuel consumption. The poor performance of the onboard system results from the extremely large distances to the nearest navigational targets encountered during the interplanetary phases of this mission.

Reduction of ephemeris error upon activation of the onboard navigation system prevails on the Earth-Jupiter leg of this mission just as it did on the same leg of the Jupiter flyby mission. This pattern also repeats on the Saturn approach of the Jupiter-Saturn leg of this mission. The percentage reduction in error is greater on the Saturn approach than the Jupiter approach because the ephemeris error for Saturn is larger than that for Jupiter, and the onboard system can be effective sooner. Tables V-2 and V-4 show, however, that by waiting until the spacecraft is within the sphere of influence of either of these planets, the ephemeris error can be reduced still further. It may be concluded therefore, that unless there is a need to reduce the ephemeris error early in the encounter, an onboard system need not be used during the interplanetary legs of this mission.

TABLE V-1

Earth - Jupiter Interplanetary Leg of the 1977 Saturn Flyby Mission

Configuration	Terminal Errors					ΔV History			
	RMS Pos. EST (km)	RMS Vel. EST (mps)	FTA (km)	RMS EPH. EST (km)	Total No.	Initial ΔV mps	Total ΔV mps	Time of Last ΔV Days	
OB Only	14,033.75	0.4991	23,314.5	554.4	3	74.66 *	81.03	310	
DSN Only	558.14	0.000304	559.4	557.6	8	52.83 **	55.997	504	
DSN & OB 10" - 60"	546.45	0.00021	1,177.2	546.02	4	52.83 **	55.55	340	
DSN & OB 3" - 60"	484.51	0.00021	1,177.2	484.01	4	52.83 **	55.55	340	
DSN & OB 1" - 60"	383.62	0.00024	603.3	382.98	5	52.83 **	55.69	426	

* at 70 Days

** at 2 Days

Time to Sphere of Influence - 513 Days.

TABLE V-2

Near Planet Results for Jupiter Passage of 1977 Saturn Flyby Mission *

Configuration	Periapsis Error Values (km)			Terminal Error				ΔV History		
	Position Estimate	Out of Path	Out of Path Corrected	RMS Pos. EST (km)	RMS Vel. EST (mps)	FTA (km)	Ephemeris RMS EST (km)	No.	Total ΔV mps	Time of Last ΔV Days
OB only	16.06	117.69	5.84	796.37	0.1786	1614.8	556.029	5	28.25	49.75
DSN Only	21.21	50.86	21.16	233.69	0.0521	340.5	75.2	5	9.43	86.88
DSN & OB 10" - No. IR	2.57	21.07	2.37	227.95	0.0507	273.9	75.3	6	4.98	92.81
DSN & OB 3" - No. IR	1.38	7.15	0.93	129.50	0.0297	233.7	75.3	7	1.99	59.42
DSN & OB 1" - No. IR	1.17	5.02	0.56	84.04	0.0204	203.9	75.5	8	1.72	59.42
DSN & OB 10" - 60"	2.33	15.95	2.09	225.61	0.0502	265.2	74.2	6	3.57	92.81
DSN & OB 60" - 60"	3.12	18.20	2.96	230.84	0.0514	693.5	75.3	5	2.80	50.04

*Terminal Time = 99.5 Days. Pericenter Time = 49.75 Days

TABLE V-3

Near Planet Results for Jupiter Passage of 1977 Saturn Flyby Mission*

Configuration	Terminal Errors					ΔV History		
	RMS Pos. EST (km)	RMS Vel EST (mps)	FTA (km)	RMS EPH. EST (km)	Total No.	Total mps	Time of Last ΔV Days	
OB Only	3915.86	0.0761	4343.6	626.8	2	10.33	585	
DSN Only	1202.75	0.0052	1274.9	1160.0	4	1.02	508	
DSN & OB 10" - 60"	1119.74	0.0052	1274.9	1074.7	4	1.02	508	
DSN & OB 3" - 60"	808.33	0.0050	1274.9	748.3	4	1.02	508	
DSN & OB 1" - 60"	556.43	0.0049	1274.9	469.1	4	1.02	508	

*Time to Sphere of Influence - 602 Days.

TABLE V-4

Near Planet Results for Jupiter Passage of 1977 Saturn Flyby Mission*

Configuration	Periapsis Error Values (km)			Terminal Error				ΔV History		
	Position Estimate	Out of Path	Out of Path Corrected	RMS Pos. EST (km)	RMS Vel. EST (mps)	FTA (km)	Ephemeris RMS EST (km)	No.	Total (mps)	Time of Last ΔV Days
OB only	86.34	685.40	49.62	20.31	3.19	4801.2	627.2	1	7.48	5.06
DSN Only	48.20	308.45	40.56	16.38	5.78	1287.5	257.3	0		
DSN & OB 10" - No. IR	13.81	241.39	6.45	7.56	0.64	540.6	255.7	1	2.79	37
DSN & OB 3" - No. IR	10.03	130.53	3.44	6.18	0.39	566.7	255.6	1	0.68	22
DSN & OB 1" - No. IR	8.03	288.57	2.30	5.78	0.31	160.5	254.9	3	5.85	40.93
DSN & OB 10" - 60"	14.76	239.07	6.78	7.89	1.50	532.1	253.0	1	2.80	37
DSN & OB 60" - 60"	28.97	2776.8	25.28	9.19	0.56	552.6	256.2	1	32.71	40.93

*Terminal Time = 43.12 Days. Pericenter Time = 42.81 Days

Table V-1 shows that, in two cases, the automatic velocity-correction scheduling algorithm did not select any midcourse corrections on the Earth-Jupiter leg in time for the advantages of the onboard instrument to appear in the FTA guidance result. This occurred in all cases on the Jupiter-Saturn leg, as seen from Table V-3. Tables V-5 and V-6 show that if a correction is made at 504 days on the Earth-Jupiter leg and 585 days into the Jupiter-Saturn leg, this benefit can be realized. The entries in Tables V-1 and V-5 include a correction of approximately 53 meters per second to remove transplanetary-injection errors.

Figures V.1 and V.2 illustrate the time history of the reduction of projected rms terminal position estimation error with increasing mission time for the case of ground-tracking-only. Figure V.1 deals with the Earth-Jupiter leg and Figure V.2 gives results for the Jupiter-Saturn leg. On the Earth-Jupiter leg the error very rapidly drops to the Jupiter ephemeris error, whereas on the Jupiter-Saturn leg it takes almost 400 days to achieve this effect. The reason is that the ability of the ground-tracking system to determine position is inversely proportional to the Earth-spacecraft separation. At the beginning of the mission, the probe is extremely close to Earth; hence the rapid reduction of errors. This favorable situation does not occur, of course, on the Jupiter-Saturn leg.

One might ask why, if tracking has been continuous since leaving Earth, a reduction of errors the size of that indicated in Figure V.2 is possible on the Jupiter-Saturn leg. The primary reason is that during the encounter with Jupiter, the mass uncertainty and trajectory dynamics of Jupiter cause the error to grow faster than tracking can drive it down. This can be seen by comparing the terminal- and periapsis-position errors in Table V-2 for the DSN-only case. When the probe leaves Jupiter, this perturbation is removed and the error can be reduced over the course of 400 days.

The major difference between the Jupiter-passage results on this mission and those on the similar passage of the mission treated in Chapter IV is that onboard-only navigation is competitive with DSN-only navigation

TABLE V-5

Fuel Requirements for Minimum FTA Error
on the Earth to Jupiter Leg
(Correction Made at 504 Days)

Configuration	Minimum FTA Error (km)	Total Fuel Consumed on Leg (mps)
OB Only	14,149	97.20
DSN only	559.4	55.997
DSN & OB 10" - 60"	547.7	57.01
DSN & OB 3" - 60"	486.2	57.05
DSN & OB 1" - 60"	386.2	56.30

TABLE V-6

Fuel Requirements for Minimum FTA
 Error on the Jupiter to Saturn Leg
 (Correction Made at 585 Days)

Configuration	Minimum FTA Error (km)	Total Fuel Consumed on Leg (mps)
OB Only	4343.6	10.33
DSN only	1204.9	1.32
DSN & OB 10" - 60"	1163.1	1.32
DSN & OB 3" - 60"	923.0	1.33
DSN & OB 1" - 60"	687.2	1.33

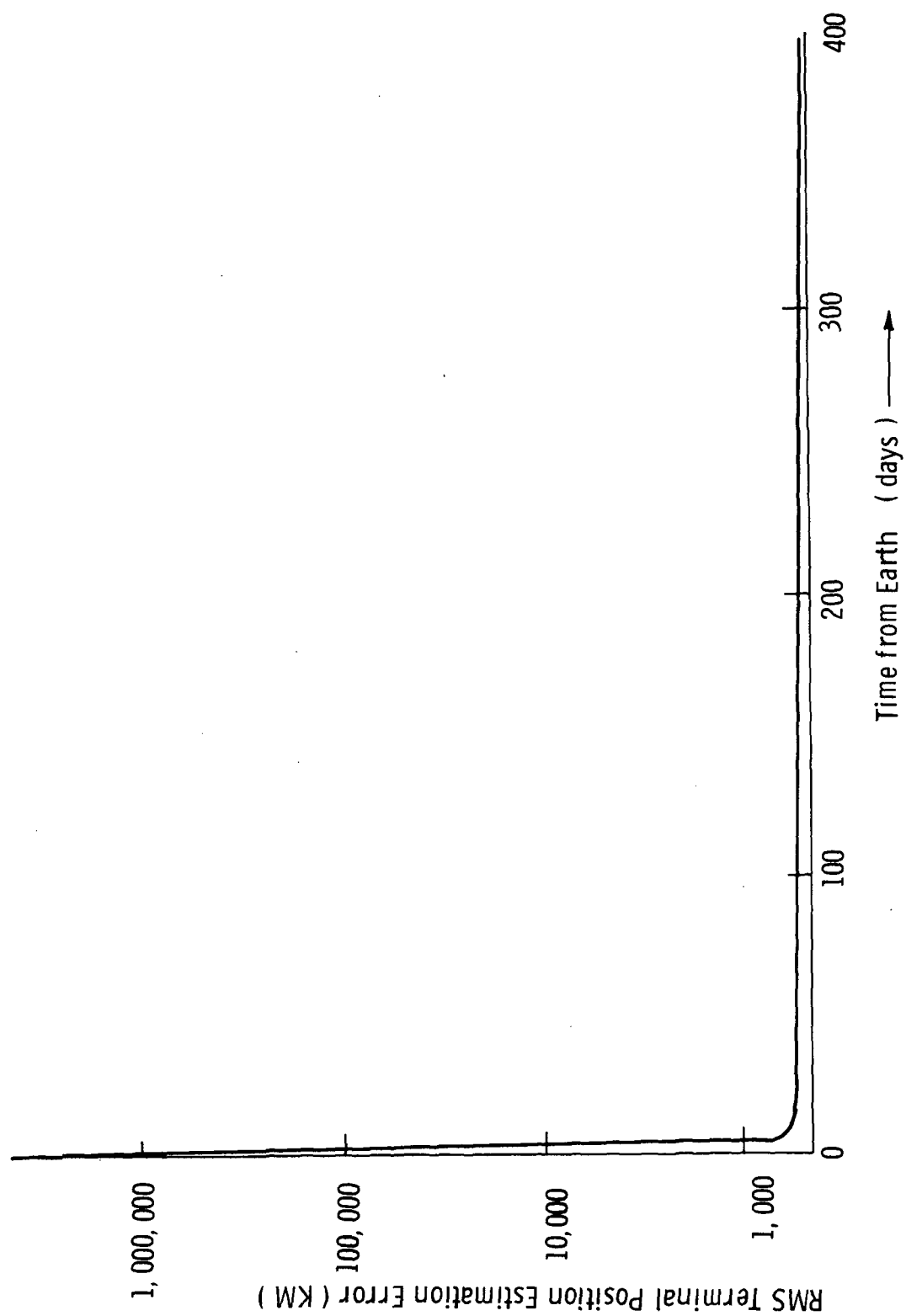


Fig. V. 1 Reduction of the Terminal Error with the DSN Only for the Earth to Jupiter Leg
of the Jupiter Swingby to Saturn

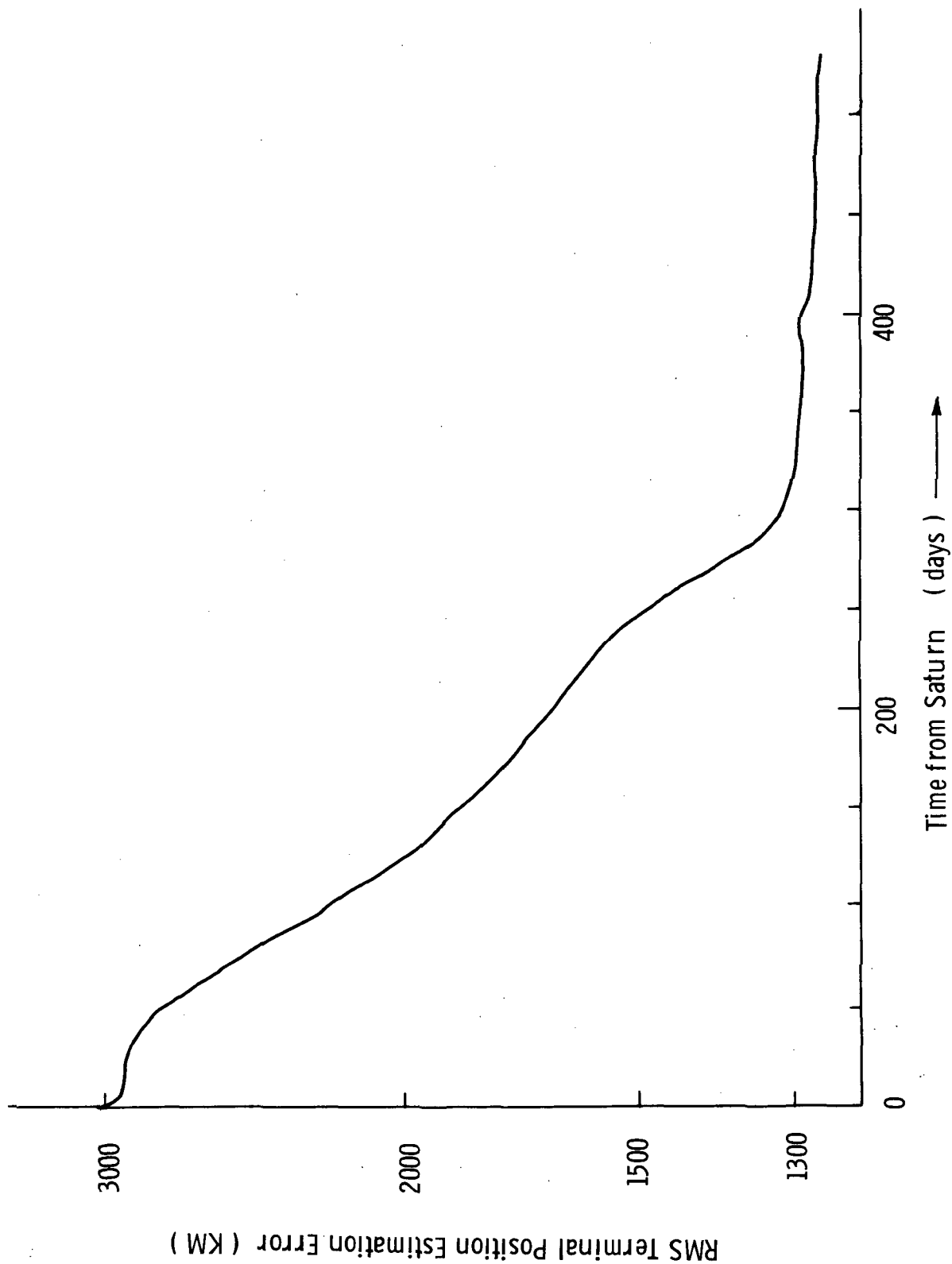


Fig. V.2 Reduction of the Terminal Error with the DSN Only for the Jupiter to Saturn Leg of the Jupiter Swingby to Saturn

when comparing errors at periplanet, particularly at Saturn. The blending of information from ground-tracking and onboard systems gives a noticeable improvement over either alone if periplanet errors are compared. Terminal-error improvement can also be achieved with the combined use of DSN and onboard systems, but only if the onboard system includes very precise visible-spectrum instruments. The onboard system does not actually work better on the mission than on the Jupiter flyby, but ground tracking is less effective because of the shorter time spent in travel from the sphere of influence to the periplanet position.

The small reduction of errors obtainable by combining onboard and ground-tracking capabilities seems to be the main benefit from using an onboard system on the first two legs of this mission. No noticeable fuel saving is gained and the early reduction of the ephemeris error probably does not justify the addition of the extra navigation capability.

In regard to the Saturn flyby summarized in Table V-4, the very small navigational errors characteristic of every periplanet point examined thus far are prevalent. The use of ground tracking during the close passage provides a means of substantially reducing the ephemeris error for Saturn. Comparison with the corresponding entries in Table VI-4 shows that the closer passage on the 1977 Grand Tour mission provides an even better opportunity to reduce the error. In both cases, however, the onboard system adds nothing to the ability to learn about the planetary ephemeris, since the location of Saturn (or of any other planet) with respect to the Earth or sun is not observable with an onboard capability unless the system sights on one of these latter two bodies. Unfortunately, they are so distant that the measurement is too noisy to be useful.

The onboard navigation system can determine the state with respect to the planet at periplanet passage so precisely because the vehicle is very close to the near body. Ground tracking is accurate at this point because on these hyperbolic flybys there is a very high angular velocity at periplanet passage. Examining the errors further out, as at the outbound intersection with the sphere of influence on the Jupiter passage of this mission, shows that neither system is

capable of reducing errors faster than the mass uncertainty and trajectory dynamics increase them.

There is substantial difference between the FTA errors and position-estimation errors for the terminal time on the Saturn passage. These could be reduced if a midcourse correction is made, for example, six hours before the probe disappears behind Saturn as viewed from Earth. These results are displayed in Table V-7. Although the data is not available, a similar reduction in the out-of-path error should also be expected. It is evident from this table that a substantial reduction in both terminal miss at Saturn and fuel required in the Saturn passage can result if the following conditions are met:

1. An onboard system with a visible-spectrum instrument of 10 seconds of arc capability or better is available.
2. A midcourse correction near periplanet is permissible.

The error reduction, but not the fuel saving, is still possible with instruments of only one-arc-minute capability.

Examining which measurement types and navigational bodies are favored, we find that planet/moon diameter measurements are rejected because the large phenomenon uncertainty associated with two edge sightings is noncompetitive during the points of closest approach when they might otherwise be useful. The light-side approaches to both planets on this mission also do not provide much opportunity for the use of star occultations.

At Jupiter, Ganymede can be used as a near body when it is closely passed, but only if an IR capability is available. Canopus is used frequently but not exclusively on all legs as a navigational star if ground tracking is active, thus indicating that a good way for the onboard capability to augment the ground-tracking function is by providing out-of-the-ecliptic positional information. Mars is used when it is the closest body and DSN capability is assumed, but it was found to be of little practical significance.

Returning to the question of implementing an onboard-system capability with a midcourse correction near periplanet, let us examine the case of DSN-only navigation compared with DSN and onboard, 1" - 60".

TABLE V-7

Terminal FTA Errors for Final ΔV 6 Hours Before
Spacecraft Passes behind Saturn

Configuration	FTA Error (km)	Total ΔV During Saturn Passage (mps)
OB Only	197.37	8.21
DSN Only	485.73	30.79
DSN & OB 10'' - No. I. R.	43.00	18.09
DSN & OB 3'' - No I. R. q	22.79	11.63
DSN & OB 1'' - No I. R.	18.56	22.37
DSN & OB 10'' - 60''	41.49	18.00
DSN & OB 60'' - 60''	55.39	189.49

A tradeoff is evaluated in Table V-8, based on ΔV results from Tables V-1, V-2, and V-3, and V-7. An initial spacecraft total weight is assumed and the rocket equation is applied for successive mission phases until the amount of fuel required for all phases is known. Subtracting total fuel from the initial gross weight gives the spacecraft dry weight. The increase in dry weight for the DSN and onboard case is a measure of the navigation-capability weight allowance available for increased accuracy, given in Table V-7. An examination of Table V-8 reveals that in no case will the fuel saving clearly buy the advantages of the onboard navigation instrument.

In conclusion, this study has shown that for the 1977 Saturn flyby, an onboard system can reduce the final FTA error, in all cases, by an order of magnitude. It has also shown, however, that the onboard system will not pay for itself in fuel savings.

TABLE V-8.
1977 Saturn Flyby Spacecraft Mass Estimates

	Velocity Budget (mps)	Final Mass (kg) at End of Each Mission Phase					
		Initial Mass 226.80 kg		Initial Mass 453.60 kg		Initial Mass 2267.99 kg	
	DSN Only	DSN Only	DSN & OB 1" - 60"	DSN Only	DSN & OB 1" - 60"	DSN Only	DSN & OB 1" - 60"
Earth-Jupiter	56.00	220.23	220.21	440.47	440.43	2202.3	2202.1
Jupiter Passage	9.43	219.17	220.02	438.35	440.05	2191.7	2200.3
Jupiter-Saturn	1.01	219.06	219.91	438.12	439.82	2191.7	2199.1
Saturn Passage	30.79	215.60	217.39	431.19	434.78	2156.2	2173.9
Mass Savings in kg over DSN only			1.79		3.59		17.64

Applicable Equation:

$$\frac{M_N}{M_N + 1} = \exp\left(-\frac{\Delta V}{I_{sp} g}\right), \text{ where } I_{sp} = 200 \text{ seconds.}$$

Page intentionally left blank

CHAPTER VI

SYSTEM REQUIREMENTS FOR THE 1977 GRAND TOUR

This chapter presents the results of the simulation study of the 1977 Grand Tour mission and discusses their implication on systems and mission requirements. The first part of the chapter delves into the reasons behind several key simulation results, and the second part emphasizes how these results might affect onboard system configuration and mission operation. Because of the different emphasis of the two sections, some overlapping of reference to specific results necessarily occurs.

A. Key Simulation Results

Tables VI-1 through VI-8 present the results of the Grand Tour mission in the same format used for the previous missions. These tables show that navigation on interplanetary legs with only an onboard system is substantially inferior to determining vehicle location with the deep space network alone. Inspection of the tables which pertain to the interplanetary legs demonstrates that ground tracking reduces the error to approximately the ephemeris error by the time the spacecraft arrives at the planetary sphere of influence. The onboard-only configuration, however, has terminal errors at this point of from 3000 to 8500 miles. The poor performance of the onboard system results from the large ranges to the navigational bodies encountered on these outer-planet missions. For example, at 1-a.u. range, a 10-arc-second pointing error amounts to a 4500-mile error. Inspection of the range data of Appendix A reveals that the range to the nearest planet frequently exceeds this 1-a.u. value.

Table VI-1 shows that using an onboard system at the end of an interplanetary leg, together with ground-tracking capability, results in

TABLE VI-1

Earth - Jupiter Interplanetary Leg of the 1977 Grand Tour Mission*

Configuration	Terminal Errors					ΔV History			
	RMS Pos. EST (km)	RMS Vel EST (mps)	FTA (km)	RMS EPH. EST (km)	Total No.	Initial ΔV mps	Total ΔV (mps)	Time of Last ΔV Days	
OB Only	12747.83	0.4893	19659.0	551.4	3	75.16 *	81.2	290	
DSN Only	555.48	0.00027	556.4	555.1	8	52.79 **	55.96	453	
DSN & OB 10" - 60"	530.30	0.00015	1007.8	530.0	4	52.79 **	55.52	310	
DSN & OB 3" - 60"	440.91	0.00015	1007.8	440.5	4	52.79 **	55.52	310	
DSN & OB 1" - 60"	279.69	0.00024	459.3	278.9	5	52.79 **	55.71	407	

* at 70 days

** at 2 days

Time to Sphere of Influence - 460.5 Days.

TABLE VI-2

Near Planet Results for Grand Tour Mission, Jupiter Passage^{*}

Configuration	Periapsis Error Values (km)			Terminal Error				ΔV History		
	Position Estimate	Out of Path	Out of Path Corrected	RMS Pos. EST (km)	RMS Vel. EST (mps)	FTA (km)	Ephemeris RMS EST (km)	No.	Total ΔV (mps)	Time of Last ΔV Days
OB only	31.99	11212.3	14.65	815.18	0.2144	1166.0	553.5	6	31.24	43.23
DSN Only	13.53	229.20	9.50	190.79	0.0497	303.0	71.8	6	8.74	70.31
DSN & OB 10" - No. IR	1.51	224.18	1.03	189.90	0.0495	491.2	71.8	6	3.73	42.73
DSN & OB 3" - No. IR	1.03	221.27	0.66	130.98	0.0342	212.0	71.8	7	2.68	51.31
DSN & OB 1" - No. IR	0.93	201.60	0.60	68.78	0.0181	91.2	71.9	9	2.30	72.31
DSN & OB 10" - 60"	1.45	280.57	0.98	190.79	0.0497	422.6	69.4	6	3.35	44.06
DSN & OB 60" - 60"	2.61	225.50	1.82	190.66	0.0497	372.7	71.8	6	3.79	65.31

^{*}Terminal Time = 84.86Days. Pericenter Time =42.43 Days.

TABLE VI-3

Jupiter - Saturn Interplanetary Leg of the 1971 Grand Tour Mission*

Configuration	Terminal Errors				ΔV History		
	RMS Pos. EST (km)	RMS Vel EST (mps)	FTA (km)	RMS EPH. EST (km)	Total No.	Total ΔV (mps)	Time of Last ΔV Days
OB Only	4811.48	0.1003	11351.7	1126.0	1	3.67	1
DSN Only	1173.07	0.0034	1227.8	1159.8	4	0.82	466
DSN & OB 10" - 60"	1106.49	0.0034	1404.0	1092.4	3	0.71	372
DSN & OB 3" - 60"	791.09	0.0033	1404.0	771.5	3	0.71	372
DSN & OB 1" - 60"	439.40	0.0037	486.3	403.8	4	2.38	524

*Time to Sphere of Influence - 543 Days.

TABLE VI-4

Near Planet Results for Grand Tour Mission, Saturn Passage*

Configuration	Periapsis Error Values (km)			Terminal Error					ΔV History		
	Position Estimate	Out of Path	Out of Path Corrected	RMS Pos. EST (km)	RMS Vel. EST (mps)	FTA (km)	Ephemeris RMS EST (km)	No.	Total ΔV (mps)	Time of Last ΔV Days	
OB only	22.18	57.29	2.06	1005.13	0.3147	1546.7	1115.3	7	33.58	37.60	
DSN Only	105.72	326.87	105.48	1481.55	0.4708	2835.02	203.3	5	123.80	52.72	
DSN & OB 10" - No. IR	9.51	14.87	1.40	950.06	0.3043	1387.3	203.1	6	19.76	37.35	
DSN & OB 3" - No. IR	9.12	5.15	0.90	829.17	0.2669	1282.01	202.9	6	8.5	37.10	
DSN & OB 1" - No. IR	9.90	5.70	0.24	844.12	0.2720	1892.59	202.5	6	3.9	36.75	
DSN & OB 10" - 60"	11.70	16.79	1.40	986.21	0.3159	1397.2	198.4	6	21.3	37.47	
DSN & OB 60" - 60"	12.79	30.06	4.52	1353.96	0.4307	2506.9	203.3	5	41.7	38.72	

*Terminal Time = 73.36 Days. Pericenter Time = 36.68 Days.

TABLE VI-5

Saturn - Uranus Interplanetary Leg of the 1977 Grand Tour Mission*

Configuration	Terminal Errors					ΔV History		
	RMS Pos. EST (km)	RMS Vel EST (mps)	FTA (km)	RMS EPH. EST (km)	Total No.	Total ΔV (mps)	Time of Last ΔV Days	
OB Only	13533.48	0.1318	34224.2	2018.3	1	1.46	20	
DSN Only	2075.95	0.0037	2128.04	2040.5	7	4.11	10.88	
DSN & OB 10" - 60"	1780.42	0.0037	2128.04	1739.7	7	4.11	10.88	
DSN & OB 3" - 60"	1071.55	0.0037	2128.04	1004.4	7	4.11	10.88	
DSN & OB 1" - 60"	726.33	0.0037	2128.04	623.9	7	4.11	10.88	

*Time to Sphere of Influence -1193 Days.

TABLE VI-6

Near Planet Results for Grand Tour Mission, Uranus Passage*

Configuration	Periapsis Error Values (km)			Terminal Error					ΔV History		
	Position Estimate	Out of Path	Out of Path Corrected	RMS Pos. EST (km)	RMS Vel. EST (mps)	FTA (km)	Ephemeris RMS EST (km)	No.	Total ΔV (mps)	Time of Last ΔV Days	
OB only	40.76	589.36	3.43	909.23	0.3794	1008.1	2025.8	11	112.58	33.03	
DSN Only	236.41	315.87	235.88	1071.99	0.4468	2037.1	425.4	6	249.03	40.53	
DSN & OB 10" - No. IR	8.06	35.44	2.04	901.03	0.3755	1345.09	426.2	7	26.1	28.05	
DSN & OB 3" - No. IR	7.39	19.91	1.29	763.64	0.3183	1835.6	427.4	6	11.53	27.83	
DSN & OB 1" - No. IR	6.74	18.49	1.32	572.32	0.2387	1114.2	427.9	7	7.74	28.03	
DSN & OB 10" - 60"	8.93	22.51	2.01	860.86	0.3587	1390.0	408.9	7	18.34	28.00	
DSN & OB 60" - 60"	10.48	97.29	5.18	1028.61	0.4288	1101.0	425.02	7	89.51	53.53	

*Terminal Time = 55.58 Days. Pericenter Time = 27.78 Days.

TABLE VI-7

Uranus - Neptune Interplanetary Leg of the 1977 Grand Tour Mission*

Configuration	Terminal Errors				ΔV History		
	RMS Pos. EST (km)	RMS Vel EST (mps)	FTA (km)	RMS EPH. EST (km)	Total No.	Total ΔV (mps)	Time of Last ΔV Days
OB Only	9698.79	0.1116	12033	3151.3	2	19.24	925
DSN Only	3660.67	0.0209	4768.7	3201.8	4	5.04	976
DSN & OB 10" - 60"	3370.29	0.0209	4768.7	2869.0	4	5.04	476
DSN & OB 3" - 60"	2414.37	0.0174	4768.7	1920.0	4	5.04	476
DSN & OB 1" - 60"	2137.70	0.0171	4768.7	1589.0	4	5.04	476

*Time to Sphere of Influence - 951 Days.

TABLE VI-8

Near Planet Results for Grand Tour Mission, Neptune Passage *

Configuration	Periapsis Error Values (km)			Terminal Error					ΔV History		
	Position Estimate	Out of Path	Out of Path Corrected	RMS Pos. EST (km)	RMS Vel. EST (mps)	FTA (km)	Ephemeris RMS EST (km)	No.	Total ΔV (mps)	Time of Last ΔV Days	
OB only	14.44	2131.7	3.40	234.02	3.1754	56269.4	3150.1	1	15.23	5.15	
DSN Only	282.97	389.32	282.29	1604.54	21.0187	21304.2	940.8	1	1.28	2	
DSN & OB 10" - No. IR	12.20	490.75	2.45	97.01	1.2827	21260.8	925.1	1	1.28	2	
DSN & OB 3" - No. IR	10.67	211.03	1.56	52.00	0.6922	5084.6	933.3	2	2.88	32	
DSN & OB 1" - No. IR	10.15	47.97	1.46	28.18	0.3816	1837.7	918.9	2	4.81	39	
DSN & OB 10" - 60"	13.20	490.83	2.43	109.00	1.4468	19539.2	919.3	1	1.29	2	
DSN & OB 60" - 60"	14.53	496.42	7.26	129.84	1.7040	21302.9	923.3	1	1.28	2	
DSN & OB 180" - No Ir	26.41	496.56	19.33	240.18	3.1712	21304.1	923.4	1	1.28	2	

*Terminal Time = 42.65 Days. Pericenter Time = 41.72 Days.

smaller errors because of the reduction of the ephemeris error possible with the onboard system. Because onboard navigation occurs directly, with respect to the planet, the ephemeris error is strongly observable. To reduce the ephemeris error by tracking from Earth would require that the vehicle be under the influence of the planet's gravity field. This effect is not strong enough during interplanetary legs to permit ground tracking to reduce the ephemeris error. Figure VI.1 displays the time history of the ephemeris-error reduction as Jupiter is approached on the first interplanetary leg of the Grand Tour. A 10 - arc-second optical device and an infrared detector with a one-arc-minute pointing error was activated 1 a. u. from Jupiter to generate this plot. The closer the spacecraft approaches Jupiter, the better is the accuracy per onboard navigational measurements. This phenomenon, which is apparent from the relative sizes of the step decreases in Fig. VI.1, results from the fact, explained above, that the pointing error becomes less dominant as the near body gets closer.

The relative improvement with combined navigational capabilities increases as the probe passes planets farther out in the solar system, since the a priori ephemeris error also increases with distance from the sun (while all planets, on this interplanetary scale, are very closely passed by the probe). Table VI-2 shows, however, that there is no advantage to adding the onboard capability if navigation can wait until the spacecraft is within the planetary sphere of influence. In the latter event, ephemeris error is reduced far below that obtainable with a combined system on the interplanetary leg; furthermore, no important additional fuel is required. Thus, through the Jupiter passage on the Grand Tour, continuous tracking with the deep space network gives results almost as good as those obtainable when an onboard capability is added. The use of an onboard system would be justified only if very small errors (such as those obtainable with a 1-arc-second sextant) were required or if for specific mission-objective reasons the ephemeris error must be reduced early in the mission. Neither of these conditions seems likely.

On the Jupiter passage just mentioned, as well as on the other

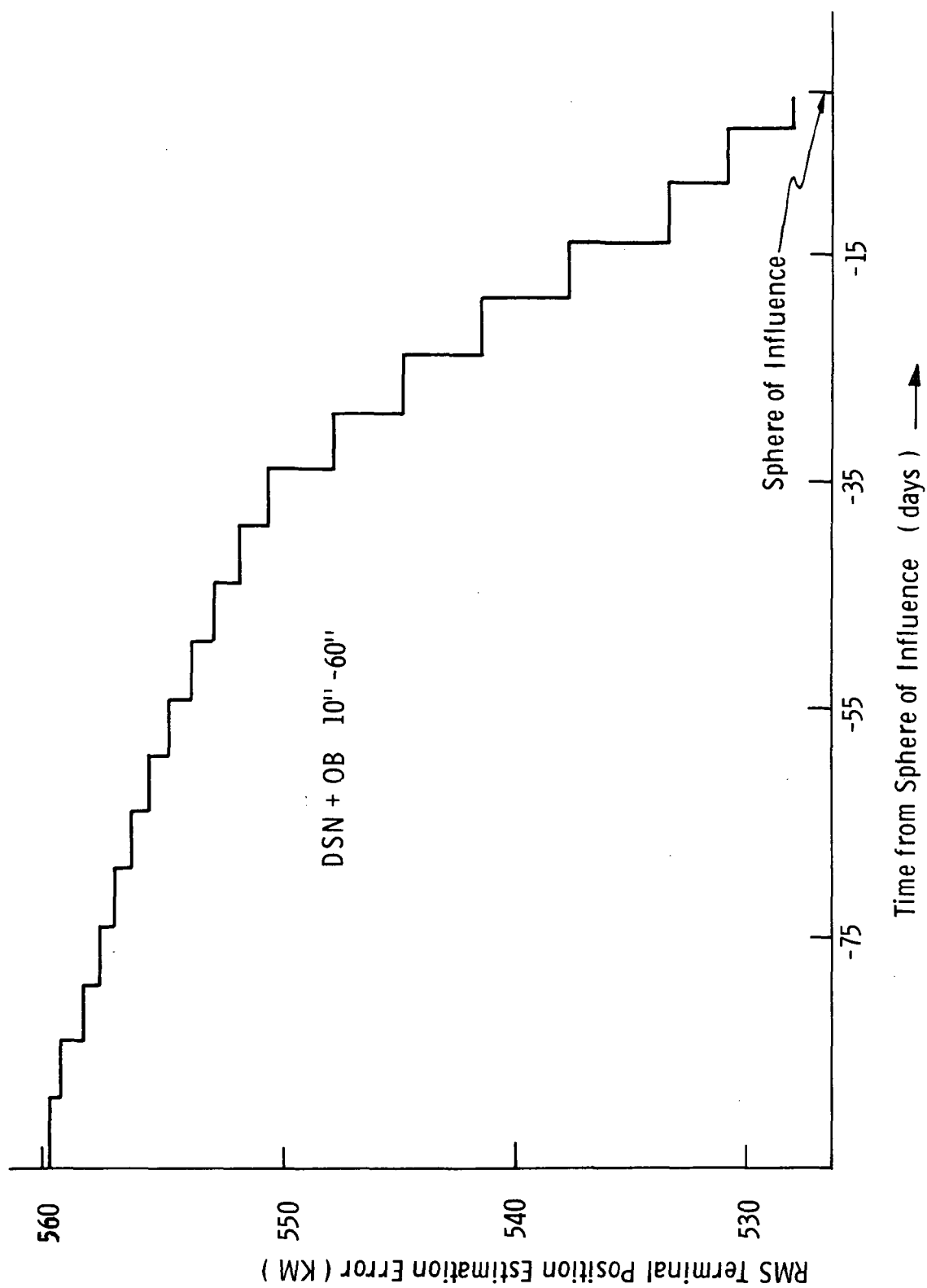


Fig. IV.1 Error Reduction with Onboard Instruments on Jupiter Approach of the Grand Tour

near-planet passes, little, if any, improvement in knowledge of ephemeris error is gained by the addition of the onboard capability, because the ephemeris error is no longer directly observable by the onboard system when the only gravitational attraction is that of the planet under consideration. No reference to any body but the planet is available. Earth-based tracking, on the other hand, always has the Earth as a reference; hence, if the probe is under the gravitational influence of another planet, the ephemeris error can be reduced using the DSN. On interplanetary legs, the DSN cannot observe the ephemeris error, but the onboard configuration can because it is operating in the sun's gravity field while directly observing the planet. During all planetary passes of this mission, the onboard system first reduces the ephemeris error on the interplanetary approach, whereupon the DSN reduces it even more on the near-planet approach. Thus, an onboard system is not the best way of learning about the planetary ephemerides.

At the Saturn passage on this Grand Tour mission, the balance between the onboard system and the DSN changes from that observed at Jupiter. The use of only onboard navigation now results in both smaller errors and smaller fuel requirements than Earth-tracking without onboard augmentation. Combining the two systems results in still smaller errors and fuel requirements. Examination of Tables VI-6 and VI-8 reveals the same pattern of results, with even larger fuel savings at Uranus and stronger reduction of errors at Neptune by adding the onboard system. We may conclude therefore, that there is a substantial reduction in Grand Tour midcourse fuel requirements and navigational errors if an onboard navigation system is employed on the approaches and encounters at Saturn, Uranus, and Neptune.

The table entries for the near-planet pass at Saturn also contain what at first may appear to be inconsistent. Specifically, the errors which result from using a 1-arc-second sextant are greater than those using a 3-arc-second device. On this passage, the probe

travels extremely close to the planet in order to fly between the surface and the inside of the innermost rings. At this low altitude, the phenomenon error dominates the sextant-pointing error when an onboard measurement is made; therefore using a better sextant does not yield significantly better results. If the sighting schedules were identical in both cases, the 1-arc-second instrument would have to give slightly better results than the 3-arc-second device. Since, in both cases, individual measurements were optimized instead of the overall schedule, the resulting sighting pattern yielded the results entered in Table VI-4.

That the phenomenon error is a more significant factor in the measurement error for the close Saturn approach than for a higher altitude pass such as at Neptune is evident by comparing the entries in Table VI-9. There is a much more substantial increase in the position-estimation errors and fuel consumption on the Saturn pass than on the Neptune flyby.

It is interesting to observe at this point the rate at which navigational information is obtained with and without an onboard system. For the Grand Tour Jupiter passage, Fig. VI.2 illustrates the reduction with time of the projected position error through the flyby; ground tracking alone is compared with ground tracking coupled with a visible horizon sensor of 10-arc-seconds pointing error. Figure VI.3 gives similar information for the Saturn passage. Note that when the onboard capability is added, there is a tremendous improvement in the obtainable information rate as periplanet is passed. Also, the DSN-only curve is relatively flat before pericenter and slopes gently but steadily downward thereafter. The explanation for these observations lies in the trajectory geometry. As is evident from the plan view of the Grand Tour displayed in Appendix A, the interplanetary trajectories bend very little. The near-planet trajectories illustrated in Appendix B sharply and suddenly change direction at periplanet, but nowhere else. Thus, as these planets are approached, the spacecraft is moving in approximately the same direction when viewed from Earth as it has since the last planetary

TABLE VI-9

Phenomena Error Sensitivity for Saturn and Neptune on the Grand Tour *

Configuration	Periapsis Error Values (km)			Terminal Error				ΔV History		
	Position Estimate	Out of Path	Out of Path Corrected	RMS Pos. EST (km)	RMS Vel. EST (mps)	FTA (km)	Ephemeris RMS EST (km)	No.	Total ΔV (mps)	Time of Last ΔV Days
Saturn Nominal	9.51	14.87	1.40	950.05	0.31	1387.3	203.1	6	19.76	37.3
Saturn X 10 phenomena error	14.71	26.36	6.95	1080.05	0.34	1266.9	203.1	6	34.36	55.7
Neptune Nominal	12.20	490.7	2.45	97.03	1.28	2109.5	925.1	1	1.28	2
Neptune X 10 Phenomena Error	20.23	490.7	12.10	93.92	1.27	2126.08	925.5	1	6.74	2

*DSN + OB 10" - No IR

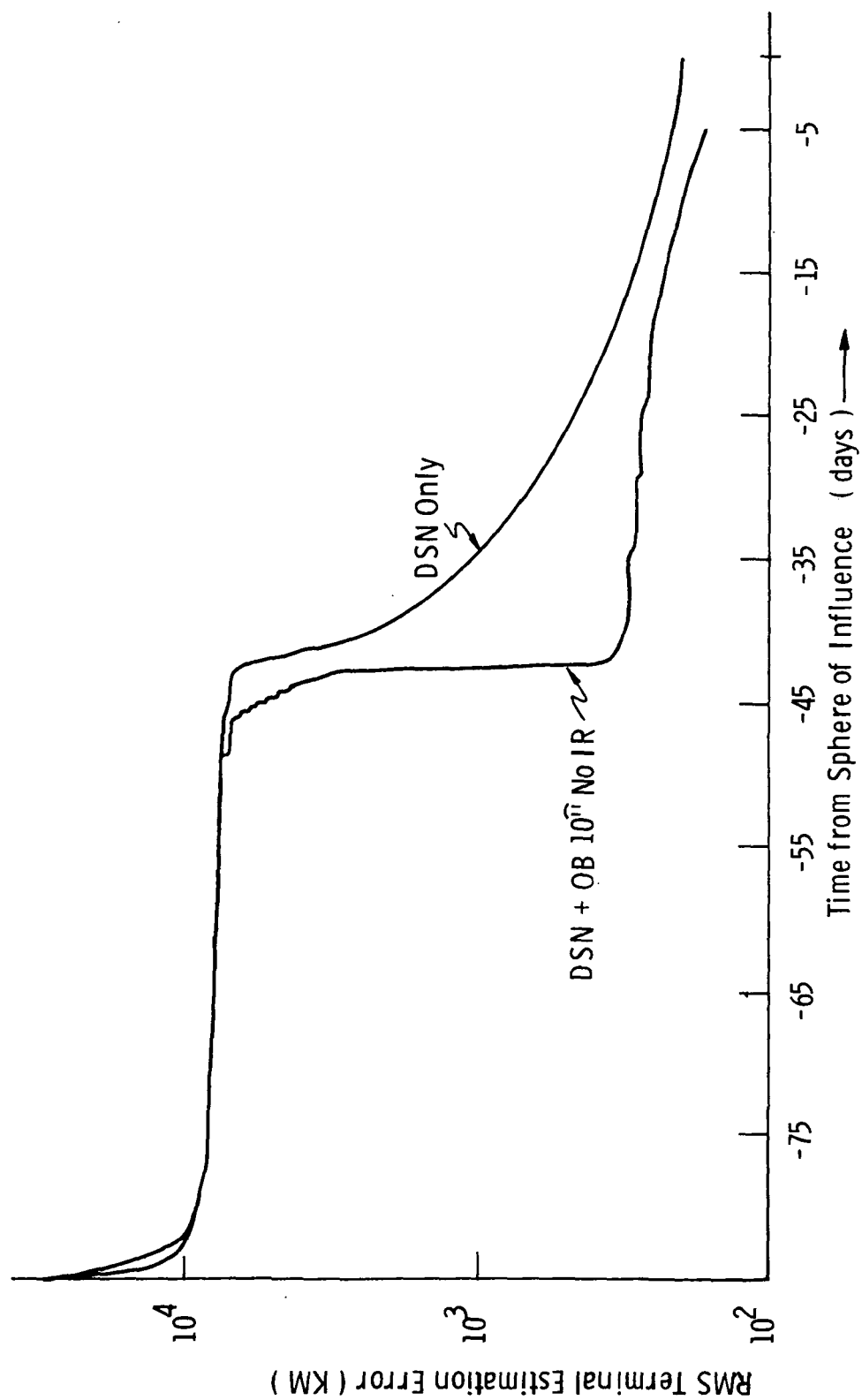


Fig. VI.2 Comparison of Terminal Error Reduction at Jupiter on the Grand Tour

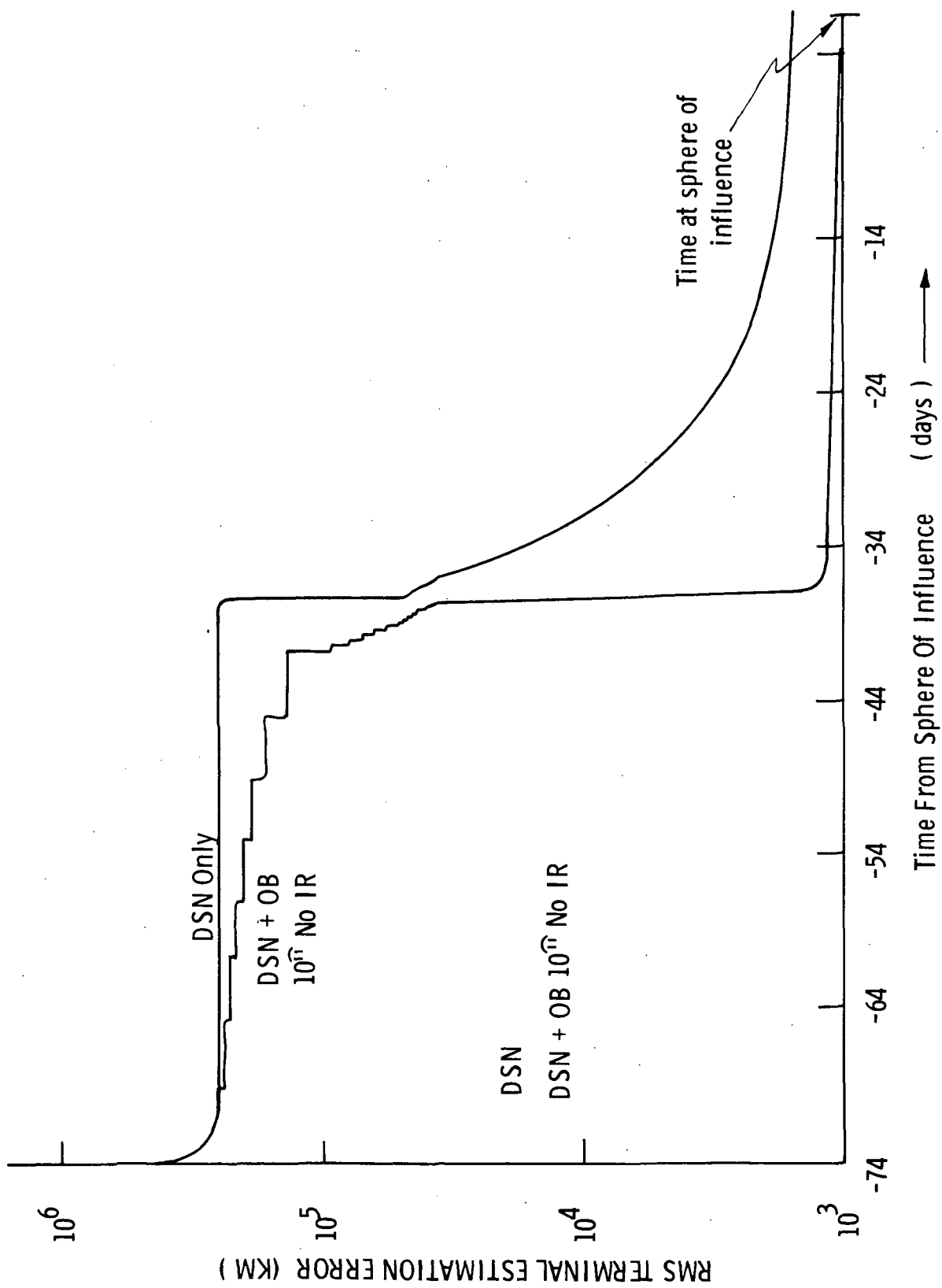


Fig. VI.3 Comparison of Terminal Error Reduction at Saturn on the Grand Tour

passage. Because the geometry has been approximately the same for so long, all the useful information obtainable from the approach configuration has long since been extracted. As soon as periplanet is passed, however, a new geometry exists and the ability of ground tracking to reduce errors accordingly improves.

Figures VI.4 and VI.5 provide insight into the data-acquisition rate for the interplanetary case. Figure VI.4 is a plot of the projected rms terminal position estimation error versus time for the Earth-Jupiter leg of the Grand Tour. Figure VI.5 gives the same information for the Jupiter-Saturn leg. Note that on the Earth-Jupiter leg the error very quickly drops to the Jupiter ephemeris error, while on the Jupiter-Saturn leg, almost the entire interplanetary-leg time is required to achieve the same result. This is because the ability of the ground-tracking system to observe the cross-range components of spacecraft position falls off the further the spacecraft moves from Earth. When the spacecraft is close to Earth, this capability is quite strong. (The partial derivatives for processing a DSN measurement are given in Appendix E.) The pattern is repeated on all the outer interplanetary legs; whereas only a few weeks are required to reduce the errors to the ephemeris error on the Earth-Jupiter leg, 400-600 days are necessary on the outer legs.

The navigational technique referred to thus far in this chapter involved building up a set of individual optimal measurements at each planet passage of the Grand Tour. (See Appendix E for a full discussion of this method.) In addition, the optimization scheme described in section F of Chapter II and developed in Appendix H was also used on the Jupiter and Saturn passages of the Grand Tour, employing only an onboard capability. Figures VI.6 through VI.9 depict the results of the optimization method compared to those of the individual-measurement technique.

Figures VI.6 and VI.7 plot the ratios of the optimization cost to individual-measurement cost, in terms of rms terminal position estimation

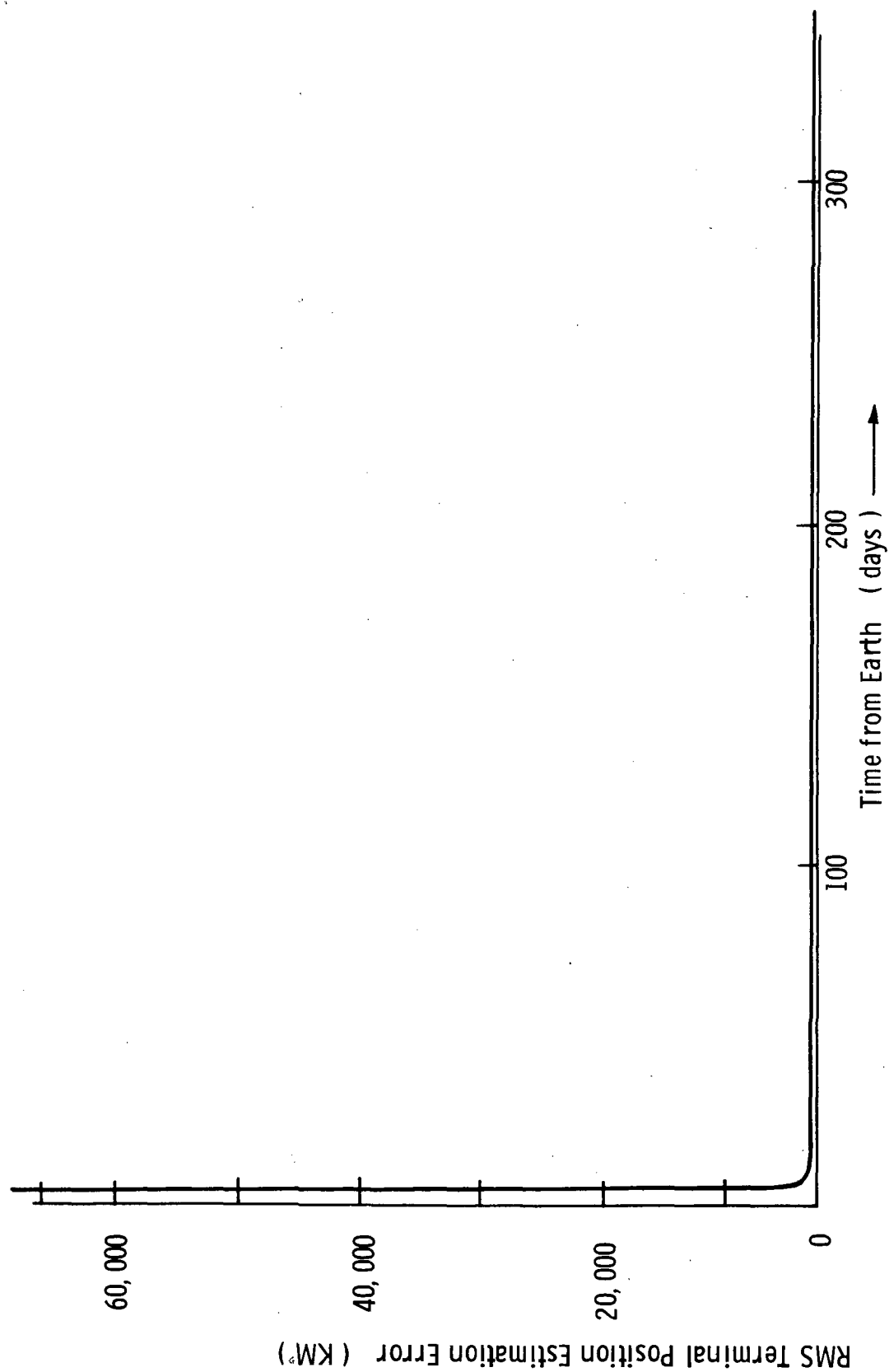


Fig. VI. 4 Reduction of Terminal Error with the DSN Only for the Earth to Jupiter Leg of the Grand Tour

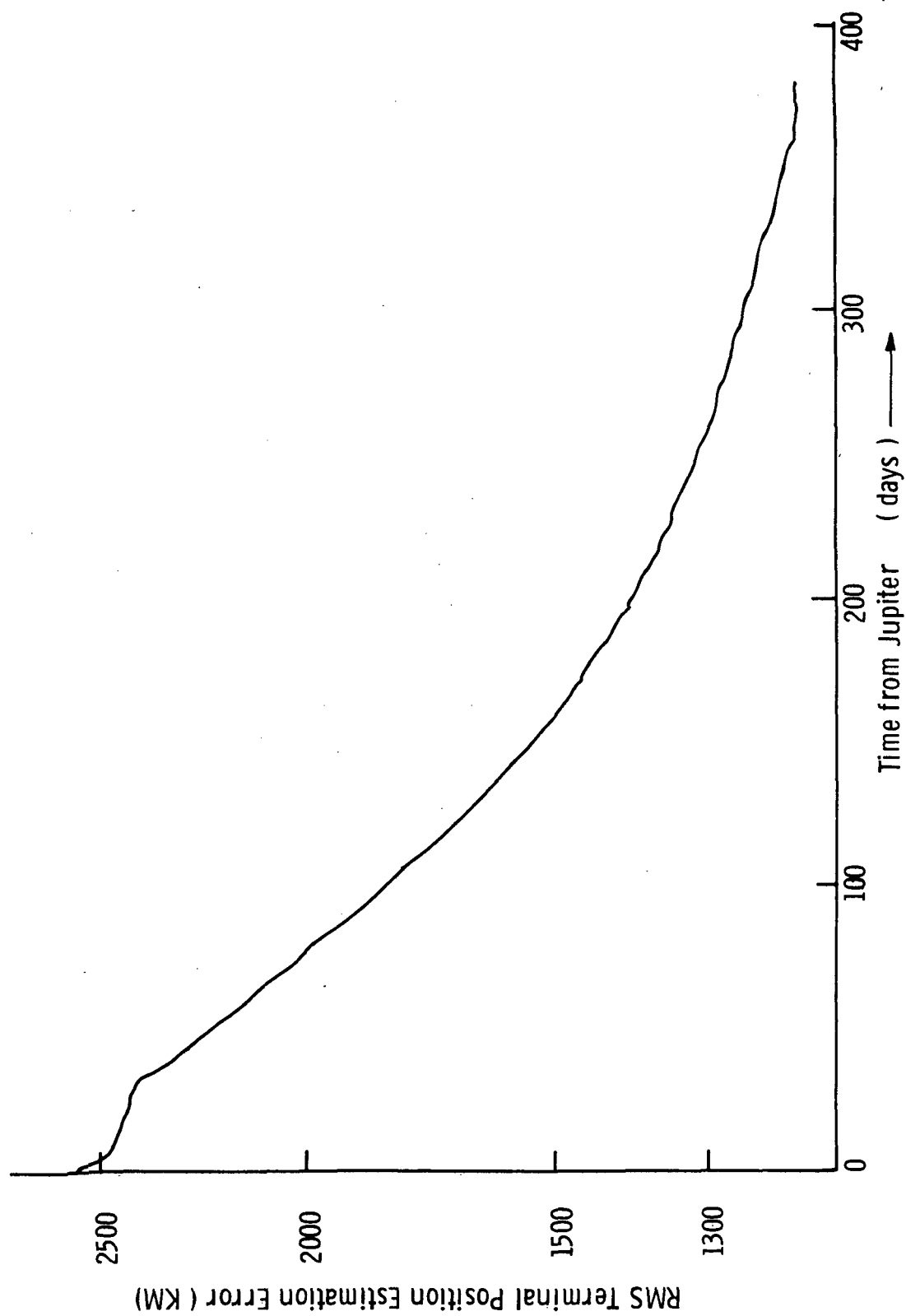


Fig. VI.5 Reduction of Terminal Error with the DSN Only for the Jupiter to Saturn Leg of the Grand Tour

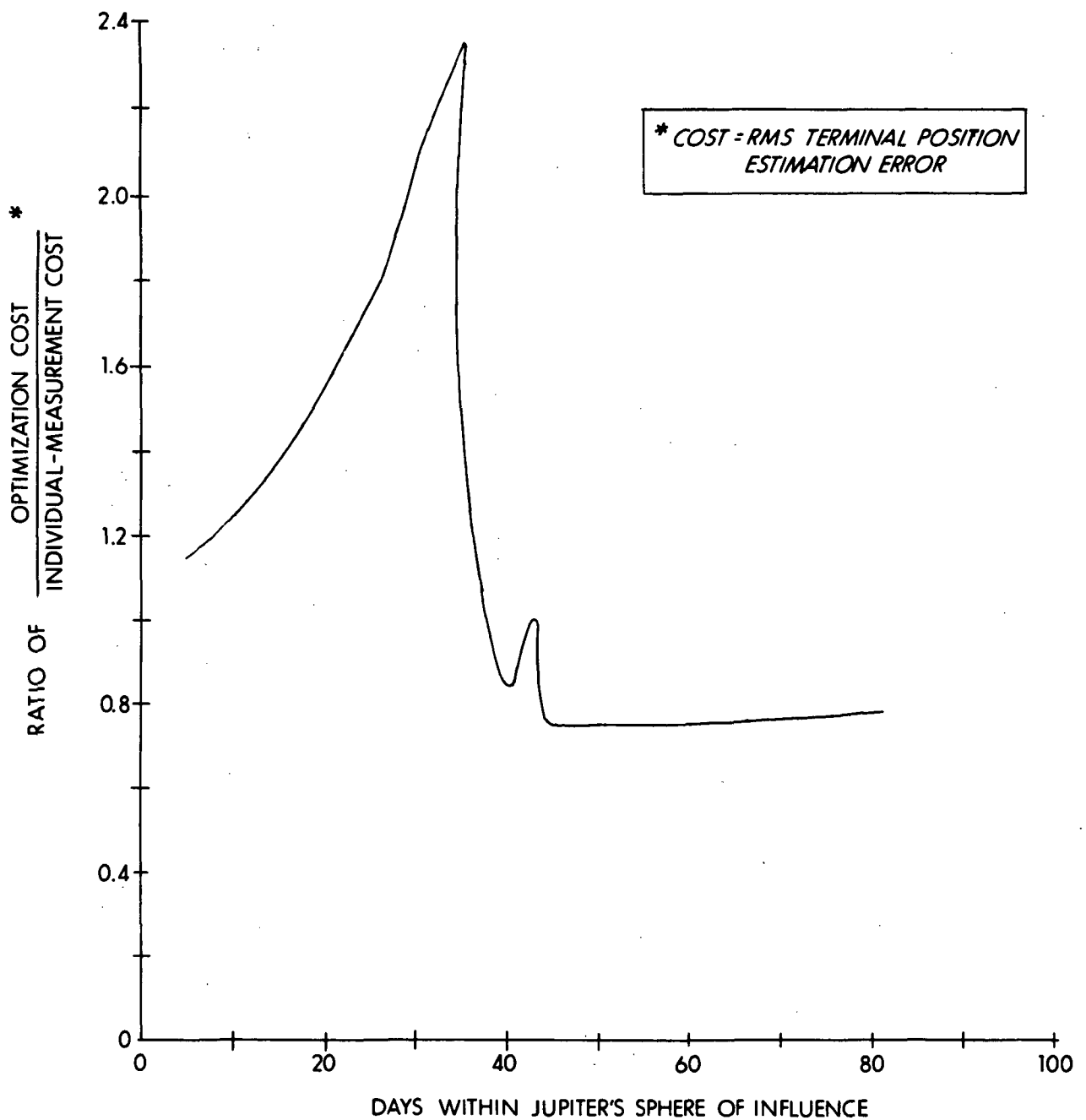


Fig. VI.6 Comparison of Measurement Scheduling Methods - Jupiter Passage

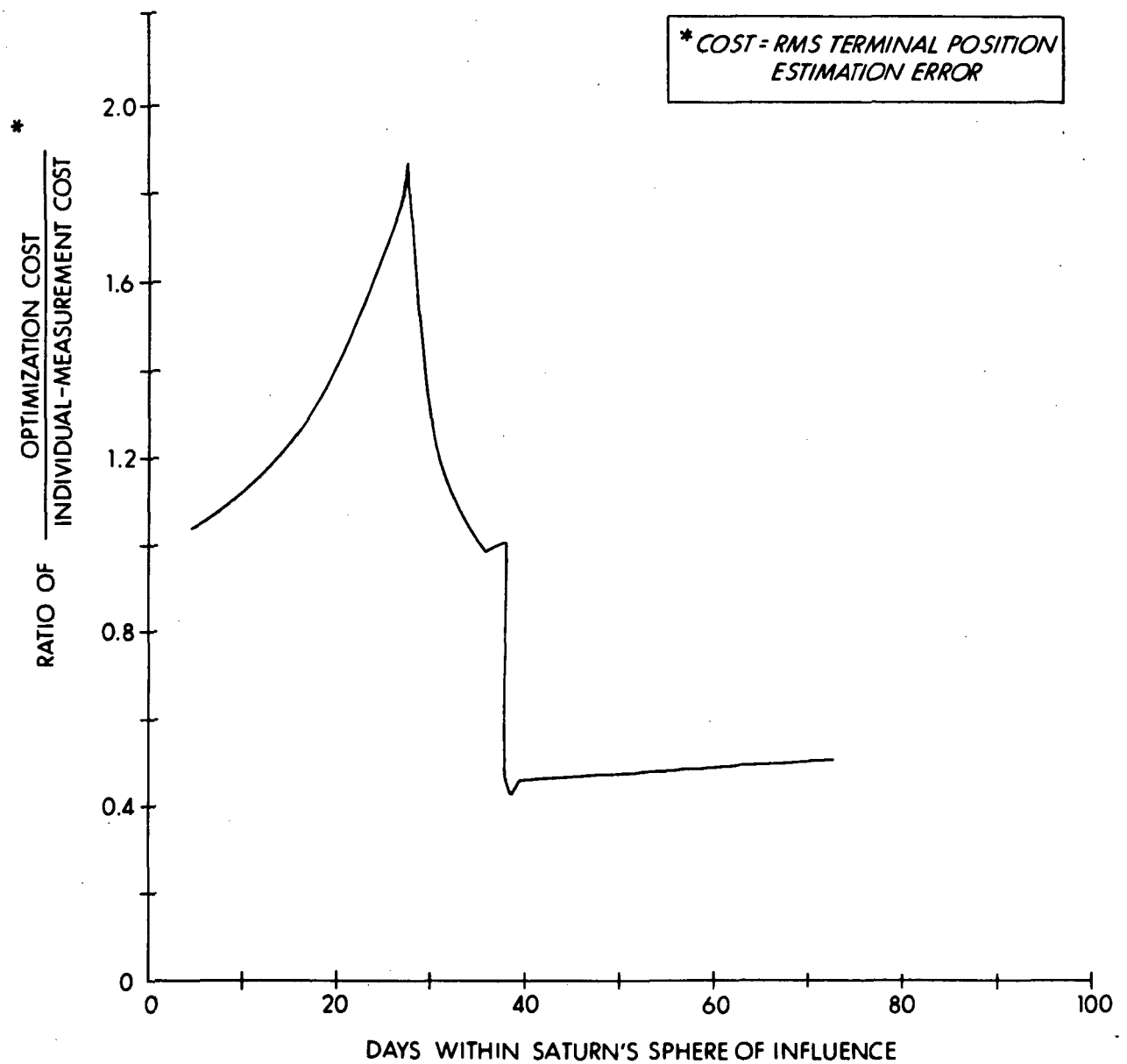


Fig. VI.7 Comparison of Measurement Scheduling Methods - Saturn Passage

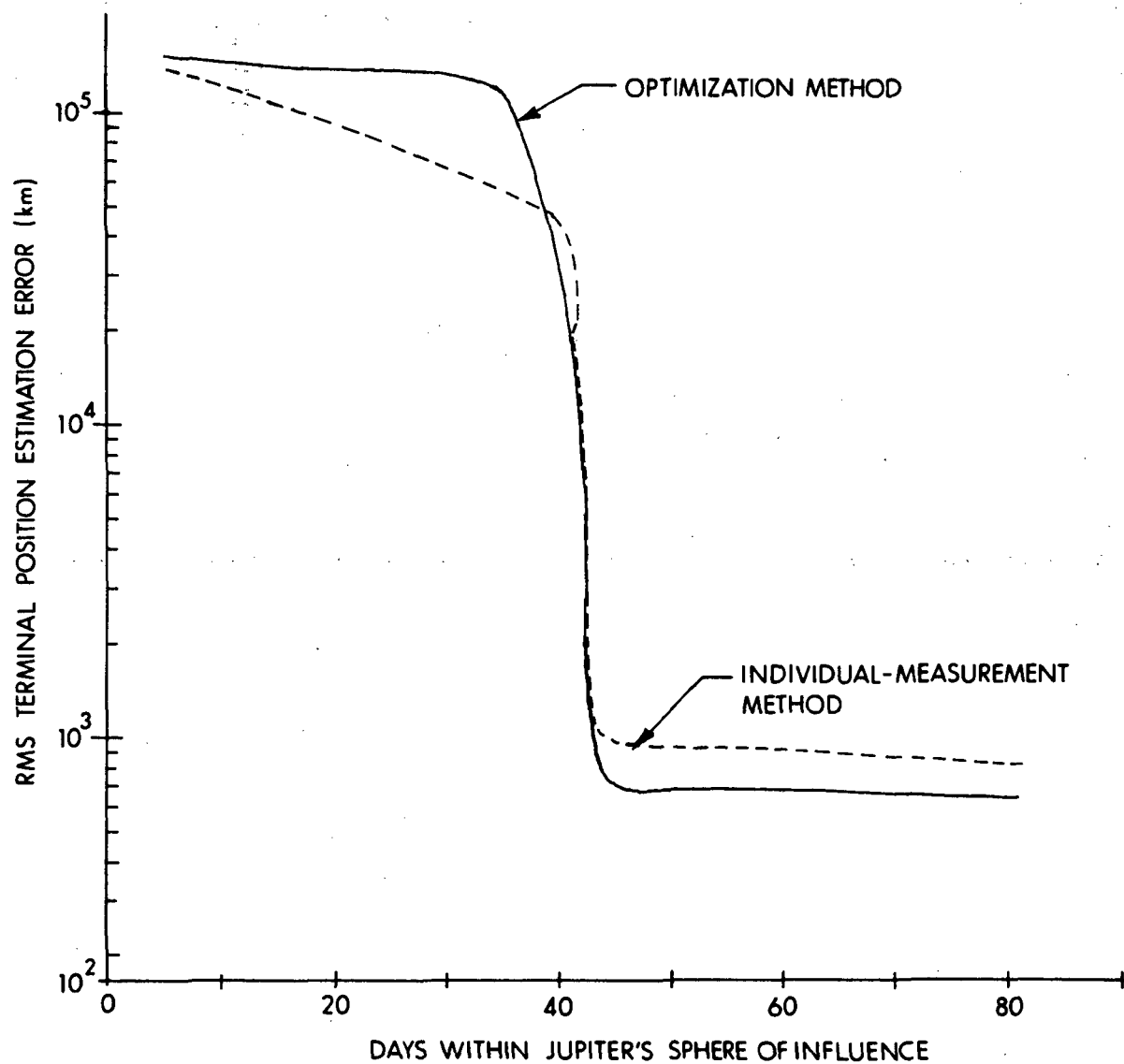


Fig. VI. 8 Position Estimation Errors for Two Measurement Scheduling Methods - Jupiter Passage

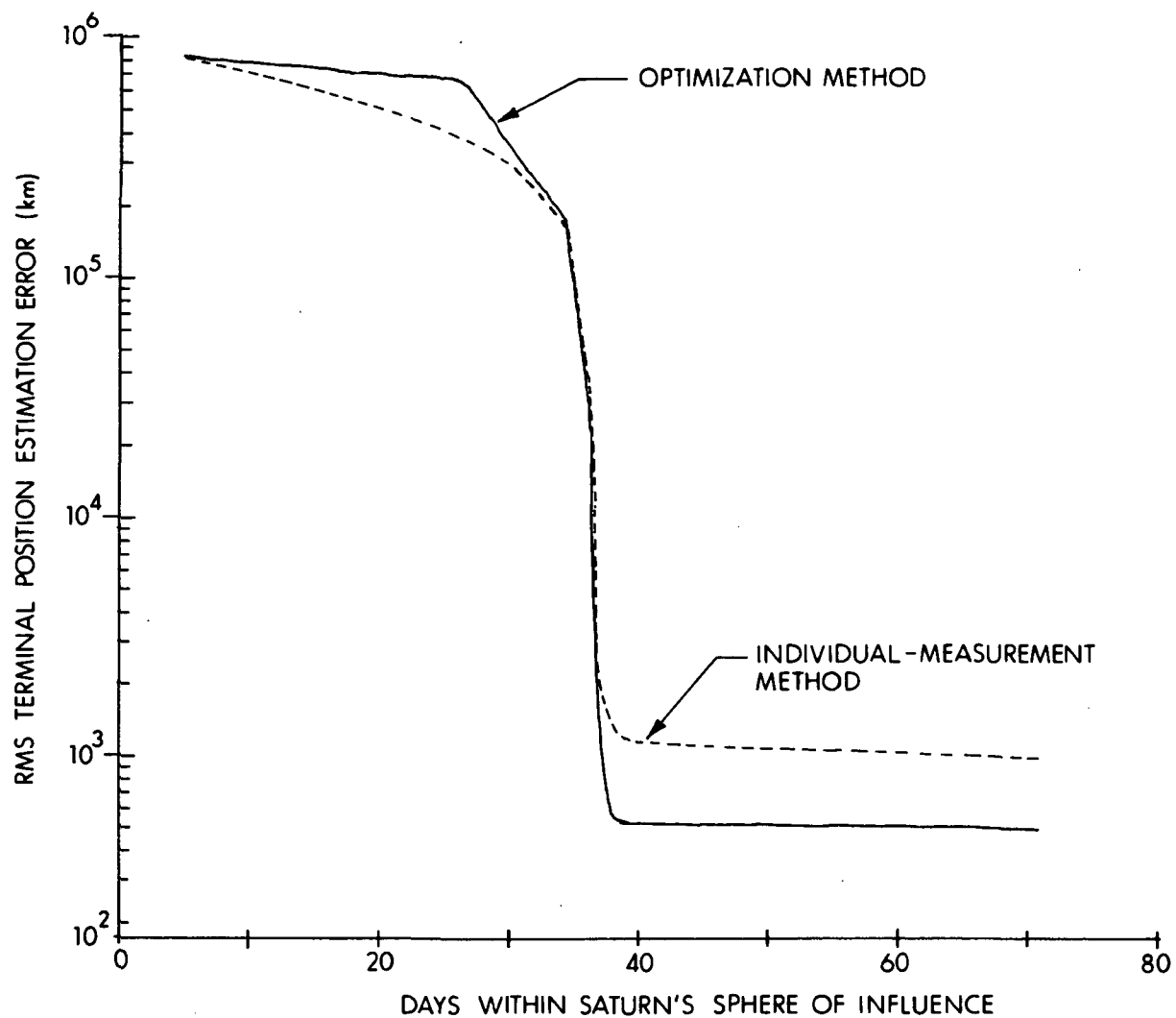


Fig. VI.9 Position Estimation Errors for Two Measurement and Stability Methods - Saturn Passage

error, for the Jupiter and Saturn passages, respectively. Note that the optimization cost at terminal time of the Jupiter passage is over 20 percent better than the individual-measurement cost, and that the optimization cost is about 45 percent better on the Saturn passage. (Better performance on the Saturn passage probably results from the closer passage to Saturn than to Jupiter.) From both figures, it is evident that most improvement occurs at periplanet passage, with little improvement afterward. Also, since the decision was made to trade off larger errors at early times for smaller errors towards the terminal time, the optimization cost is larger than the individual measurement cost during the early stages of both passages.

Figures VI.8 and VI.9 are combination plots showing the mechanics of how the optimization method presents an improvement over the individual-measurement method, for the Jupiter and Saturn passages, respectively. While Figures VI.6 and VI.7 provided the ratio of costs for the two methods, Figures VI.8 and VI.9 compare the actual values of the rms terminal position estimation error. The latter two plots each demonstrate that the individual-measurement technique at first yields smaller terminal estimation errors, but larger errors as terminal time approaches. Both methods provide the most complete information at periplanet passage.

On the Saturn-Uranus and Uranus-Neptune interplanetary legs, no velocity corrections are indicated. This is a consequence of the fact that the automatic correction-scheduling algorithm rejected all midcourse corrections because the ratio of uncertainty to magnitude of the velocity correction remains greater than the prespecified minimum value for a correction (0.2 in this case). As a result, the correction is made inside the sphere of influence of Uranus and Neptune. At Neptune no effort is made to control the passage after periapsis, so there is no clear-cut fuel saving of one navigation method over another. As pointed out above, however, there remains the substantial improvement of position and velocity determination as a result of adding the onboard system.

It is worth reemphasizing that all velocity-correction values given in the standard tables are approximate one-sigma numbers. In an actual mission, of course, the midcourse corrections would not be made at the same times as scheduled by the automatic algorithm. Because the method assures that the corrections are efficient, however, the total fuel requirements tabulated herein are approximately those that would be required by an actual correction schedule.

In a few circumstances the correction pattern which results from this automatic procedure is difficult to interpret. As noted above, one instance of this occurs during the Neptune passage on the Grand Tour. To clarify this situation, the minimum obtainable terminal error and the velocity correction required to obtain it are continuously computed. Through selection of a particular time, an evaluation can be made of the fuel required to obtain the minimum possible deviation from the reference trajectory at the terminal time. This evaluation, of course, is a function of the time selected. Table VI-10 gives these results on the Neptune passage for a final correction made at 41.47 days--just prior to periplanet, and a day before the probe reappears from behind Neptune. Note that there is a substantial reduction in minimum obtainable error with no appreciable increase in fuel if an onboard system is added to the ground-tracking capability. It is also evident that a sizeable reduction can be obtained if a 10-arc-second instrument is used instead of a one-arc-minute device.

Before leaving the subject of fuel consumption, a comment with regard to transplanetary-injection errors is appropriate. Most of the fuel consumed on the Earth-Jupiter leg of this Grand Tour mission (52.6 mps out of approximately 55.9 mps) was used to remove the injection errors after ground tracking measured them. The size of this first correction is, in all cases, directly proportional to the injection errors, assuming, of course, that sufficient time (a few weeks at most) is provided before the correction, for the ground-tracking system to determine the errors.

TABLE VI-10

Fuel Requirements for Obtaining Minimum Miss
at Neptune on the 1977 Grand Tour

Configuration	Minimum Obtainable Miss (km)	Total Fuel Required (mps) At Neptune
OB Only	690	23
DSN Only	7942	9
DSN + OB 10" - no IR	627.6	10
DSN + OB 3" - no IR	354	13.7
DSN + OB 1" - no IR	254	15.8
DSN + OB 10" - 60"	569.7	9
DSN + OB 60" - 60"	2607	9.7
DSN + OB 180" - no IR	5352.6	10

In the last entry in Tables VI-8 and VI-10, ground tracking is aided by a 3-arc-minute optical device to determine the result if one of the higher-accuracy sextants degrades into a 3-arc-minute device by the time the spacecraft arrived at Neptune. As can be seen from these entries, substantial improvement over ground-tracking alone is still achievable.

Interestingly, Tables VI-2, VI-4, VI-6, and VI-8 show that the terminal ephemeris error can be less than the error in estimating the position of the probe with respect to the planet. The planet-mass uncertainty and trajectory dynamics drive the error in position of the spacecraft with respect to the planet but not the error in location of the planet with respect to the sun. This driving term increases the error in the estimate of position with respect to the planet; only measurements can reduce it again. The result of this increase with time is evident by comparing the terminal position estimation errors to the same quantity at periapsis. Table VI-11 illustrates what the results would be if there were zero planet-mass uncertainty at Neptune. Here we see that with an onboard navigation capability, the terminal position errors with respect to the planet can be reduced below the ephemeris errors. With ground tracking alone, however, this is still not possible at Neptune. This comparison demonstrates the advantage of navigating directly with respect to the planet--something an onboard system can do, but which the DSN cannot.

Tables VI-12, VI-13 and VI-14 and Fig. VI.10 and VI.11 provide the results of varying key DSN parameters for the Uranus-Neptune and Neptune flyby legs of the Grand Tour. Ground tracking only was assumed for the Uranus to Neptune leg and two cases, DSN only and DSN augmented with a 10-arc-second sextant, were explored for the Neptune flyby. The frequency of DSN tracking and the station-location errors were varied. The nominal points, which are taken from Tables VI-7 and VI-8, represent continuous ground tracking with three stations. Each station has a location error of 1 meter off the spin axis and 2 meters in effective longitude. The station location errors were raised to 10 and 20 meters and 50 and 100 meters, respectively. The tracking frequency was

TABLE NO. VI-11

Sensitivity to Planet Mass Uncertainty at Neptune on Grand Tour

	Periapsis Error Values (km)			Terminal Error				ΔV History		
	Position Estimate	Out of Path	Out of Path Corrected	RMS Pos. EST (km)	RMS Vel. EST (mps)	FTA (km)	Ephemeris RMS EST (km)	No.	Total ΔV (mps)	Time of Last ΔV Days
Configuration										
DSN & OB 10" No. IR Nominal	12.20	490.75	2.45	97.01	1.28	21260.8	925.1	1	1.28	2
DSN & OB 10" No. IR Mass UNC = 0	3.07	266.96	2.33	13.66	0.18	6429	906.30	2	10.24	40
DSN Only Nominal	282.97	389.32	282.28	1604.54	21.02	21304.2	940.8	1	1.28	2
DSN Only Mass UNC = 0	277.39	389.3	277.13	1602.04	20.98	21290.2	923.3	1	1.28	2

TABLE VI-12

Sensitivity to DSN Parameter on Uranus*
Neptune Leg of Grand Tour DSN Only

Configuration	Terminal Errors				ΔV History		
	RMS Pos. EST (km)	RMS Vel EST (mps)	FTA (km)	RMS EPH. EST (km)	Total ΔV (mps)	Total ΔV (mps)	Time of Last ΔV Days
Nominal	3660.67	0.02	4768.7	3185.7	4	5.04	476
Station Location Uncertainty X10	4051.64	0.03	6913.4	3186.0	3	5.07	474
Station Location Uncertainty X50	4052.83	0.03	6915.2	3186.0	3	5.07	474
1 DSN Pass Per Day	3686.7	0.11	4621.1	3186.0	4	5.04	482
1 DSN Pass Per 3 Days	3722.44	0.11	4610.0	3186.0	4	5.06	514

*Time to Sphere of Influence - 951 Days.

TABLE VI-13

Sensitivity to DSN Parameters at Neptune on Grand Tour - DSN Only*

Configuration	Periapsis Error Values (km)			Terminal Error				ΔV History		
	Position Estimate	Out of Path	Out of Path Corrected	RMS Pos. EST (km)	RMS Vel. EST (mps)	FTA (km)	Ephemeris RMS EST (km)	No.	Total ΔV (mps)	Time of Last ΔV Days
Nominal	282.97	389.32	282.28	1604.54	21.02	21304.2	940.8	1	1.28	2
Station Location Uncertainty X10	1463.97	1623.8	1462.56	10662.95	139.67	36578.7	1693.5	1	3.61	22
Station Location Uncertainty X50	1580.75	3745.1	1579.20	34319.68	449.53	90737.9	2008.6	0		
1 DSN Pass Per Day	309.04	456.7	308.35	2628.18	34.42	24001.6	1004.9	1	1.25	3
1 DSN Pass Per 3 Days	350.00	506.3	349.32	4193.73	54.93	25460.2	1104.7	1	1.34	6

* Terminal Time = 42.65 Days. Pericenter Time = 41.72 Days.

TABLE VI-14

Sensitivity to DSN Parameter at Neptune on Grand Tour
DSN & 10" No IR^{*}

Configuration	Periapsis Error Values (km)			Terminal Error				ΔV History		
	Position Estimate	Out of Path	Out of Path Corrected	RMS Pos. EST (km)	RMS Vel. EST (mps)	FTA (km)	Ephemeris RMS EST (km)	No.	Total ΔV (mps)	Time of Last ΔV Days
Nominal	12.20	490.75	2.45	97.01	1.28	21260.8	925.1	1	1.28	2
Station Location Uncertainties X50	13.00	554.11	2.45	95.93	1.26	11301.5	1654.2	2	4.79	32
Station Location Uncertainties X50	13.04	559.43	2.45	95.90	1.26	11380.3	1660.2	2	4.95	32
1 DSN Pass Per Day	12.38	270.13	2.46	98.65	1.31	7469.5	974.9	2	7.68	39
1 DSN Pass Per 3 Days	11.99	285.24	2.48	96.96	1.29	8385.8	1059.3	2	8.13	39

^{*}Terminal Time = 42.65 Days. Pericenter Time = 41.72 Days.

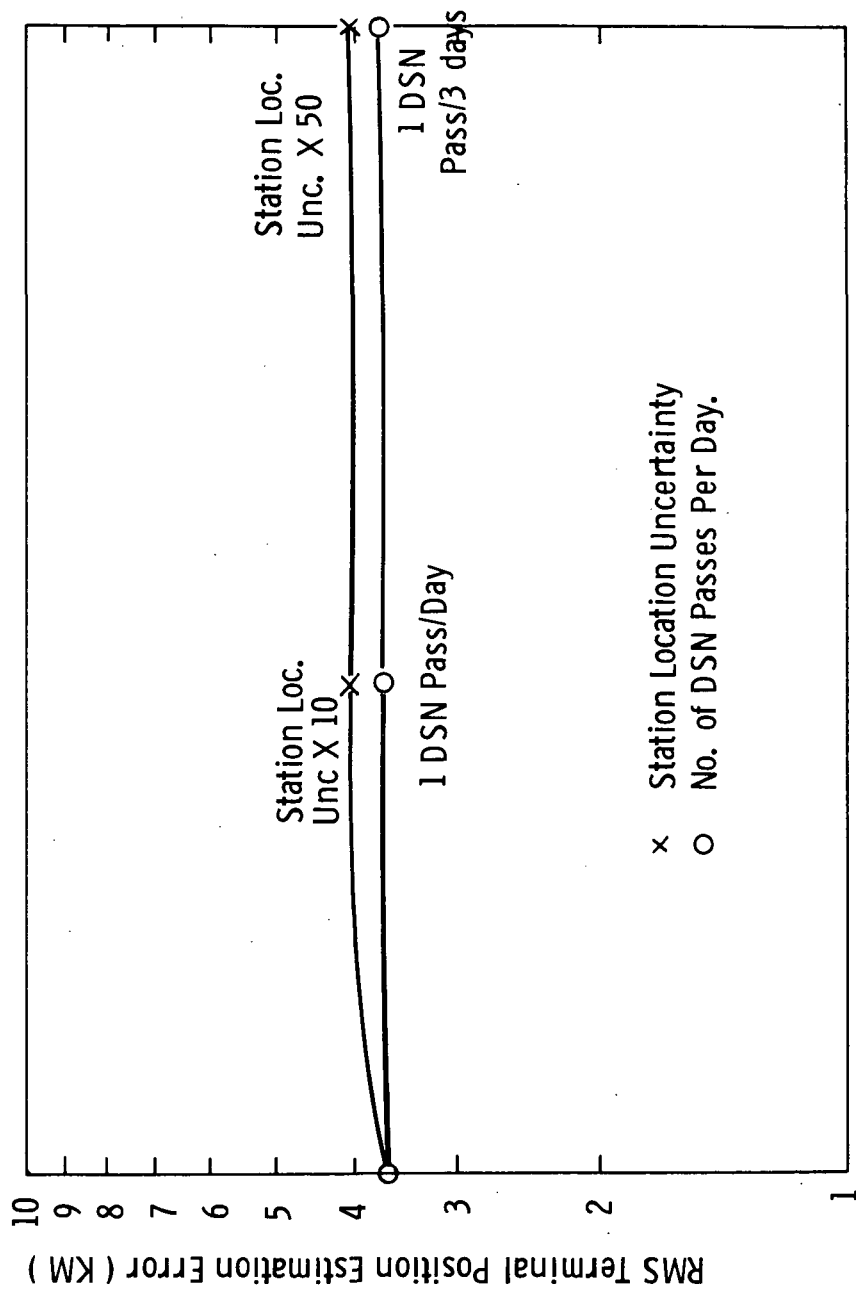


Fig. VI.10 Effect of DSN Parameters on Terminal Position Estimation Error on Uranus to Neptune Leg of the Grand Tour

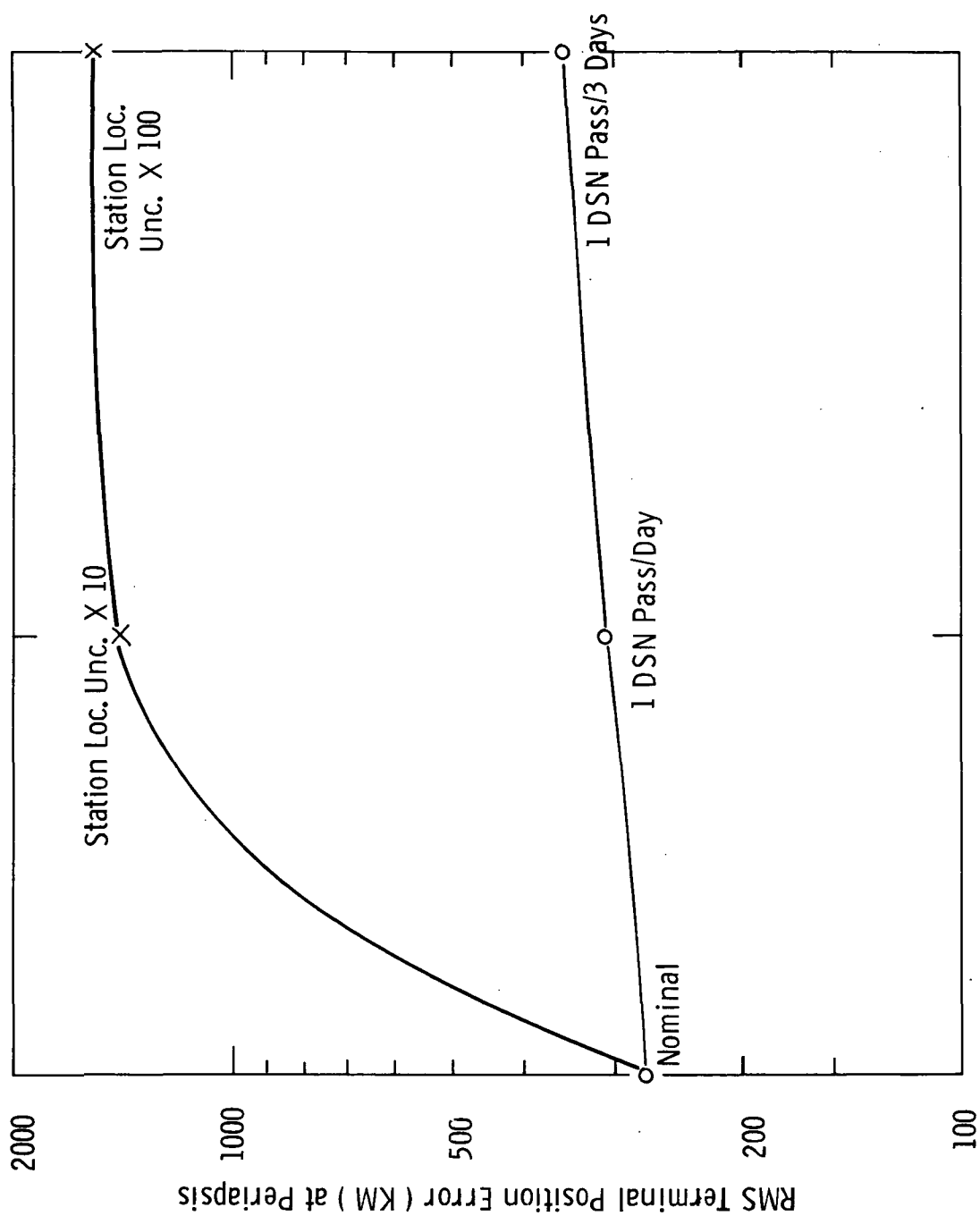


Fig. VI.11 Effect of DSN Parameters on the Terminal Position Estimation Error at Neptune
on the Grand Tour-DSN Only

reduced to continuous tracking with one station and tracking with another station every third day.

Table VI- 12 and Fig. VI- 10 reveal that on the Uranus-Neptune interplanetary leg, there is more sensitivity to station-location errors than to tracking frequency; the 300-mile difference, however, is not important since these errors can be significantly reduced during the actual encounter with Neptune. Turning to Tables VI- 13 and VI- 14 and Fig. VI.11,, we see that with an onboard capability, there is negligible sensitivity to these DSN parameters. Without this onboard navigation system, there is a noticeable increase of errors as tracking frequency falls off, and an enormous sensitivity to station-location errors in the ranges explored. This adds one more justification for carrying along an onboard navigation system.

The final comments in this section refer to the measurement types and navigational bodies chosen by the onboard system. Planet/moon diameter measurements and star occultations were rarely used. The geometry of the mission with its light-side planetary approaches provides only rare opportunities for dark-edge star occultations. The use of light-edge occultation, although perhaps practical, was not explored. Planet-diameter measurements only become strong at very close ranges to the planet, but at this point the uncertainty involved with sighting on two horizons causes the optimum measurement-selecting scheme to reject this mode in favor of others. Sun-star measurements are not useful on outer planet missions because of the great range to the sun compared with that to the planets.

Only at Jupiter was a planetary satellite selected, and the geometry of the situation demands that an IR sensor be available to make the sighting. The satellite selected was Callisto, which, as can be seen from the plots in Appendix B, is quite closely approached. No such close passage is available at any of the other planets. The rings of Saturn were not used to aid in the determination of range to the planet-- again probably because of the double edge phenomena uncertainty involved.

On the Earth-Jupiter leg, the measurement optimization scheme selects only Canopus as a navigational star. This use of a single star is not found anywhere else in the mission. Canopus is a frequent choice on the other legs, as is γ Velorum. The reason for the frequent choice of these stars is that they both lie almost orthogonal to the plane of motion and thus provide an opportunity to gather out-of-plane navigational information.

B. Onboard System Requirements

In reviewing the results from the simulation program discussed in the previous section, the need for an onboard navigation instrument was of primary interest. Of secondary interest were the accuracy benefits and the need for an IR capability. The interplanetary legs (Tables VI-1, VI-3, VI-5, and VI-7) of the Grand Tour all show the onboard system alone to be the worst choice. The DSN-only errors are not excessive and are only modestly reduced in a linear fashion by adding the onboard capability. We concluded that for the interplanetary legs of the Grand Tour, the onboard instrument is not needed.

From Table VI-2, it is apparent that the Jupiter passage of the Grand Tour does not benefit from the onboard navigation capability by itself. However, the periapsis position estimate and out-of-path corrected position benefit decidedly from the combined capabilities of onboard navigation and Earth-based tracking. Response to accuracy improvement in the combination system is modest in the range from 10 to 1 seconds of arc. Addition of the infrared capability does not help, probably because the Jupiter approach is from the sunlight side.

The Saturn passage, described in Table VI-4, is the first instance of a case where onboard-only capability proves better than DSN alone. Combining the two navigation methods, however, is most advantageous of all, in terms of minimizing both errors at passage and fuel consumption. Also, the errors do not respond strongly either to infrared capability or to enhanced accuracy.

Remembering that this trajectory goes between Saturn and its rings (essentially at periplanet passage), guidance errors must be minimized. Even the 60" - 60" system reduces the out-of-path component from 327 to 30 km, a factor of ten. With the addition of a final velocity correction, the onboard 60" - 60" capability reduces the out-of-path value from the DSN-only value of 105 km to 4.5 km.

The onboard system is not justifiable in terms of significantly reduced uncertainties at exit from Saturn's sphere of influence enroute to Uranus. However, the same size state-vector uncertainties and guidance errors are achieved with significantly less fuel. Still referring to Table VI-4, the use of the 60" - 60" configuration reduces the total velocity change requirement from 124 mps to 42 mps.

The passage by Uranus is described in Table VI-6. At periapsis, the onboard system improves the position estimate by a factor of six. However, the combination of the onboard and DSN systems has a smaller position uncertainty by a factor of 30.

The exit from the Uranus sphere of influence is another situation where the onboard-only system exhibits comparable position estimate, velocity estimate, and guidance errors to the DSN-only operation. The combination of DSN and onboard information does not reduce the position, velocity, and guidance errors significantly from the DSN-only case. The addition of an onboard system to the DSN-only case, however, results in substantial reduction in fuel requirements. Referring again to Table VI-6, it can be seen that even the 60" - 60" instrument can reduce the ΔV requirement from 249 mps for the DSN-only case to 89.5 mps.

In considering the Neptune passage described in Table VI-8, attention should be focused on the periapsis error values, since the terminal conditions are not of significant interest. The runs in this particular set have a varying ΔV timing pattern which affects the out-of-path errors and the fuel consumption pattern. However, the periapsis position estimate and the out-of-path corrected error show a strong response to the addition of the onboard instrument. There is no clear

benefit to adding IR capability. In addition, the increased accuracy does not produce substantial benefits.

Before drawing conclusions about the onboard navigation requirements, it is desirable to consider the guidance answers derived for the Grand Tour. Although guidance-error studies were not run for all legs of the mission, the conclusions presented here are for the Uranus-Neptune interplanetary leg (Table VI-15 and Fig. VI.12). In these simulations, a single midcourse correction of 10.80 mps was implemented at 582 days. From this figure, it is apparent that the nominal guidance values selected are non-critical and that the bias could be increased to 1 cm/sec^2 and the scale-factor error to 5000 ppm without significant impact. Uncertainties in cutoff time again appear as the most critical item.

Guidance-error sensitivity for the Neptune flyby is the subject of Table VI-16 and Figures VI.13 and VI.14. For these cases, two midcourse corrections were applied--one at 3 and the other at 42.1 days. In the figures, only a small insensitivity to accelerometer performance is evident until the bias approaches 10 times its nominal value.

Table VI-17 compares the effects of limiting velocity correction on the Grand Tour Saturn passage to a single impulse three weeks after the spacecraft enters the sphere of influence. These numbers should be compared with their equivalent cases in Table VI-4, where the velocity corrections are determined only by the algorithms discussed in Chapter II. It is apparent that planetary passage without the ability to make a corrective maneuver soon after passage produces excessively high guidance errors (FTA) at exit from Saturn's sphere of influence.

This observation leads to the first comment on requirements for Grand Tour onboard systems. Enough onboard decision and control autonomy should be provided to implement necessary velocity corrections quickly and efficiently, even near but not necessarily during planetary passages. Thus, the onboard computer must have a sufficient level of authority and reliability. This requirement tends to reinforce the selection of the 8.2-kg - 30 watt computer over the 4.1-kg version as listed in Table III-4.

TABLE VI-15

Guidance Error Survey for Uranus - Neptune Leg of Grand Tour

Configuration	RMS Pos EST (Km)	RMS Vel EST (Mps)	FTA (km)	Size of Velocity Correction at 582 Days (mps)
Nominal	3662.62	0.0222	18194.2	10.80
Engine Cutoff Uncertainty X10	3662.62	0.0222	23106.7	10.80
Engine Cutoff Uncertainty X100	3662.62	0.0222	144301.9	10.80
Accelerometer Bias X10	3665.55	0.0344	18473.1	10.80
Accelerometer Bias X100	3665.43	0.0361	36934.8	10.80
Accelerometer Scale Factor X10	3662.87	0.0223	18194.8	10.80
Accelerometer Scale Factor X100	3664.76	0.0292	18262.2	10.80

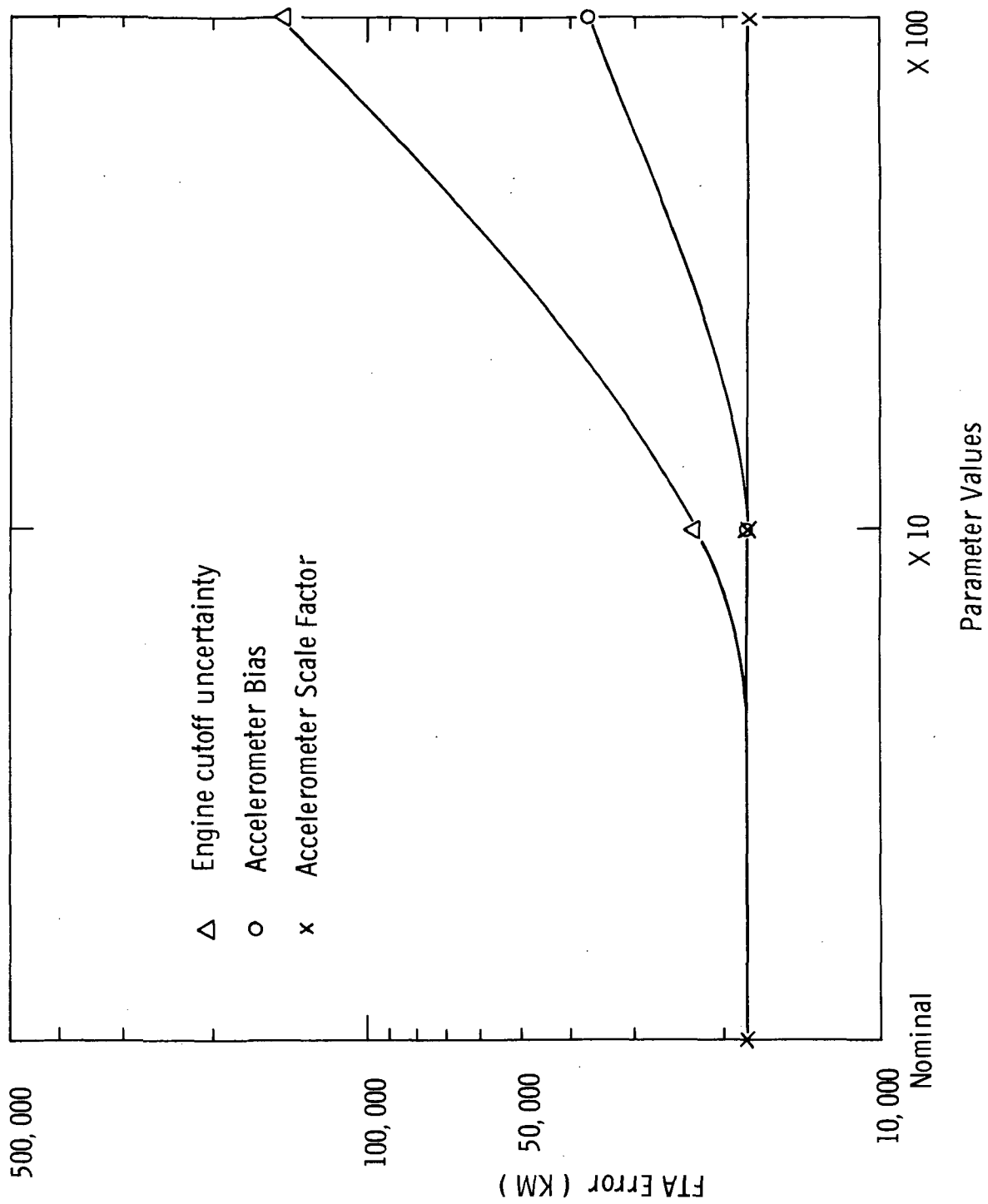


Fig. VI.12 Effect of Guidance Error on FTA Error on Uranus - Neptune Leg of Grand Tour
DSN Only

TABLE VI-16

Guidance Error Survey for Neptune on Grand Tour
DSN & OB 10" No IR

Configuration	Periapsis Error Values (km)			Terminal Error				Amount of Velocity Correction at 2 Days (mps)
	Position Estimate	Out of Path	Out of Path Corrected	RMS Pos. EST (km)	RMS Vel. EST (mps)	FTA (km)	Ephemeris RMS EST (km)	
Nominal	12.65	1279.77	2.45	102.03	1.38	113.9	853.0	476.26
Engine Cutoff Uncertainty X10	12.65	1481.16	2.45	102.69	1.41	117.8	852.6	635.91
Engine Cutoff Uncertainty X100	12.01	6804.5	2.61	143.30	2.66	323.6	865.02	4310.13
Accelerometer Bias X10	12.65	1290.83	2.46	154.11	2.92	254.1	854.6	480.86
Accelerometer Bias X100	12.75	2143.8	3.02	216.84	4.92	5015.9	895.5	1078.85
Accelerometer Scale Factor X10	12.65	1280.01	2.45	102.24	1.39	114.4	853.1	476.35
Accelerometer Scale Factor X100	12.65	1286.37	2.46	119.04	1.94	159.3	853.9	478.83

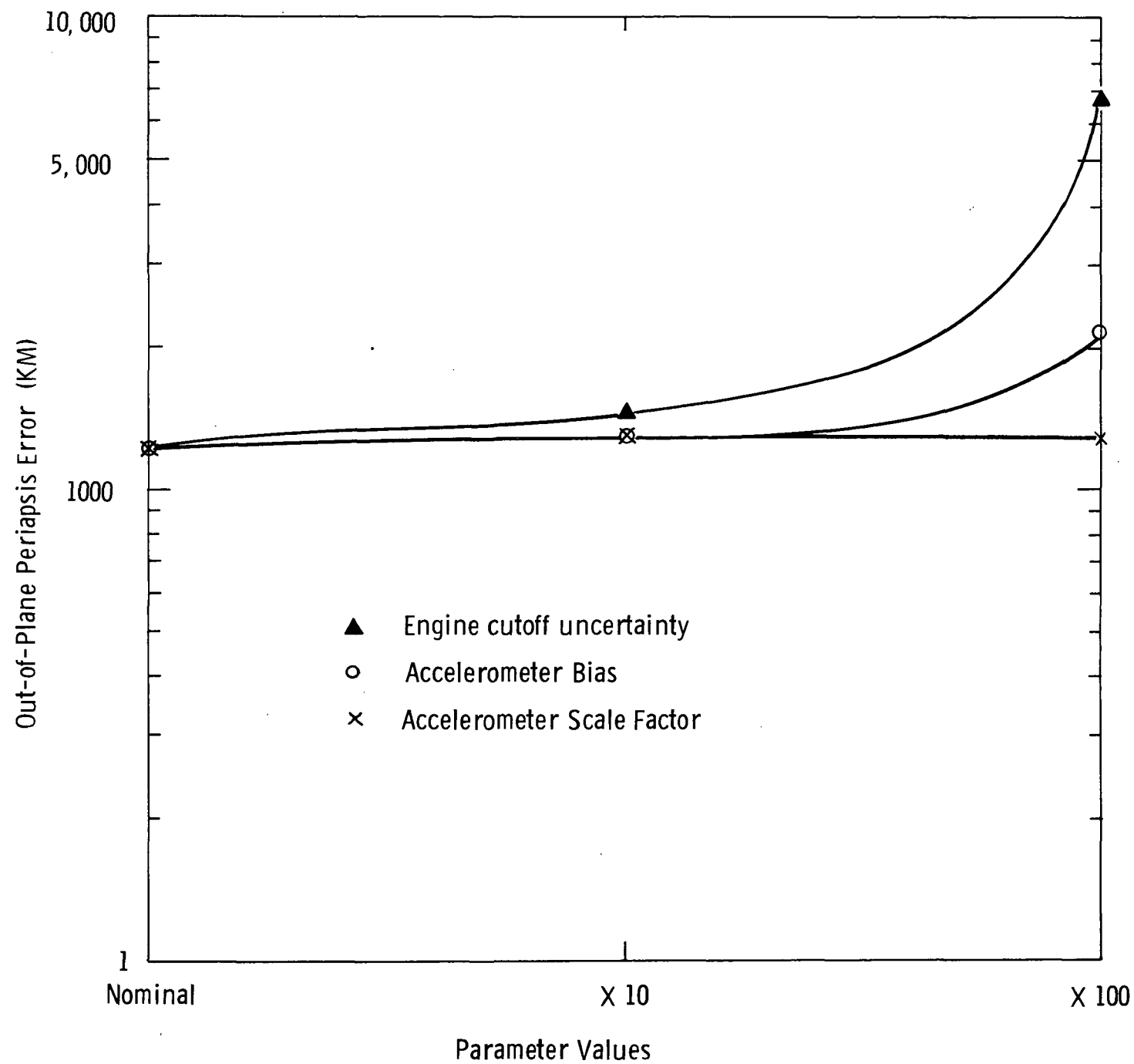


Fig. VI. 13 Effect of Guidance Error on the Out of Plane Deviation at
Pericenter at Neptune on the Grand Tour DSN 10" - No IR

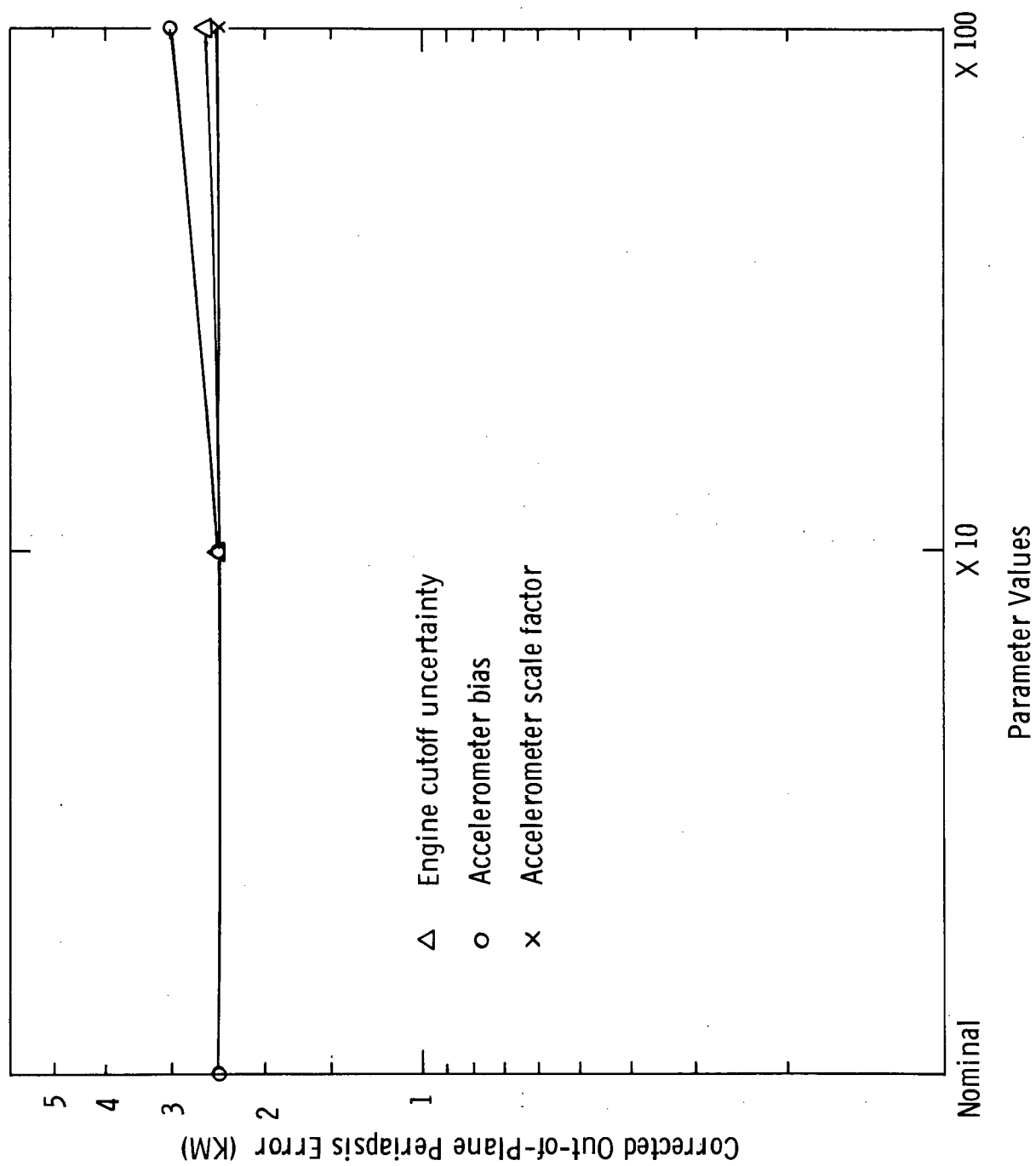


Fig. VI. 14 Effect of Guidance Error on Minimum Obtainable Out of Plane Error Corrected
at Neptune on the Grand Tour. DSN + 10" No IR

TABLE VI-17

Comparison of Errors at Saturn for Single ΔV at 21 Days*

Configuration	Error Values at 36.7969 Days (km)			Terminal Error				Total ΔV
	Position Estimate	Out of Path	Out of Path Corrected	RMS Pos. EST (km)	RMS Vel. EST (mps)	FTA (km)	Ephemeris RMS EST (km)	
DSN Only	242.94	405.66	104.77	1466.01	0.47	261015.1	204.1	1.69
DSN & OB 10" - No IR	9.51	137.21	1.40	949.97	0.31	210216.4	203.9	1.72
DSN & OB 60" - No IR	12.20	170.20	5.49	1411.82	0.45	259025.0	204.1	1.69

*Terminal Time = Days. Pericenter Time = Days.

Also regarding guidance requirements, it appears that accelerometer bias as large as $1 - 10 \text{ cm/sec}^2$ and scale-factor errors in excess of 500 ppm may be acceptable at the end of a nine-year mission. Sensors meeting the highest known standards of performance must be designed to ensure that the above values will exist after nine years.

Considering now specific requirements for the onboard system, an examination of Table VI-18 shows that the onboard navigation sensor produces substantial savings in total-mission fuel, except for the comparison at Neptune passage. In those cases where better navigation estimates by an onboard system cause an additional velocity correction, the FTA guidance errors are also reduced substantially. The same table contains estimates of fuel savings made available by an onboard capability. These estimates can, for a specific spacecraft design, be converted into a fuel penalty. No representative spacecraft designs were provided for this study.

To pursue the subject of tradeoff between DSN-only and DSN-onboard capabilities further, a comparison was made using spacecraft with assumed initial weights. The results of this study are shown in Table VI-19, which is similar in content to Table V-8 in the previous chapter. Velocity totals for each of the eight mission legs of the Grand Tour were chosen for the DSN-only and the DSN-onboard (1" - 60") cases. The three spacecraft weights at earth departure were chosen as 226.8, 453.6 and 2268.0 kg. The resulting gross-mass savings using the DSN and onboard combination are given below. These mass savings predictions are quite conservative inasmuch as the additional savings obtainable through associated reduction in tank and structure mass is not included. They indicate a compelling reason to use onboard navigation on the Grand Tour:

<u>Initial Mass of Spacecraft (kg)</u>	<u>Gross-Mass Saving (kg)</u>
226.8	40.4
453.6	80.8
2268.0	404.0

TABLE VI-18

Fuel Savings Indicated During Four Planet Encounters on the Grand Tour,
with Accompanying Fixed-Time-of-Arrival Guidance Errors

DSN ONLY	ONBOARD 10" - 60"		ONBOARD 10" - No IR		ONBOARD 3" - No IR		ONBOARD 1" - No IR	
	FTA(km)	$\Delta V(\text{mps})$	FTA(km)	$\Delta V(\text{mps})$	FTA(km)	$\Delta V(\text{mps})$	FTA(km)	$\Delta V(\text{mps})$
Jupiter	206.8	9.47	210.8	4.29	209.9	4.87	134.4	3.10
Saturn	1514.7	134.33	996.8	25.58	959.3	24.16	841.8	12.75
Uranus	1203.6	252.80	874.8	20.11	916.3	27.68	772.5	14.26
Neptune	7941.9	9.00	569.6	9.00	627.6	10.00	354.0	13.7
TOTAL (mps)		405.75		59.42		66.77		43.83
SAVINGS (mps)		N/A		346.32		338.98		361.92
								39.01
								366.73

TABLE VI-19

Grand Tour Spacecraft Weight Estimates

MISSION PHASE	Velocity Budget (mps)		Final Mass (kg) at End of Mission Phases					
	DSN Only	DSN&OB 1" - 60"	W _O = 226.8 (kg)		W _O = 453.6 (kg)		W _O = 2268.0 (kg)	
Earth-Jupiter	56.0	56.1	220.2	220.2	440.5	440.4	2202.4	2202.1
Jupiter Passage	9.47	2.60	219.2	219.9	438.4	439.8	2218.9	2199.2
Jupiter-Saturn	1.1	2.4	219.0	219.7	438.1	439.3	2190.5	2196.6
Saturn- Passage	134.33	11.28	203.5	218.4	407.1	436.8	2035.4	2183.9
Saturn-Uranus	4.6	6.13	203.1	217.7	406.1	435.4	2030.5	2177.1
Uranus Passage	252.80	9.29	175.1	216.7	350.3	433.4	1751.5	2166.8
Uranus-Neptune	9.0	9.05	174.4	215.7	348.7	431.4	1743.5	2156.7
Neptune Passage	9.1	15.85	173.5	213.9	347.0	427.9	1735.3	2139.3
Mass Savings-kg (Gross)			40.4		80.8		404.0	

The gross-weight savings in these cases are roughly proportional to the spacecraft gross weight (18%). Of course, the net-weight savings involve the direct and indirect weight and reliability penalties incurred by actually adding the equipment.

Tables VI-20 and VI-21 compare navigation and guidance sub-systems weight and power on a total basis in the three navigation concepts for both the heliocentric and near planet mission phases. Turning to Table VI-20 for the heliocentric or interplanetary portions of the Grand Tour mission, we note the navigation errors and guidance errors for the onboard-only, DSN-only, and the DSN combined with a 10-arc-second visible and 60-arc second infrared onboard systems. This material was presented earlier in the chapter, but is now organized for a synoptic view. Total velocity change is given along with spacecraft-subsystem parameters. The two classes of computer weights are differentiated by onboard capability for navigation and autonomous guidance in the 8.2-kg unit versus only limited onboard control capability and no navigation computations in the 3.6-kg unit. The three degree-of-freedom, sequential-type, navigation instrument is listed. From this table, it is plain that onboard only is a noncompetitive concept for interplanetary legs of the Grand Tour. In comparison with DSN only, the onboard units yield no advantage and a net penalty of 22.2 kg and 22 watts.

The onboard-only case having been rejected because of its unsuitability for the interplanetary legs, the near-planet mission phases summarized in Table VI-21 can be examined. Here, a DSN-only case is compared with a minimum-onboard capability (60" - 60" instrument) and a maximum capability of 1" visible edge only. The 60" - 60" instrument was again assumed to be the three-degree-of-freedom sequential telescope. The 1" instrument was the same instrument with the addition of an inertially-torqued capability in the command of the telescope in the measuring plane. Both onboard instruments require the augmented or 8.2-kg

TABLE VI-20

Comparison of Three Navigation Concepts on a Total G & N Subsystem Basis
for the Heliocentric or Interplanetary Legs of the Grand Tour

	OB ONLY		DSN ONLY		DSN&OB 1" - 60"	
	mps	km	mps	km	mps	km
NAV ERRORS						
Earth-Jupiter	0.4893	12747.0	0.0003	555.0	0.0002	280.0
Jupiter-Saturn	0.1003	4811.8	0.0034	1173.0	0.0037	439.0
Saturn-Uranus	0.1318	13532.6	0.0037	2075.9	0.0037	725.8
Uranus-Neptune	0.1116	9699.0	0.0209	3661.0	0.0171	2137.0
		km		km		km
FTA GUID						
Earth-Jupiter		12932.0		555.0		304.0
Jupiter-Saturn		5121.0		1174.7		439.0
Saturn-Uranus		14020.0		2075.9		909.0
Uranus-Neptune		11004.0		3661.0		2874.0
TOTAL ΔV (mps)	162.4		70.6		73.7	
S/C PENALTIES						
ITEM	Mass (kg)	PWR. (Wts)	Mass (kg)	PWR. (Wts)	Mass (kg)	PWR. (Wts)
Computer	8	30	4	30	8	30
Sensor	18	22	-	-	18.5	23
	26	52	4	30	26.8	53

TABLE VI-21

Comparison of Two Navigation Concepts on a Total G & N Subsystem Basis
for the Near Planet Portions of the Grand Tour

	DSN ONLY				Minimum Onboard with DSN Capability (60" - 60")		Accurate Onboard with DSN Capability (1" - No IR)	
	ΔV mps	Error km	ΔV mps	Error km	ΔV mps	Error km	ΔV mps	Error km
Navigation Uncertainties								
Jupiter	0.0497	190.78	0.0497	190.65	0.0181	68.78		
Saturn	0.4708	1481.51	0.4307	1353.92	0.2720	844.09		
Uranus	0.4468	1071.95	0.4288	1028.58	0.2387	572.30		
Neptune	21.0200	1604.48	1.7040	129.84	0.3820	28.18		
FTA Guidance Errors								
Jupiter		206.8		211.8		71.9		
Saturn		1514.7		1371.8		859.5		
Uranus		1203.6		1028.5		592.1		
Neptune		7941.8		2607.0		254.0		
Total ΔV (mps)	405.72		155.08		39.01			
S/C Penalties	Item	Mass(kg)	PWR. (Wts)	Mass(kg)	PWR. (Wts)	Mass(kg)	PWR. (Wts)	
Computer		4	30	8	30	8	30	
Nav-Sensor		-	-	18	22	18.6	23	
Total		4	30	26	52	26.6	53	

computer unit, and their mechanizations use only a portion of the 40.4-kg. savings predicted in the 226.8-kg spacecraft studies of Table VI-19.

The potential minimization of fuel described in the Grand Tour results for this chapter can be achieved by combining accurate measurement capability with the autonomy necessary to correct a state-vector error soon after its detection. This implies a requirement for accurate, flexible navigation measurements, and a computer capability well beyond that used in unmanned space missions to date. Guidance requirements are dominated by accelerometer parameters.

CHAPTER VII

CONCLUSIONS AND RECOMMENDATIONS

A. Conclusions

1. 1973 Jupiter Flyby

Simulation of the 1973 Jupiter Flyby indicated that onboard navigation can make no significant contribution to reducing the navigation error. Thus, for this mission there was no evaluation of attitude-control requirements of the onboard instrument, no estimate of the power, weight and volume impact of the onboard equipment, and no study of total-system trade-off. An evaluation of the effects of accelerometer errors and propulsion cut-off uncertainty on the guidance implementation of DSN-generated midcourse velocity corrections was made. The fixed-time-of-arrival (FTA) error was found to be very sensitive to accelerometer bias and propulsion cut-off uncertainty. A bias level below 0.10 cm/sec^2 and a thrust cut-off uncertainty of 0.05 sec should be maintained.

2. 1977 Jupiter Swingby to Saturn

For the 1977 Jupiter swingby to Saturn, onboard navigation did not make a significant impact upon navigational accuracy until the actual Saturn passage at three radii was being approached. At this point, combining onboard navigation measurements with DSN navigation reduced the FTA guidance error of almost 500 km by an order of magnitude. Because at three Saturn radii the position vector at passage may not be a critical flyby mission parameter, this FTA guidance-error reduction may not be very beneficial. On a total-system basis, in any event, the fuel saving produced by this potentially improved navigational accuracy did not approach paying in weight for the additional weight required by the onboard system.

The guidance requirements again were sensitive to accelerometer bias and propulsion cut-off uncertainty.

3. 1977 Grand Tour

In the analysis of the 1977 Grand Tour simulation, the addition of onboard measurements to DSN navigation again began to pay for itself at the Saturn passage and its contribution became successively more marked for the Uranus and Neptune passages. One should not interpret this conclusion to mean that a totally on-board system should be used. DSN data will be available and should be utilized. However, it does indicate that DSN scheduling can be determined from science and engineering data return or operational requirements rather than navigational requirements.

The combination of on board navigation with DSN resulted in both lower errors and fuel savings. For the complete mission, the savings in required onboard fuel for a given initial spacecraft weight amounted to about 18 percent of initial weight, enough to justify the penalty of the navigation sensor. The onboard instrument was shown to require a visible-light sensitivity only, since the dark side of the planet was not frequently called up for an IR measurement.

As on the previous missions, the guidance requirements emphasized accelerometer bias and cut-off time uncertainty. At the outer planets, however, the FTA guidance sensitivity to these errors did not appear until they had been increased generally by more than a factor of ten from the selected nominal values.

The attitude-control requirements were involved in a trade-off with the navigation instrument. The simplest body-fixed sensor required complete maneuver and precision hold from the attitude-control system. Navigation sensors of increasing weight, power and complexity required less and less performance from the attitude control system. Specific examples were given for a range of sensors, with accompanying statements regarding their impact on attitude-control requirements. Power, weight and volume requirements were estimated and tabulated.

Specific system choice will require additional design information from the spacecraft and other subsystem areas. However, the results of the Grand Tour evaluation clearly imply the need for an onboard-navigation system.

B. Recommendations.

Looking towards a Grand Tour program and a launch date a scant seven or eight years away, several recommendations can be made.

1. Navigation.

a. Future Phenomena Studies.

Presuming that it is desirable, for outer-planet scientific-experiment purposes, to know the probe-planet range as accurately as possible, the probe position-error ellipsoid volume must therefore be minimized. Because, at close ranges, the volume of the error ellipsoid is proportional to phenomena uncertainties, these uncertainties must be minimized.

Minimization of phenomena uncertainties will require a considerable amount of work beginning now and continuing through the outer-planet missions. Data on all the pertinent experiments performed to date need to be gathered and correlated. Further experiments to complement the data on hand need to be designed and performed. Models of the radiative-transfer processes need to be developed so that mathematical simulations can be constructed. It is anticipated that simulations will help separate useful from spurious experimental data, and will provide the best possible horizon profiles prior to flight.

Tangential ephemeris errors might possibly be reduced by star-occultation experiments, or error analyses applied to planetary satellite positions. The effects on radius uncertainties of latitude and cloud thickness and composition should be determined. The range of radius values based on star occultation resulting from differential and ordinary refraction should be determined. Aerosol composition, shape

and size, and number disturbances should be estimated. Models of meteorological phenomena should be formulated so that the variations in horizon profiles can be estimated. Finally, the error models associated with the combining of instrument and phenomena errors should be expanded to include the results of multiple measurement filtering.

b. Navigation Instrument-Design Studies.

This crucial area presents program planners with a particularly challenging task, for several reasons. First, instrument design must be predicated on an admittedly meager knowledge of phenomena physics; better knowledge of phenomena physics will only come, however, through operational use of a properly designed instrument. Second, whereas inertial - sensor and computer subsystems currently under development show survivability or graceful degradation, the navigation-sensor subsystem clearly lacks a conceptual approach to reliability. Intensive design work must begin now to provide for an orderly and well-managed instrument developmental program. The instrument finally chosen should be flown at the earliest possible date on an inner solar-system planetary mission so that operational experience can be gained.

2. Guidance

The guidance "problem" actually relates to prediction of reliability and to control of velocity-correction vector length. In the area of guidance, developmental programs should aim toward single specific-force sensors for the outer-planet mission environments. Improved control and prediction of variation in the propulsion system "tail-off" impulse are also required.

3. Systems

The systems study was conducted without a series of candidate or representative spacecraft designs. Nevertheless, the need was repeatedly demonstrated for an onboard control digital computer to allow the spacecraft mission operation both autonomy and flexibility. The onboard measurements on the Grand Tour will require this support just for the operation of the instrument in the measuring cycle.

As candidate spacecraft are defined in future studies, it would then be possible to make more satisfactory trade-offs in flexibility and precision between spacecraft orientation and instrument orientation.

Finally, the Grand Tour must meet the long-term mean-time-to-first-failure requirement imposed by the eight-year mission length. It appears that this requirement can be met only by design concepts which allow for graceful degradation, implemented with the highest standards of design practice and fabrication.

Page intentionally left blank

APPENDIX A

INTERPLANETARY TRAJECTORY GEOMETRIES

The purpose of this appendix is to present the geometrical properties of the interplanetary legs of each of the three missions under study here. The plots included herein are invaluable to the scheduling of the on-board navigation system. In addition, they display mission phenomena such as distances to navigational targets and sun angles which are basic to the design and implementation of the onboard navigational system.

There are five plots included for each interplanetary leg. The first in each series displays the overall mission geometry and is used primarily to provide geometrical support for the other plots. The markings on the spacecraft and planet trajectories are at the same equal time intervals to aid in determining the relative positions of the planets and spacecraft.

The second plot in each group of five gives the range to the possible planets of interest. This is valuable for deciding which planet to use for navigation sightings as the spacecraft proceeds along its trajectory. In the absence of other constraints which would prohibit the measurement, those measurements which employ the closest near body are potentially the most useful. This plot is also used to decide during what periods the various planets are too far away to detect with an I. R. instrument and to provide the navigation system designer with information about the target ranges his sensors must deal with.

The third plot in each series gives the spacecraft-Earth-sun angle. The purpose of this plot is to identify those phases of the mission where the spacecraft line of sight (from Earth) comes too close to the sun line of sight to permit tracking of the vehicle from Earth. A check of all these plots reveals the fact that there are very few times the ground based antennas will not be able to track the spacecraft because it is behind the sun. Note that only on the Saturn-Uranus leg of the Grand Tour does one of these periods even come close to an encounter time.

The fourth graph in each group provides the sun-spacecraft-planet angle for each leg. This is of much use in setting up the on board measurement schedule because it displays those periods in which the line-of-sight to the planet is too close to the line of sight to the sun to permit use of the planet for navigational purposes. It also informs the sensor designer what range of sun angles his instrument will encounter.

The final plot in each group gives the Earth-spacecraft-planet angle for each leg. This is of interest to the systems designer because he must be aware of the relative location of the planet and Earth so that functions related to each body can be coordinated. As an example of such coordination consider the problem of orienting the spacecraft, communications antenna, star tracker, and/or planet sensor such that a navigational sighting can be performed without losing communication with the Earth.

Tables A-1 through A-7 provide the results of using these plots to develop candidate on board measurement schedules for all the interplanetary legs of the three missions used in this study. The actual measurements used in the results presented in Chapters IV through VI were selected from those indicated as available in these tables.

As an example of using these plots to create a candidate on board measurement schedule consider the construction of Table A-1 from Figures A1.2 and A1.4. To do this we will use an I.R. instrument maximum useful range of 1 a.u. and an angle of 20 degrees as the closest any instrument may point toward the sun. First we note from Figure A1.4 that Jupiter is never in a position such that the sun angle constraint prevents a measurement. Since Jupiter is thus always available as a navigational body we will use it as a potential near body throughout this interplanetary leg; thus the column of "yes's" under Jupiter in Table A-1. The reason for this is that the ephemeris error is so large that it is often useful to begin sighting on Jupiter earlier than would otherwise be expected so that the ephemeris error can be reduced.

Turning now to the question of what other near bodies should be used throughout the leg we note from Figure A1.2 that Earth is the closest planet until 140 days, when Venus becomes closest. From Figure A1.4 we see that after 125 days the Venus line of sight is too close to the sun to use Venus. Since Earth is considerably closer than Venus prior to 125 days we elect not to use Venus at all on this leg; thus the column of "no's" under Venus in Table A-1. Examining Figure A1.4 again we see that from 40 days to 90 days Earth is inside the sun angle limit and cannot be used for navigation sightings; thus the "no" entry under Earth in Table A-1 from 40 to 90 days. Prior to 40 days Earth is acceptable, thus the "yes" under Earth for the first 40 days. Earth is less than 1 a. u. away during this period hence the "yes" entry for I. R. during these first 40 days. Mars and Jupiter are the only feasible near body condidates during the 40-90 day period but are both too far away to use I. R. , as is seen from Figure A1.2; thus the "no" entry under I. R. during this period.

During the period from 90 to 205 days Earth is outside the sun angle constraint but at 190 days Jupiter, which is a prime target because of the need to reduce the ephemeris error, becomes the closest planet. Since Jupiter is more desirable as a navigational target we elect to use only it after it becomes the closest body; thus the "no's" under Earth and Mars after 190 days. From 90 - 190 days we see from Figure A1.2 that Earth is closer than Mars so we elect to use only Earth and Jupiter during this period; thus the "no's" from 90 - 190 days under Mars in Table A-1.

To complete the construction of Table A-1 we must decide upon the feasibility of I. R. after 90 days. Turning to Figure A1.2 we see that from 90 - 110 days Earth is close enough to use I. R. and that Jupiter meets this condition after 520 days; hence we enter "yes" under I. R. from 90 - 110 days and after 520 days and enter "no" from 110 days to 520 days.

TABLE A-1

On Board Measurement Schedule for Earth-Jupiter Leg
of the 1973 Low Energy Jupiter Flyby

Beginning of Interval (days)	End of Interval (days)	Time Step for Interval (days)	I. R. Feasible?	Venus Used?	Earth Used?	Mars Used?	Jupiter Used?
Injection	40	10	yes	no	yes	no	yes
40	20	10	no	no	no	yes	yes
90	110	10	yes	no	yes	no	yes
110	190	10	no	no	yes	no	yes
190	520	10	no	no	no	no	yes
520	Jupiter sphere of influence	10	yes	no	no	no	yes

TABLE A-2
On Board Measurement Schedule for the Earth-Jupiter Leg
of 1977 Jupiter Swingby to Saturn

Beginning of Interval (Days)	End of Interval (Days)	Time Step for Interval (Days)	I. R. Feasible?	Venus Used?	Earth Used?	Mars Used?	Jupiter Used?	Saturn Used?	Uranus Used?	Neptune Used?
Injection	10	1	yes	no	yes	no	no	no	no	no
10	60	10	yes	no	yes	no	no	no	no	no
60	120	10	yes	no	no	yes	no	no	no	no
120	220	10	no	no	yes	yes	yes	no	no	no
220	360	10	no	no	no	yes	yes	no	no	no
360	Jupiter Sphere of Influence	10	yes	no	no	no	yes	no	no	no

On Board Measurement Schedule for Jupiter-Saturn Leg
of the 1977 Jupiter Swingby to Saturn

Beginning of Interval (Days)	End of Interval (Days)	Time Step for Interval (Days)	I. R. Feasible?	Venus Used?	Earth Used?	Mars Used?	Jupiter Used?	Saturn Used?	Uranus Used?	Neptune Used?
Jupiter Sphere of Influence	50	5	yes	no	no	no	yes	no	no	no
50	170	10	yes	no	no	no	yes	yes	no	no
170	370	10	no	no	no	no	yes	yes	no	no
370	530	10	no	no	no	no	no	yes	no	no
530	Saturn Sphere of Influence	5	yes	no	no	no	no	yes	no	no

TABLE A-4
On Board Measurement Schedule for the Earth-Jupiter Leg
of the 1977 Grand Tour

Beginning of Interval (Days)	End of Interval (Days)	Time Step for Interval (Days)	L.R. Feasible?	Venus Used?	Earth Used?	Mars Used?	Jupiter Used?	Saturn Used?	Uranus Used?	Neptune Used?
Injection	10	1	yes	no	yes	no	no	no	no	no
10	60	10	yes	no	yes	no	no	no	no	no
60	210	10	yes	no	no	yes	yes	no	no	no
210	370	10	no	no	no	no	yes	no	no	no
370	Jupiter Sphere of Influence	10	yes	no	no	no	yes	no	no	no

TABLE A-5

On Board Measurement Schedule for the Jupiter-Saturn
Leg of the 1977 Grand Tour

Beginning of Interval (Days)	End of Interval (Days)	Time Step for Interval (Days)	I.R. Feasible?	Venus Used?	Earth Used?	Mars Used?	Jupiter Used?	Saturn Used?	Uranus Used?	Neptune Used?
Jupiter Sphere of Influence	10	1	yes	no	no	no	yes	no	no	no
10	150	10	yes	no	no	no	yes	no	no	no
150	350	10	no	no	no	no	yes	yes	no	no
350	490	10	no	no	no	no	yes	yes	no	no
490	Saturn Sphere of Influence	10	yes	no	no	no	no	yes	no	no

TABLE A-6

On Board Measurement Schedule for the Saturn-Uranus
Leg of the 1977 Grand Tour

Beginning of Interval (Days)	End of Interval (Days)	Time Step for Interval (Days)	L.R. Feasible?	Venus Used?	Earth Used?	Mars Used?	Jupiter Used?	Saturn Used?	Uranus Used?	Neptune Used?
Saturn Sphere of Influence	100	20	yes	no	no	no	no	yes	no	no
100	680	20	no	no	no	no	no	yes	no	no
680	1140	20	no	no	no	no	no	no	yes	no
1140	Uranus Sphere of Influence	10	no	no	no	no	no	no	yes	no

TABLE A-7

On Board Measurement Schedule for the Uranus - Neptune Leg
of the 1977 Grand Tour

Beginning of Interval (Days)	End of Interval (Days)	Time Step for Interval (Days)	I. R. Feasible?	Venus Used?	Earth Used?	Mars Used?	Jupiter Used?	Saturn Used?	Uranus Used?	Neptune Used?
Uranus Sphere of Influence	80	10	yes	no	no	no	no	no	yes	no
80	320	20	no	no	no	no	no	no	yes	no
320	720	20	no	no	no	no	no	no	no	yes
720	Neptune Sphere of Influence	5	no	no	no	no	no	no	no	yes

Interplanetary Trajectory Geometries

* Trajectory Parameter Summary Page*

1. 1973 LOW ENERGY JUPITER FLYBY

Fig. A1.1 Trajectory Diagram for Low Energy Jupiter Flyby

Fig. A1.2 Ranges to Solar System Planets for Low Energy
Jupiter Flyby

Fig. A1.3 Spacecraft- Earth-Sun Angle for Low Energy Jupiter
Flyby

Fig. A1.4 Sun-Spacecraft-Planet Angles for Low Energy Jupiter
Flyby

Fig. A1.5 Earth-Spacecraft-Planet Angles for Low Energy
Jupiter Flyby

2. 1977 JUPITER FLYBY TO SATURN

Fig. A2.1 Trajectory Diagram for Jupiter Flyby to Saturn

Fig. A2.2 Ranges to Solar System Planets for Earth-Jupiter
Leg of 1977 Jupiter Flyby to Saturn

Fig. A2.3 Spacecraft-Earth-Sun Angle for Earth-Jupiter Leg
of 1977 Jupiter Flyby to Saturn

Fig. A2.4 Sun-Spacecraft-Planet Angles for Earth-Jupiter Leg
of 1977 Jupiter Flyby to Saturn

Fig. A2.5 Earth-Spacecraft-Planet Angles for Earth-Jupiter
Leg of 1977 Jupiter Flyby to Saturn

Fig. A2.6 Range to Solar System Planets for Jupiter-Saturn
Leg of 1977 Jupiter Flyby to Saturn

- Fig. A2.7 Spacecraft-Earth-Sun Angle for Jupiter-Saturn Leg of 1977 Jupiter Flyby to Saturn
- Fig. A2.8 Sun-Spacecraft-Planet Angles for Jupiter-Saturn Leg of 1977 Jupiter Flyby to Saturn
- Fig. A2.9 Earth-Spacecraft-Planet Angles for Jupiter-Saturn Leg of 1977 Jupiter Flyby to Saturn

3. 1977 GRAND TOUR

- Fig. A3.1 Trajectory Diagram for 1977 Grand Tour
- Fig. A3.2 Ranges to Solar System Planets for Earth-Jupiter Leg of 1977 Grand Tour
- Fig. A3.3 Spacecraft-Earth-Sun Angle for Earth-Jupiter Leg of 1977 Grand Tour
- Fig. A3.4 Sun-Spacecraft-Planet Angles for Earth-Jupiter Leg of 1977 Grand Tour
- Fig. A3.5 Earth-Spacecraft-Planet Angles for Earth-Jupiter Leg of 1977 Grand Tour
- Fig. A3.6 Ranges to Solar System Planets for Jupiter-Saturn Leg of 1977 Grand Tour
- Fig. A3.7 Spacecraft-Earth-Sun Angle for Jupiter-Saturn Leg of 1977 Grand Tour
- Fig. A3.8 Sun-Spacecraft-Planet Angles for Jupiter-Saturn Leg of 1977 Grand Tour
- Fig. A3.9 Earth-Spacecraft-Planet Angles for Jupiter-Saturn Leg of 1977 Grand Tour
- Fig. A3.10 Ranges to Solar System Planets for Saturn-Uranus Leg of 1977 Grand Tour
- Fig. A3.11 Spacecraft-Earth-Sun Angle for Saturn-Uranus Leg of 1977 Grand Tour

- Fig. A3.12 Sun-Spacecraft-Planet Angles for Saturn-Uranus
Leg of 1977 Grand Tour
- Fig. A3.13 Earth-Spacecraft Planet Angles for Saturn-Uranus
Leg of 1977 Grand Tour
- Fig. A3.14 Ranges to Solar System Planets for Uranus-Neptune
Leg of 1977 Grand Tour
- Fig. A3.15 Spacecraft-DSN-Sun Angle for Uranus-Neptune Leg
of 1977 Grand Tour
- Fig. A3.16 Sun-Spacecraft-Planet Angles for Uranus-Neptune
Leg of 1977 Grand Tour
- Fig. A3.17 Earth-Spacecraft-Planet Angles for Uranus-Neptune
Leg of 1977 Grand Tour

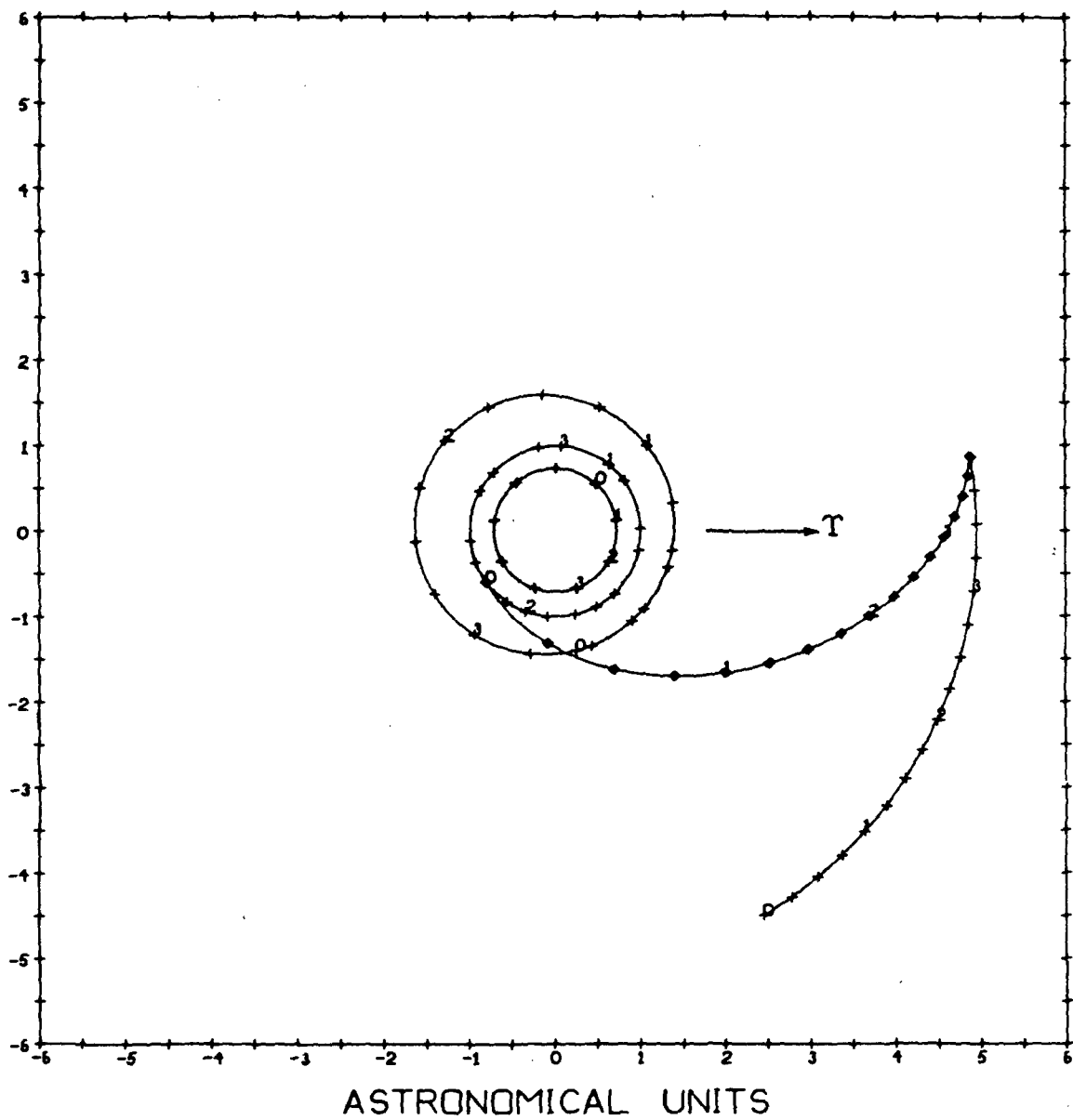


Fig. A1.1 Trajectory Diagram for Low Energy Jupiter Flyby

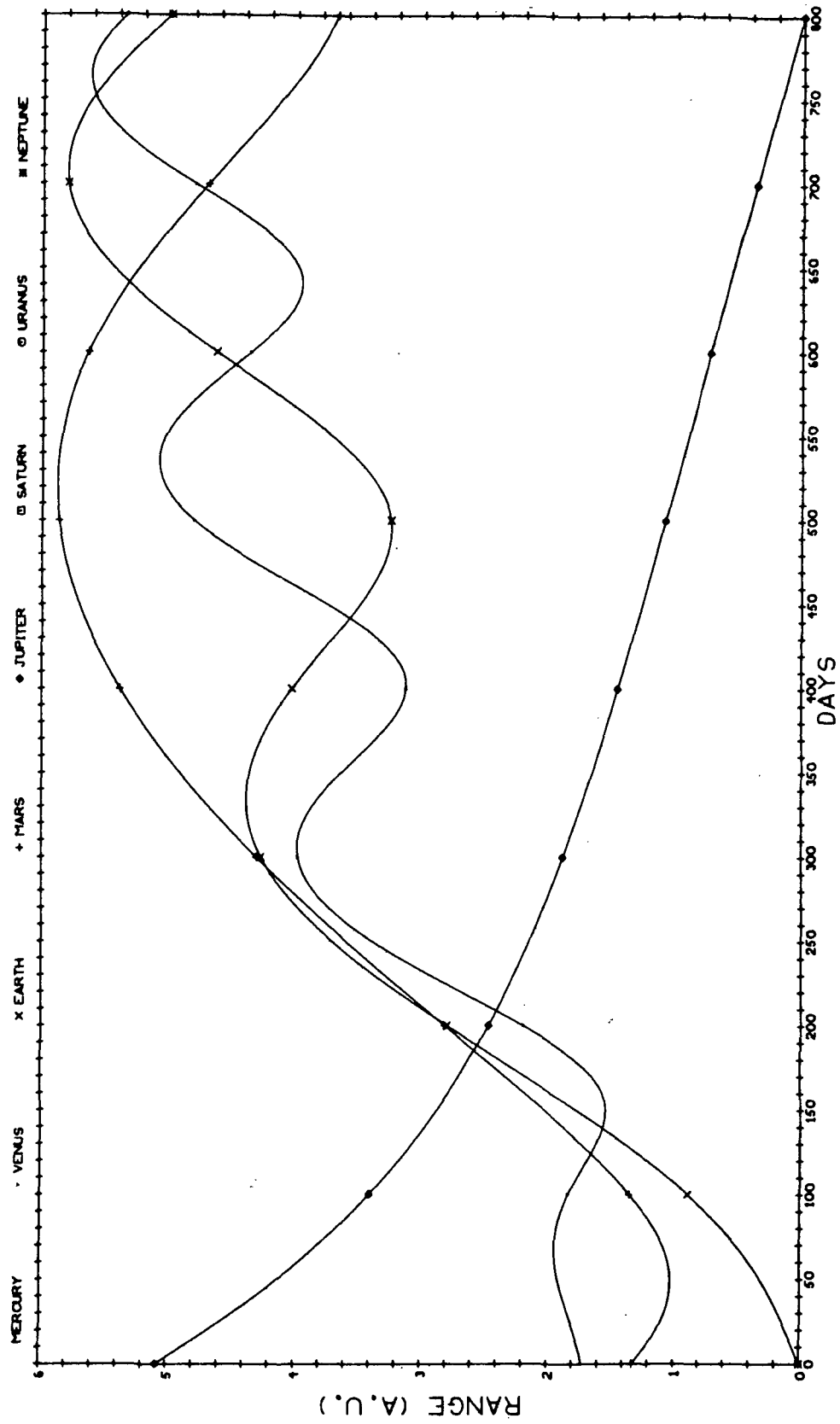


Fig. A1.2 Ranges to Solar System Planets for Low Energy Jupiter Flyby

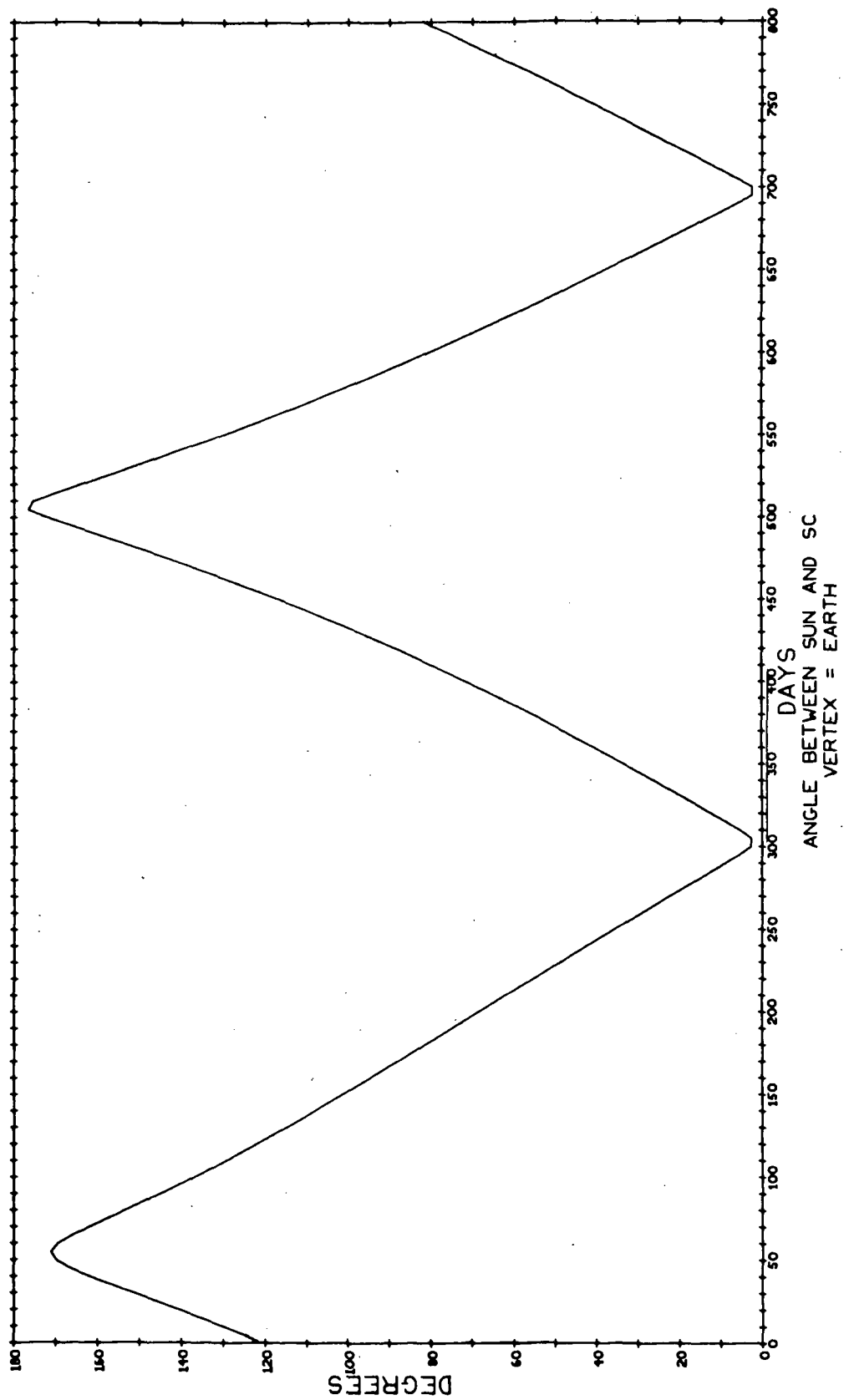


Fig. A1.3 Spacecraft-Earth-Sun Angle for Low Energy Jupiter Flyby

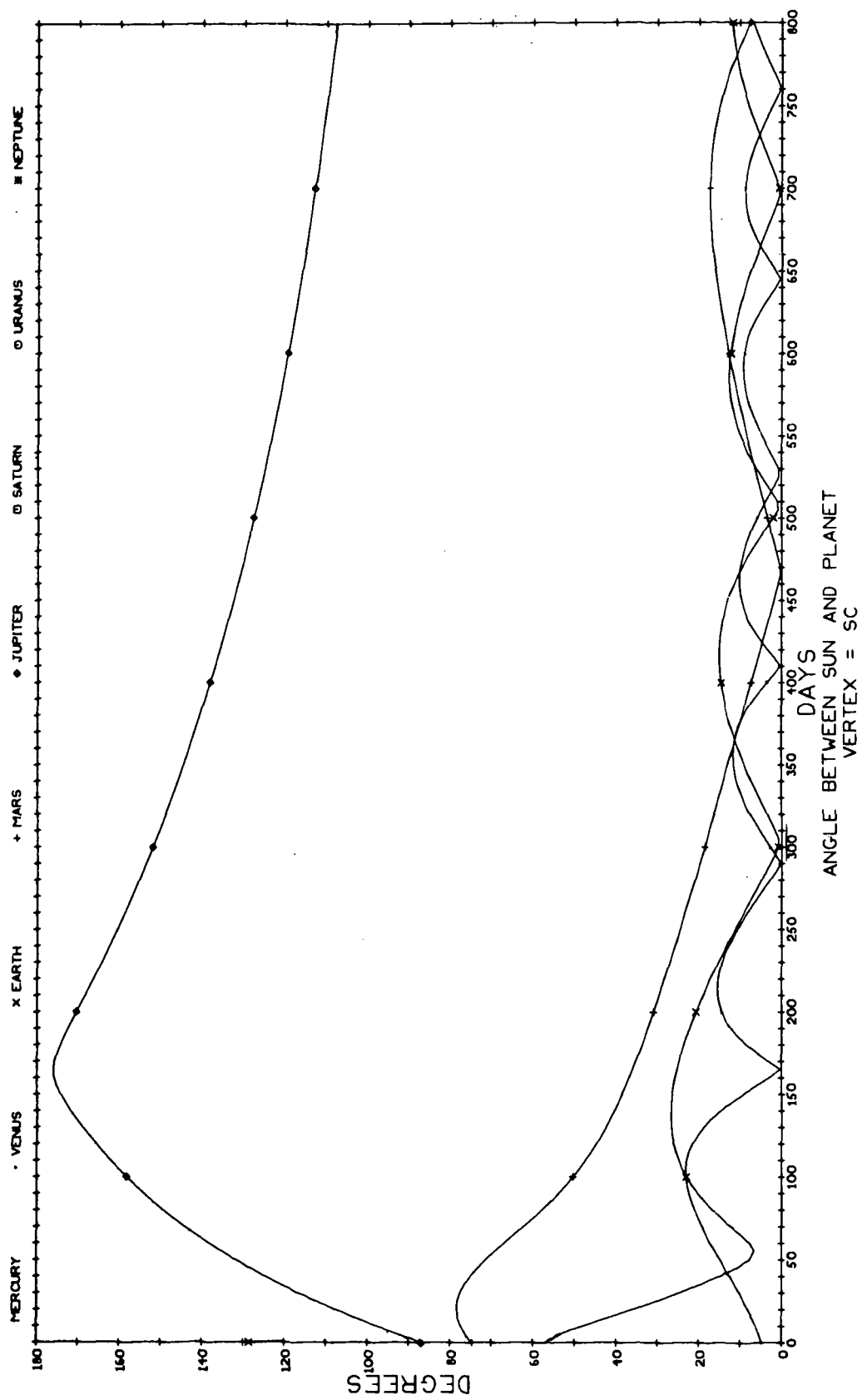


Fig. A1.4 Sun-Spacecraft-Planet Angles for Low Energy Jupiter Flyby

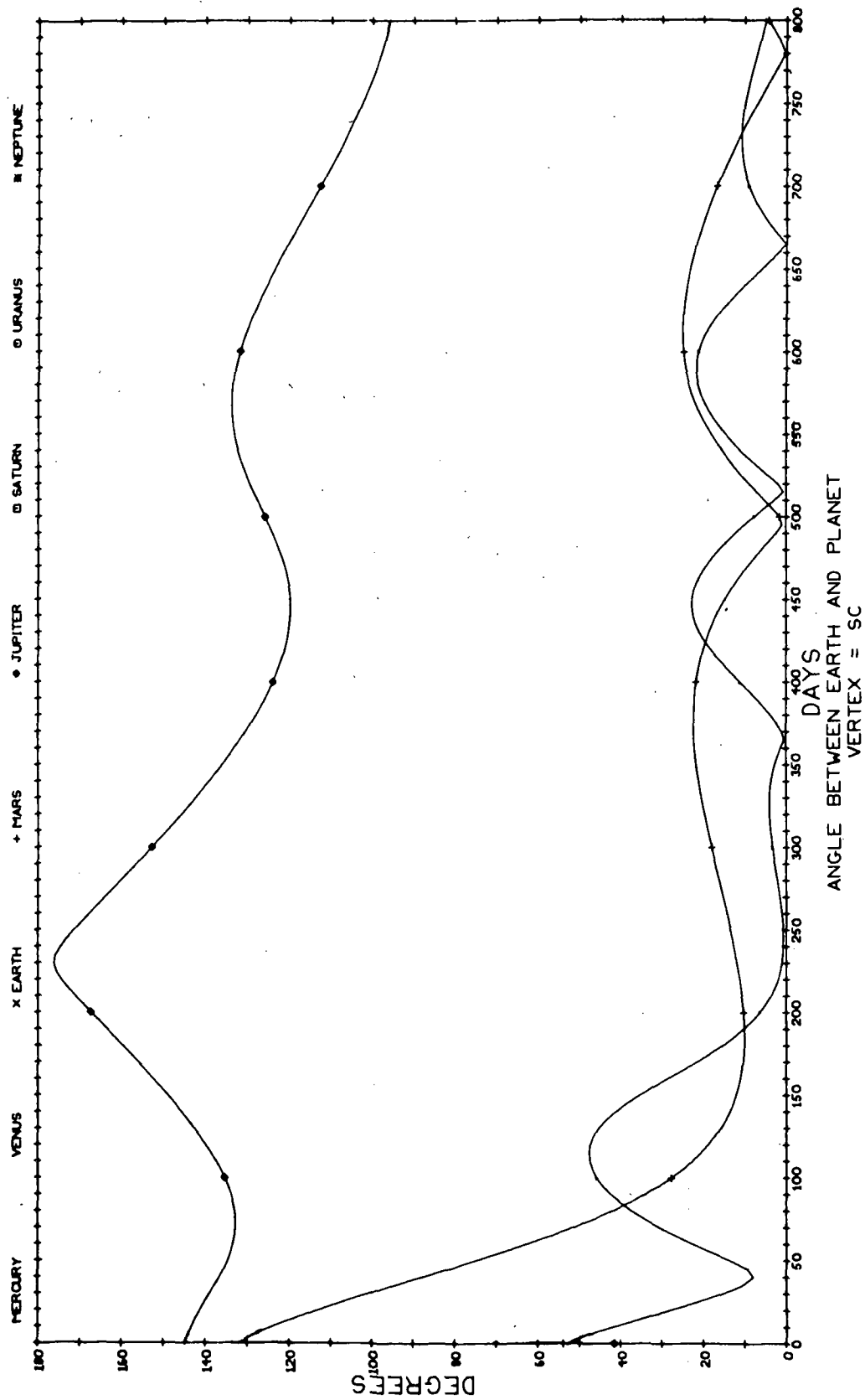


Fig. A1.5 Earth-Spacecraft-Planet Angles for Low Energy Jupiter Flyby

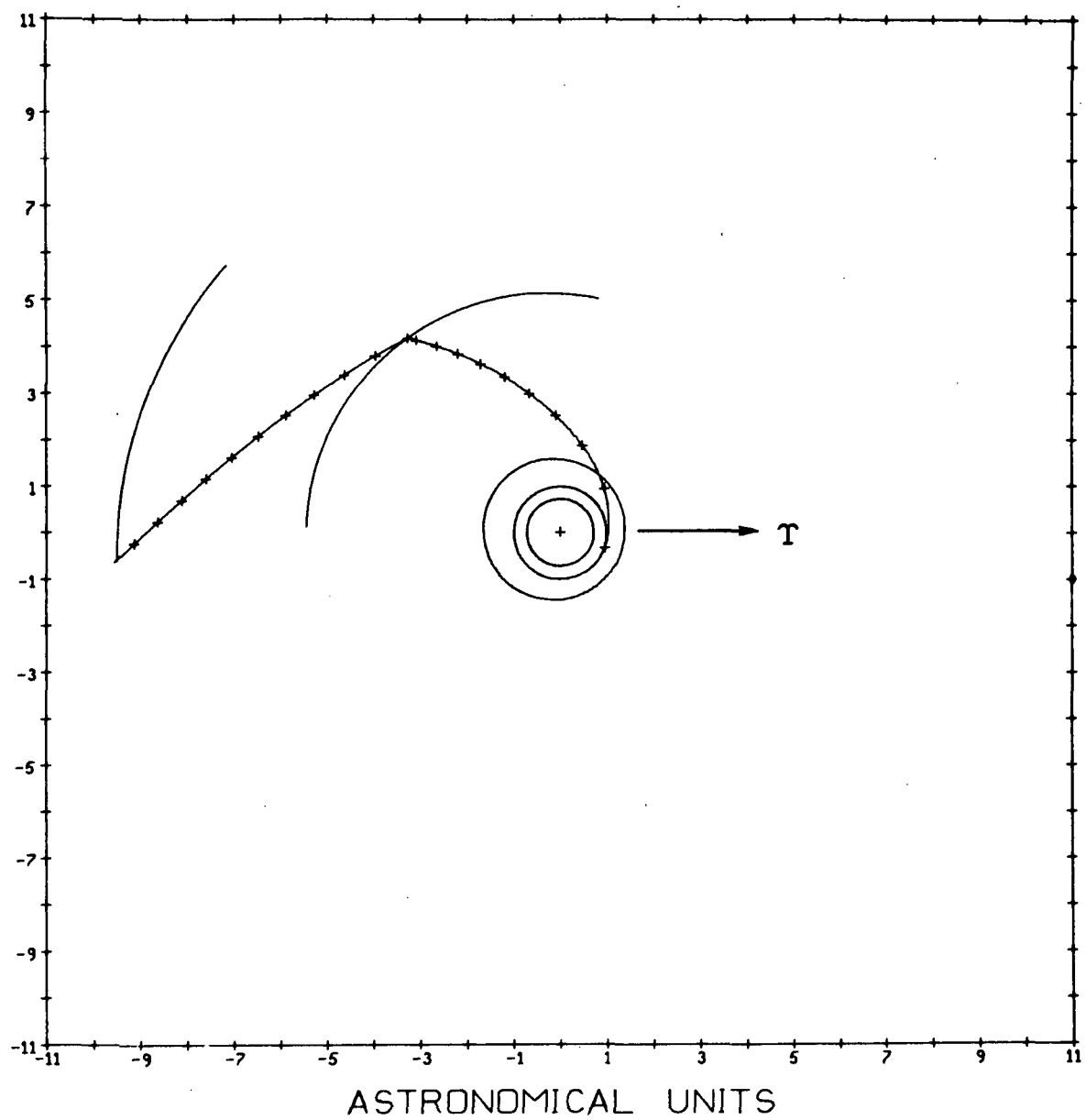


Fig. A2.1 Trajectory Diagram for Jupiter Flyby to Saturn

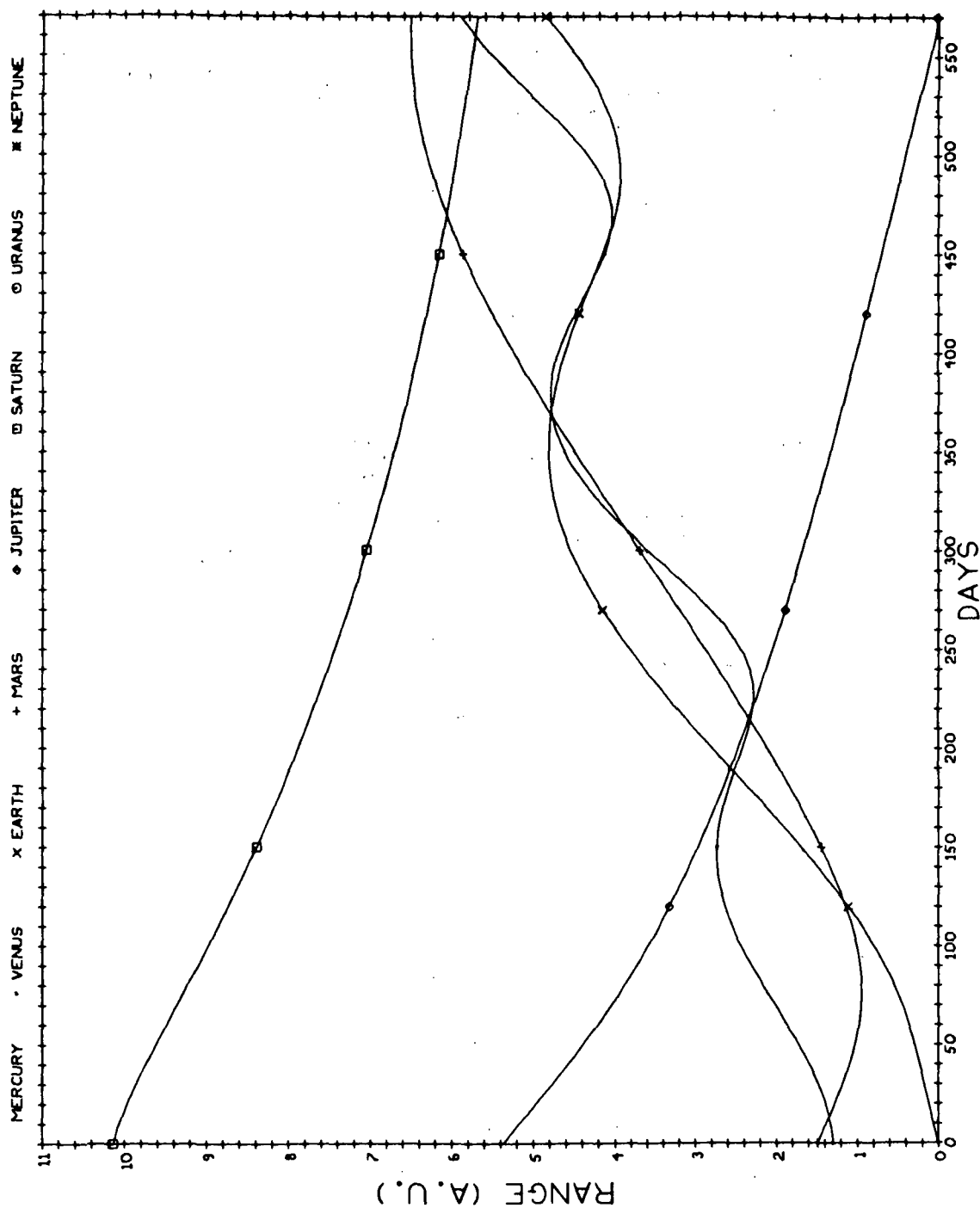


Fig. A2.2 Ranges to Solar System Planets for Earth-Jupiter Leg of 1977
Jupiter Flyby to Saturn

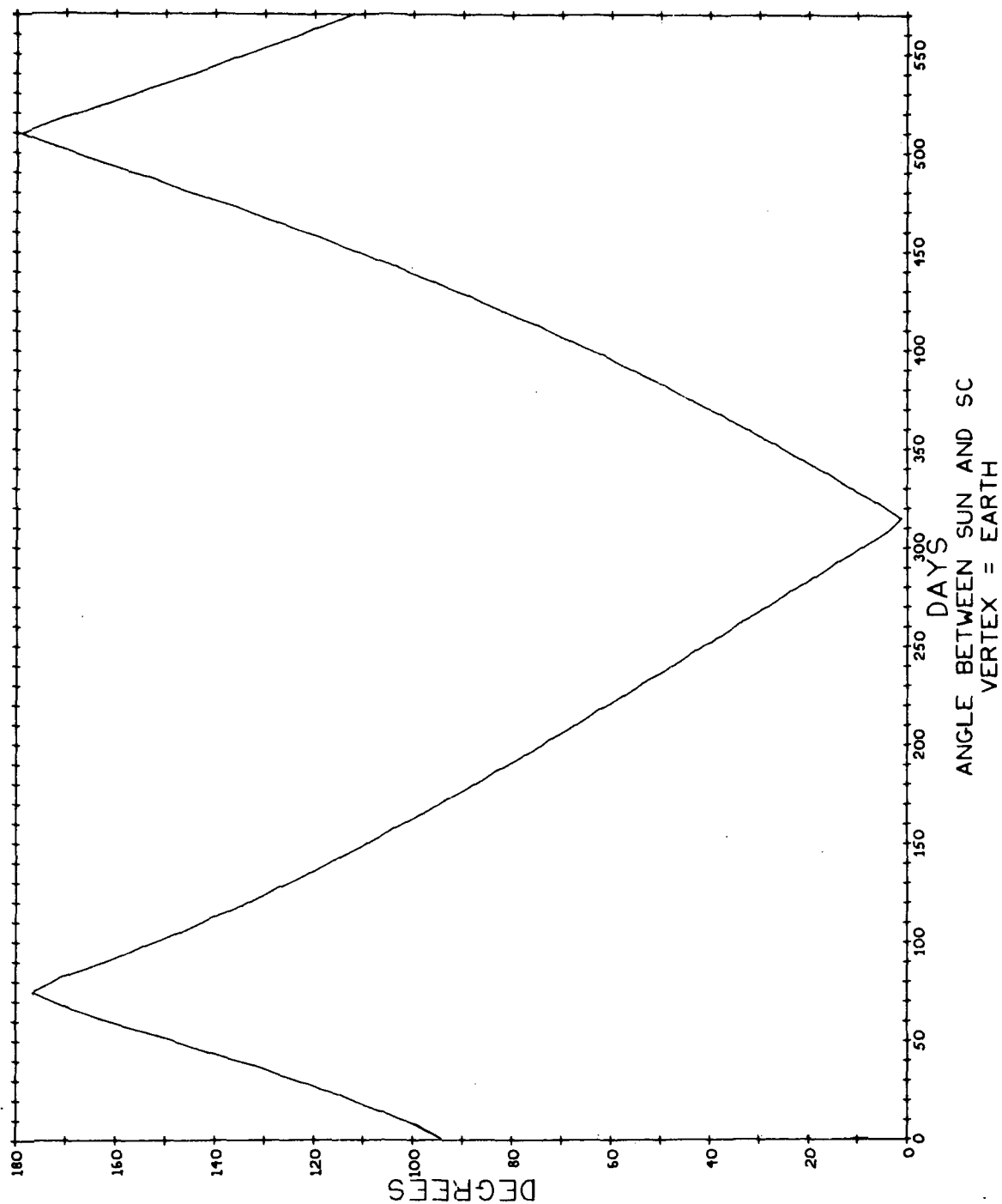


Fig. A2.3 Spacecraft-Earth-Sun Angle for Earth-Jupiter Leg of 1977
Jupiter Flyby to Saturn

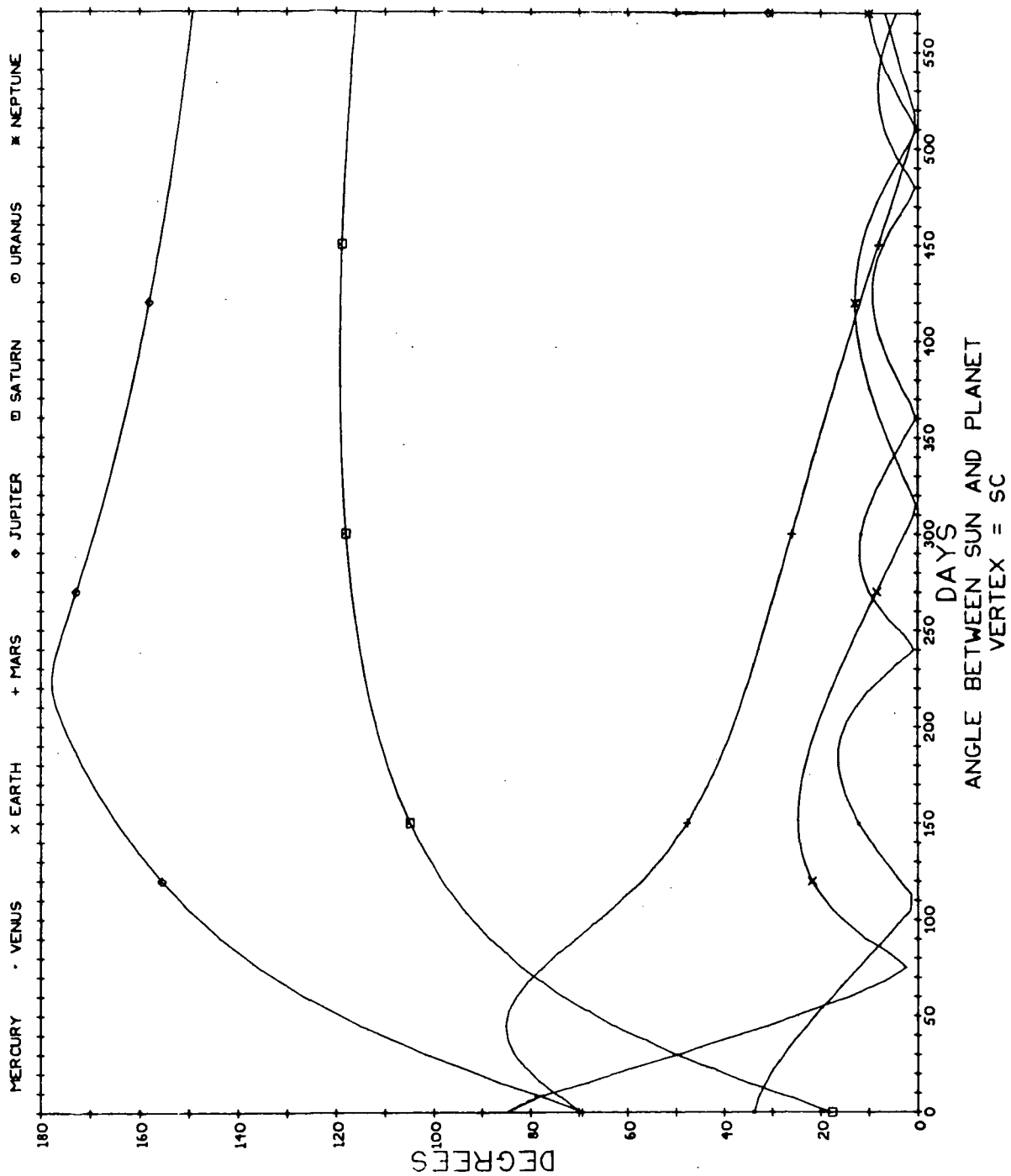


Fig. A2.4 Sun-Spacecraft - Planet Angles for Earth-Jupiter Leg of 1977 Jupiter Flyby to Saturn

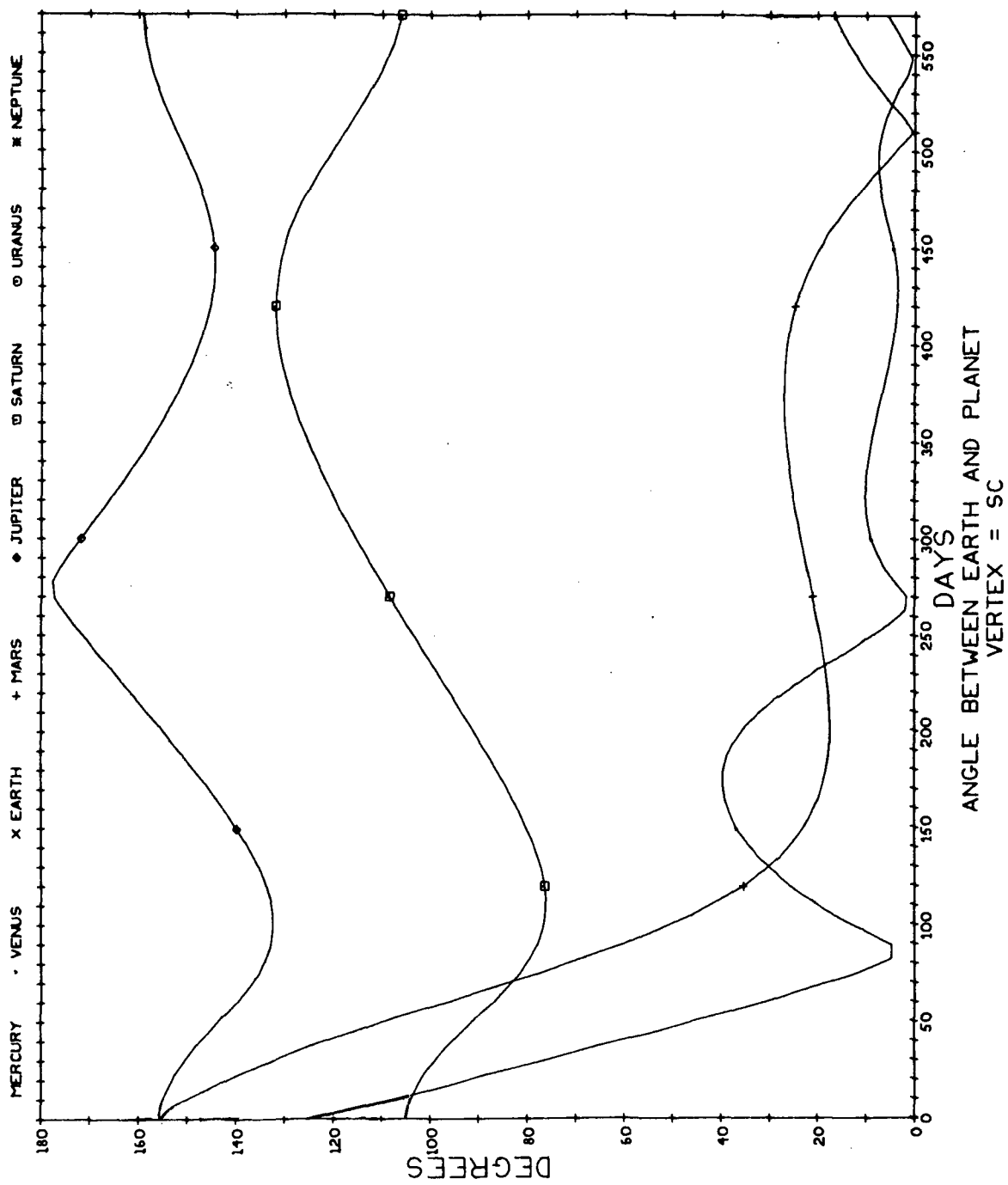


Fig. A2.5 Earth-Spacecraft - Planet Angles for Earth-Jupiter Leg of 1977 Jupiter Flyby to Saturn

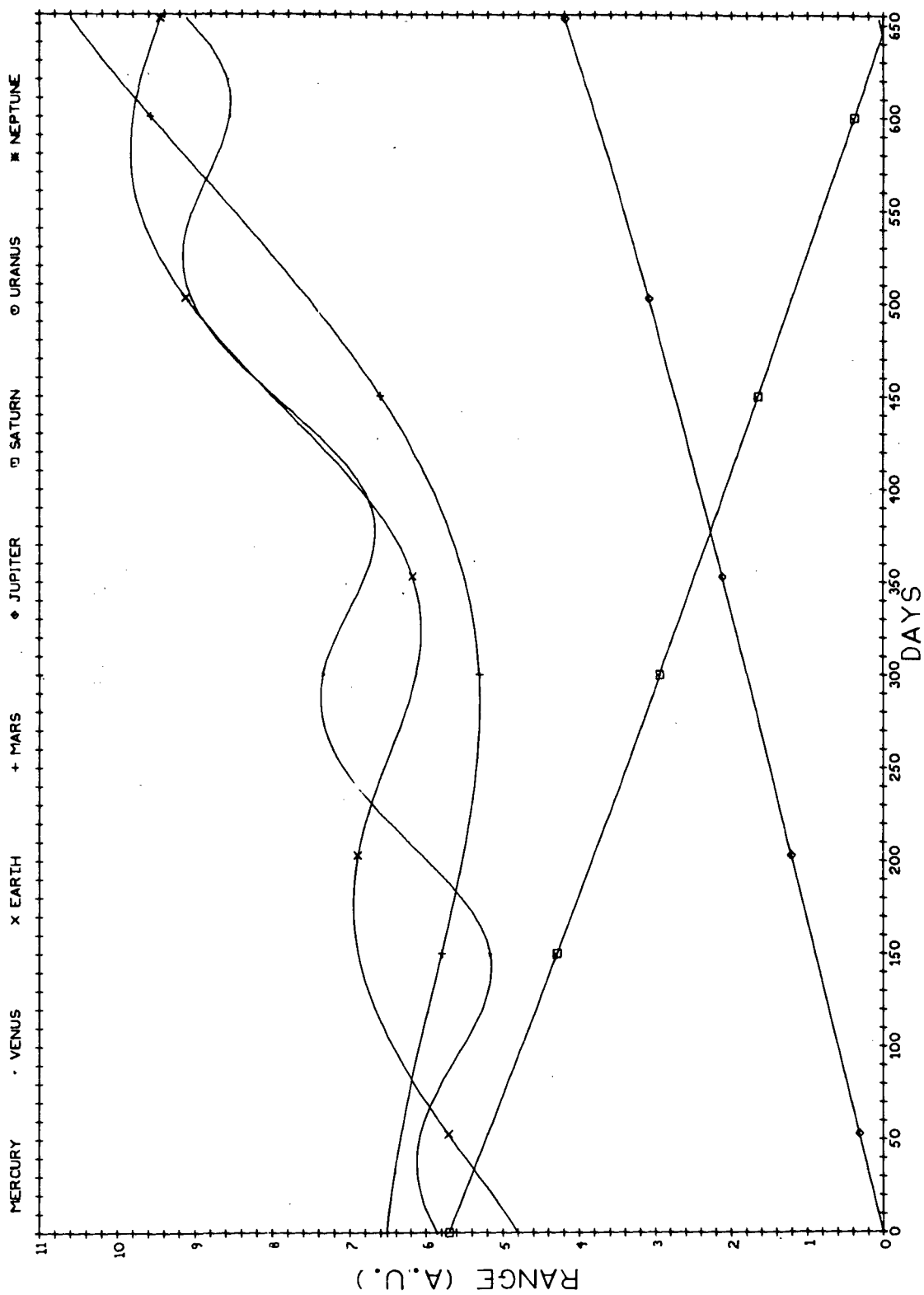


Fig. A2.6 Range to Solar System Planets for Jupiter - Saturn Leg of 1977 Jupiter Flyby to Saturn

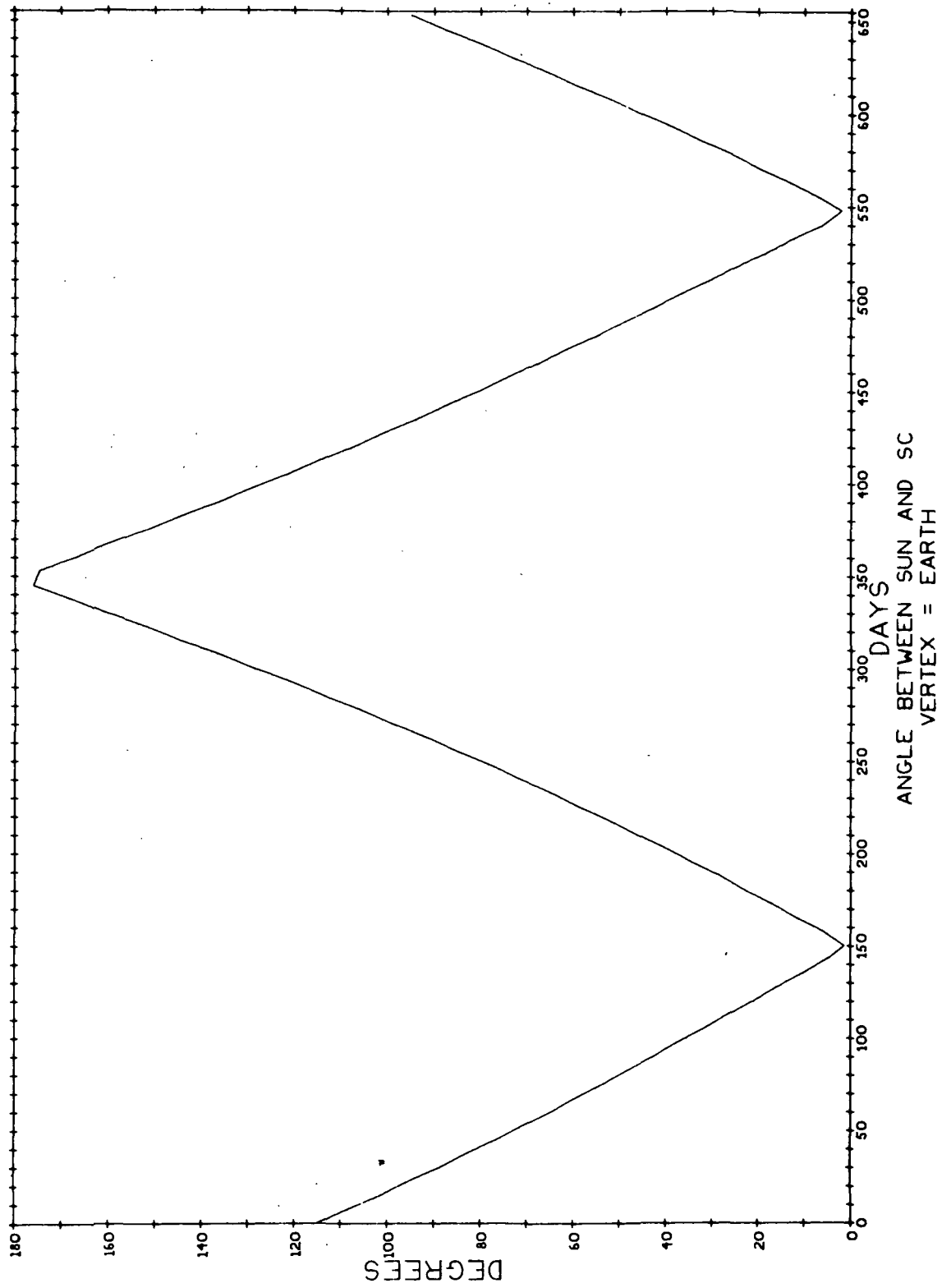


Fig. A2.7 Spacecraft - Earth - Sun Angle for Jupiter - Saturn Leg of 1977 Jupiter Flyby to Saturn

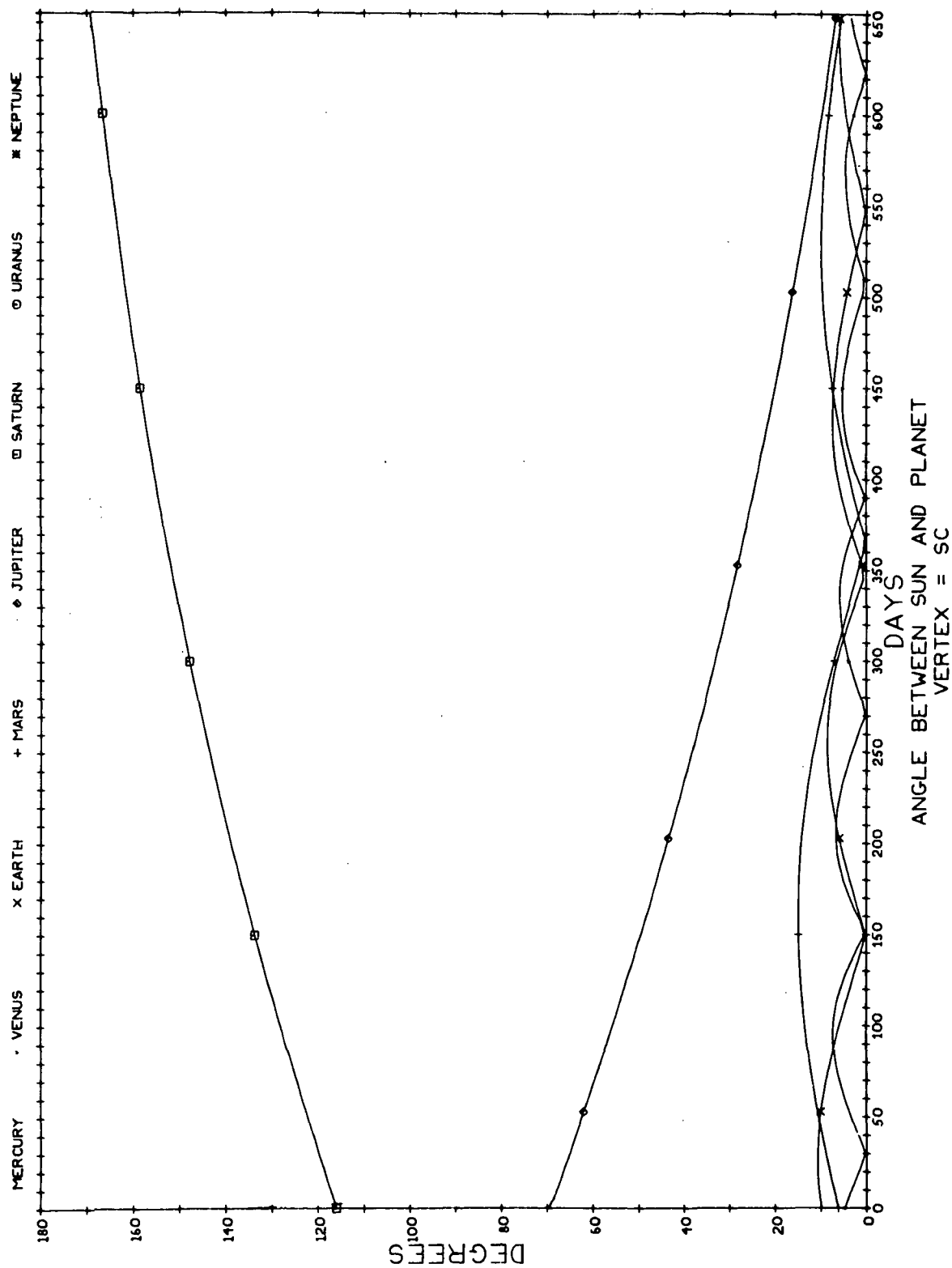


Fig. A2.8 Sun - Planet Angles for Jupiter - Saturn Leg of 1977 Jupiter Flyby to Saturn

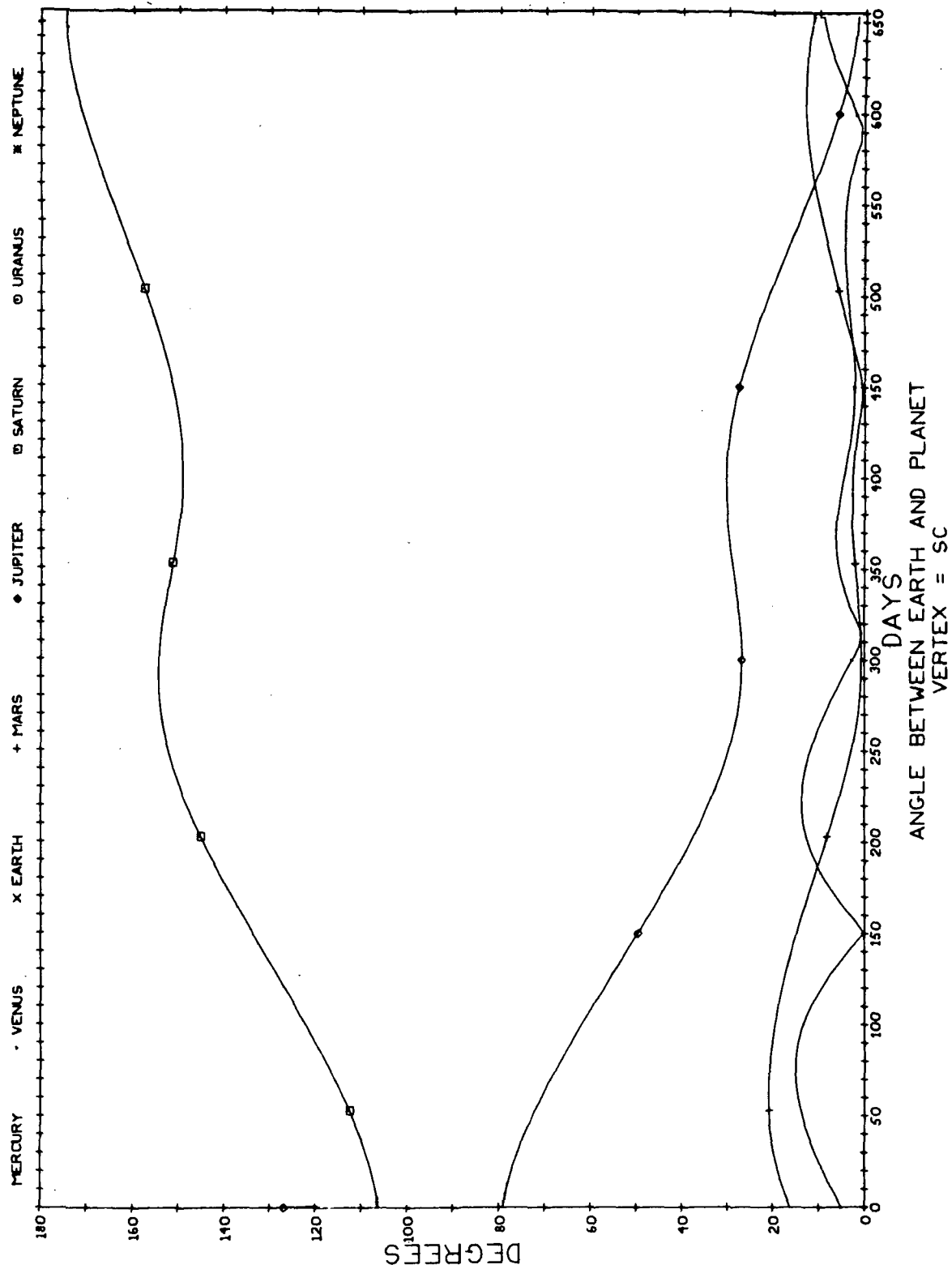


Fig. A2.9 Earth - Spacecraft - Planet Angles for Jupiter - Saturn Leg of 1977 Jupiter Flyby to Saturn
VERTEX = SC

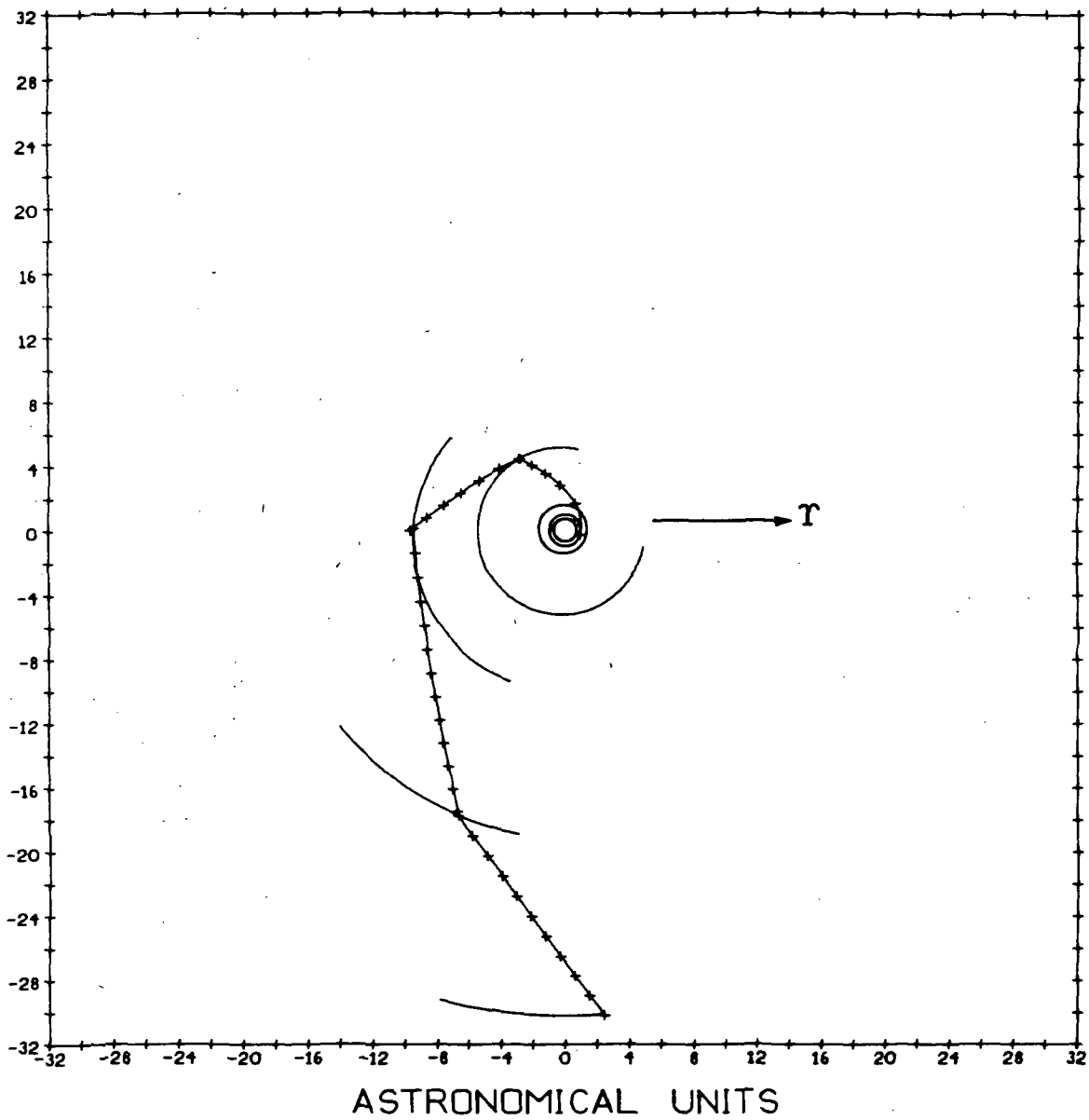


Fig. A3.1. Trajectory Diagram for 1977 Grand Tour.

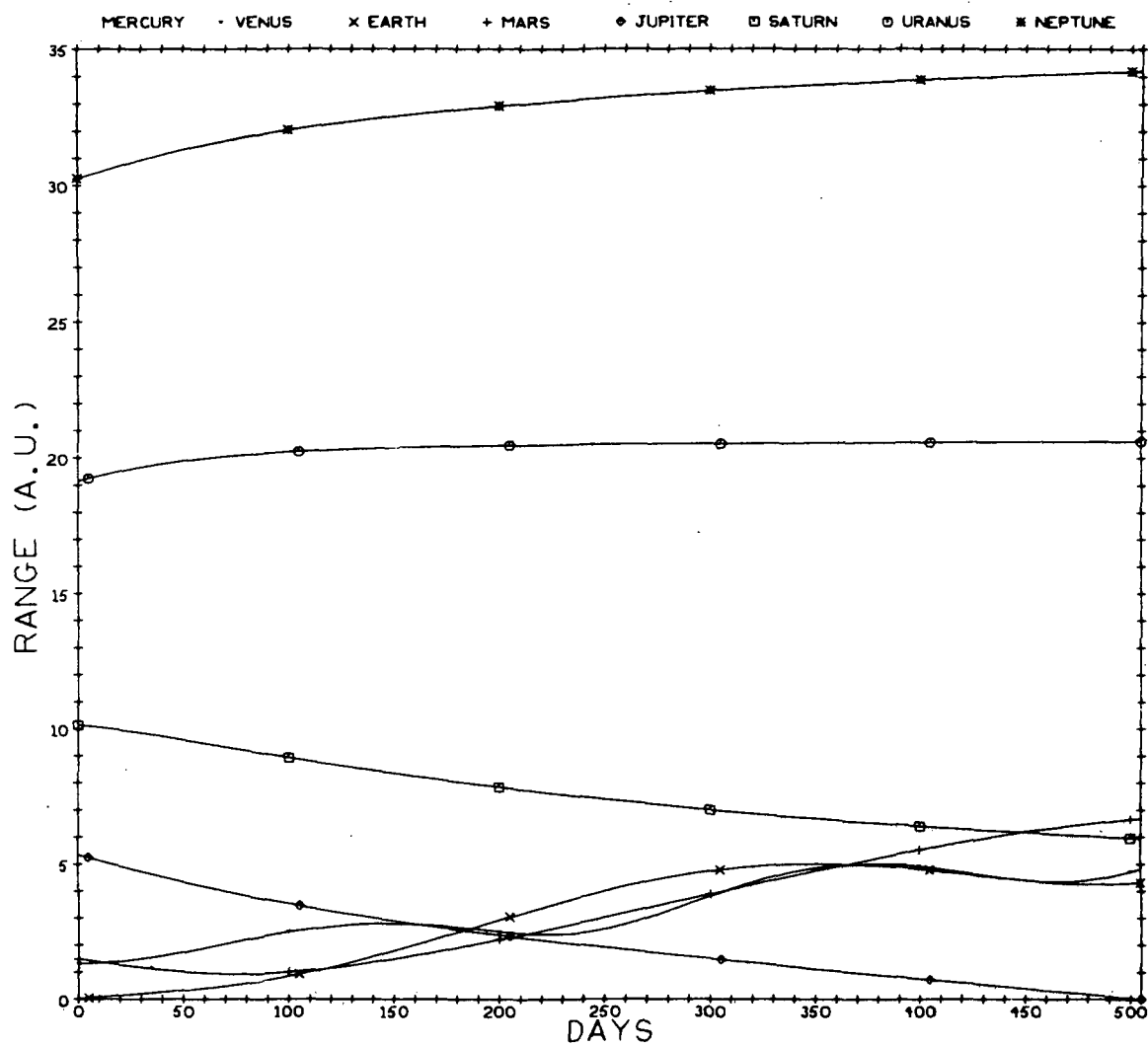


Fig. A3.2 Ranges to Solar System Planets for Earth-Jupiter Leg of 1977 Grand Tour

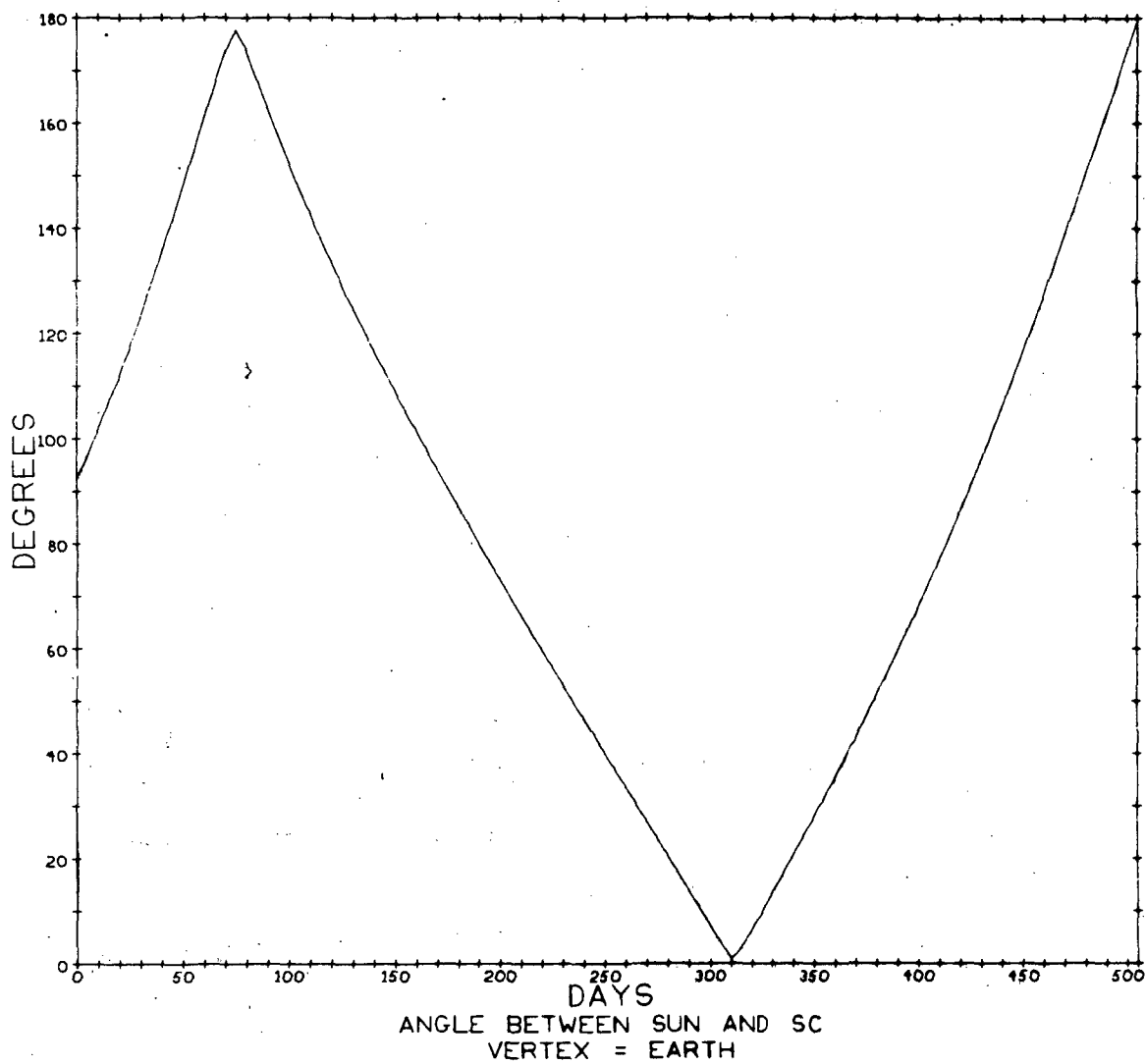


Fig. A3.3 Spacecraft-Earth-Sun Angle for Earth-Jupiter Leg of 1977 Grand Tour

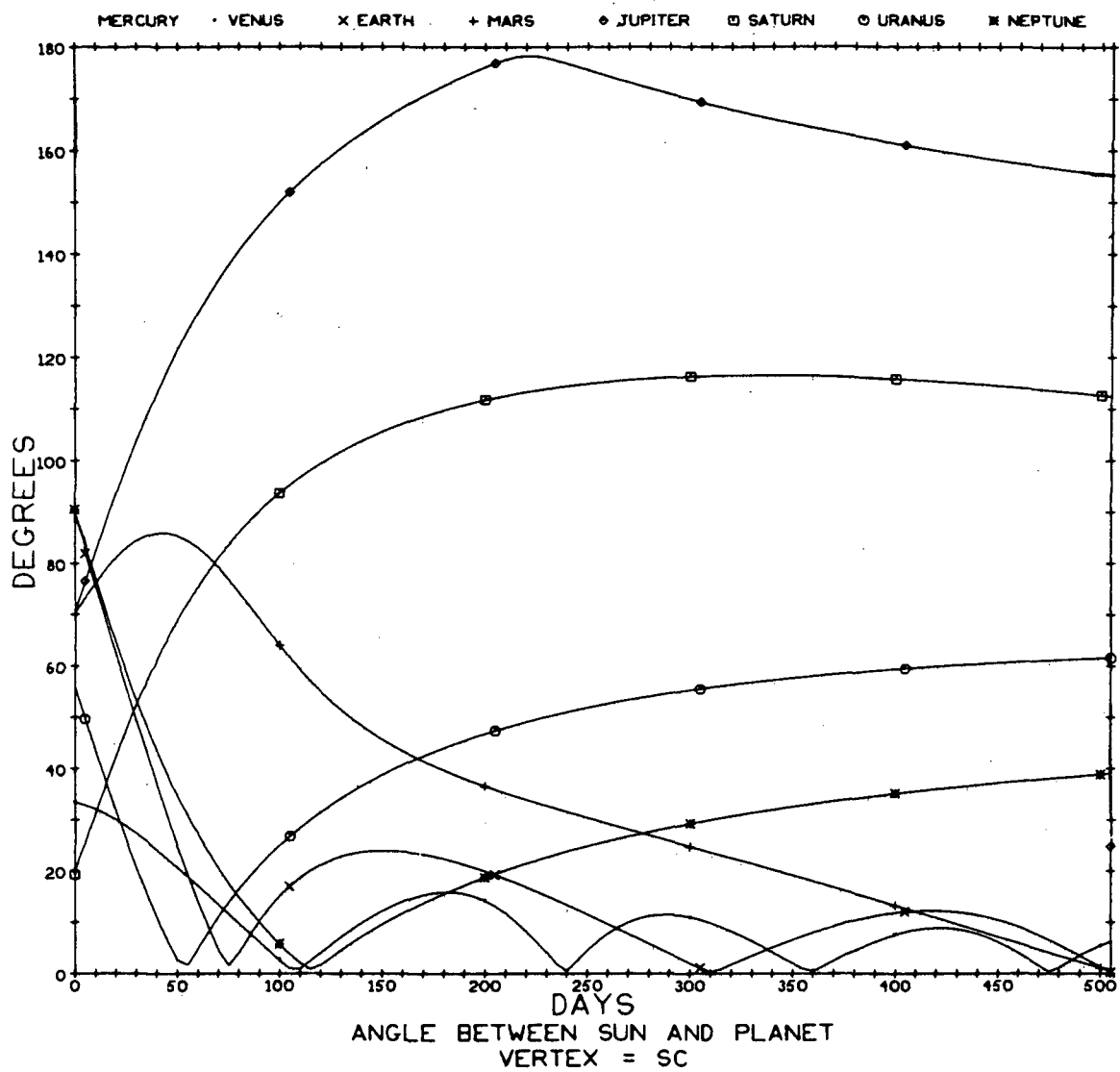


Fig. A3.4 Sun-Spacecraft-Planet Angles for Earth-Jupiter Leg of 1977 Grand Tour

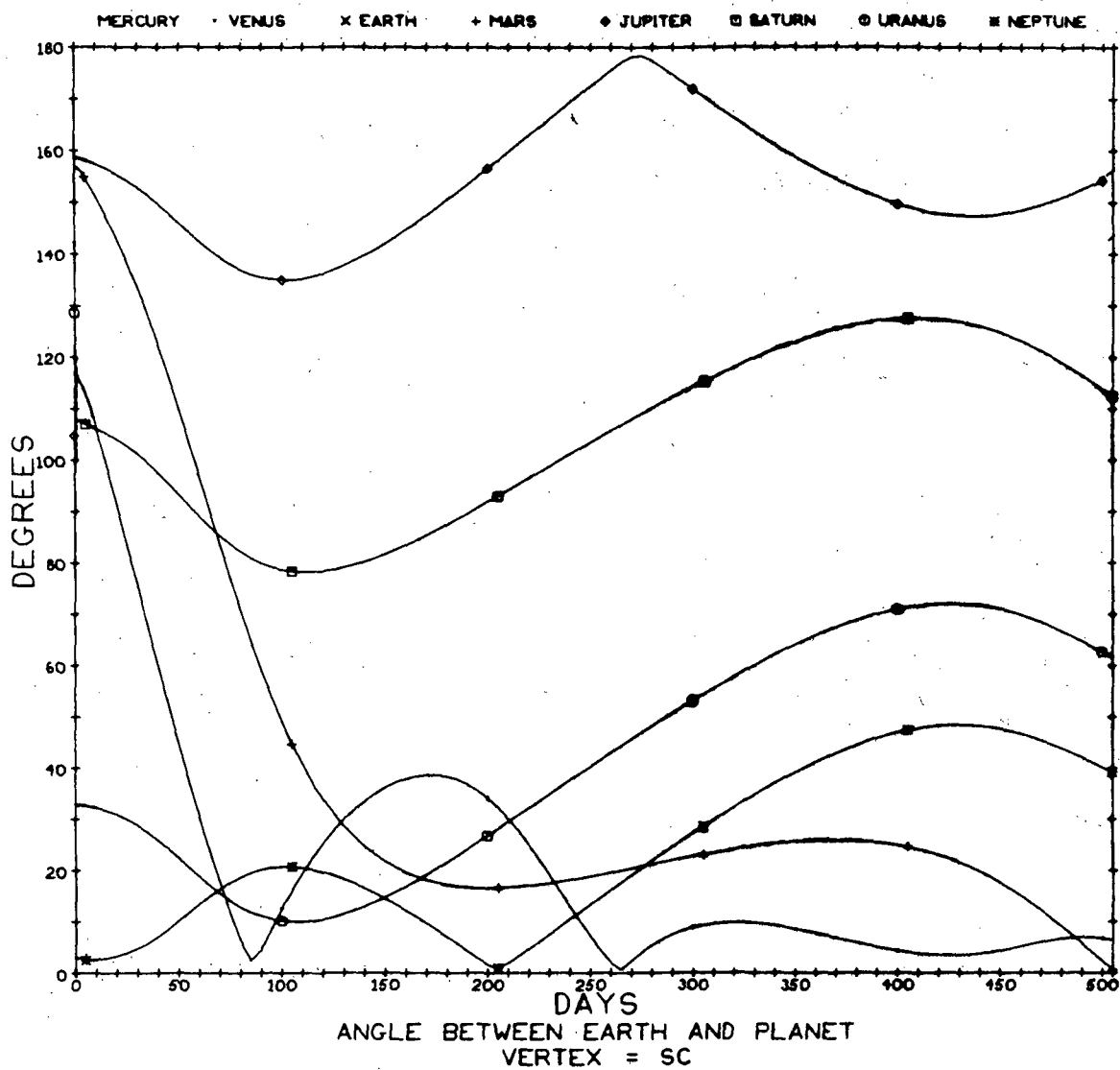


Fig. A3.5 Earth-Spacecraft-Planet Angles for Earth-Jupiter Leg of 1977 Grand Tour

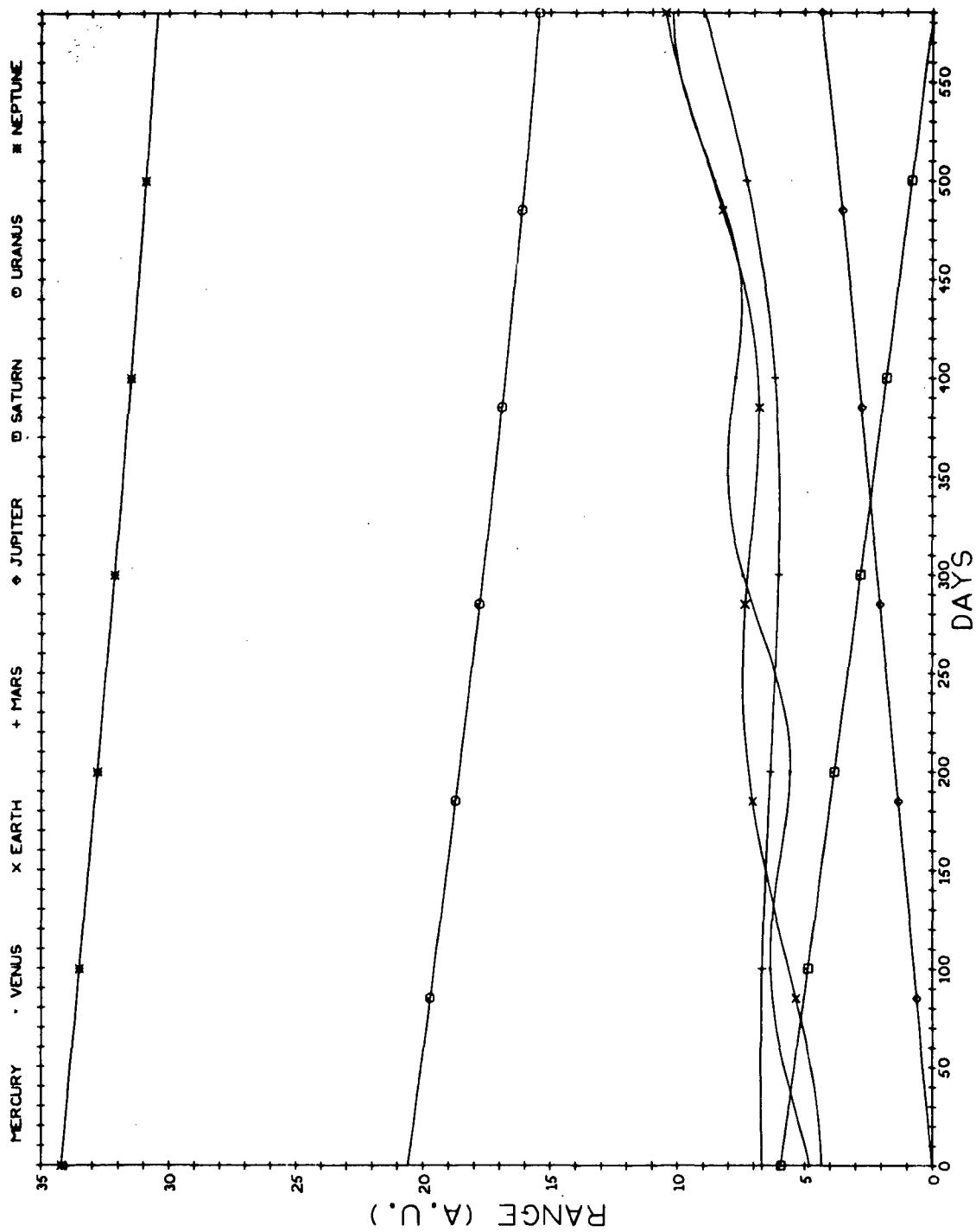


Fig. A3.6 Ranges to Solar System Planets for Jupiter-Saturn Leg of 1977 Grand Tour

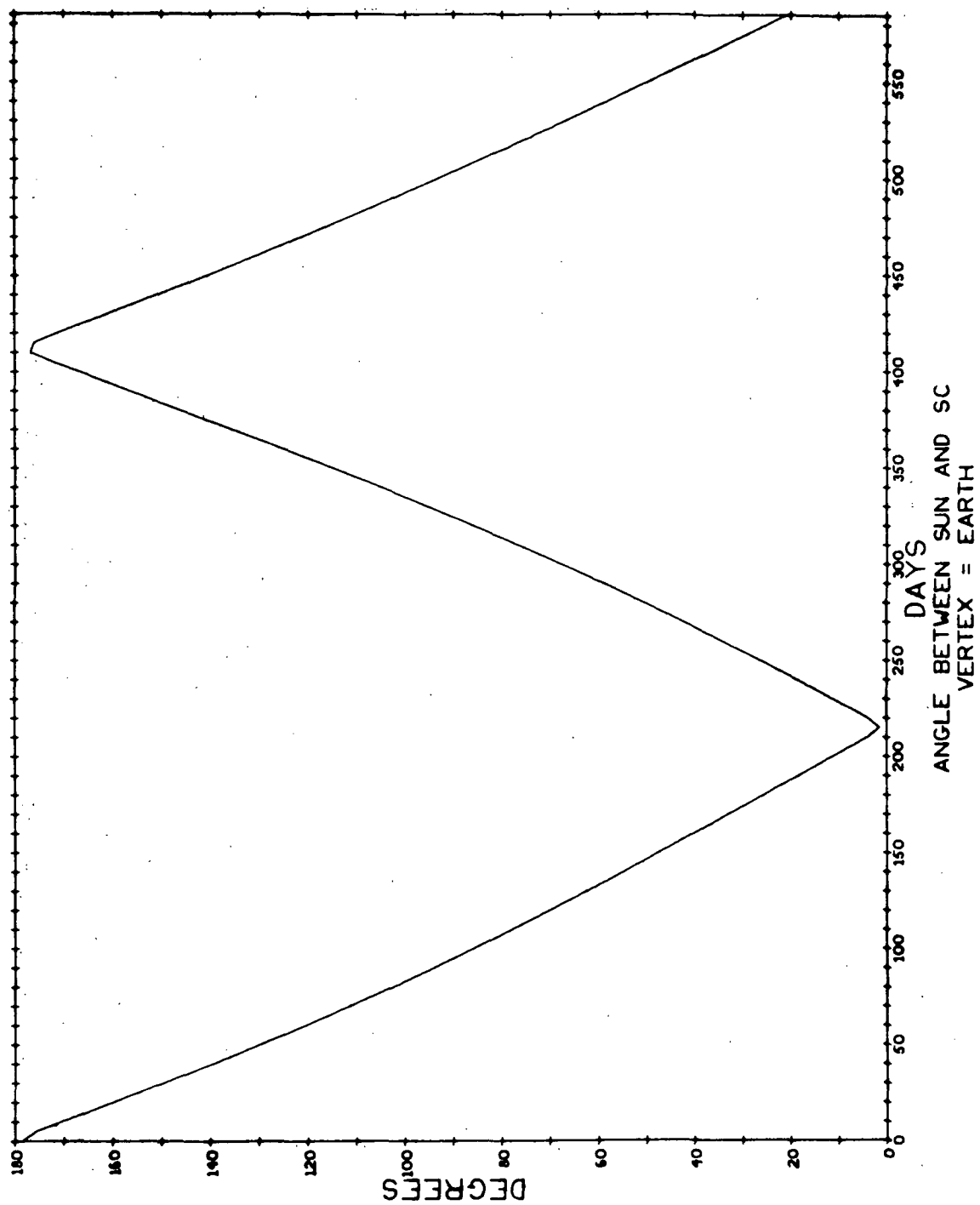


Fig. A3.7 Spacecraft-Earth-Sun Angle for Jupiter-Saturn Leg of 1977 Grand Tour

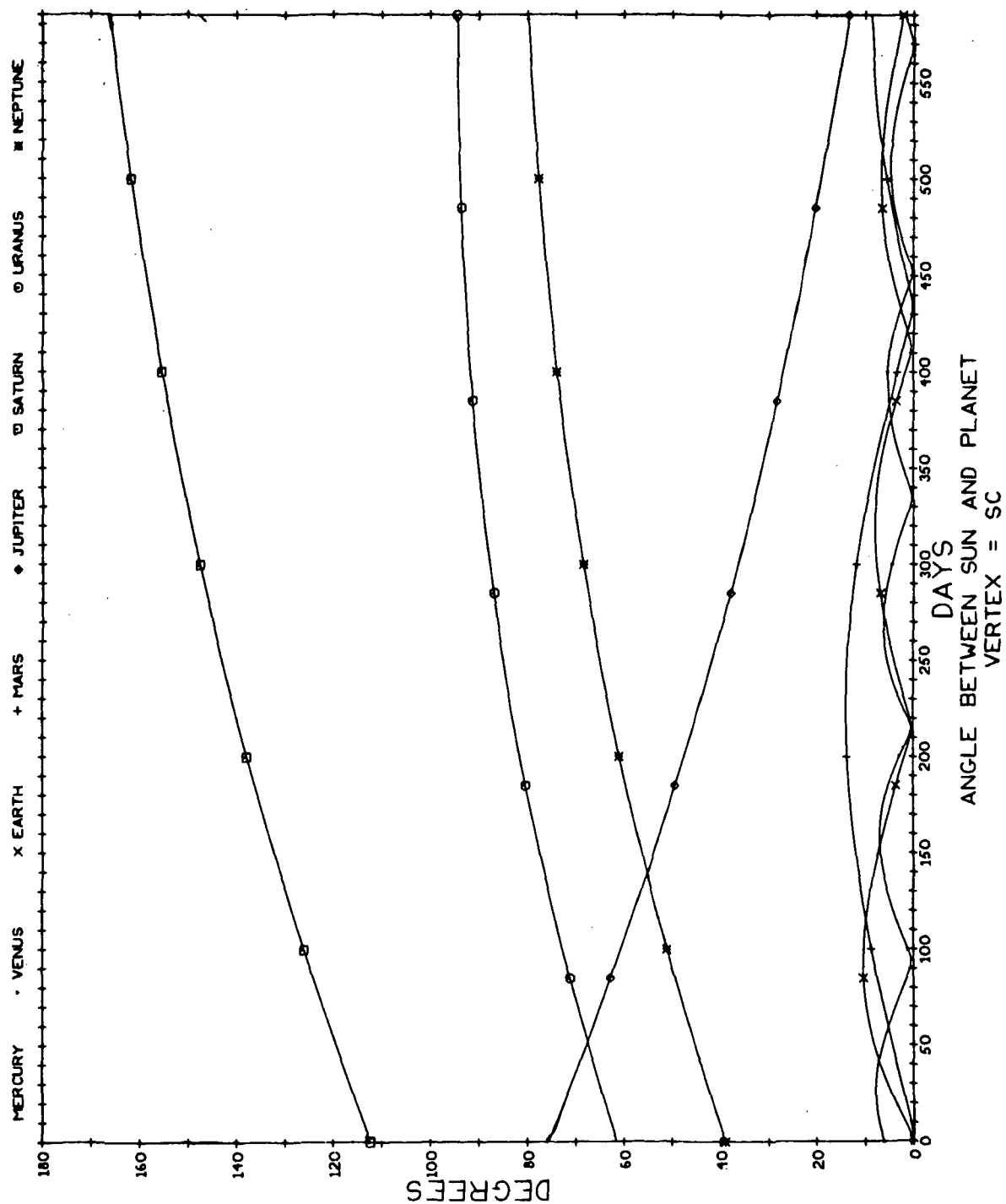


Fig. A3.8 Sun-Spacecraft-Planet Angles for Jupiter-Saturn Leg of 1977 Grand Tour

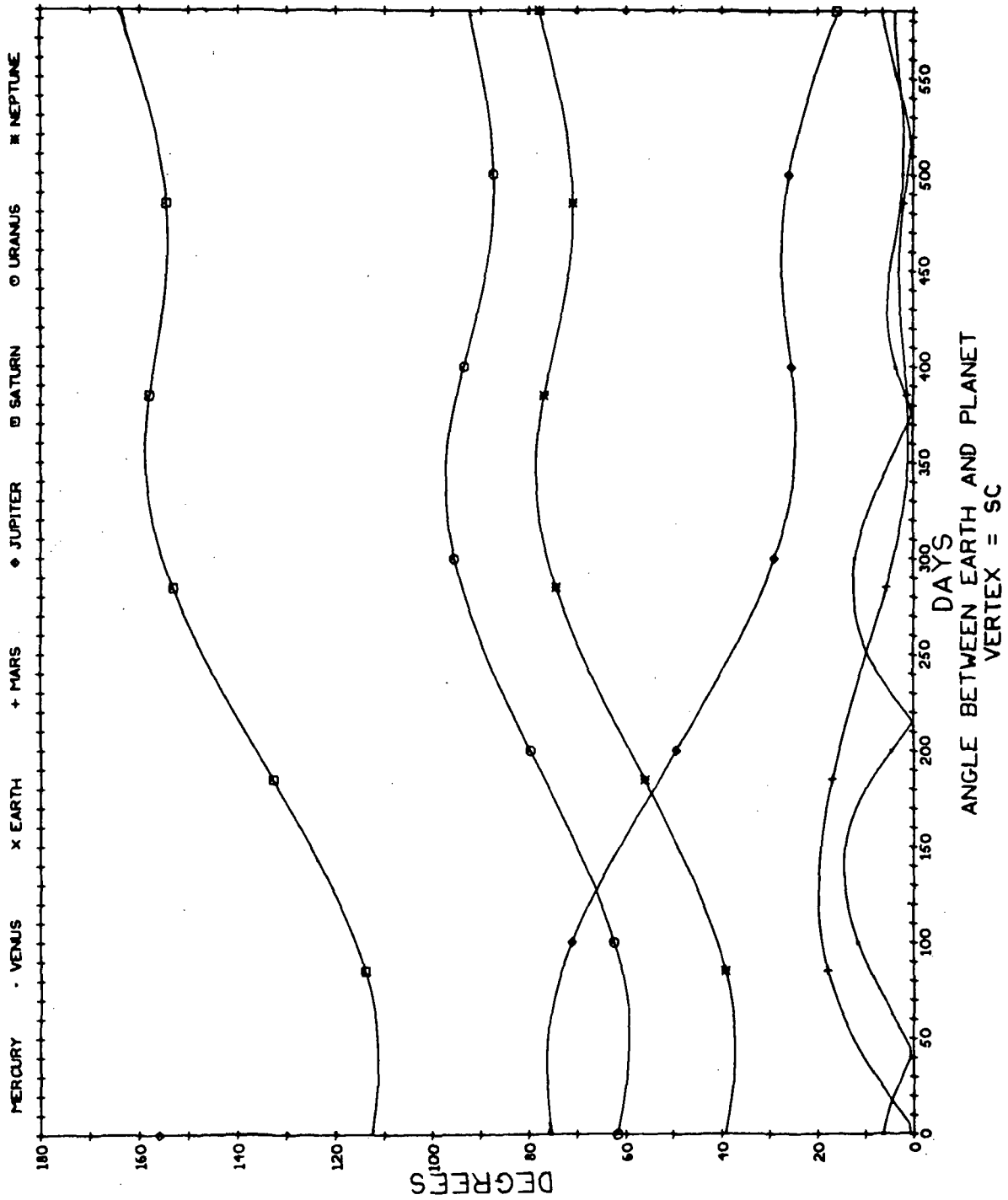


Fig. A3.9 Earth-Spacecraft-Planet Angles for Jupiter-Saturn-Leg of 1977 Grand Tour

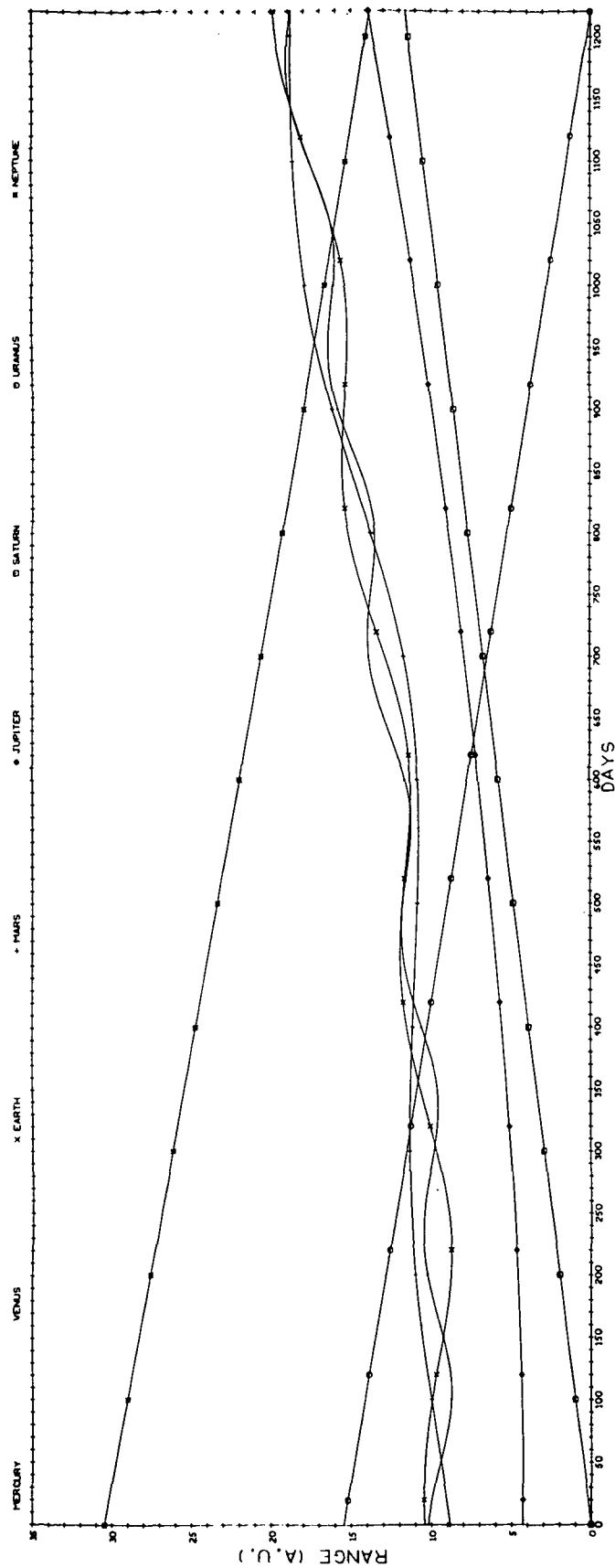


Fig. A3.10 Ranges to Solar System Planets for Saturn-Uranus Leg of 1977 Grand Tour

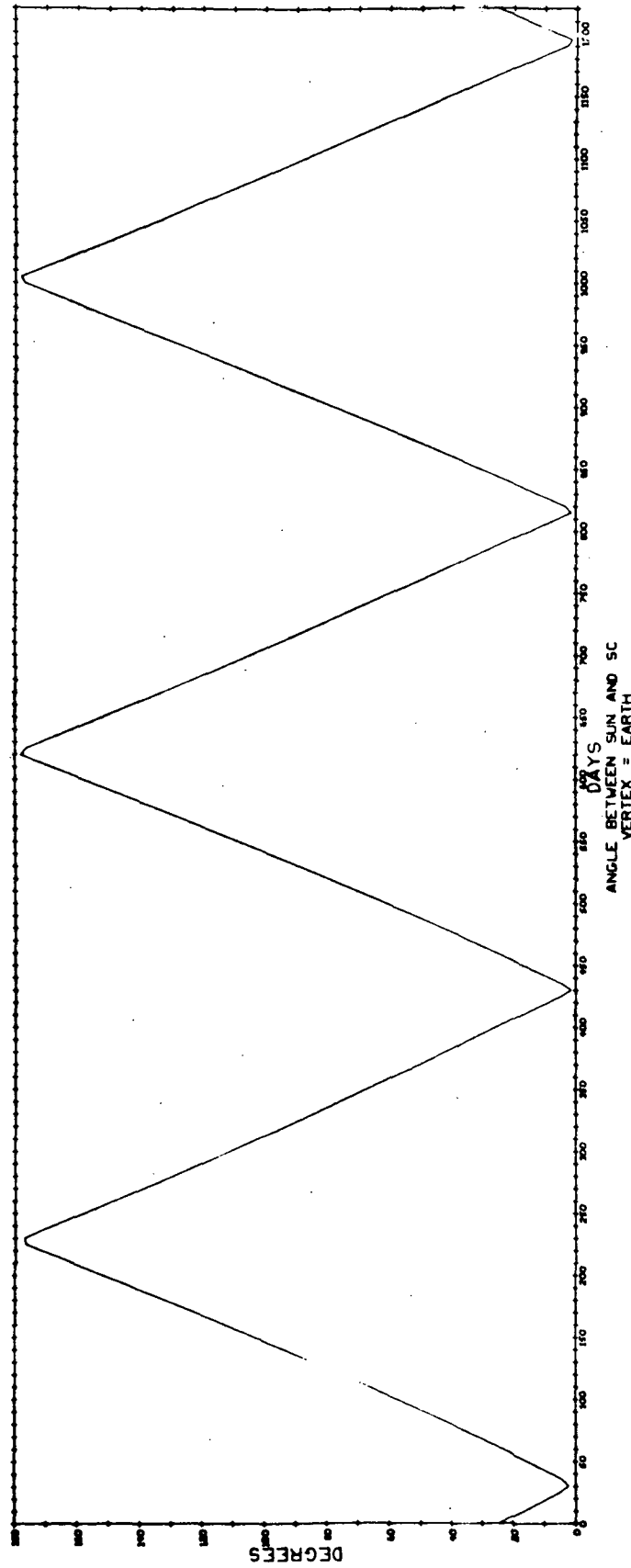


Fig. A3-11 Spacecraft-Earth-Sun Angle for Saturn-Uranus Leg of 1977 Grand Tour

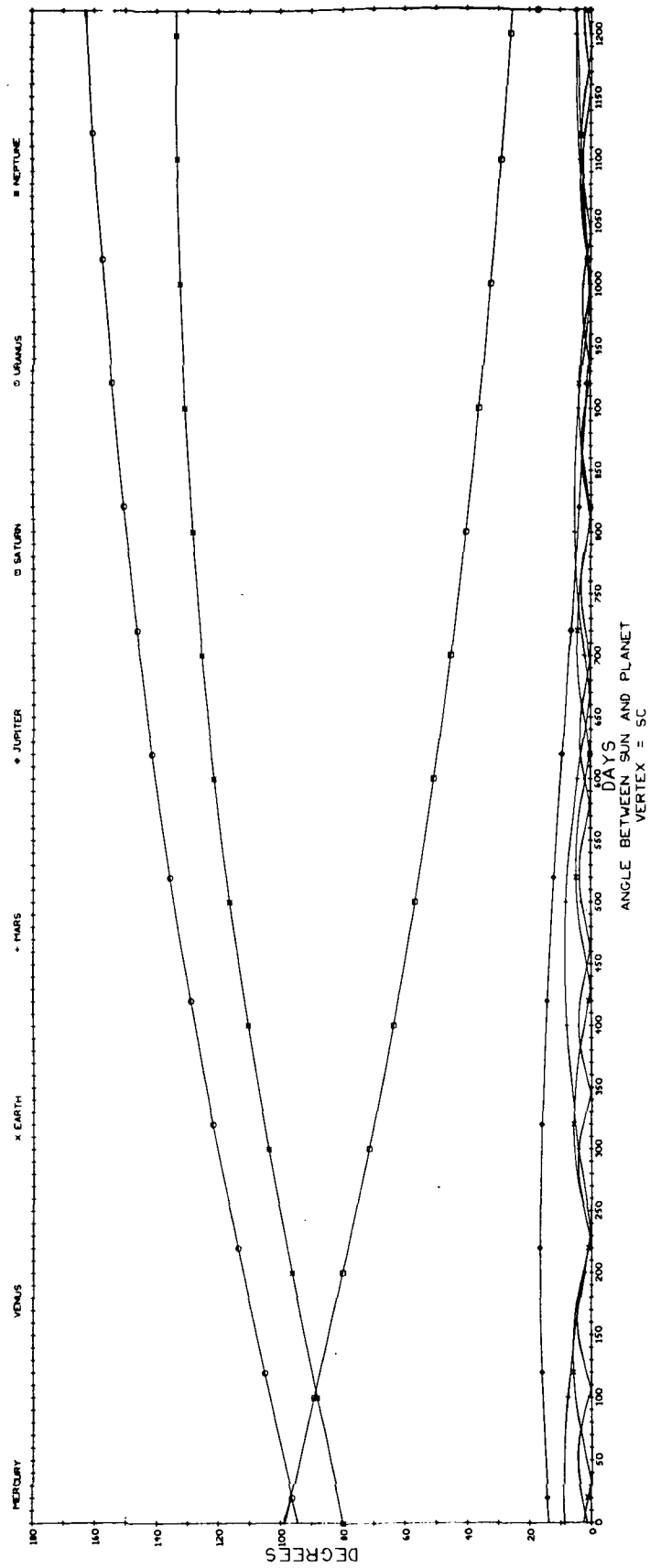


Fig. A3. 12 Sun-Spacecraft-Planet Angles for Saturn-Uranus Leg of 1977 Grand Tour

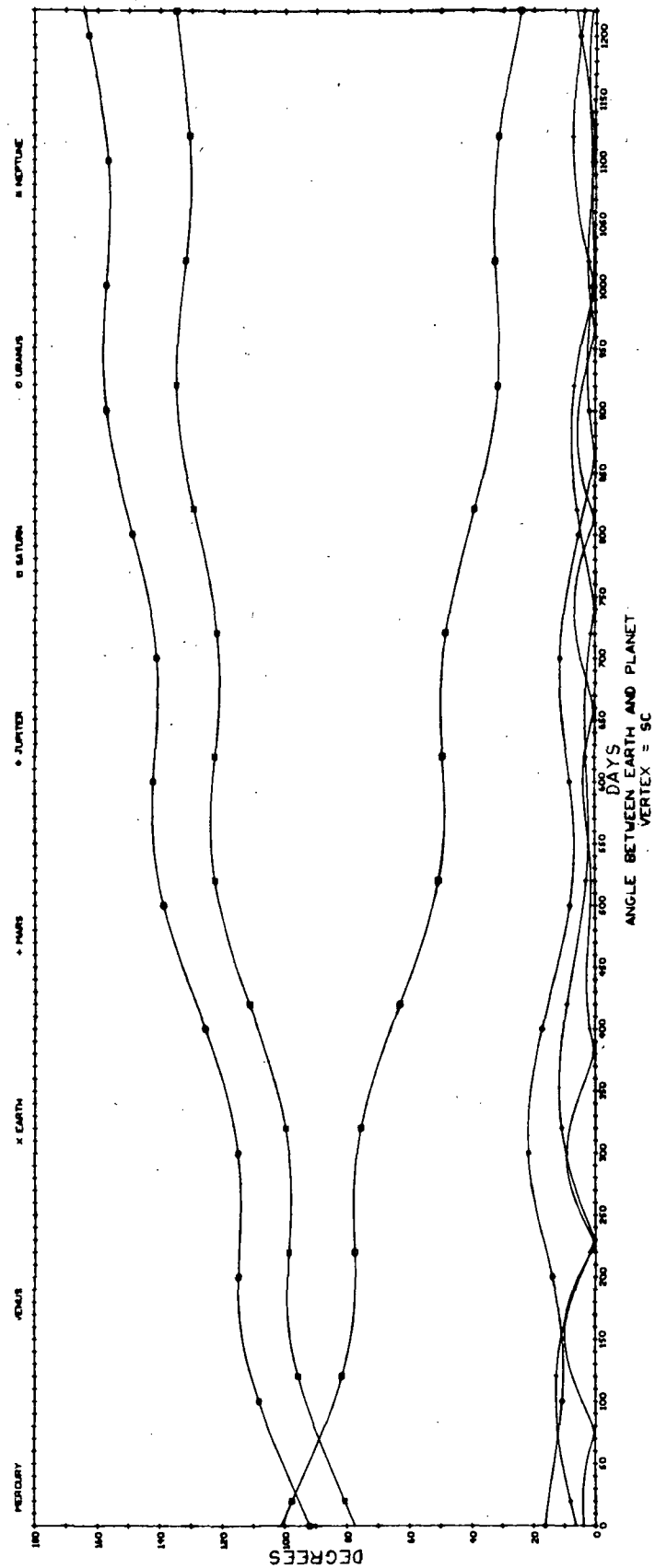


Fig. A3.13 Earth-Spacecraft Planet Angles for Saturn-Uranus Leg of 1977 Grand Tour

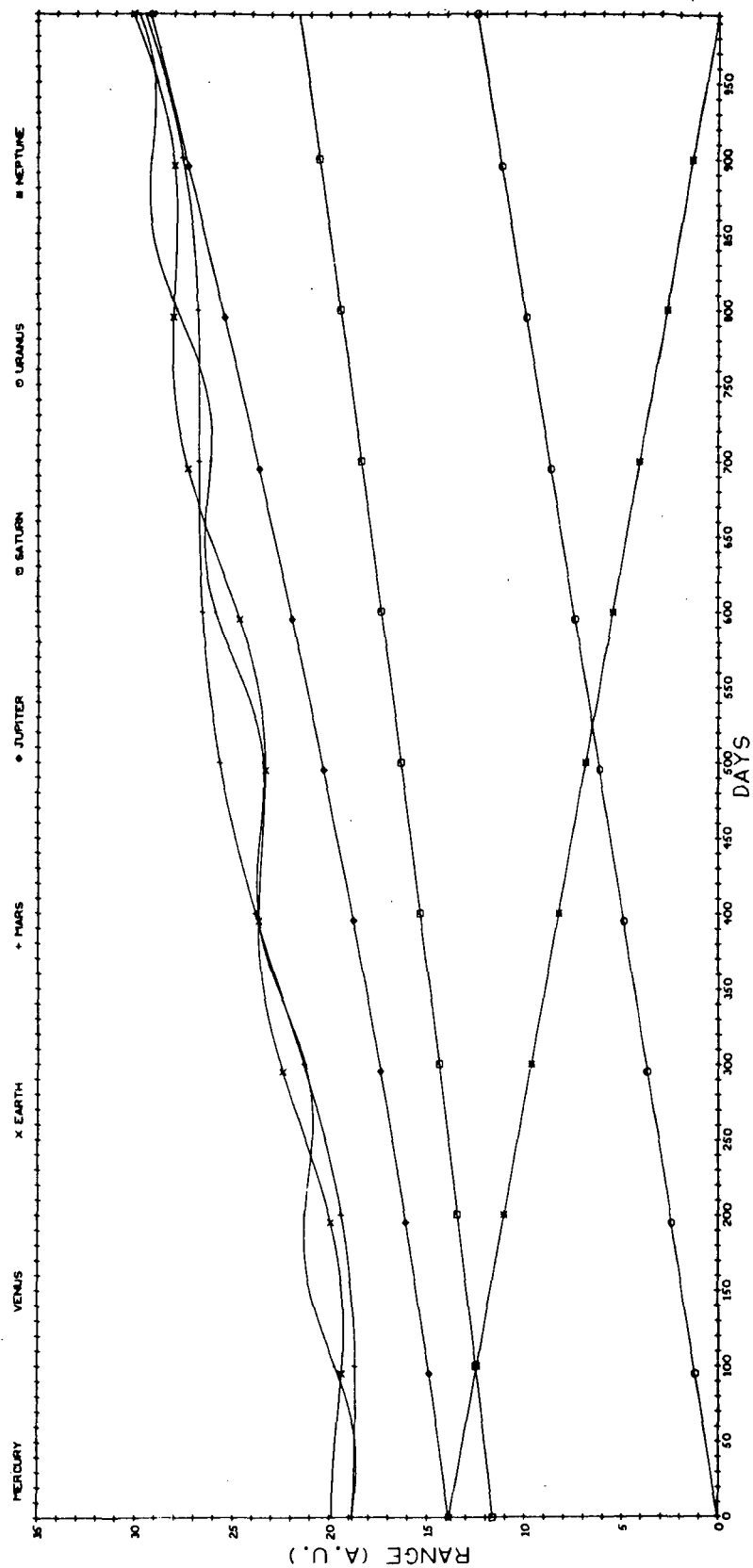


Fig. A3.14 Ranges to Solar System Planets for Uranus-Neptune Leg of 1977 Grand Tour

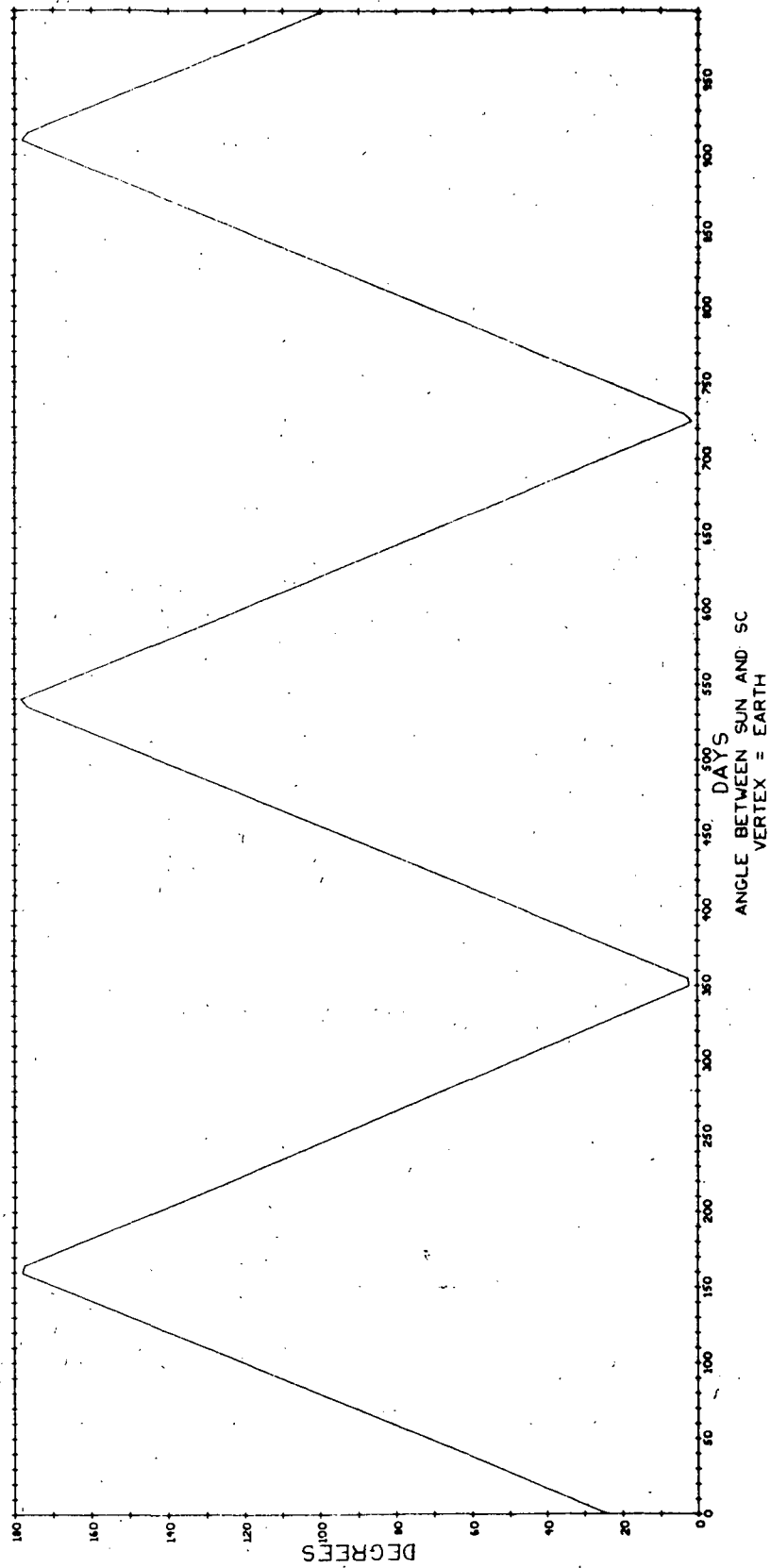


Fig. A3.15 Spacecraft-Earth-Sun Angle for Uranus-Neptune Leg of 1977 Grand Tour

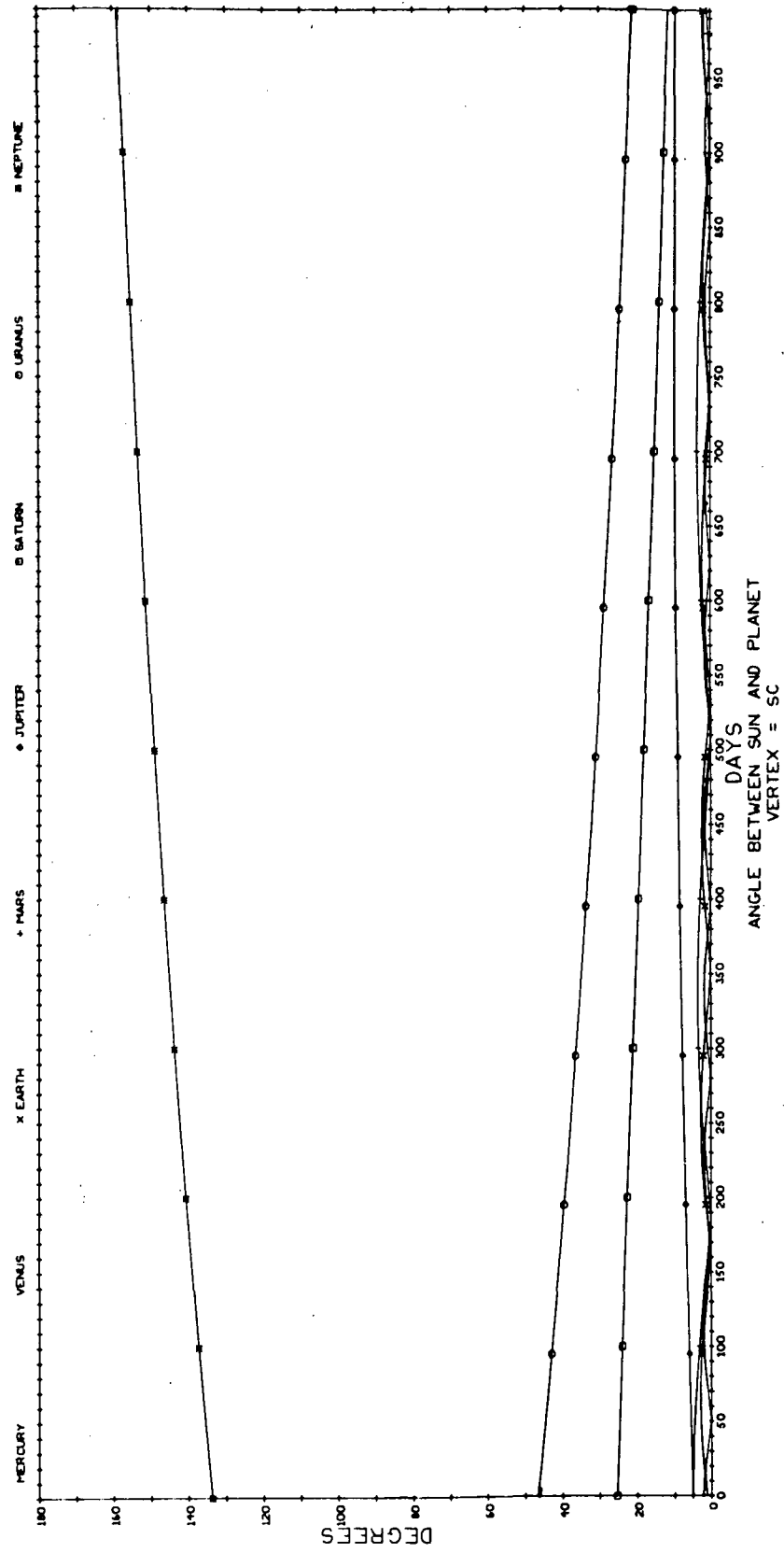


Fig. A3.16 Sun-Spacecraft-Planet Angles for Uranus-Neptune Leg of 1977 Grand Tour

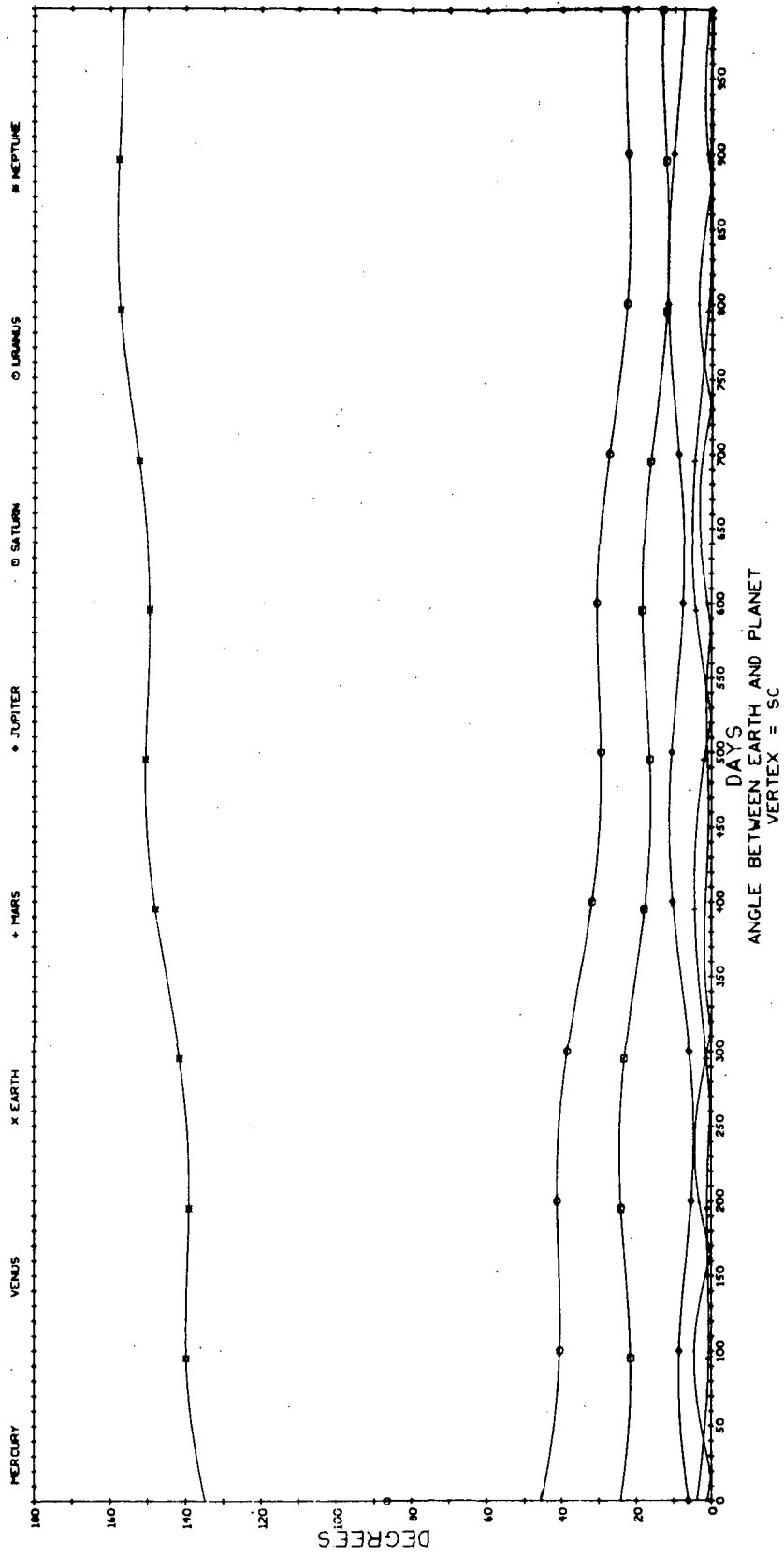


Fig. A3.17 Earth-Spacecraft-Planet Angles for Uranus-Neptune Leg of 1977 Grand Tour

APPENDIX B

PLANETARY PASSAGE TRAJECTORY GEOMETRIES

In this appendix are presented the key physical parameters which are indispensable for a preliminary analysis of the use of an onboard navigation system during the period in which the spacecraft is well within the sphere of influence of a planet. These characteristics are illustrated here for all the planetary encounters of the three missions used as examples in this study. The value of the data contained in these plots should not be underestimated - the overall scheduling and measurement selection which can be performed with this information eliminates the need for a costly computer search through a much larger set of possible measurement combinations.

The first plot in each series is a plan view of the hyperbolic pass of the planet. It provides an overall view of the passage. The direction of the sun is indicated on both the closeup and large field view in every case. By using this, one determines which side of the terminator line (which is drawn on the planet) is sunlit. In all cases passage is from right to left around the planet; thus in every case where the planet is not the last to be encountered the approach is made from the direction of the sun. This results in an approach to the light side and a retreat from the dark side of the planet. This is not necessarily true for the last planet involved as can be seen from Figures B1. 1. In the case of Saturn the inner edge of the rings is drawn on the plan view. The dotted edge is below the plane of the paper. Note the interior ring passage of Saturn on the Grand Tour. The plan view is also useful for determining when star occultations might be available. Star occultations are potentially useful measurements only when the relative motion is such that a dark edge of the planet passes into the star field. Note that until the spacecraft is very close to the planet there is very little relative motion of this type. If the planet has an atmosphere, as the outer planets seem to have, the intersection of the star with the edge must occur far enough from the terminator so that there is no light leakage. If we assume a central angle value of about 20° for this distance we see that when the

approach is made from out of the sun there isn't much opportunity to find good star occultations.

The final use to be mentioned here is that by simply noting whether a light edge is available at any given time one can determine whether or not an IR capability is required to make a measurement at that time.

The second plot in each group gives the range to the planet in planet radii and kilometers. Note that in all cases very little time is spent close to periplanet. Use of this together with the ranges to the planetary satellites given in the sixth plot of each group enables one to determine whether or not a satellite might be a better navigational target than the planet. This could be the case if the distance to the satellite is much less than the distance to the planet.

The third graph gives the angle subtended by the planet versus time. Again the tremendous speed at which the probe passes periplanet is apparent from this plot. This plot and the previous one have much meaning to the instrument designer as they provide information on the size and distance of the near body. In addition, this plot is useful to determine during what period planet diameter measurements will be useful. The geometry is favorable only during the time the subtended angle is large - which isn't very long. The fourth plot gives either the Earth-probe-planet angle, or sun-probe-planet angle, or both, for each case. Besides giving information to the systems designer and mission planner the Earth-probe-planet angle plot reveals during what period the spacecraft is behind the planet as viewed from Earth. Note that it is never occulted for more than a few hours. The sun-spacecraft-planet angle is extremely useful to onboard system scheduling because it reveals when the lines of sight to the planet and sun are too close to permit using the planet for sightings. For the near planet passages this doesn't occur for any significant length of time.

The fifth plot in each group gives the ranges to the principle satellites of each planet. A use of this plot was discussed above in

conjunction with the planetary range figure. The code for the satellites is given in Table B-1. For example, moon 3 at Jupiter is Ganymede. It is of interest to note that on the Uranus passage no satellite is ever very close. Because the moons of Uranus orbit almost perpendicular to the ecliptic it is not likely that on a mission such as the Grand Tour in which all motion is close to the ecliptic plane that one would have a close encounter to one of these moons. Such is not the case for Jupiter where on this Grand Tour the approach to Callisto is actually closer than to the planet itself. The mission might be planned to either avoid such a close encounter in order to limit the perturbation on the trajectory, or to capitalize upon it for scientific information. In either case the orbital period of Jupiter's satellites is so small compared to the trip time to Jupiter that fixed time of arrival guidance would be a necessity for mission success.

The sixth graph in each group gives the moon-spacecraft-planet angle and thus reveals the location of the satellite relative to the planet. Although satellite-planet measurements have been eliminated due to the large phenomena error which would result, this plot is still useful because it identifies those times the satellite is not visible from the spacecraft. The sun-satellite-spacecraft angle is used to determine whether or not the satellite is sunlit at a potential navigation sighting time. This information, which is given in the seventh plot of each group, reveals whether or not an I. R. capability is required to make a measurement.

The final plot in each group gives the sun-probe-satellite angle. This has precisely the same uses as the sun-probe-planet angle. For example, on the Jupiter passage of the Grand Tour moon 4 (Callisto) might still be useful 21 to 14 hours before periplanet but the line of sight to the moon is too close to the line of sight to the sun for this to be a useable measurement.

Tables B-2 through B-8 give the results of using these plots to determine candidate on board measurement schedules. The measurements actually used to generate the results given in Chapters IV through VI were selected from those indicated as available in these tables. These

tables correspond to Tables A-1 through A-7 and the selection of individual entries in Tables B-1 through B-7 is performed in the same way as outlined in the example in Appendix A. As an example of how to read these tables note in Table B-3 that in the period from 20 hours before pericenter to 9 hours before pericenter the following measurement types are searched for the optimum measurement every hour using both Jupiter and Ganymede as near bodies:

1. Planet/moon diameter measurement.
2. Planet/moon center to star measurements.
3. Planet/moon limb to star measurements.

TABLE B-1

Code For Planetary Satellites

Planet	Satellite	Code Number
Jupiter	Io	1
	Europa	2
	Ganymede	3
	Callisto	4
Saturn	Titan	1
Uranus	Ariel	1
	Umbriel	2
	Titania	3
	Oberon	4
Neptune	Triton	1

TABLE B-2.
On Board Measurement Schedule for the Jupiter
Leg of the 1973 Jupiter Flyby

Beginning of Interval* (hrs)	End of Interval* (hrs)	Time Step for Interval	Satellites Used	Planet/Moon Diameter Measurement	Planet/Moon Center to Star Measurement	Star Occultation	Planet/Moon Limb to Star Measurement
Jupiter Sphere of Influence	-81	5 days	none	no	yes	no	yes
-81	-70	4 hr 25 min	none	no	yes	no	yes
-70	-46	4 hr	Io	no	yes	no	yes
-46	-18	2 hr	Ganymede	no	yes	no	yes
-18	-10	1 hr	Ganymede	no	yes	no	yes
-10	-5	1 hr	Ganymede	no	yes	yes	yes
-5	-2	30 min	none	yes	yes	yes	yes
-2	End of Mission	20 min	none	yes	yes	yes	yes

* Times are relative to periplanet passage

TABLE B-3

On Board Measurement Schedule for Jupiter Passage on
1977 Swingby to Saturn

Beginning of Interval (hrs)	End of Interval (hrs)	Time Step for Interval	Satellites Used	Planet/Moon Diameter Measurement	Planet/Moon Center to Star Measurement	Star Occultation	Planet/Moon Limb to Star Measurement
Sphere of Influence	-72	5 days	none	no	yes	no	yes
-72	-20	4 hr	none	no	yes	no	yes
-20	-9	1 hr	Ganymede	yes	yes	no	yes
-9	-2	1 hr	none	no	yes	no	yes
-2	0	30 min	none	yes	yes	no	yes
0	+2	30 min	none	yes	yes	yes	yes
+2	+10	1 hr	none	no	yes	yes	yes
+10	+20	2 hr	none	no	yes	no	yes
+20	+72	4 hr	none	no	yes	no	yes
72	Sphere of Influence	5 days	none	no	yes	no	yes

* Times are relative to periplanet passage.

TABLE B-4

On Board Measurement Schedule for the Saturn Leg
of 1977 Jupiter Swingby to Saturn

Beginning of Interval	End of Interval	Time Step for Interval	Satellites Used	Planet/Moon Diameter Measurement	Planet/Moon Center to Star Measurement	Star Occultation	Planet/Moon Limb to Star Measurement
Saturn Sphere of Influence	-60 hr 52 min	5 days	none	no	yes	no	yes
-60 hr 52 min	-58 hr 30 min	12 hr 22 min	none	no	yes	no	yes
-58 hr 30 min	-8 hr 30 min	5 hr	none	yes	yes	no	yes
-8 hr 30 min	-5 hr 30 min	5 hr	none	yes	yes	no	yes
-5 hr 30 min	-1 hr 30 min	20 min	none	yes	yes	yes	yes
1 hr 30 min	end of mission	30 min	none	yes	yes	yes	yes

TABLE B-5
On Board Measurement Schedule for the Jupiter Leg
of the Grand Tour

Beginning of Interval	End of Interval	Time Step for Interval	Satellites Used	Planet/Moon Diameter Measurement	Planet/Moon Center to Star Measurement	Star Occultation	Planet/Moon Limb to Star Measurement
Jupiter Sphere of Influence	-82 hr 32 min	5 day	none	no	yes	no	yes
-82 hr. 32 min	-73 hr 40 min	8 hr 51.6 min	none	no	yes	no	yes
-73 hr 40 min	-40 hr 40 min	7 hr	Callisto	no	yes	no	yes
-40 hr 40 min	-26 hr 40 min	1 hr	Callisto	yes	yes	yes	yes
-26 hr 40 min	-12 hr 40 min	2 hr	none	no	yes	no	yes
-12 hr 40 min	-7 hr 40 min	30 min	none	yes	yes	yes	yes
-7 hr 40 min	-5 hr 40 min	20 min	none	yes	yes	yes	yes
-5 hr 40 min	-4 hr	20 min	none	yes	yes	no	yes
-4 hr	+1 hr	30 min	none	yes	yes	no	yes
+1 hr	+7 hr	2 hr	3	no	yes	no	yes
+7 hr	+67 hr	10 hr	none	no	yes	no	yes
+67 hr	Leaving Jupiters Sphere of Influence	5 day	none	no	yes	no	yes

TABLE B-6

On Board Measurement Schedule for the Saturn
Leg of the Grand Tour

Beginning of Interval	End of Interval	Time Step for Interval	Satellites Used	Planet/Moon Diameter Measurement	Planet/Moon Center to Star Measurement	Star Occultation	Planet/Moon Limb to Star Measurement
Saturn Sphere of Influence	-62 hr	4 days	none	no	yes	no	yes
-62 hr	-46 hr 40 min	15 hr 20 min	none	no	yes	no	yes
-46 hr 40 min	- 1 hr 40 min	3 hr	Titan, Rings	yes	yes	no	yes
-1 hr 40 min	0	20 min	Rings	yes	yes	no	yes
0	+2 hr 20 min	20 min	none	yes	yes	yes	yes
+2 hr 20 min	+ 5 hr	20 min	none	yes	yes	yes	yes
+ 5 hr	+13 hr 20 min	20 min	Rings	yes	yes	yes	yes
+13 hr 20 min	+58 hr 20 min	3 hr	Rings	yes	yes	no	yes
+58 hr 20 min	Leaving Saturn's Sphere of Influence	4 days	none	no	yes	no	yes

TABLE B-7
On Board Measurement Schedule for the Uranus
Leg of the Grand Tour

Beginning of Interval	End of Interval	Time Step for Interval	Satellites Used	Planet/Moon Diameter Measurement	Planet/Moon Center to Star Measurement	Star Occultation	Planet/Moon Limb to Star Measurement
Uranus Sphere of Influence	- 18 hr 42 min	4 days	none	no	yes	no	yes
- 18 hr 42 min	- 18 hr	42 min	none	no	yes	no	yes
- 18 hr	- 2 hr	30 min	none	no	yes	no	yes
- 2 hr	- 1 hr	20 min	none	yes	yes	no	yes
- 1 hr	+ 2 hr	20 min	none	yes	yes	yes	yes
+ 2 hr	+ 18 hr	30 min	none	no	yes	yes	yes
+ 18 hr	Leaving Uranus's Sphere of Influence	1 day	none	no	yes	no	yes

TABLE B-8

On Board Measurement Schedule for the Neptune Leg
of the Grand Tour

Beginning of Interval	End of Interval	Time Step for Interval	Satellites Used	Planet/Moon Diameter Measurement	Planet/Moon Center to Star Measurement	Star Occultation	Planet/Moon Limb to Star Measurement
Neptune Sphere of Influence	-39 hr 37.5 min	5 days	none	no	yes	no	yes
-39 hr 37.5 min	-35 hr 20 min	4.29 hr	none	no	yes	no	yes
-35 hr 20 min	-24 hr 20 min	30 min	none	no	yes	no	yes
-24 hr 20 min	-23 hr 20 min	20 min	none	yes	yes	no	yes
-23 hr 20 min	End of mission	20 min	none	yes	yes	yes	yes

Planetary Passage Trajectory Geometries

* Trajectory Parameter Summary Page *

1. 1977 LOW ENERGY JUPITER FLYBY

Jupiter Passage:

- Fig. B1.1 Trajectory Plan View During Jovian Passage on 1973 Low Energy Jupiter Flyby.
 a. 100 Radii Field
 b. 12 Radii Field
- Fig. B1.2 Range to Planet During Jovian Passage on 1973 Low Energy Jupiter Flyby.
- Fig. B1.3 Angle Subtended by Planetary Limbs During Jovian Passage on 1973 Low Energy Jupiter Flyby.
- Fig. B1.4a Earth-SC-Planet Angle During Jovian Passage on 1973 Low Energy Jupiter Flyby.
- Fig. B1.4b Sun-SC-Planet Angle During Jovian Passage on 1973 Low Energy Jupiter Flyby.
- Fig. B1.5 Range to Principle Moons During Jovian Passage on 1973 Low Energy Jupiter Flyby.
- Fig. B1.6 Moon-SC-Planet Angle During Jovian Passage on 1973 Low Energy Jupiter Flyby.
 a. 144 Hour Frame
 b. 9.8 Hour Frame
- Fig. B1.7 Sun-Moon-SC Angle During Jovian Passage on 1973 Low Energy Jupiter Flyby.
- Fig. B1.8 Sun-SC-Moon Angle During Jovian Passage on 1973 Low Energy Jupiter Flyby.

2. 1977 JUPITER FLYBY TO SATURN

Jupiter Passage

- Fig. B2.1 Trajectory Plan View During Jovian Passage on 1977
Jupiter Swingby to Saturn.
 a. 100 Radii Field
 b. 24 Radii Field
- Fig. B2.2 Range to Planet During Jovian Passage on 1977
Jupiter Swingby to Saturn.
- Fig. B2.3 Angle Subtended by Planetary Limbs During Jovian
Passage on 1977 Jupiter Swingby to Saturn.
- Fig. B2.4a Earth-SC-Planet Angle During Jovian Passage on 1977
Jupiter Swingby to Saturn.
- Fig. B2.4b Sun-SC-Planet Angle During Jovian Passage on 1977
- Fig. B2.5 Range to Moons During Jovian Passage on 1977 Jupiter
Swingby to Saturn.
- Fig. B2.6 Moon-SC-Planet Angle During Jovian Passage on 1977
Jupiter Swingby to Saturn.
- Fig. B2.7 Sun-Moon-SC Angle During Jovian Passage on 1977
Jupiter Swingby to Saturn.
- Fig. B2.8 Sun-SC-Moon Angle During Jovian Passage on 1977
Jupiter Swingby to Saturn.

Saturn Passage

Fig. B3. 1 Trajectory Plan View During Saturn Flyby on 1977
Jupiter Swingby to Saturn.

a. 100 Radii Field

b. 12 Radii Field

(Note: Solid Ring Image is above Plane of Passage Orbit.)

Fig. B3. 2 Range to Planet During Saturn Flyby on 1977 Jupiter
Swingby to Saturn.

Fig. B3. 3 Angle Subtended by Planetary Limbs During Saturn
Flyby on 1977 Jupiter Swingby to Saturn.

Fig. B3. 4a Earth-SC- Planet Angle During Saturn Flyby on 1977
Jupiter Swingby to Saturn.

Fig. B3. 4b Sun-SC- Planet Angle During Saturn Flyby on 1977
Jupiter Swingby to Saturn.

Fig. B3. 5 Range to Titan During Saturn Flyby on 1977 Jupiter
Swingby to Saturn.

Fig. B3. 6 Titan-SC- Planet Angle During Saturn Flyby on 1977
Jupiter Swingby to Saturn.

Fig. B3. 7 Sun-Titan- SC Angle During Saturn Flyby on 1977
Jupiter Swingby to Saturn.

Fig. B3. 8 Sun-SC-Titan Angle During Saturn Flyby on 1977
Swingby to Saturn.

3. 1977 GRAND TOUR

Jupiter Passage

- Fig. B4. 1a Trajectory Plan View During Jovian Passage on the 1977 Grand Tour;
 a. 100 Radii Field
 b. 20 Radii Field
- Fig. B4. 2 Range to Planet During Jovian Passage on the 1977 Grand Tour.
- Fig. B4. 3 Angle Subtended by Planetary Limbs During Jovian Passage on the 1977 Grand Tour.
- Fig. B4. 4 Sun-SC-Planet Angle During Jovian Passage on the 1977 Grand Tour.
 a. 140 Hour Frame
 b. 15 Hour Frame
- Fig. B4. 5 Range to Principle Moons During Jovian Passage on the 1977 Grand Tour.
- Fig. B4. 6 Moon-SC-Planet Angle During Jovian Passage on the 1977 Grand Tour.
 a. 140 Hour Frame
 b. 15 Hour Frame
- Fig. B4. 7 Sun-Moon-SC Angle During Jovian Passage on the 1977 Grand Tour.
- Fig. B4. 8 Sun-SC-Moon Angle During Jovian Passage on the 1977 Grand Tour.

Saturn Passage

- Fig. B5. 1a Trajectory Plan View During Saturn Flyby on 1977 Grand Tour.
 a. 100 Radii Field
 b. 12 Radii Field
- Fig. B5. 2 Range to Planet During Saturn Flyby on 1977 Grand Tour.
- Fig. B5. 3 Angle Subtended by Planetary Limbs During Saturn Flyby on 1977 Grand Tour.
- Fig. B5. 4 Sun-SC-Planet Angle During Saturn Flyby on 1977 Grand Tour.
 a. 96 Hour Frame
 b. 8.4 Hour Frame
- Fig. B5. 5 Range to Titan During Saturn Flyby on 1977 Grand Tour.
- Fig. B5. 6 Tital-SC-Planet Angle During Saturn Flyby on 1977 Grand Tour.
- Fig. B5. 7 Sun-Titan-SC Angle During Saturn Flyby on 1977 Grand Tour.
- Fig. B5. 8 Sun-SC-Titan Angle During Saturn Flyby on 1977 Grand Tour.

Uranus Passage

- Fig. B6. 1 Trajectory Plan View During Uranus Passage on the 1977 Grand Tour.
 a. 100 Radii Field
 b. 12 Radii Field
- Fig. B6. 2 Range to Planet During Uranus Passage on the 1977 Grand Tour.
- Fig. B6. 3 Angle Subtended by Planetary Limbs During Uranus Passage on the 1977 Grand Tour.
- Fig. B6. 4 Sun-SC-Planet Angle During Uranus Passage on the 1977 Grand Tour.
 a. 12 Radii Field
 b. 3.2 Hour Frame
- Fig. B6. 5 Range to Principle Moons During Uranus Passage on the 1977 Grand Tour.
- Fig. B6. 6 Moon-SC-Planet Angles During Uranus Passage on the 1977 Grand Tour.
 a. 36 Hour Frame
 b. 3.2 Hour Frame
- Fig. B6. 7 Sun-Moon-SC Angle During Uranus Passage on the 1977 Grand Tour.
- Fig. B6. 8 Sun-SC-Moon Angle During Uranus Passage on the 1977 Grand Tour.

Neptune Passage

- Fig. B7. 1 Trajectory Plan View During Neptune Flyby on the
 1977 Grand Tour.
 a. 100 Radii Field
 b. 12 Radii Field
- Fig. B7. 2 Range to Planet During Neptune Flyby on the 1977
 Grand Tour.
- Fig. B7. 3 Angle Subtended by Planetary Limbs During Neptune
 Flyby on the 1977 Grand Tour.
- Fig. B7. 4 Sun-SC-Planet Angle During Neptune Flyby on the
 1977 Grand Tour.
 a. 26 Hour Frame
 b. 3 Hour Frame
- Fig. B7. 5 Range to Triton During Neptune Flyby on the 1977
 Grand Tour.
- Fig. B7. 6 Triton-SC-Planet Angle During Neptune Flyby on
 the 1977 Grand Tour.
- Fig. B7. 7 Sun-Triton-SC Angle During Neptune Flyby on the
 1977 Grand Tour.
- Fig. B7. 8 Sun-SC-Triton Angle During Neptune Flyby on the
 1977 Grand Tour.

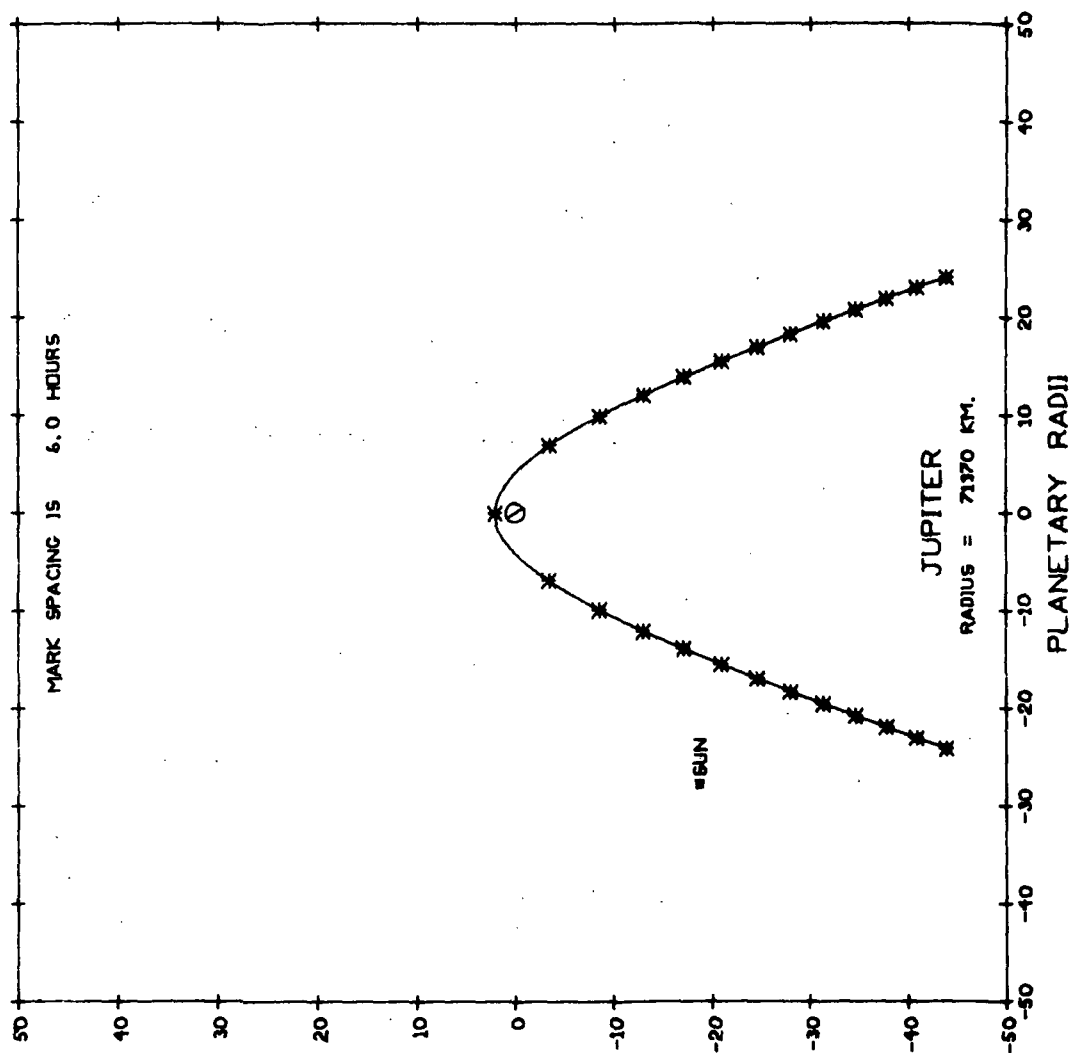


Fig. Bl. la Trajectory Plan View During Jovian Passage on 1973
Low Energy Jupiter Flyby; 100-Radii Field.

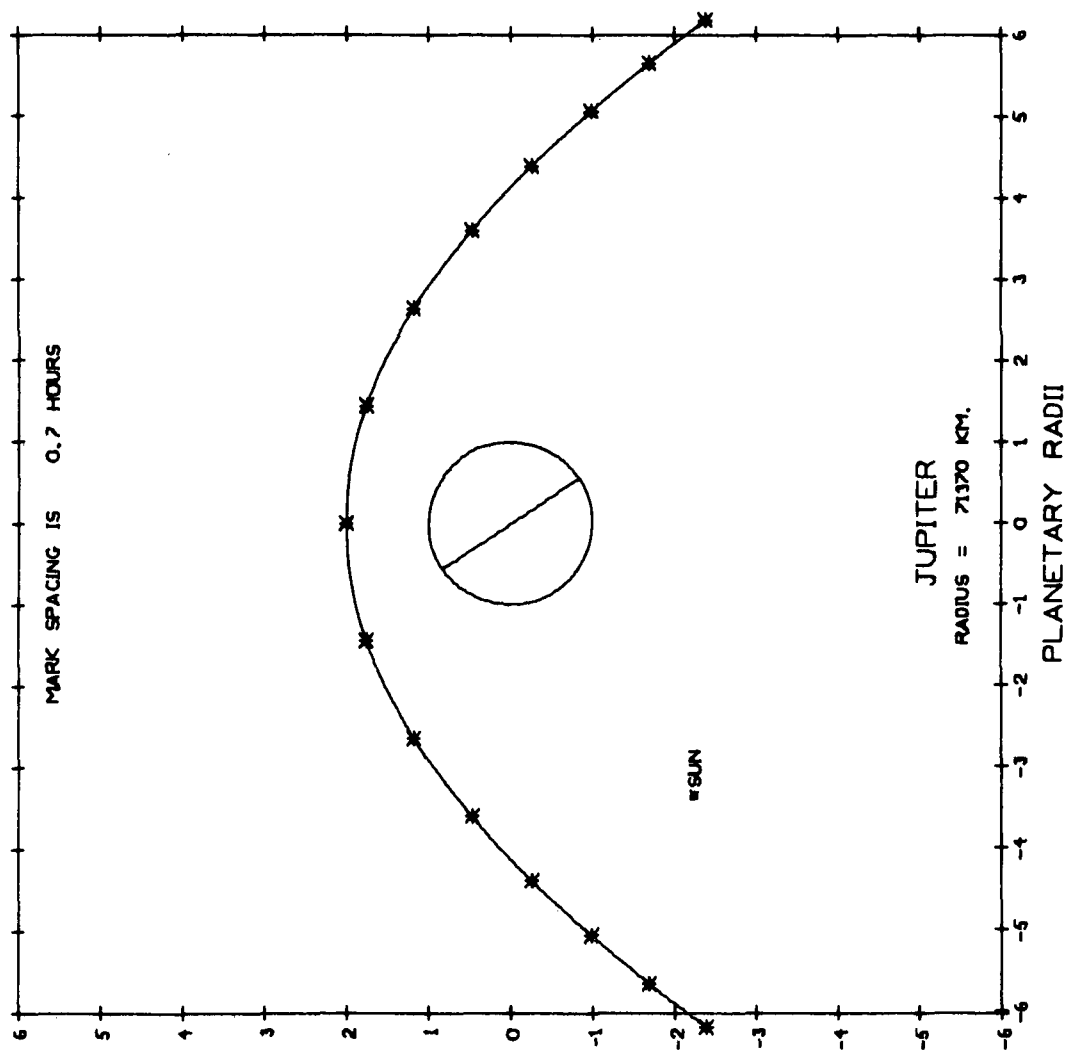


Fig. Bl. lb Trajectory Plan View During Jovian Passage on 1973
Low Energy Jupiter Flyby; 12-Radii Field.

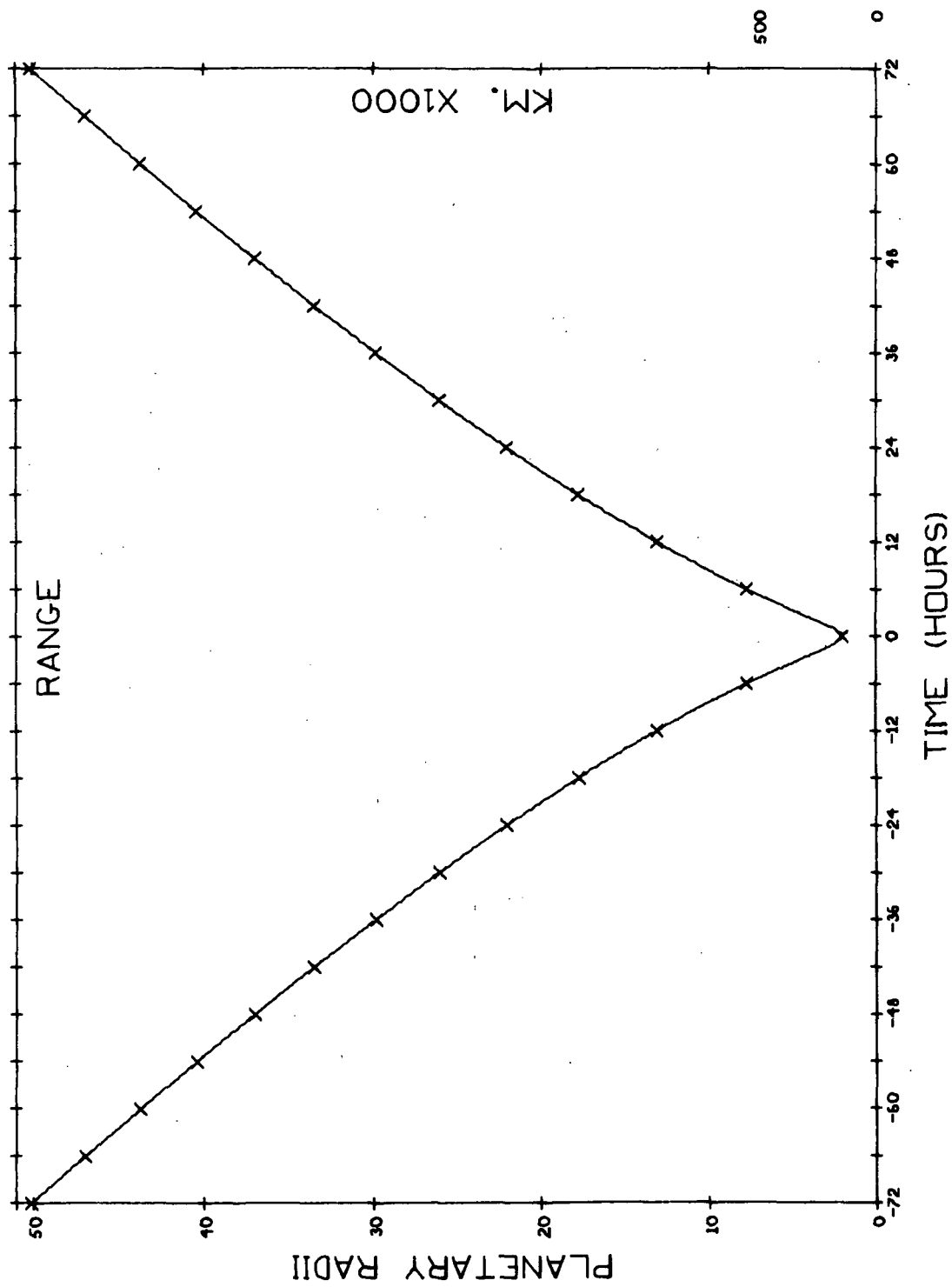


Fig. Bl. 2 Range to Planet During Jovian Passage on 1973 Low Energy Jupiter Flyby.

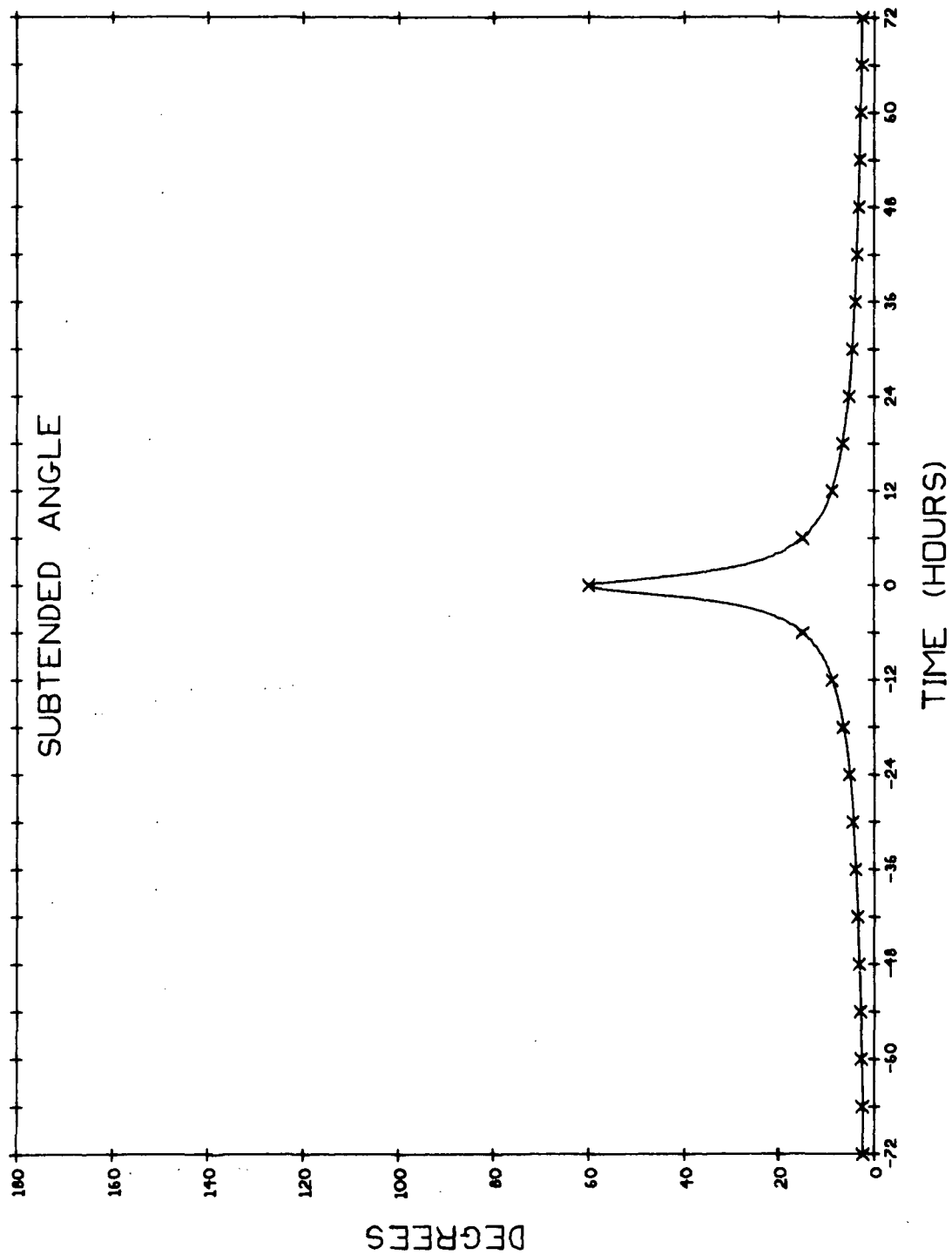


Fig. Bl. 3 Angle Subtended by Planetary Limbs During Jovian Passage on 1973 Low Energy Jupiter Flyby.

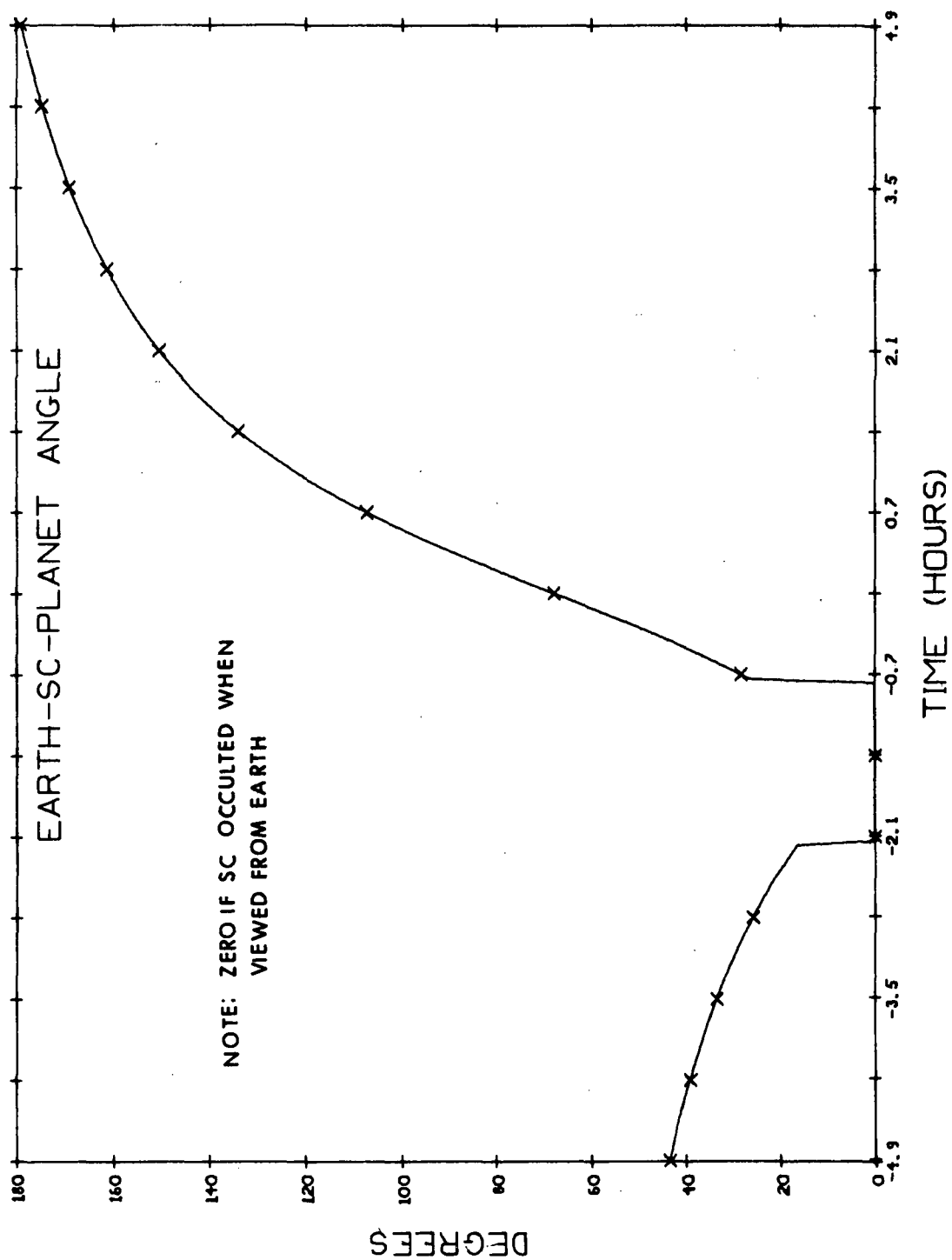


Fig. Bl. 4a Earth-SC-Planet Angle During Jovian Passage on 1973 Low Energy Jupiter Flyby.

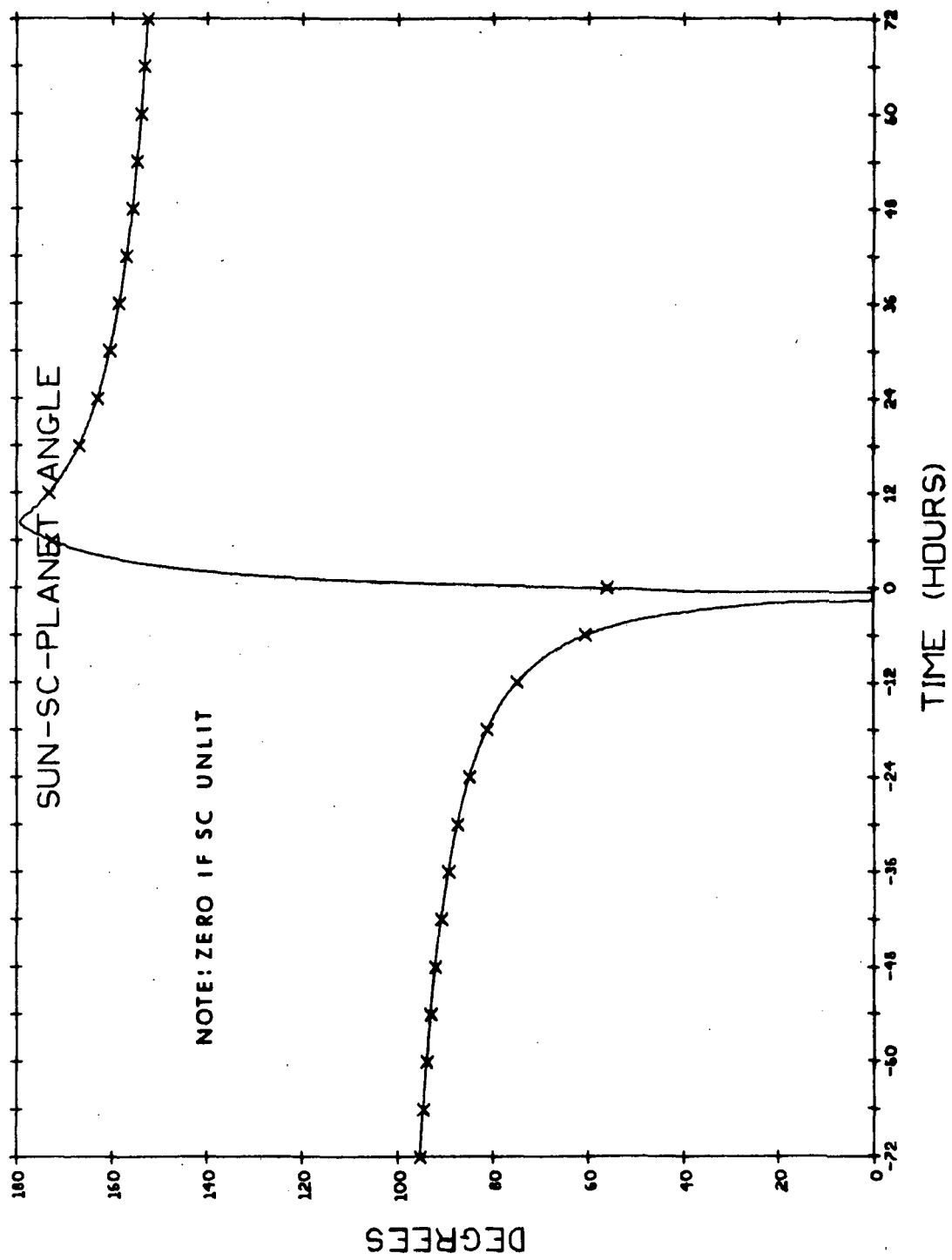


Fig. Bl. 4b Sun-SC-Planet Angle During Jovian Passage on 1973 Low Energy Jupiter Flyby.

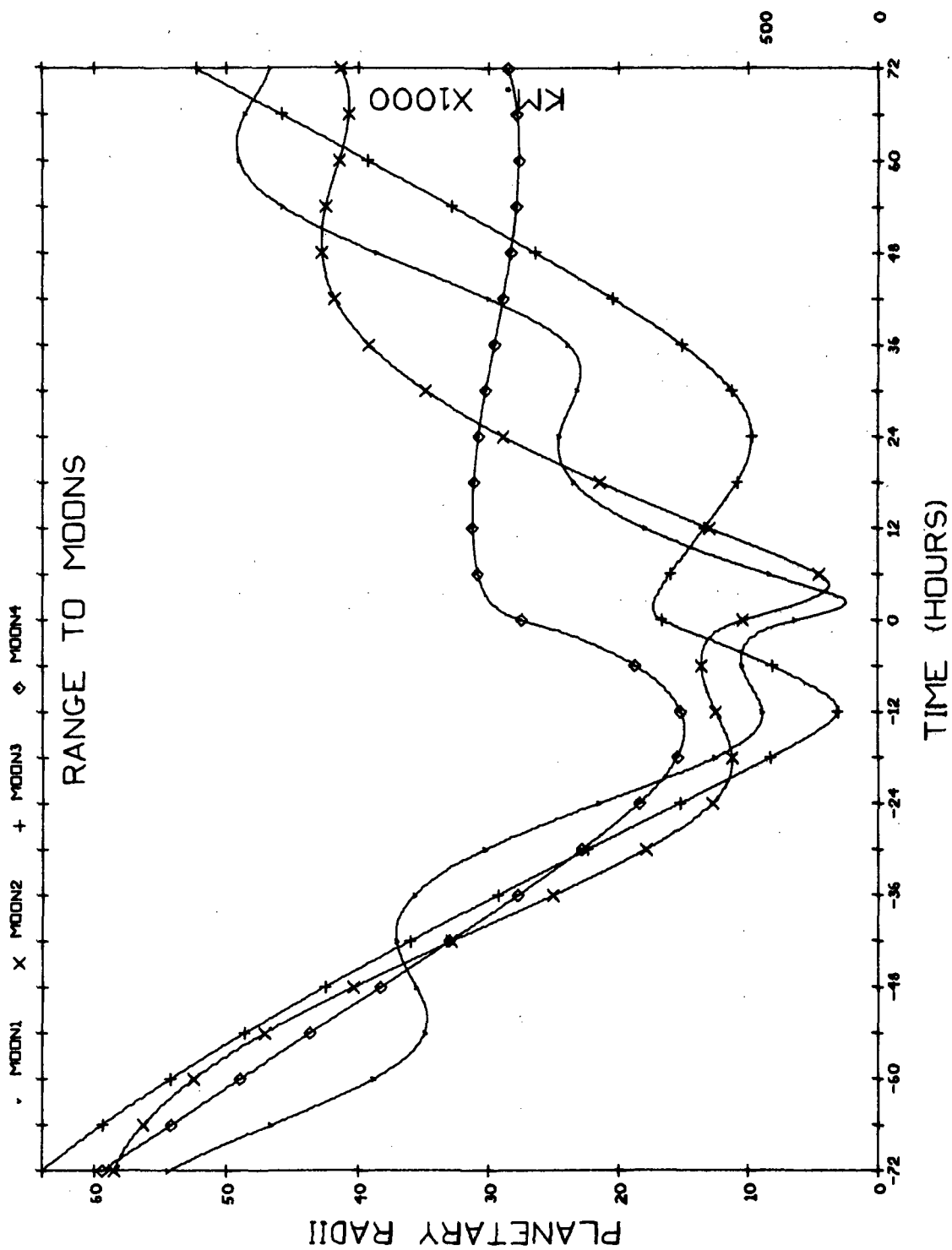


Fig. Bl. 5 Range to Principle Moons During Jovian Passage on 1973 Low Energy Jupiter Flyby.

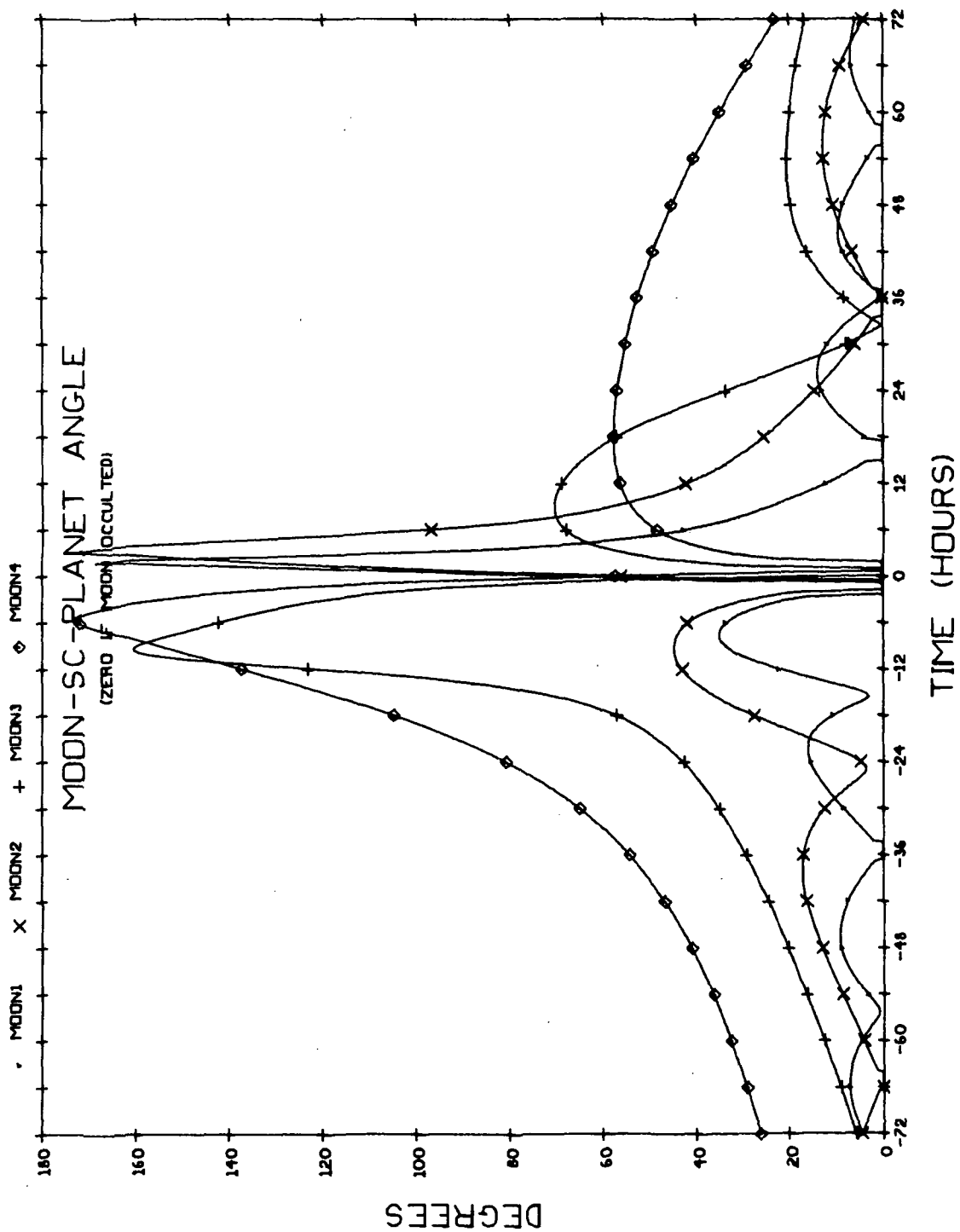


Fig. Bl. 6a Moon-SC-Planet Angle During Jovian Passage on 1973 Low Energy Jupiter Flyby;
144-Hour Frame.

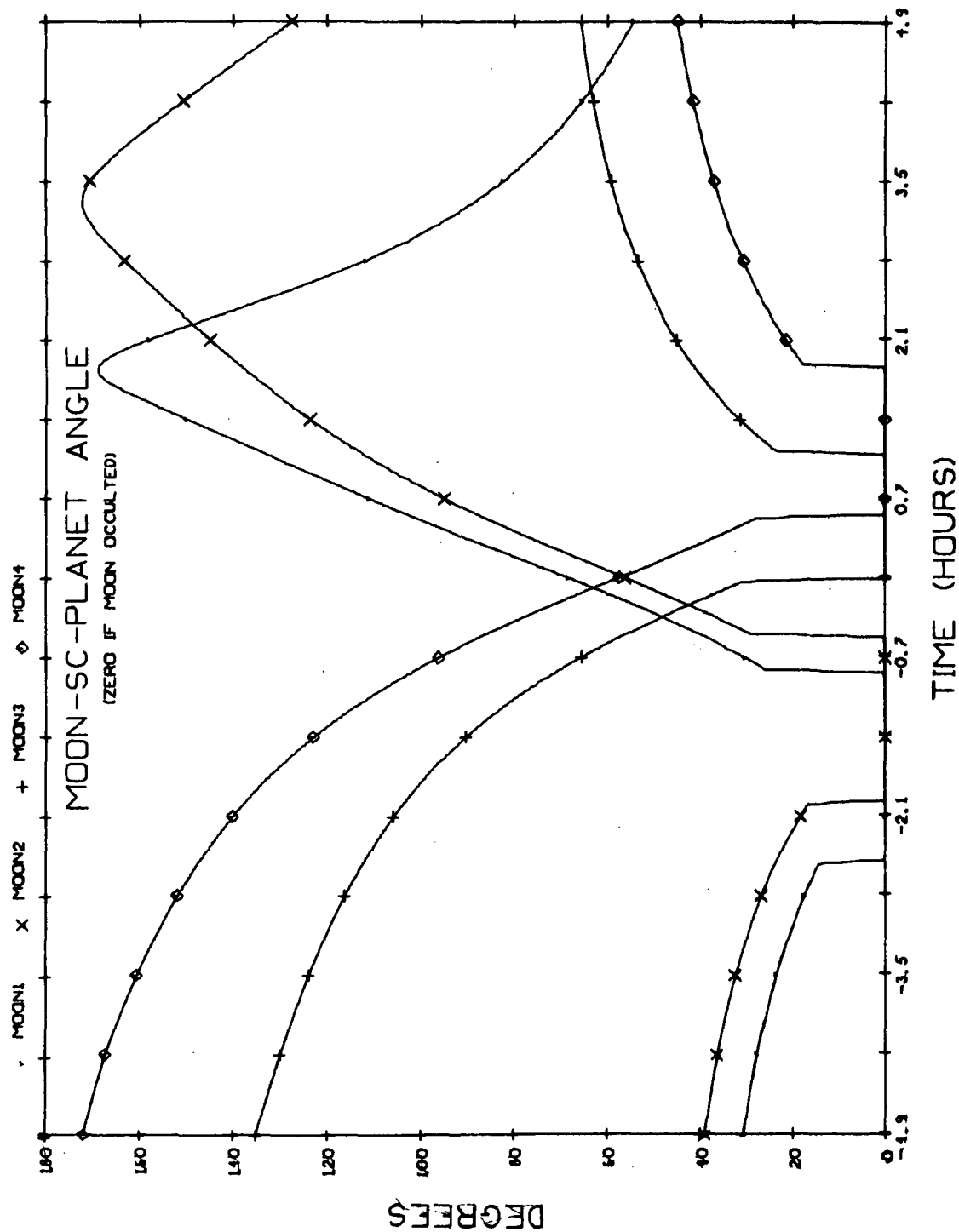


Fig. Bl. 6b Moon-SC-Planet Angle During Jovian Passage on 1973 Low Energy Jupiter Flyby;
9.8-Hour Frame.

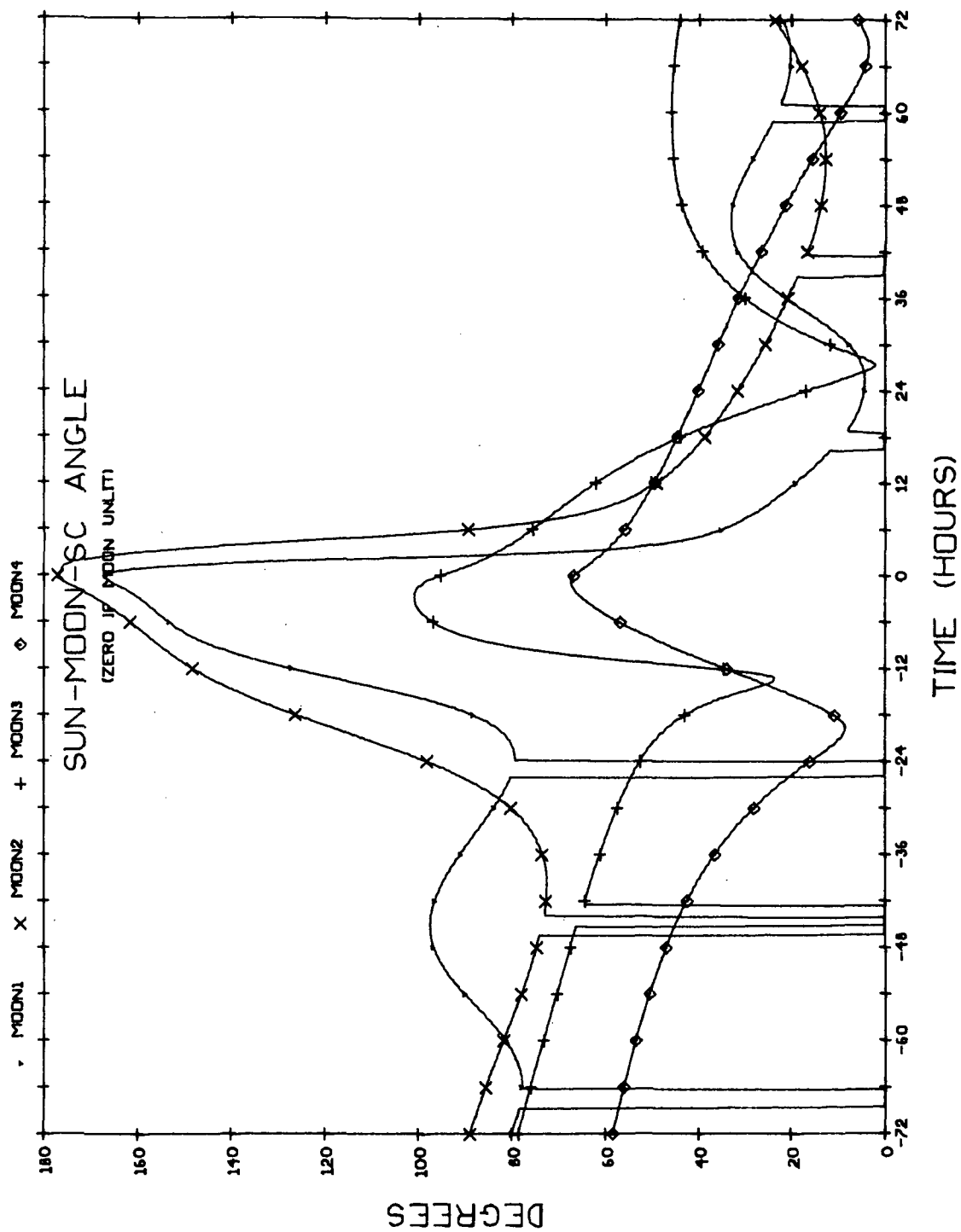


Fig. Bl. 7 Sun-Moon-SC Angle During Jovian Passage on 1973 Low Energy Jupiter Flyby.

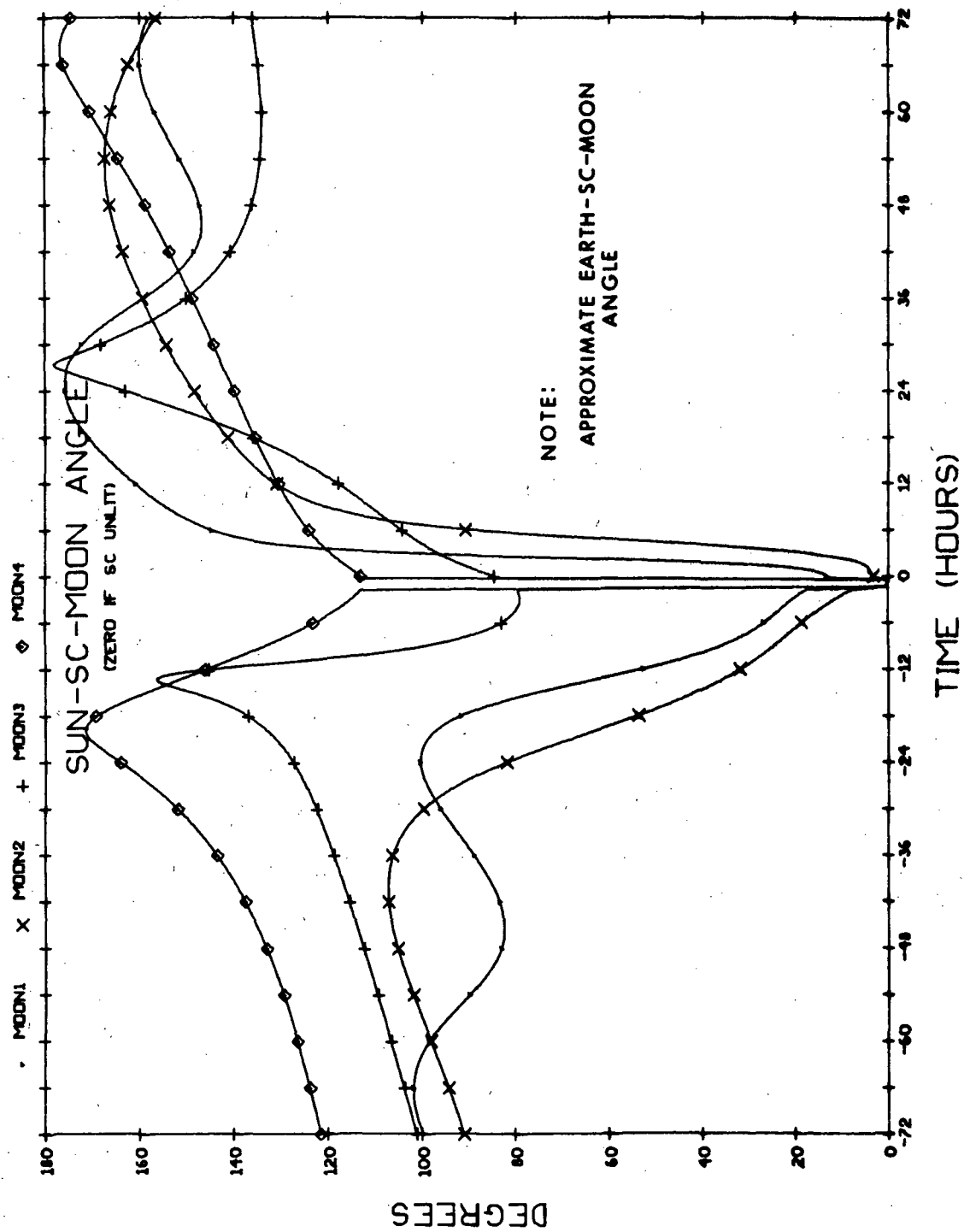


Fig. Bl. 8 Sun-SC-Moon Angle During Jovian Passage on 1973 Low Energy Jupiter Flyby.

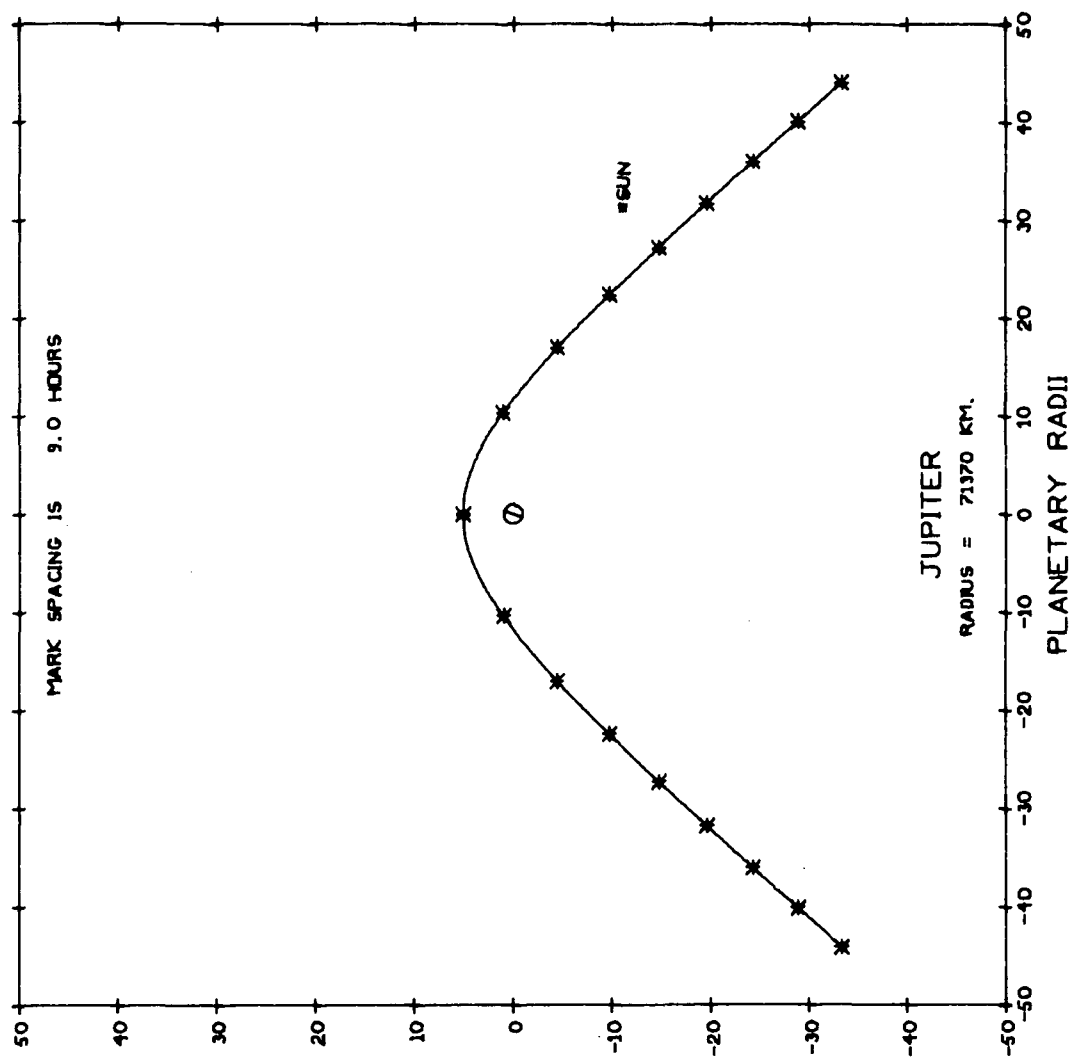


Fig. B2.1a Trajectory Plan View During Jovian Passage on 1977
Jupiter Swingby to Saturn; 100-Radii Field.

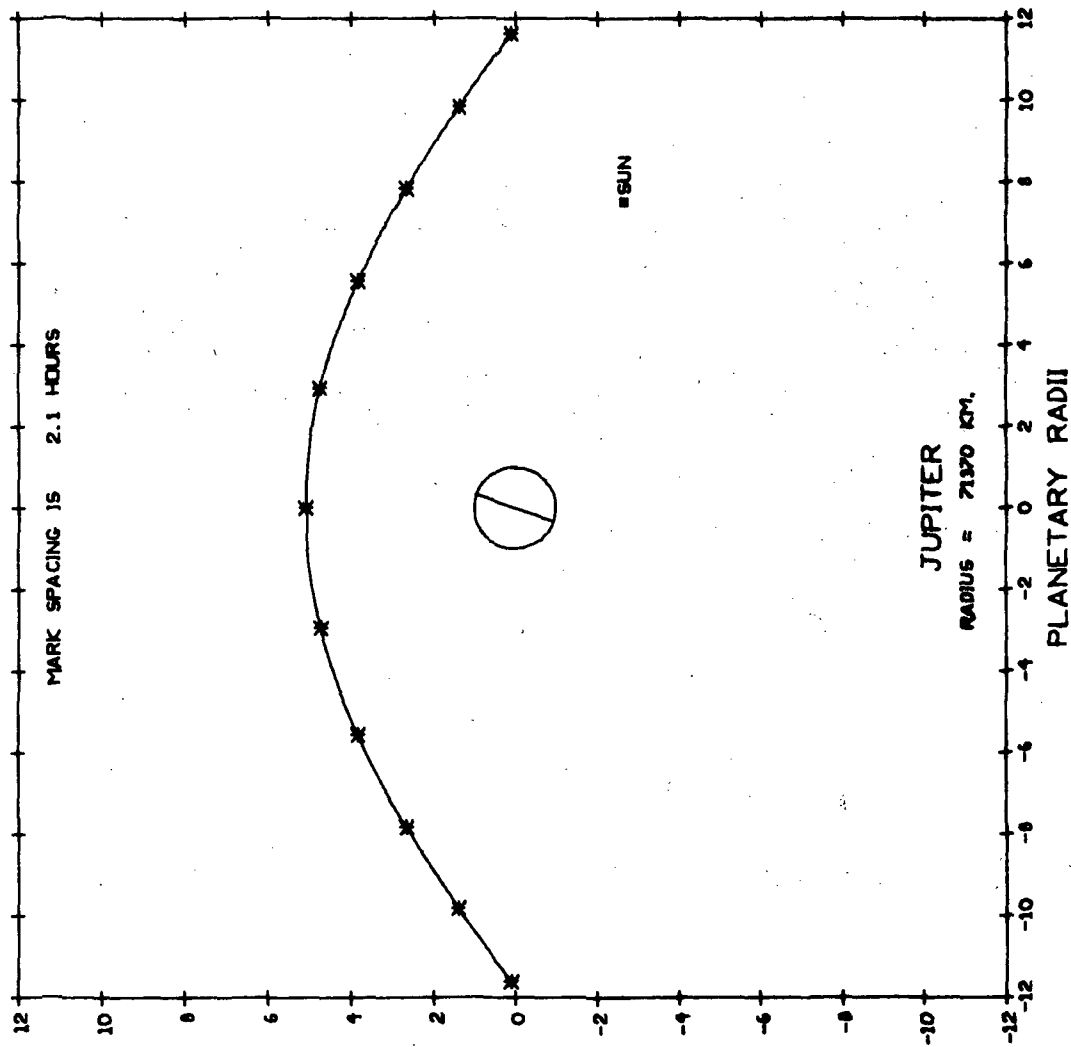


Fig. B2.1b Trajectory Plan View During Jovian Passage on 1977
Jupiter Swingby to Saturn; 24-Radii Field.

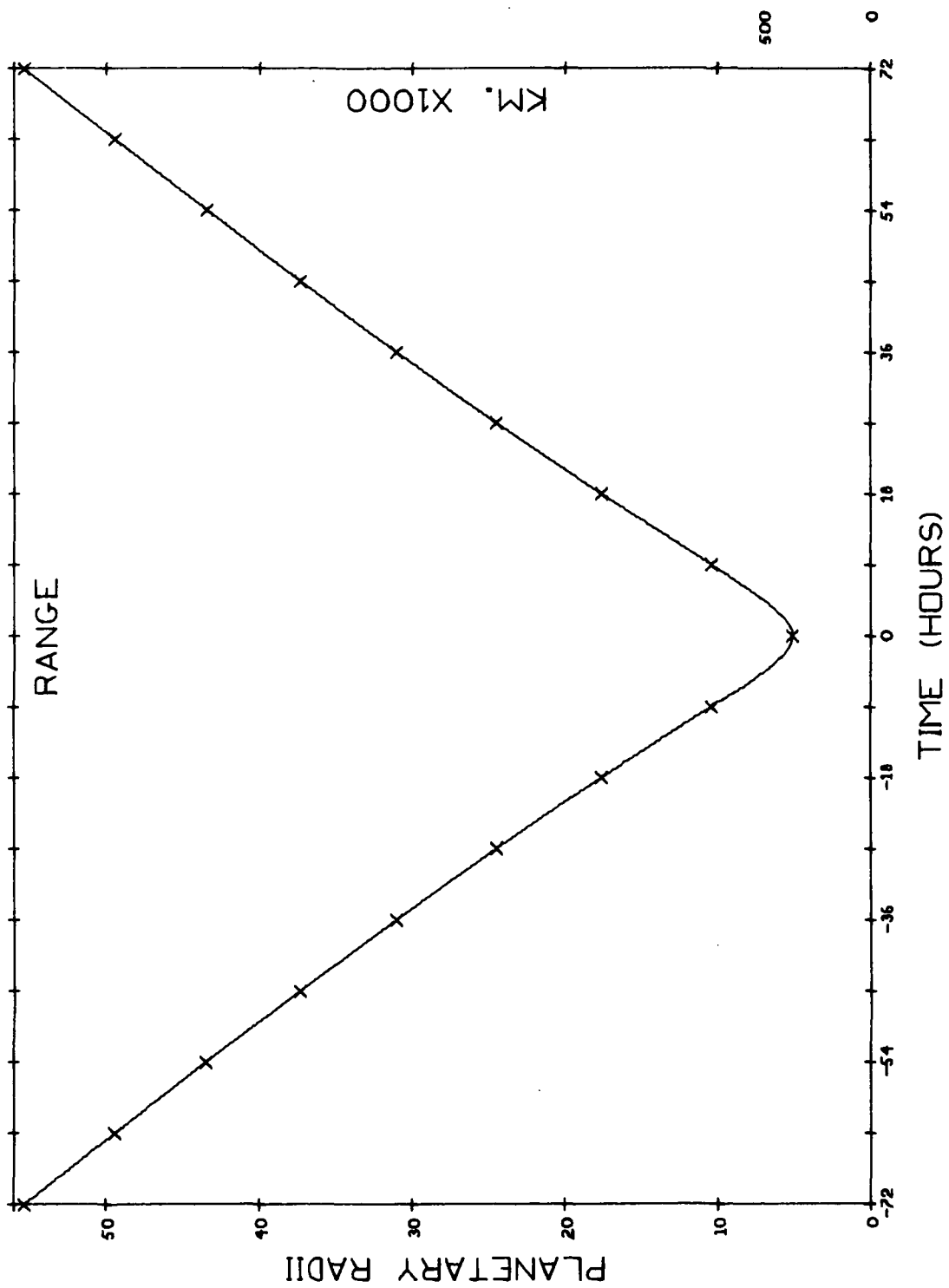


Fig. B2.2 Range to Planet During Jovian Passage on 1977 Jupiter Swingby to Saturn.

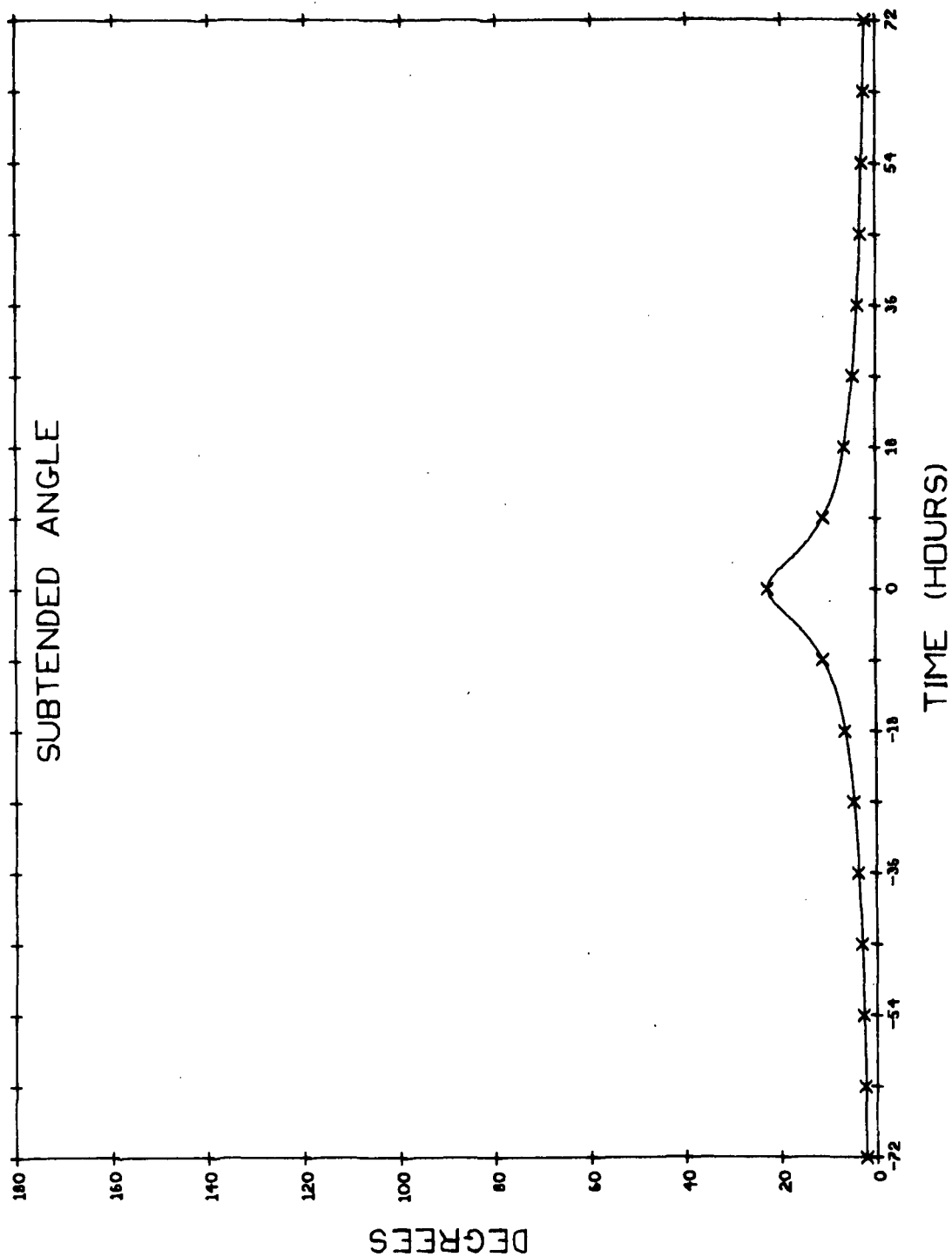


Fig. B2.3 Angle Subtended by Planetary Limbs During Jovian Passage on 1977 Jupiter Swingby to Saturn.

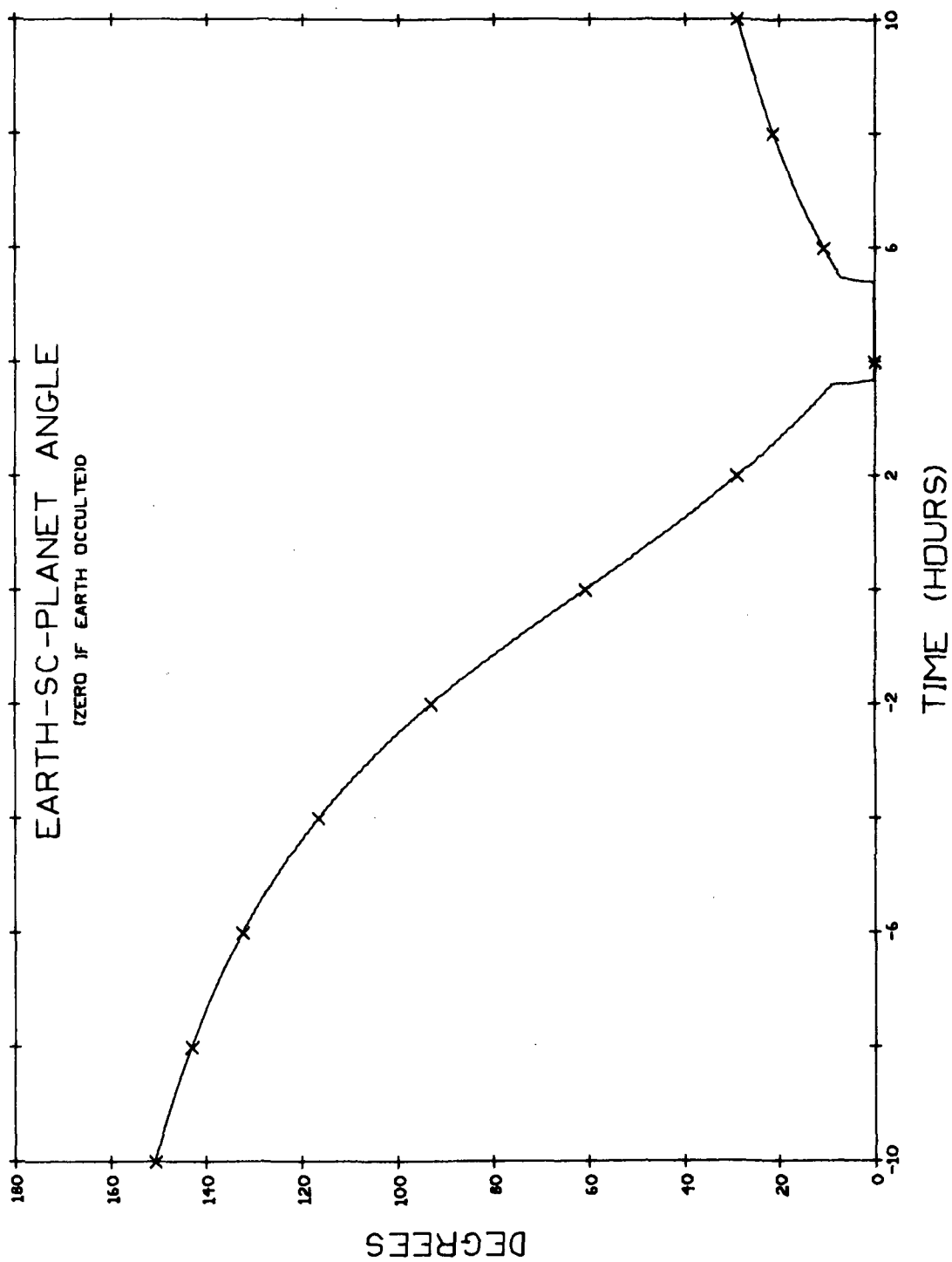


Fig. B2.4a Earth-SC-Planet Angle During Jovian Passage on 1977 Jupiter Swingby to Saturn.

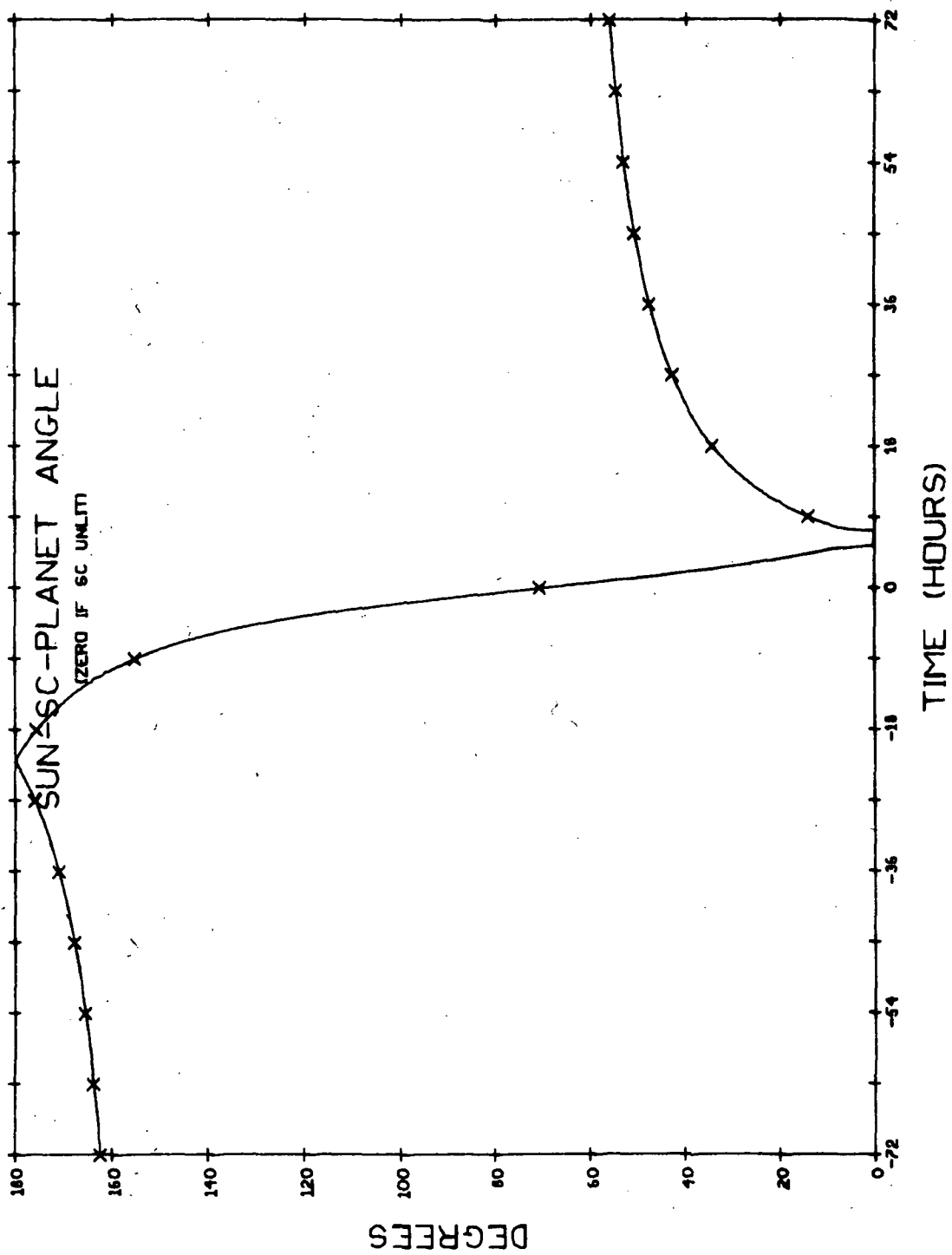


Fig. B2. 4b Sun-SC-Planet Angle During Jovian Passage on 1977 Jupiter Swingby to Saturn.

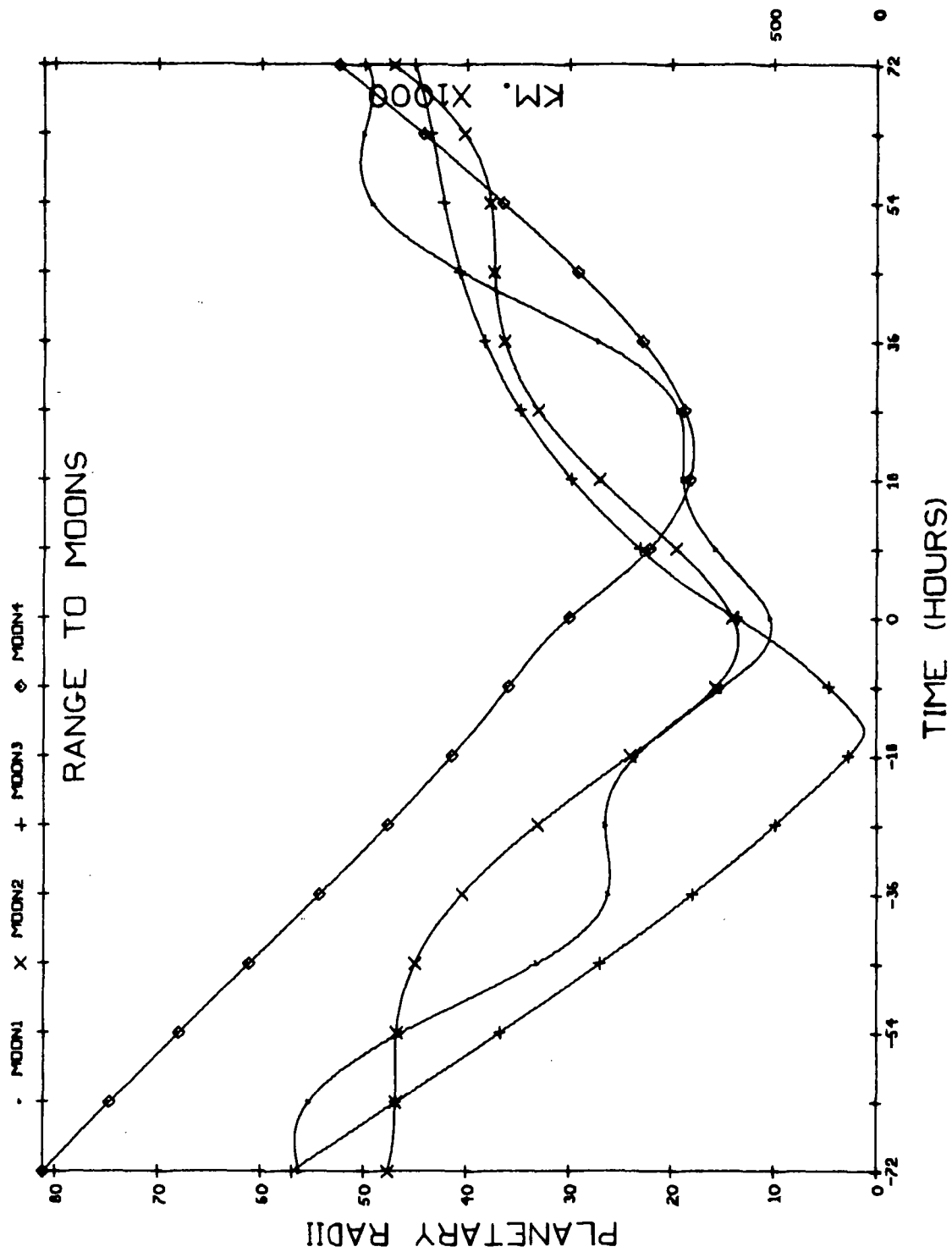


Fig. B2.5 Range to Moons During Jovian Passage on 1977 Jupiter Swingby to Saturn.

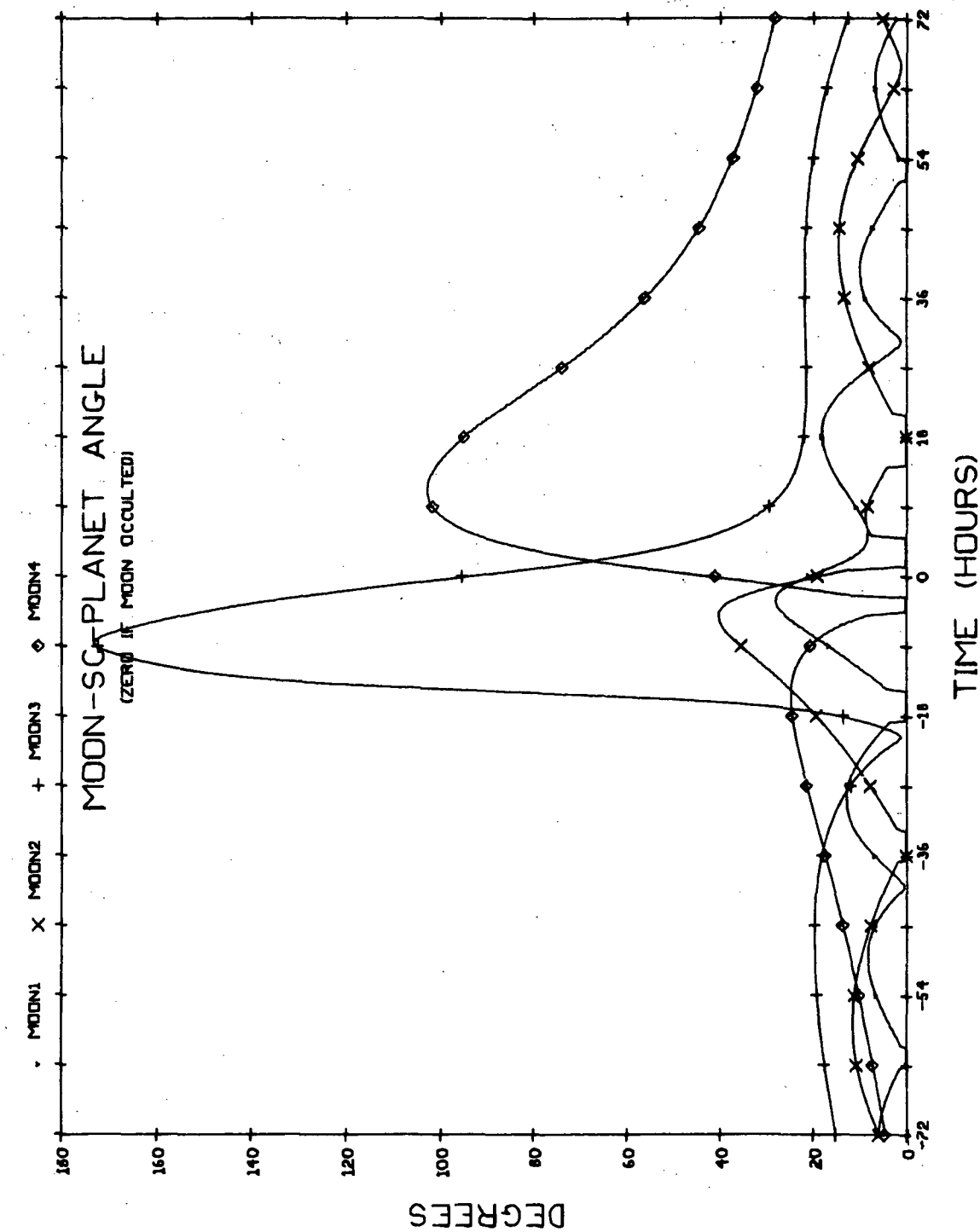


Fig. B2.6 Moon-SC-Planet Angle During Jovian Passage on 1977 Jupiter Swingby to Saturn.

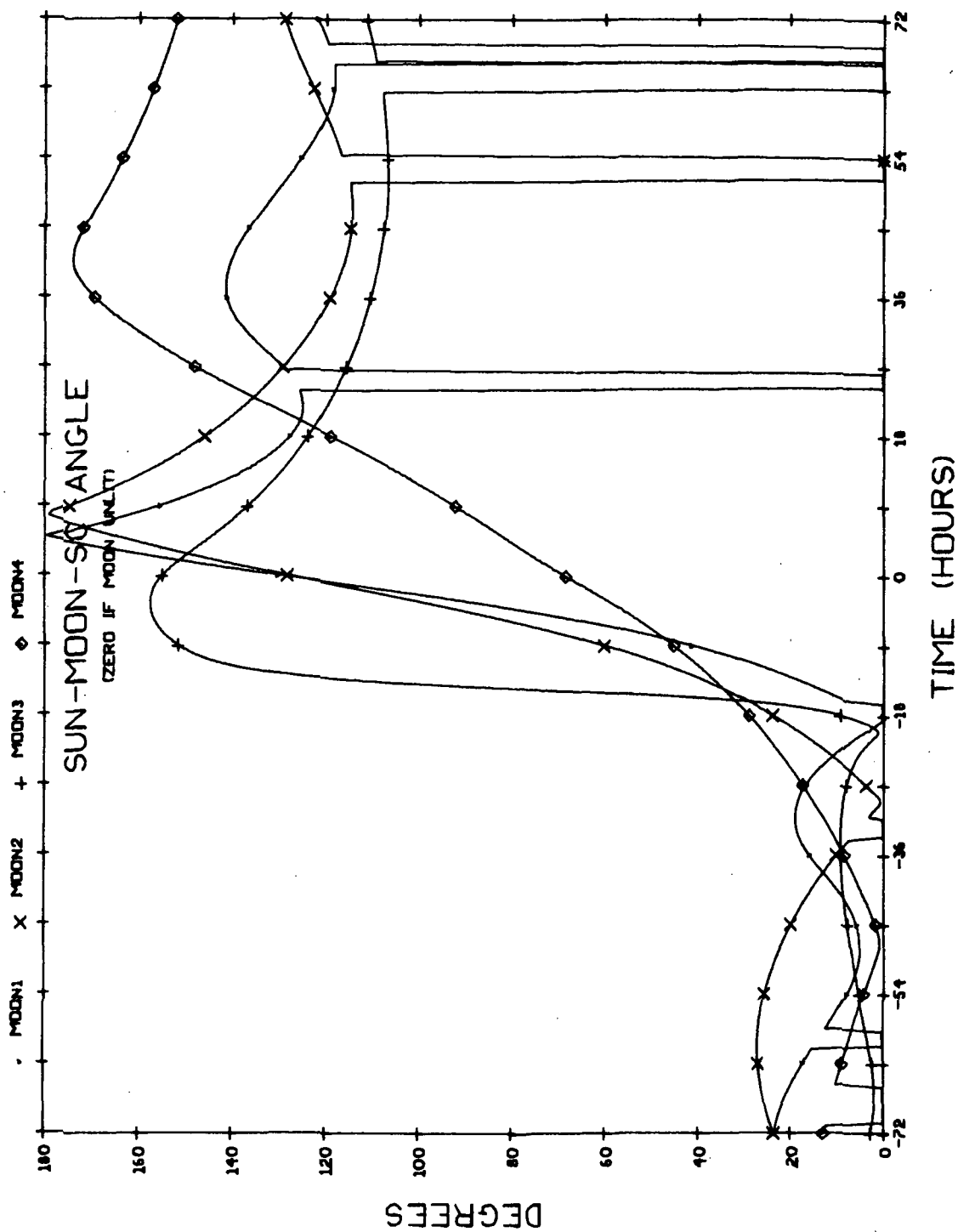


Fig. B2.7 Sun-Moon-SC Angle During Jovian Passage on 1977 Jupiter Swingby to Saturn.

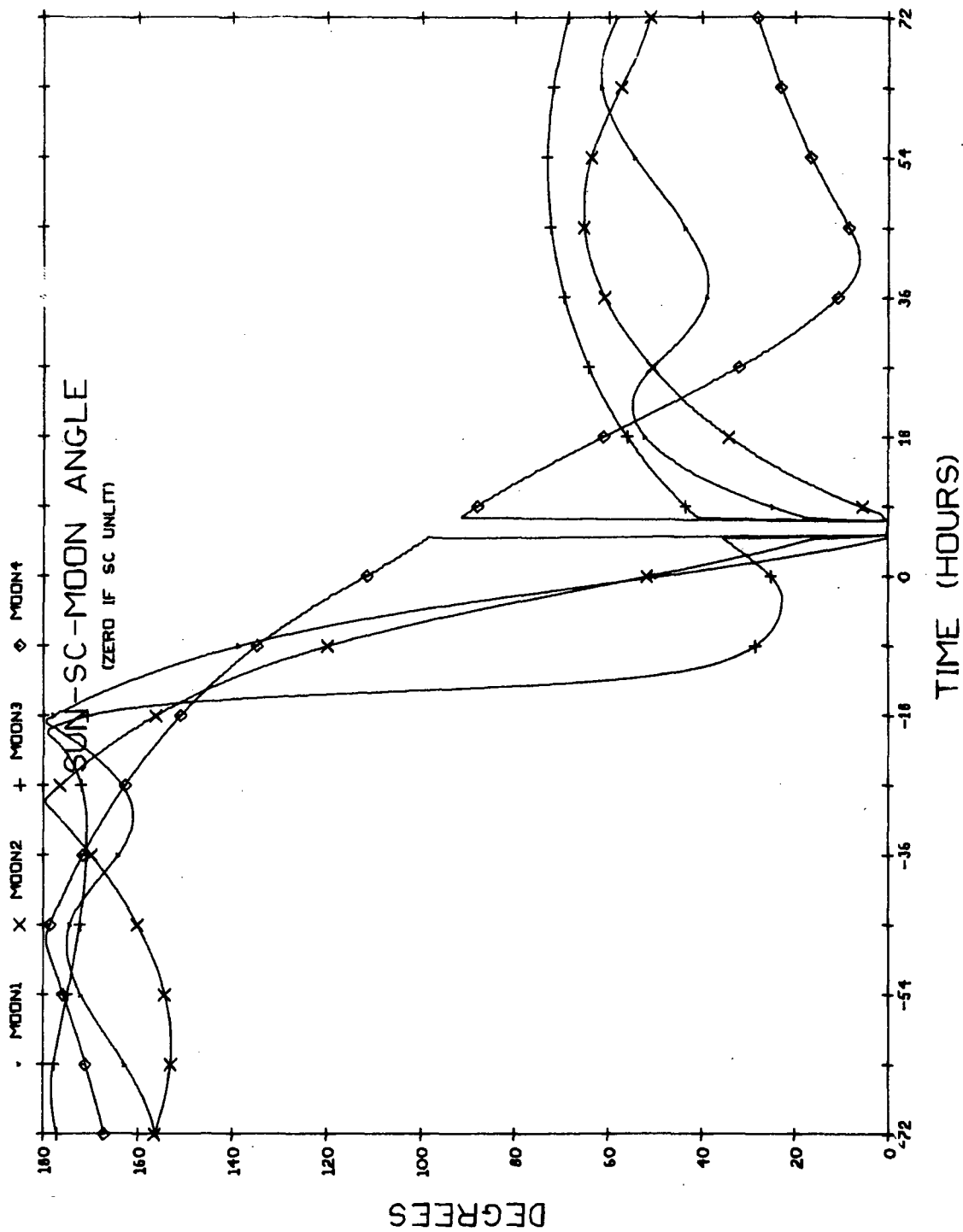


Fig. B2.8 Sun-SC-Moon Angle During Jovian Passage on 1977 Jupiter Swingby to Saturn.

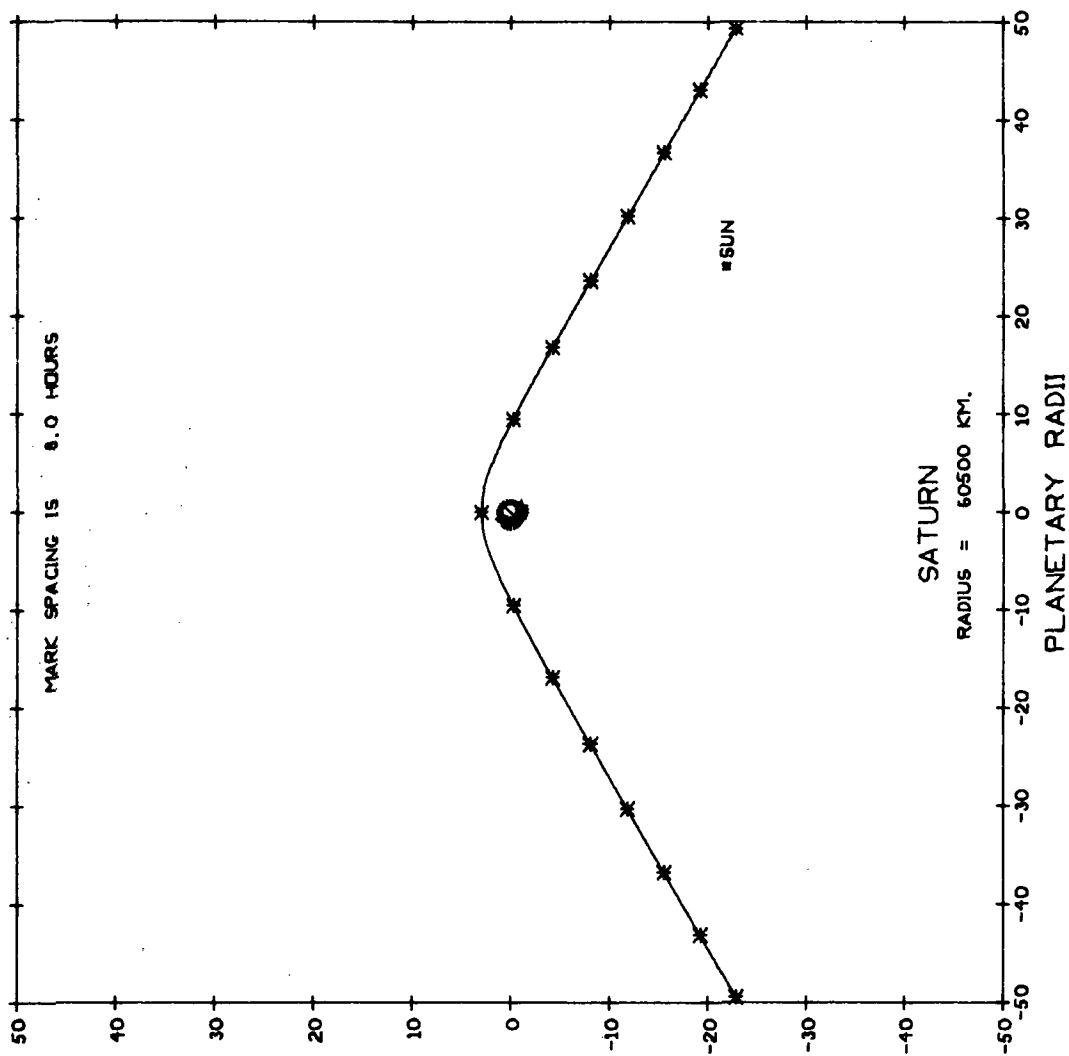


Fig. B3.1a Trajectory Plan View During Saturn Flyby on 1977
Jupiter Swingby to Saturn; 100-Radii Field.

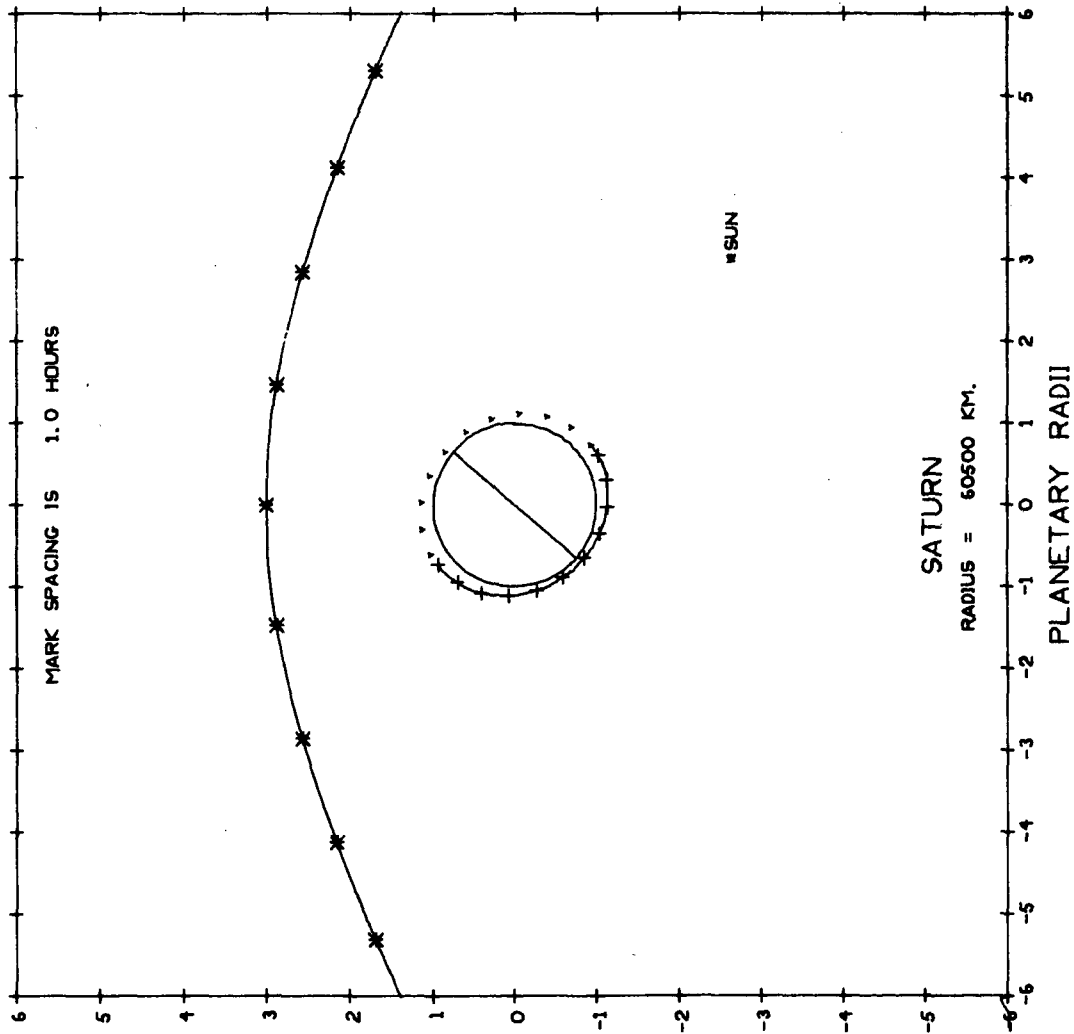


Fig. B3, lb Trajectory Plan View During Saturn Flyby on 1977
Jupiter Swingby to Saturn; 12-Radii Field.

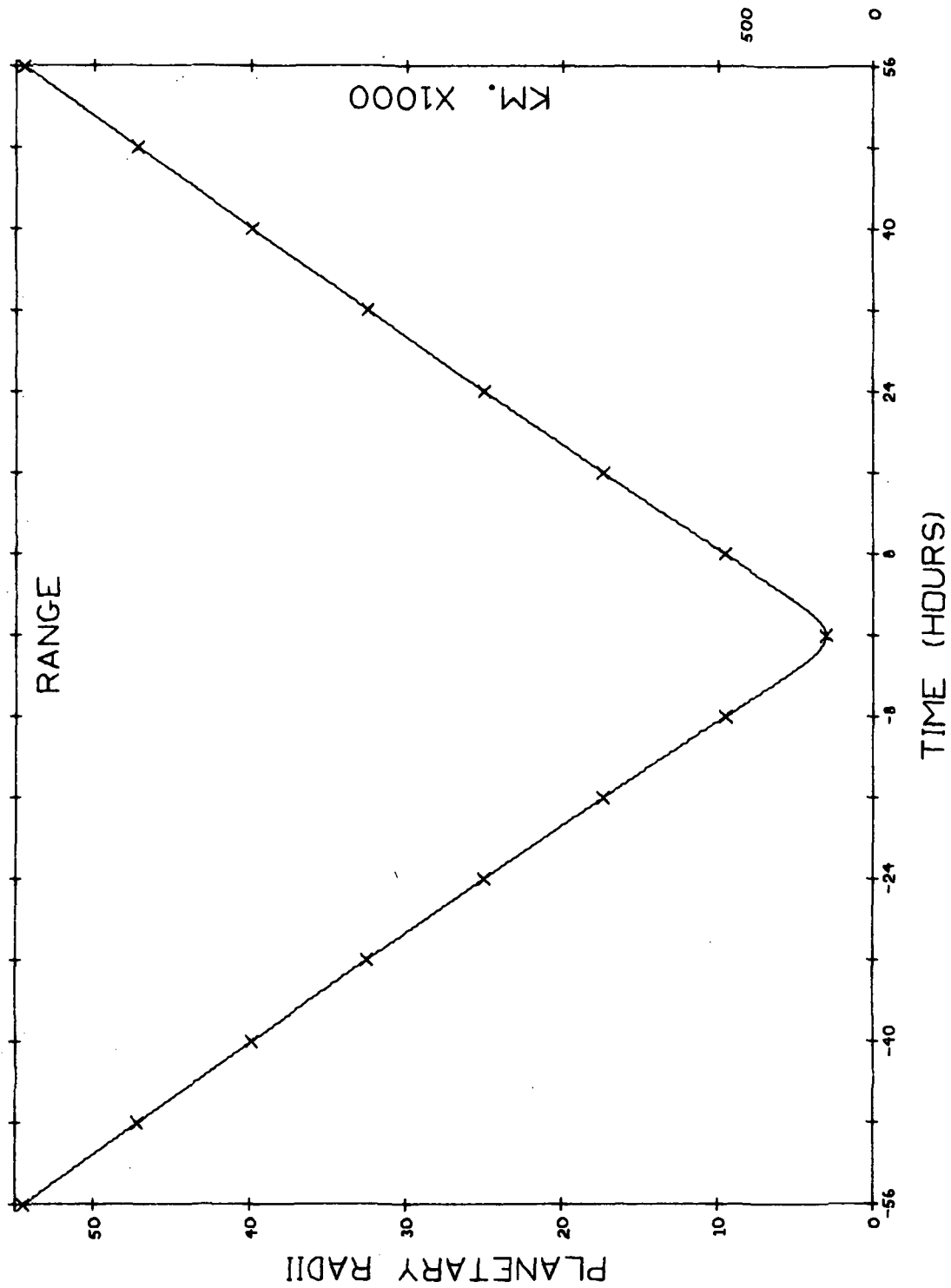


Fig. B3. 2 Range to Planet During Saturn Flyby on 1977 Jupiter Swingby to Saturn.

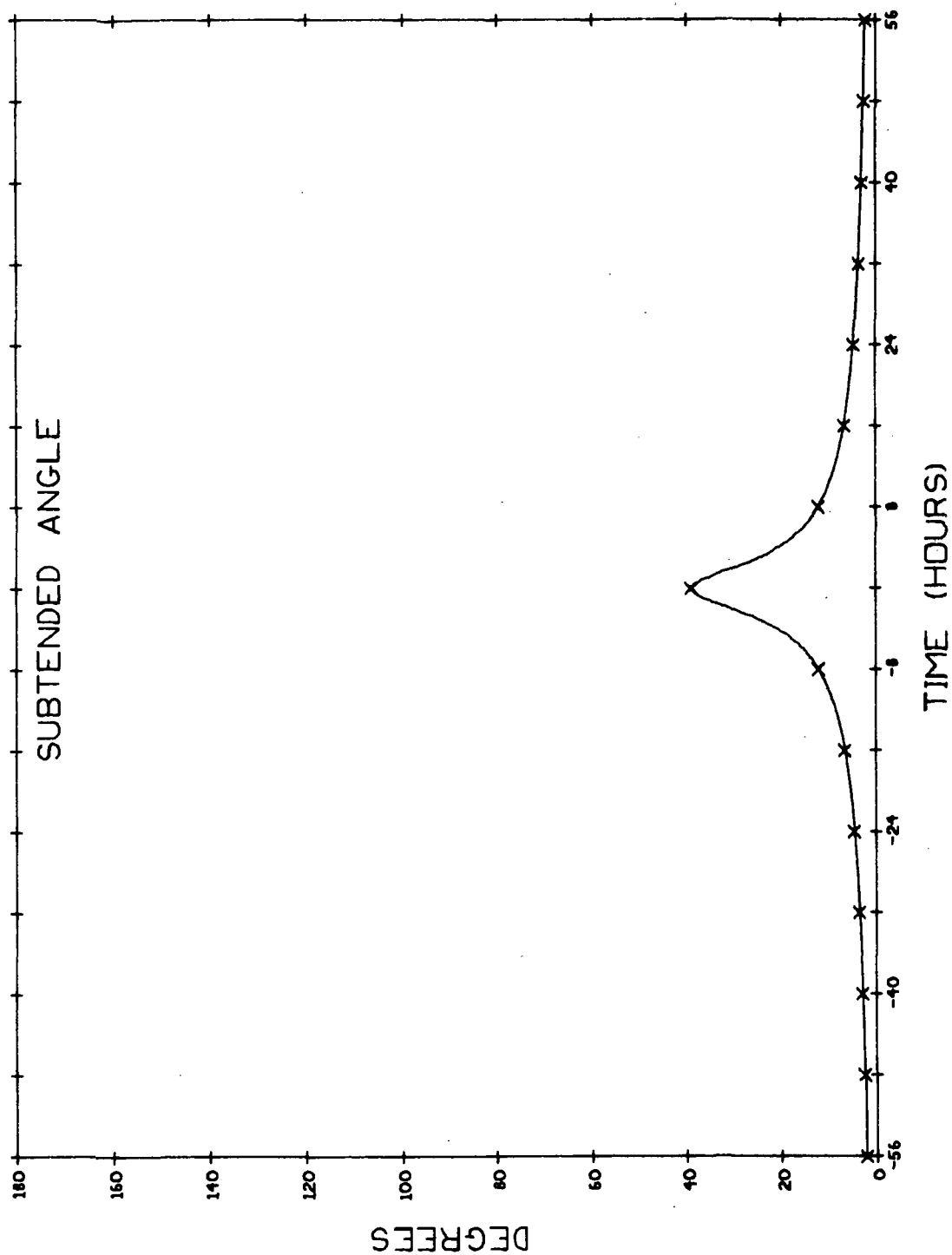


Fig. B3. 3 Angle Subtended by Planetary Limbs During Saturn Flyby on 1977 Jupiter
Swingby to Saturn.

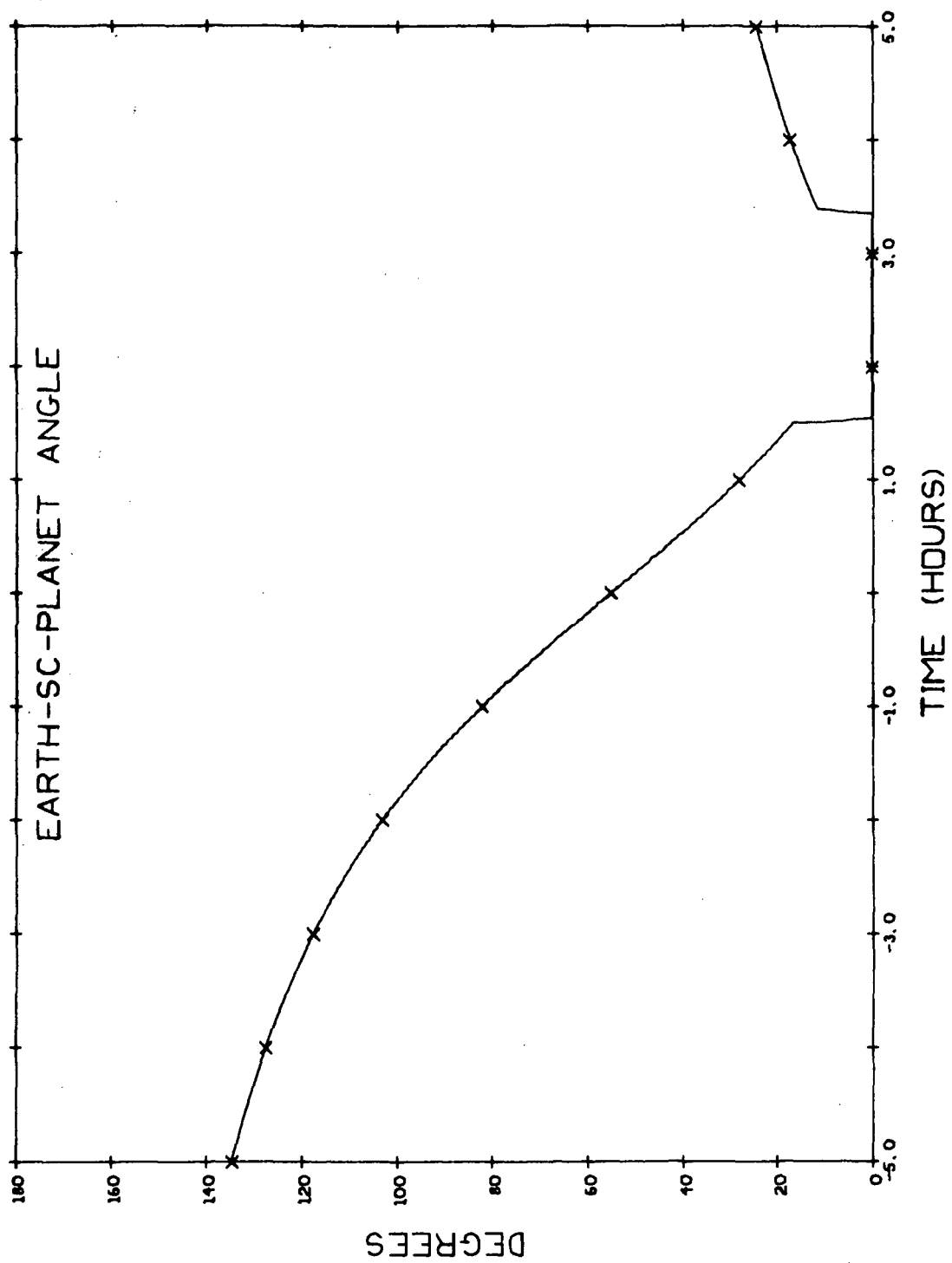


Fig. B3.4a Earth-SC-Planet Angle During Saturn Flyby on 1977 Jupiter Swingby to Saturn.

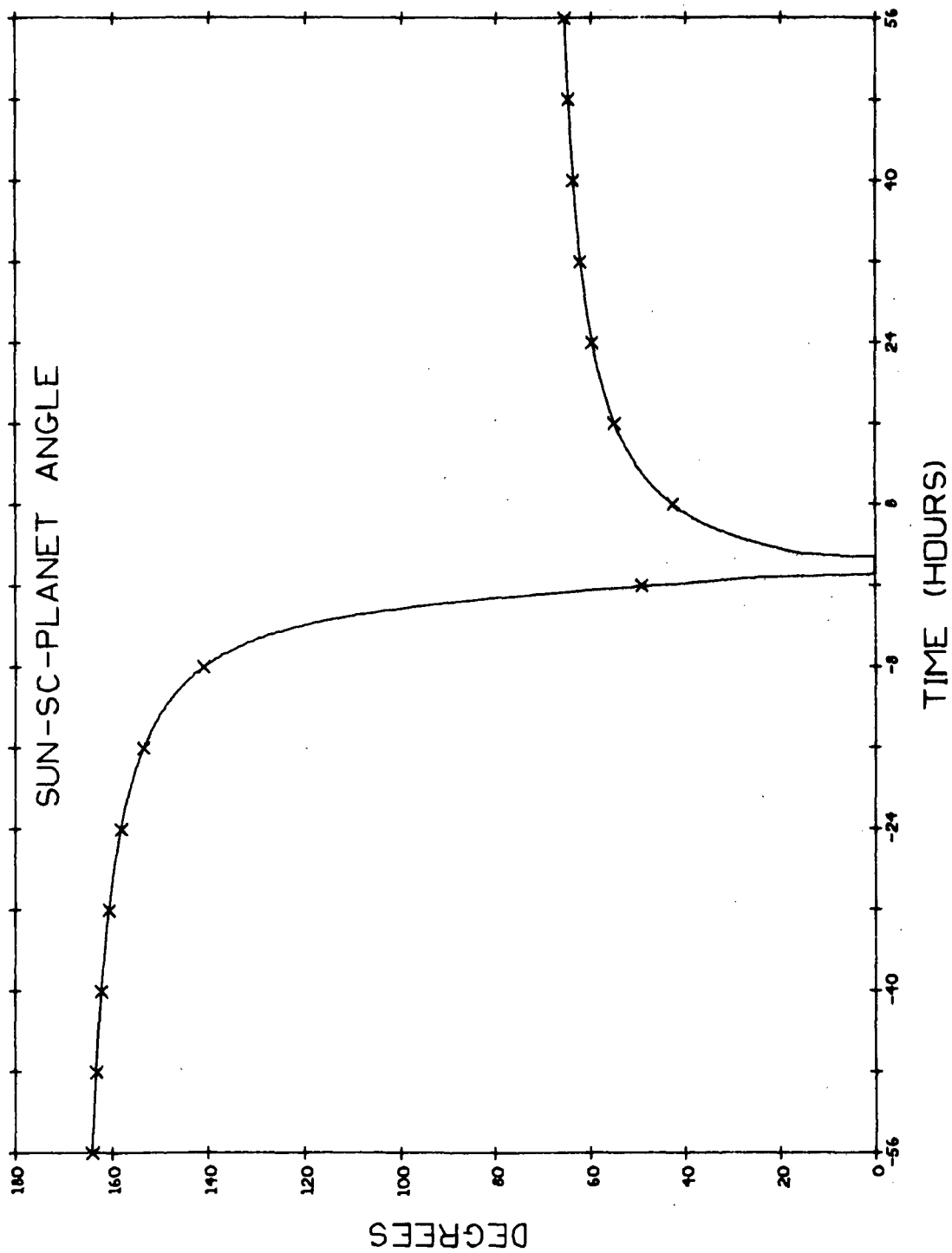


Fig. B3.4b Sun-SC-Planet Angle During Saturn Flyby on 1977 Jupiter Swingby to Saturn.

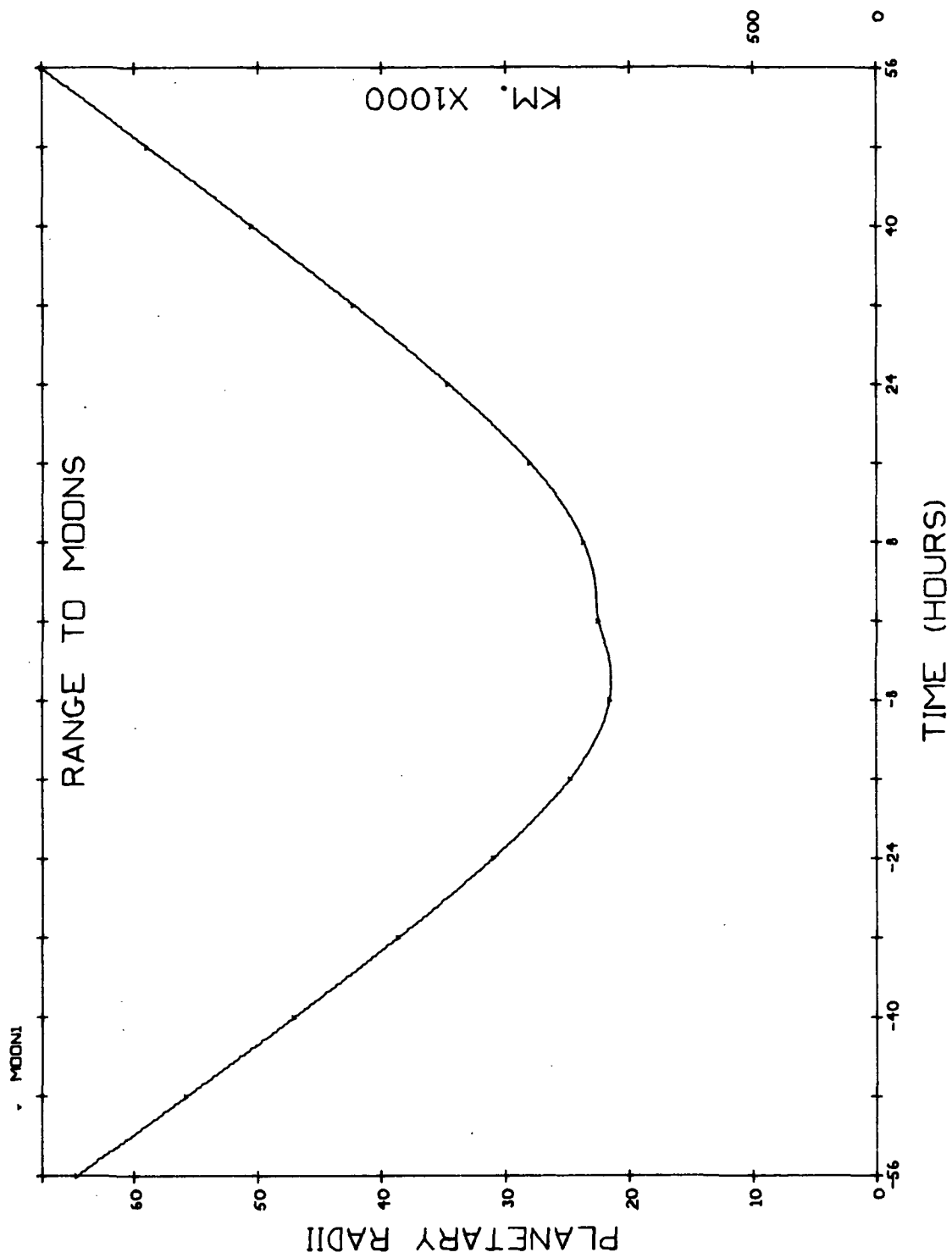


Fig. B3.5 Range to Titan During Saturn Flyby on 1977 Jupiter Swingby to Saturn.

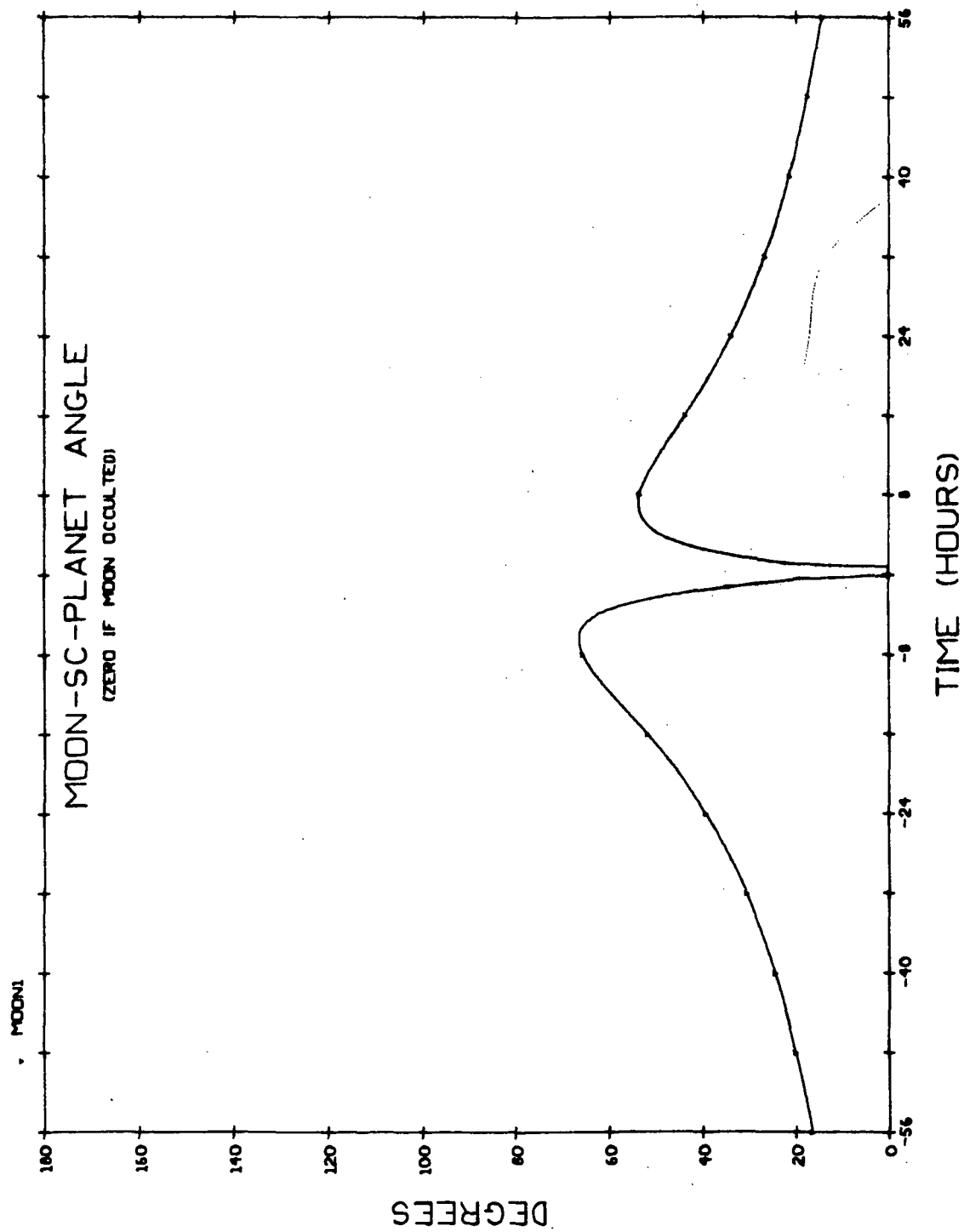


Fig. B3. 6 Titan-SC-Planet Angle During Saturn Flyby on 1977 Jupiter Swingby to Saturn.

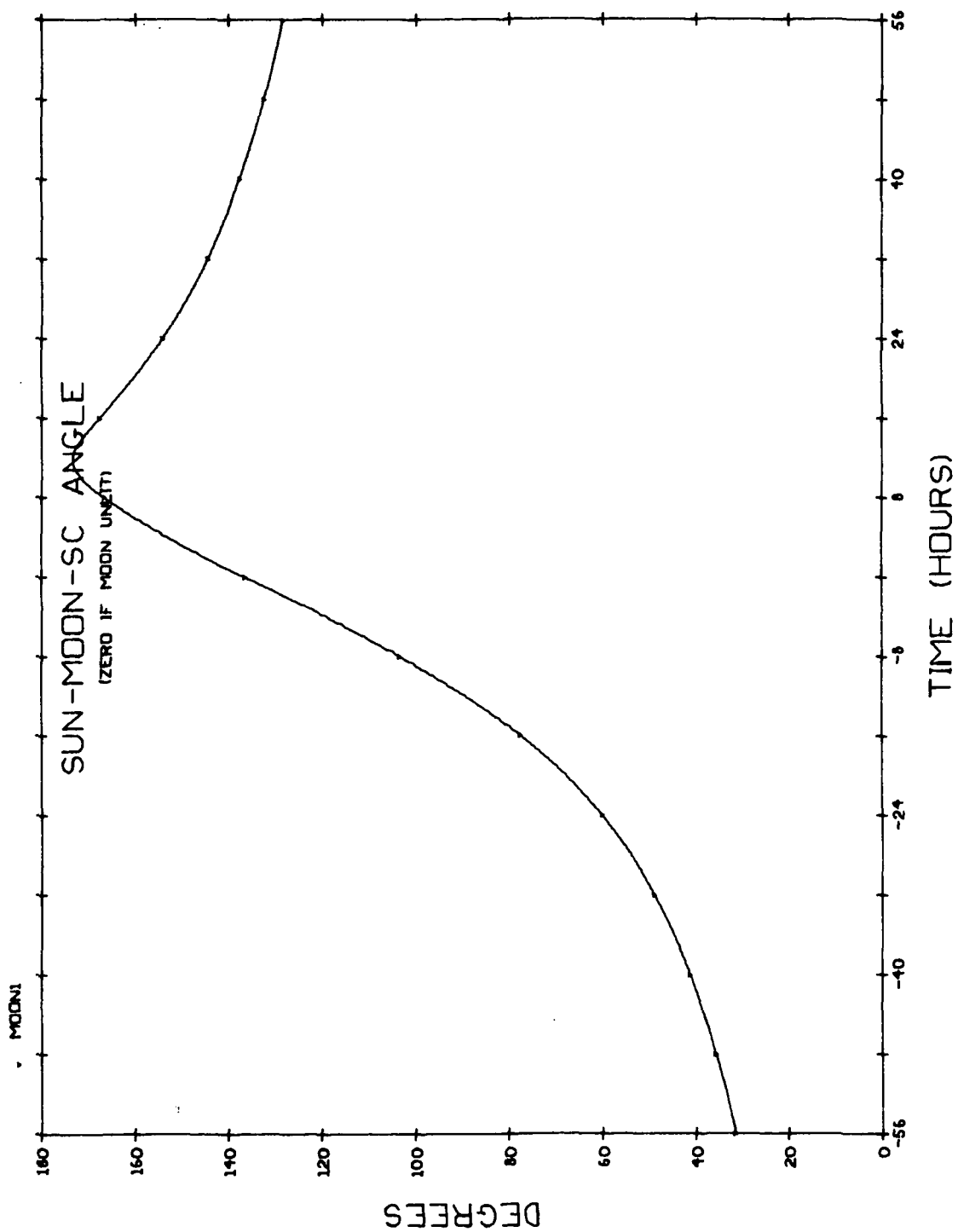


Fig. B3.7 Sun-Titan-SC Angle During Saturn Flyby on 1977 Jupiter Swingby to Saturn.

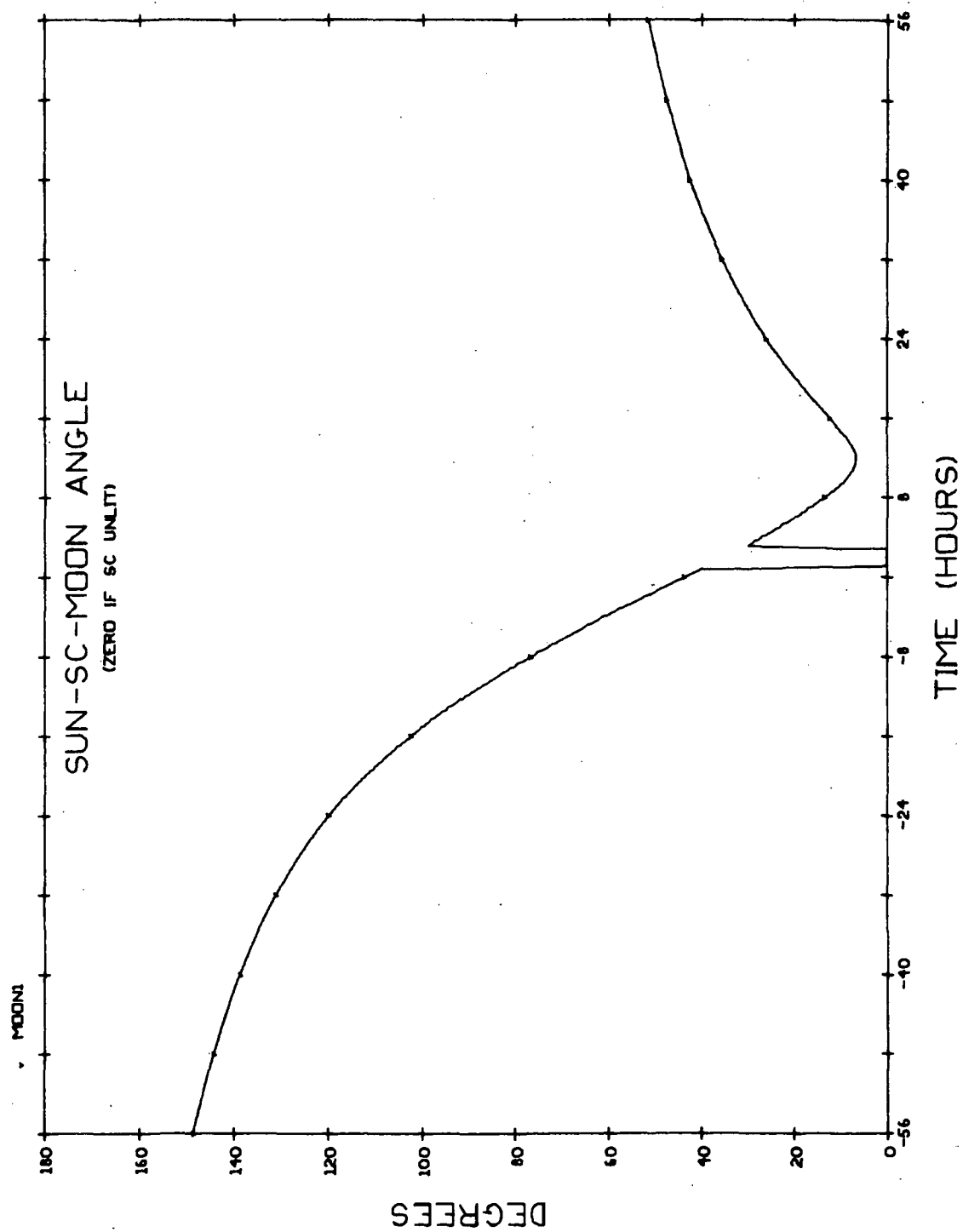


Fig. B3.8 Sun-SC-Titan Angle During Saturn Flyby on 1977 Swingby to Saturn.

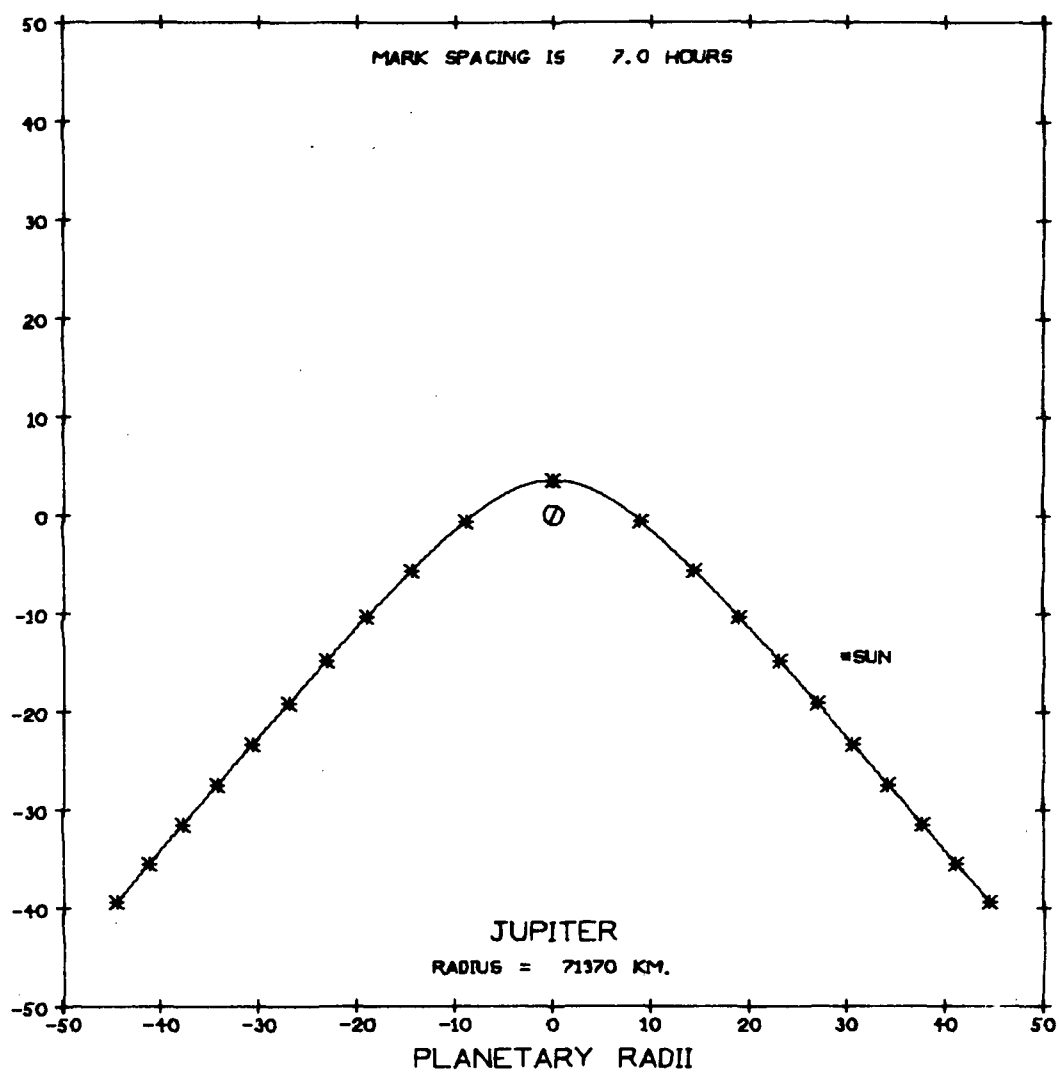


Fig. B4.1a Trajectory Plan View During Jovian Passage on the 1977 Grand Tour; 100 Radii Field

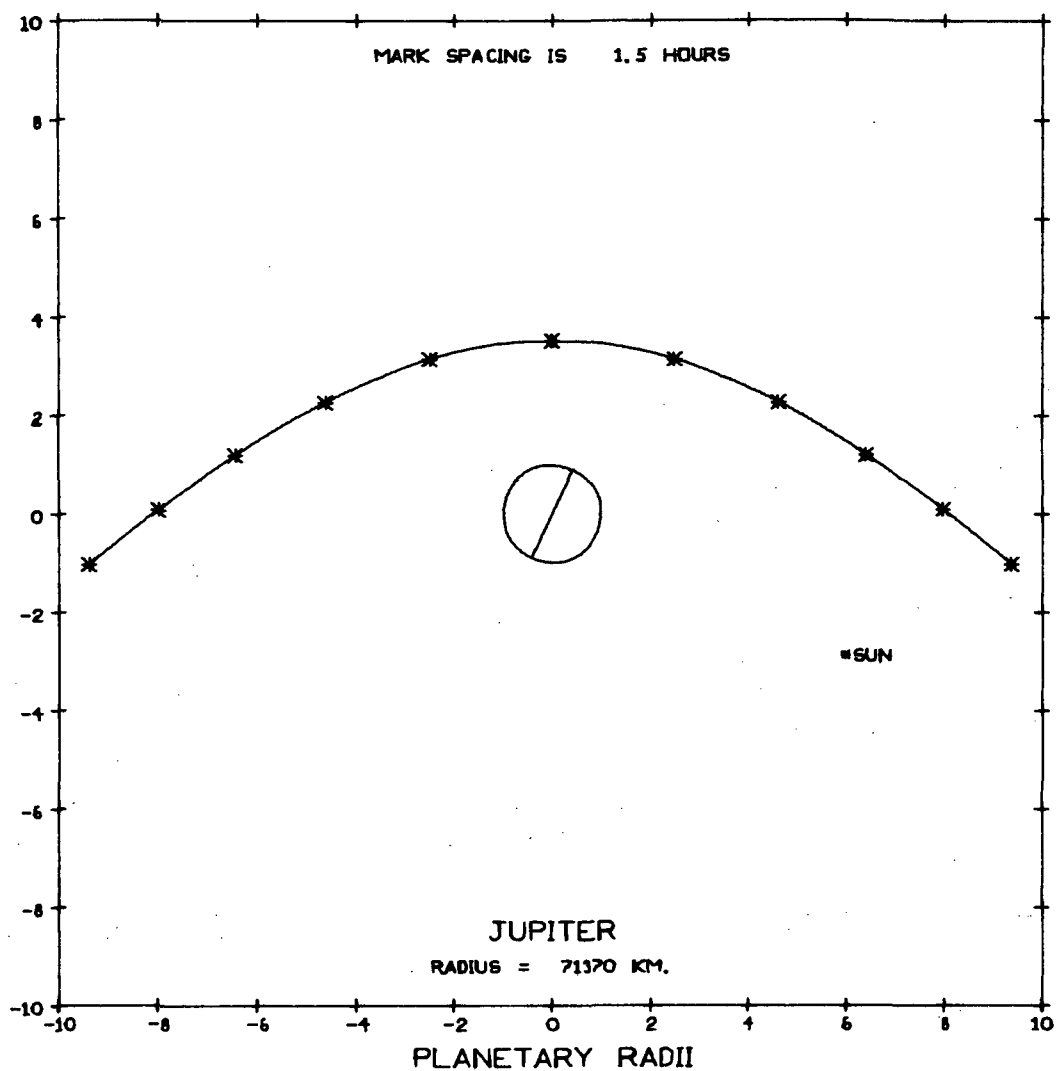


Fig. B4.1b Trajectory Plan View During Jovian Passage on the 1977 Grand Tour; 20 Radii Field

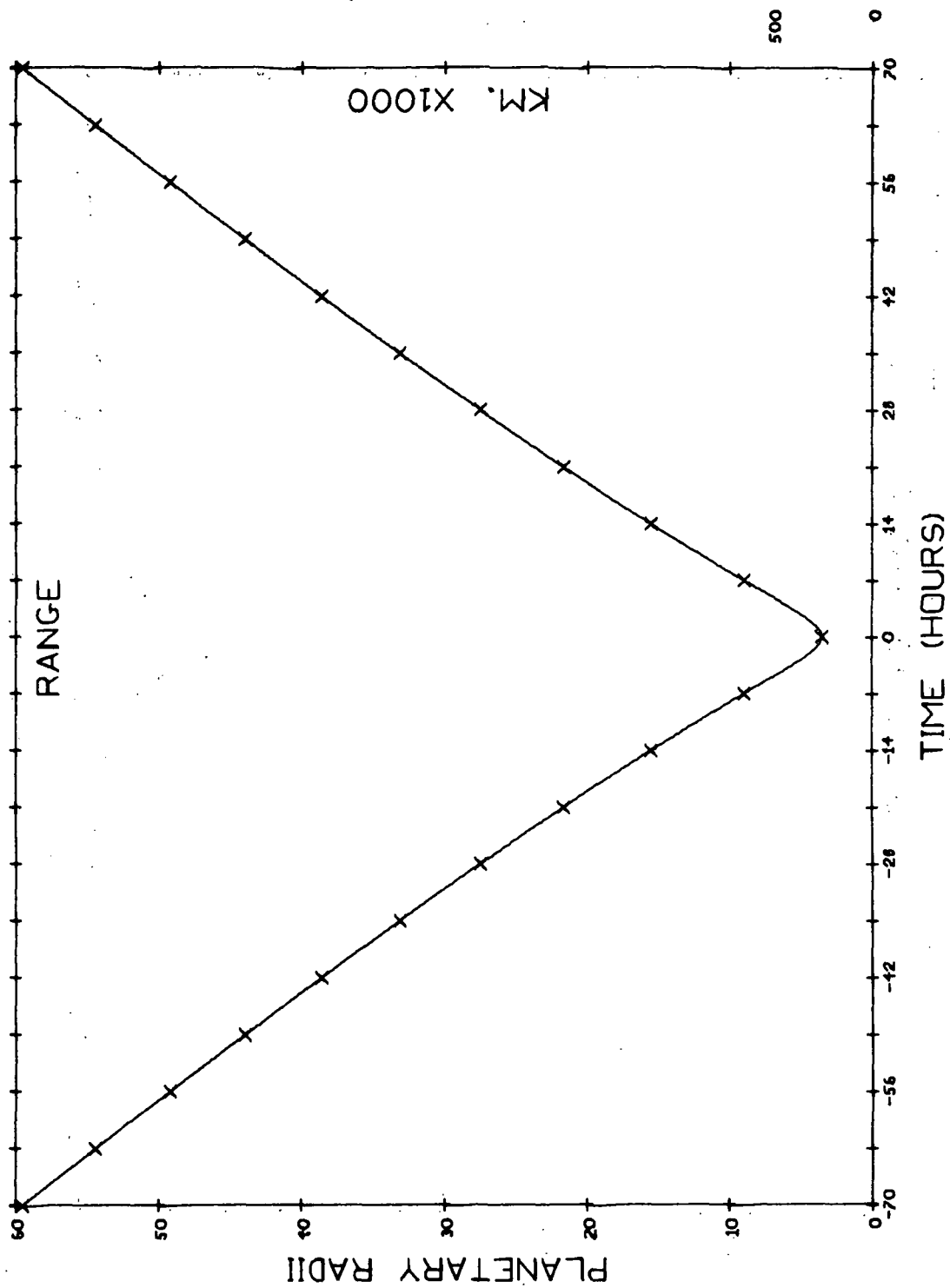


Fig. B4.2 Range to Planet During Jovian Passage on the 1977 Grand Tour

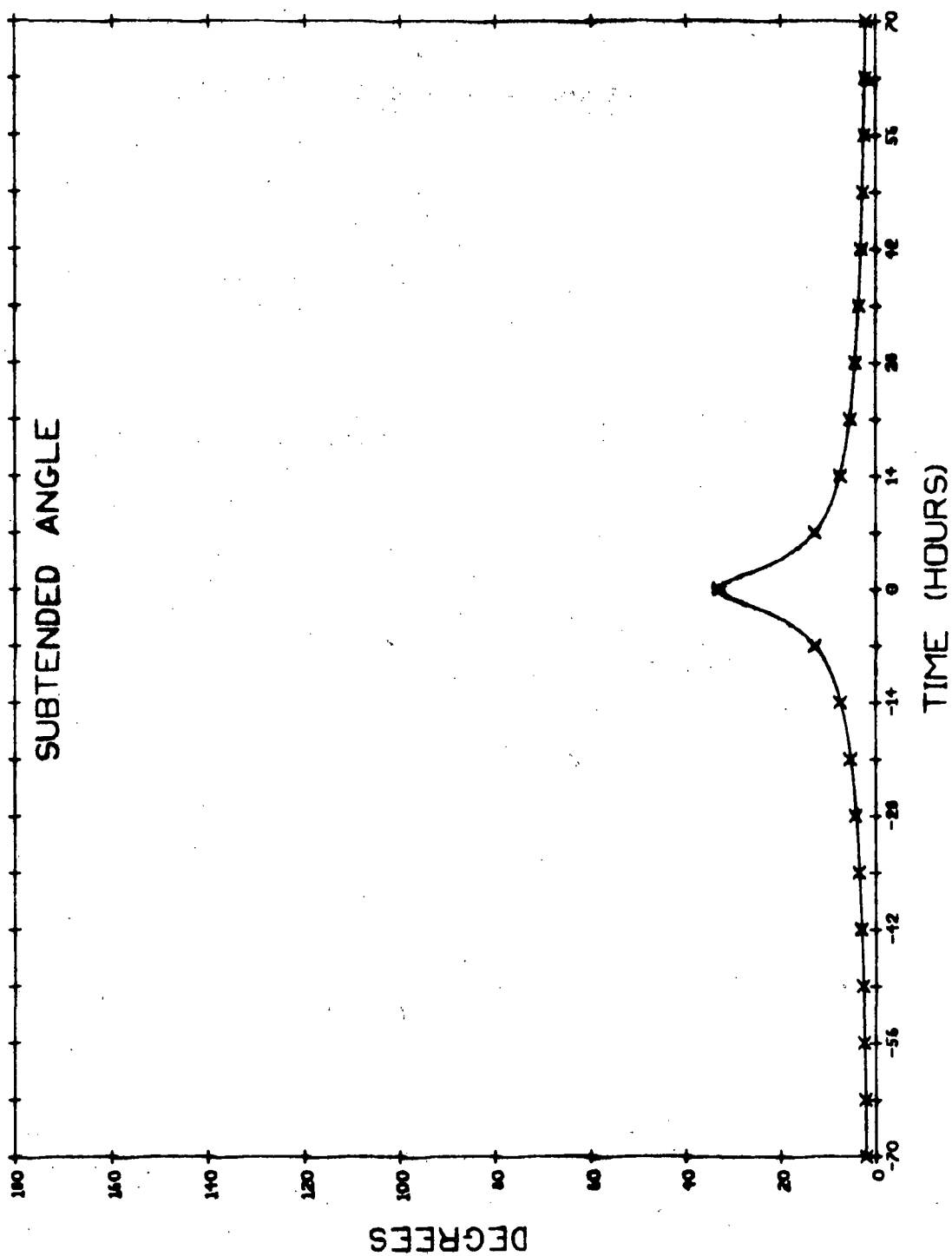


Fig. B4.3 Angle Subtended by Planetary Limbs During Jovian Passage on the 1977 Grand Tour

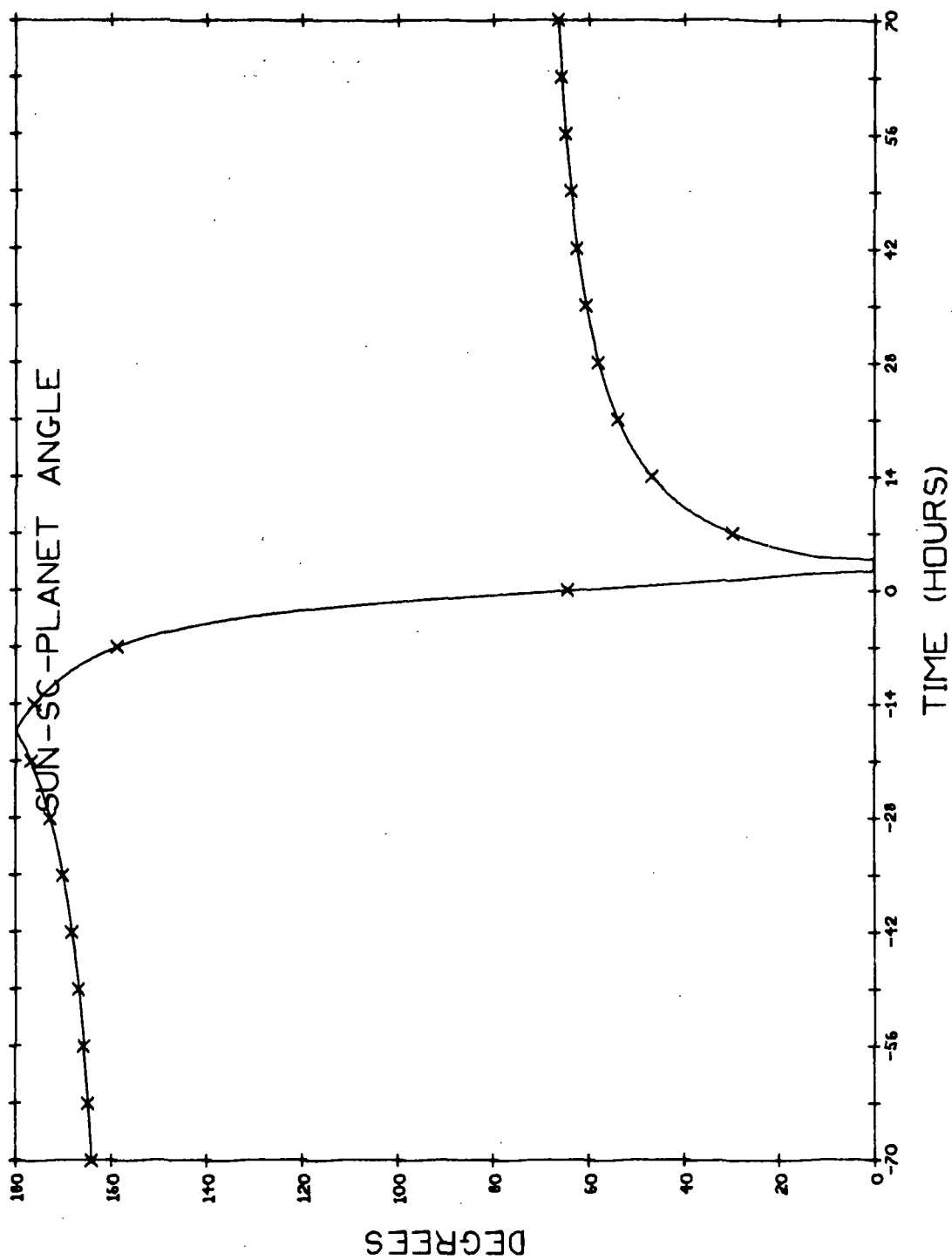


Fig. B4. 4a Sun-SC-Planet Angle During Jovian Passage on the 1977 Grand Tour, 140 Hour Frame

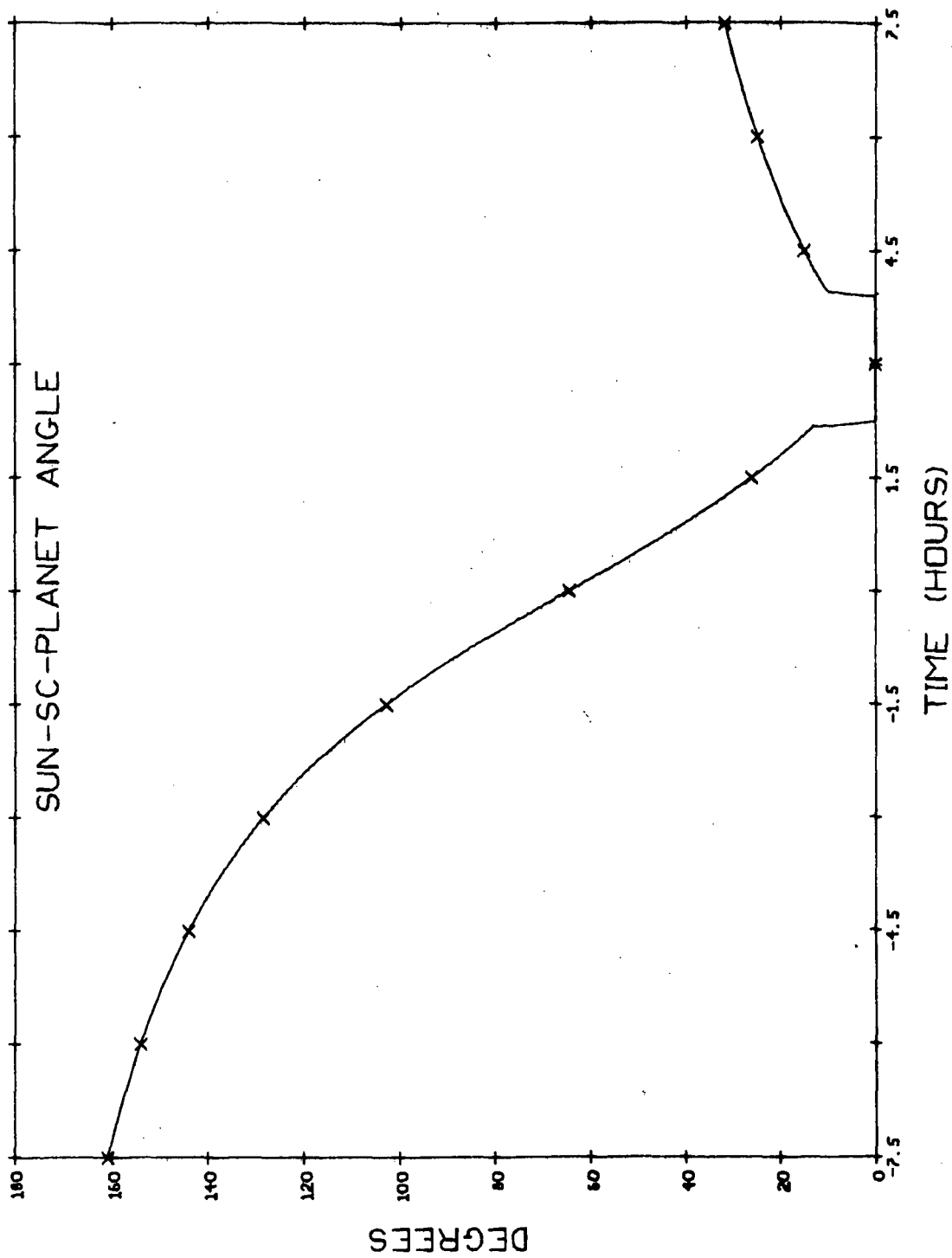


Fig. B4. 4b Sun-SC-Planet Angle During Jovian Passage on the 1977 Grand Tour. 15 Hour Frame

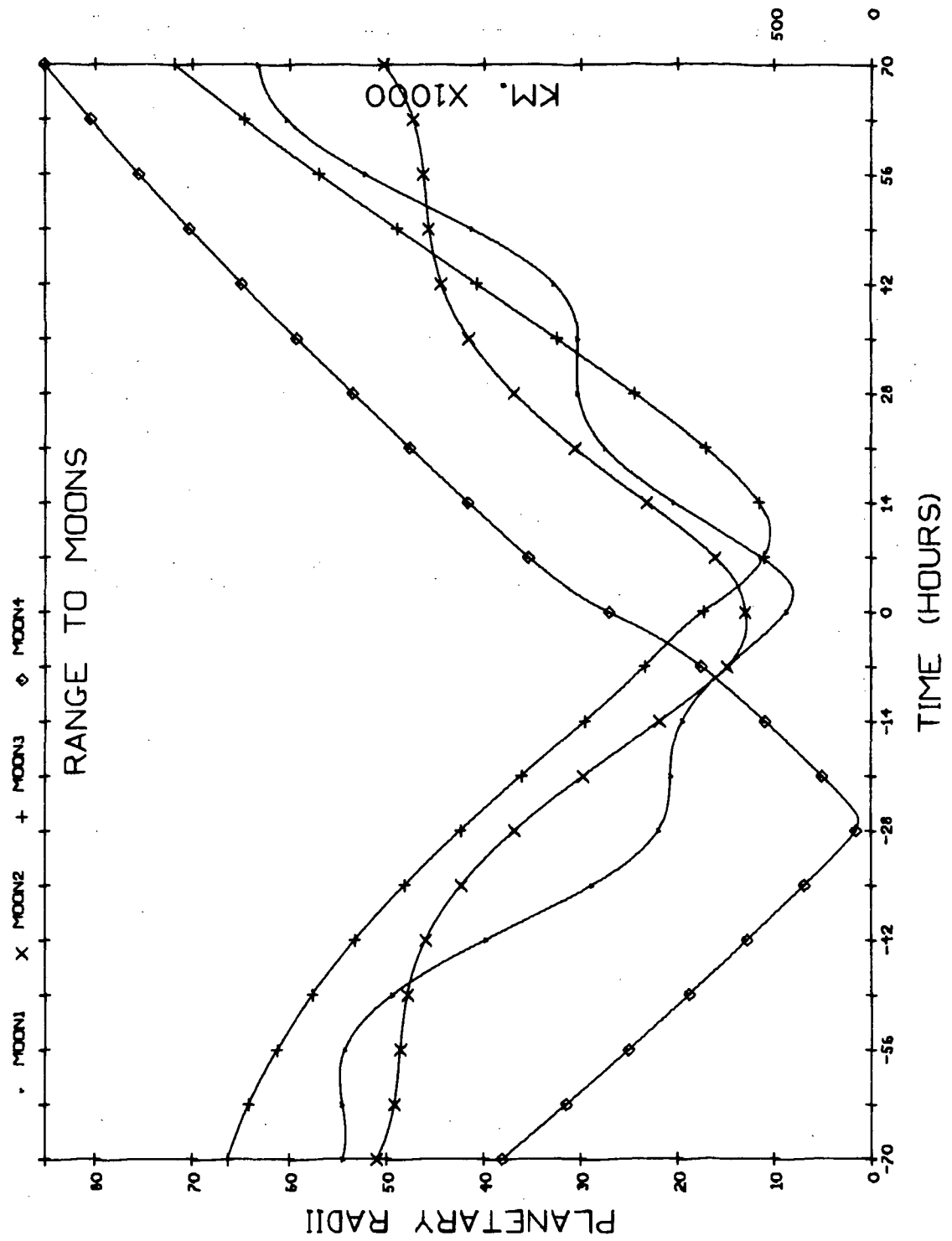


Fig. B4.5 Range to Principle Moons During Jovian Passage on the 1977 Grand Tour

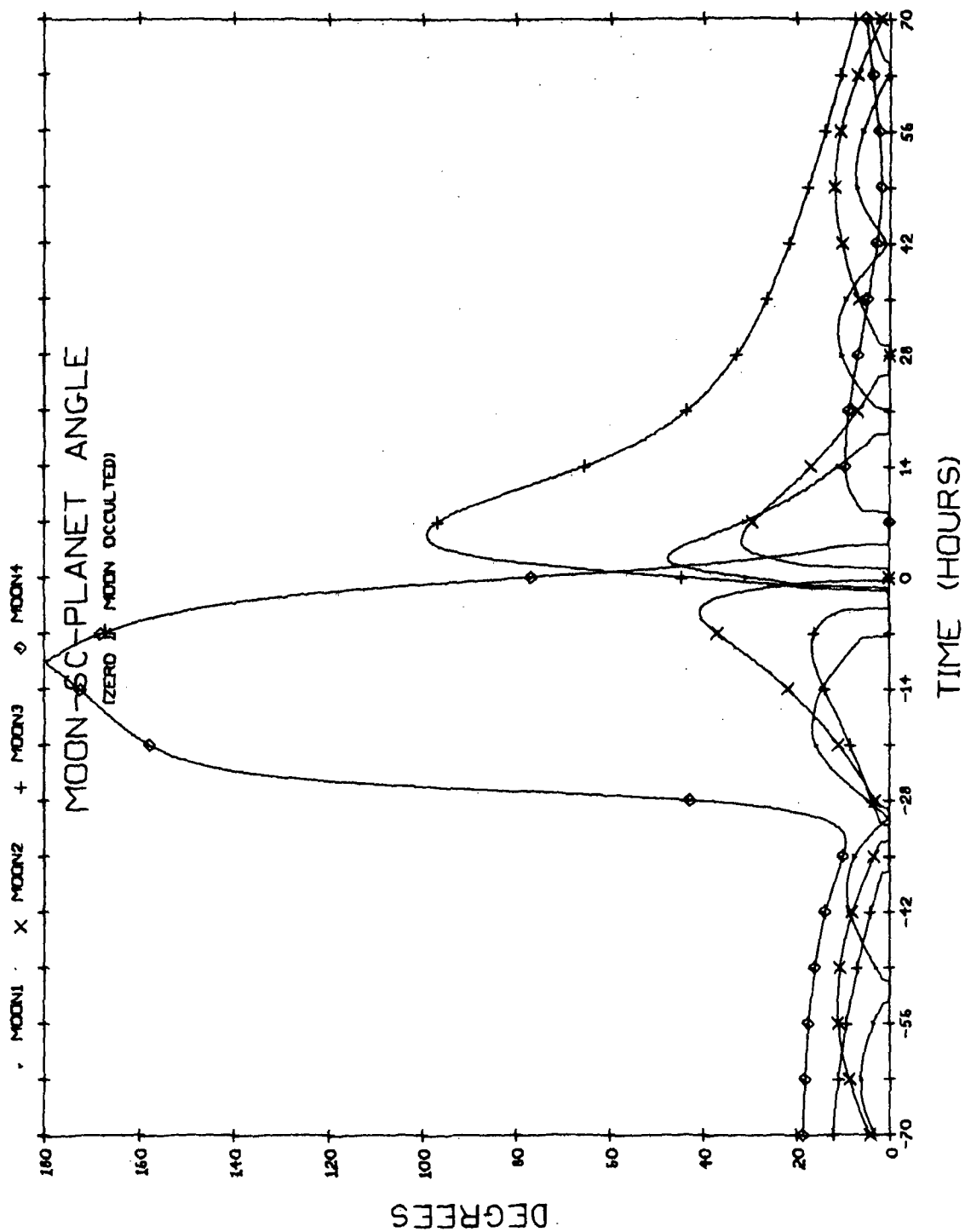


Fig. B4.6a Moon-SC-Planet Angle During Jovian Passage on the 1977 Grand Tour; 140 Hour Frame

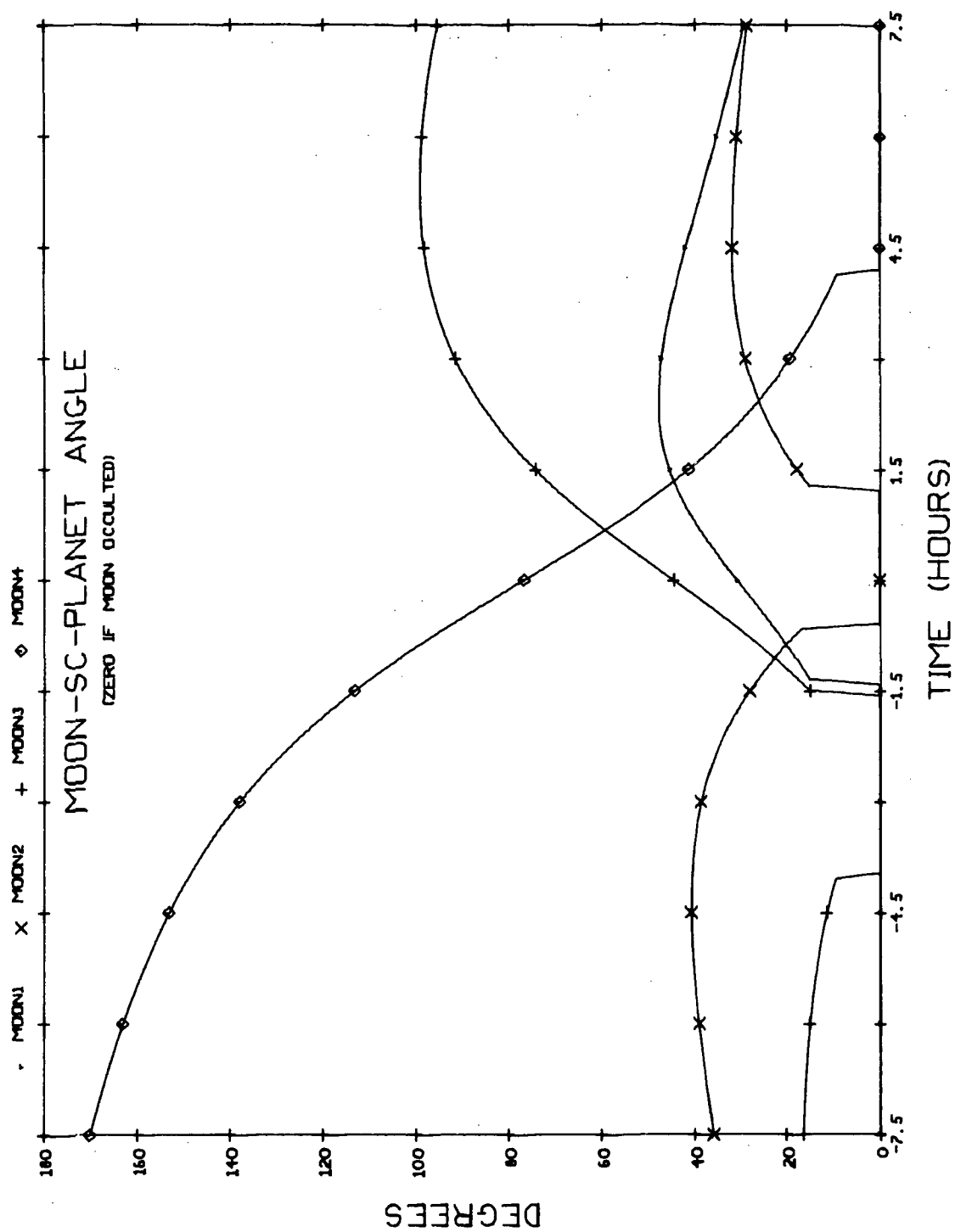


Fig. B4.6b Moon-SC-Planet Angle During Jovian Passage on the 1977 Grand Tour; 15 Hour Frame

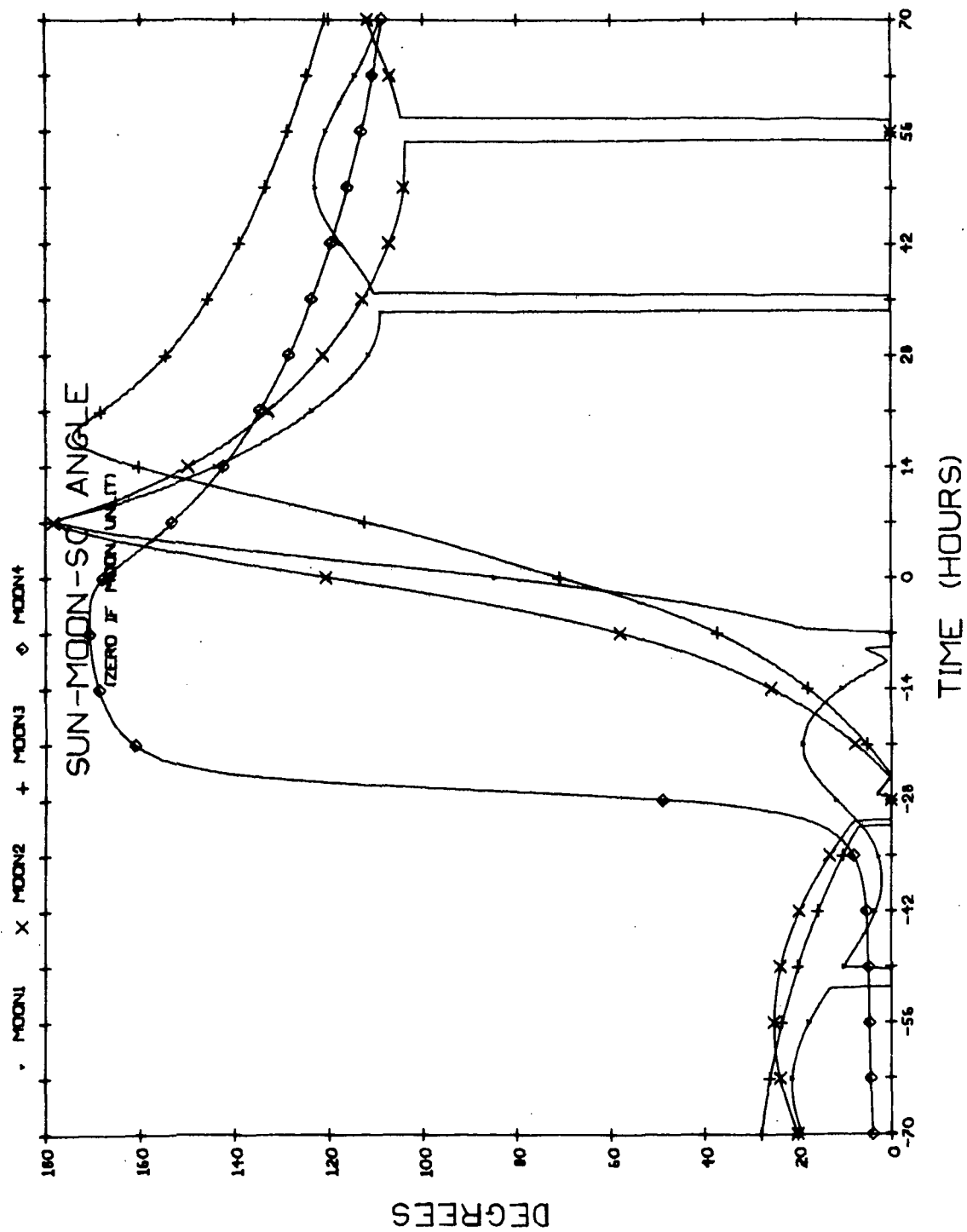


Fig. B4.7 Sun-Moon-SC Angle During Jovian Passage on the 1977 Grand Tour

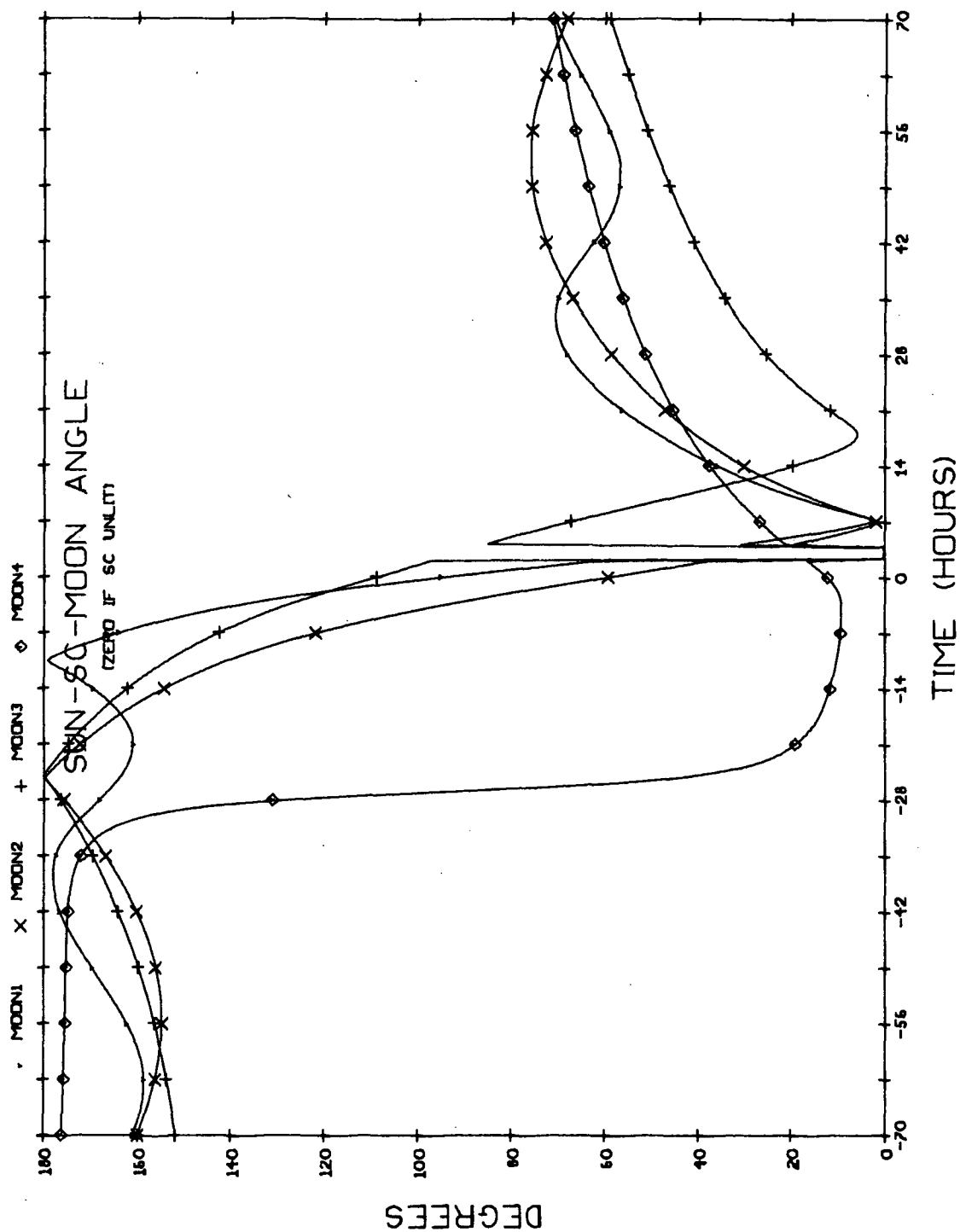


Fig. B4.8 Sun-SC-Moon Angle During Jovian Passage on the 1977 Grand Tour

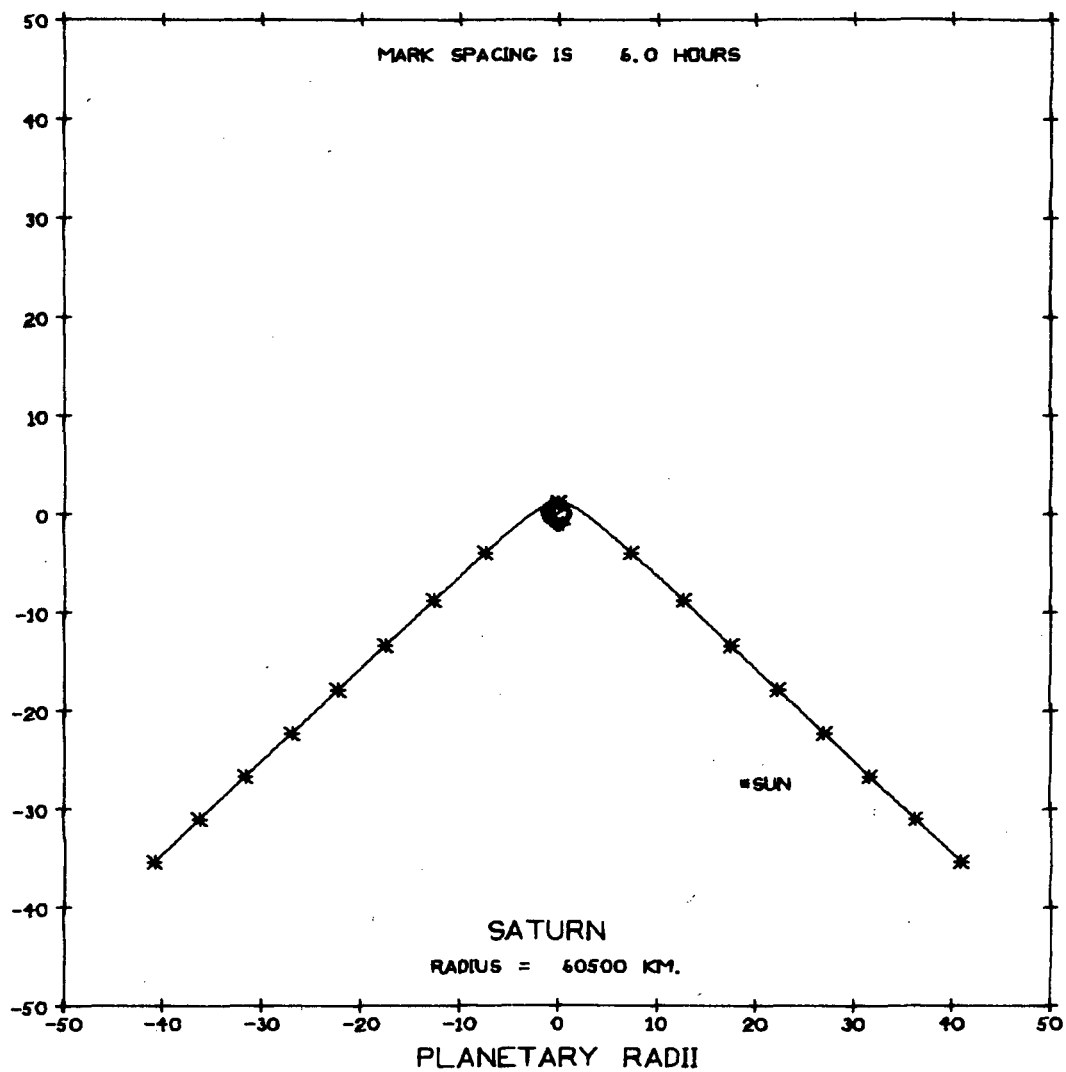


Fig. B5.1a Trajectory Plan View During Saturn Flyby on 1977 Grant Tour; 100 Radii Field

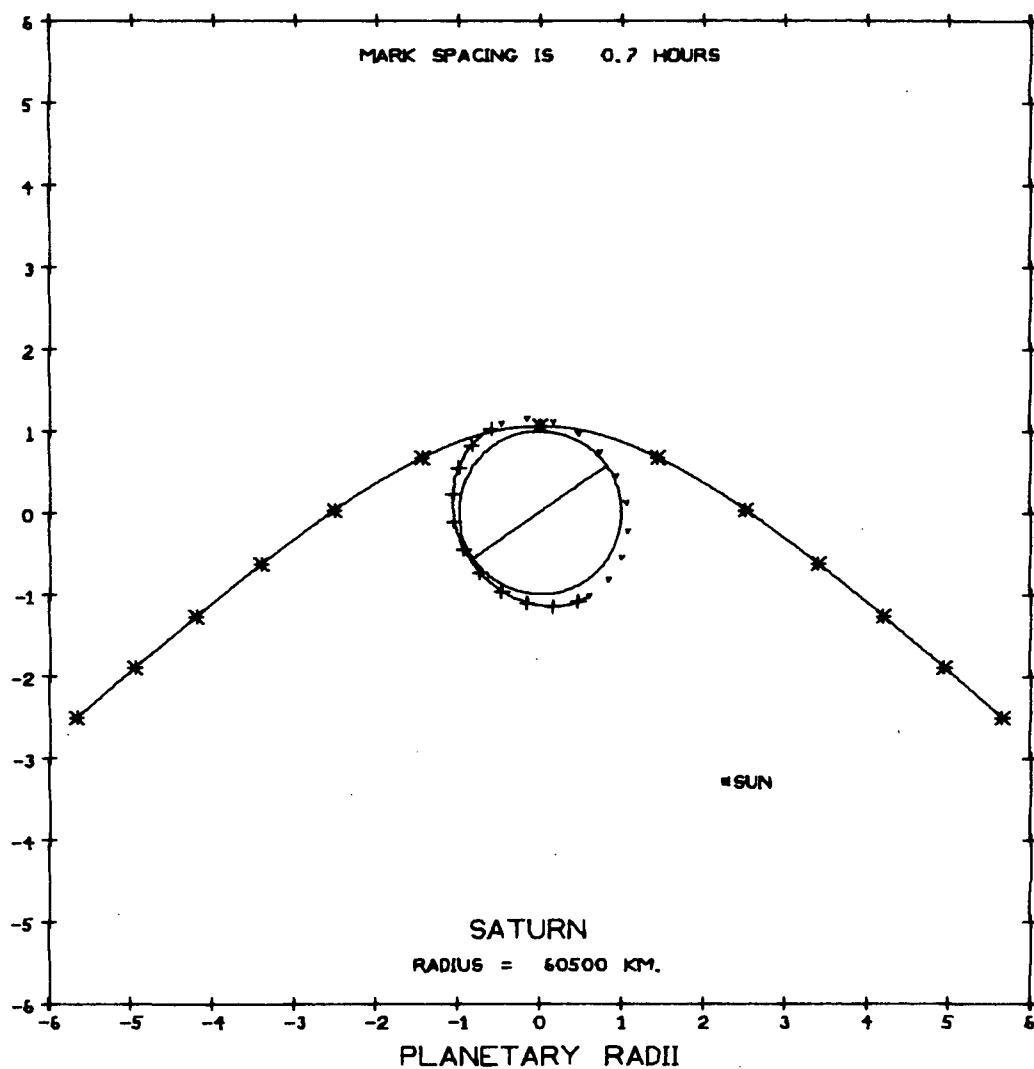


Fig. B5.1b Trajectory Plan View During Saturn Flyby on 1977 Grand Tour; 12 Radii Field

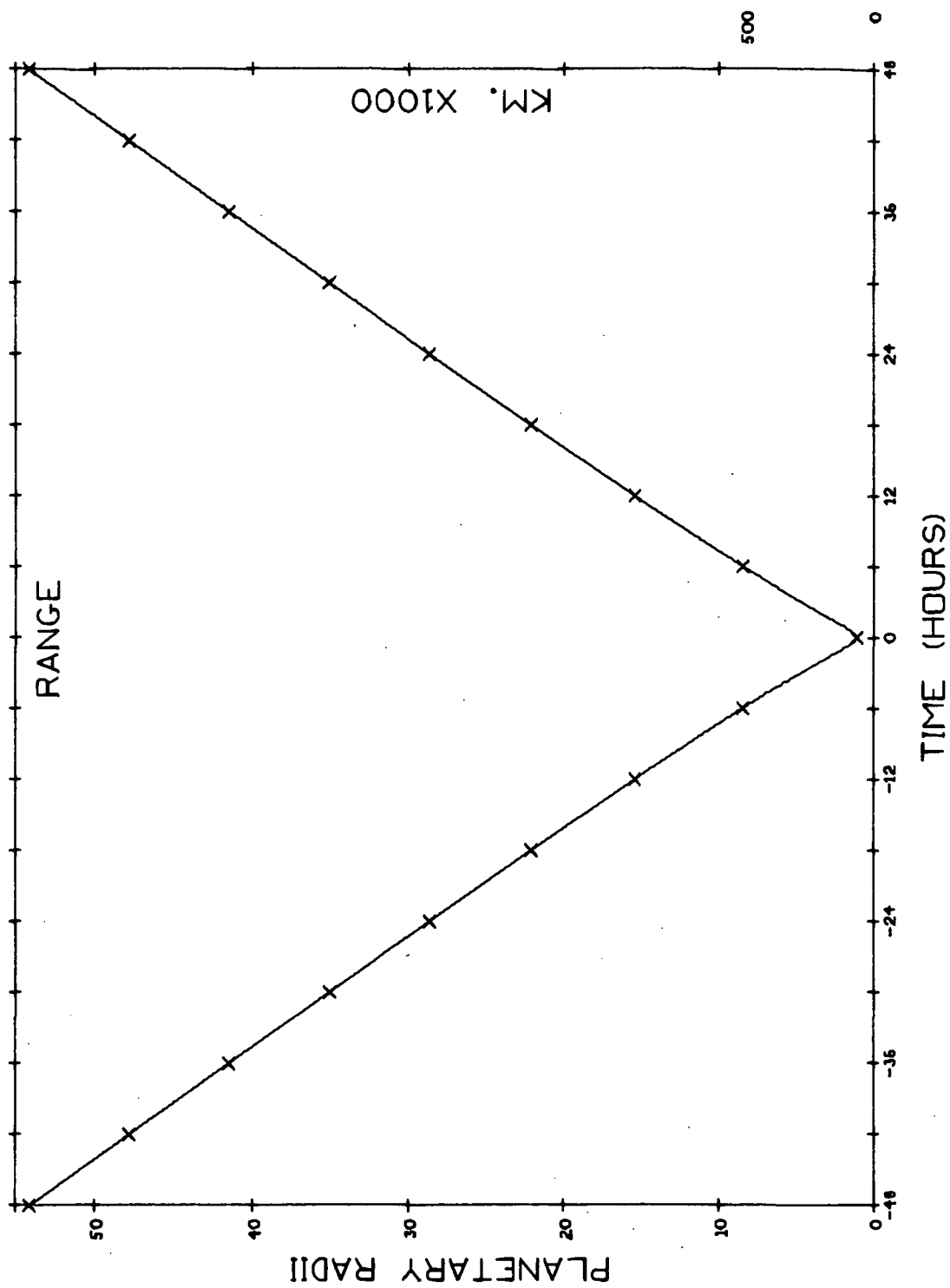


Fig. B5. 2. Range to Planet During Saturn Flyby on 1977 Grand Tour

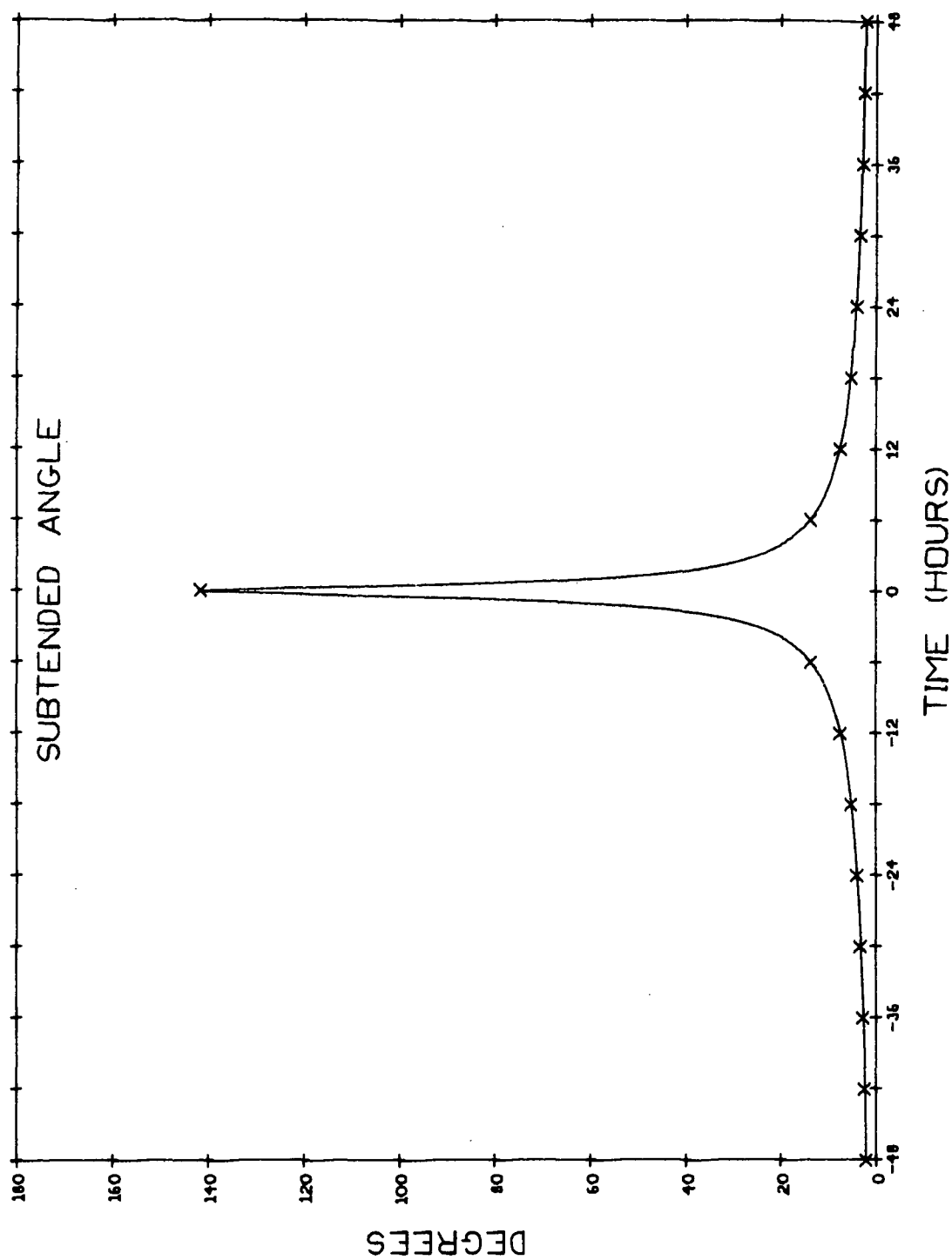


Fig. B5.3 Angle Subtended by Planetary Limbs During Saturn Flyby on 1977 Grand Tour

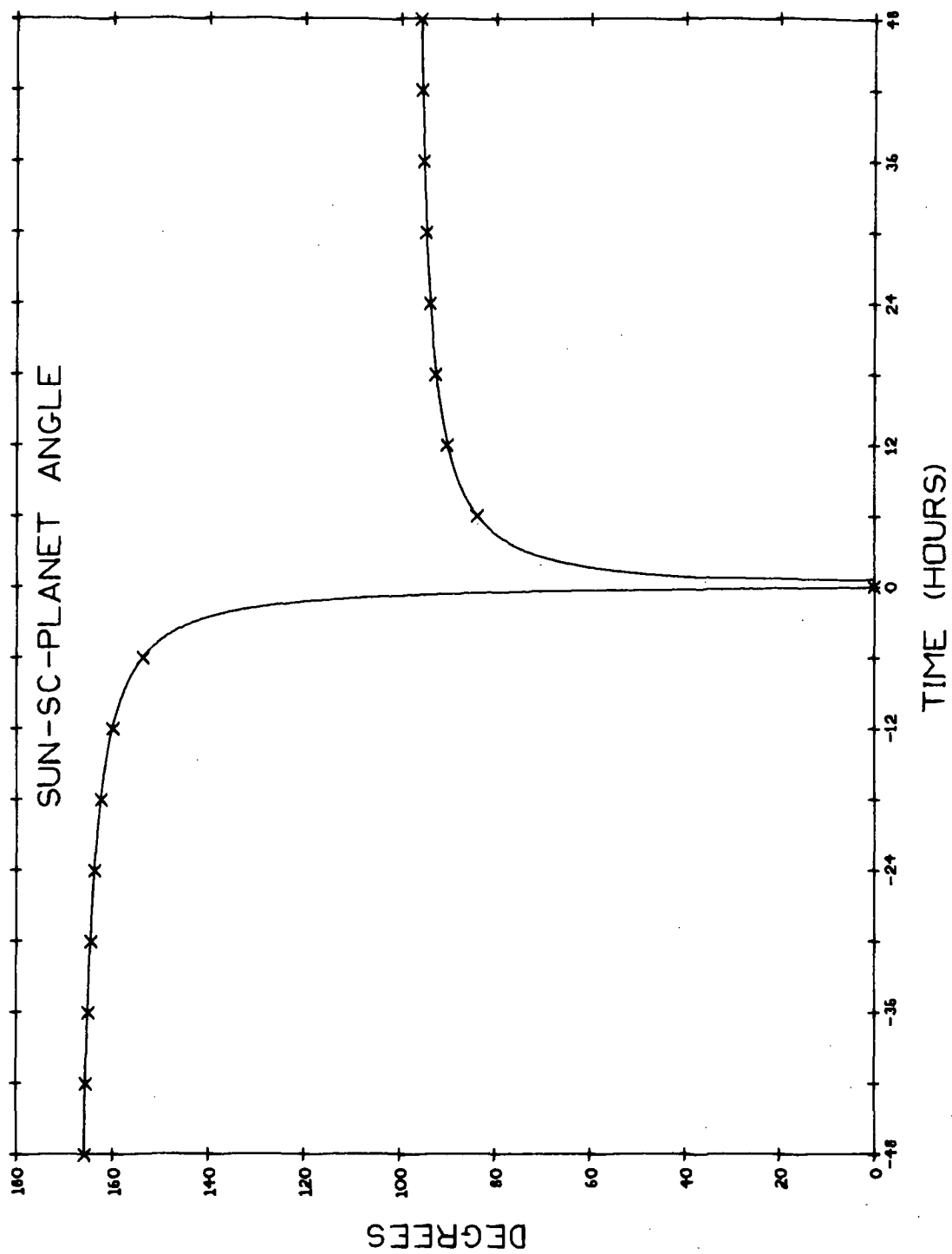


Fig. B5.4a Sun-SC-Planet Angle During Saturn Flyby on 1977 Grand Tour; 96 Hour Frame

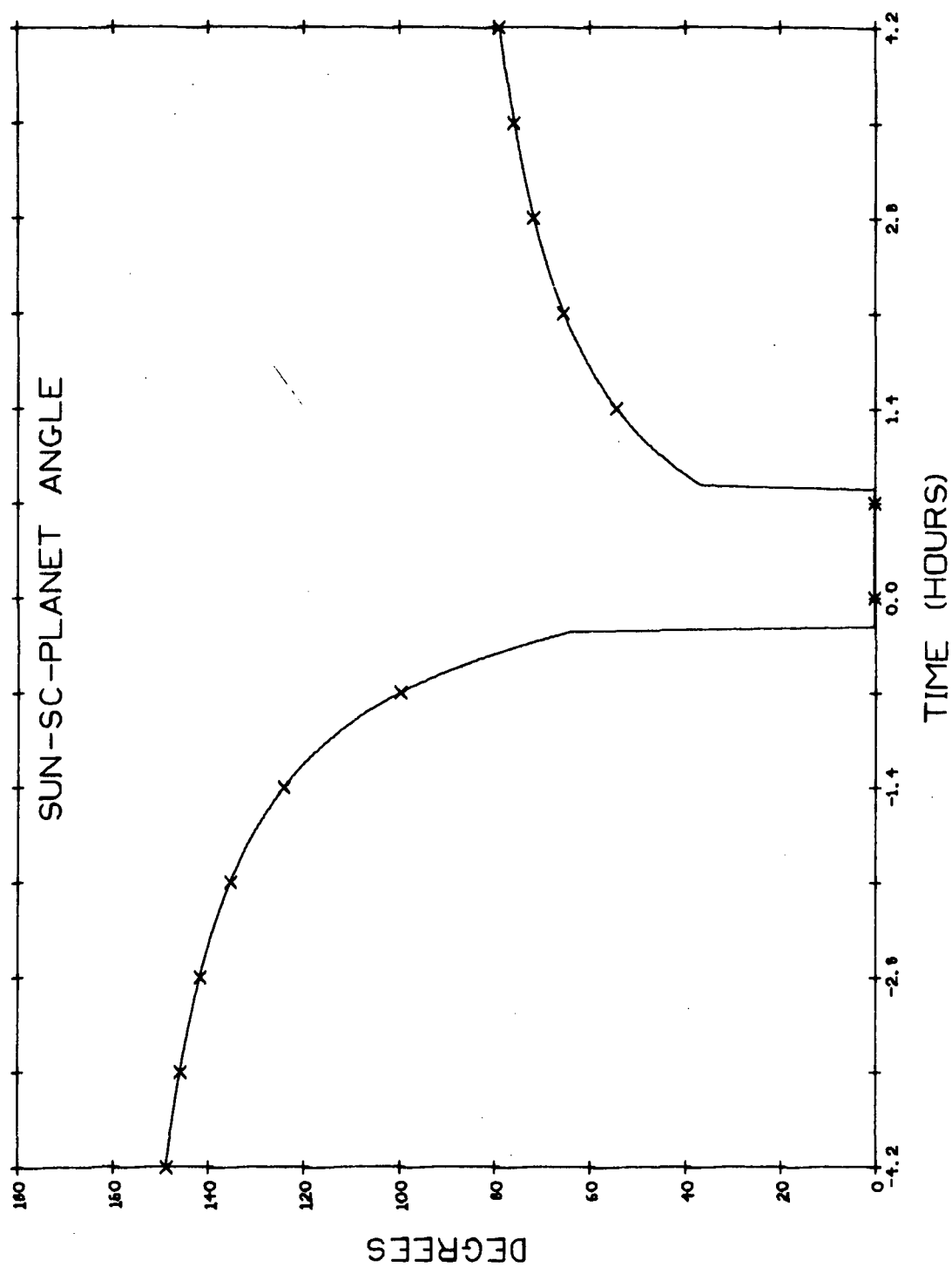


Fig. B5. 4b Sun-SC-Planet Angle During Saturn Flyby on 1977 Grand Tour; 8.4 Hour Frame

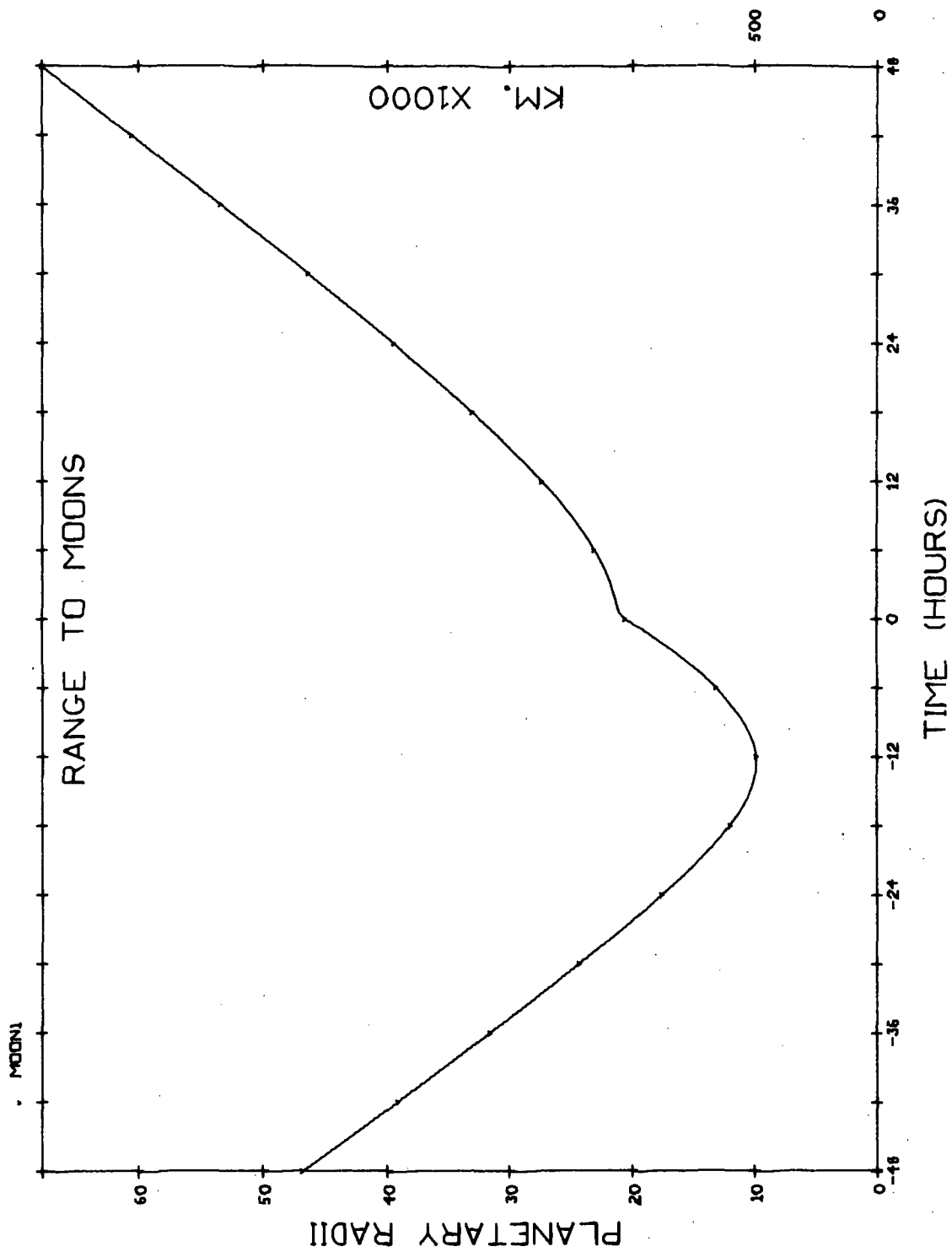


Fig. B5.5 Range to Titan During Saturn Flyby on 1977 Grand Tour

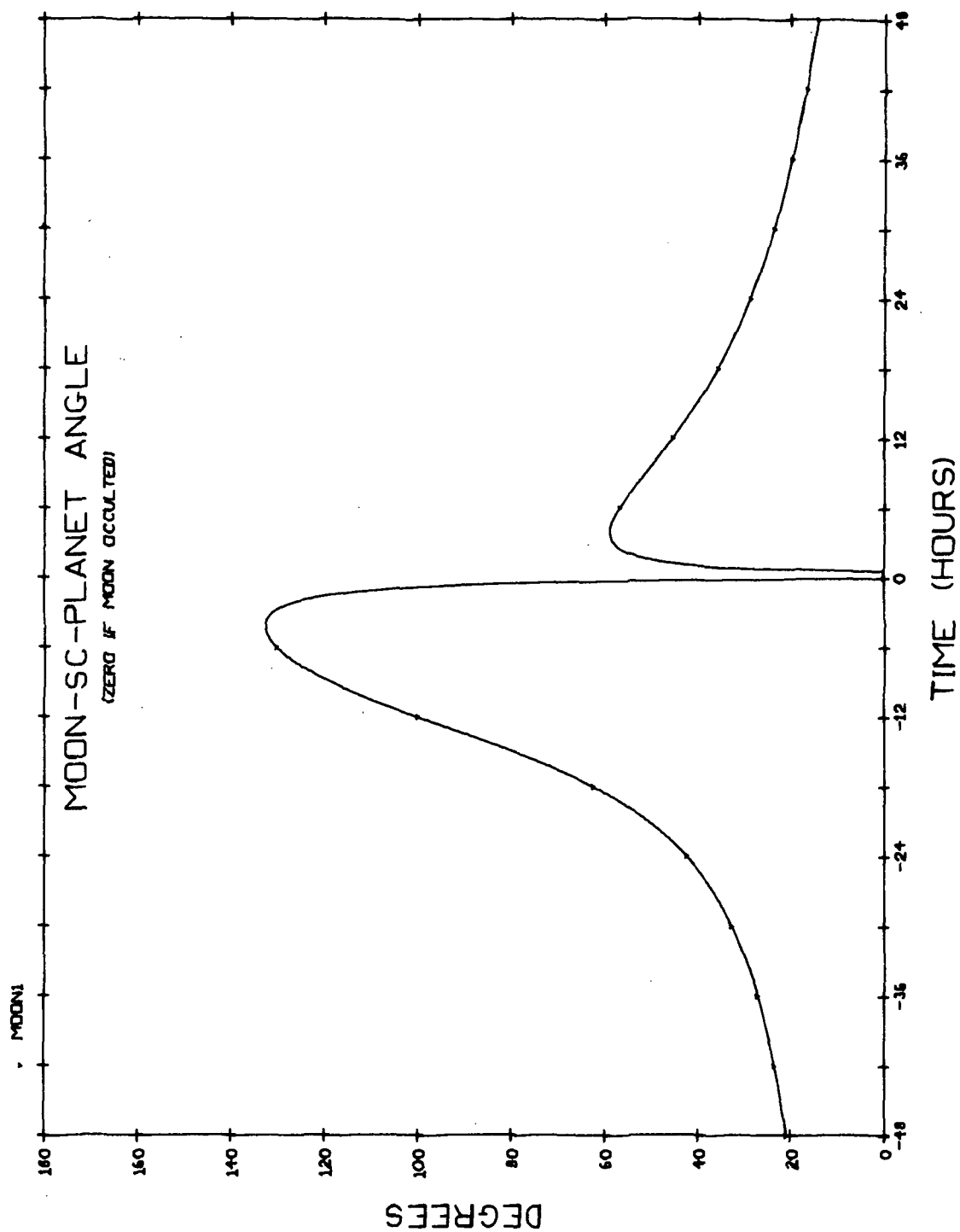


Fig. B5.6 Titan-SC-Planet Angle During Saturn Flyby on 1977 Grand Tour

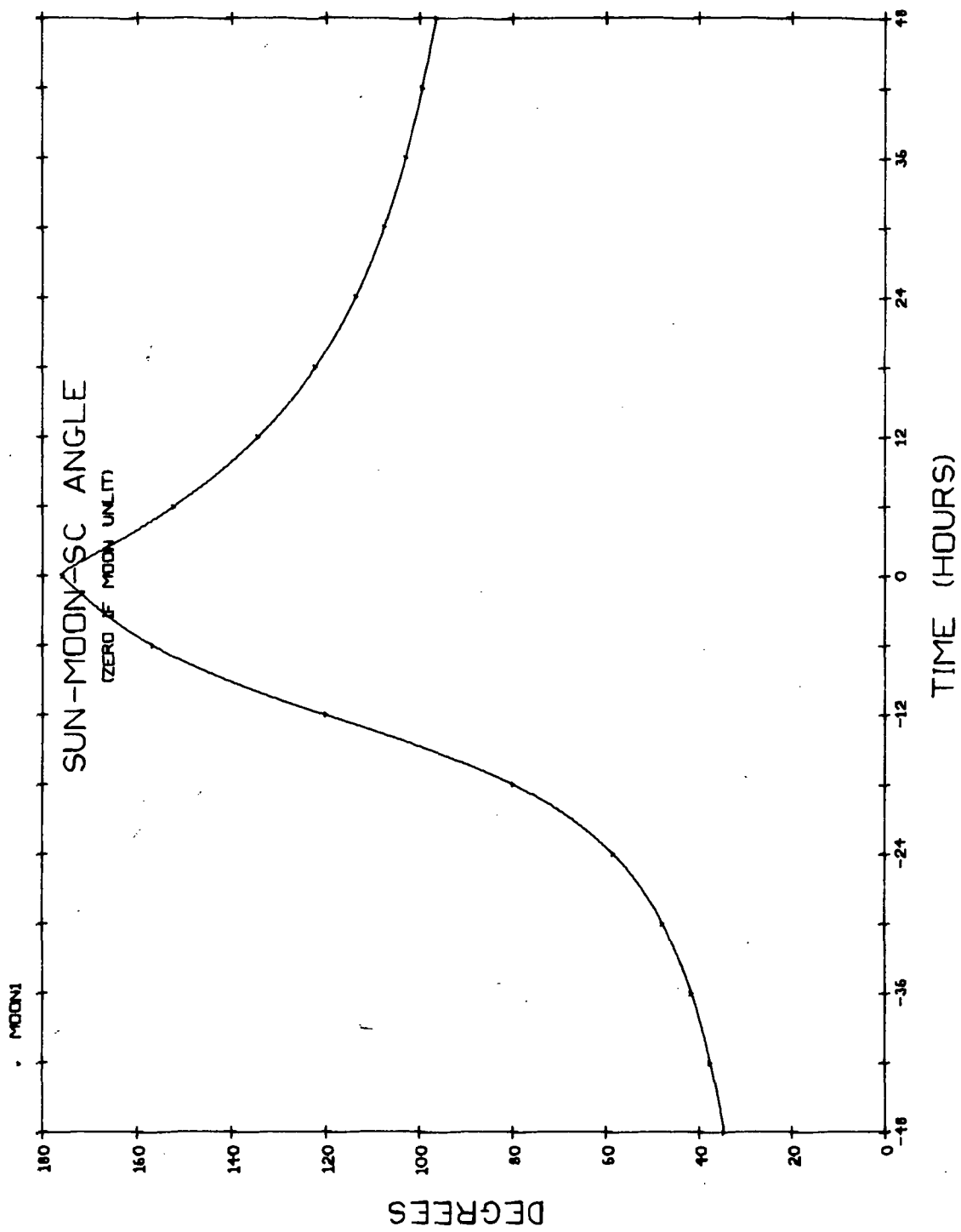


Fig. B5.7 Sun-Titan-SC Angle During Saturn Flyby on 1977 Grand Tour

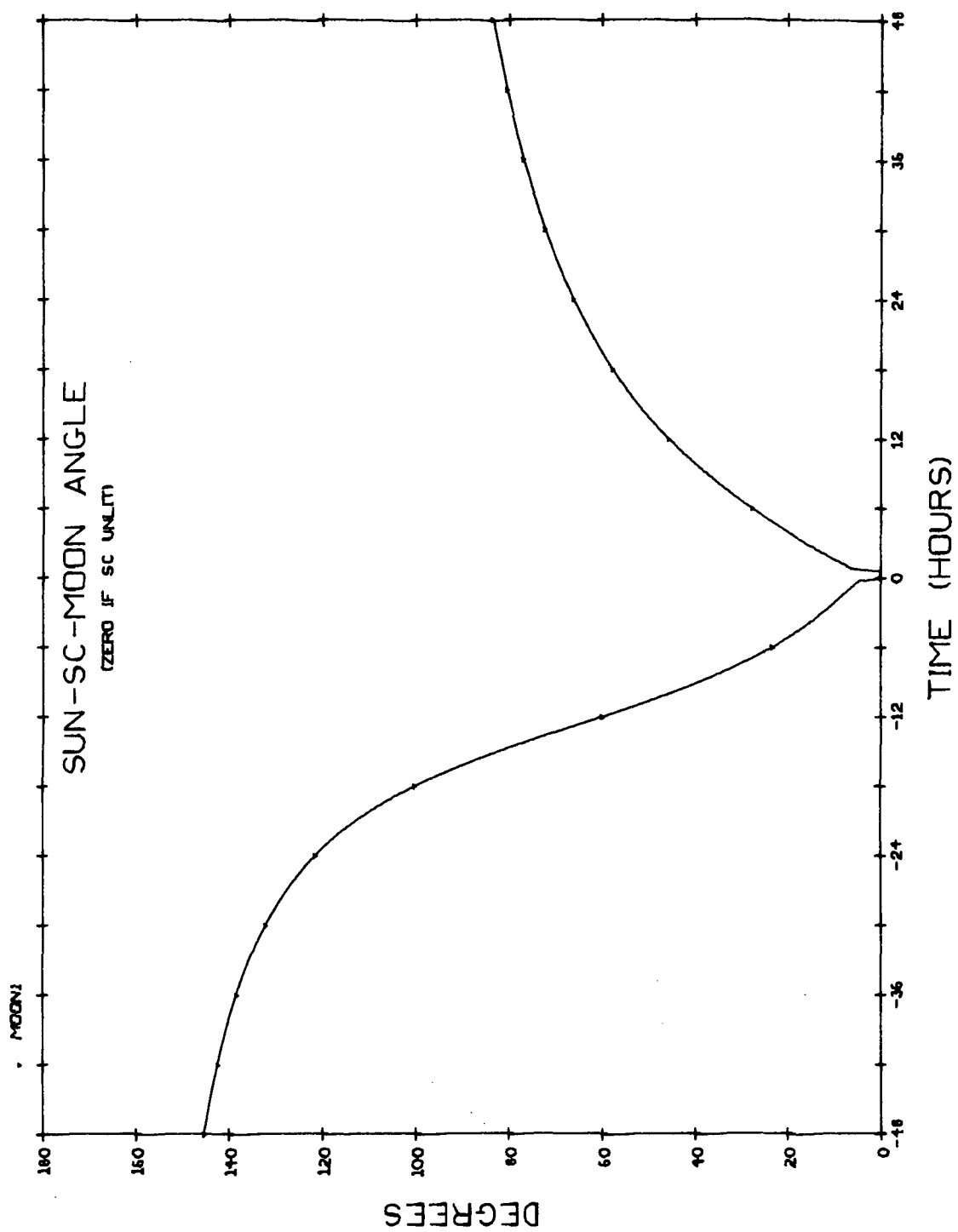


Fig. B5.8 Sun-SC-Titan Angle During Saturn Flyby on 1977 Grand Tour

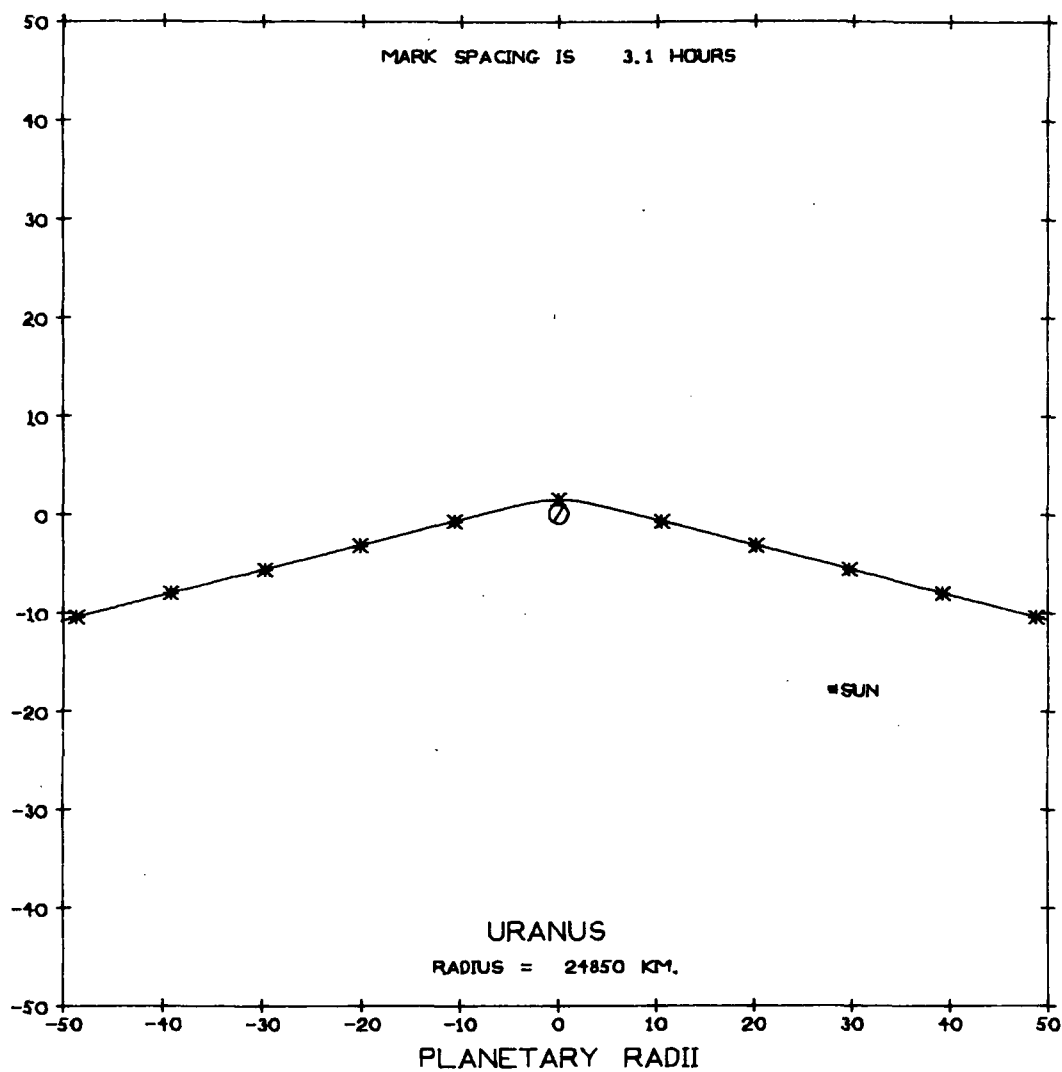


Fig. B6.1a Trajectory Plan View During Uranus Passage on the 1977 Grand Tour; 100 Radii Field

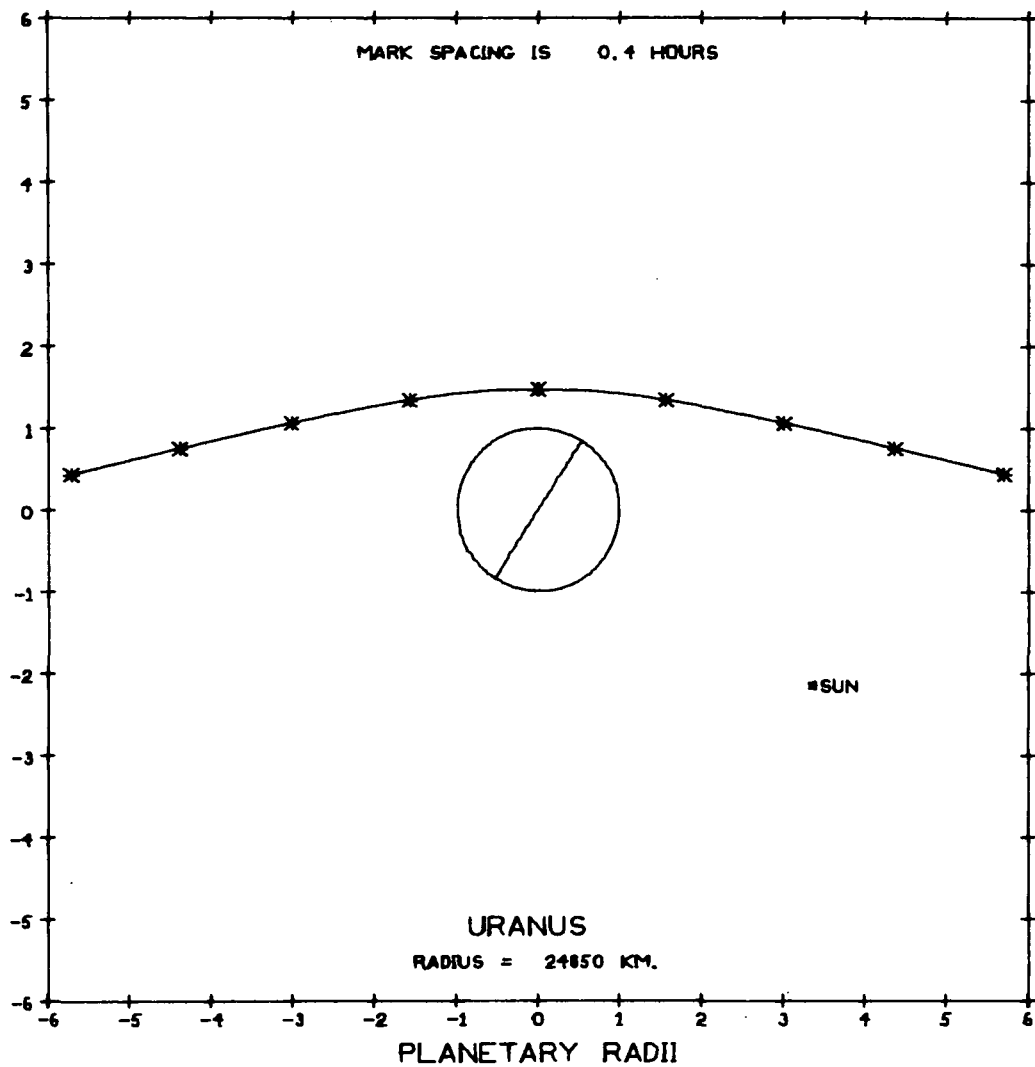


Fig. B6.1b Trajectory Plan View During Uranus Passage on the 1977 Grand Tour; 12 Radii Field

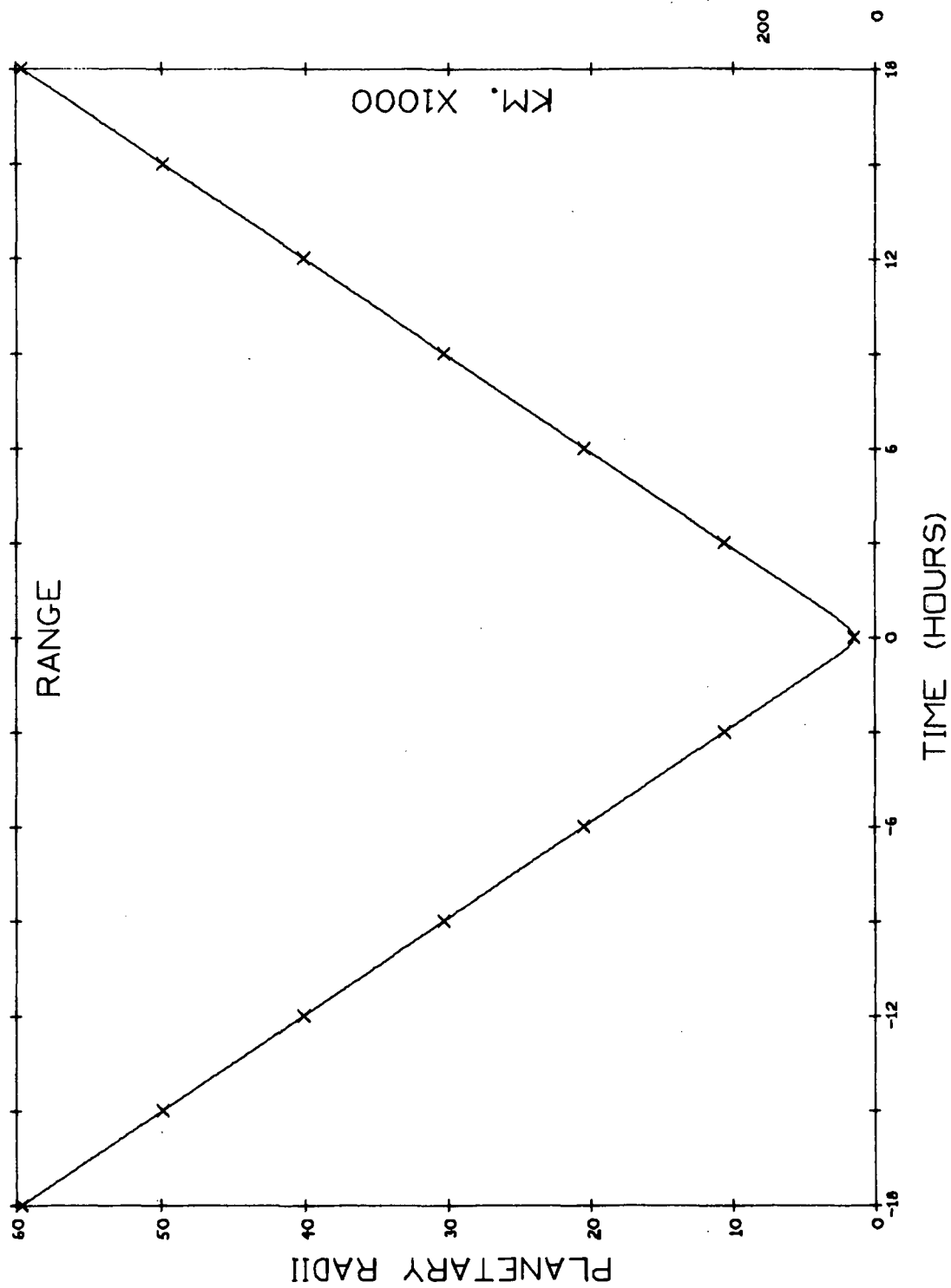


Fig. B6.2 Range to Planet During Uranus Passage on the 1977 Grand Tour

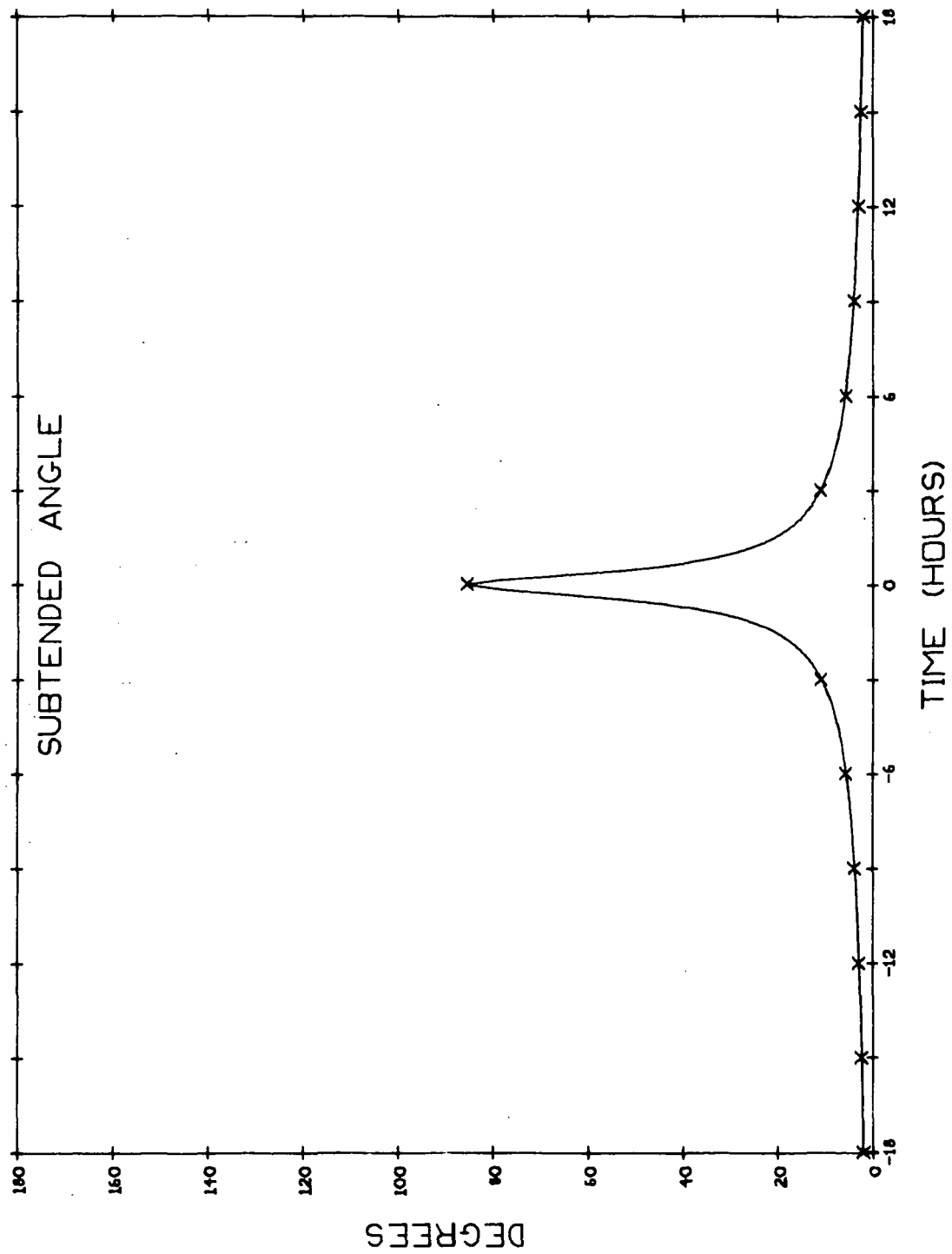


Fig. B6. 3 Angle Subtended by Planetary Limbs During Uranus Passage on the 1977 Grand Tour

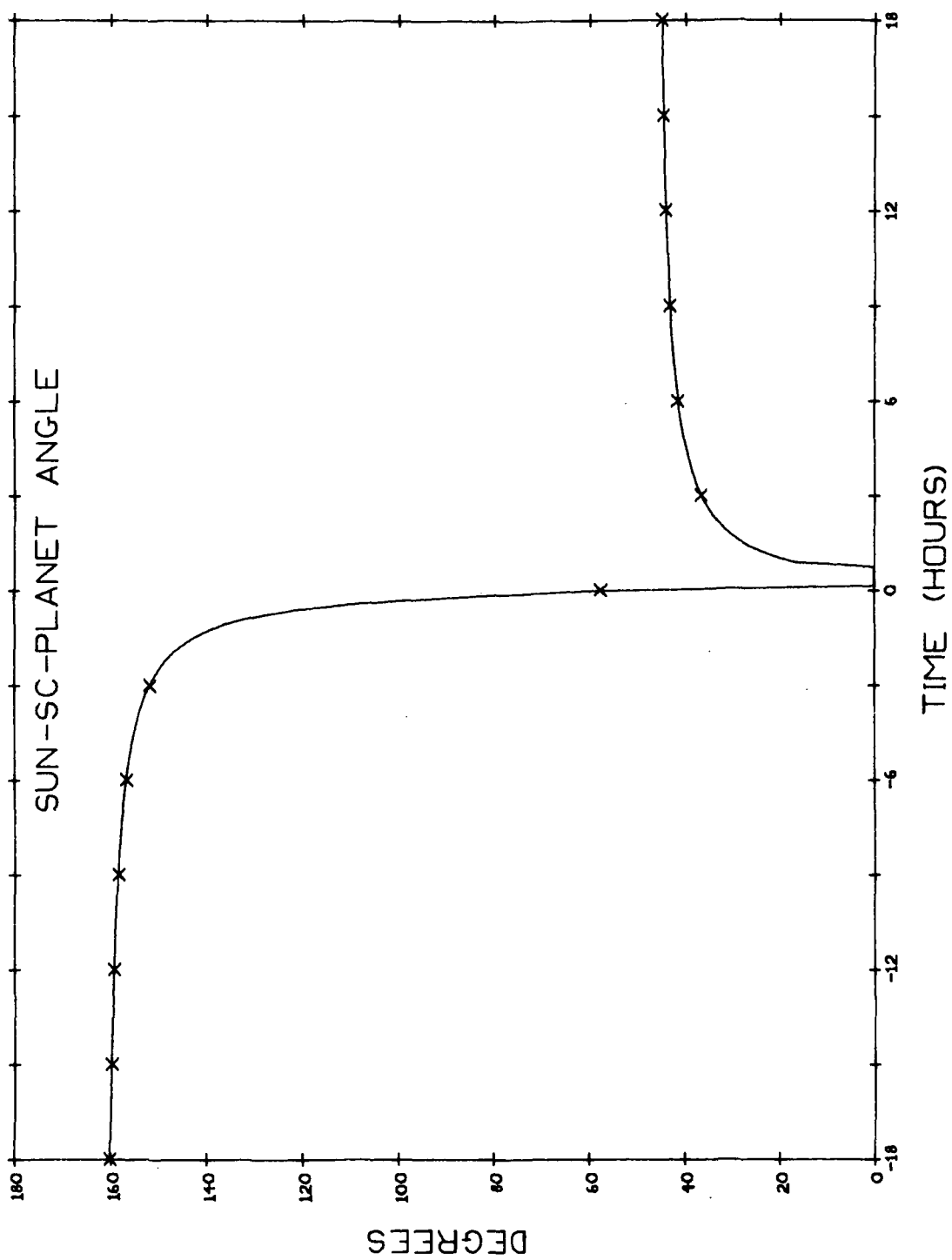


Fig. B6. 4a Sun-SC-Planet Angle During Uranus Passage on the 1977 Grand Tour;
12 Radii Field. 36 Hour Frame

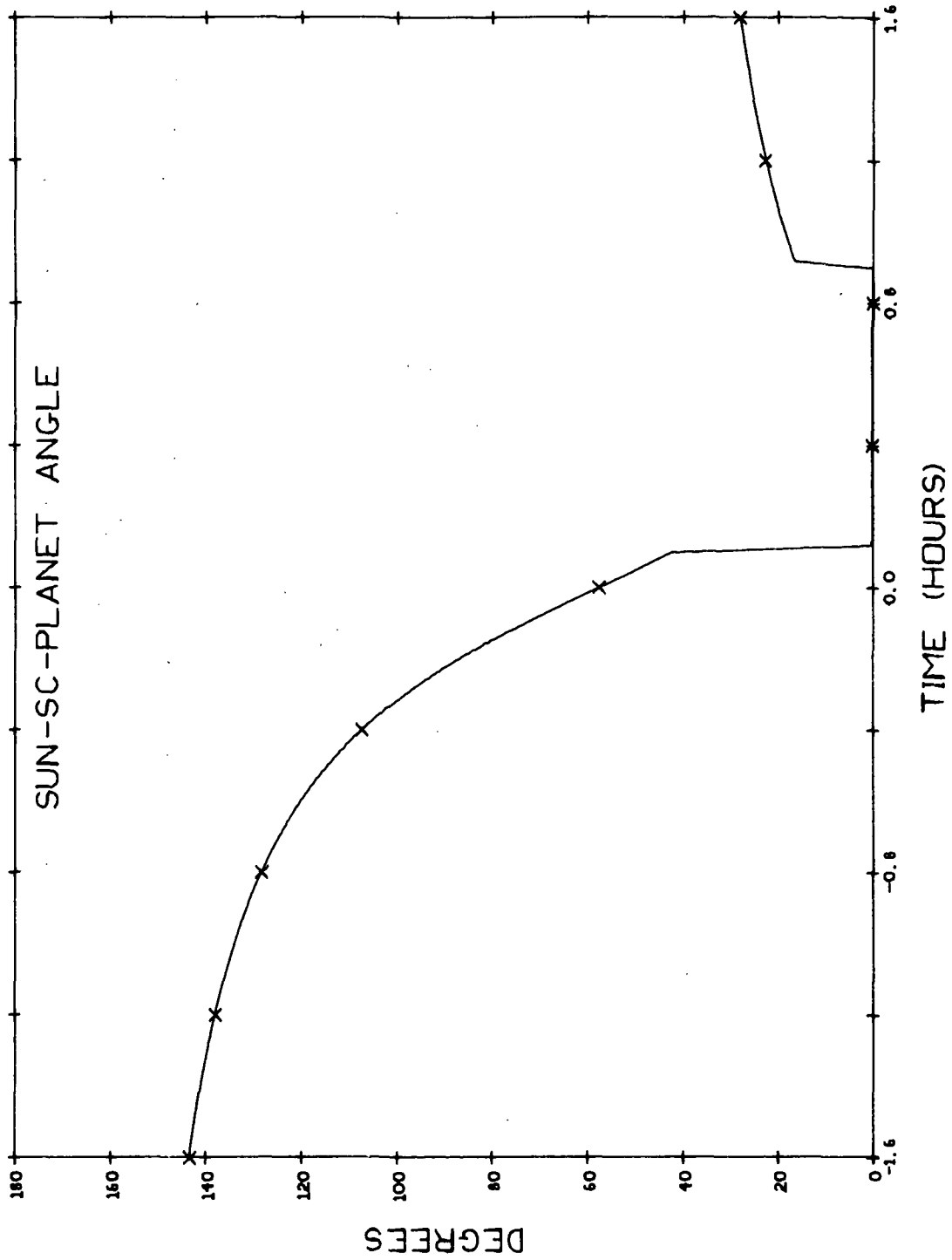


Fig. B6.4b Sun-SC-Planet Angle During Uranus Passage on the 1977 Grand Tour;
3.2 Hour Frame

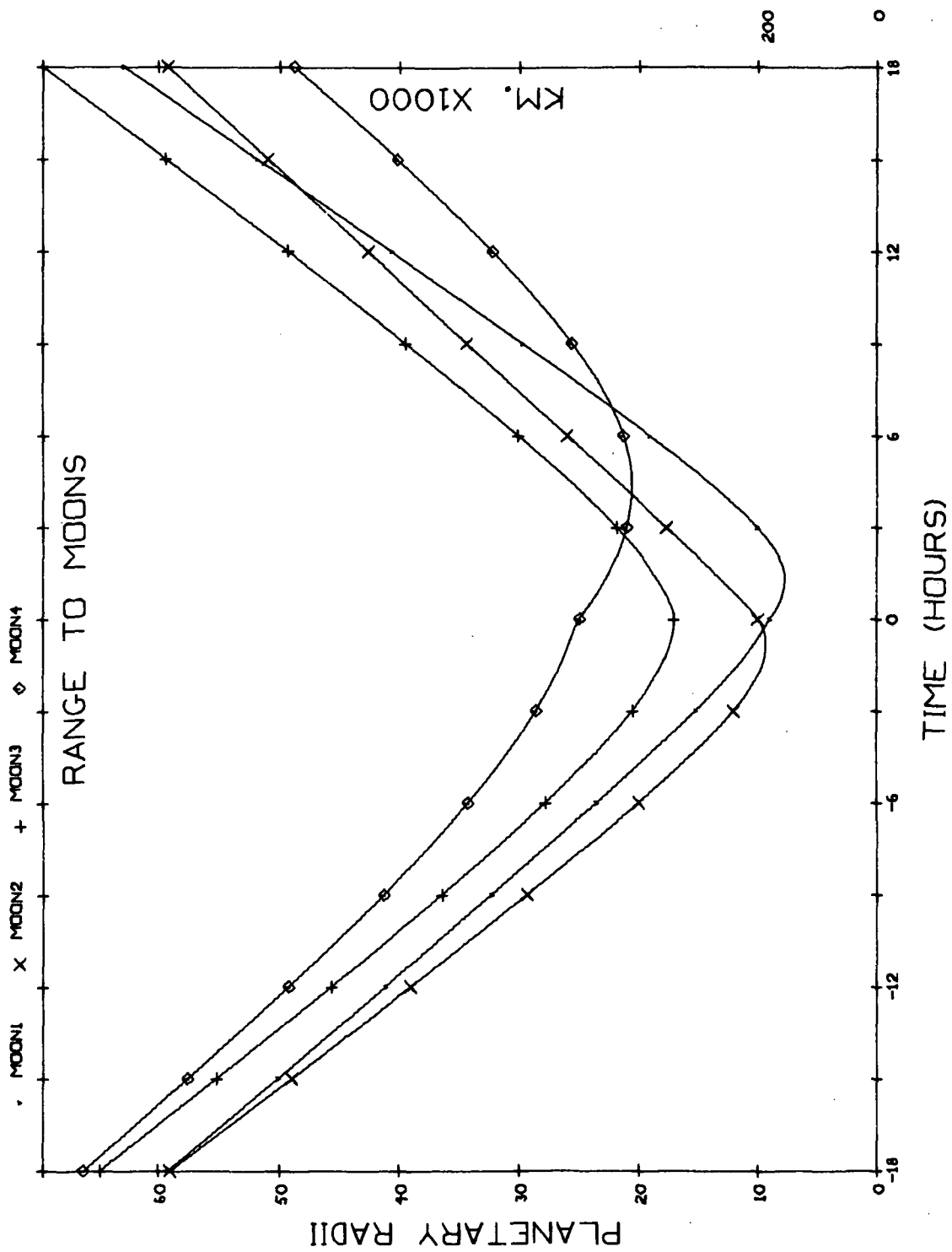


Fig. B6.5 Range to Principle Moons During Uranus Passage on the 1977 Grand Tour

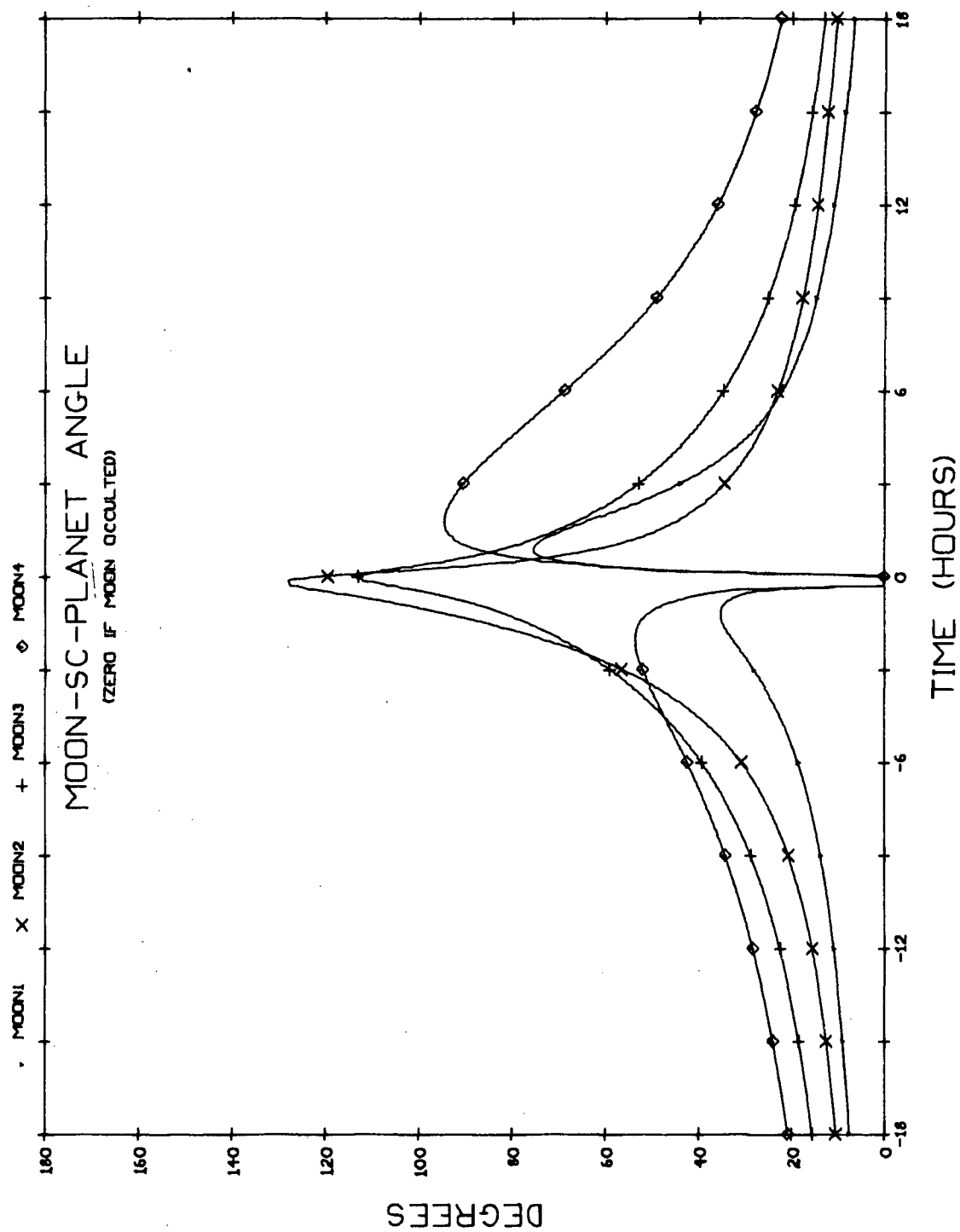


Fig. B6. 6a Moon-SC-Planet Angles During Uranus Passage on the 1977 Grand Tour; 36 Hour Frame

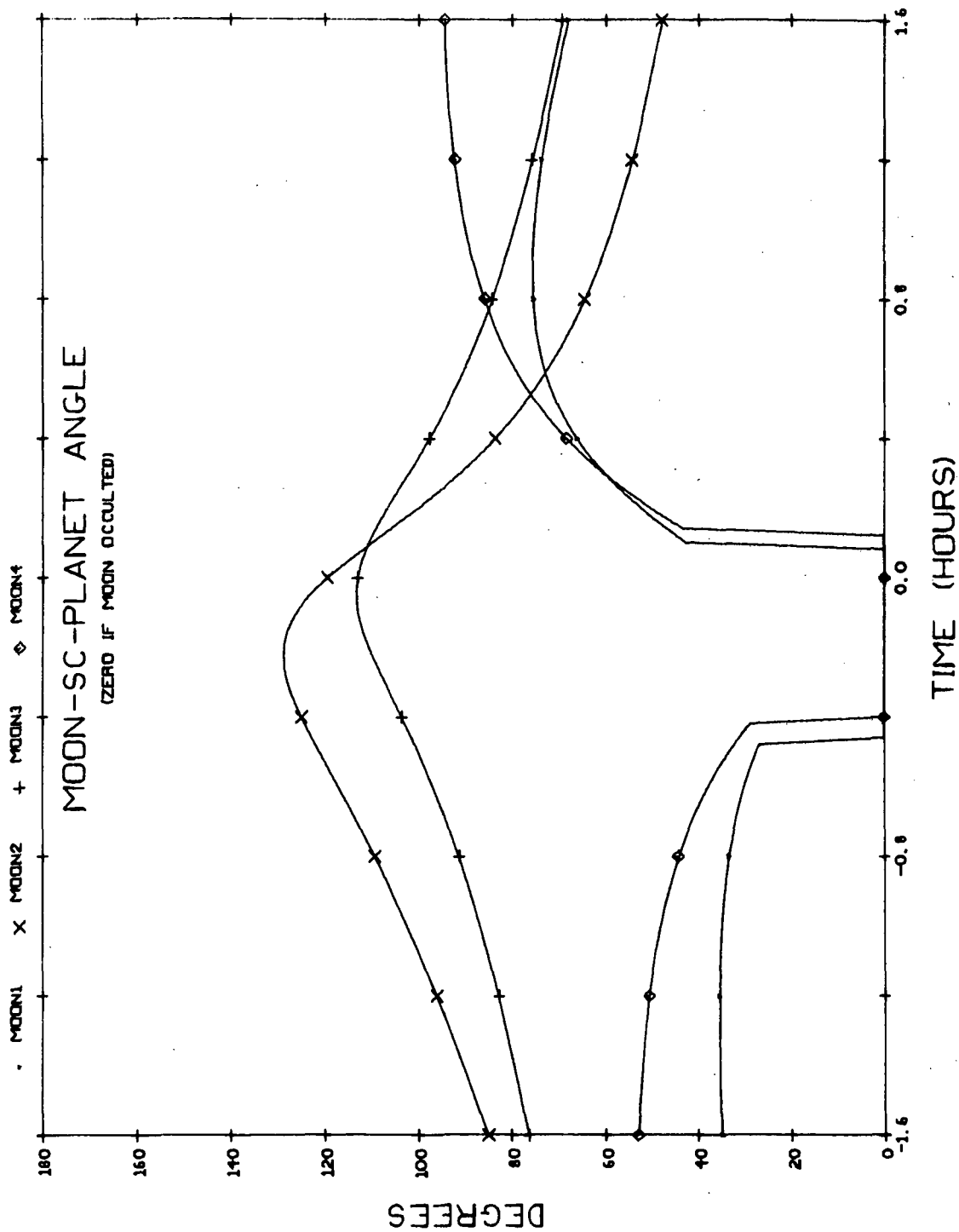


Fig. B6. 6b Moon-SC-Planet Angles During Uranus Passage on the 1977 Grand Tour;
3.2 Hour Frame

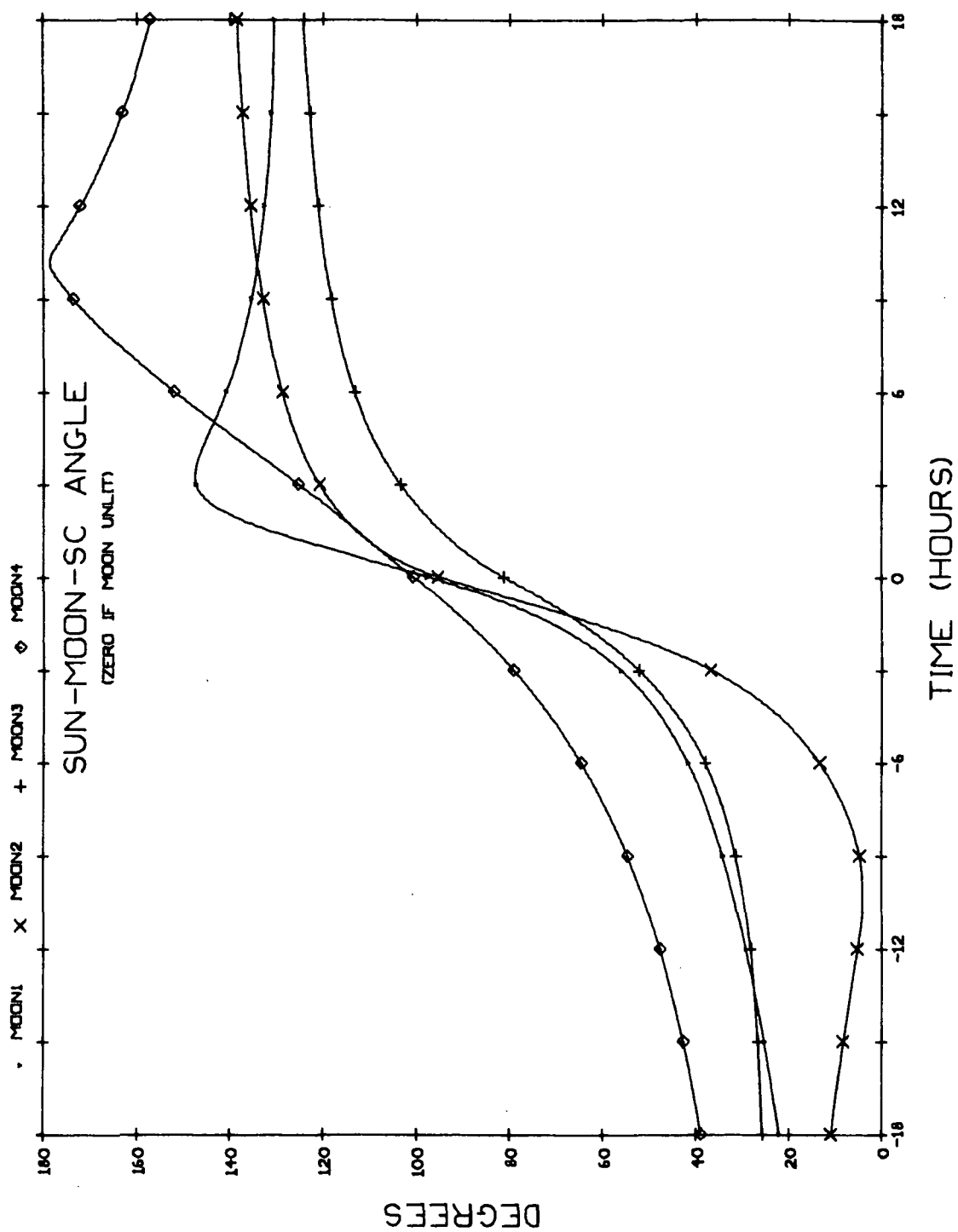


Fig. B6.7 Sun-Moon-SC Angle During Uranus Passage on the 1977 Grand Tour

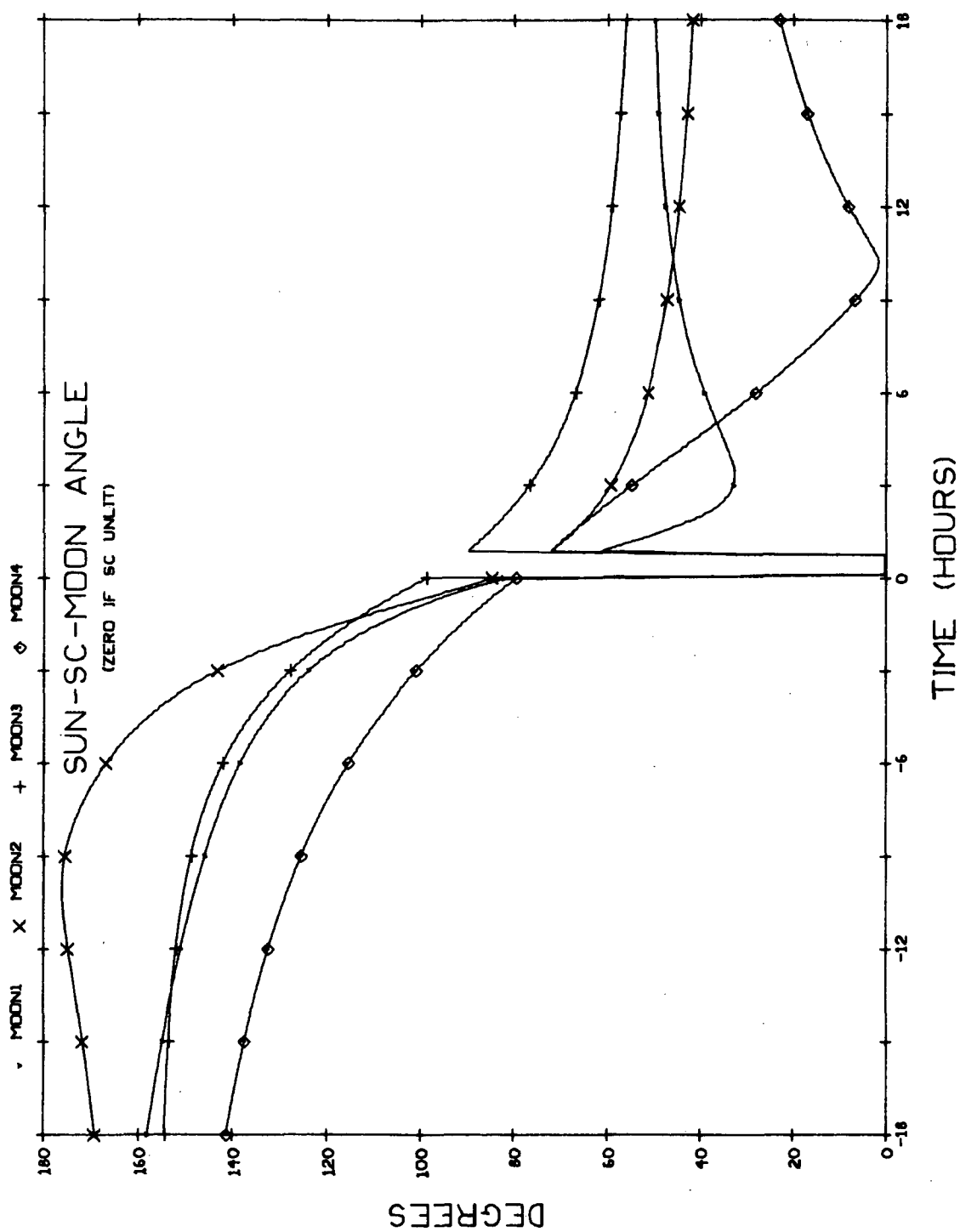


Fig. B6.8 Sun-SC-Moon Angle During Uranus Passage on the 1977 Grand Tour

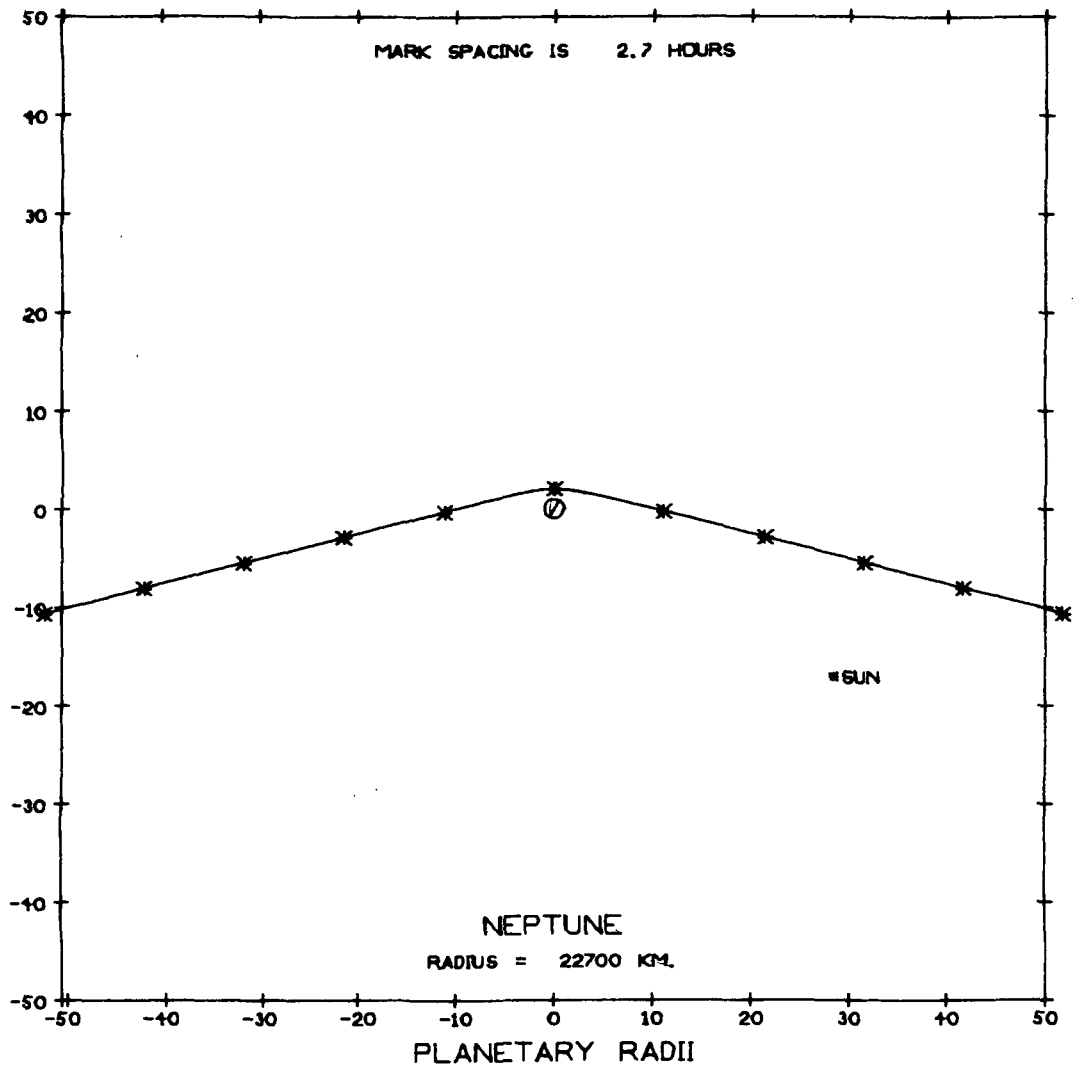


Fig. B7.1a Trajectory Plan View During Neptune Flyby on the 1977 Grand Tour; 100 Radii Field

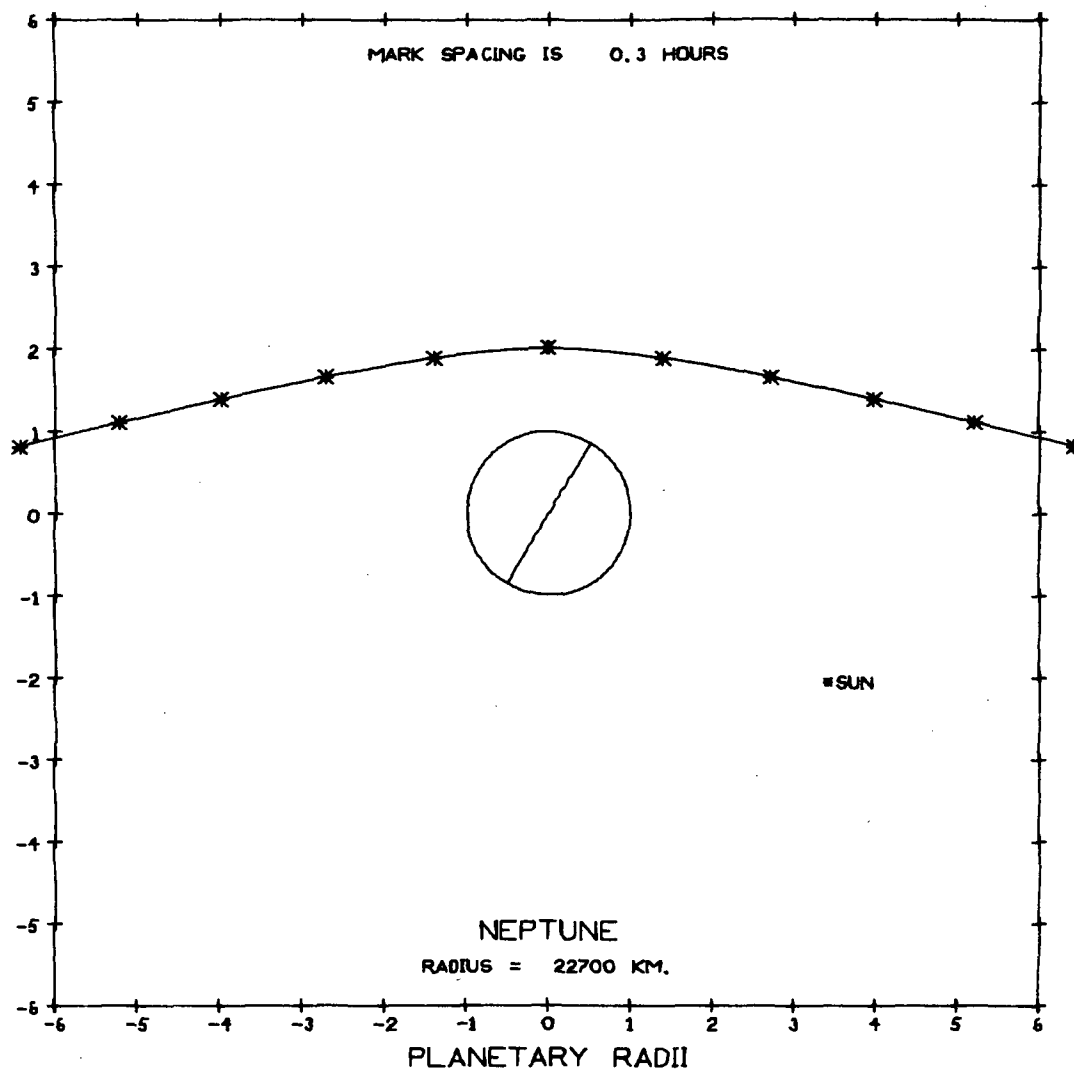


Fig. B7.1b Trajectory Plan View During Neptune Flyby on the 1977 Grand Tour; 12 Radii Field

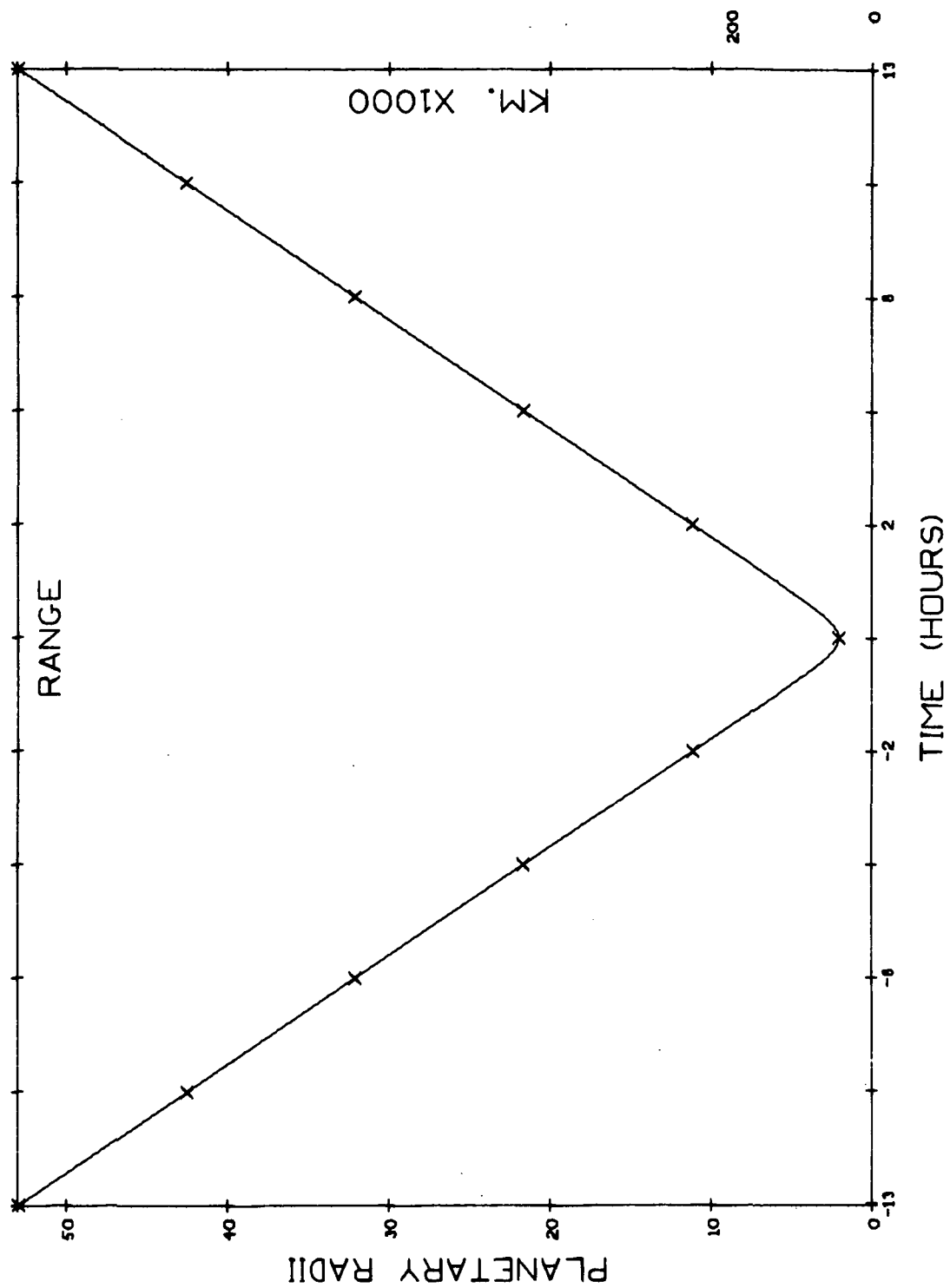


Fig. B7.2 Range to Planet During Neptune Flyby on the 1977 Grand Tour

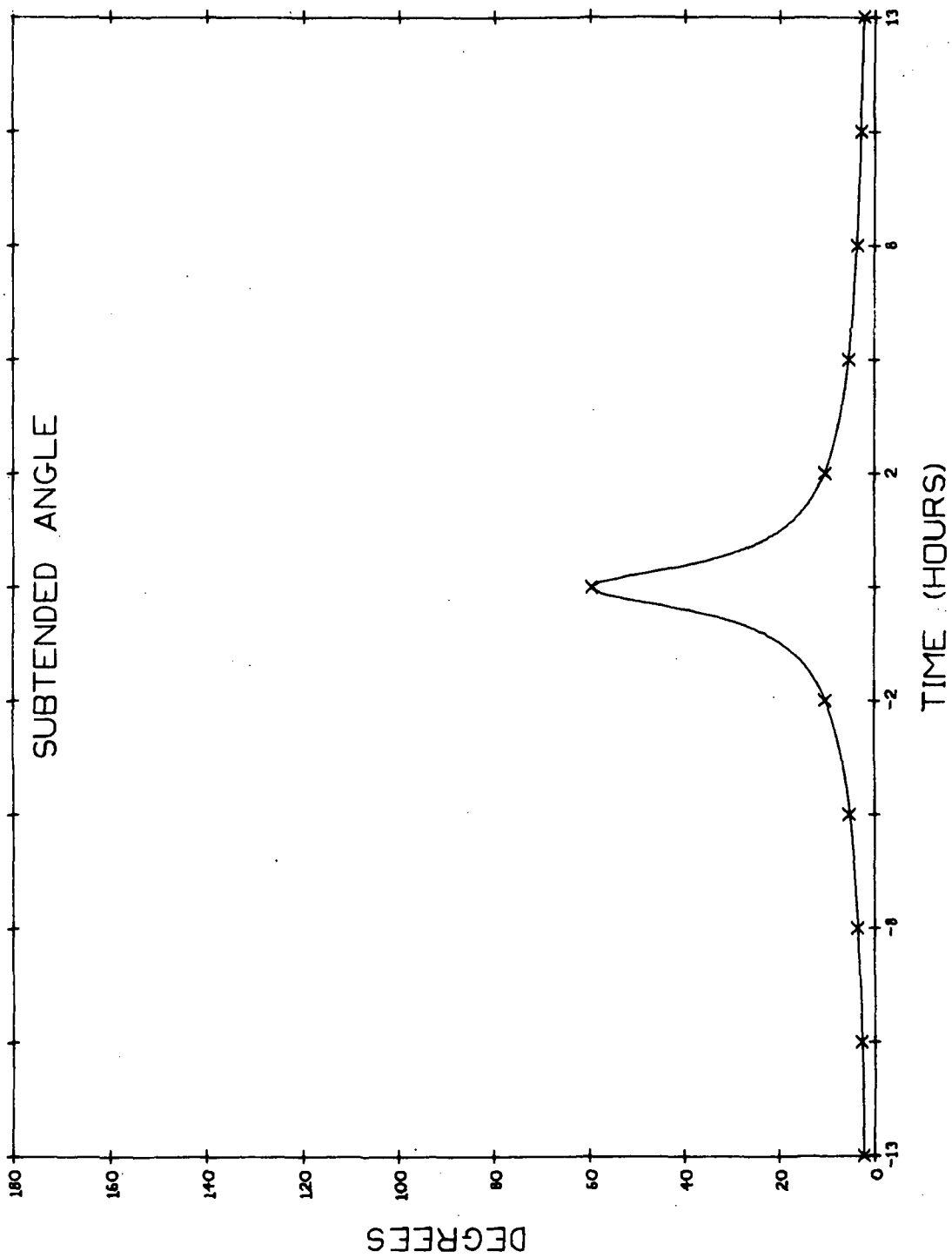


Fig. B7.3 Angle Subtended by Planetary Limbs During Neptune Flyby on the 1977 Grand Tour

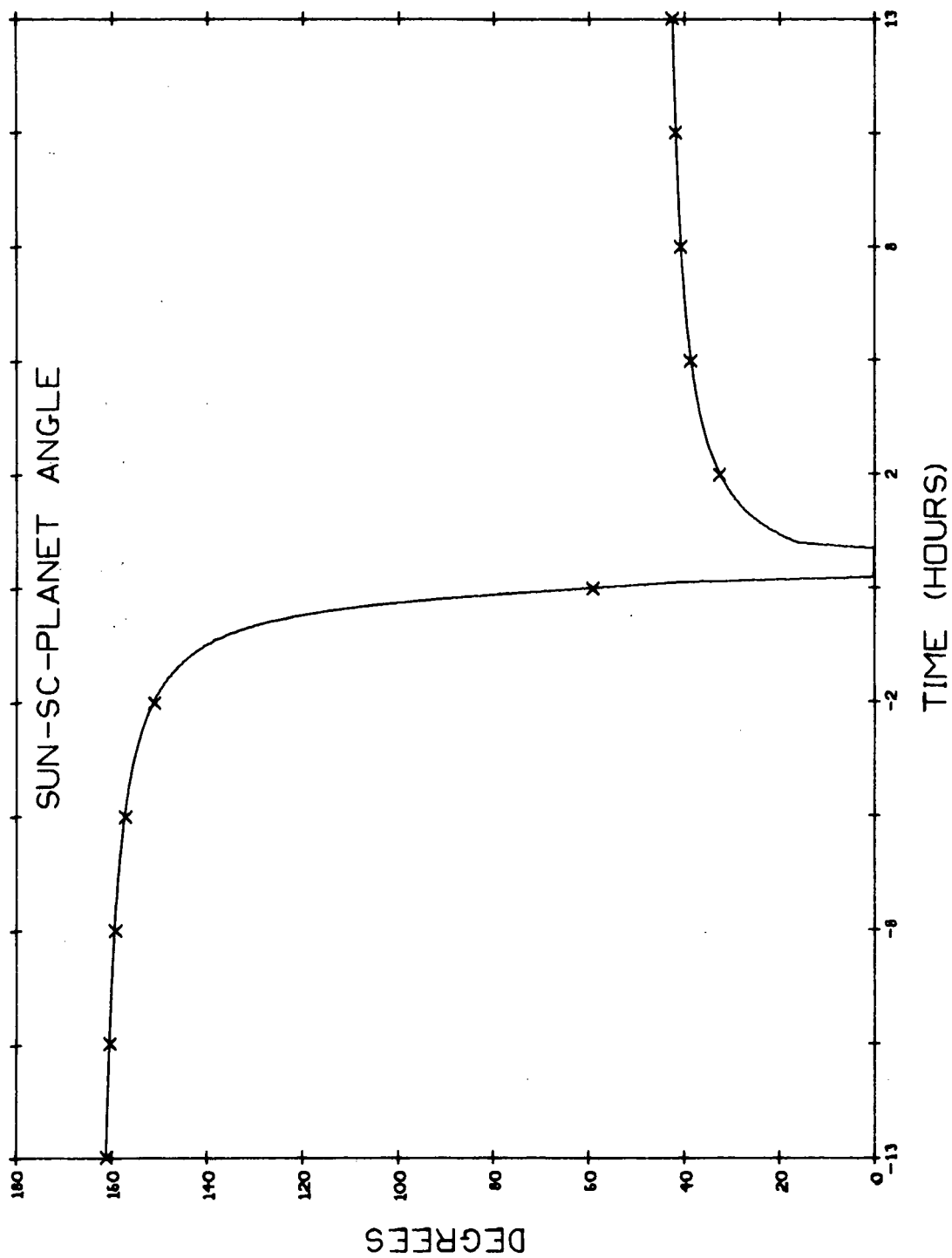


Fig. B7. 4a Sun-SC-Planet Angle During Neptune Flyby on the 1977 Grand Tour;
26 Hour Frame

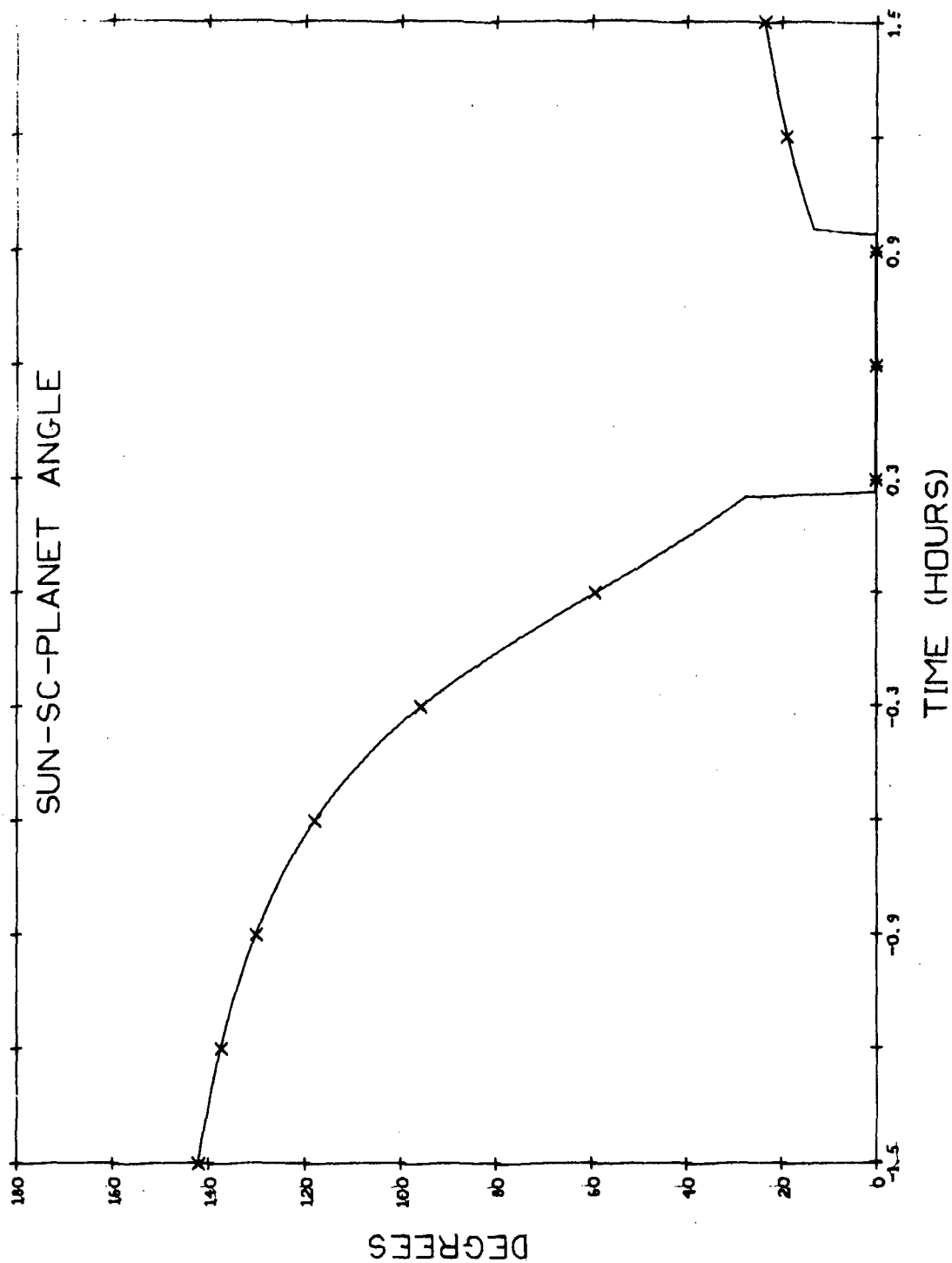


Fig. B7.4b Sun-SC-Planet Angle During Neptune Flyby on the 1977 Grand Tour;
3 Hour Frame

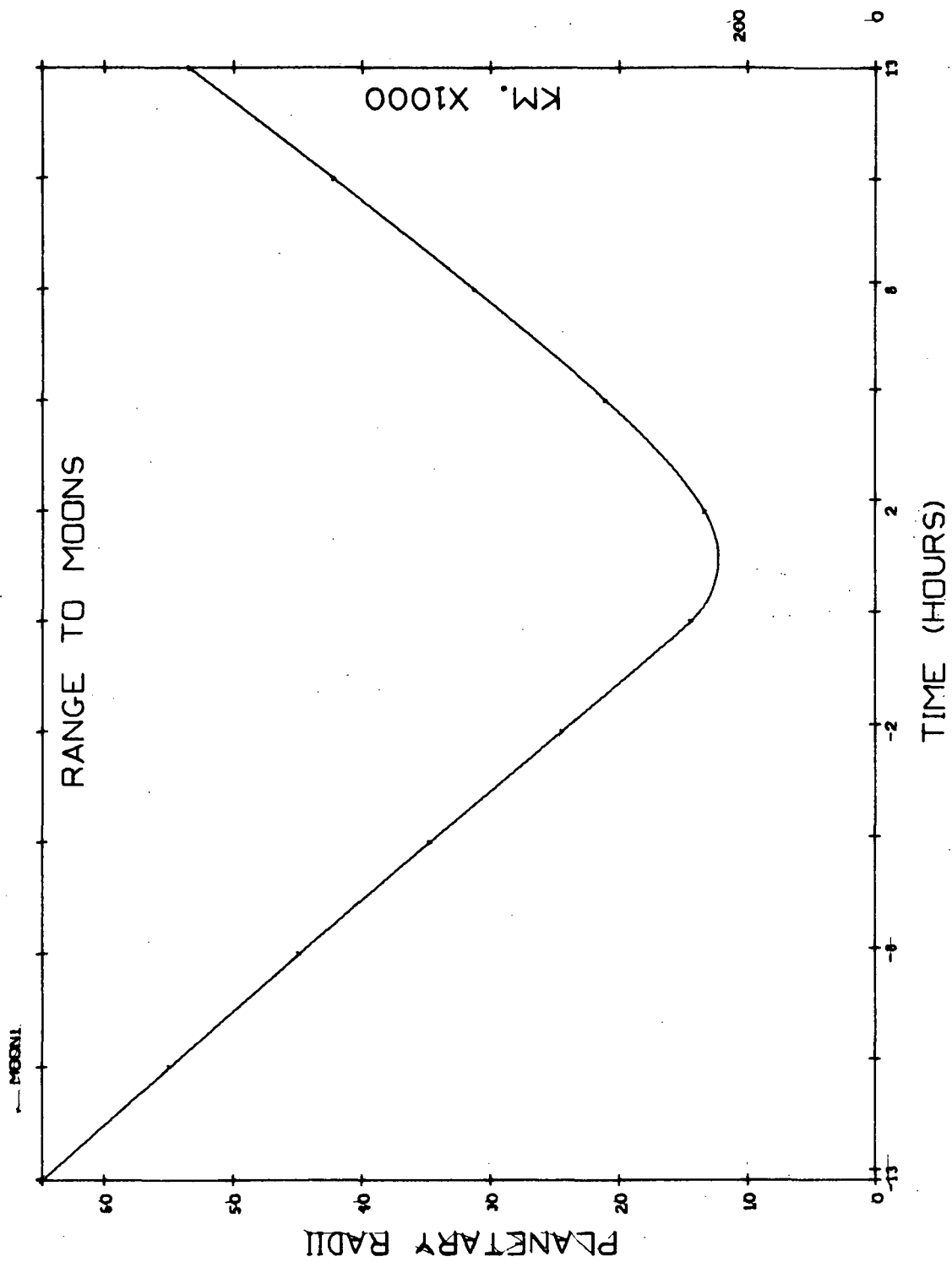


Fig. B7.5 Range to Triton During Neptune Flyby on the 1977 Grand Tour

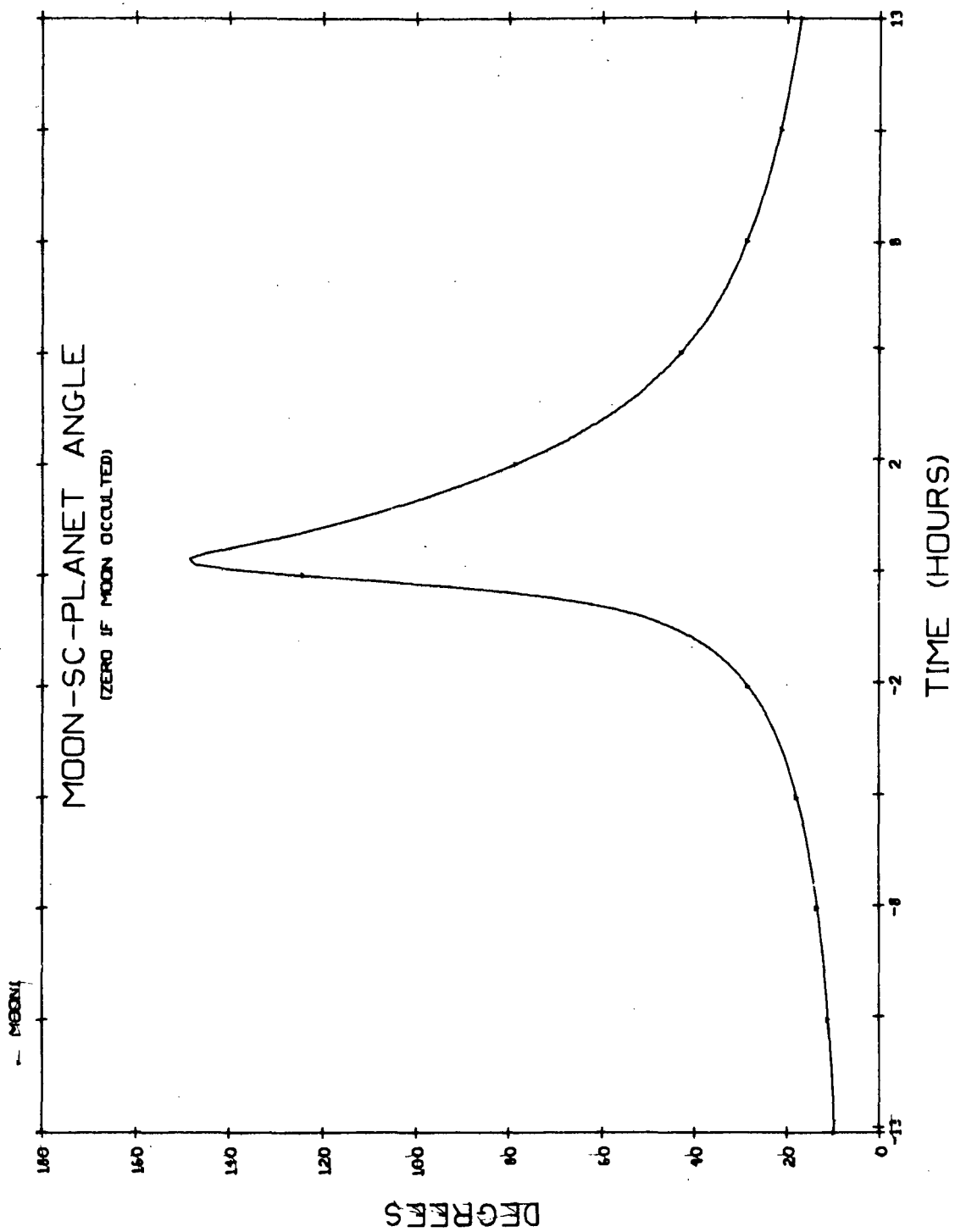


Fig. B7.6 Triton-SC-Planet Angle During Neptune Flyby on the 1977 Grand Tour

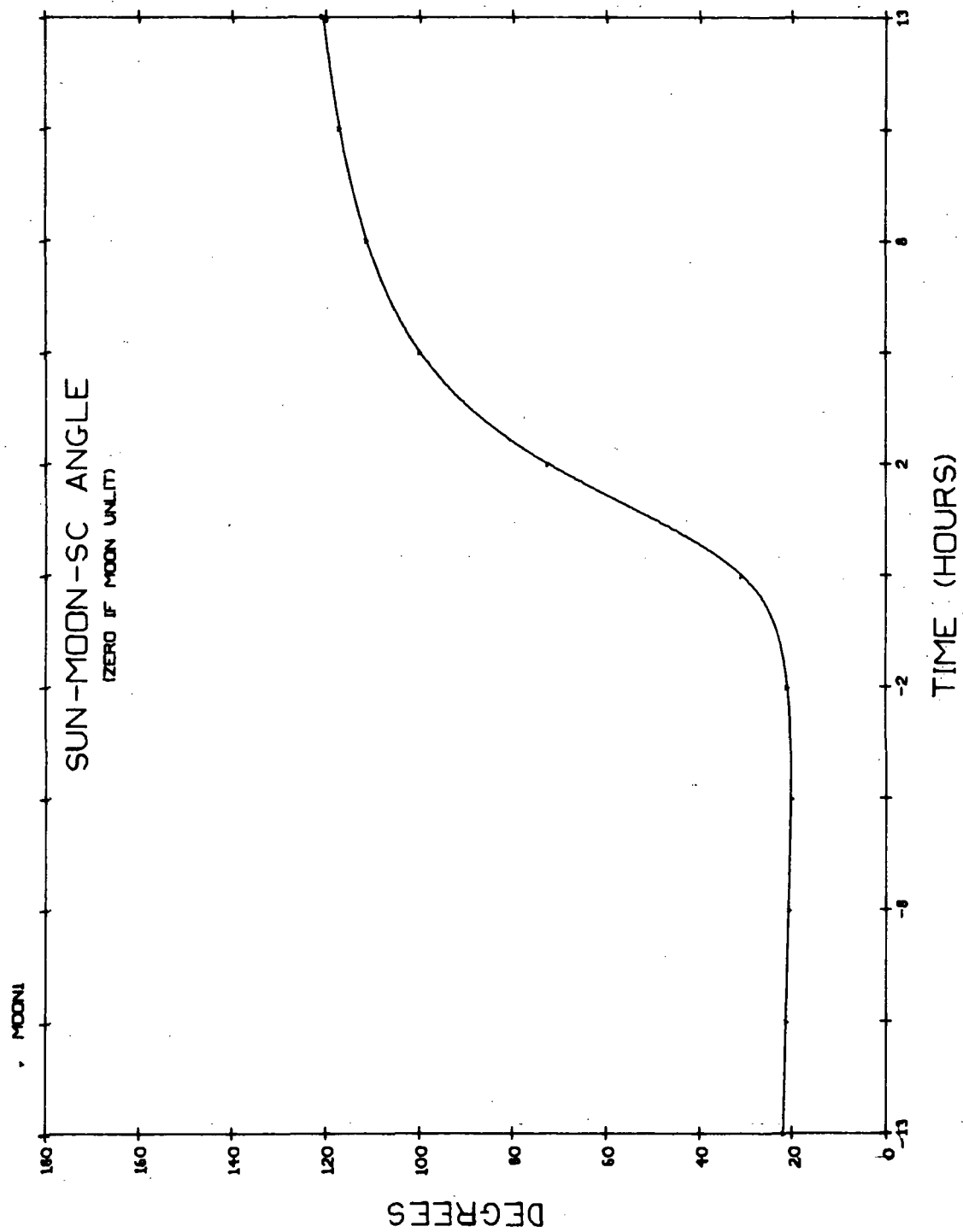


Fig. B7.7 Sun-Triton-SC Angle During Neptune Flyby on the 1977 Grand Tour

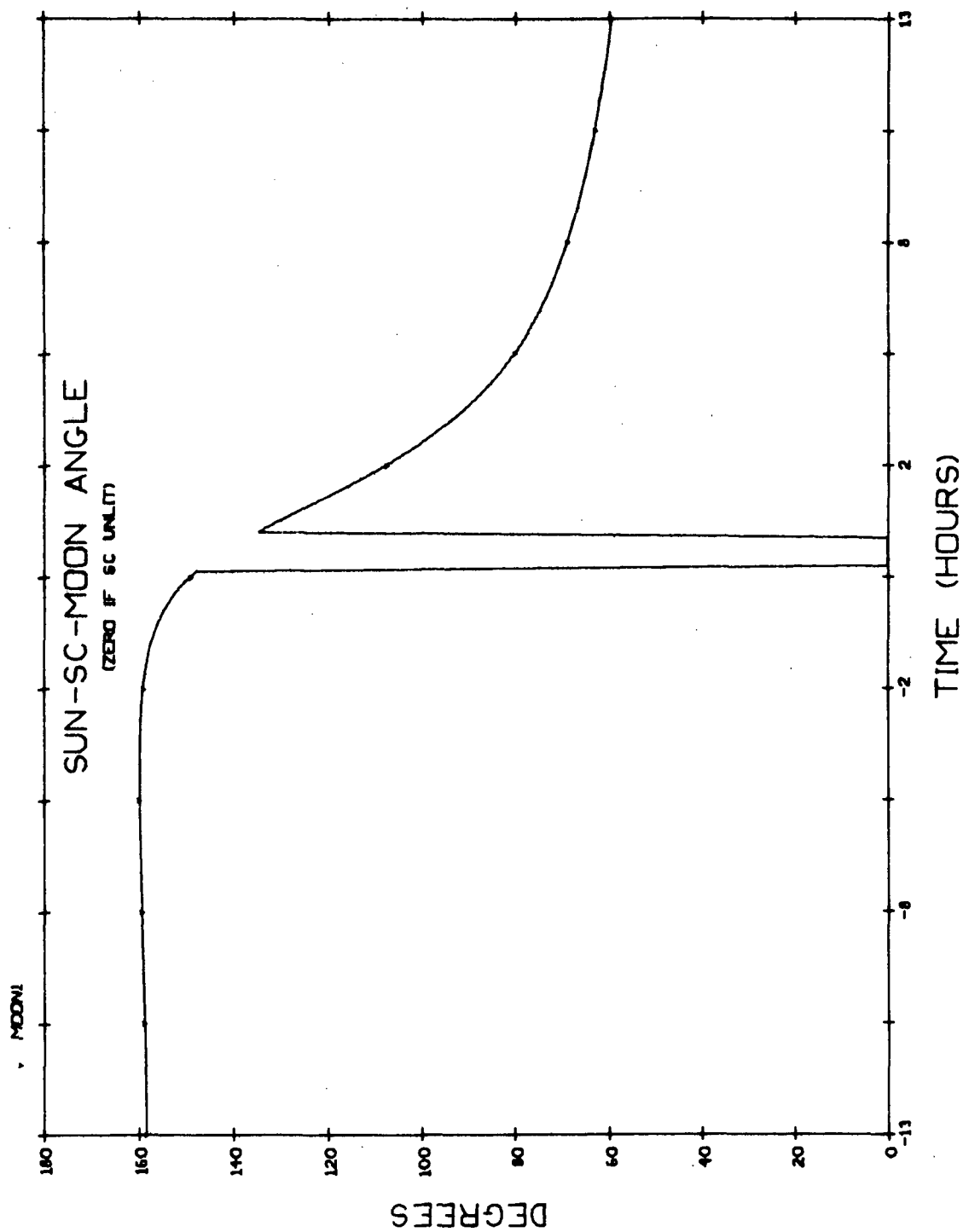


Fig. B7.8 Sun-SC-Triton Angle During Neptune Flyby on the 1977 Grand Tour

APPENDIX C

GUIDANCE ERROR SENSITIVITIES

In this appendix the complete sensitivity matrices from which the data of Chapter I was assembled are presented. Additional information is provided enabling the user to identify directional sensitivity information which was not made available in the first chapter.

The first table provides the key to interpreting the remaining tables. Partitioning the 6×6 matrix into four 3×3 's we have the fact that the upper left and lower right 3×3 's are dimensionless. The upper right 3×3 has the dimensions of kilometers per meter per second while the lower left 3×3 has dimensions of meters per second per kilometer. The terminal time (T) is the end of the interplanetary leg while the initial time (i) is the beginning. Note in all cases the extreme sensitivity of terminal position errors to the initial velocity errors. This, of course, is due to the large integration time. The x component is along the velocity vector at the time indicated, the y component is in the plane of motion perpendicular to the velocity vector, and the z component completes the orthogonal set.

These tables for the interplanetary legs are followed by graphs giving the guidance error sensitivities as a function of time for the near planet passes. These show the RSS position and velocity error which would result from a unit error in each component of position and velocity as the probe makes its inbound intersection with the sphere of influence. The coordinates x, y, z have the same meaning as in the interplanetary case. All position units are in kilometers and all velocity units are in meters per second. Note the rapid increase of errors as periplanet is passed. The implication here is that it will be difficult to predict position and velocity through pericenter unless the input of new navigational information offsets this loss. Stated differently, this means that without a strong navigation function during this period large guidance errors will ensue. The data presented in this appendix displays only the effect of trajectory dynamics - no planet mass uncertainty is included.

$\frac{\partial r_x(T)}{\partial r_x(i)}$	$\frac{\partial r_x(T)}{\partial r_y(i)}$	$\frac{\partial r_x(T)}{\partial r_z(i)}$	$\frac{\partial r_x(T)}{\partial v_x(i)}$	$\frac{\partial r_x(T)}{\partial v_y(i)}$	$\frac{\partial r_x(T)}{\partial v_z(i)}$
$\frac{\partial r_y(T)}{\partial r_x(i)}$	$\frac{\partial r_y(T)}{\partial r_y(i)}$	$\frac{\partial r_y(T)}{\partial r_z(i)}$	$\frac{\partial r_y(T)}{\partial v_x(i)}$	$\frac{\partial r_y(T)}{\partial v_y(i)}$	$\frac{\partial r_y(T)}{\partial v_z(i)}$
$\frac{\partial r_z(T)}{\partial r_x(i)}$	$\frac{\partial r_z(T)}{\partial r_y(i)}$	$\frac{\partial r_z(T)}{\partial r_z(i)}$	$\frac{\partial r_z(T)}{\partial v_x(i)}$	$\frac{\partial r_z(T)}{\partial v_y(i)}$	$\frac{\partial r_z(T)}{\partial v_z(i)}$
$\frac{\partial v_x(T)}{\partial r_x(i)}$	$\frac{\partial v_x(T)}{\partial r_y(i)}$	$\frac{\partial v_x(T)}{\partial r_z(i)}$	$\frac{\partial v_x(T)}{\partial v_x(i)}$	$\frac{\partial v_x(T)}{\partial v_y(i)}$	$\frac{\partial v_x(T)}{\partial v_z(i)}$
$\frac{\partial v_y(T)}{\partial r_x(i)}$	$\frac{\partial v_y(T)}{\partial r_y(i)}$	$\frac{\partial v_y(T)}{\partial r_z(i)}$	$\frac{\partial v_y(T)}{\partial v_x(i)}$	$\frac{\partial v_y(T)}{\partial v_y(i)}$	$\frac{\partial v_y(T)}{\partial v_z(i)}$
$\frac{\partial v_z(T)}{\partial r_x(i)}$	$\frac{\partial v_z(T)}{\partial r_y(i)}$	$\frac{\partial v_z(T)}{\partial r_z(i)}$	$\frac{\partial v_z(T)}{\partial v_x(i)}$	$\frac{\partial v_z(T)}{\partial v_y(i)}$	$\frac{\partial v_z(T)}{\partial v_z(i)}$

x = Along Velocity Vector at time T or i
 y = In Plane of Motion \perp Velocity Vector at time T or i
 z = Cross Product of x into y

TABLE C-1 Standard Key to Sensitivity Matrix Tables

TABLE C-2

Sensitivity Matrix for Earth to Jupiter Interplanetary Leg
of 1973 Low Energy Jupiter Flyby

(For Matrix Element Identification See Table C-1)

-9.148	19.493	0	2909.658	5296.052	182.332
-6.485	31.440	0	5080.045	9243.961	318.321
0	0	-4.700	4272.553	7763.888	267.646
-1.405	0.775	-0.042	-0.619	0.055	0
-17.616	9.719	-0.705	-6.396	0.460	0
0.013	0.024	-0.898	0	0	-0.159

TABLE C-3

Sensitivity Matrix for Earth to Jupiter Interplanetary Leg
of 1977 Jupiter Flyby to Saturn

(For Matrix Element Identification See Table C-1)

-3.481	0.147	0	82.507	-235.920	-1.650
-5.181	21.017	0	-886.564	2544.927	17.727
0	0	-4.418	3526.165	-10166.611	-70.508
-2.771	-0.961	0.049	1.632	0.036	0
2.743	0.952	-0.114	-3.696	0.666	0
-0.005	0.016	-2.520	0	0	-0.032

TABLE C-4

Sensitivity Matrix for Jupiter to Saturn Leg
of 1977 Jupiter Swingby to Saturn

(For Matrix Element Identification See Table C-1)

0.832	0.059	0	-2022.529	1056.619	91.087
-0.560	1.381	0	940.197	-489.116	-42.337
0	0	0.742	-46160.258	24086.842	2078.809
-0.111	-0.213	0.003	0.999	0.096	0
0.072	0.139	-0.016	-0.499	1.081	0
-0.008	0.004	-0.220	0	0	0.857

TABLE C-5

Sensitivity Matrix for Earth to Jupiter Leg
of 1977 Grand Tour

(For Matrix Element Identification See Table C-1)

-2.643	-1.331	0	96.410	-310.190	-1.374
-5.145	17.258	0	-452.595	1460.401	6.450
0	0	-4.034	3656.664	-11879.427	-52.112
-2.565	-0.790	0.032	1.678	0.036	0
1.233	0.380	-0.064	-3.161	0.742	0
-0.004	0.012	-2.931	0	0	0.038

TABLE C-6

Sensitivity Matrix for Jupiter to Saturn Leg

of 1977 Grand Tour

(For Matrix Element Identification See Table C-1)

0.862	0.050	0	-1851.270	860.859	81.534
-0.456	1.325	0	728.190	-336.807	-32.065
0	0	0.784	-42919.922	19935.340	1890.224
-0.095	-0.205	0.002	1.002	0.078	0
0.069	0.150	-0.014	-0.411	1.076	0
-0.007	0.003	-0.207	0	0	0.880

TABLE C-7

Sensitivity Matrix for Saturn to Uranus Leg

of 1977 Grand Tour

(For Matrix Element Identification See Table C-1)

0.887	0.028	0	-126.301	-2062.600	-81.788
-0.268	1.283	0	-245.613	-3896.550	-154.624
0	0	0.824	6306.527	100400.625	3983.772
-0.021	0.001	0.003	1.008	0.033	0
-0.078	0.005	-0.004	-0.256	1.066	0
0	0.003	-0.078	0	0	0.912

TABLE C-8

Sensitivity Matrix for Uranus to Neptune Leg
of 1977 Grand Tour

(For Matrix Element Identification See Table C-1)

1.004	0.003	0	-2418.401	-3397.161	-230.054
-0.044	1.009	0	-1596.866	-2237.813	-151.726
0	0	0.986	49475.287	69421.408	4703.828
0.009	-0.006	0	1.006	0.011	0
-0.010	0.007	0	-0.036	1.002	0
0	0	0.008	0	0	0.991

Planetary Passage Guidance Sensitivities

* Sensitivity Figure Summary Page *

1. 1973 LOW ENERGY JUPITER FLYBY

Fig. C1.1 RSS Position Error Propagation due to Initial Position and Velocity Errors for Jovian Passage on 1973 Low Energy Jupiter Flyby.

Fig. C1.2 RSS Velocity Error Propagation due to Initial Position and Velocity Errors for Jovian Passage on 1973 Low Energy Jupiter Flyby.

2. 1977 JUPITER SWINGBY TO SATURN, JUPITER PASSAGE

Fig. C2.1 RSS Position Error Propagation due to Initial Position and Velocity Errors for Jovian Passage of 1977 Jupiter Swingby to Saturn.

Fig. C2.2 RSS Velocity Error Propagation due to Initial Position and Velocity Errors for Jovian Passage of 1977 Jupiter Swingby to Saturn.

3. 1977 JUPITER SWINGBY TO SATURN, SATURN PASSAGE

Fig. C3.1 RSS Position Error Propagation due to Initial Position and Velocity Errors for Saturn Flyby of 1977 Jupiter Swingby to Saturn.

Fig. C3.2 RSS Velocity Error Propagation due to Initial Position and Velocity Errors for Saturn Flyby of 1977 Jupiter Swingby to Saturn.

4. 1977 GRAND TOUR, JUPITER PASSAGE

Fig. C4.1 RSS Position Error Propagation due to Initial Position and Velocity Errors for Jovian Passage of 1977 Grand Tour.

Fig. C4.2 RSS Velocity Propagation Error due to Initial Position and Velocity Errors for Jovian Passage of 1977 Grand Tour.

5. 1977 GRAND TOUR, SATURN PASSAGE

Fig. C5.1 RSS Position Error Propagation due to Initial Position and Velocity Errors for Saturn Passage of 1977 Grand Tour.

Fig. C5.2 RSS Velocity Error Propagation due to Initial Position and Velocity Errors for Saturn Passage of 1977 Grand Tour.

6. 1977 GRAND TOUR, URANUS PASSAGE

Fig. C6.1 RSS Position Error Propagation due to Initial Position and Velocity Errors for Uranus Passage of 1977 Grand Tour.

Fig. C6.2 RSS Velocity Error Propagation due to Initial Position and Velocity Errors for Uranus Passage of 1977 Grand Tour.

7. 1977 GRAND TOUR, NEPTUNE PASSAGE

Fig. C7.1 RSS Position Error Propagation due to Initial Position and Velocity Errors for Neptune Flyby of 1977 Grand Tour.

Fig. C7.2 RSS Velocity Error Propagation due to Initial Position and Velocity Errors for Neptune Flyby of 1977 Grand Tour.

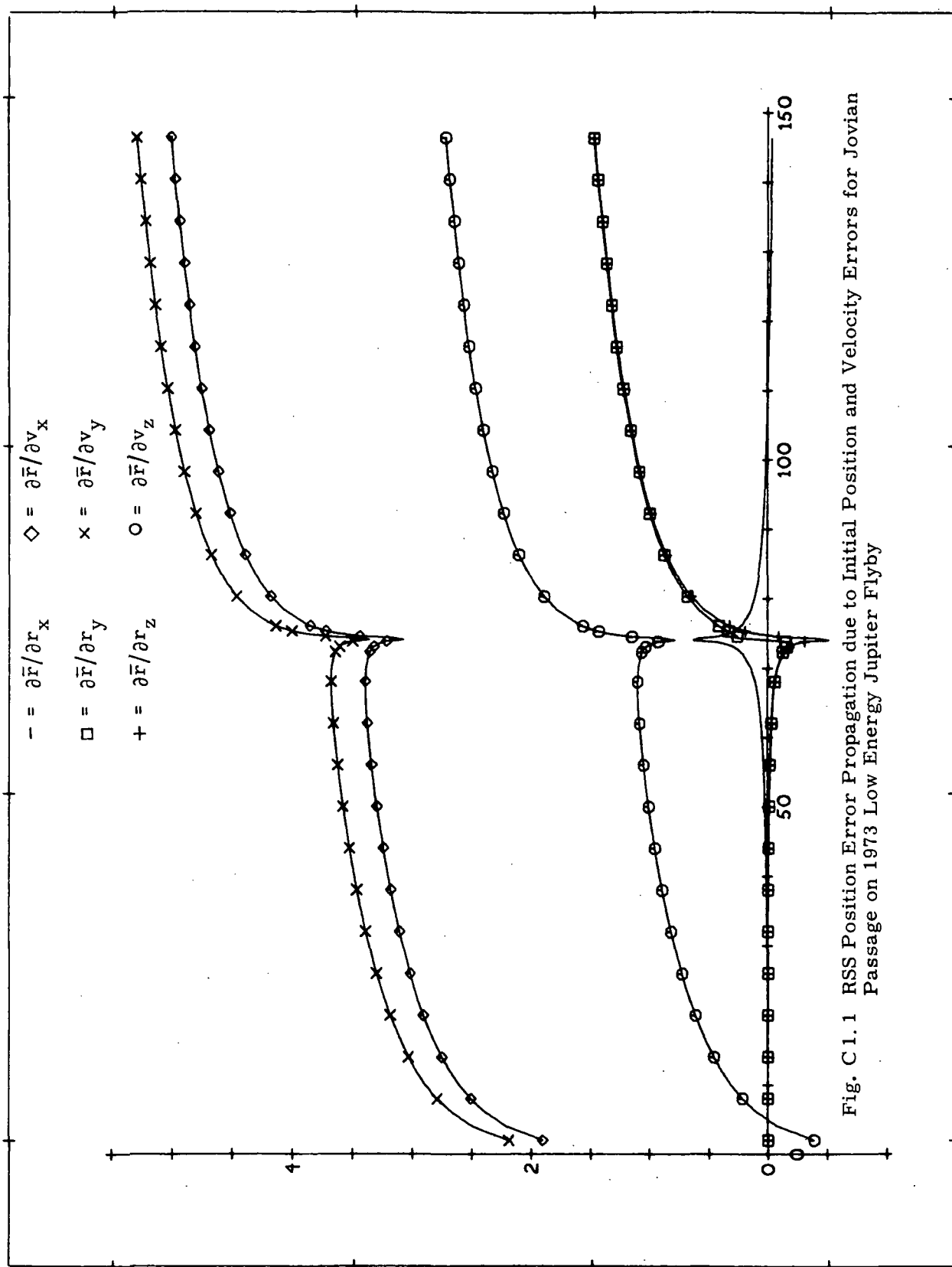


Fig. C1.1 RSS Position Error Propagation due to Initial Position and Velocity Errors for Jovian Passage on 1973 Low Energy Jupiter Flyby

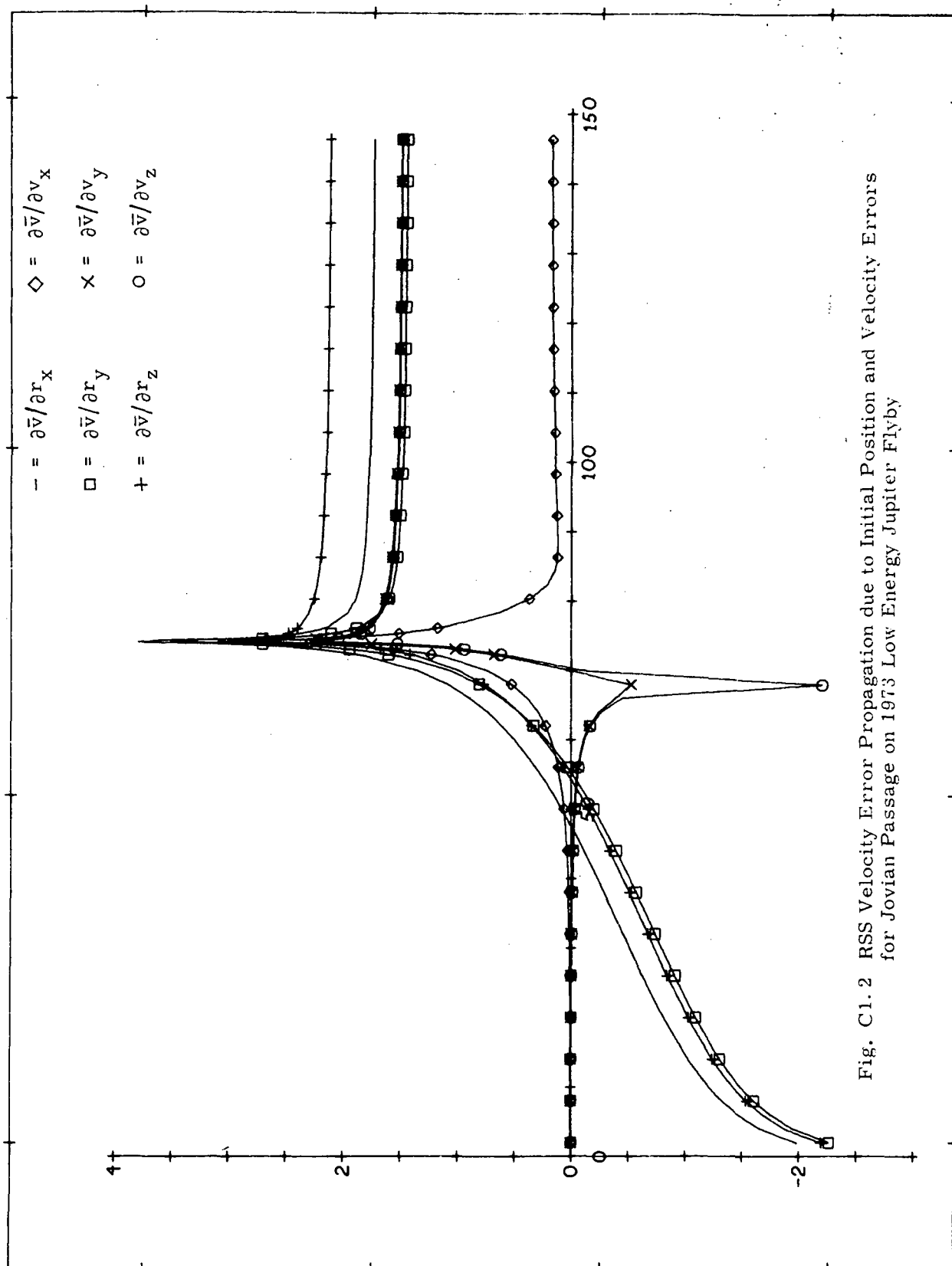


Fig. C1.2 RSS Velocity Error Propagation due to Initial Position and Velocity Errors for Jovian Passage on 1973 Low Energy Jupiter Flyby

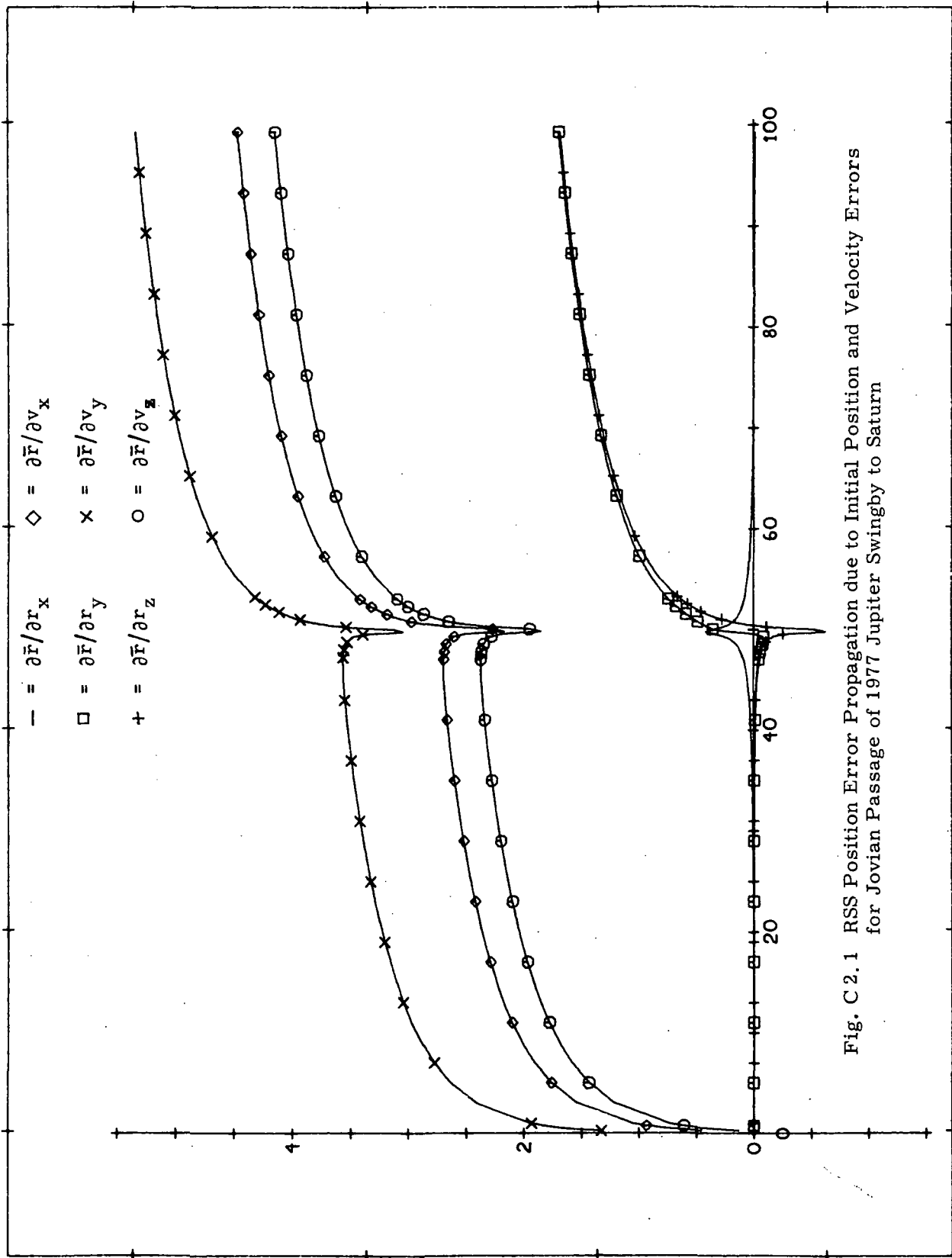


Fig. C 2.1 RSS Position Error Propagation due to Initial Position and Velocity Errors for Jovian Passage of 1977 Jupiter Swingby to Saturn

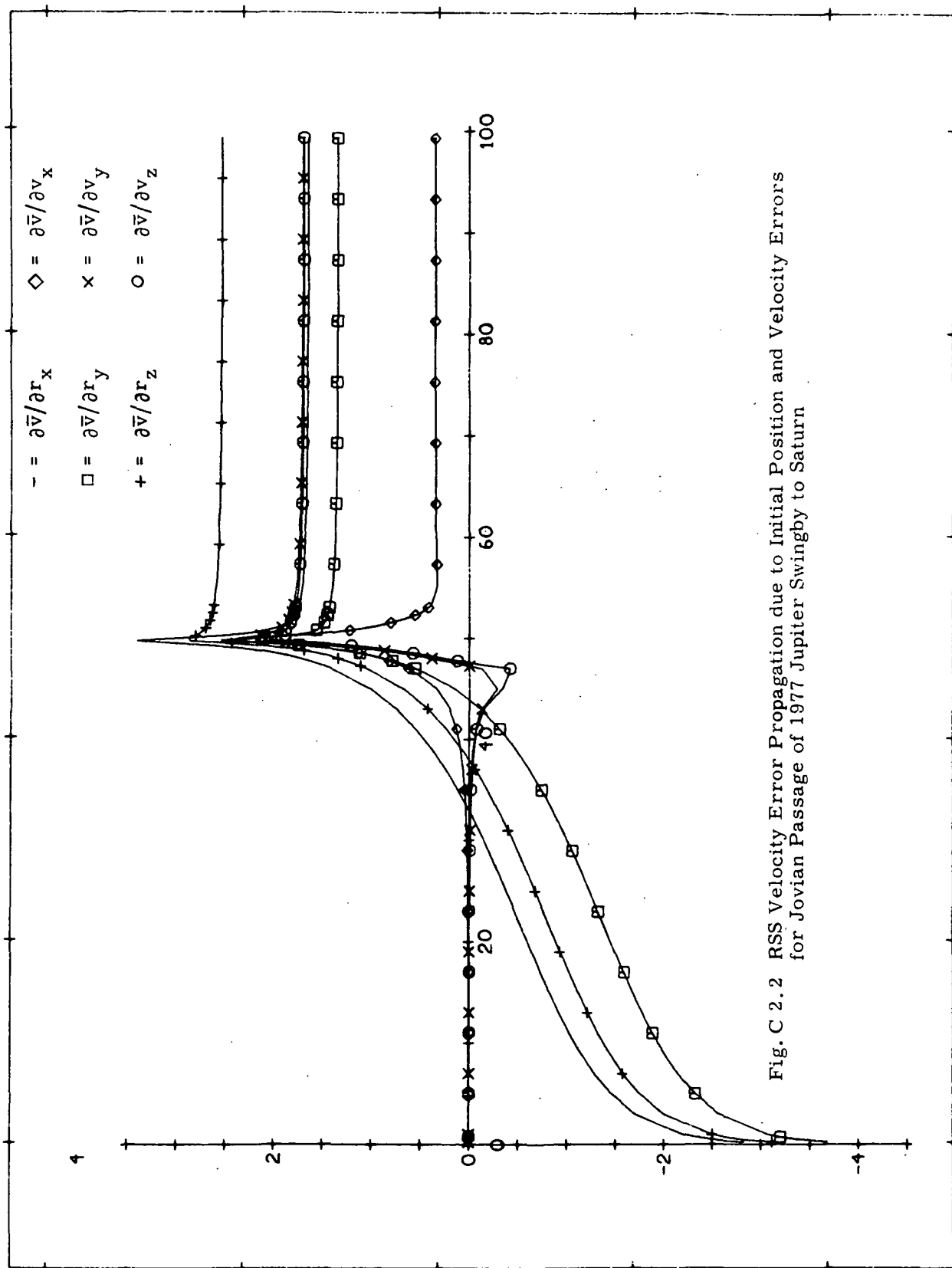


Fig. C 2.2 RSS Velocity Error Propagation due to Initial Position and Velocity Errors for Jovian Passage of 1977 Jupiter Swingby to Saturn

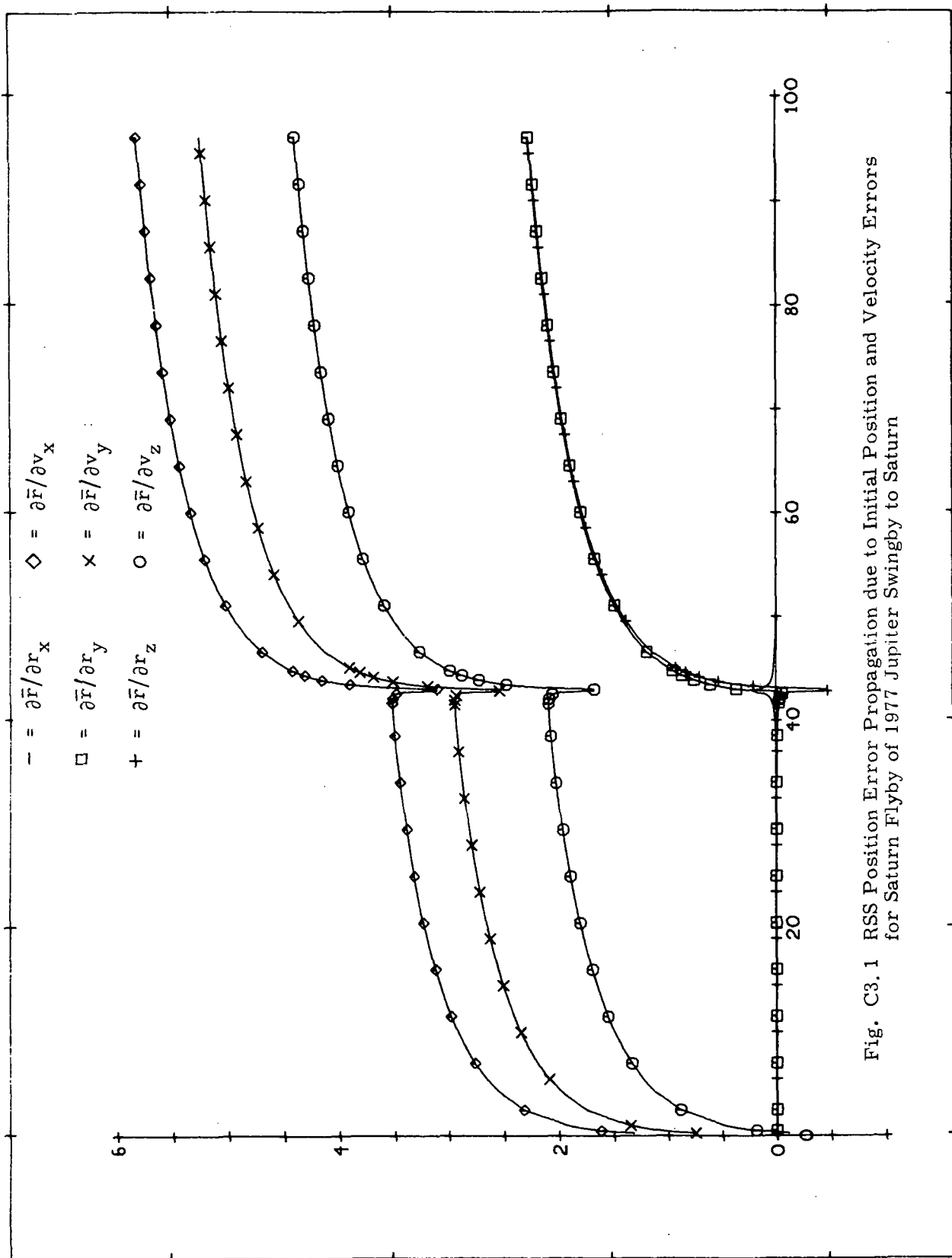


Fig. C3.1 RSS Position Error Propagation due to Initial Position and Velocity Errors for Saturn Flyby of 1977 Jupiter Swingby to Saturn

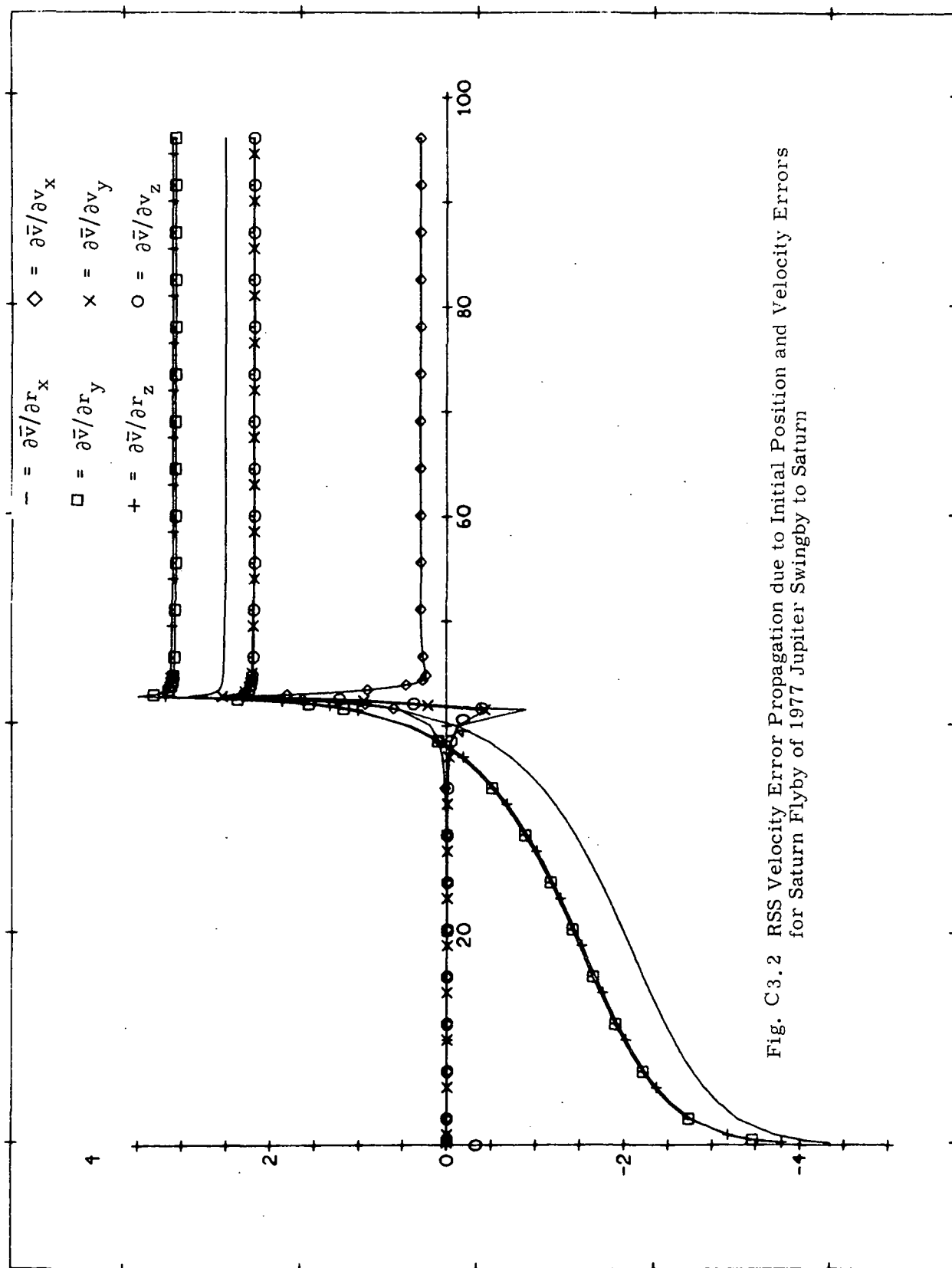


Fig. C3.2 RSS Velocity Error Propagation due to Initial Position and Velocity Errors for Saturn Flyby of 1977 Jupiter Swingby to Saturn

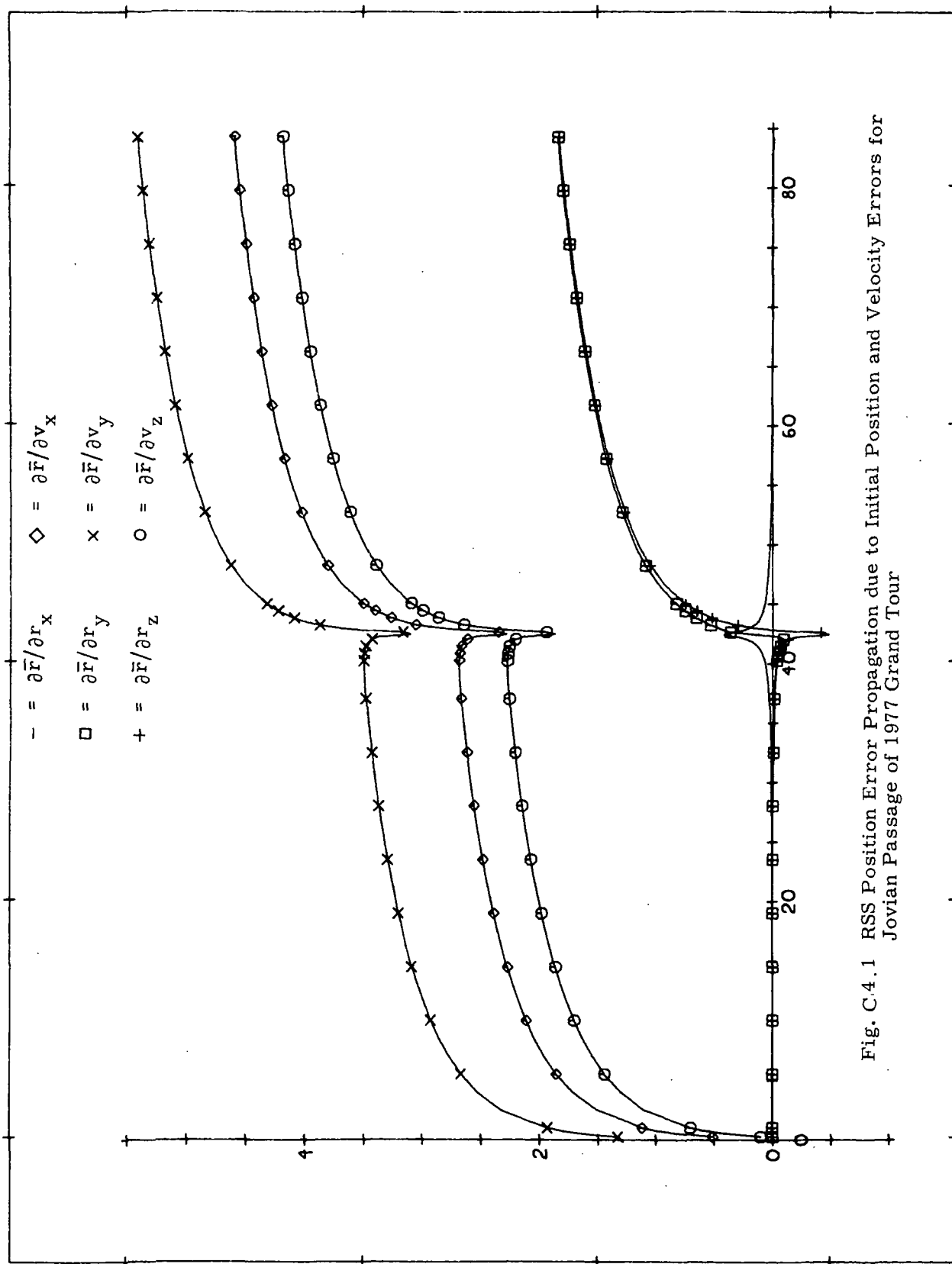


Fig. C4.1 RSS Position Error Propagation due to Initial Position and Velocity Errors for Jovian Passage of 1977 Grand Tour

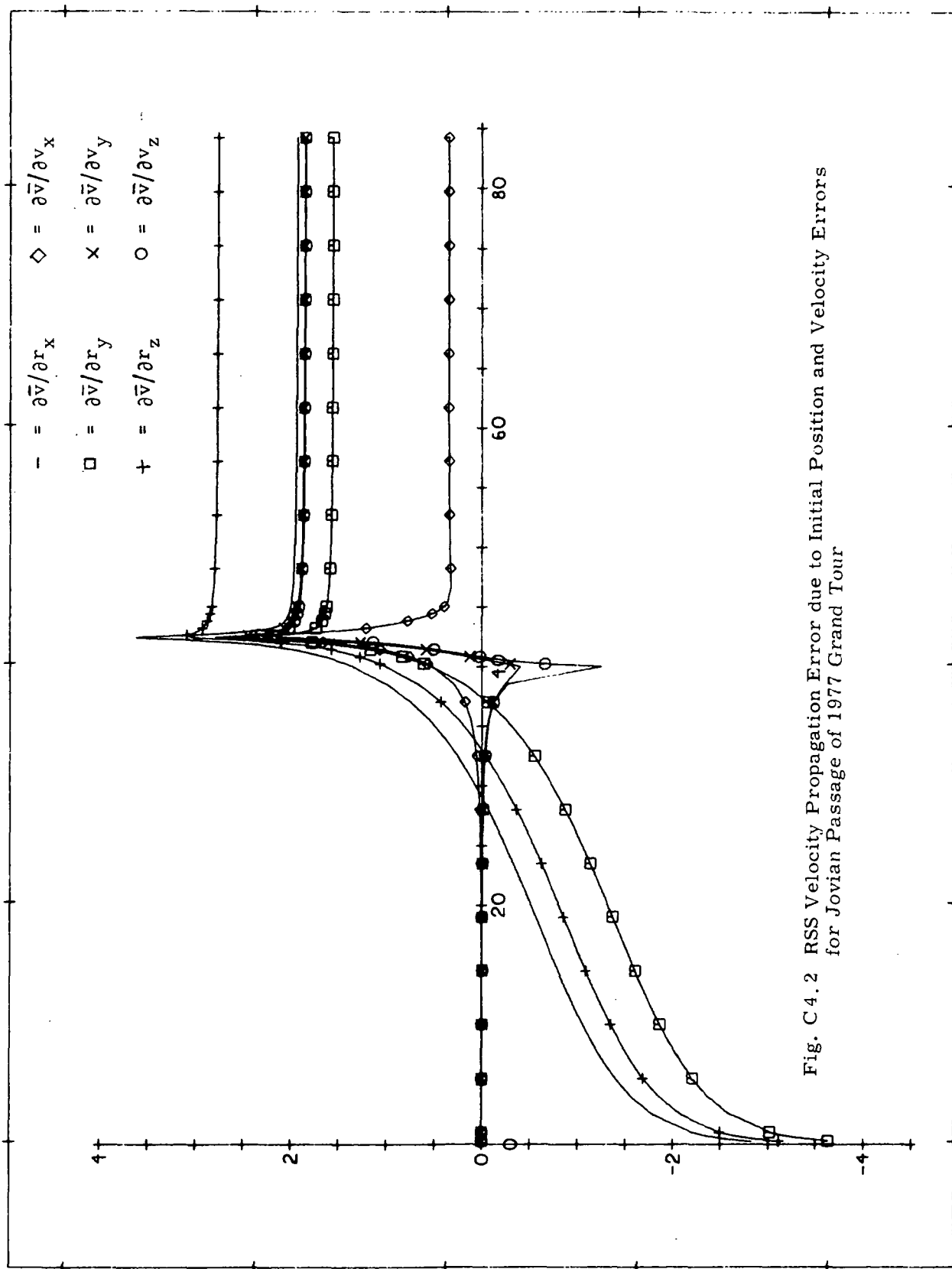


Fig. C4.2 RSS Velocity Propagation Error due to Initial Position and Velocity Errors
for Jovian Passage of 1977 Grand Tour

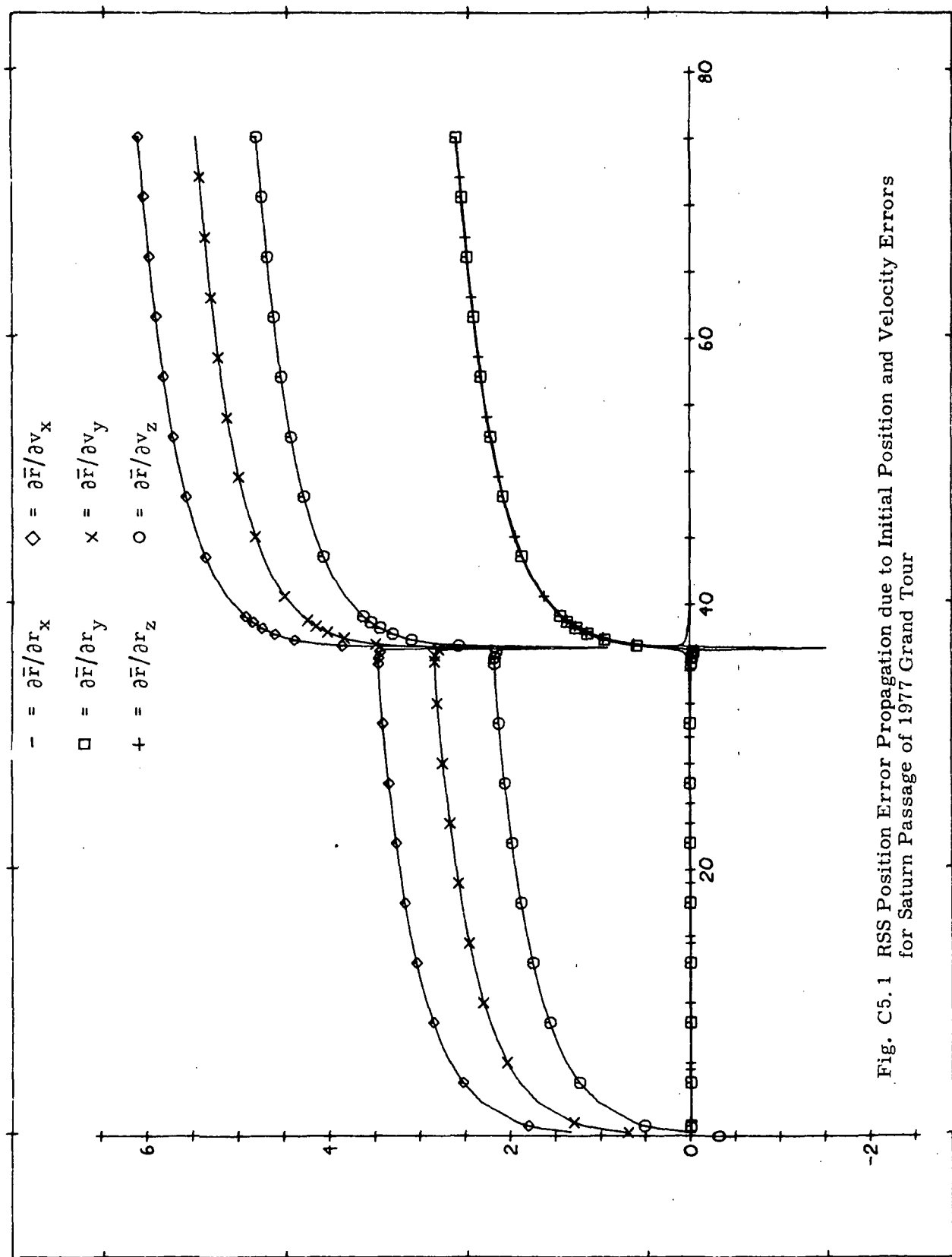


Fig. C5.1 RSS Position Error Propagation due to Initial Position and Velocity Errors for Saturn Passage of 1977 Grand Tour

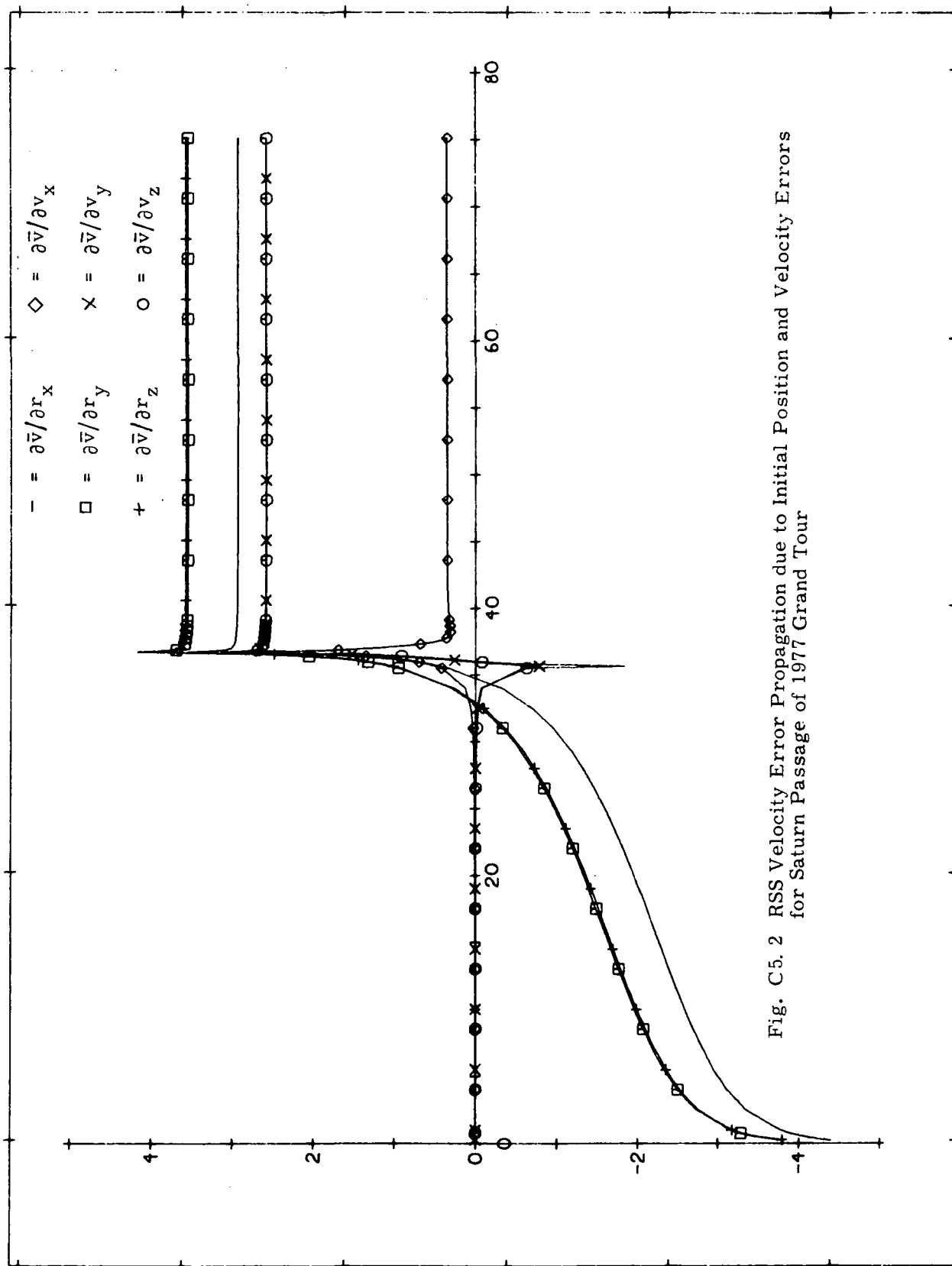


Fig. C5. 2 RSS Velocity Error Propagation due to Initial Position and Velocity Errors for Saturn Passage of 1977 Grand Tour

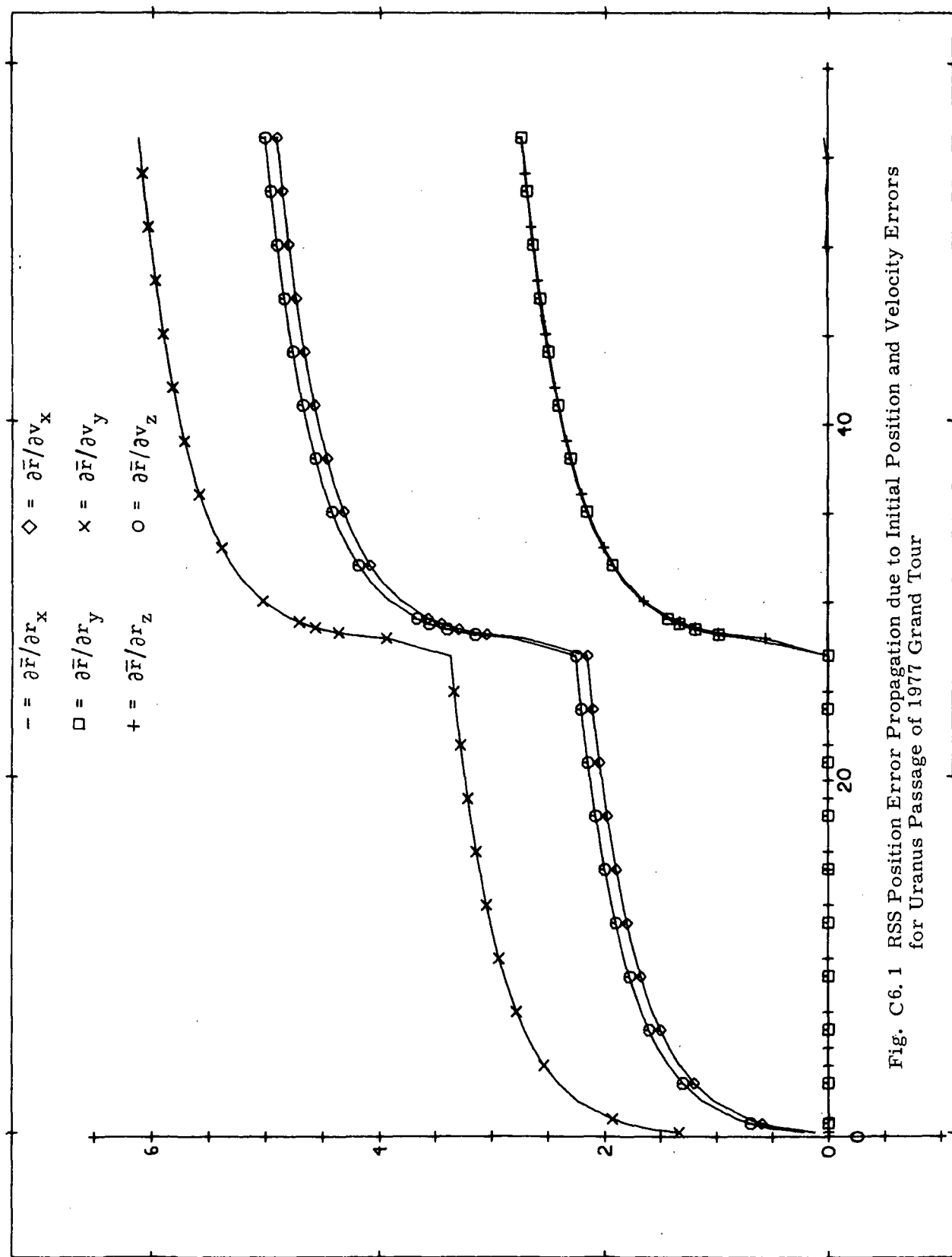


Fig. C6.1 RSS Position Error Propagation due to Initial Position and Velocity Errors
for Uranus Passage of 1977 Grand Tour

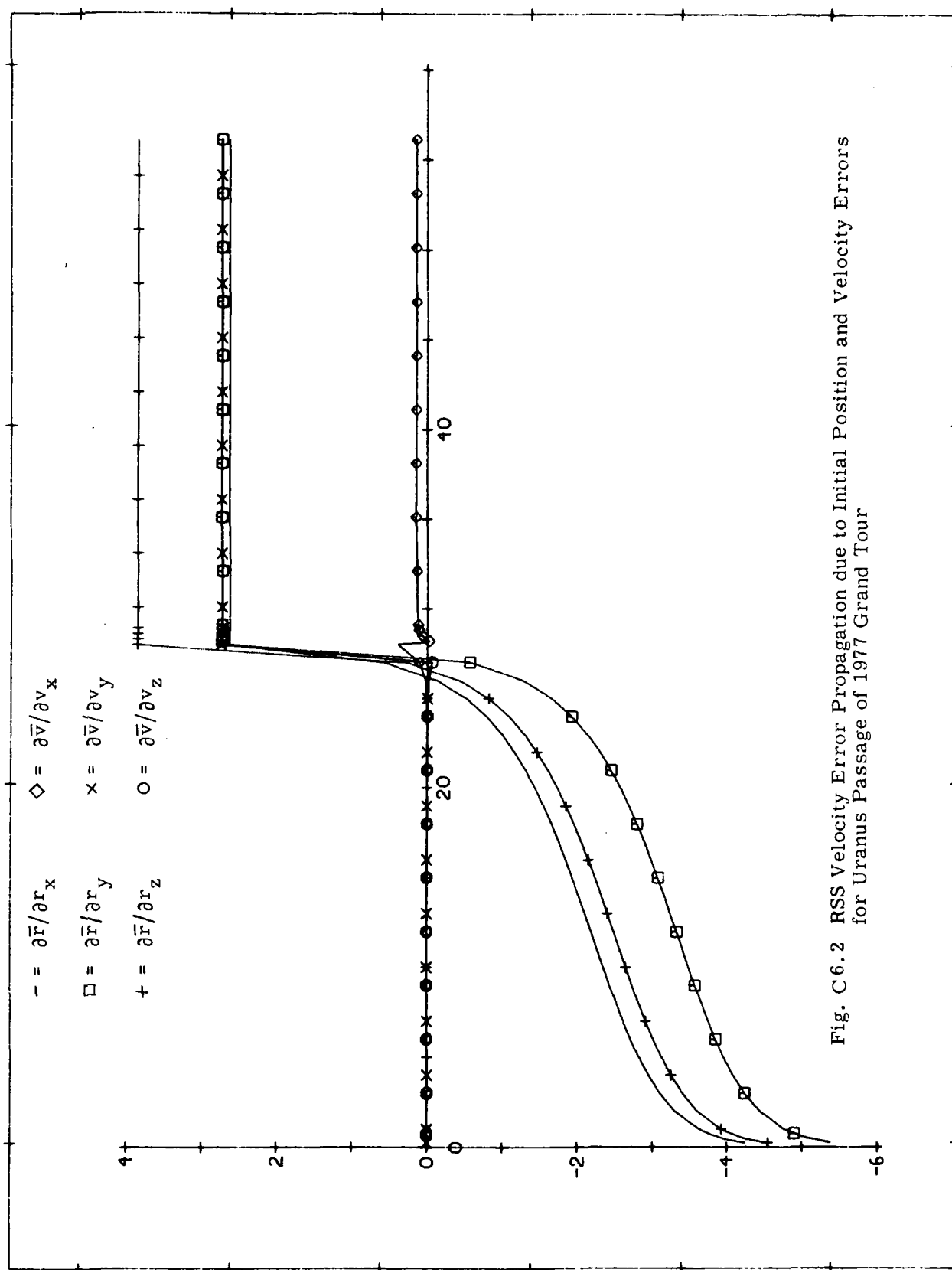


Fig. C6.2 RSS Velocity Error Propagation due to Initial Position and Velocity Errors
for Uranus Passage of 1977 Grand Tour

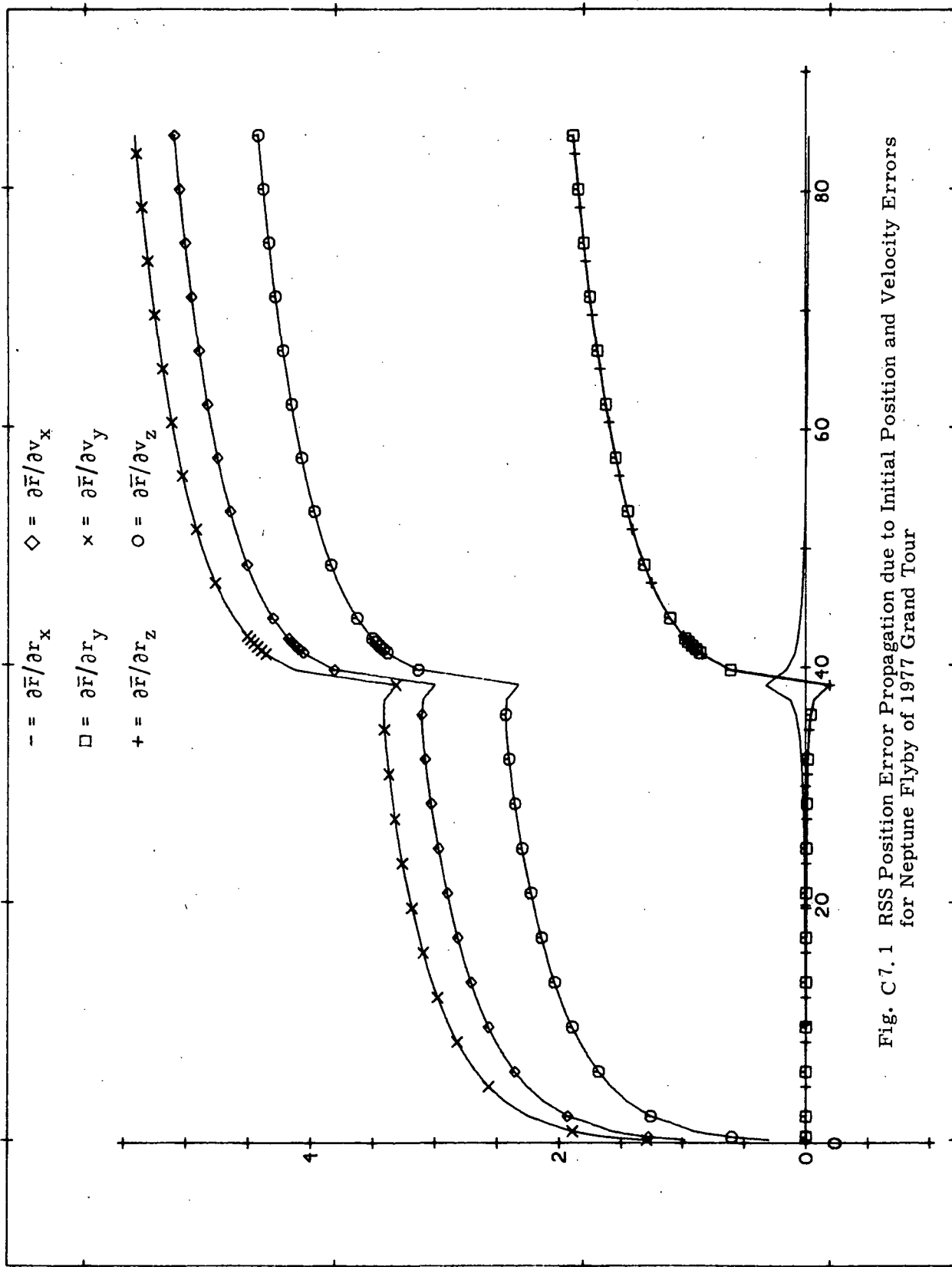


Fig. C7.1 RSS Position Error Propagation due to Initial Position and Velocity Errors for Neptune Flyby of 1977 Grand Tour

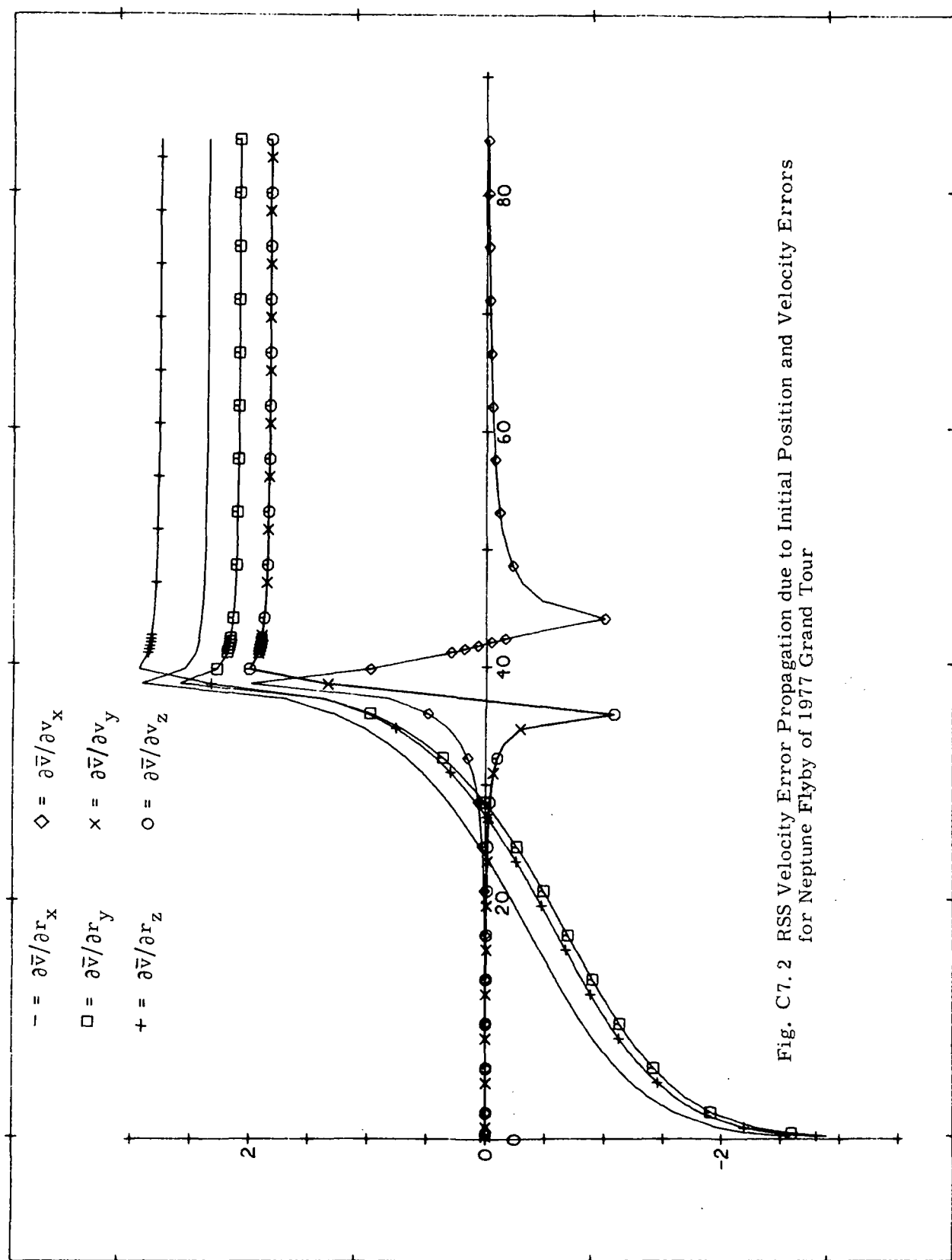


Fig. C7.2 RSS Velocity Error Propagation due to Initial Position and Velocity Errors
for Neptune Flyby of 1977 Grand Tour

Page intentionally left blank

APPENDIX D

ASPECT PROGRAM PLOTS

Early in the Phase A Study, frequent discussions were held involving the geometry of the following elements of the navigation sighting:

- a) Planet Subtended Angle
- b) Orientation of Terminator and sunlit/dark sides
- c) Star orientation
- d) Navigation Instrument slit geometry.

It was decided to program the sighting geometry. The graphical results of this program applied to outer planet sighting situations is given in this Appendix. It was never intended that this pictorialization would play a significant part in the generation of the contract end items. It was thought rather that the visual portrayal would assist in interpreting the end item results, and supplementing the understanding gained from the numerical answers.

From these plots for example, we learn that sighting geometry produced by out-of-plane star locations (see Fig. D. 1) will place the planet horizon substellar point near the intersection of the terminator with the planet outline. This is an inferior horizon segment to be forced to use, because it is near the transition from lightside to darkside. A description of the plotting routine is given below:

1. "Star" and "Sun" are the projections of these unit vectors into the viewing plane. The x and y components of these vectors are seen in the picture, which means that the z component is either into or out of the plane. For example Figure D.1 shows Jupiter and the Star and sun: the sun is "behind" you or up out of the plane of view.

2. The small box in the center represents the dimensions of an optical slit 10 seconds of arc by 1 min. of arc. The outer dimensions are scaled off of the slit dimensions such that the vertical dimension is 40 times the slit vertical dimension, and the horizontal dimension is 1.5 times the

vertical regardless of the horizontal dimension of the optical slit.

3. SUNLIT and UNLIT tell whether the point on the planet that you are viewing, as defined by the aim point cross within the small box, is Sunlit or dark.

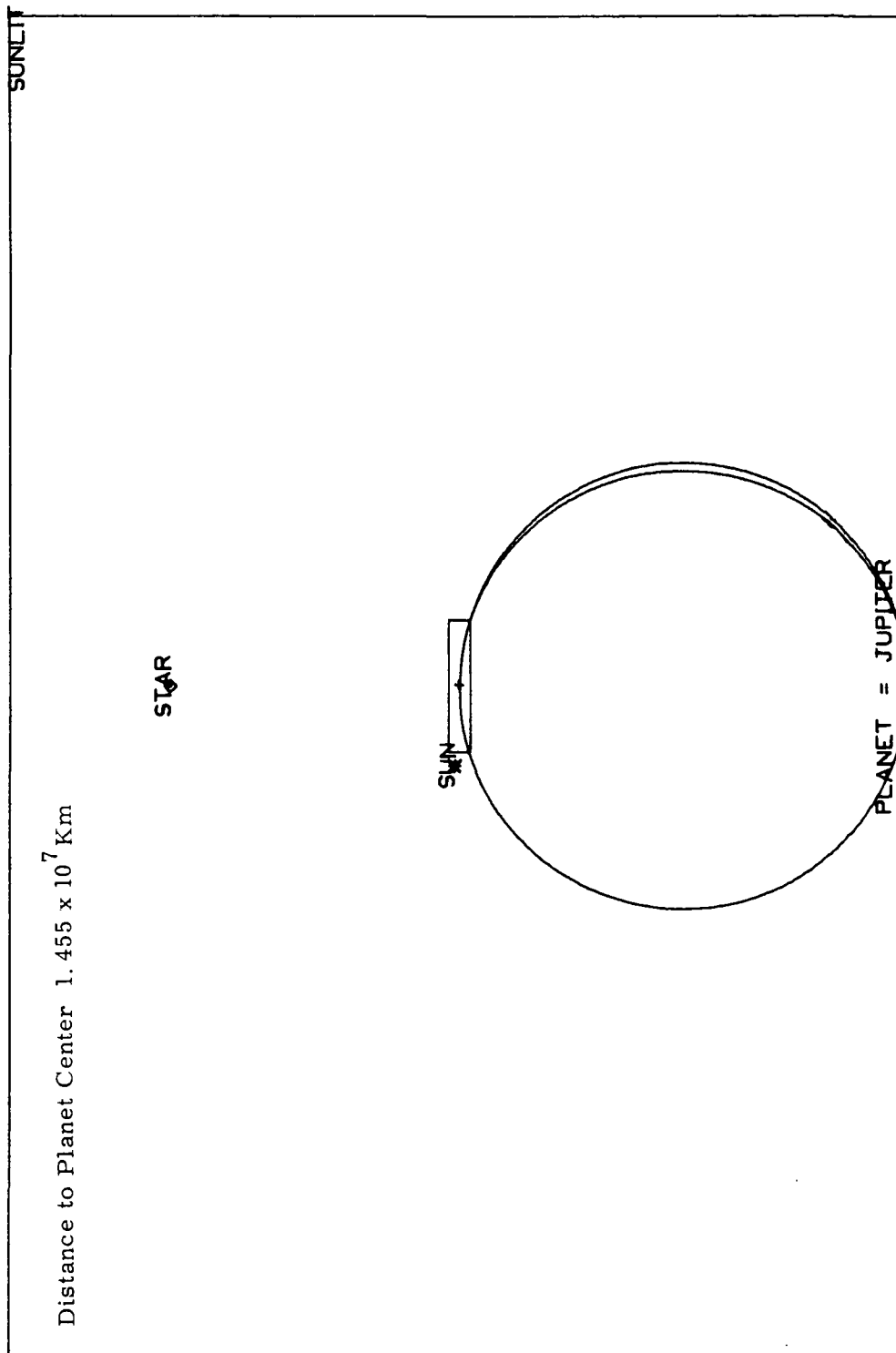


Fig. D. 1. Aspect of Jupiter on the Earth-Jupiter Leg of the Grand Tour at 371 Days.
Star = Canopus.

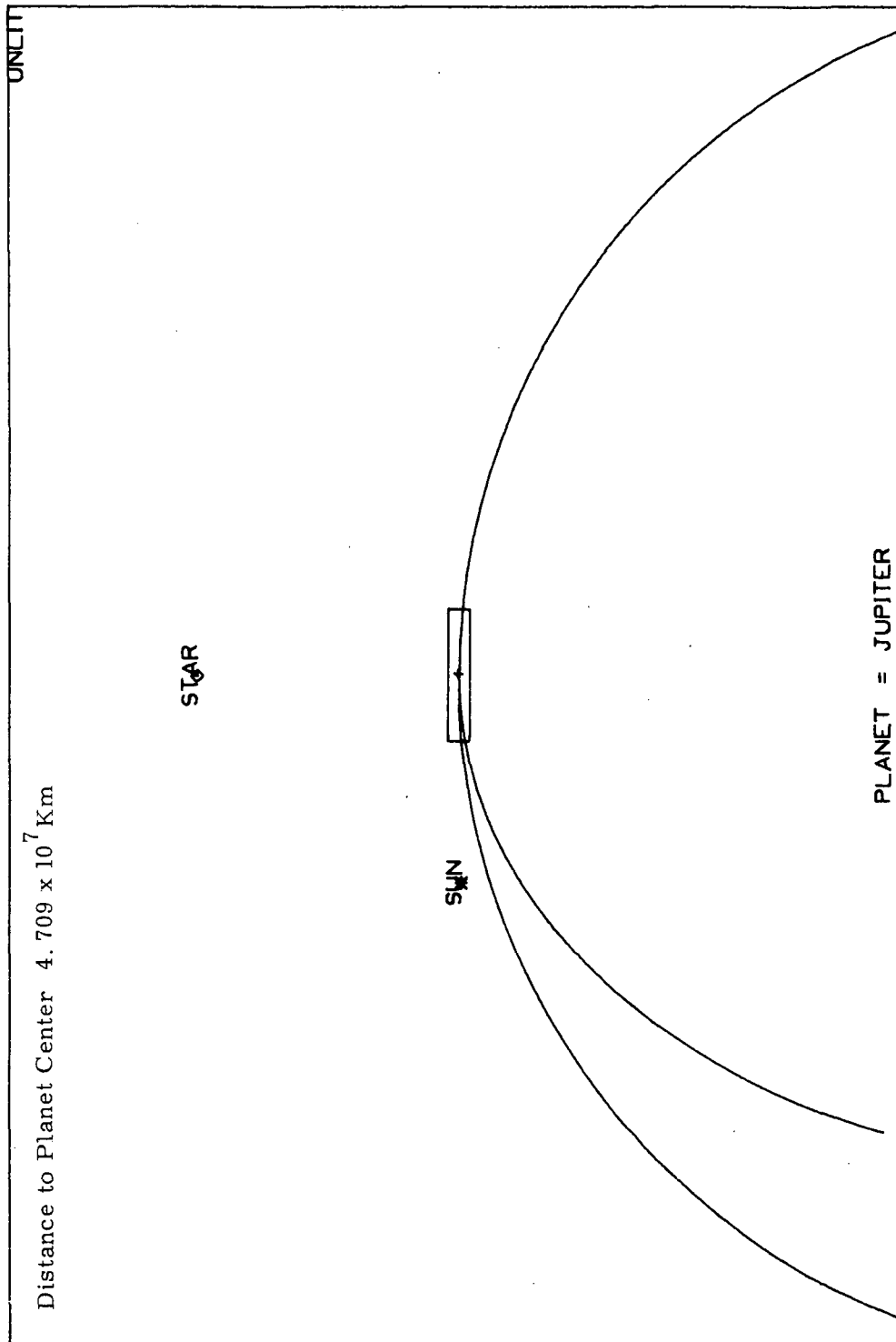


Fig. D. 2. Aspect of Jupiter on the Passage Phase of the Grand Tour
at 1 Day within the Sphere of Influence.
Star = Vega

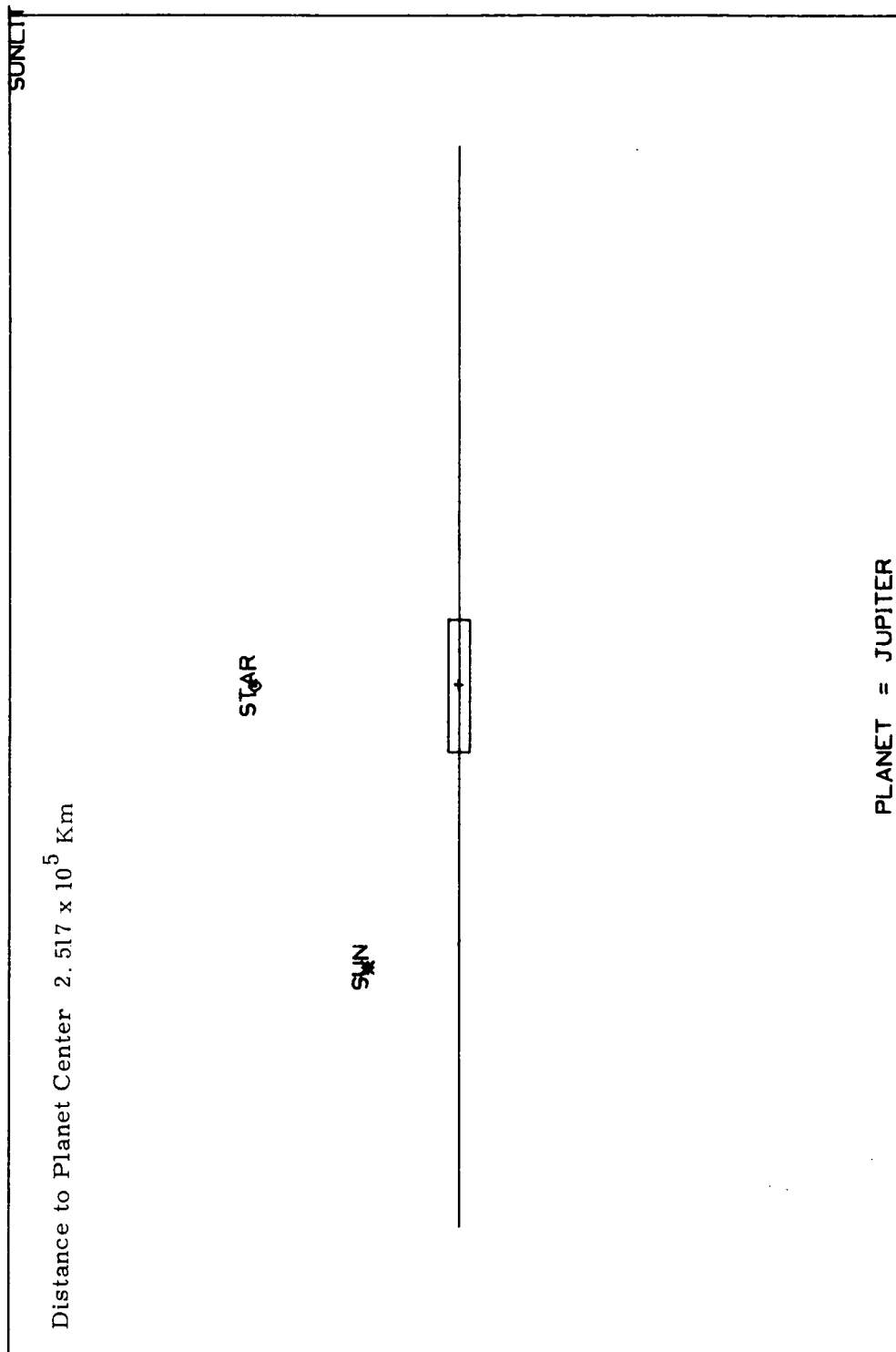
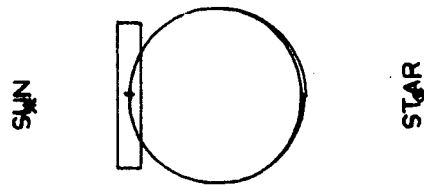


Fig. D. 3. Aspect of Jupiter on the Passage Phase at Periplanet of the Grand Tour.
Star = Eridani

Distance to Planet Center 1.416×10^8 Km



PLANET = URANUS

Fig. D. 4. Aspect of Uranus on the Saturn-Uranus Leg After 1142 Days.
Star: Virginus.

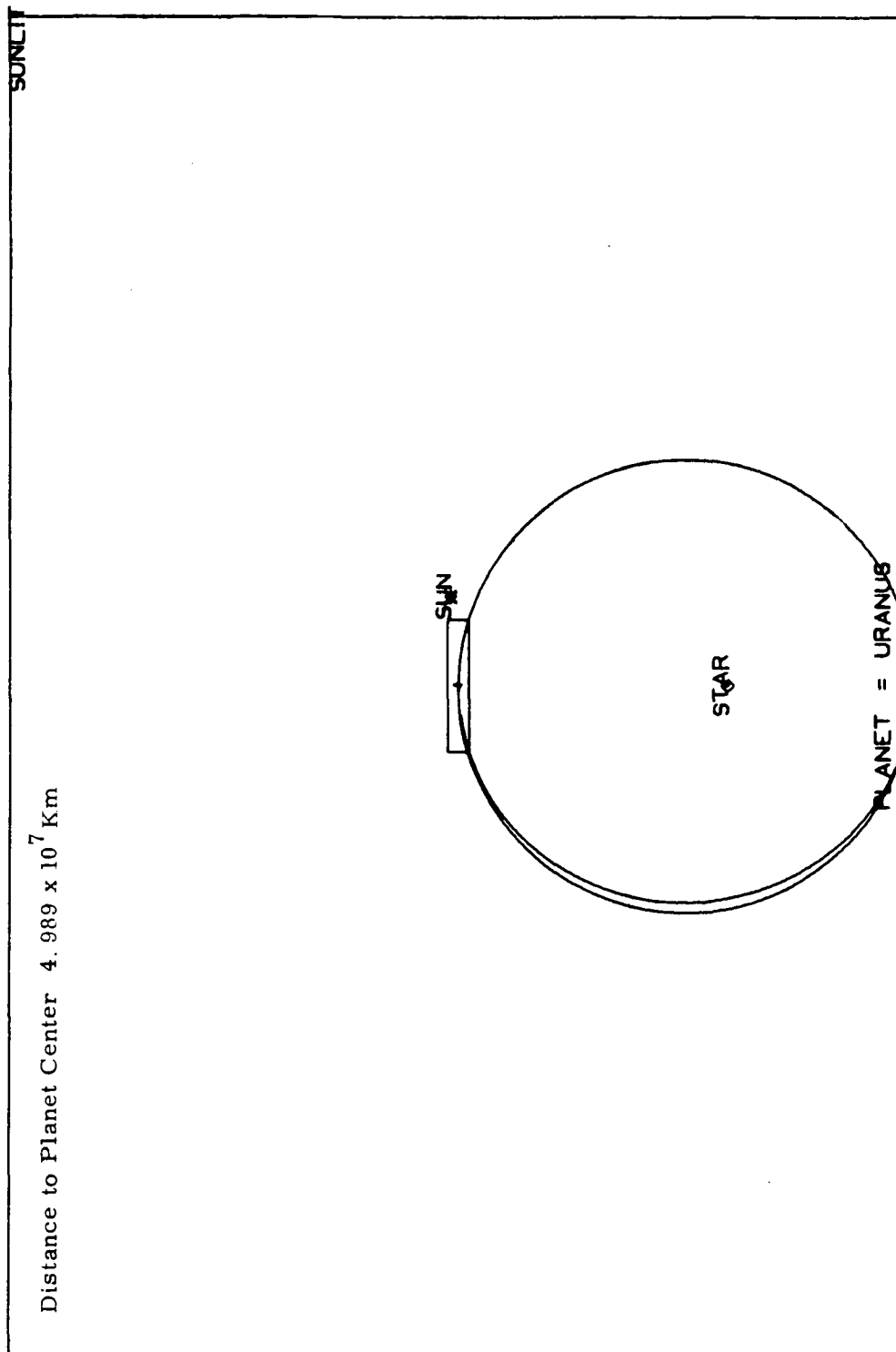


Fig. D. 5. Aspect of Uranus During Uranus Passage 1 Day into the Sphere of Influence Star: Polaris

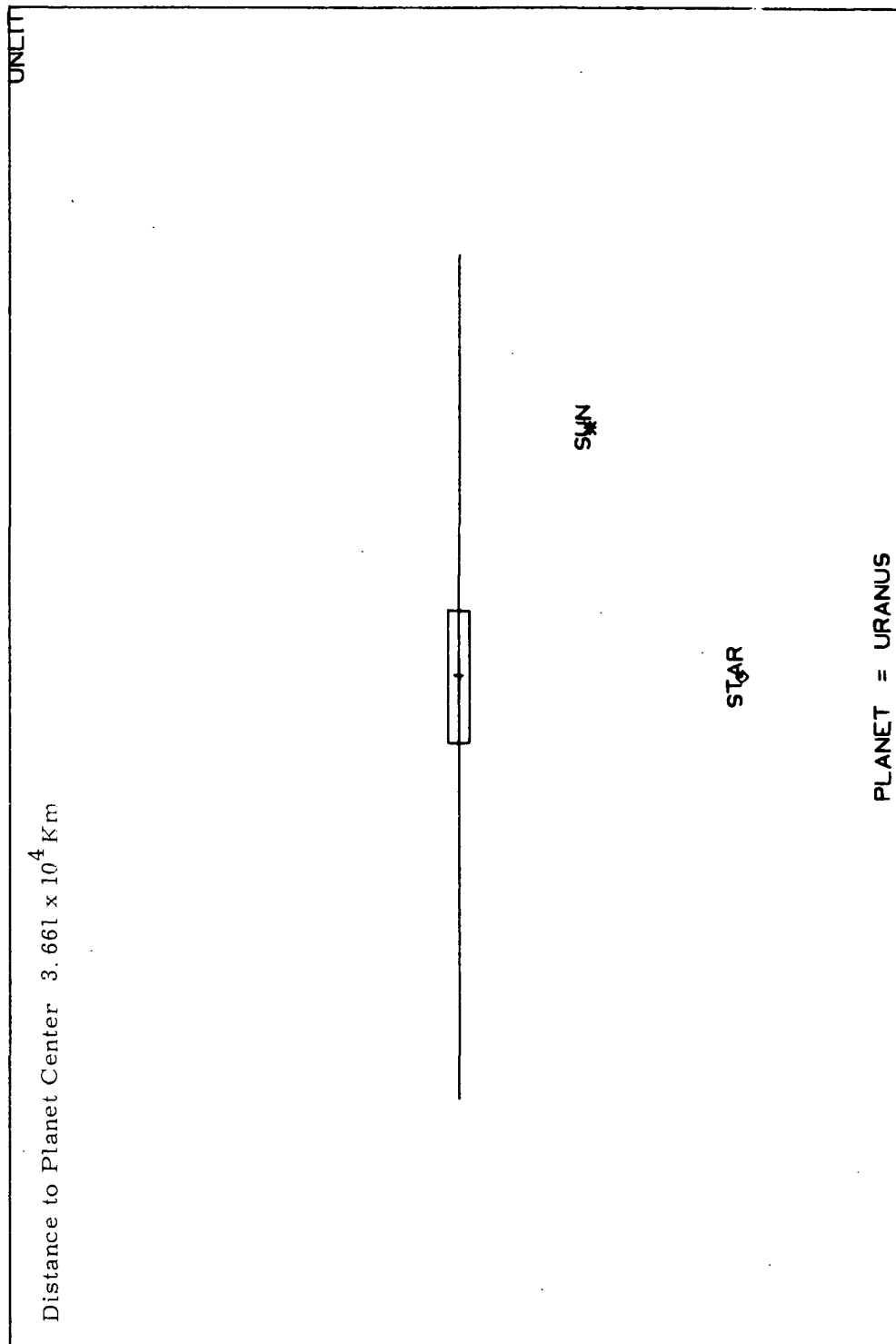


Fig. D. 6. Aspect of Uranus During Uranus Passage 28 Days into the Sphere of Influence.
Star: Andromeda

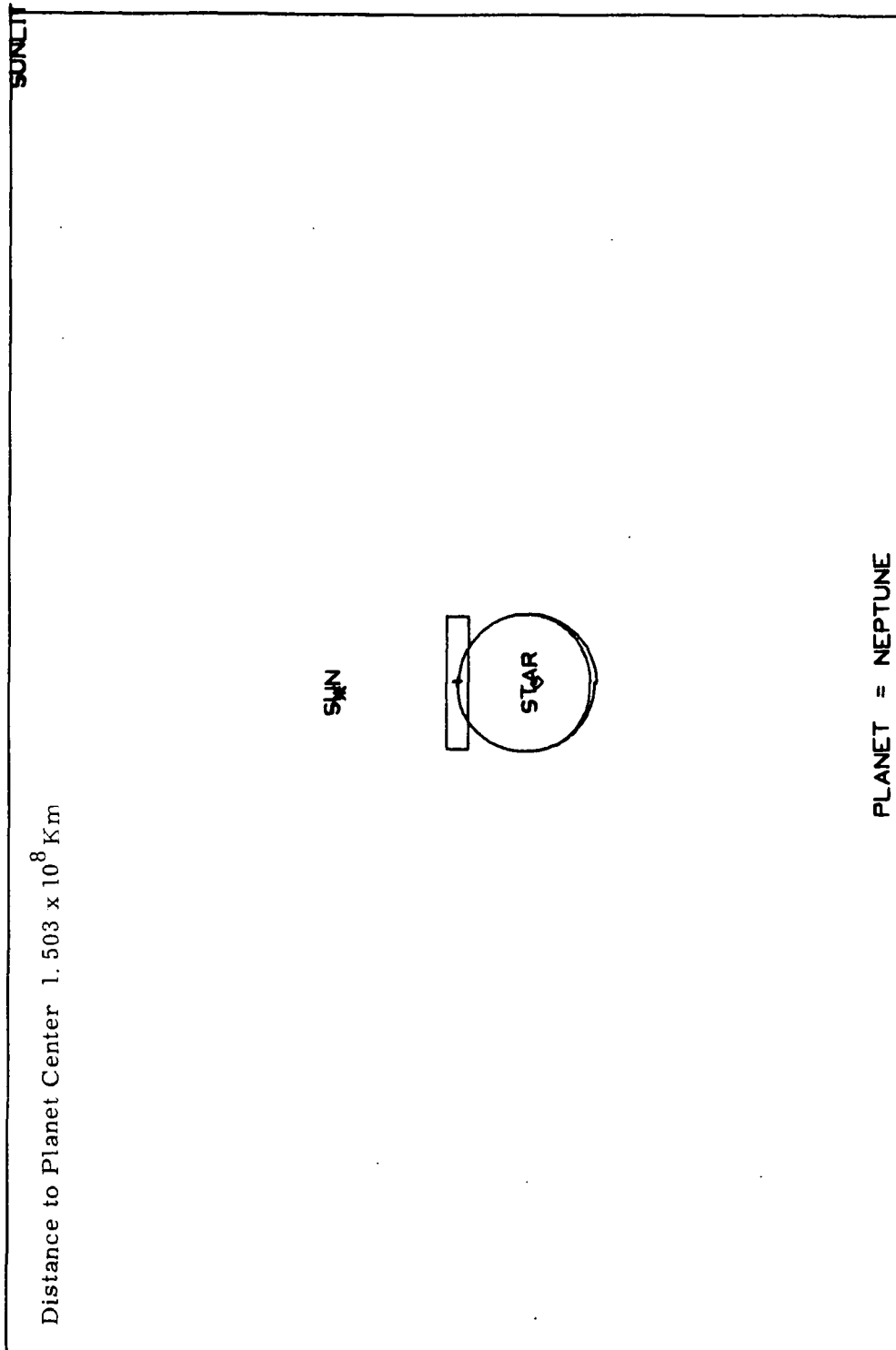
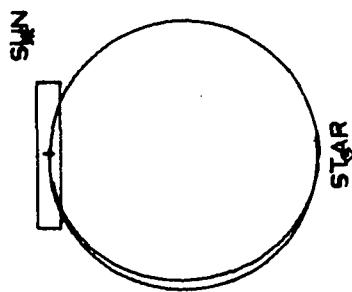


Fig. D. 7. Aspect of Neptune on the Uranus-Neptune Leg of the Grand Tour, at
922 Days
Star = Sagittarius

Distance to Planet Center 8.467×10^7 Km



PLANET = NEPTUNE

Fig. D. 8. Aspect of Neptune During Neptune Passage on the Grand Tour,
1 Day Within the Sphere of Influence,
Star: Vega

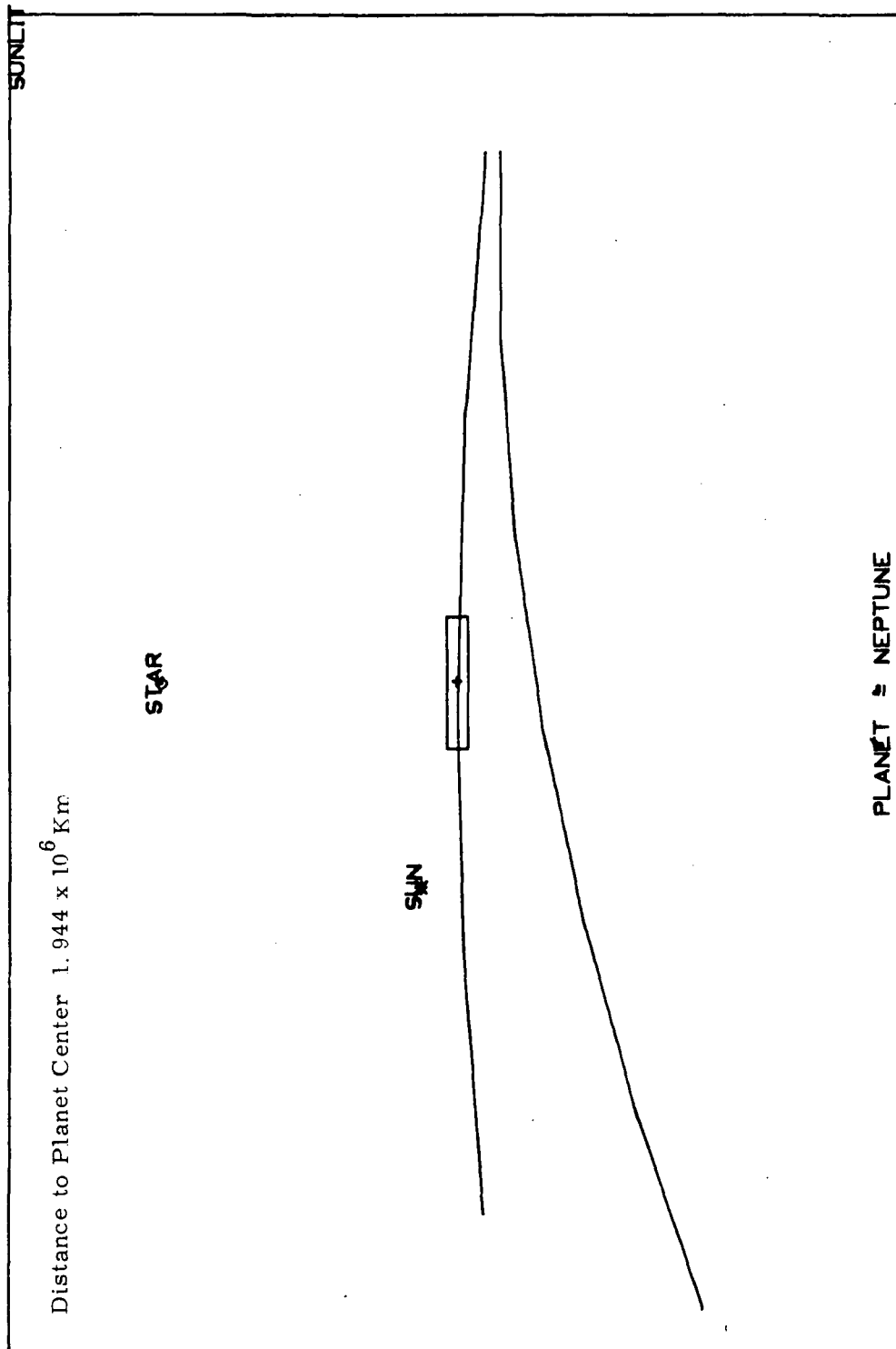


Fig. D. 9. Aspect of Neptune During Periplanet Passage on the Grand Tour.
Star = Canopus

Page intentionally left blank

APPENDIX E

DERIVATION OF THE FILTER ALGORITHMS

A general description of the analytic approach used to perform the error analysis which is fundamental to the tradeoff between the candidate navigation schemes was given in Chapter II. In this appendix the equations which this error analysis consists of are derived in detail. The resulting equations have the form of a set of recursion formulas.

A. Recursive Filtering with Unestimated Biases

The following quantities will be necessary for a complete statistical simulation of the guided flight:

E The covariance matrix of state estimation errors:

$$\overline{\underline{e} \underline{e}^T} \quad (9 \times 9)^*$$

X The covariance matrix of actual state deviations from

the reference trajectory: $\overline{\underline{\delta x} \underline{\delta x}^T} \quad (9 \times 9)$

S The correlation between the error in the estimate of the state and the station location biases:

$$\overline{\underline{e} \underline{b}^T} \quad (9 \times 2)$$

*Numbers in parenthesis indicate the dimension of the variable for a nine dimensional state, for a two dimensional station location error, and for a scalar gravitational parameter uncertainty.

- v The correlation between the error in the state estimate and the planet gravitational parameter uncertainty:

$$\overline{\underline{e} \delta \mu} \quad (9 \times 1)$$

- j The correlation between the actual state deviation from the reference trajectory and the planet gravitational

$$\text{parameter uncertainty: } \overline{\delta \underline{x} \delta \mu} \quad (9 \times 1)$$

- C The correlation between the state estimate and the error in the state estimate (zero for "Kalman" filter but not here because of the planet gravitational

$$\text{parameter uncertainty): } \overline{\delta \underline{x}^{\wedge} \underline{e}^T} \quad (9 \times 9)$$

Before beginning with the development of these recursion formulas it is useful to note how the state estimate ($\delta \underline{x}^{\wedge}$), error in the state estimate (\underline{e}), and actual deviation from the reference trajectory ($\delta \underline{x}$) behave during each of the steps mentioned above. The notion of statistically describing actual deviations to completely simulate guided flight is due to Battin²⁹.

EXTRAPOLATION:

$$\delta \underline{x}_{n+1}^{\wedge} = \Phi_{n+1,n} \delta \underline{x}_n^{\wedge}$$

$$\underline{e}_{n+1}' = \Phi_{n+1,n} \underline{e}_n - \underline{m}_{n+1,n} \delta \mu$$

$$\delta \underline{x}_{n+1}' = \Phi_{n+1,n} \delta \underline{x}_n + \underline{m}_{n+1,n} \delta \mu$$

where:

$\Phi_{n+1,n}$ = state transition matrix for the linearized state equations

$$\underline{m}_{n+1,n} = \frac{\partial \underline{x}_{n+1}}{\partial \mu}$$

$$\underline{e}_n \triangleq \delta \hat{\underline{x}}_n - \delta \underline{x}_n$$

and primed quantities (double or single) indicate that the measurement has not been incorporated at the indicated time.

MIDCOURSE VELOCITY CORRECTION:

$$\delta \hat{\underline{x}}_n'' = (I + M B_n) \delta \hat{\underline{x}}_n'$$

$$\underline{e}_n'' = \underline{e}_n' + M \underline{\nu}_n$$

$$\delta \hat{\underline{x}}_n'' = (I + M B_n) \delta \hat{\underline{x}}_n' + M B_n \underline{e}_n' - M \underline{\nu}_n^{\#}$$

where:

$\underline{\nu}_n$ = unobservable part of velocity correction implementation error (due to instrument errors)

$\underline{\nu}_n^{\#}$ = velocity correction implementation error.

$$M = \begin{bmatrix} 0 \\ I \end{bmatrix}$$

$$B_n = [C_n^* - I]$$

and C_n^* is a 3×3 matrix which is the partial derivative of the correlated velocity at time t_n with respect to the position at time t_n . The correlated

velocity at time t_n is that velocity required by the spacecraft to travel in free fall under the action of gravity only from its present position to the target point. Methods for evaluating C_n^* are given in Reference 29.

ONBOARD NAVIGATION MEASUREMENT:

$$\hat{\delta \underline{x}}_{-n} = \hat{\delta \underline{x}}_{-n}' + \underline{w}_n (z_n - \underline{h}_{-n}^T \hat{\delta \underline{x}}_{-n}')$$

$$\underline{e}_{-n} = (I - \underline{w}_n \underline{h}_{-n}^T) \underline{e}_{-n}' + \underline{w}_n \eta_n$$

$$\delta \underline{x}_{-n} = \delta \underline{x}_{-n}'$$

where

$$z_n = \text{the measurement}$$

$$\underline{h}_{-n} = (\partial z_n / \partial \underline{x}_{-n})^T$$

$$\underline{w}_n = \text{gain vector to be computed below.}$$

$$\eta_n = \text{white measurement noise.}$$

DSN MEASUREMENT:

$$\hat{\delta \underline{x}}_{-n} = \hat{\delta \underline{x}}_{-n}' + W_n (z_n - H_n \hat{\delta \underline{x}}_{-n}')$$

$$\underline{e}_{-n} = (I - W_n H_n) \underline{e}_{-n}' + W_n (G_n b + \eta_n)$$

$$\delta \underline{x}_{-n} = \delta \underline{x}_{-n}'$$

where \underline{z}_n , H_n , W_n and $\underline{\eta}_n$ have analogous definitions to the onboard measurement case.

Recursion formulas for each of the required statistical variables will now be obtained.

E matrix:

Extrapolation:

$$\begin{aligned} E_n' &= \overline{\underline{e}_n' \underline{e}_n'^T} = \Phi_{n,n-1} \overline{\underline{e}_{n-1} \underline{e}_{n-1}^T} \Phi_{n,n-1}^T \\ &\quad - \Phi_{n,n-1} \overline{\underline{e}_{n-1} \delta\mu \underline{m}_{n,n-1}^T} - \overline{\underline{m}_{n,n-1} \delta\mu \underline{e}_{n-1}^T} \Phi_{n,n-1}^T \\ &\quad + \overline{\underline{m}_{n,n-1} \delta\mu^2 \underline{m}_{n,n-1}^T} \end{aligned}$$

$$\begin{aligned} E_n' &= \Phi_{n,n-1} E_{n-1} \Phi_{n,n-1}^T - \Phi_{n,n-1} \overline{\underline{v}_{n-1} \underline{m}_{n,n-1}^T} \\ &\quad - \overline{\underline{m}_{n,n-1} \underline{v}_{n-1}^T} \Phi_{n,n-1}^T + \overline{\underline{m}_{n,n-1} \underline{m}_{n,n-1}^T \delta\mu^2} \end{aligned}$$

Velocity Correction:

$$E_n'' = \overline{\underline{e}_n'' \underline{e}_n''^T} = \overline{\underline{e}_n' \underline{e}_n'^T} + M \overline{\underline{\nu}_n \underline{\nu}_n^T} M^T$$

$$E_n'' = E_n' + M Q_n M^T$$

$$\text{where } Q_n = \overline{\underline{\nu}_n \underline{\nu}_n^T}$$

Onboard Measurement:

$$\begin{aligned} E_n = \overline{e_n e_n^T} &= (I - \underline{w}_n \underline{h}_n^T) \overline{e_n' e_n'^T} (I - \underline{w}_n \underline{h}_n^T)^T \\ &+ \underline{w}_n \overline{\eta_n^2} \underline{w}_n^T \end{aligned}$$

$$E_n = (I - \underline{w}_n \underline{h}_n^T) E_n' (I - \underline{w}_n \underline{h}_n^T)^T + \underline{w}_n r_n \underline{w}_n^T$$

where

$$r_n = \overline{\eta_n^2}$$

DSN Measurement:

$$\begin{aligned} E_n = \overline{e_n e_n^T} &= (I - W_n H_n^T) \overline{e_n' e_n'^T} (I - W_n H_n^T)^T \\ &+ (I - W_n H_n^T) \overline{e_n' b^T} G_n^T W_n^T + W_n G_n \overline{b e_n'^T} (I - W_n H_n^T)^T \\ &+ W_n G_n \overline{b b^T} G_n^T W_n^T + W_n \overline{\eta_n \eta_n^T} W_n^T \end{aligned}$$

$$\begin{aligned} E_n &= (I - W_n H_n^T) E_n' (I - W_n H_n^T)^T + (I - W_n H_n^T) S_n' G_n^T W_n^T \\ &+ W_n G_n S_n'^T (I - W_n H_n^T)^T + W_n G_n \beta G_n^T W_n^T \\ &+ W_n R_n W_n^T \end{aligned}$$

(E. 1)

$$\text{where } \beta = \overline{b b^T}, R_n = \overline{\eta_n \eta_n^T}$$

X Matrix:

Extrapolation:

$$\begin{aligned}
 \underline{X}_n' &= \overline{\delta \underline{x}_n' \delta \underline{x}_n'^T} = \overline{\Phi_{n,n-1} \delta \underline{x}_{n-1} \delta \underline{x}_{n-1}^T \Phi_{n,n-1}^T} \\
 &+ \overline{\Phi_{n,n-1} \delta \underline{x}_{n-1} \delta \mu \underline{m}_{n,n-1}^T} + \overline{\underline{m}_{n,n-1} \delta \mu \delta \underline{x}_{n-1}^T \Phi_{n,n-1}^T} \\
 &+ \overline{\underline{m}_{n,n-1} \delta \mu^2 \underline{m}_{n,n-1}^T} \\
 \underline{X}_n' &= \Phi_{n,n-1} \underline{X}_{n-1} \Phi_{n,n-1}^T + \Phi_{n,n-1} \underline{j}_{n-1} \underline{m}_{n,n-1}^T \\
 &+ \underline{m}_{n,n-1} \underline{j}_{n-1}^T \Phi_{n,n-1}^T + \underline{m}_{n,n-1} \overline{\delta \mu^2} \underline{m}_{n,n-1}^T
 \end{aligned}$$

Velocity Correction:

$$\begin{aligned}
 \underline{X}_n'' &= \overline{\delta \underline{x}_n'' \delta \underline{x}_n''^T} = (I + M B_n) \overline{\delta \underline{x}_n' \delta \underline{x}_n'^T} (I + M B_n)^T \\
 &+ (I + M B_n) \overline{\delta \underline{x}_n' \underline{e}_n'^T B_n^T M^T} + \overline{M B_n \underline{e}_n' \delta \underline{x}_n'^T} (I + M B_n)^T \\
 &+ \overline{M B_n \underline{e}_n' \underline{e}_n'^T B_n^T M^T} + \overline{M \underline{\nu}_n^\# \underline{\nu}_n^\#^T M^T} \\
 \underline{X}_n'' &= (I + M B_n) (\underline{X}_n' - E_n') (I + M B_n)^T + (I + M B_n) C_n' B_n^T M^T \\
 &+ M B_n C_n'^T (I + M B_n)^T + M Q_n^\# M^T + E_n'
 \end{aligned}$$

Onboard or DSN Measurement:

$$\begin{aligned}
 \underline{X}_n &= \overline{\delta \underline{x}_n \delta \underline{x}_n^T} = \overline{\delta \underline{x}_n' \delta \underline{x}_n'^T} \\
 \underline{X}_n &= \underline{X}_n'
 \end{aligned}$$

S Matrix:

Extrapolation:

$$\underline{S}_n' = \overline{\underline{e}_n' \underline{b}^T} = \underline{\Phi}_{n,n-1} \overline{\underline{e}_{n-1} \underline{b}^T} - \underline{m}_{n,n-1} \overline{\delta \underline{\mu} \underline{b}^T}$$

$$\underline{S}_n' = \underline{\Phi}_{n,n-1} \underline{S}_{n-1}$$

Velocity Correction:

$$\underline{S}_n'' = \overline{\underline{e}_n'' \underline{b}^T} = \overline{\underline{e}_n' \underline{b}^T} + M \overline{\underline{\nu} \underline{b}^T}$$

$$\underline{S}_n'' = \underline{S}_n'$$

Onboard Measurement:

$$\underline{S}_n = \overline{\underline{e}_n \underline{b}^T} = (\underline{I} - \underline{w}_n \underline{h}_n^T) \overline{\underline{e}_n' \underline{b}^T} + \underline{w}_n \overline{\eta_n \underline{b}^T}$$

$$\underline{S}_n = (\underline{I} - \underline{w}_n \underline{h}_n^T) \underline{S}_n'$$

DSN Measurement:

$$\underline{S}_n = \overline{\underline{e}_n \underline{b}^T} = (\underline{I} - \underline{W}_n \underline{H}_n) \overline{\underline{e}_n' \underline{b}^T} + \underline{W}_n (\overline{\underline{G}_n \underline{b} \underline{b}^T} + \underline{\eta}_n \underline{b}^T)$$

$$\underline{S}_n = (\underline{I} - \underline{W}_n \underline{H}_n) \underline{S}_n' + \underline{W}_n \underline{G}_n \underline{\beta}$$

v vector :

Extrapolation:

$$\underline{v}_n' = \overline{\underline{e}_n \delta \mu} = \Phi_{n,n-1} \overline{\underline{e}_{n-1} \delta \mu} + \overline{\underline{m}_{n,n-1} \delta \mu^2}$$

$$\underline{v}_n' = \Phi_{n,n-1} \underline{v}_{n-1} - \overline{\underline{m}_{n,n-1} \delta \mu^2}$$

Velocity Correction:

$$\underline{v}_n'' = \overline{\underline{e}_n'' \delta \mu} = \overline{\underline{e}_n' \delta \mu} + M \overline{\underline{v}_n \delta \mu}$$

$$\underline{v}_n'' = \underline{v}_n'$$

Onboard Measurement:

$$\underline{v}_n = \overline{\underline{e}_n \delta \mu} = (I - \underline{w}_n \underline{h}_n^T) \overline{\underline{e}_n' \delta \mu} + \overline{\underline{w}_n \eta_n \delta \mu}$$

$$\underline{v}_n = (I - \underline{w}_n \underline{h}_n^T) \underline{v}_n'$$

DSN Measurement:

$$\underline{v}_n = \overline{\underline{e}_n \delta \mu} = (I - \underline{W}_n \underline{H}_n) \overline{\underline{e}_n' \delta \mu} + \overline{\underline{W}_n (\underline{G}_n \underline{b} \delta \mu + \underline{\eta}_n \delta \mu)}$$

$$\underline{v}_n = (I - \underline{W}_n \underline{H}_n) \underline{v}_n'$$

j vector:

Extrapolation:

$$\underline{j}_n' = \overline{\delta \underline{x}_n'} \delta \mu = \overline{\Phi_{n,n-1} \delta \underline{x}_{n-1}'} \delta \mu + \overline{m_{n,n-1} \delta \mu^2}$$

$$\underline{j}_n = \Phi_{n,n-1} \underline{j}_{n-1} + \overline{m_{n,n-1} \delta \mu^2}$$

Velocity Correction .

$$\begin{aligned} \underline{j}_n'' &= \overline{\delta \underline{x}_n''} \delta \mu = \overline{(I + M B_n) \delta \underline{x}_n'} \delta \mu + \overline{M B_n \underline{e}_n'} \delta \mu \\ &\quad - \overline{M \underline{v}_n^{\#}} \delta \mu \end{aligned}$$

$$\underline{j}_n'' = (I + M B_n) \underline{j}_n' + M B_n \underline{v}_n'$$

Onboard or DSN Measurement

$$\underline{j}_n = \overline{\delta \underline{x}} \delta \mu = \overline{\delta \underline{x}'} \delta \mu$$

$$\underline{j}_n = \underline{j}_n'$$

C Matrix:

Extrapolation:

$$C_n' = \overline{\delta \underline{x}_n' e_n'^T} = \Phi_{n,n-1} \overline{\delta \underline{x}_{n-1}' e_{n-1}'^T} \Phi_{n,n-1}^T \\ - \Phi_{n,n-1} \overline{\delta \underline{x}_{n-1}' \delta \mu m_{n,n-1}^T}$$

$$C_n' = \Phi_{n,n-1} C_{n-1} \Phi_{n,n-1}^T - \Phi_{n,n-1} (j_{n-1} + v_{n-1}) m_{n,n-1}^T$$

Velocity Correction

$$C_n'' = \overline{\delta \underline{x}_n'' e_n''^T} = (I + M B_n) \left[\overline{\delta \underline{x}_n' e_n'^T} + \overline{\delta \underline{x}_n' v_n^T} M^T \right]$$

$$C_n'' = (I + M B_n) C_n'$$

Onboard Measurement

is added to the state estimate and the covariance matrix is updated as follows:

$$C_n = \overline{\delta \underline{x}_n e_n^T} = \left[\overline{\delta \underline{x}_n'} + \underline{w}_n (\underline{h}_n^T \underline{e}_n' + \eta_n) \right] \overline{\delta \underline{x}_n'^T}$$

where \underline{e}_n is the measurement residual, η_n is the measurement noise, and \underline{w}_n is the Kalman gain.

$$\left[(I - \underline{w}_n \underline{h}_n^T) \underline{e}_n' + \underline{w}_n \eta_n \right]^T$$

$$C_n = C_n' (I - \underline{w}_n \underline{h}_n^T)^T - \underline{w}_n \underline{h}_n^T \overline{\delta \underline{x}_n' e_n'^T} (I - \underline{w}_n \underline{h}_n^T)^T$$

where \underline{e}_n is the measurement residual, η_n is the measurement noise, and \underline{w}_n is the Kalman gain.

$$+ \underline{w}_n \underline{r}_n \underline{w}_n^T$$

Using (E.1) to evaluate the covariance matrix, the updated covariance matrix is given by:

(E. 2)

$$\hat{C}_n = (I - \underline{w}_n \underline{h}_n^T) \hat{C}_{n-1} (I - \underline{w}_n \underline{h}_n^T)^T - \underline{w}_n \underline{h}_n^T \hat{C}_{n-1} \underline{h}_n \underline{w}_n^T + \underline{w}_n \underline{r}_n \underline{w}_n^T$$

$$\hat{C}_n = (I - \underline{w}_n \underline{h}_n^T) \hat{C}_{n-1} (I - \underline{w}_n \underline{h}_n^T)^T - \underline{w}_n \underline{h}_n^T \hat{C}_{n-1} \underline{h}_n \underline{w}_n^T + \underline{w}_n \underline{r}_n \underline{w}_n^T$$

$$\hat{C}_n = (I - \underline{w}_n \underline{h}_n^T) \hat{C}_{n-1} (I - \underline{w}_n \underline{h}_n^T)^T - \underline{w}_n \underline{h}_n^T \hat{C}_{n-1} \underline{h}_n \underline{w}_n^T + \underline{w}_n \underline{r}_n \underline{w}_n^T$$

DSN Measurement:

$$\begin{aligned}
 C_n \delta \hat{x}_n e_n^T &= \frac{[\delta \hat{x}_n^T + W_n (-H_n e_n^T + G_n b + \eta_n)]}{[(I - W_n H_n) e_n^T + W_n (G_n b + \eta_n)]^T} \\
 C_n &= (C_n^T - W_n H_n E_n^T + W_n G_n S_n^T) (I - W_n H_n)^T \\
 &\quad - W_n H_n S_n^T G_n^T W_n^T + W_n G_n \beta G_n^T W_n^T \\
 &\quad + W_n R_n W_n^T
 \end{aligned} \tag{E. 3}$$

The only remaining part of this scheme to be defined is the optimal choice of the gains W_n and w_n . This is the solution to an algebraic variational problem as follows:

Let us minimize some linear combination of the error E_n :

$$\text{minimize } J = \text{tr} (L E_n)$$

where L is an arbitrary real matrix

Using Eq. (E.1) to evaluate J for a DSN measurement gives:

$$\begin{aligned}
 J = \text{tr} (L E_n) &= \text{tr} [L \{ (I - W_n H_n) E_n (I - W_n H_n)^T \\
 &\quad + (I - W_n H_n) S_n^T G_n^T W_n^T + W_n G_n S_n^T (I - W_n H_n)^T \\
 &\quad + W_n G_n \beta G_n^T W_n^T + W_n R_n W_n^T \}]
 \end{aligned}$$

Taking the variation of J and keeping only those terms which depend upon W_n yields, using the commutative property of conformable quantities inside the argument of the trace:

$$\delta J = 0 = \text{tr} \{ 2 (G_n S_n'^T - H_n E_n') L \delta W_n + K W_n^T L \delta W_n + K W_n^T L \delta W_n \}$$

where

$$K = H_n E_n' H_n^T - H_n S_n' G_n^T - G_n S_n'^T H_n^T + G_n \beta G_n^T + R_n$$

solving for W_n yields the desired result:

$$W_n = (E_n' H_n^T - S_n' G_n^T) (H_n E_n' H_n^T + G_n \beta G_n^T + R_n - G_n S_n'^T H_n^T - H_n S_n' G_n^T)^{-1} \quad (\text{E. 4})$$

Performing a similar analysis for the onboard case gives:

$$\underline{w}_n = E_n' \underline{h}_n (\underline{h}_n^T E_n' \underline{h}_n + r_n)^{-1} \quad (\text{E. 5})$$

which is the familiar "Kalman" gain expression since no uncalibrated bias is assumed to be on the onboard measurement.

If Eqs. (E. 4) and (E. 5) are substituted into Eqs. (E. 2) and (E. 3) the following simplification results:

Onboard Measurement:

$$C_n = C_n' (I - \underline{w}_n \underline{h}_n^T)^T$$

DSN Measurement:

$$C_n = C_n' (I - W_n H_n)^T + S_n' G_n^T W_n^T$$

Summarizing these results we have the following set of recursion formulas:

Extrapolation:

$$\begin{aligned} E_n' &= \Phi_{n,n-1} E_{n-1} \Phi_{n,n-1}^T - \Phi_{n,n-1} \underline{v}_{n-1} \underline{m}_{n,n-1}^T \\ &\quad - \underline{m}_{n,n-1} \underline{v}_{n-1}^T \Phi_{n,n-1}^T + \underline{m}_{n,n-1} \overline{\delta\mu^2} \underline{m}_{n,n-1}^T \end{aligned}$$

$$\begin{aligned} X_n' &= \Phi_{n,n-1} X_{n-1} \Phi_{n,n-1}^T + \Phi_{n,n-1} \underline{j}_{n-1} \underline{m}_{n,n-1}^T \\ &\quad + \underline{m}_{n,n-1} \underline{j}_{n-1}^T \Phi_{n,n-1}^T + \underline{m}_{n,n-1} \overline{\delta\mu^2} \underline{m}_{n,n-1}^T \end{aligned}$$

$$S_n' = \Phi_{n,n-1} S_{n-1}$$

$$\underline{v}_n' = \Phi_{n,n-1} \underline{v}_{n-1} - \underline{m}_{n,n-1} \overline{\delta\mu^2}$$

$$\underline{j}_n' = \Phi_{n,n-1} \underline{j}_{n-1} + \underline{m}_{n,n-1} \overline{\delta\mu^2}$$

$$C_n' = \Phi_{n,n-1} C_{n-1} \Phi_{n,n-1}^T - \Phi_{n,n-1} (\underline{j}_{n-1} + \underline{v}_{n-1}) \underline{m}_{n,n-1}^T$$

Velocity Correction:

$$\underline{E}_n'' = \underline{E}_n' + M \underline{Q}_n M^T$$

$$\begin{aligned} \underline{X}_n'' &= (I + M \underline{B}_n) (\underline{X}_n' - \underline{E}_n') (I + M \underline{B}_n)^T \\ &\quad + (I + M \underline{B}_n) \underline{C}_n' \underline{B}_n^T M^T + M \underline{B}_n \underline{C}_n' (I + M \underline{B}_n)^T \\ &\quad + M \underline{Q}_n^{\#} M^T + \underline{E}_n' \end{aligned}$$

$$\underline{S}_n'' = \underline{S}_n'$$

$$\underline{v}_n'' = \underline{v}_n'$$

$$\underline{j}_n'' = (I + M \underline{B}_n) \underline{j}_n' + M \underline{B}_n \underline{v}_n'$$

$$\underline{C}_n'' = (I + M \underline{B}_n) \underline{C}_n'$$

Onboard Measurement:

$$\underline{w}_n = \underline{E}_n' \underline{h}_n (\underline{h}_n^T \underline{E}_n' \underline{h}_n + \underline{r}_n)^{-1}$$

$$\underline{E}_n = (I - \underline{w}_n \underline{h}_n^T) \underline{E}_n' (I - \underline{w}_n \underline{h}_n^T)^T \underline{w}_n \underline{r}_n \underline{w}_n^T$$

$$\underline{X}_n = \underline{X}_n'$$

$$\underline{S}_n = (I - \underline{w}_n \underline{h}_n^T) \underline{S}_n'$$

$$\underline{v}_n = (I - \underline{w}_n \underline{h}_n^T) \underline{v}_n'$$

$$\underline{j}_n = \underline{j}_n'$$

$$\underline{C}_n = \underline{C}_n' (I - \underline{w}_n \underline{h}_n^T)^T$$

DSN Measurement:

$$W_n = (E_n' H_n^T - S_n' G_n^T) (H_n E_n' H_n^T + G_n \beta G_n^T + R_n \\ - G_n S_n' H_n^T - H_n S_n' G_n^T)^{-1}$$

$$E_n = (I - W_n H_n) E_n' (I - W_n H_n)^T + (I - W_n H_n) S_n' G_n^T W_n^T \\ + W_n G_n S_n' H_n^T (I - W_n H_n)^T + W_n G_n \beta G_n^T W_n^T \\ + W_n R_n W_n^T$$

$$X_n = X_n'$$

$$S_n = (I - W_n H_n) S_n' + W_n G_n \beta$$

$$\underline{v}_n = (I - W_n H_n) \underline{v}_n'$$

$$\underline{j}_n = \underline{j}_n'$$

$$C_n = C_n' (I - W_n H_n)^T + S_n' G_n^T W_n^T$$

B. Coordinate Definitions

The purpose of this section is twofold: 1) to define the state vector used for the study; 2) to develop the transformations which must be performed on the matrices of the previous section when changing coordinate centers.

State Definition.

Different state definitions are used depending upon whether the phase under study is a near planet (inside one Laplacian sphere of influence) or interplanetary part of the mission. In both cases the basic state vector is nine dimensional*. Six of these are the vehicle position and velocity deviations with respect to a two body reference trajectory for which the gravitational center is the center of coordinates. The other three are the components of the planetary positional ephemeris error. The use of only the position components of the ephemeris error instead of both position and velocity components is an approximation which is made in the interest of simplicity and economy. The approximation made is that the velocity error is not significant compared to the positional error. This is valid for two reasons: 1) if the velocity error were not small its integrated effect on the position error would be larger than reported position errors and would be calibrated out; 2) the position errors have the most impact upon the use of the onboard system and are the components which ultimately figure in the miss distance at the target planet.

In applying the filter equations derived in the previous section the most time consuming computations are the matrix multiplications involved in processing the optimal linear filter equations. The computer time required is approximately proportional to the cube of the dimension of the state. (If n is the dimension of the state, each of the n^2 elements of the result of a matrix product requires n multiplications and $n-1$ additions). As a suitable compromise to this eight fold increase in computer time costs, only the three position components of the ephemeris error have been added to the state.

*In the near planet phase, capability for adjoining the planet radius deviation to the state is available.

Figure E. 1 defines the variables of interest for the interplanetary case while Figure E. 2 does the same for the near planet situation. The state vector used in each case is:

$$\delta \underline{x} = \begin{bmatrix} \delta \underline{r} \\ \delta \underline{v} \\ \delta \underline{y} \end{bmatrix}$$

where the velocity \underline{v} is measured in whichever coordinate system is being used. In both cases an ecliptic coordinate system is used with the x axis in the direction of the vernal equinox and the z direction orthogonal to the ecliptic.

Changing Coordinate Centers

If the state convention just defined is adopted, the correlation matrices for the filtering technique developed in the previous section must be adjusted when changing coordinate centers. When changing from sun centered to planet centered coordinates we have:

$$\delta \underline{r}' = \delta \underline{r} - \delta \underline{y}$$

$$\delta \underline{v}' = \delta \underline{v}$$

$$\delta \underline{y}' = \delta \underline{y}$$

where the approximation has been made that the position of the Earth with respect to the sun is known much better than the position of any of the outer planets with respect to either the sun or the Earth. This is the equivalent to the transformation

$$\delta \underline{x}' = A \delta \underline{x}$$

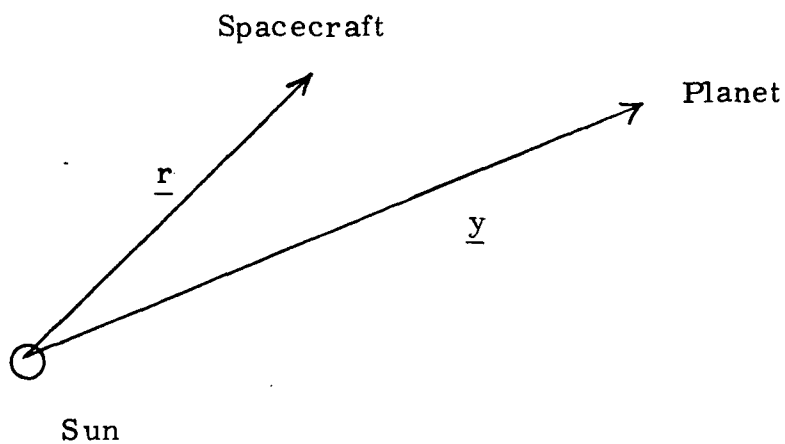


Figure E. 1 Definition of Positional State Variables for Sun Centered Case

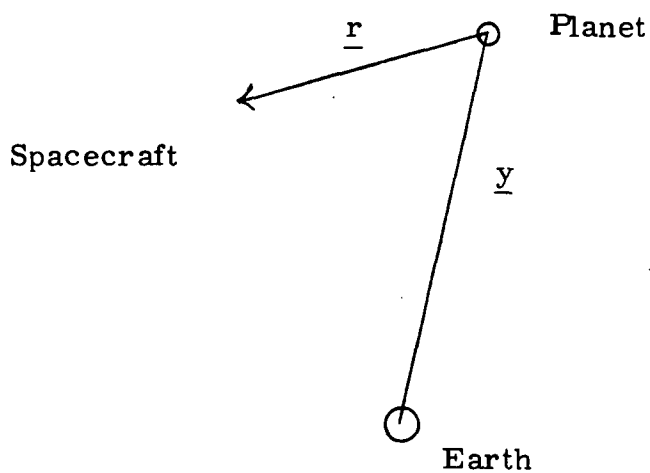


Figure E. 2 Definition of Positional State Variables for Planet Centered Case.

where

$$A = \begin{bmatrix} I & O & -I \\ O & I & O \\ O & O & I \end{bmatrix}$$

where A has been defined in terms of its 3×3 partitions.

For the case of changing from planet centered to sun centered coordinates we have

$$\delta \underline{r}' = \delta \underline{r} + \delta \underline{y}$$

$$\delta \underline{v}' = \delta \underline{v}$$

$$\delta \underline{y}' = \text{value for the next planet}$$

Here it will be convenient to define

$$A' = \begin{bmatrix} I & O & I \\ O & I & O \\ O & O & O \end{bmatrix}$$

and

$$P_E = \begin{bmatrix} O & O & O \\ O & O & O \\ O & O & \delta \underline{y}_O \delta \underline{y}_O^T \end{bmatrix}$$

where $\delta \underline{y}_O \delta \underline{y}_O^T$ is the initial covariance matrix for the position ephemeris of the new destination planet.

By noting that the error in the state estimate, state estimate, and actual deviation from the reference trajectory behave as follows:

Sun to Planet Centered:

$$\begin{aligned}\underline{e} &= A \underline{e} \\ \delta \underline{\hat{x}} &= A \delta \underline{\hat{x}} \\ \delta \underline{x} &= A \delta \underline{x}\end{aligned}$$

Planet to Sun Centered:

$$\begin{aligned}\underline{e} &= A' \underline{e} - \begin{bmatrix} \underline{0} \\ \underline{0} \\ \delta \underline{y}_o \end{bmatrix} \\ \delta \underline{\hat{x}} &= A' \delta \underline{\hat{x}} \\ \delta \underline{x} &= A' \delta \underline{x} + \begin{bmatrix} \underline{0} \\ \underline{0} \\ \delta \underline{y}_o \end{bmatrix}\end{aligned}$$

One can develop the following transformations for the correlation matrices:

Sun Centered to Planet Centered:

$$\begin{aligned}\underline{E}' &= A \underline{E} A^T \\ \underline{X}' &= A \underline{X} A^T \\ \underline{S}' &= A \underline{S} \\ \underline{v}' &= \underline{0} \\ \underline{j}' &= \underline{0} \\ \underline{d}' &= \underline{0} \\ \underline{C}' &= A \underline{C} A^T\end{aligned}$$

where \underline{v}' , \underline{j}' , \underline{d}' , are zero because by definition of the two body motion assumed throughout, the planet mass uncertainty does not affect the motion until the near planet phase; thus the initial values of these correlations for the near planet phase are zero.

Planet Centered to Sun Centered:

$$\underline{E}' = \underline{A}' \underline{E} \underline{A}'^T + \underline{P}_E$$

$$\underline{X}' = \underline{A}' \underline{X} \underline{A}'^T + \underline{P}_E$$

$$\underline{S}' = \underline{A}' \underline{S}$$

$$\underline{v}' = \underline{0}$$

$$\underline{j}' = \underline{0}$$

$$\underline{d}' = \underline{0}$$

$$\underline{C}' = \underline{A}' \underline{C} \underline{A}'^T$$

where \underline{v}' , \underline{j}' , \underline{d}' , are zero because no solar mass uncertainty has been included. Even if it were included these would be zero because they would be changing from accounting for the correlation with planet mass uncertainty to accounting for solar mass uncertainty.

C. The Measurement Partial and Data Compression

In this section the partial derivatives H_n and G_n used in incorporating a DSN measurement are developed. The part of the partial h_n for an onboard measurement corresponding to the vehicle position vector is treated for all measurement types used here by Battin²⁹. The part corresponding to the ephemeris variable, \underline{y} , has the same form as for the position vector in the interplanetary case and is zero for the near planet case.

The following derivation follows closely that of Kingsland and Bollman¹. The differences are 1) the state is defined differently and

2) the effect of compressing a pass of data must be treated differently, due to the use of a different filtering technique. The derivation will be performed here for the planet centered case first.

As in Reference 1 we begin with the range rate equation.

$$\dot{\rho} = \dot{r}' + \Omega r_s \cos \delta \sin \Omega (t - t_0) \quad (\text{E.6})$$

where

- ρ = distance from the tracking station to the spacecraft
- r' = distance from the center of the Earth to the spacecraft
- Ω = Earth's angular velocity about its spin axis
- r_s = distance of the tracking station off the spin axis of the Earth
- δ = geocentric equatorial declination of the spacecraft
- t = observation time
- t_0 = time of the maximum elevation of the spacecraft with respect to the tracking station

This expression for range rate is due to Hamilton and Melbourne². Following the example of Kingsland and Bollman we will define the partial derivative as follows:

$$\begin{aligned} \underline{h}' &= \left(\frac{\partial \dot{\rho}}{\partial \underline{x}} \right)^T = \underline{a} + \underline{b} \cos \Omega (t - t_0) \\ &\quad + \underline{c} \sin \Omega (t - t_0) \end{aligned} \quad (\text{E.7})$$

where:

$$\begin{aligned}\underline{a} &= \left(\frac{\partial \dot{\underline{r}}'}{\partial \underline{x}} \right)^T \\ \underline{b} &= \Omega r_s \cos \delta \left\{ \frac{\partial [\Omega (t - t_0)]}{\partial \underline{x}} \right\}^T \\ \underline{c} &= -\Omega r_s \sin \delta \left(\frac{\partial \delta}{\partial \underline{x}} \right)^T\end{aligned}$$

With reference to Figure E. 2 we can proceed with the development of an expression for \underline{a} :

$$\underline{r}' = \underline{r} + \underline{y} \quad (\text{E. 8})$$

$$\dot{\underline{r}}' = \frac{(\dot{\underline{r}} + \dot{\underline{y}}) \cdot (\underline{r} + \underline{y})}{|\underline{r} + \underline{y}|}$$

$$\frac{\partial \dot{\underline{r}}'}{\partial \underline{r}} = \frac{\partial \dot{\underline{r}}'}{\partial \underline{y}} = \frac{1}{|\underline{r}|} \underline{r}' - \frac{\dot{\underline{r}}'}{|\underline{r}|^2} \underline{r} \quad (\text{E. 9})$$

$$\frac{\partial \dot{\underline{r}}'}{\partial \underline{v}} = \frac{1}{|\underline{r}|} \underline{r}'$$

Rewriting Eq. (E. 9) there results:

$$\underline{a} = \begin{bmatrix} \frac{1}{|\underline{r}'|^3} \left\{ \underline{r}' \times (\dot{\underline{r}}' \times \underline{r}) \right\} \\ \frac{1}{|\underline{r}'|^3} \underline{r}' \\ \frac{1}{|\underline{r}'|^3} \left\{ \underline{r}' \times (\dot{\underline{r}}' \times \underline{r}) \right\} \end{bmatrix} \quad (\text{E. 10})$$

Note that there are no components of \underline{a} in the range direction of \underline{r} or \underline{y} and that the only velocity component is along the range line.

As defined in reference 1:

$$\Omega(t - t_o) = \Omega t_u + \alpha_s + \lambda_s - \alpha$$

where

t_u = true universal time

α_s = instantaneous right ascension of the mean sun

λ_s = longitude of the tracking station with respect to the Greenwich meridian

α = geocentric equatorial right ascension of the spacecraft

Thus

$$\underline{b} = \left(\frac{\partial [\Omega(t - t_o)]}{\partial \underline{x}} \right)^T = - \left(\frac{\partial \alpha}{\partial \underline{x}} \right)^T$$

in terms of \underline{r}' as defined by Eq. (E. 8):

$$\alpha = \tan^{-1} \left[\frac{r'_y \cos \gamma - r'_z \sin \gamma}{r'_x} \right]$$

where γ is the obliquity of the ecliptic.

With this identification of α we have:

$$\frac{\partial \alpha}{\partial \underline{x}} = \frac{1}{1 + \tan^2 \alpha} \frac{\partial \tan \alpha}{\partial \underline{x}}$$

Thus:

$$\frac{\partial [\Omega(t - t_0)]}{\partial \underline{r}} = \frac{\partial [\Omega(t - t_0)]}{\partial \underline{y}} = - \frac{1}{r'_x (1 + \tan^2 \alpha)} \begin{bmatrix} -\tan \alpha \\ \cos \gamma \\ -\sin \gamma \end{bmatrix}^T$$

$$\frac{\partial [\Omega(t - t_0)]}{\partial \underline{v}} = 0$$

or:

$$\underline{b} = - \frac{1}{r'_x (1 + \tan^2 \alpha)} \begin{bmatrix} -\tan \alpha \\ \cos \gamma \\ -\sin \gamma \\ 0 \\ 0 \\ 0 \\ -\tan \alpha \\ \cos \gamma \\ -\sin \gamma \end{bmatrix} \quad (\text{E. 11})$$

Note that \underline{b} has no components in the velocity directions of the nine space. Next by forming the projection

$$\underline{\xi} = \underline{r}' \cdot \begin{bmatrix} -\tan \alpha \\ \cos \gamma \\ -\sin \gamma \end{bmatrix}$$

with \underline{r}' defined by Eq. (E. 8) we find that

$$\xi = 0$$

or that there is no position or ephemeris component along the range line from the center of the Earth.

To evaluate the remaining term in \underline{h}' note that

$$\delta = \sin^{-1} \left[\frac{r'_y \sin \gamma + r'_z \cos \gamma}{|\underline{r}'|} \right]$$

Thus:

$$\frac{\partial \delta}{\partial \underline{x}} = \frac{1}{\cos \delta} \frac{\partial \sin \delta}{\partial \underline{x}}$$

hence:

$$\frac{\partial \delta}{\partial \underline{r}} = \frac{\partial \delta}{\partial \underline{y}} = \frac{1}{|\underline{r}'| \cos \delta} \left\{ \begin{bmatrix} 0 \\ \sin \gamma \\ \cos \gamma \end{bmatrix} - \frac{\sin \delta}{|\underline{r}'|} \underline{r}' \right\}^T$$

$$\frac{\partial \delta}{\partial \underline{v}} = \underline{0}$$

or:

$$\underline{c} = \frac{1}{|\underline{r}'| \cos \delta} \begin{bmatrix} \begin{bmatrix} 0 \\ \sin \gamma \\ \cos \gamma \end{bmatrix} - \frac{\sin \delta}{|\underline{r}'|} \underline{r}' \\ 0 \\ \begin{bmatrix} 0 \\ \sin \gamma \\ \cos \gamma \end{bmatrix} - \frac{\sin \delta}{|\underline{r}'|} \underline{r}' \end{bmatrix} \quad (\text{E. 12})$$

Again note that there are no velocity components in this part of the partial and that the projection

$$\xi = \underline{r}' \cdot \left\{ \begin{bmatrix} 0 \\ \sin \gamma \\ \cos \gamma \end{bmatrix} - \frac{\sin \delta}{|\underline{r}'|} \underline{r}' \right\}$$

is zero hence there is no component of position or ephemeris along the range line from the center of the Earth.

The partial derivatives for the sun centered case are identical to those for the near planet case except that the partial with respect to the ephemeris variables are zero, that is:

$$\frac{\partial \dot{\rho}}{\partial \underline{y}} = 0$$

The physical reason for this is that until the probe is influenced by the gravity field of the planet, tracking the probe from Earth yields no information about the location of the planet.

Performing a similar analysis to determine the partial derivatives with respect to the two components of tracking station location yields:

$$\frac{\partial \dot{\rho}}{\partial r_s} = \Omega \cos \delta \sin \Omega (t - t_0) \quad (\text{E. 13})$$

$$\frac{\partial \dot{\rho}}{\partial \lambda_s} = \Omega r_s \cos \delta \cos \Omega (t - t_0)$$

By defining an "equivalent longitude"

$$d_s = r_s \lambda_s$$

we obtain

$$\frac{\partial \dot{\rho}}{\partial d_s} = \Omega \cos \delta \cos \Omega (t - t_0) \quad (\text{E. 14})$$

For convenience we will collect Eqs. (E.13) and (E. 14) into a single vector equation:

$$\underline{\log'} = \begin{bmatrix} \frac{\partial \dot{\rho}}{\partial r_s} \\ \frac{\partial \dot{\rho}}{\partial d_s} \end{bmatrix} = \Omega \cos \delta \begin{bmatrix} \sin \Omega (t - t_0) \\ \cos \Omega (t - t_0) \end{bmatrix}$$

During a tracking period data is taken continuously. After a smoothing period of one minute the one sigma rms error in range rate is about 1 mm/sec (Ref. 2). In order to avoid processing the filter equations presented above once per minute throughout the entire period ground tracking is active on one of these outer planet missions, it is desirable to "compress" the information in a DSN tracking pass.

Let us begin this compression process by forming a "pseudo measurement" consisting of k of the scalar measurements each of which have been smoothed for one minute. Then:

$$\underline{z}^{\#} = \begin{bmatrix} z_1 \\ z_2 \\ \vdots \\ z_k \end{bmatrix} \quad (k \times 1)$$

$$H^{\#} = \begin{bmatrix} h_1 \\ h_2 \\ \vdots \\ h_k \end{bmatrix} \quad (k \times 9)$$

$$G^{\#} = \begin{bmatrix} g_1 \\ g_2 \\ \vdots \\ g_k \end{bmatrix} \quad (k \times 2)$$

$$r^{\#} = \begin{bmatrix} \sigma_1^2 & & 0 \\ & \sigma_2^2 & \\ 0 & & \ddots \\ & & & \sigma_k^2 \end{bmatrix} \quad (k \times k) \quad \underline{\eta}^{\#} = \begin{bmatrix} \eta_1 \\ \eta_2 \\ \vdots \\ \eta_k \end{bmatrix} \quad (k \times 1)$$

By approximating the estimate over these k measurements with the least squares estimate we obtain:

$$\delta \hat{\underline{x}} = (H^{\#T} r^{\#-1} H^{\#})^{-1} H^{\#T} r^{\#-1} \underline{z}^{\#} \quad (E. 15)$$

since

$$\begin{aligned} \underline{z}^{\#} &= H^{\#} \delta \underline{x} + G^{\#} \underline{b} + \underline{\eta}^{\#} \\ \underline{e} &= \delta \hat{\underline{x}} - \delta \underline{x} = (H^{\#T} r^{\#-1} H^{\#})^{-1} H^{\#T} r^{\#-1} G^{\#} \underline{b} \\ &\quad + (H^{\#T} r^{\#-1} H^{\#})^{-1} H^{\#T} r^{\#-1} \underline{\eta}^{\#} \end{aligned}$$

If we incorporate $\delta \hat{\underline{x}}$ into the state as if it were a measurement we have:

$$\delta \hat{\underline{x}} = \delta \underline{x} + \widetilde{\underline{\eta}} + G_p \underline{b}$$

where

$$\overline{\tilde{\eta} \tilde{\eta}^T} = (H^{\#T} R^{-1} H^{\#})^{-1} \triangleq R_p \quad (E. 16)$$

$$G_p = R_p H^{\#T} R^{\#-1} G^{\#} \quad (E. 17)$$

Kingsland and Bollman¹, by making the following assumptions:

- 1) the sums indicated in Eqs. (E. 16) and (E. 17) can be replaced by integrals
- 2) the geometry is constant over a pass of data
- 3) the pass is symmetric about the zenith

show that the information matrix, J, is given by:

$$J \triangleq \int_{t_I}^{t_f} \frac{1}{\sigma^2} \underline{h}' \underline{h}'^T dt \approx H^{\#T} R^{-1} H^{\#} \quad (E. 18)$$

The j-k element of J is:

$$J_{jk} = \frac{1}{\sigma^2} \left[a_j a_k + (a_j b_k + a_k b_j) \frac{\sin \psi}{\psi} + \frac{b_j b_k}{2} \left(1 + \frac{\sin \psi \cos \psi}{\psi} \right) + \frac{c_j c_k}{2} \left(1 - \frac{\sin \psi \cos \psi}{\psi} \right) \right]$$

where ψ is the half pass width:

$$\psi = \frac{\Omega}{2} (t_f - t_I)$$

and t_f and t_I are respectively the times of the end and beginning of the pass. The equivalent data noise σ^2 is given by:

$$\sigma_{\dot{\rho}}^2 = \frac{\sigma_{\dot{\rho}}^2}{N} \left(\frac{\pi}{\psi} \right) \left(\frac{1}{\Delta T} \right)$$

The coefficients a_i , b_i , c_i refer to the elements of the vectors \underline{a} , \underline{b} and \underline{c} defined by Eqs. (E. 10), (E. 11) and (E. 12) and

$$\sigma_{\dot{\rho}}^2 = \text{data noise for a one minute smoothing time}$$

$$N = \text{number of tracking stations}$$

$$\Delta T = \text{time since the last evaluation of the partial derivatives that tracking was active (measured in minutes)}$$

In a similar way we can define the cross integral between the state and station location partials as follows:

$$G' \triangleq \int_{t_I}^{t_f} \frac{1}{\sigma_{\dot{\rho}}^2} \underline{h}' \begin{bmatrix} \frac{\partial \dot{\rho}}{\partial r_s} \\ \frac{\partial \dot{\rho}}{\partial d_s} \end{bmatrix}^T dt \approx H^{\#T} R^{\#-1} G^{\#}$$

or

$$G' = \frac{\Omega \cos \delta}{\sigma^2} \left[\underline{c} \left(1 - \frac{\sin \psi \cos \psi}{\psi} \right), \underline{b} \left(1 + \frac{\sin \psi \cos \psi}{\psi} \right) \right] \quad (E. 19)$$

where \underline{b} and \underline{c} are the column vectors defined in Eqs. (E. 11) and (E. 12).

All that remains now is to use these integrals in identifying H_n , R_n and G_n in the filter equations for incorporating a DSN measurement given above. Note that if R_p could be evaluated directly using Eq. (E. 15) then we would have:

$$R_n = R_p, \quad G_n = G_p, \quad H_n = I$$

Unfortunately because $H^{\#T} R^{\#-1} H^{\#}$ is singular this approach will not work. To avoid this dilemma let us reduce the dimension of the measurement to the point where the pseudo measurement noise covariance matrix is non singular.

In evaluating the partial derivatives we noted that there were no components of the position and ephemeris in the range direction nor of the velocity in the two cross range directions. The information matrix can thus have a maximum rank of five. In the interplanetary case there are no ephemeris partials so the rank is then three. For the near planet case the rank is also three because the position and ephemeris partials are identical. Thus by defining a rotation matrix as follows:

$$T = \begin{bmatrix} \underline{u}_y & 0 & k \underline{u}_y \\ \underline{u}_z & 0 & k \underline{u}_z \\ 0 & \underline{u}_x & 0 \end{bmatrix} \quad 3 \times 9$$

where

$$k = \begin{cases} 0 & \text{for interplanetary case} \\ 1 & \text{for near planet case} \end{cases}$$

$$\underline{u}_x = \frac{1}{|\underline{r}'|} \underline{r}'$$

$$\underline{u}_z = \frac{1}{|\underline{r}' \times \dot{\underline{r}}'|} (\underline{r}' \times \dot{\underline{r}}')$$

$$\underline{u}_y = \underline{u}_z \times \underline{u}_x$$

we can form a new pseudo measurement:

$$\underline{\tilde{z}} = T \underline{\hat{x}}$$

where $\underline{\hat{x}}$ is given by Eq. (E. 15).

By doing this we can write

$$R_n = (T J T^T)^{-1}$$

where J is given by Eq. (E. 18)

$$H_n = T$$

$$G_n = T G'$$

where G' is given by Eq. (E. 19). These are then to be used in the DSN measurement incorporation formulas.

APPENDIX F

A COMPARISON OF FILTERING TECHNIQUES

During the course of this study three approaches to the problem of how to perform the statistical error analysis were considered. The one used to actually perform the study is described in detail in Chapter II and Appendix E. The purpose of this appendix is to identify the other two methods and compare the important characteristics of all three.

The first of the alternate two methods is to apply directly the so called "Kalman filter" technique to the problem. Two ways of doing this are important to discuss. The first is to simply ignore the biases on the problem and apply the filter equations directly. Previous experience by workers at the Jet Propulsion Laboratory indicates that this is not a good approximation to the actual situation. Artificially increasing the data noise to offset the fact that the biases were neglected also gives poor results.

The second "Kalman filter" approach is the one mentioned in Chapter II whereby the important biases of the problem, in this case two components of each tracking station location error and planet mass uncertainty, are adjoined to the state and estimated. In this way the "Kalman filter" requirement that all measurement and driving noises have white distributions in time is fulfilled. As pointed out in Chapter II, unless some method is included to put a lower bound on the estimation error for these biases the estimation error continuously decreases. The point is soon reached where in a practical sense these biases become perfectly known and should be dropped from the problem. In reality this cannot happen because there are limiting phenomena such as wander of the Earth's spin axis and higher order terms in the expansion of the planetary potential function which prevent this. Because these limiting phenomena are currently not well modelled it is not practical to introduce them into the filtering

scheme; thus this approach has the disadvantage that the errors can become unrealistically small.

As a demonstration of this tendency for the bias errors to continuously shrink see Table F. 1. This table contains results from all three missions used as examples in this study. In all cases the entry in the table is for the point 1. a. u. away from Jupiter. All cases were started with an off spin axis station location error of one meter and equivalent longitude error of two meters. Two items of interest are contained in this data. First, the station location errors have already been reduced to unrealistically small values which is the objection to using this approach. Second, the ratio of corresponding errors from mission to mission is very close to being inversely proportional to the square root of the elapsed time to the data point. Using this rule one can quickly estimate just how small the station location errors would be at the end of the nine year Grand Tour mission.

The remaining method to be described is the "consider option" approach used in reference 1. In its recursive form this method is very closely related to the one presented in Appendix E. The only difference is in the choice of the filter gains \underline{w}_n and W_n which are used to process the measurements. In the method of Appendix E the optimal gains are chosen and a minimum variance estimate results. In the "consider option" method the Kalman gains are used as the filter gains - the result is sub-optimal in that a minimum variance estimator is not obtained.

To be more specific the gains in the "consider option" mode are computed by carrying along another set of covariance matrix equations:

Extrapolation:

$$P_{n+1}' = \Phi_{n+1,n} P_n \Phi_{n+1,n}^T$$

TABLE F.1

Result of Estimating Biases on Earth-Jupiter Legs

Mission	* Final Station Location Error (meters)	* Final Station Location Error (meters)	* Equivalent Longitude Station Location Error (meters)	Elapsed Time to Terminal Time (Days)
1973 Low Energy Jupiter Flyby	.044	.029		518
1977 Jupiter Swingby to Saturn	.052	.034		394
1977 Grand Tour	.054	.035		365

*Final point in all cases is 1 a.u. from Jupiter.

Initial off spin axis station location error = 1 meter

Initial equivalent longitude station location error = 2 meters

Midcourse Correction:

$$P_n'' = P_n' + M Q_n M^T$$

Onboard Measurement:

$$\underline{w}_n = P_n' \underline{h}_n / (\underline{h}_n^T P_n' \underline{h}_n + r_n)^{-1}$$

$$P_n = (I - \underline{w}_n \underline{h}_n^T) P_n' (I - \underline{w}_n \underline{h}_n^T)^T + \underline{w}_n r_n \underline{w}_n^T \quad (F. 1)$$

DSN Measurement:

$$W_n = P_n' H_n^T (H_n P_n' H_n^T + R_n)^{-1}$$

$$P_n = (I - W_n H_n) P_n' (I - W_n H_n)^T + W_n R_n W_n^T \quad (F. 2)$$

If the \underline{w}_n and W_n from Eqs. (F. 1) and (F. 2) are used in place of those defined in Chapter II then the result is the "consider option".

Note, however, that these are not the optimal gains.

In words, what the three methods amount to is as follows: The pure Kalman approach as defined here without estimating the biases is the optimal policy if there are no biases. The method of Appendix F is the optimal policy in recognizing the biases if they are not estimated. The "consider option" is a sub optimal conservative method which is effectively the same as using the Kalman filter approach then, after completion, going back and evaluating what the real estimation errors are using the same gains but including the effect of biases. The errors obtained using the "consider option" can never be less than those computed using the method of Appendix F. As an example of a case where the estimation

error increases when the "consider option" is used to treat the station location errors see Figure F. 1. This displays the projected RMS terminal position error versus time. With the pure Kalman filter approach or the method of Chapter II this quantity could never rise unless a midcourse velocity correction was made. Note the periodic increase evident in Figure F. 1. This periodic property is correlated with Earth's motion about the sun. It is just such an increase as this that makes it difficult to use this approach in a trade-off study.

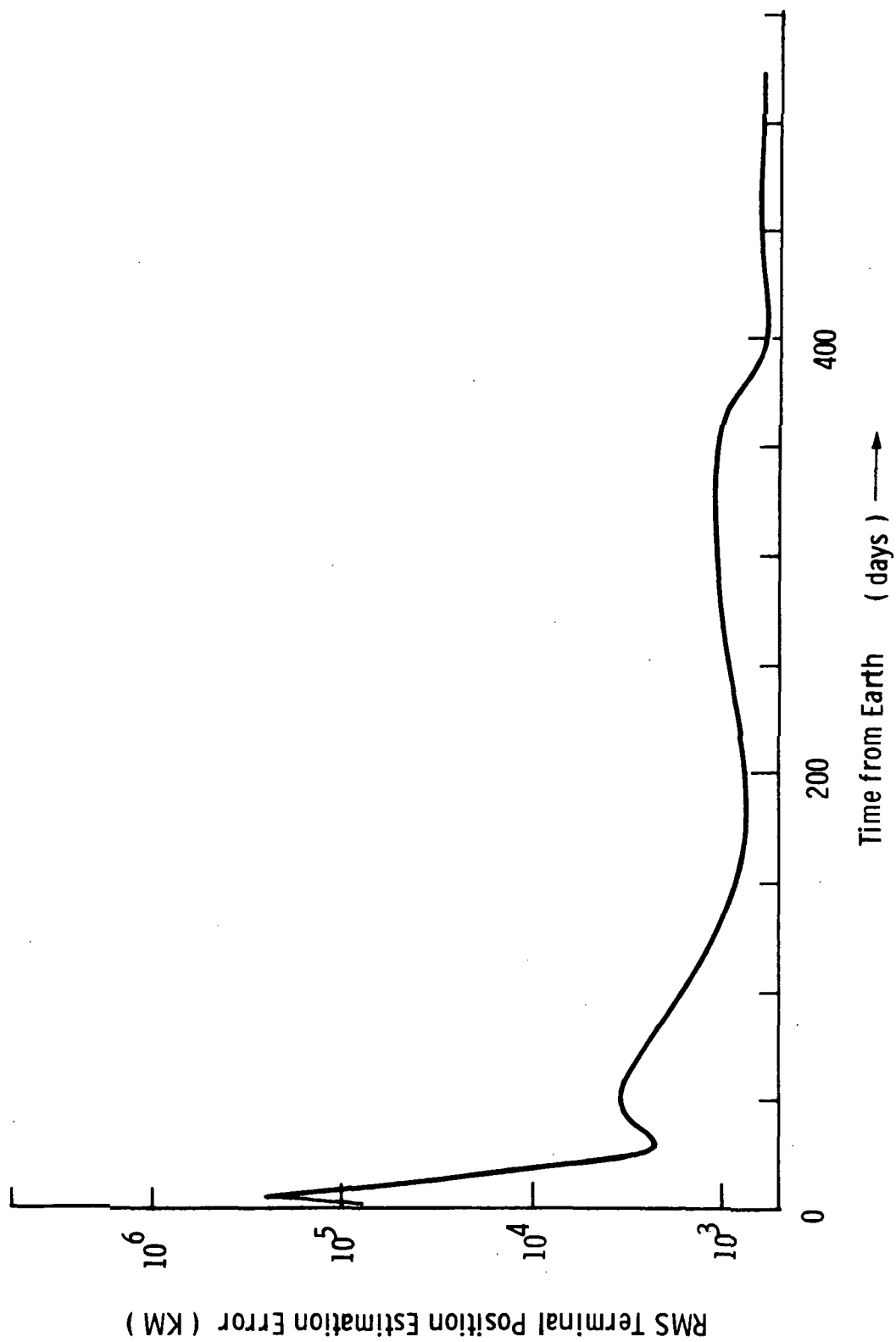


Fig. F1 Projected RMS Position Error when Filtering with Non optimal Gains

APPENDIX G

SENSOR DESIGN CHARACTERISTICS

Detailed discussions of sensor design are given in this appendix. Section G1 contains estimates of weight, power, and volume requirements for sensors with 0, 1, and 3 rotational degrees of freedom. Section G2 discusses telescope design factors such as materials, aperture area, field of view, and detector selections. G3 presents the results of some accuracy calculations for a nominal choice of parameters.

G1 Navigation Sensor Physical Characteristics

1. Weight

The material of the mounting brackets, flanges, telescope tube and mirrors is beryllium with a density of about 1600 kg/m^3 , and the gears, bearings, and bearing raceways are of stainless steel at about 7800 kg/m^3 . Estimated design weights for systems having a telescope of 100 cm^2 aperture area are 18.2 kg for the three degree of freedom instrument, 11.4 kg for the one degree of freedom instrument, and 5.5 kg for the strapped down system. The scaling of sensor weight with aperture diameter can be characterized as follows. Since the accuracy of the angle resolvers is directly proportional to their diameter, a significant reduction in their size is not likely, and the resolver weight forms a lower limit to the overall weight. For the three degree of freedom instrument, the resolver-servomotor weight is expected to be about 12 kg. For the single degree instrument, precision resolver is expected to weigh about 5.5 kg. The telescope in each case is expected to scale somewhere between the square and the cube of aperture diameter. Based on these assumptions, Figure G.1 shows the expected weight ranges for the three instruments as a function of aperture area. Each curve converges on the target design weight at 100 cm^2 effective aperture, and is asymptotic to the resolver-bearing motor weight for small effective apertures. These estimated masses represent conceptual maxima in order to produce conservative results.

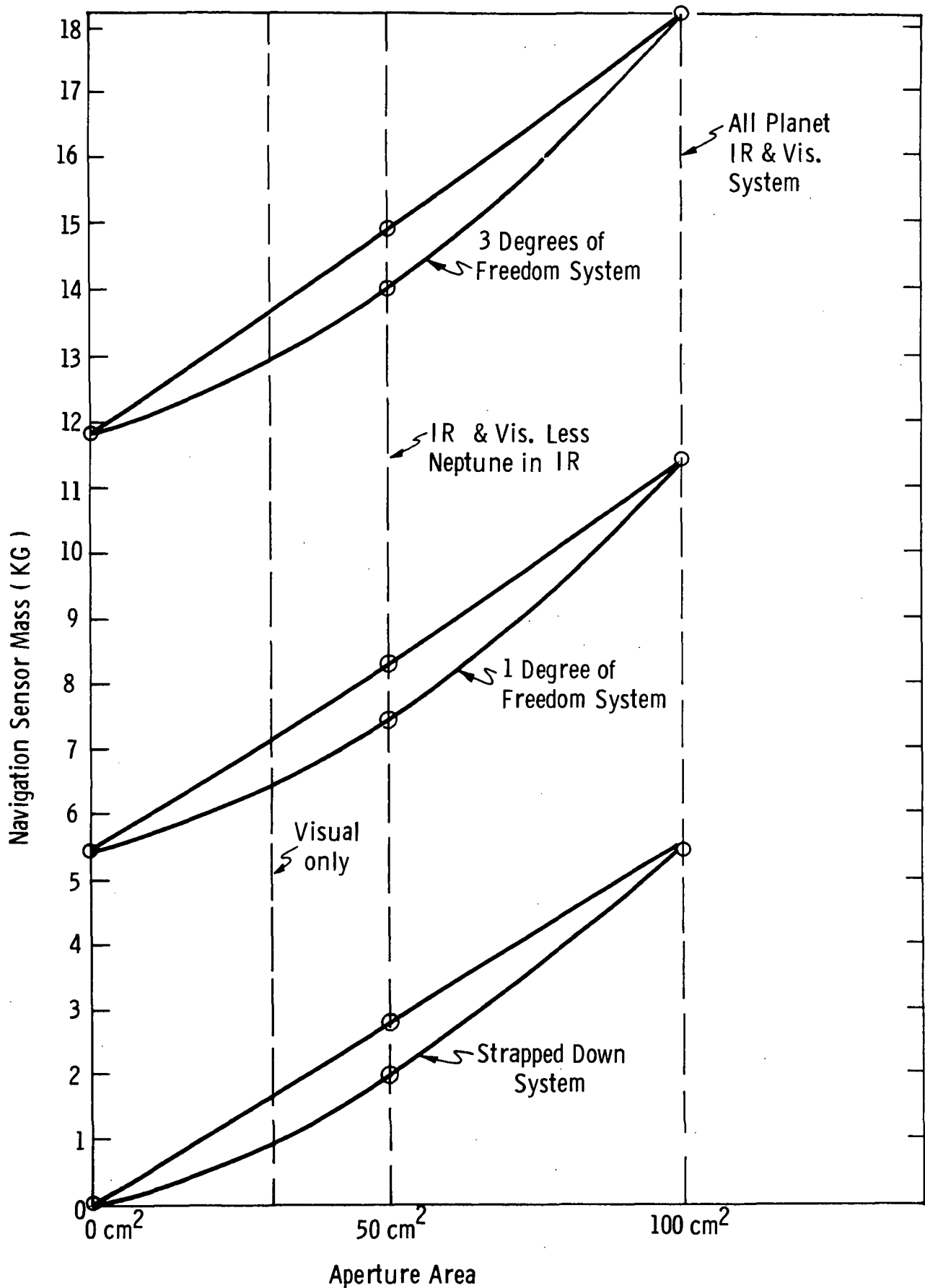


Fig. G. 1 Sensor Weight Ranges

2. Volume

Total rectangular enclosure volume for the three degree of freedom instrument is approximately $21,200 \text{ cm}^3$ with outside dimensions in the upright position of 35.5 cm high by 33 cm long by 17.8 cm wide for a 100 cm^2 effective aperture area. For a 50 cm^2 effective aperture area the volume reduces to about $16,387 \text{ cm}^3$. The 100 cm^2 aperture single degree of freedom instrument has a volume of $11,500 \text{ cm}^3$ which reduces to 7800 cm^3 at 50 cm^2 effective aperture. For the strapped down system, the volume is slightly larger than the telescope tube volume which means about 6550 cm^3 at 100 cm^2 effective aperture, and 4600 cm^3 at 50 cm^2 effective aperture.

3. Power

Items directly associated with the sensor package that require a significant amount of power are the servo-tach motors and the detector - amplifier combination. For the latter, it is estimated that approximately one watt each will be required for both the visible and the infrared detector-amplifier combination. Servo motor power requirements are proportional to the motor rate. If we select a standard No. 8 AC motor with maximum no load speed of 6500 rpm, and match this maximum speed with the maximum required scan rate of about 1000 arcseconds/second through a gear train of ratio 150,000/1, then the required power is about 6.5 watts maximum for one motor. No appreciable power is expected to be expended against bearing friction. Also resistive power losses in the resolvers are expected to be negligible. The 6.5 watt motor value includes 1.5 watts for the tachometer, and 2.5 watts for the control phase of the two phase motor. Thus at low rpm the motor will still draw about 4 watts.

For the 3 degree of freedom sensor, total maximum power required will be about 22 watts. For the one degree of freedom model about 9 watts are needed, and the strapped down telescope uses from one to two watts depending upon whether or not both infrared and visible sensors are employed.

G2 Telescope Design

1. Mechanical Features

Regardless of the number of degrees of freedom assigned to the sensor and spacecraft, the relative values of detector noise equivalent radiance and navigation phenomena radiance require that the navigation sensor have light gathering capability. Therefore, a telescope of some sort is required. The sensors shown in Figures III-2 and III-3 have cassegranian telescopes which are relatively simple to design and do an adequate job. The telescope barrel, the mirrors, and the supporting structures are constructed of beryllium with appropriate coatings. Gears, bearings, and bearing raceways are stainless steel. The bearings are angular contact, paired in opposition to prevent parallel shaft loading. Bearings are oil labyrinth lubricated and sealed to prevent vacuum welding. Angular resolution to within a few arcseconds is obtained from an air core inductosyn affixed to the precision scan axis. In the case of the three axis system, the two non-precision axis angles are obtained from ferrite core resolvers which are capable of fifteen arcsecond accuracy.

Detectors are located behind the focal plane which contain field limiting slits. Behind the detectors, room is allotted in the telescope barrel for the detector signal amplifiers.

2. Aperture Area

There are, of course, a number of factors which influence the choice of aperture area. Each selected radiation detector has its related noise equivalent power which needs to be compared to the total power placed on the detector by the telescope. This in turn depends upon the radiance of the astronomical source, the field of view of the field limiting aperture, and the aperture, and the aperture area. The choice of detectors, as will be seen below, is based substantially on factors other than noise

equivalent power. Therefore, given a chosen detector with its concomitant noise equivalent power, and given the fixed planet radiance, one is left with only telescopic factors as variables. The aperture area differs among the astronomical sources and radiation bandwidths, and so the various possibilities are examined according to source.

The aperture area for a planet limb scan with an infrared detector depends on the planet temperature, therefore, sufficient aperture for the planet Neptune will also be sufficient for the other grand tour planets. The temperature of Neptune is estimated to be about 40°K which indicates black body infrared emission of about 4.6×10^{-6} watts/cm² str in the sensitive region of a thermistor detector. If one chooses an aperture area of 100 cm², and if the full image is placed on the detector, say at 1 a. u. from the planet, then the signal strength is about 10^{-11} watts. The noise equivalent power of the detector, if it has a state of the art time constant of 0.04 seconds, a physical area (for f/4 optics) of 10^{-4} cm², and a noise filter bandwidth of 0.004 Hz, is 0.25×10^{-11} watts. The signal to noise ratio for this situation is about 15 arcseconds based upon the rough rule of thumb that the error is equal to the slit height (when filled) divided by the signal to noise ratio. But if the field of view is limited to say one square minute, because of diffraction, the actual signal to noise ratio will be lower. In fact it drops to about 0.5 which corresponds to about 100 arcseconds uncertainty. These are probably unacceptable values, and since the only easily adjustable parameter associated with the sensor is the aperture area, it appears that one needs to consider eliminating I. R. measurements at 1 a. u. on Neptune or increasing the aperture area above 100 cm² which would increase weight and volume penalties. At 1/100 a. u. with a $1' \times 20'$ field of view and corresponding thermistor of 2×10^{-3} cm² area, the I. R. sensor accuracy can be increased to the $\pm 1\sigma = 30''$ range. At present, it is not clear what the navigation requirements will be on the Uranus - Neptune leg of the grand tour. Since at Neptune there will be no requirement for a precision impact parameter for purposes of getting to another planet, the need for accuracy will be dictated by the scientific package requirements. It is anticipated that I. R. measurements will be most useful over the range from a few planet diameters upon approach to a dozen diameters on recession. For Neptune

then, I. R. measurements can probably be eliminated. At Uranus, a signal to noise ratio of 10 can be maintained with an aperture of 50 cm^2 at half maximum intensity with a $1' \times 20'$ field of view. It appears, therefore, that 50 cm^2 is a lower useful limit to the aperture area of an I. R. telescope for the grand tour mission.

In the visible spectral region, Neptune will again determine the minimum limiting aperture area. The effective radiance of Neptune over the sensitive band of a silicon photodiode is about 0.25×10^{-4} watts/cm² str. For an aperture area of 100 cm^2 this becomes approximately 2.5×10^{-14} watts per square arcsecond of planet within the field of view. The noise equivalent power of the photodiode is about 8×10^{-14} watts with a 3 Hz noise filter bandwidth. Thus, about 40 square arcseconds worth of Neptune must be focussed on the detector to yield a signal to noise ratio of 10. Depending on the range, this amounts to scanning a few arcseconds or less into the planet limb. If we require a signal to noise ratio of 10 at half maximum signal coupled with few arcsecond sensitivity, then the minimum allowable aperture area is about 25 cm^2 .

The aperture requirements for star detection during a simple scan depend on the detector response and the star type. It is assumed here that the same detector will be used for the star scan as for the planet limb. Various star types have an effective temperature range of about 3×10^3 to 30×10^3 °K, or a range of total energy output of about 10^4 . This means of course that there is no simple relationship between the visual magnitude of a star and the corresponding diode output, because the energy sensed by the diode depends on star type as well as magnitude. We therefore, choose an average star for discussion purposes, namely a type AO with photosphere temperature of about 10^4 °K. According to reference 35, a star of this type, and of zero visual magnitude delivers a signal of 3.8×10^{-9} erg/cm² sec Å to a point just outside the earth's atmosphere at a wavelength of 5560 Å. The radiation peak for a 10^4 °K star is around 3000 Å, while the silicon photodiode is most sensitive at 9000 Å, thus the diode output will come mainly from the long wavelength side of the star output curve, and this region closely approximates black body radiation.

Therefore, to calculate the expected signal, a 10^4 °K blackbody curve has been scaled with respect to the above mentioned 5560 Å output from a zero magnitude, type AO star, and the diode sensitivity curve has been integrated over the blackbody curve. The result, when scaled down to 2nd magnitude, is about 10^{-13} watts/cm² signal strength. This is about the same as the noise levels of the detector and background combined, therefore a signal to noise ratio of 10 is obtainable with an aperture of 10 cm².

In summary, a wide range of aperture areas are usable and specific choices depend on navigation requirements, signal to noise ratios, star characteristics, etc. Figure G.2 summarizes some of the plausible aperture requirements.

3. Planet Limb Sensor Slit Size and Shape.

Slit size and shape form another loop in the total system problem. The type and accuracy of the spacecraft attitude control system determine the gross slit size, while the estimated accuracy of angle measurements with a given slit affect the total system navigation ability and thrusting requirements. Some of the important considerations are as follows.

There are no doubt a number of complex slit shapes that after considerable analysis could be shown to be useful for planet limb sensing. But if it can be shown that the usual simple shapes are adequate, a lot of unnecessary research can be avoided. The analysis in the Navigation Sensor Accuracy section shows that good accuracy is attainable with the rectangular slit. A rectangular shape has the advantage that, assuming it is of adequate width, its characteristics with respect to the limb are constant over a wide range of sensor-planet distances.

By using a photo engraving process, any shape of field of view can be produced with accuracies of approximately one ten thousandth of an inch.

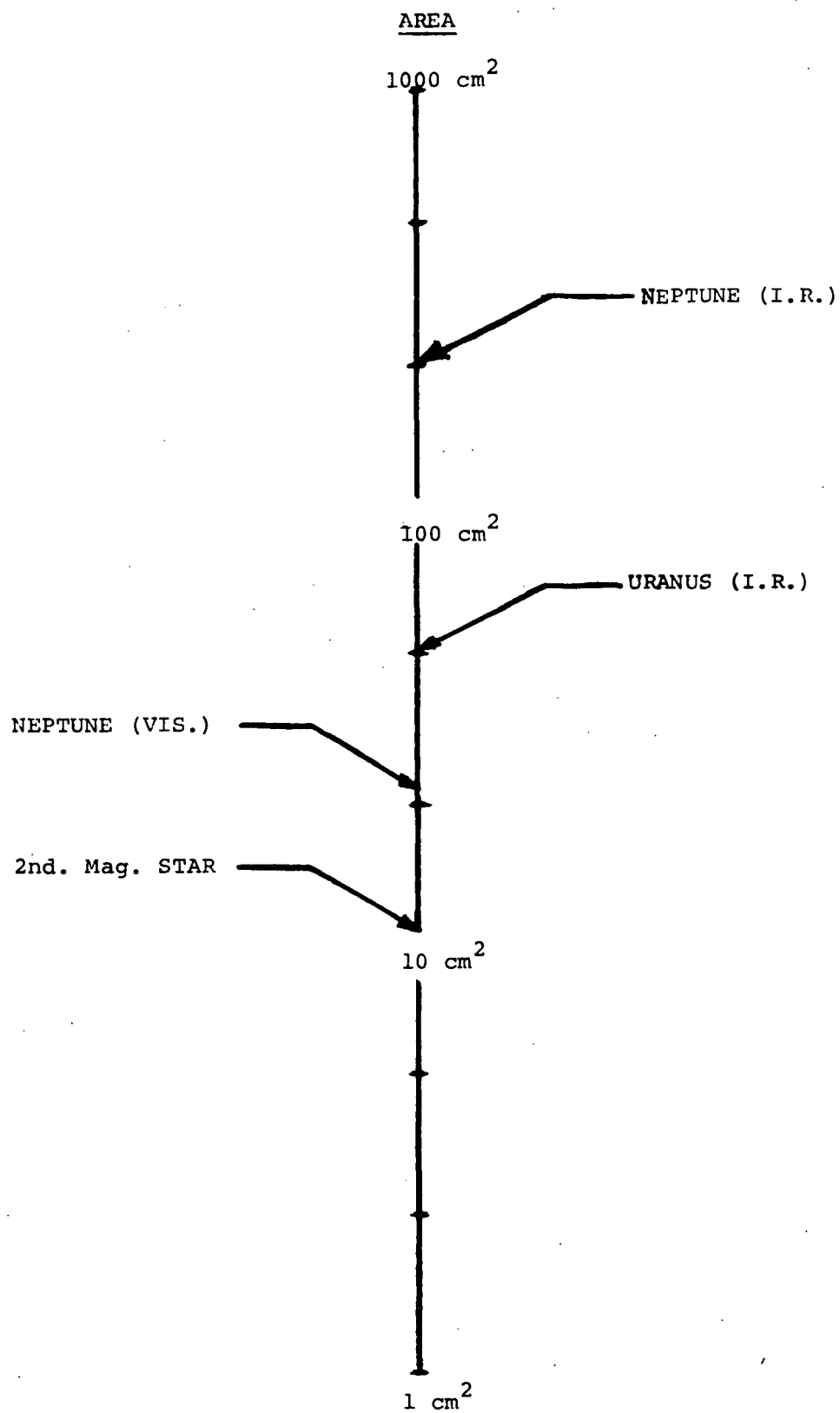


Fig. G.2 Aperture Area Requirements

The general width is determined primarily by the expected coarse attitude control system accuracy. For example, if coarse alignment is good to within 1° , then at 1 A. U. to insure that the slit hits the planet (if the star-planet angle is 60°) a 0.84° wide slit is required. In practice, the width must be optimized to minimize background noise at long ranges, and to maximize the signal at close ranges. A 1° width is felt to be representative, and is assumed in the section on system accuracy.

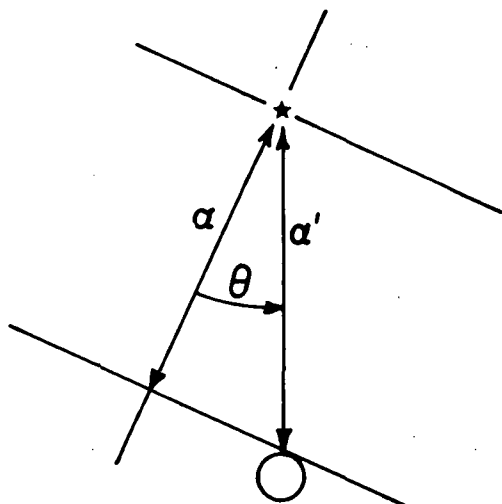
Slit height is determined primarily by consideration of accuracy, and signal characteristics such as the slope of the signal rise curve as a function of scan angle. For example a narrow slit provides fine definition, but also is characterized by a weaker signal and a smaller slope, since the signal rises slowly after the total slit height is immersed in the planet disk (at long ranges). The height value of $10''$ chosen for the accuracy analysis is felt to represent a reasonable compromise between definition and total signal.

It is possible to increase star position accuracy by using a several slit, correlation technique; however the same thing can be accomplished with a single slit by using a signal centroid technique. (See Section 10 below.) Therefore it is proposed to use a single main slit with the addition of a corrector slit.

Of the several types of tilt and offset errors, the more important ones and some possible correction schemes are shown in Figures G3. A- E. Figure G3. A shows the scan plane orientation error (θ) for a tracker scanner configuration where the tracker is locked on to the star. If $\theta = 20$ arc minutes, $|\alpha - \alpha'| \simeq 2$ arc second of error when $\alpha = 60^\circ$. It is hoped that θ can be controlled to within a few arc minutes rather than 20 so that this error is a fraction of an arc second.

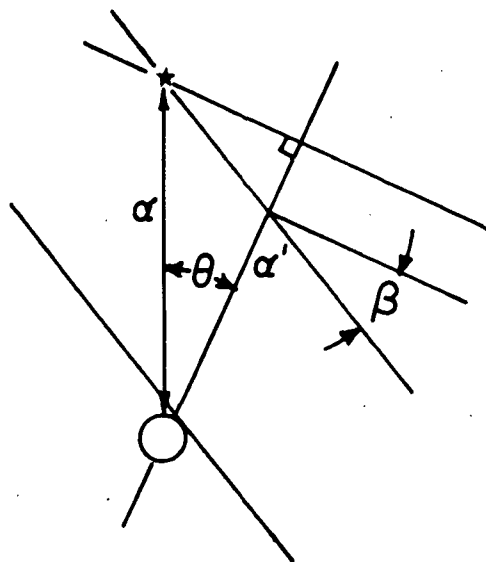
Figure G3. b shows the additional error resulting from a deviation from a perpendicular alignment of the scanning slit to the scan axis. The angle β is expected to be of the order of a few minutes resulting in an error comparable to the scan plane alignment error.

A.



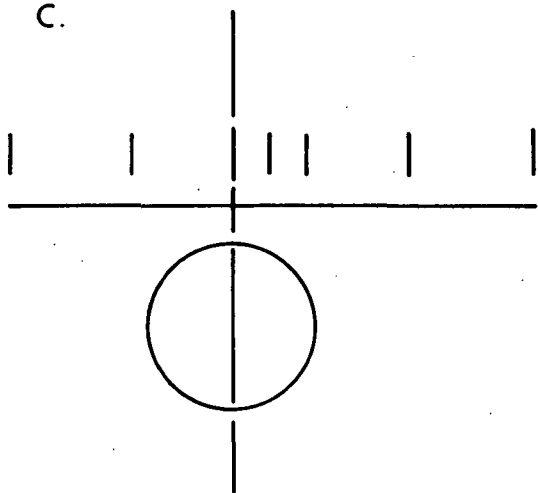
$$\frac{(\alpha - \alpha')}{\alpha} = (1 - \cos \theta)$$

B.

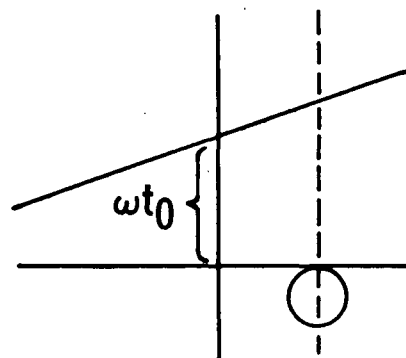


$$\frac{(\alpha - \alpha')}{\alpha} = (1 - \cos \theta + \sin \theta \tan \theta)$$

C.



D.



$$\Delta \theta \alpha \omega \Delta t$$

E.

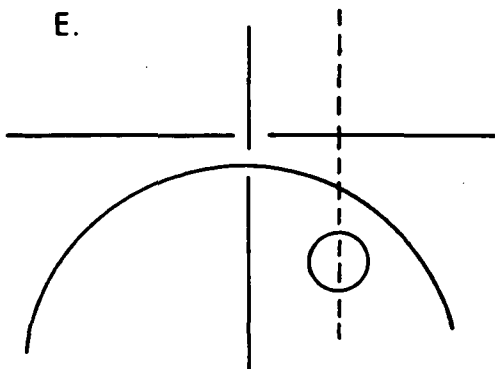


Fig. G3. Slit Characteristics

The remaining figures show some slits that could be used to correct scan plane orientation errors. Figure G3. C has a group of small slits perpendicular to the main slit, each with its own detector. Asymetries in the signal are then fed to the attitude control system. In Figure G3. D two slits are used, the second of which is at an angle. Time differences in the occurrence of a given signal level are used to correct scan plane orientation errors. Figure G3. E shows a circular slit with a pair of straight error ocrrections. Each scheme has a certain set of planet ranges over which it is effective.

At very short ranges the problem changes. The uncertainty in the direction of the planet center increases as the range decreases. Thus at 1 a. u. the planet center direction is measurable to arcsecond accuracy, while at ranges of the order of planet radii, the uncertainty is of the order of arcminutes. As a specific example, consider the Saturn Flyby (Mission II). At perigee, the planet center is approximately 118,000 miles from the spacecraft. The uncertainty in estimating the planet center direction (assuming no on-board planet sensor has been employed) is composed of contributions from the ephemeris and spacecraft position uncertainties. Considering the worst case, i. e., onboard navigation only, the simulation results show an ephemeris error or 389 miles. The spacecraft position error is about 53 miles. Summing these uncertainties as the variances of independent variables gives about 400 miles position uncertainty of the planet center with respect to the spacecraft. This is an angular uncertainty of about 11 arcminutes. Since the slit width of 1° is much smaller than the 28° subtense of the planet, the error in horizon-star measurements in this situation is not the $(1 - \cos \theta)$ value of Figure G3. A above, but is dependent on the planet surface curvature. Thus the error in star-horizon angle is approximately $\Delta \alpha = r - \sqrt{r^2 - (\Delta \theta)^2}$, where r is the planet radius angular subtense and $\Delta \theta$ is the 11 arcminute uncertainty in planet center direction. In the situation under consideration, the star - horizon angle uncertainty from this source is approximately 0.07 arcminutes. This should be compared to the phenomenon error at this range of approximately 0.4 arcminutes. The important thing is that the error due to planet center direction uncertainty should be less than the phenomenon uncertainty.

If this isn't true, then a more sophisticated means of finding the proper scan plane is needed to make full use of the sensor measurement capability.

The navigation angle between the star and the planet center can be obtained by measuring the star-planet limit angle, and adding to this value the angle between the planet limb and center as calculated from earth-based knowledge of the planet diameter and planet - spacecraft range. Errors will be contributed to the total angle from the star-limb error, the limb-center error, and the range error.

4. Detector Selection .

A. Infrared Detector Choice.

There are basically two types of infrared detectors that have a useful response in the far infrared where the outer planet thermal emission is centered. These are the extrinsic, or doped semi-conductor type, and the thermal, or intrinsic type. In the thermal type each molecule is a potential charge donor, hence the term "intrinsic".

Both detector types have spectral responses ranging over the required region. For example, Cadmium doped Germanium detectivity peaks at about 16μ , Zinc doped Germanium at 36μ , and Boron doped Germanium at 100μ . The polycrystalline thermistor has a flat spectral response, and the spectral region of absorption is determined by the characteristics of the absorptive coating.

Because of their wide band spectral response, the thermal type detectors appear to be the best choice, although new developments may change this conclusion. The wider spectral response of the thermistor compensates for its lower detectivity, and the magnitude of the mission time scale allows the required low scan rates. Another attribute of the thermistor is that it operates with a relatively low bias voltage of say 20 - 100 volts.

B. Visible Detector Choice

There are a number of general considerations involved in the choice of visible light detectors such as relative spectral response, quantum efficiency, linearity, response time, temperature sensitivity, noise level, bias voltage, and related circuitry problems. The general problem of overall reliability and ruggedness is of prime importance for the outer planet mission. Also of prime importance is the the minimum detectable star brightness, and which may limit the accuracy of planetary limb sightings.

Photomultipliers feature the lowest noise levels of visible detectors, and if this were the overriding consideration, these devices would be advocated. However, the photomultiplier has a low (on the order of 15%) quantum efficiency which means that the ratio of signal out to signal in is small. It also requires bias voltages of a few thousand volts, which can lead to breakdown problems.

Photodiodes have noise levels that are a couple of orders of magnitude above those of photomultipliers, but adjustments of the noise filter bandwidth and the telescope aperture can be made to produce an adequate signal to noise ratio. It is anticipated that the photodiode would be used in a photoelectric mode, that is, as a current generator with no applied bias voltage. It appears that there may be some low temperature problems in the Uranus-Neptune region of space where equilibrium temperatures are of the order of 50°K. Quantum efficiency drops for extremely low temperatures, but so does noise. Just how these effects affect the signal to noise ratio will have to be determined. Low temperatures may affect other elements of the circuitry as well, so it may be necessary to regulate the circuit and detector thermal environment.

G3 Navigation Sensor Accuracy

1. Introduction

There are a number of ways to operate on sensor output and to arrange scan geometry so that navigation accuracy will be maximized, but fundamental to any of these operational techniques will be the basic, single scan accuracy with which the direction of an astronomical phenomenon can be determined. It is the basic angular accuracy that is estimated here. The calculations assume certain sensor characteristics such as a specific detector and a set of telescope design factors. These are coupled with the radiation outputs from relevant astronomical phenomena to provide curves of detector signal output as a function of scan angle. Phenomena signals can then be compared with the noise levels, and by applying conservative estimates of the accuracy of calibrating the sensor to the signal, angular accuracy can be estimated.

Basic planetary limb measurement accuracy is presented first for visible and infrared sensors. A bias error is introduced into these measurements by diffraction and the limb intensity profile, and the relationship between this error and threshold levels is discussed. Scan rates are estimated for various situations. Estimates of star position determination accuracy are then presented. The section concludes with a list of studies that should be made if navigation system accuracy is to be optimized.

2. Visible Horizon Locator Selection

The locator selection problem cannot be simply isolated from the total instrument design problem, but there are enough "constants" in the outer planet probe studies to allow some arguments about locators to be made. For example, the planetary reflected radiative intensities and radii are known, and this allows curves of signal versus scan angle to be constructed for various ranges. Also the detector spectral and electronic frequency responses are known so that signal to noise ratios

can be estimated. With the "constants" in hand, the locator selection problem reduces to considerations of scattered light levels, sweep rates, noise filter bandwidths, signal to noise ratios, bias errors, diffraction effects, horizon scale heights, and accuracy.

Assumptions

Since the problem has too many variables to be analyzed in general, we chose a representative sensor for analysis purposes having a silicon diode detector, receiving reflected solar radiation in the $0.5-1.1\mu$ spectral region, through a reflecting telescope of 100 cm^2 aperture, and through a field limiting slit of 10 arcseconds height and one degree width. The detector noise equivalent power at 3Hz electrical bandwidth is 8×10^{-4} watts. Signal and noise level curves for various ranges to the outer planets are shown in Figure G.4. In the figure, the ordinate is in watts, and the abscissa is in arcseconds, with zero representing the coincidence of the slit center of field of view and the planet edge. The signal curves are only applicable to long ranges, namely more than $1/20$ astronomical unit. At ranges smaller than this, the angular subtense of the atmospheric scale (taken as 100 Km) becomes as large as the diffraction width (3.3 arcseconds), and the signal curves become atmospheric profile rather than diffraction profile dependent.

Fixed S/N Locator

One manner of classifying locators is according to whether they are absolute and detector related, or relative and planet related. The detector related locator is a fixed threshold value - some multiple of the noise level - which is related to some point on a planet limb by, say, analog calculations which change for each planet and each range. The planet related locator places the planet edge at a constant (which is close to unity) times the angle at which the signal reaches some fraction of its maximum. For the present, problems of locator instability resulting from atmospheric seasonal and latitudinal fluctuations will be ignored. Arguments for and against the two basic types of locator, namely absolute and relative, will be given. Basic to the discussion below

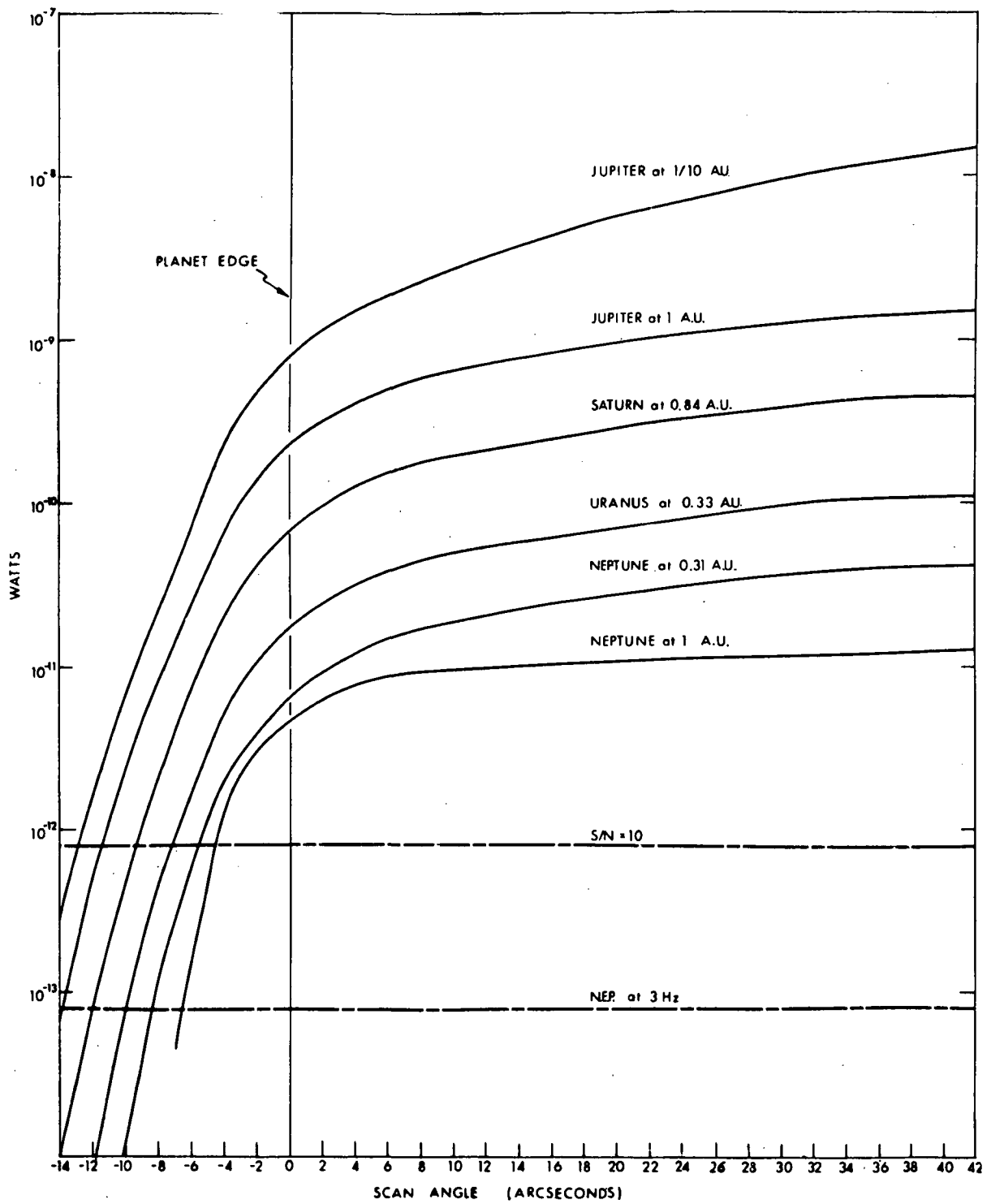


Fig. G. 4 Visible Light Signal Curves for Various Ranges

will be the estimate, based on engineering judgment, that absolute threshold settings will have a $\pm 3\sigma$ error range no greater than factors of $+2 (+3\sigma)$ and $-1/2 (-3\sigma)$ times the threshold signal level. Similarly, it is assumed that half-max thresholds have an error range of $\pm 3\sigma = \pm 25\%$ of max intensity.

The absolute threshold locator has some potentially strong attributes, namely, high accuracy and relative simplicity of electronic design. For example, on Neptune, at 0.31 a. u., if the threshold is set at $S/N = 10$, and the seven arcsecond bias error is removed, the $\pm 3\sigma$ error is just 1.8 arcseconds. However, it may not be easy to remove the bias error. One impractical solution would be to let the telescope aperture diameter get very large, which would effectively force the left part of the Figure G.4 signal curves to become asymptotic to the zero line. Alternatively, a constant bias setting of say -9 arcseconds would lead to roughly a 4 arcsecond bias error at the extremes of Jupiter at 1/10 a. u. and Neptune at 1 a. u. If such a bias error is not acceptable, it could be reduced by applying a planet correction factor (assuming each planet is used for navigation only over a unique range) which would reduce the error to about 1 arcsecond over the 1 to 0.1 a. u. distances. Complete elimination of the bias error would require the addition of a range correction.

A possible problem with the low level threshold type locator is scattered light effects. For Jupiter at say 1/20 a. u., the threshold setting of $S/N = 10$ is six orders of magnitude or 60 db below the total power of the half planet image on the slit plate or what ever part of the telescope gets hit with the non slit part of the image. Although it is felt that a scattered light problem of this order can be eliminated by proper telescope design, experimental results show that the probability that scattered rays will enter a slit increases dramatically as the angle between these rays and the field of view axis gets down around one minute of arc. Therefore, the problem is not felt to be ignorable and must be considered as an important telescope design constraint.

Another disadvantage of the low level fixed threshold is that it leads to slow sweep rates. If we consider the signal to be approximately

a ramp at the threshold and if the sensor response is approximately linear, then the output signal from the sensor is

$$\text{Sig.} = k [t - \tau (1 - e^{-t/\tau})]$$

where : k = slope of the signal curve,

τ = sensor electrical time constant.

For a 10 Hz bandwidth $\tau = 0.016$ seconds. To calculate sweep rates it is assumed that the steady state is obtained at say 0.1 seconds; then by setting the difference between true and lag signals equal to the 1σ noise, and converting k to angular units, one obtains the rate equation

$$\dot{\theta} = \frac{1. \sigma \text{ Noise}}{\tau k}$$

For the low level, fixed threshold this gives rates on the order of 25 arcsec/sec compared to the rates of four or five times this value for higher level fractional thresholds.

If an error exists in the calculated signal curves a bias error will result. The size of the angular error will depend on the magnitude and direction of the signal error. Overestimating the signal results in a larger angular bias error than underestimating. The same effect will result from an error in the threshold setting of the sensor.

At a S/N value of 10, the photon flux rate is about 10^7 photons/second. At a sweep rate of 25 arcsec/sec, the signal fluctuations due to the statistics of photon arrival time, are of the order of 10^{-3} arcseconds (Ref. 36). Thus it appears that photon rate fluctuations are ignorable as an error source for visible planet limbs.

A final problem with the fixed, low level threshold is that at short ranges ($< 1/100$ A. U.) the signal curves become dominated by the atmospheric limb effects. Two things are happening. First, the threshold level signal occurs at a greater angular altitude above the planetary radius reference point, thus either introducing an increasing bias error or the requirement for a bias range correction. Secondly, the slopes of the signal curves are smaller at the higher altitudes which magnifies the calibration error. Therefore it would seem advisable, assuming one is interested in taking advantage of the low level fixed threshold accuracy at long ranges, to switch either to higher threshold or a relative, fractional type threshold at close ranges.

Fractional Threshold Locator

On the basis of the assumed slit, the relative or fractional threshold turns out to have much lower accuracy at long ranges than the fixed S/N value. This is due to the reduced slopes of the signal curves in the normally chosen fraction region when the planet is small compared to the width of the detector field of view. For example, at the $1/2$ max point on any of the signal curves of Figure G.4, the total error range, based on the assumed $\pm 25\%$, 3σ detection uncertainty is approximately $3\sigma = 14$ arcseconds (See Figure G.4). It is interesting that this error range is approximately constant, independent of planet and range. This is one of the attributes of the half max locator, when employed at long ranges with a slit such as the one assumed here. On the other hand, with the relative threshold setting some of the problems associated with fixed low level thresholds disappear. For example, the scattered light levels will be negligible, the sweep rates will be higher, S/N ratios are large, and the sensor bias error will not change drastically at close ranges. These

advantages are bought, however, with a decrease in accuracy at the long ranges. The final choice of threshold type may be decided by the accuracy of the DSN. If this system is accurate enough, navigation measurements involving the planets may not be required outside the near (1/20 A. U.) range, thus necessitating the use of a relative threshold.

3. Visible Planet Limb Accuracy

Some rough curves of angular error for the two classes of locators are given in Figures G. 5 and G. 6. These values are taken directly from the signal curves of Figure G. 4 using the assumed calibration uncertainty of $\pm 3\sigma = \pm 25\%$ maximum signal for the 1/2 maximum locator, and $+3\sigma = 2$ times threshold, $-3\sigma = 1/2$ of threshold for all others. Figure G. 5 shows the 1σ uncertainties for several locaters: obviously the 1σ error is inversely proportional to the signal curve slope in the region of the threshold level. Fixed low level threshold errors are the smallest as would be expected. Bias error (Figure G. 6) presents a more complicated picture. Relative thresholds can be chosen to eliminate bias at one range for each planet. For example, if the threshold is picked at 1/6.4 maximum, the bias error is approximately zero for Jupiter at 1 A. U., Saturn at 0.84 A. U., Uranus at 0.33 A. U., Neptune at 0.31 A. U. At close ranges to the planets atmospheric limb profiles dominate the signal curves. Figure G. 7 is a representative limb profile for Jupiter. Although the parameters which determine this profile such as cloudtop pressure and atmospheric scale height are not well known, the curve is felt to be representative. At 1/100 A. U. the sensor signal curve would look like the horizon profile since the representative slit height of 10 arcseconds is much smaller than the curve scale and the planetary subtense greatly exceeds the detector width. The half-max locator would then be on the order of 25 arcseconds above the cloud tops, while the fixed S/N locator would be at an extreme altitude, and at a point of very small slope on the signal curve. Obviously, at these ranges a fractional threshold is required.

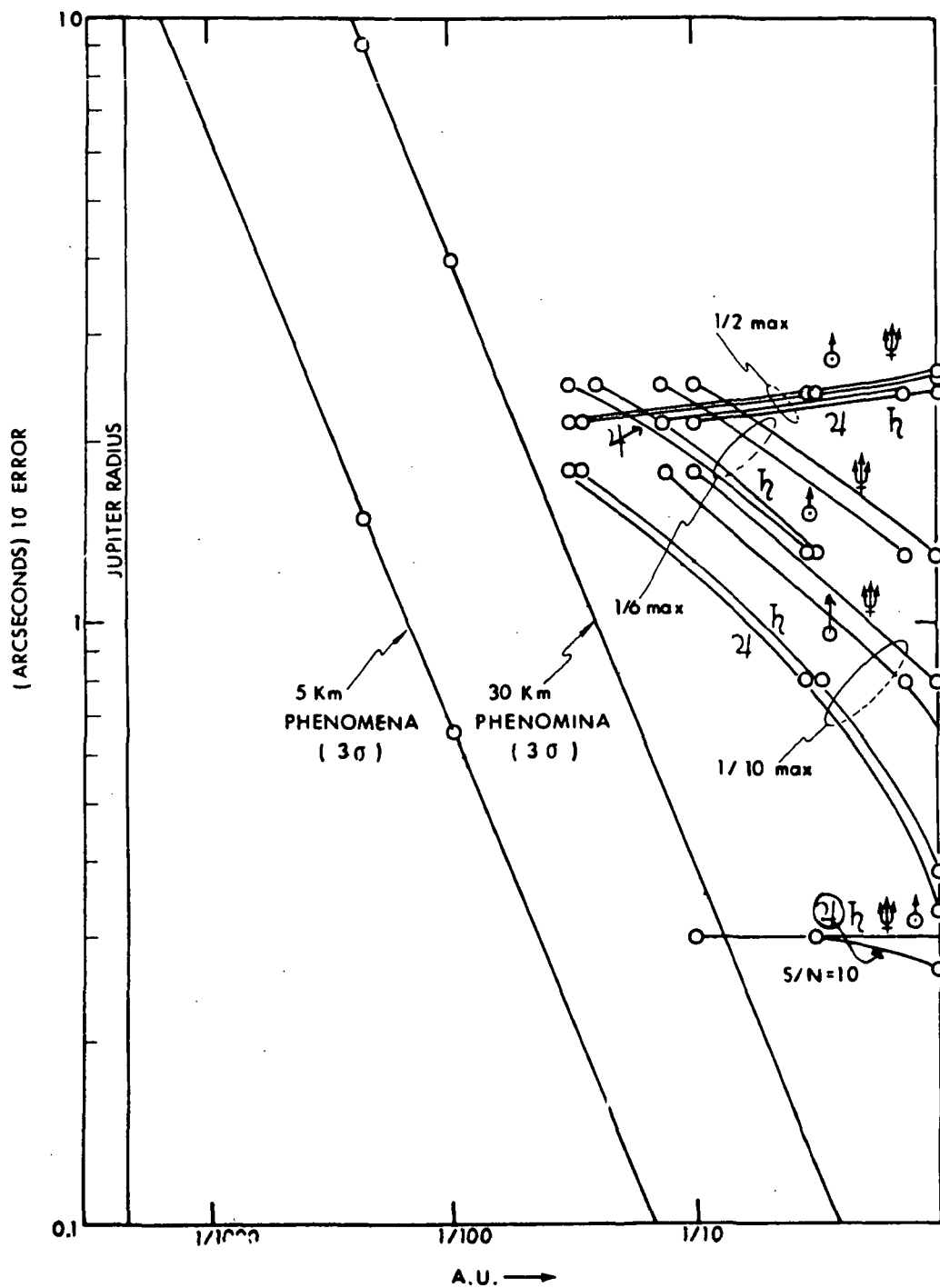


Fig. G.5 1σ Errors-Visible Light (Bias Removed)

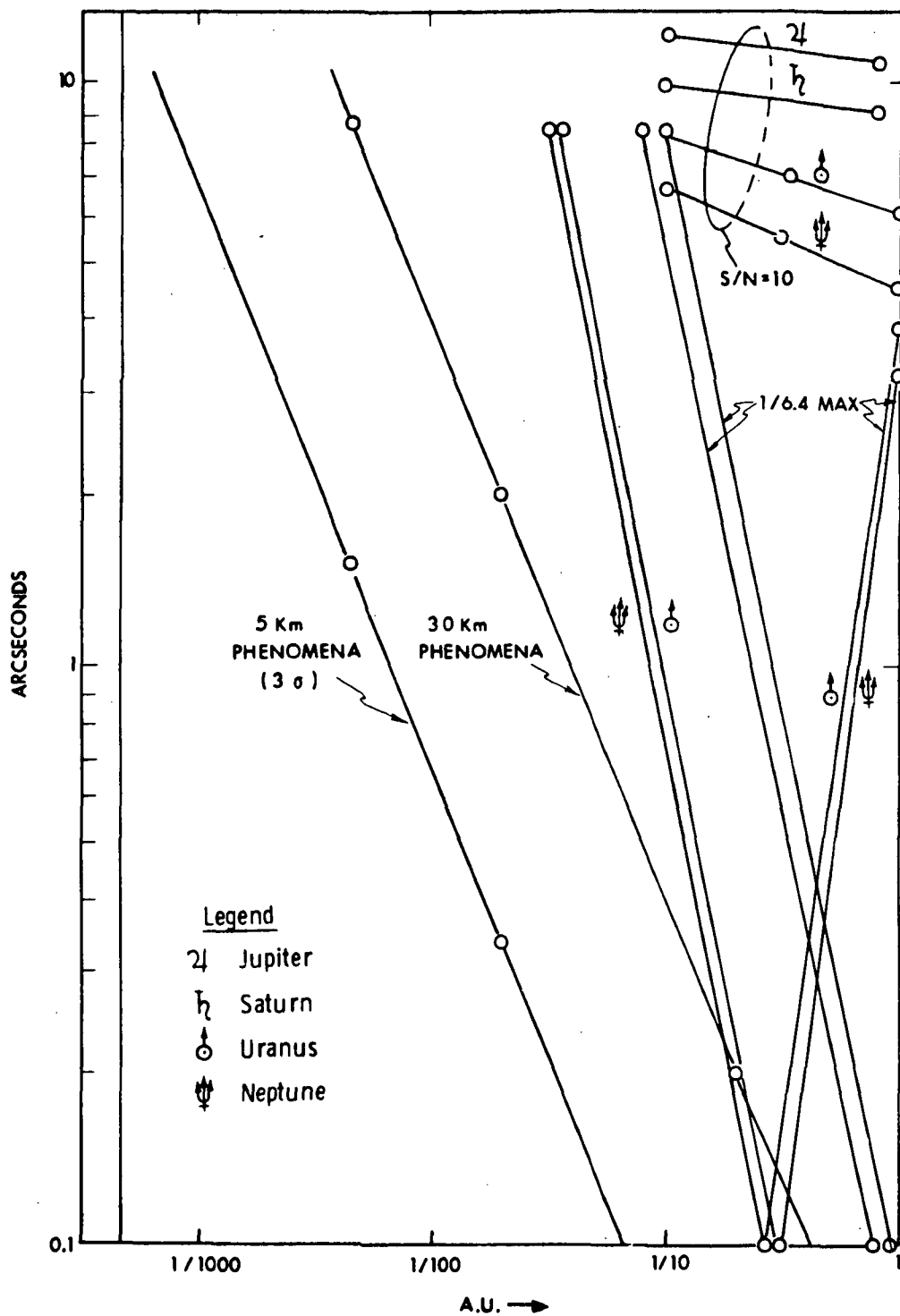


Fig. G.6 Bias Errors Caused by Diffraction

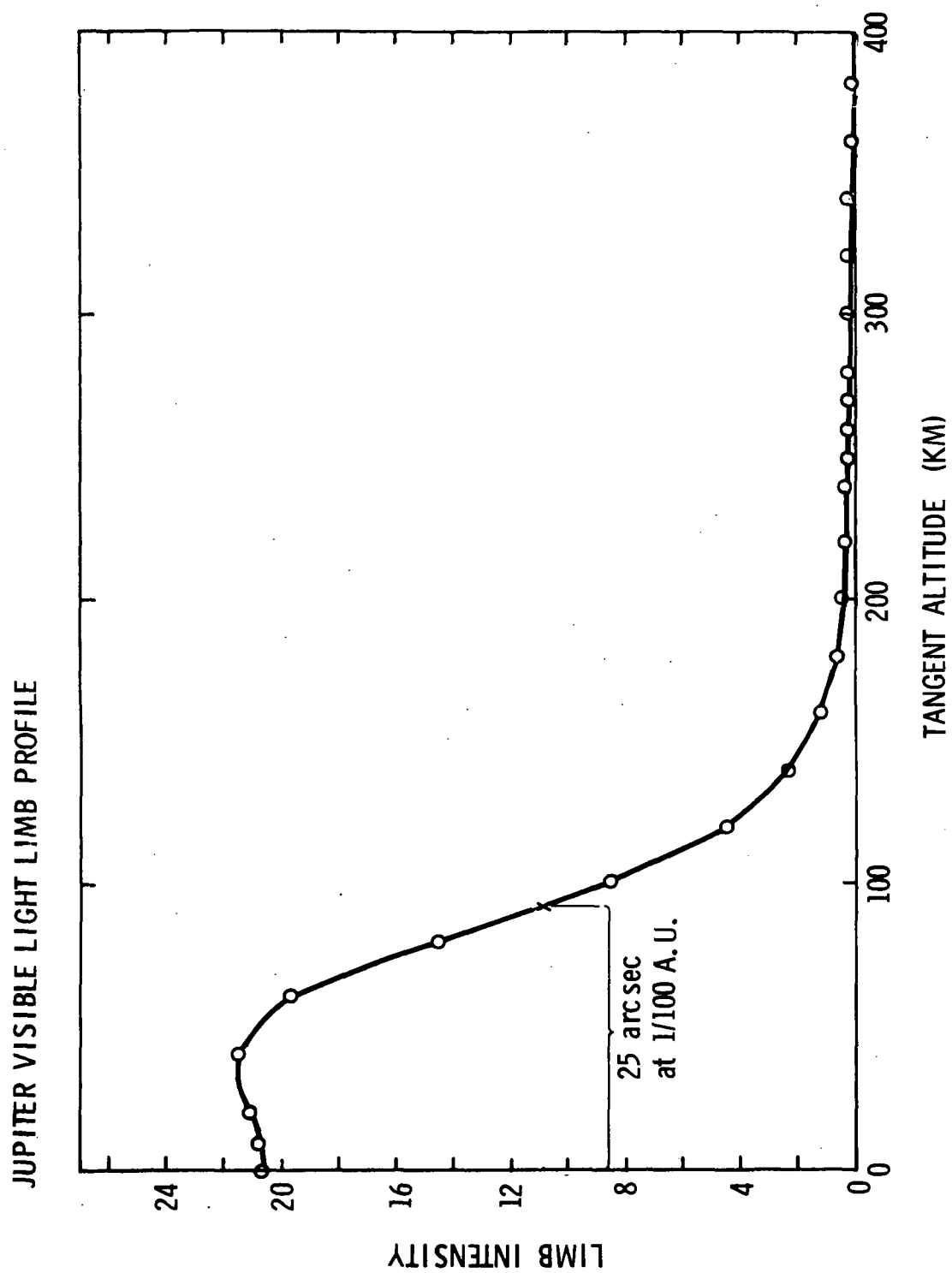


Fig. G. 7 Jupiter Visible Light Limb Profile

4. Visible Scan Rates

Using the formula for scan rate given previously, representative rates were calculated for the half maximum and fixed $S/N = 10$ threshold levels. Signal rise curve slopes (k) were obtained graphically from the signal curves (Figure G.4). The results are given in Figure G.8. Rates for the fixed threshold remain fairly constant as a function of range because they result from the diffraction region of the signal curves, however, at shorter ranges where the atmospheric scale becomes important, these rates increase rapidly because of the small slope of the signal curves (see Figures G.7 and G.4). Half-maximum related rates, by contrast, start high at 1 a.u. and eventually decrease at short range where the atmospheric horizon profile has greater slope than does the diffraction curve at larger ranges. Differences between planets are due to the differing angular radii of the planets for a given range.

5. Infrared Assumptions

To make some estimates of accuracy it is necessary to make some assumptions about the detector and its environment.

It is assumed that a thermistor bolometer detector will be mounted adjacent to another identical detector, with one detector sensing the source planet, and the other cold space. The signals coming from the two detectors are subtracted leaving a difference signal which is nearly independent of ambient thermal environmental conditions (see References 37 and 38 for a detailed and thorough exposition of the theory and engineering of thermistor-bolometer detectors). The planets are assumed to radiate as black bodies with temperatures of 149°K -Jupiter, 111°K -Saturn, 60°K -Uranus, 40°K -Neptune. Corresponding peak radiation wavelengths are 19.4, 26.05, 48.2, 72.5 microns respectively. Radiation in the wavelength range of 10-100 microns is assumed to be detectable. The detector is assumed to have the state of the art time constant of 40 seconds, and is seated at the focal point of a reflecting telescope of 100 cm^2 aperture.

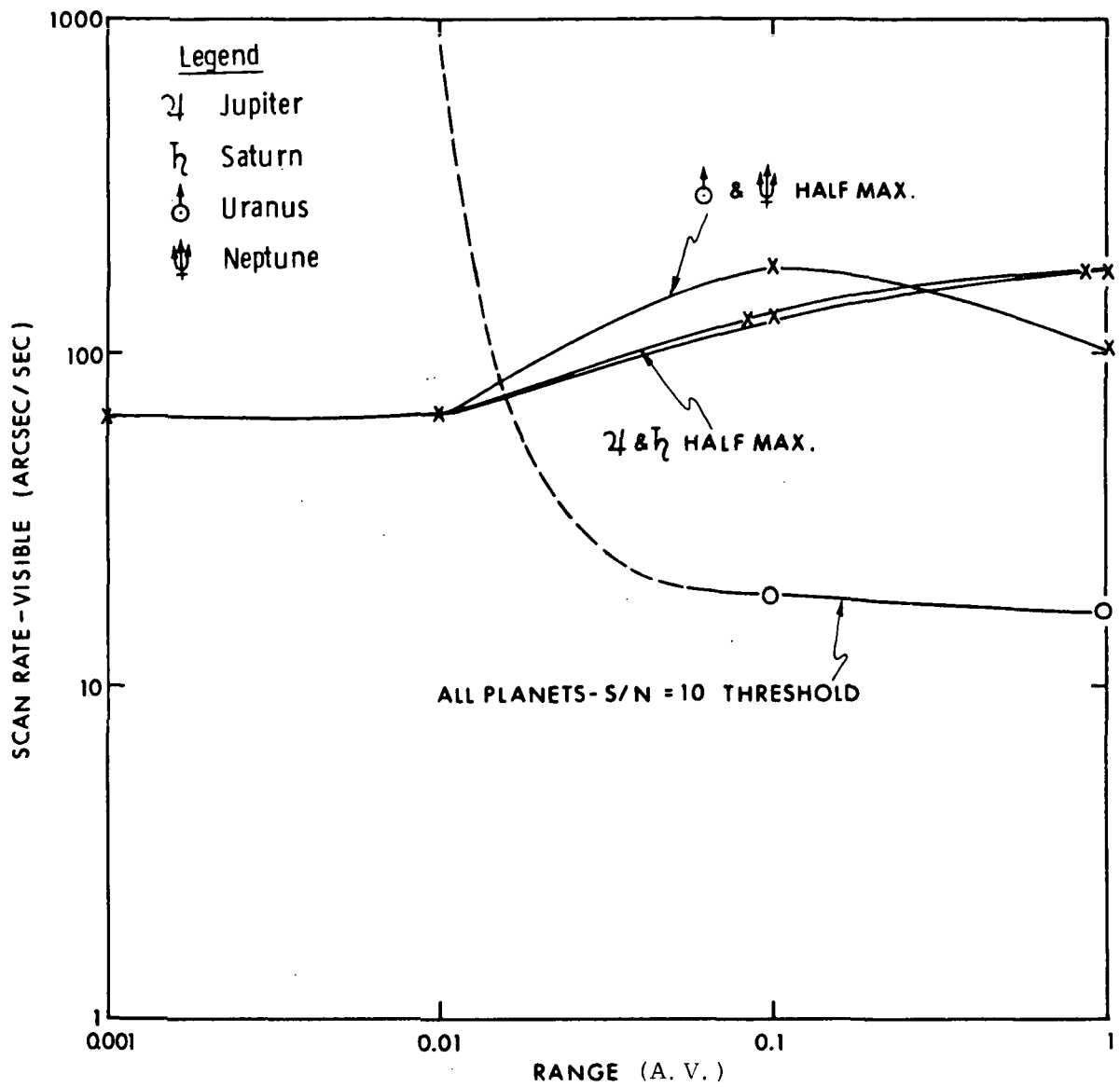


Fig. G. 8 Scan Rate vs Range for Half-Max and S/N = 10 Locators

Two field of view limiting slits were chosen for analysis. The first, one minute of arc by one minute, represents the order of size required to sense the colder planets when the field of view is filled. For this aperture, the main signal curve shaping effecting is diffraction. The $1' \times 20'$ field of view was selected to determine the effects of planet curvature, and higher signal to noise ratio on accuracy and scan rate.

6. I. R. Horizon Locator Selection

There does not appear to be much choice for an I. R. threshold. Signal to noise ratios are low for Uranus and Neptune, which implies that the threshold should be set as high as possible; and diffraction effects dominate the signal rise curves for a single limb scan which implies that the best choice of locator is at or near the maximum slope point. For the $1' \times 1'$ field of view, the point of maximum slope is very close to the half maximum intensity as can be seen in Figure G. 9. This is true for all four planets over most of the range. Maximum slopes in the $1' \times 20'$ field of view case vary in angular separation from the planet edge and in fractional intensity level. Variations occur among planets and as a function of range. For example, Figure G. 10 shows the signal curves for the four outer planets as a function of scan angle between planet edge (cloud top) and the center of the sensor field of view. It is clear from the figure that for Uranus and Neptune, the threshold has to be set as high as possible, consistent with a reasonable error, to preserve a reasonable S/N. Jupiter and Saturn allow more leeway with respect to S/N, but the threshold levels at maximum signal curve slope occur just below the half maximum point. In the cases of Uranus and Neptune the maximum slope points are even closer to the half maximum points. Thus choosing the half maximum as a threshold for all four planets does not appreciably affect the accuracy in each case. The alternative is a variable fractional threshold that changes with each planet. At long (1 a. u.) ranges the signal curves are essentially diffraction shaped, and the half maximum intensity lies on the maximum slope part of the sweep signal curve. At very small range ($< 1/500$ a. u.) the curves are atmospheric structure dependent and probably resemble the visible wavelength curve (Figure G. 7).

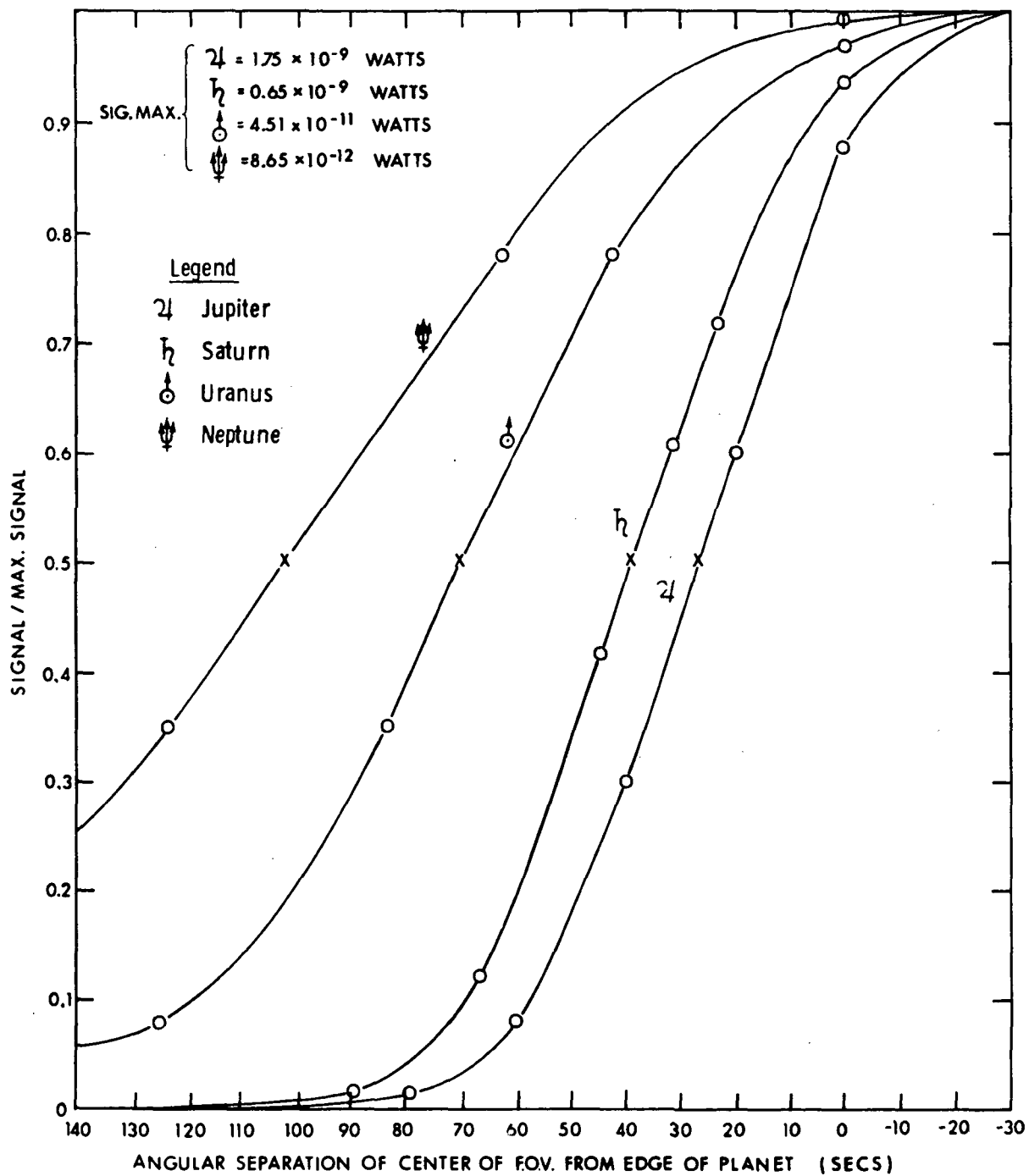


Fig. G. 9 . Normalized Infrared Signal for 1'x1' Field of View

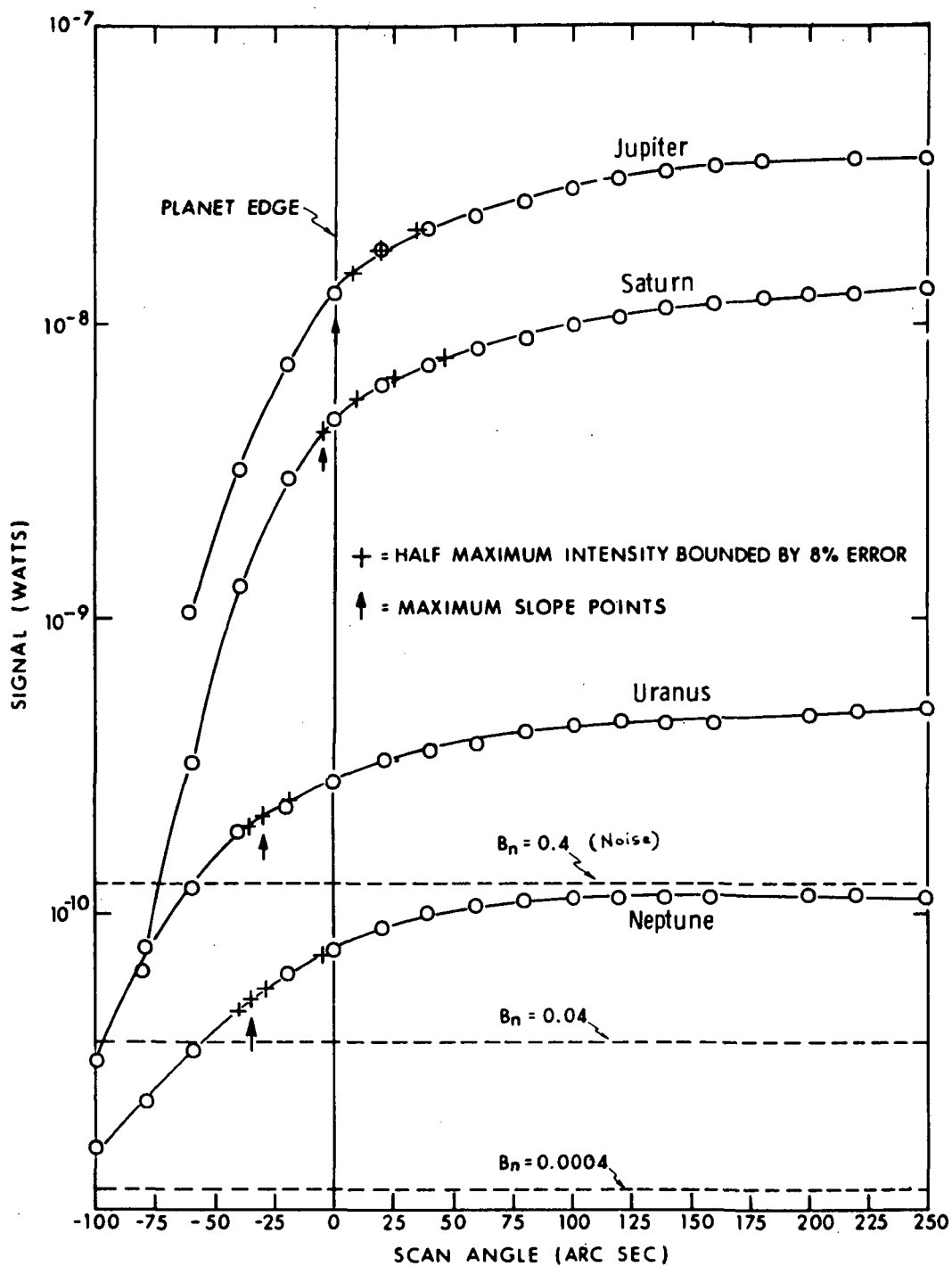


Fig. G.10 Infrared Scan Signal for a $1' \times 20'$ Fiew of View at $1/10$ A. U.

7. Infrared Accuracy

Curves of angular and bias error for the two fields of view are given in Figure G. 11 and G. 12. Noise filter bandwidth is the parameter while range is the independent variable. These curves have all been calculated by assuming an 8% 1σ calibration error on either side of a half maximum threshold setting. Where it is important, noise from the detector has been added linearly to the calibration error. 1σ noise has been computed using a formula from Reference 38, namely:

$$1\sigma \text{ noise} = 3.5 \times 10^{-10} (A/\tau)^{1/2} \times \text{noise filter bandwidth}^{1/2},$$

where A is the detector area in cm^2 , and τ is the detector time constant in seconds. For the $1' \times 1'$ field of view, A is taken as $0.775 \times 10^{-4} \text{ cm}^2$. The value of $\tau = 0.04$ sec has been estimated in Reference 39 as the state of the art in the 70's.

Figures G. 11 and G. 12 show the noise and calibration errors for the two slits. At long range, the large area detector errors are huge for Uranus and Neptune because the signal is buried in detector noise. For the $1' \times 20'$ case for Jupiter and Saturn the error increases at 1/100 a. u. over that at 1 a. u. This is caused by the effects of planet curvature which flatten the signal curves. At very small ranges, the $1' \times 20'$ field of view errors are smaller than the $1' \times 1'$ values which is to be expected because the signal increases with field of view while the noise only increases with the square root of detector area.

To illustrate the effect of noise filter bandwidth (B_n), Figure G. 13 has been constructed for the $1' \times 1'$ case. It shows the angular error increasing rapidly with B_n for Uranus and Neptune. For Jupiter and Saturn, however, the calibration error is much larger than the detector noise, and so increasing B_n over the indicated range has little effect.

Figure G. 14 shows the bias errors that would result if the half maximum locator were taken to be the planet limb. Uncertainty in atmospheric transmission for the outer planets makes bias errors uncertain in turn. If optical depths in the upper atmosphere are small over most wavelengths, then the limbs will be sharp and bias errors will diminish

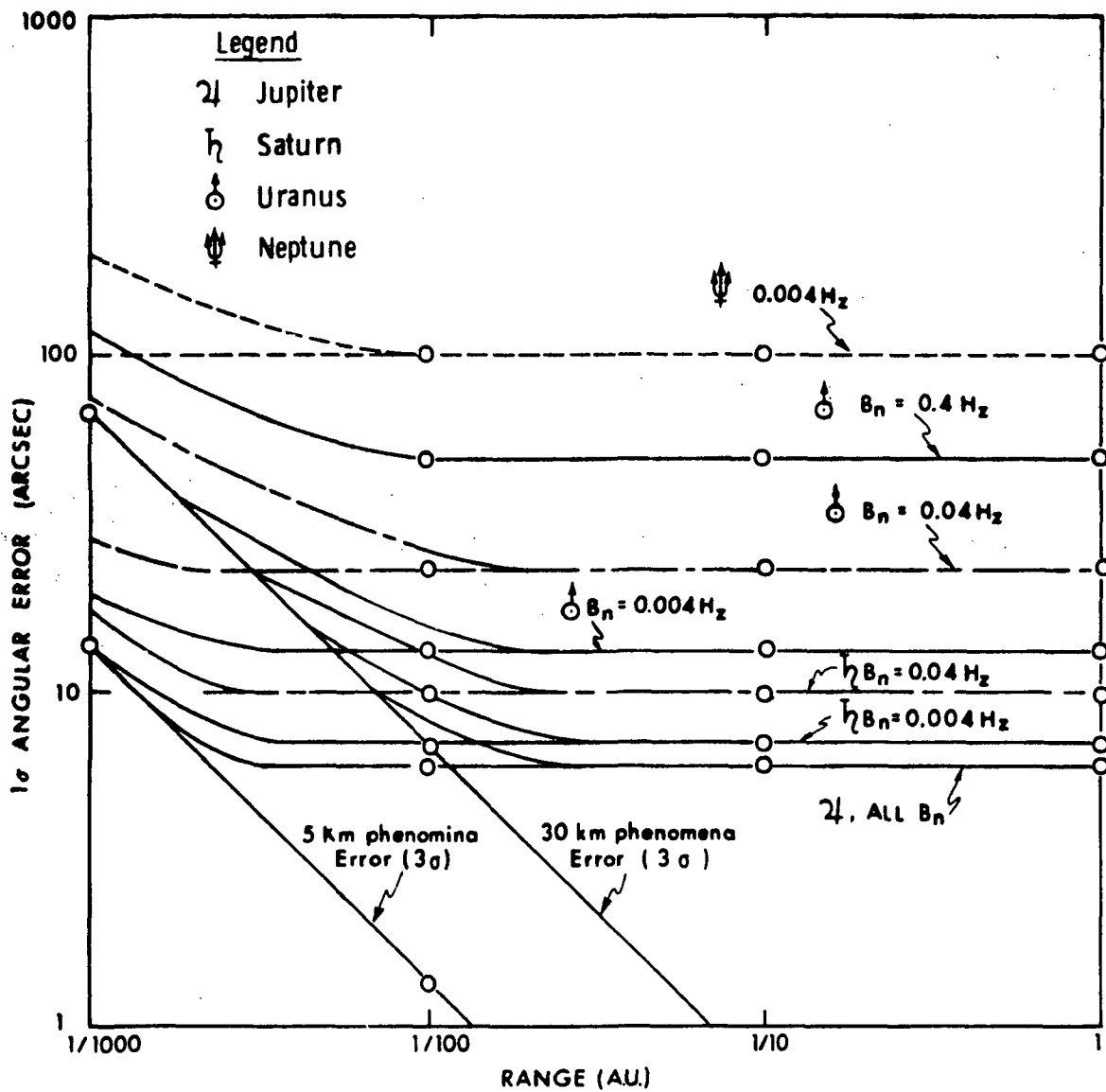


Fig. G. 11 Infrared Scan 1σ Error (Bias Removed) $1' \times 1'$ Field of View

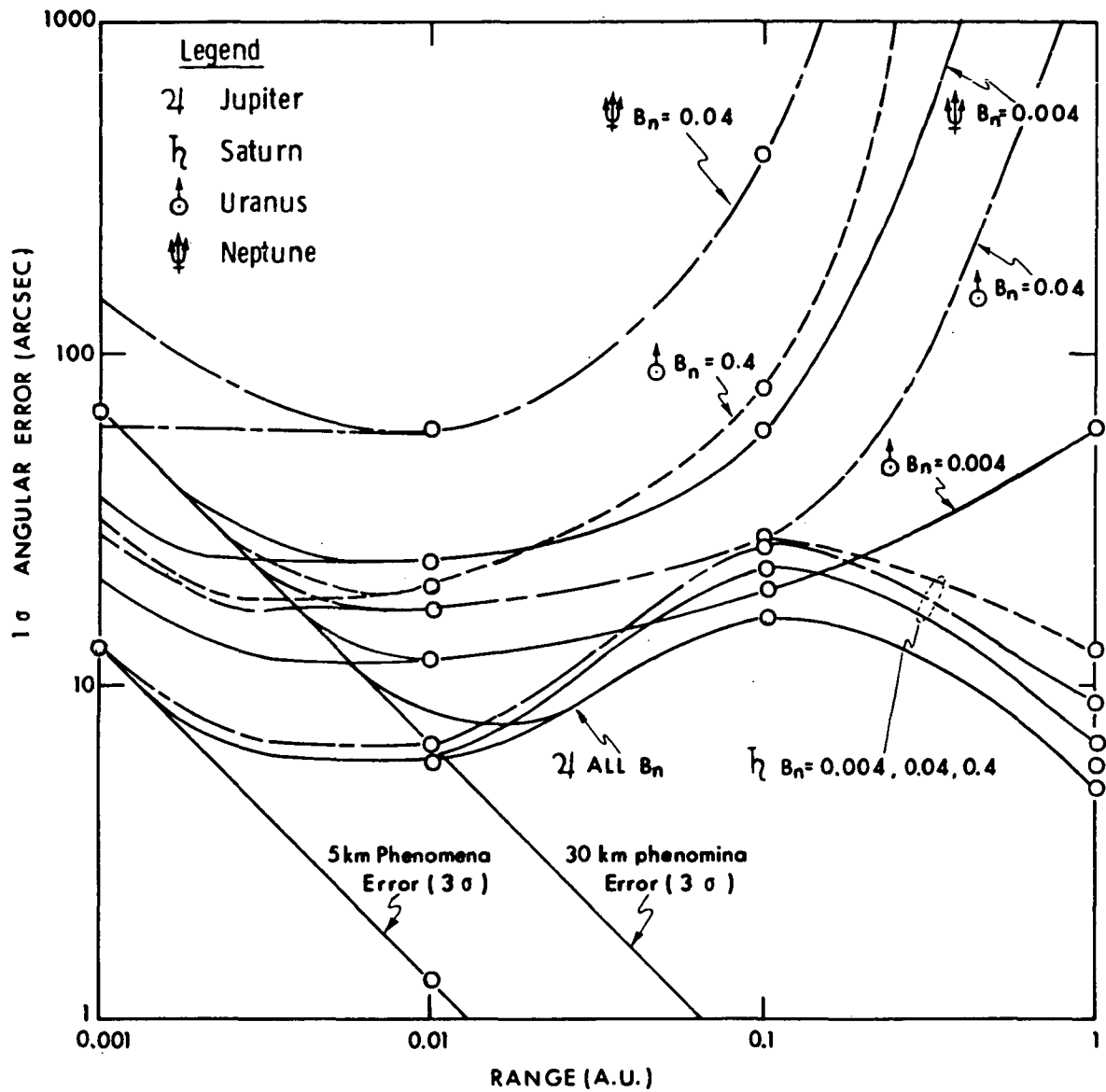


Fig. G. 12 Infrared 1σ Scan Error - $1' \times 20'$ Field of View

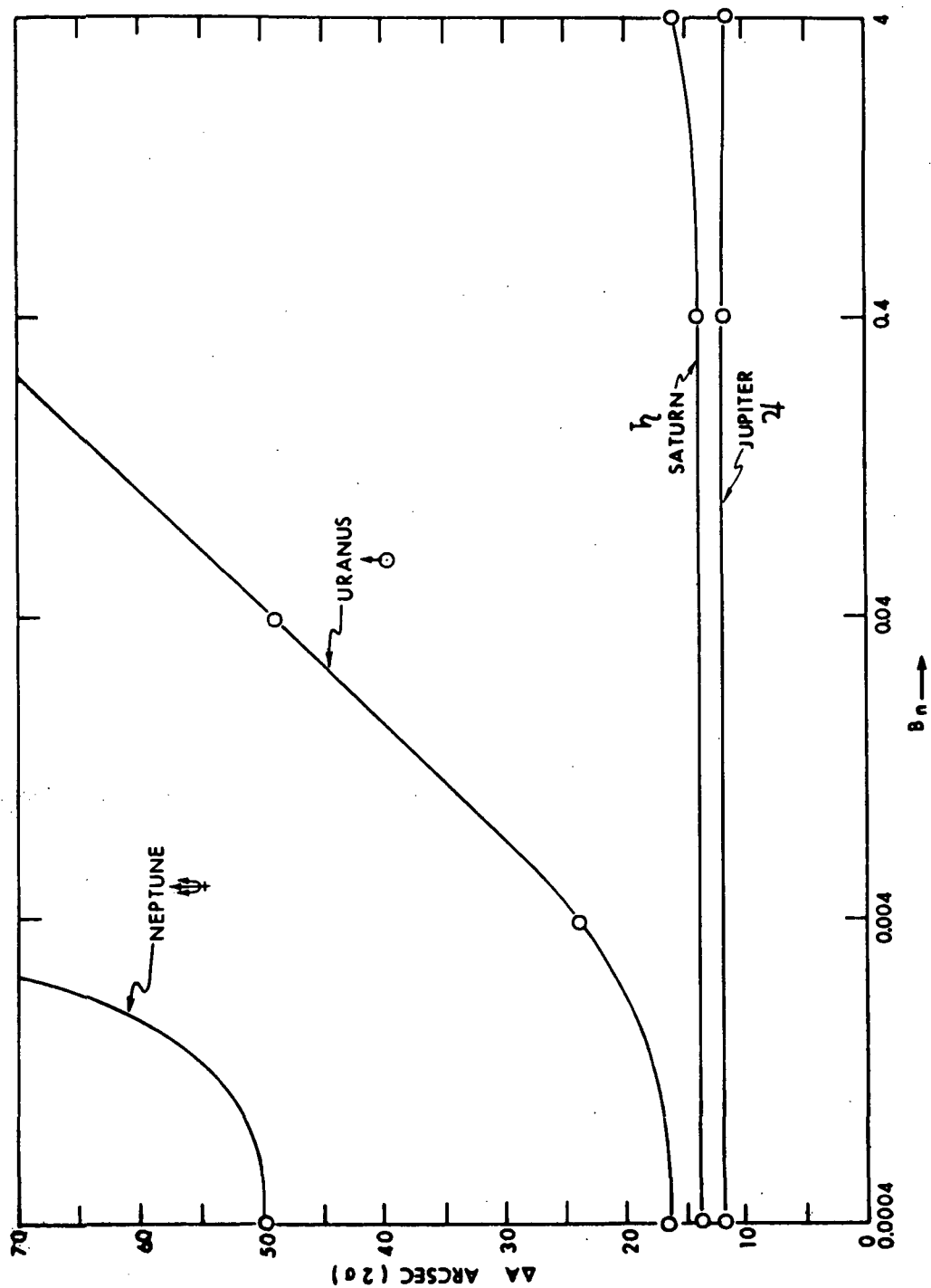


Fig. G. 13 Infrared 1σ Scan Error vs Noise Filter Bandwidth ($1' \times 1'$ Field of View)

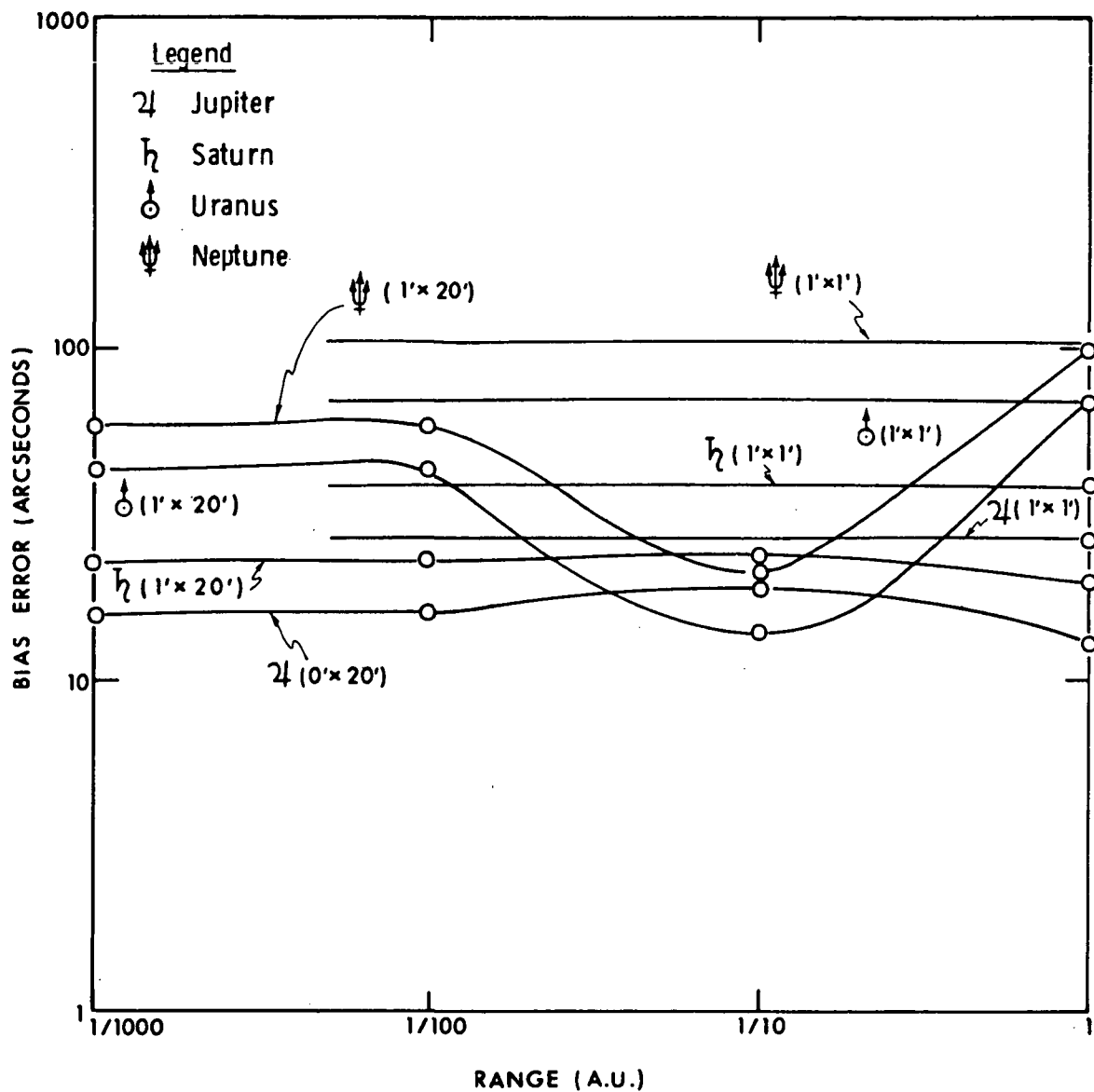


Fig. G. 14 Infrared Bias Error from Diffraction Using Half-Max Locator, $1' \times 1'$ Slit

close in, and vice versa. It looks like the choice of a constant bias correction for a given field of view could keep the bias error down to say a half minute of arc.

8. Infrared Scan Rates

Scan rates were calculated by applying the same equation used for visible rates. Figure G. 15 shows rates for the $1' \times 1'$ field of view as a function of noise filter bandwidth, with each planet represented by a curve. Neptune rates are indeterminate by means of the given equation because the 1σ noise exceeds the signal for all the chosen filter bandwidths. Figure G. 16 and G. 17 show the $1' \times 20'$ field of view rates for the planets Jupiter and Neptune which are the limiting cases on the two extremes. Jupiter rates show the bulge at $1/10$ a. u. caused by geometric effects on the signal curve slope at half maximum. The larger field of view and its corresponding larger detector area admit more noise, causing rates to go indeterminate for Neptune at the larger ranges.

9. Further Investigations - I. R. and Visible Accuracy

Although it is felt that the above results are representative of the accuracies that will be obtained by a simple scan solid state detector, the calculations are gross and will require much refinement. In addition, there are a number of non-negligible factors whose effects haven't been included, even roughly, in the above results.

The signal rise curves for a simple scan need to be calculated accurately at all ranges, combining the effects of limb structure, telescope diffraction, and planet curvature. Presumably this would be done by computer simulation although planet curvature can be treated analytically, and the diffraction problem may be possibly formulated using Fourier transform optics. Limb profiles, at close ranges where the field of view height is much less than the angle subtended by the atmospheres, need to be determined as accurately as possible. This will involve atmospheric modeling and the solution of transfer equations using the scanty and variable data available.

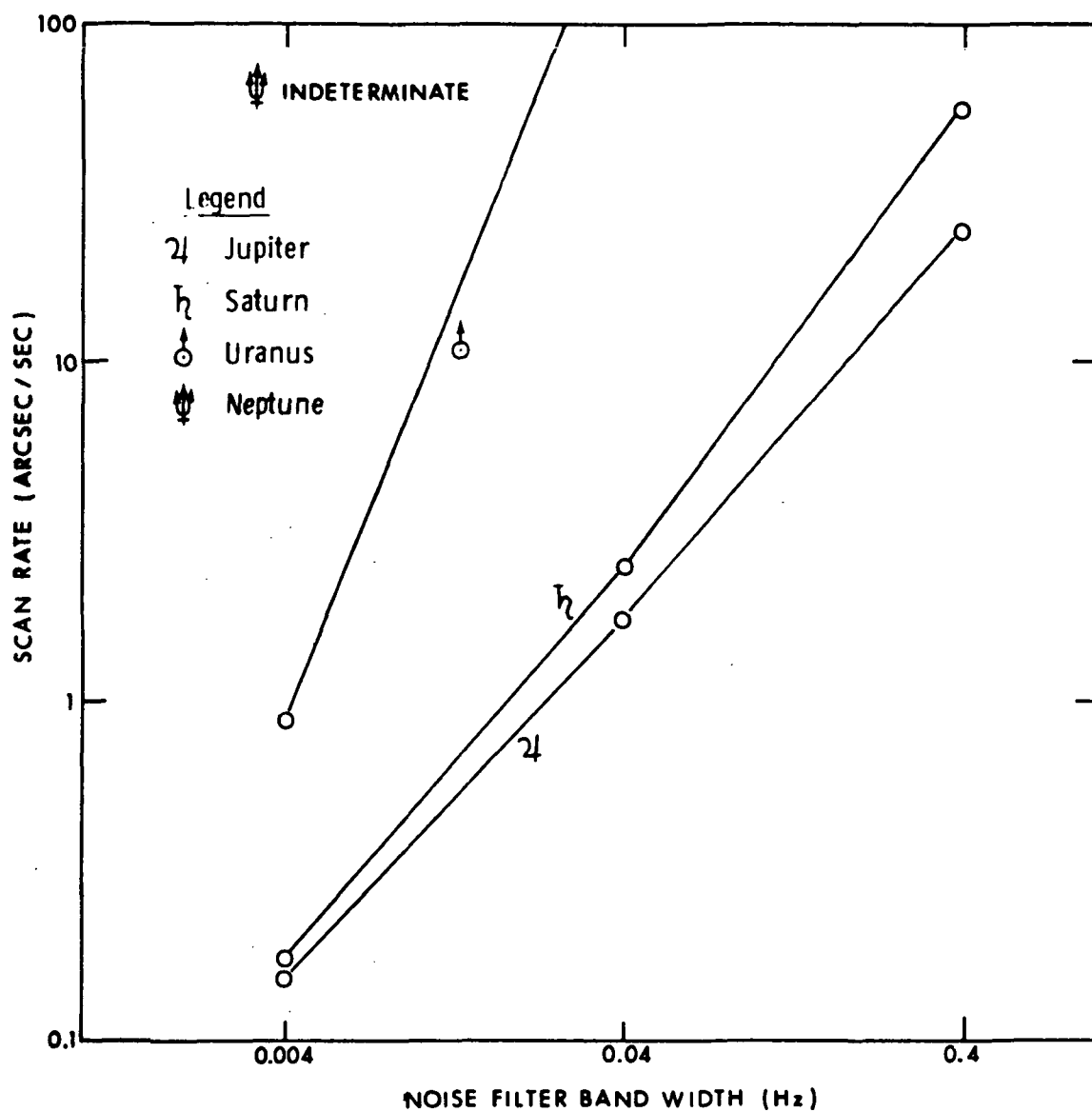


Fig. G. 15 Infrared Scan Rates, 1'x1' Slit, vs Noise Filter Bandwidth

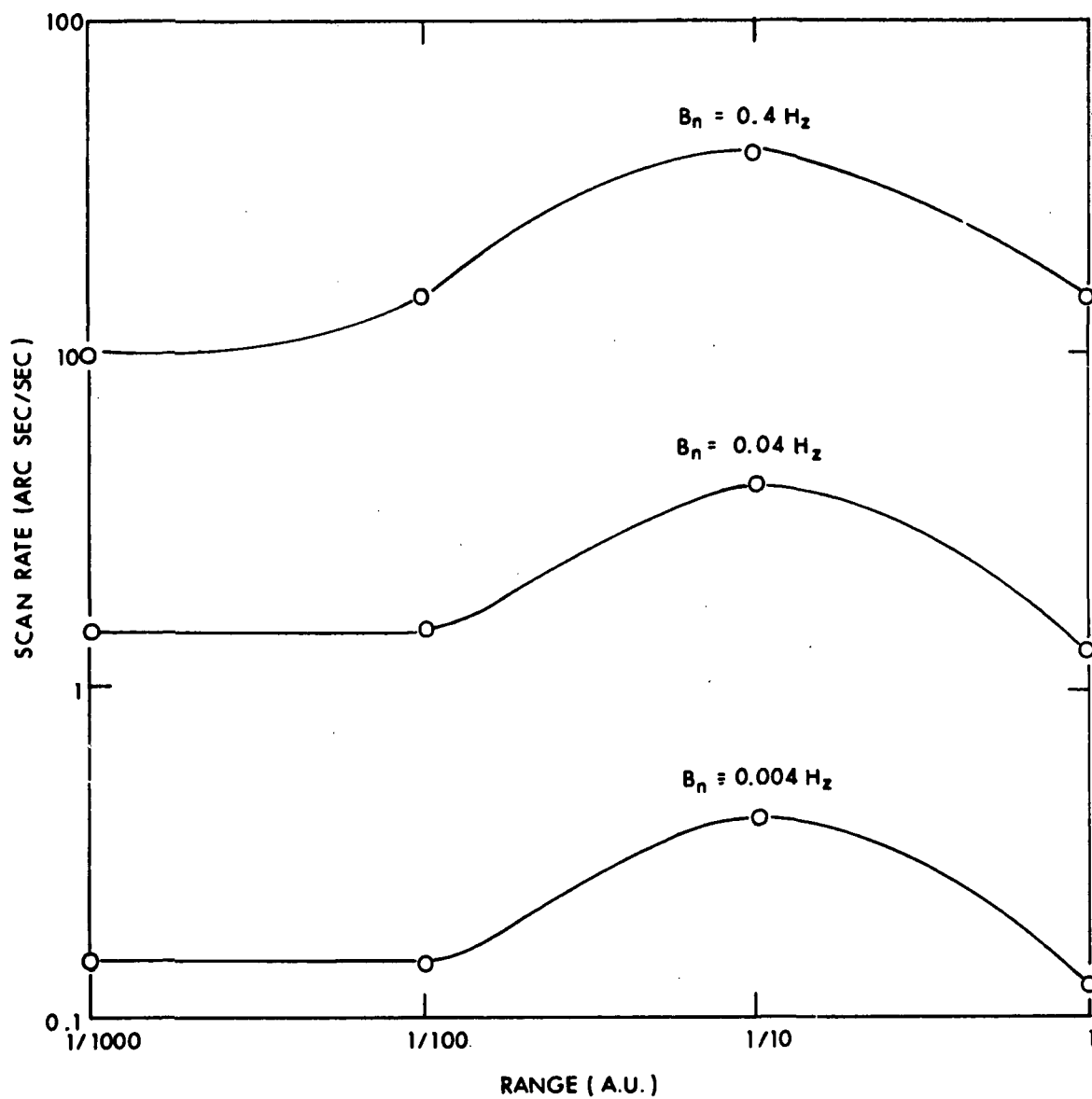


Fig. G. 16 Jupiter Infrared Scan Rates for 1' \times 20' Slit

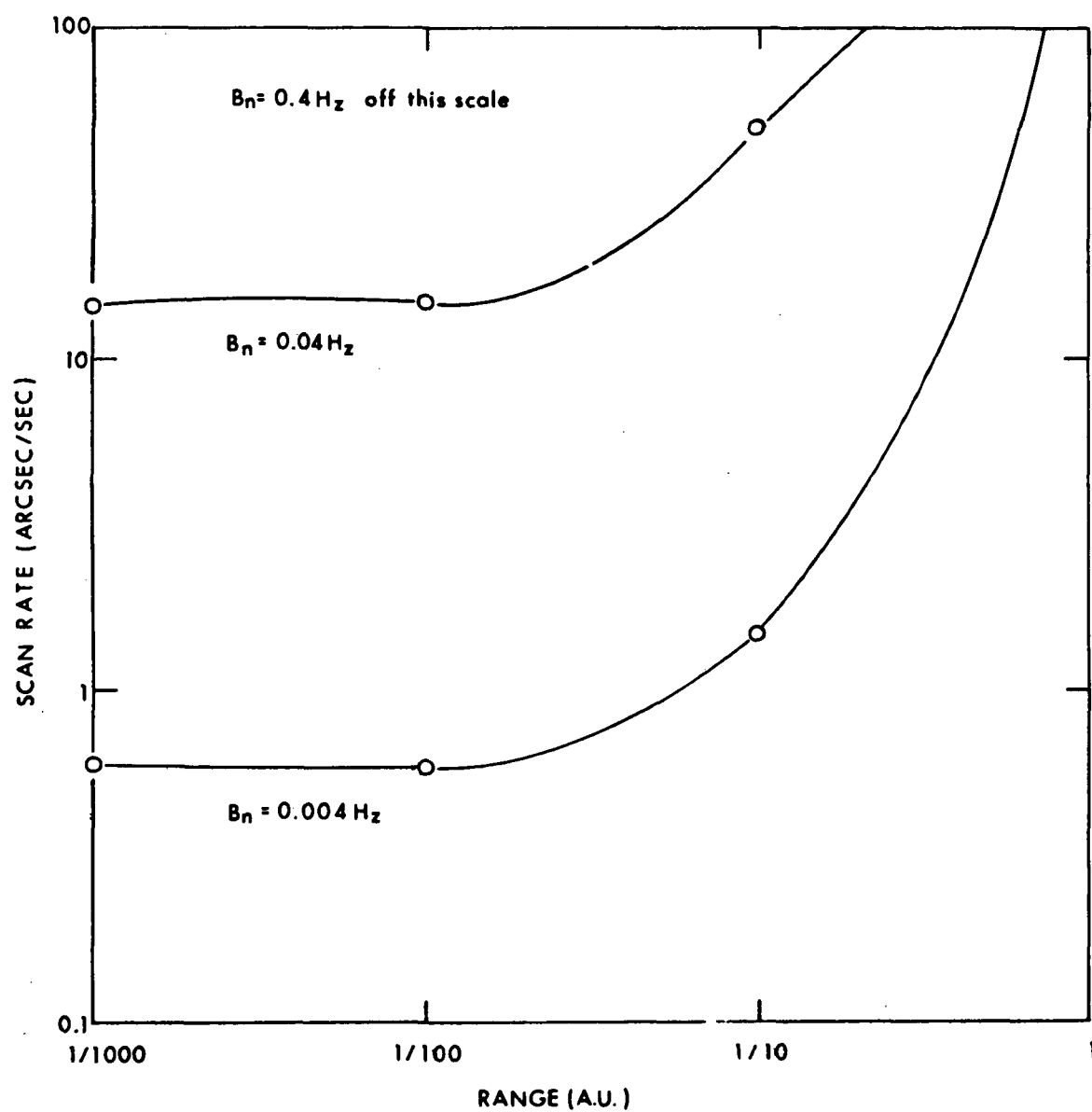


Fig. G. 17 Neptune Infrared Scan Rates for 1' x 20' Slit

If there are significant temperature variations with latitude, the variations and resultant effects on the signal curves need to be calculated. This problem is complicated by a wide field of view that collects radiation from a band of latitudes simultaneously.

In the same general area, errors caused by offset and rotated fields of view must be determined. This problem has been worked many times before, but not under the outer planet conditions.

It is apparent that regardless of the choice of threshold, there will be bias errors, and a scheme to correct these needs to be developed. The scan signal may be transmitted back to earth for processing which would effectively remove the bias error; however, if there is a backup capability in case of failure of uplink, the bias correction will still be required.

Scattered light from the sun in near planet situations and from the portion of the planet out of the field of view in far planet situations may be a problem.

Background radiation from space may cause significant additions to the errors in the case of Neptune, particularly at 1 a. u. , with the larger fields of view.

In the case of I. R. there are possibilities that small amounts of heat dissipated from various operating electrical and mechanical parts of the spacecraft may end up in some detectable part of the sensor. These possibilities need to be engineered away if they can be shown to seriously affect accuracy.

Finally, given the best possible scan signal curves, it will be necessary to optimize the sweep rates, which can probably best be done by use of an analog-digital simulation.

10. Star Sensing Accuracy

The signal from a second magnitude, type AO star is about 100 times the noise level of the SCG-100 diode, so a simple threshold device could be used to indicate the sensing of a star. However, since the central region of the star diffraction image ranges from about 2 to 4 arcseconds in width depending on the aperture diameter and the wavelength, some procedure is needed to account for the bias error of a simple threshold device if star direction errors are to be reduced to the fractional arcsecond range. A simple solution to this problem is to average the position of entrance and exit thresholds. A more accurate method is to calculate the signal centroid by integrating the signal over a small scan interval. The theory of this type of computation is given in Reference 40. The interval of integration is chosen by varying the scan rate such that the rate is fast enough to avoid getting too large a noise contribution to the integral, but slow enough to get sufficient signal. The procedure is mechanized by using three slits. The first triggers the integration, the second samples the signal, and the trailing slit stops the integration. A computer simulation of this technique is presently being constructed, and although no complete calculations have been made yet, the estimated error of the star position for B-Grius (second magnitude) is shown in Figure G. 18.

11. Angle Resolver Accuracy

The two non-precision axes of the three degree of freedom sensor use iron core resolvers for angle measurement which are accurate to within about 15 arcseconds. This is well within the requirement for scan plane alignment. The precision axis resolver is an Inductosyn of approximately 5" diameter. This device is capable of an estimated 1 arc-second precision given that it requires use of error correction determined from calibration in order that its accuracy be limited only by its stability. Repeatabilities are significantly better than their linearity. These corrections, obtained either from pre-flight calibration and/or in-flight calibration can be expressed and stored as a few dominant Fourier

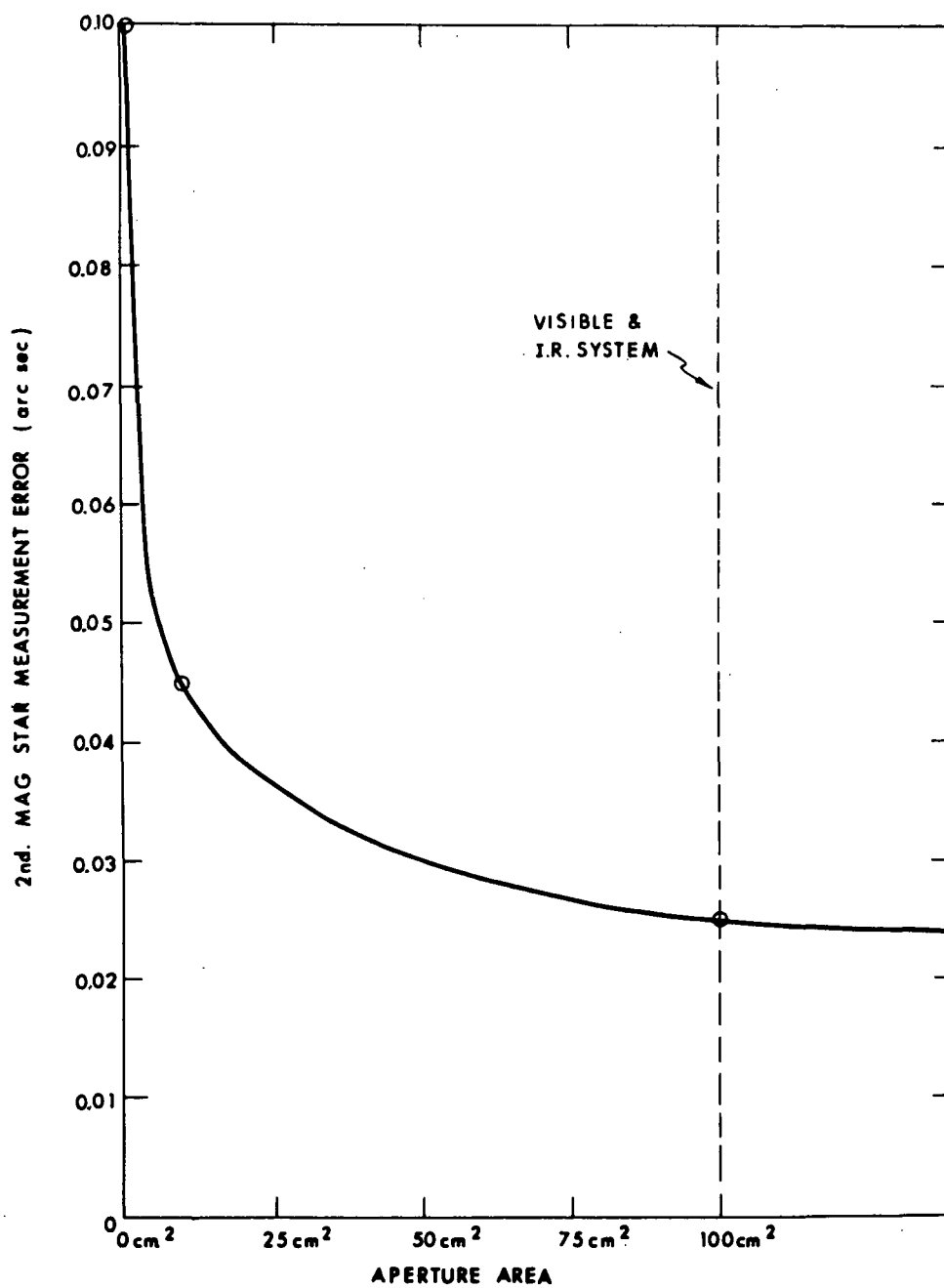


Fig. G.18 Star Direction Error Estimate

coefficients, and used by the flight computer to calculate corrections to the indicated angle of any measurement made.

If the limiting accuracy of an angle measurement is 1 arcsecond, then obviously sophisticated techniques for determining star position to within a small fraction of an arcsecond are unnecessary. To match resolver and electronic star position accuracies, a highly accurate resolver like the ring laser (Reference 41) would be required.

Page intentionally left blank

APPENDIX H

OPTIMIZATION OF THE ONBOARD MEASUREMENT SCHEDULE

The measurement selection method given in Chapter II finds the optimum measurement at any given measurement time; the effect of measurements taken at future times is not considered in that procedure; moreover the measurements selected at the previous times were fixed once they were selected. In this Appendix a method is given for optimizing the overall measurement schedule for the case where only onboard measurements are made. This method is basically that developed in Reference 42; it is repeated here for the current application.

The equations used for extrapolating and incorporating the state covariance matrix, E , are

$$E_n' = \Phi_{n, n-1} E_{n-1} \Phi_{n, n-1}^T \quad (\text{H. 1})$$

and

$$E_n = E_n' - E_n' h_n (h_n^T E_n' h_n + R_n)^{-1} h_n^T E_n' \quad (\text{H. 2})$$

where $n = 0, 1, \dots, N$ and N is the total number of measurement times. It is assumed that the measurement times are prespecified, but the particular measurement to be made at any time is to be determined from a given selection, $\theta = [\theta_1, \theta_2, \dots, \theta_K]$ with the associated h_i 's and R_i 's given and where K is the total number of measurement opportunities at the measurement time under consideration. The cost function used to evaluate the quality of a given measurement sequence is

$$J = \text{tr} \begin{bmatrix} I & O \\ O & cI \end{bmatrix} E_N \quad (\text{H. 3})$$

where c is a weighting coefficient.

We now seek the impulse response of J to small perturbations in the present measurement sequence. From the impulse response, the effect on J of a small change* in the choice of measurement at a particular measurement time can be determined.

From Eq. (H. 1) one obtains the following equation for the extrapolation of the first variation of the covariance matrix.

$$\delta E_n' = \Phi_{n,n-1} \delta E_{n-1} \Phi_{n,n-1}^T \quad (H. 4)$$

From Eq. (H. 2) one obtains the following equation for the effects on the first variation of the covariance matrix of incorporating a measurement.

$$\begin{aligned} \delta E_n = & \delta E_n' - \delta E_n' \underline{h}_n a_n^{-1} \underline{h}_n^T E_n' - E_n' \delta \underline{h}_n a_n^{-1} \underline{h}_n^T E_n' \\ & + E_n' \underline{h}_n a_n^{-1} (\delta \underline{h}_n^T E_n \underline{h}_n + \underline{h}_n^T \delta E_n' \underline{h}_n + \underline{h}_n^T E_n' \delta \underline{h}_n + \delta R_n) a_n^{-1} \underline{h}_n^T E_n' \\ & - E_n' \underline{h}_n a_n^{-1} \delta \underline{h}_n^T E_n' - E_n' \underline{h}_n a_n^{-1} \underline{h}_n^T \delta E_n' \end{aligned} \quad (H. 5)$$

where

$$a_n = \underline{h}_n^T E_n' \underline{h}_n + R_n \quad (H. 6)$$

Substituting Eq. (H. 4) into Eq. (H. 5), premultiplying the results by L_n , and employing the properties that $\text{Tr}(AB) = \text{Tr}(BA)$ and $\text{Tr}(A + B + C) = \text{Tr}(A) + \text{Tr}(B) + \text{Tr}(C)$ yields:

$$\begin{aligned} \text{tr } L_n \delta E_n = & \text{tr } L_{n-1} \delta E_{n-1} \\ & - 2 \text{tr } B_n L_n E_n \delta \underline{h}_n + \text{tr } B_n L_n B_n^T \delta R_n, \end{aligned} \quad (H. 7)$$

*Small change infers that $\underline{h}_i' - \underline{h}_i$ and $R_i' - R_i$ are small.

where

$$A_n \triangleq \underline{h}_n a_n^{-1} \underline{h}_n^T E_n \quad (H. 8)$$

$$B_n \triangleq a_n^{-1} \underline{h}_n^T E_n \quad (H. 9)$$

$$L_{n-1} \triangleq \Phi_{n,n-1}^T [L_n - A_n L_n - L_n A_n^T + A_n L_n A_n^T]$$

Summing (Eq. H. 7) and invoking the boundary condition $\delta E_0 = 0$ yields:

$$\text{tr } L_N \delta E_N = \sum_{n=1}^{N-1} (\text{tr } \underline{\lambda}_n^T \delta \underline{h}_n + \epsilon_n \delta R_n), \quad (H.10)$$

where

$$\underline{\lambda}_n = -2E_n L_n B_n^T \quad (H. 11)$$

$$\epsilon_n = B_n L_n B_n^T \quad (H. 12)$$

Equation (H. 10) is the desired result; that is, it can be used to determine the effect of changing a measurement at any measurement time.

The criterion used for keeping the change in a measurement small was

$$\delta \underline{h}_n^T A \delta \underline{h}_n + b \delta R_n \leq k,$$

where the matrix A and the scalars b and k must be chosen by experience. Repeated passes through the trajectory are made; on each pass the optimum measurement at each time is selected using Eq. (H. 10). When an improvement is no longer obtained, the procedure is stopped since the optimum overall onboard measurement schedule has been found.

Page intentionally left blank

REFERENCES

1. Kingsland, L. , Bollman, W. E. , "An Approximate Solution to the Estimate of the Navigational Accuracy of a Deep Space Probe", Jet Propulsion Laboratory Technical Memorandum 312-884, May 21, 1969, Pasadena, California
2. Hamilton, T.W. , Melbourne, W.G. , "Information Content of a Single Pass of Doppler Data From a Distant Spacecraft", Jet Propulsion Laboratory Space Programs Summary 37-39, Vol. III, March - April 1966, Pasadena California.
3. Dollfus, A. , Planets and Satellites, G.P. Kuiper Ed. , U. of Chicago Press, Chicago, 1961. (pp 545)
4. Mintz, B.F. , "Observations of Bright Minor Planets and Comets", Astronomical Journal, Vol. 73, No. 1, pp 49, Feb. 1968.
5. Cesco, C. U. , Klemola, A.R. , "Observations of the Satellites Jupiter VI and VII", Astronomical Journal, Vol. 72, No. 8, pp 951, Oct. 1967.
6. Scott, F. P. , "Limitations Imposed on Celestial Navigation Due to Inaccuracies of Star Positions", Navigation, Vol. 11, No. 1, pp 20, Spring 1964.
7. Duncombe, R. L. , "Personal Communication," U.S. Nautical Almanac Office, Naval Observatory, Washington, D. C. , June 31, 1968.
8. Allen, C. W. , "Astrophysical Quantities", the Athlone Press, U. of London, 1955.

9. Manning, L. A., "letter to J. H. Flanders of MIT/IL", NASA/OART Mission Analysis Division, August 5, 1968.
10. Peebles, P. J. E., "The Structure and Composition of Jupiter and Saturn", Astrophysical Journal, Vol. 140, No. 1, pp 328, July 1964.
11. "Handbook of the Physical Properties of the Planet Jupiter", NASA Publication SP-3031, 1967.
12. Manning, L. A., "Letter to MIT/IL", NASA/OART Mission Analysis Division, July 10, 1968.
13. Squires, P., "The Equatorial Clouds of Jupiter", Astrophysical Journal, Vol. 126, No. 1, pp 185, January 1957.
14. Urey, H. C., "Handebuch Der Physik", S. Flugge Ed., Vol. 52, pp 363, Springer-Verlag, Berlin, 1959.
15. Taylor, G. E., "New Determination of the Diameter of Neptune", Nature, Vol. 219, pp 475, August 3, 1968.
16. Spinrad, H., Trafton, L. M., "High Dispersion Spectra of the Outer Planets (1.) Jupiter in the Visual and Red", Icarus, Vol. 2, No. 1, pp 19, June 1963.
17. "The Atmosphere of the Earth and Planets", G. P. Kuiper Ed., U. of Chicago Press, Chicago, pp 382, 1957.
18. Wildey, R. L., "On the Infrared Opacity of Jupiter's Outer Atmosphere", Icarus, Vol. 3, pp 322, June 1964.
19. Moroz, V. I., "The Spectra of Jupiter and Saturn in the 1.0 - 2.5 μ Region", Soviet Astronomy, Vol. 10, No. 3. pp 457, December 1967.

20. Taylor, D. J., "Spectrophotometry of Jupiter's 3400 - 10,000 Å Spectrum and a Bolometric Albedo for Jupiter", *Icarus*, Vol. 4, pp 362, September 1965.
21. Jaschek, C., Jaschek, M., "Some Considerations on the Asteroid Families", *Astronomical Journal*, Vol. 68, pp 108, March 1963.
22. Beckman, J. E., "The Pressure at the Cloud Top and the Abundance of Hydrogen in the Atmosphere of Jupiter", *Astrophysical Journal*, Vol. 149, pp 453, August 1967.
23. Öpik, E. J., "Jupiter: Chemical Composition, Structure, and Origin of a Giant Planet", *Icarus*, Vol. 1, No. 3, pp 200, October 1962.
24. Handbook of the Astronomical Association of Britain, C. Dinwoodie Ed., 303 Bass Road, Hounslow West, Middlesex England. 1968 edition.
25. Alexander, A. F., The Planet Saturn, Faber and Faber, London, 1962.
26. Herbig, G. H., Worley, C. E., "Some Basic Astronomical Data", *Astronomical Society of the Pacific*, Leaflet No. 325, June 1956.
27. Battin, R. H., "Class Notes for an MIT Course in Astronautical Guidance", MIT Department of Aeronautics and Astronautics, Cambridge, Mass.
28. Goodyear, W. H., "A General Method for Computation of C Coordinates and Partial Derivatives of the Two Body Problem", NASA CR-522, September 1966.

29. Battin, R. H., Astronautical Guidance, McGraw Hill, Inc., New York, 1964.
30. The American Ephemeris and Nautical Almanac, U. S. Government Printing Office, Washington, D. C., 1969.
31. Explanatory Supplement to the Ephemeris, Her Majesty's Stationary Office, London, 1961.
32. Allen, C. W., Astrophysical Quantities, Althene Press, U. of London, 1963.
33. "Control Guidance and Navigation for Advanced Manned Missions", MIT Instrumentation Laboratory Report R-600, Vol. III, Cambridge, Mass., Jan. 1968.
34. "Control Guidance and Navigation for Advanced Manned Missions", MIT Instrumentation Laboratory Report R-600, Vol. II, Cambridge Mass., Jan. 1968.
35. Code, A., Stellar Atmospheres, Vol. 6 of Stars and Stellar Systems, J. L. Greenstein Ed., U. of Chicago Press, Chicago, 1960.
36. McGarty, T. P., "Estimation of the Center of Gravity of a Photon Density Profile in Noise", MIT Instrumentation Laboratory O & N Memo No 112, September 1968.
37. Smith, M. A., "Radiometer Development - First Milestone Report", MIT Instrumentation Laboratory Research Note R 169, August 1968.
38. Smith, M. A., "Radiometer Development - 2nd Milestone Report", MIT Instrumentation Laboratory Research Note R 630, February 1969.
39. Smith, M. A., Ogletree, G., "Preliminary Design Exercise for I. R. Planet Sensor", MIT Instrumentation Laboratory Internal Memo, November 21, 1968.

40. McGarty, T. P., "Some Comments on Nonhomogeneous Poisson Processes With Applications to Position Estimation With a Photodiode", MIT Instrumentation Laboratory O & N Memo No. 122, April 22, 1969.
41. Coccoli, D., Lawson, J., "Ring Laser Angle Encoder", NASA Tech Brief 69-10015, April 1969.
42. Denham, W. F., Speyer, J. L., "Optimal Measurement and Velocity Correction Programs for Mid Course Guidance", AIAA Journal, May, 1964.

R-678
Distribution

O. Anderson
R. Battin
P. Bowditch
S. Croopnick
J. Deckert
T. Edelbaum
P. Felleman
D. Fraser (50)
C. Gray
D. Gustafson
D. Hoag
P. Kachmar
A. Klumpp
B. Kriegsman
L. Larson
G. Levine
H. Malchow (5)
E. Muller
G. Ogletree
T. Parr
P. Philliou
P. Pollock
W. Robertson
L. Sackett(2)
N. Sears
W. Tempelman
MIT/CSDL Library (10)
Apollo Library (2)

R-678

Distribution - External

NASA Headquarters - Washington, D. C. 20546

OART

R/Mr. Oran W. Nicks
RP/Mr. Adelbert O. Tischler
RE/Mr. Frank J. Sullivan
REE/Mr. Charles E. Pontious
REG/Mr. Jules I. Kanter
REI/Mr. Gene A. Vacca
RES/Mr. Charles H. Gould
RET/Mr. Henry L. Anderton
RN/Mr. William H. Woodward
RNT/Mr. James Lazar
RMD/Mr. Richard J. Wisniewski
RR/Dr. Hermann H. Kurzweg
RV/Mr. Milton B. Ames, Jr.
REG/Mr. Theodore S. Michaels

OSSA

S/Dr. John E. Naugle
SS/Dr. Henry J. Smith
SL/Mr. Robert S. Kraemer
SL/Mr. Norri Sirri

OMSF

M/Mr. Dale D. Myers

Ames Research Center - NASA, Moffett Field, California 94035

Mr. C. A. Syvertson, Mail Stop 200-2
Dr. Leonard Roberts, Mail Stop 200-3
Mr. John S. White, Mail Stop 210-3
Mr. Charles F. Hall, Mail Stop 244-8
Mr. Howard F. Matthews, Mail Stop 244-7

Goddard Space Flight Center - NASA, Greenbelt, Maryland 20771

Mr. Donald P. Hearth, Code 100
Dr. Rydolf A. Stampfl, Code 401
Mr. Robert T. Groves, Code 551
Mr. Kenneth I. Duck, Code 734

Jet Propulsion Laboratory - 4800 Oak Grove Dr., Pasadena, Calif. 91103

Dr. Donald Rea, Mail Stop 180-404
Mr. Peter N. Hauran, Mail Stop 180-302
Dr. R. Rhoads Stephenson, Mail Stop 156-203
Mr. James Long, Mail Stop 180-302
Mr. Tom W. Hamilton, Mail Stop 180-402
Mr. John R. Scull, Mail Stop 198-226
Dr. James F. Jordan, Mail Stop 156-229
Dr. Roger D. Bourke, Mail Stop 126-235
Mr. Robert G. Nagler, Mail Stop 180-703

Langley Research Center - NASA, Langley Station, Hampton, Va. 23365

Mr. William H. Phillips, Mail Stop 152
Mr. George B. Graves, Jr., Mail Stop 476
Mr. Richard C. Dingeldein, Mail Stop 156

Lewis Research Center - NASA, 21000 Brookpark Road, Cleveland, Ohio 44135

Dr. Seymour C. Himmel, Mail Stop 173-303
Mr. Richard J. Wever, Mail Stop 501-302

Marshall Space Flight Center - NASA, Marshall Space Flight Center, Ala. 35812

PD/DIR/Mr. William R. Lucas
S&E-Aero-G/Mr. Clyde D. Baker
S&E-Aero-M/Mr. J. P. Lindberg

Outside Agencies

North American Rockwell
Space Division
12214 Lakewood Boulevard
Downey, California 90241

Mr. Robert Epple, D192-400
Mr. J. R. Eyman, BB77
Mr. E. J. Dazzo, BB57

Mr. George Townsend
North American Rockwell
Suite 143
3322 South Memorial Parkway, S. W.
Huntsville, Alabama 35801

TRW Systems Group
One Space Park
Redondo Beach, California 90278

Mr. H. F. Meissinger, R5/2291
Mr. Robert A. Park, R5/2291

Mr. Brian T. Howard
Director, Space Sciences and
Advanced Manned Missions Division
Bellcomm, Inc.
955 L'Enfant Plaza No. S.W.
Washington, D. C. 20024

Mr. Alan L. Friedlander
IIT Research Institute
10 West 35 Street
Chicago, Illinois 60616

Mr. B. Gentry Lee
Viking Projects Mission Analysis
SSB 8947
Martin Marietta Corp.
P. O. Box 179
Denver, Colorado 80201

Mr. B. Galman
Re-Entry and Environmental Systems Div.
General Electric Co.
3198 Chestnut Street
Philadelphia, Pennsylvania 19101

Mr. D. D. Fields
AVCO Systems Division
201 Lowell Street
Wilmington, Massachusetts 01887